Supplement to NCHRP Report 316

LABORATORY EVALUATION OF PILES INSTALLED WITH VIBRATORY DRIVERS

Appendices B-Q

FINAL REPORT

Volume 2 of 2

Prepared for

National Cooperative Highway Research Program
Transportation Research Board
National Research Council

M. W. O'Neill and C. Vipulanandan

University of Houston
Houston, Texas
NCHRP Project 24-3

December, 1988

Supplement to NCHRP Report 316

LABORATORY EVALUATION OF PILES INSTALLED WITH VIBRATORY DRIVERS

Appendices B-Q

FINAL REPORT

Volume 2 of 2

Prepared for

National Cooperative Highway Research Program
Transportation Research Board
National Research Council

M. W. O'Neill and C. Vipulanandan

University of Houston
Houston, Texas
NCHRP Project 24-3

December, 1988

TABLE OF CONTENTS

LIST OF FIGURES

LIST OF TABLES

APPENDIX B

Summary of Tests

This appendix provides a synoptic description of the pile tests that were conducted during the study. Three general types of tests were conducted according to the method of installation (vibratory installation without restriking the pile ("Vibratory"), vibratory installation with restrike of the pile with the impact hammer approximately one hour after vibration, with the distance of restrike equal to one-half of a pile diameter ("Vibratory w/ Restrike"), and driving of the pile to full penetration with the impact hammer without restriking the pile ("Impact"). There were also two categories of tests according to the purpose of the test: "parameter" tests to investigate the effects of vibrator frequency, eccentric moment and bias mass on the rate of penetration of the pile into saturated sands of varying properties (density, confining pressure, d_{10}), and "capacity" tests, in which the vibrator characteristics were taken to be the optimum operating characteristics from the "parameter" tests and were not varied during a test (except for initial "spudding in" of the pile, which was always executed without the use of bias mass. The test identification numbers, test types and conditions that were employed for each of the tests are outlined in Table B.1.

One definition requires further explanation. The term "bias mass" refers to the additional weight that was applied to the vibrator above the isolation springs (Fig. E.1.). The carriage on which these weights were placed was present in all tests, so that no test was conducted with a truly zero bias mass. The carriage weight was 380 lb. With the laboratory driver that was designed and constructed for this study, it was possible to add another 1620 lbs in increments to the carriage weight, making the maximum available total bias weight 2000 lb. Therefore, the values recorded as "bias mass" in Table B.1 were actually added bias weights.

The test numbering scheme is the numbering scheme that was established at the outset of the project. Because of structural problems at the head of the pile that evolved early in the test program from fatigue produced by a fixed connection between the vibro-driver and the head of the pile (which were later rectified) and synchronization problems with the vibro-driver motors (which were also later rectified), the chronological sequence of testing did not follow the numerical sequence, which was initially planned to be the chronological sequence. Because of the difficulties described above, some tests had to be either "rerun" (meaning the scheduled test had been completed but data appeared to be of inferior quality due to driver malfunctions) or "continued" (meaning that it had been impossible to drive the pile to its intended penetration because of either cracking of the steel at the head of the pile or lack of synchronization of the vibrator's motors).

Table B.1. Summary of Tests

Test No.	Date	Test Type	Conditions	Details (Unbal. mom./ bias mass)	Comments
1a / 1b	3/9 & 3/10 1987	Vibratory (parameter)	•SJR sand; •90% rel. den. •No bias mass •Variable chamber pressure, frequency, ecc. moment	0-44": 50 "# @10 psi 44-46": 50 "# @20 psi 46" : 100 "# @20 psi	•Did not drive @ 46 " (100 "# / 20 psi / no bias mass) •Motor sync OK •Pile head cracked •Test terminated @ 46" •Cracked head repaired
1b, Cont'd	7/10 1987	Vibratory (parameter)	•SJR sand •90% rel. den. •No bias mass •Variable frequency	0-21": 100"# @20 psi	•Hammer desynchronized •Pile head cracked •Test terminated @ 21" •Cracked head repaired/ swivel-head designed & built to eliminate bending moments due to lateral vibration of hammer in leads in chronologically future tests.
2a / 2b	9/8 1987	Vibratory (parameter)	•SJR sand •65% rel. den. •No bias mass •Variable chamber pressure, frequency	0-67": 100"# @ 10psi 67-71": 100"# @ 20 psi	•Pile could not be driven past 71" •Excellent and consistent hammer performance •See Note 5
3a	4/1 - 4/3 1987	Vibratory (parameter)	•SJR Sand •90% rel. den. •10 psi chamber press. •Variable frequency, ecc. moment, bias mass	0-13": 50"# @10 psi (0 bias mass) 13-44": 100"# @10 psi (0 bias mass) 44-59": 50"# @10 psi (930 lb bias mass) 59-61": 50"# @10psi (558 lb bias mass) 61-78": 100"# @10 psi (558 lb bias mass)	•Intermittent hammer synchronization problems
3a (Re-run)	9/30 1987	Vibratory (parameter)	•SJR sand •90% rel. ren. •10 psi chamber press. •Variable frequency, bias mass •50 "# ecc. moment	0-30": No bias mass 30-79": 1620 lb bias mass	•Retest under good hammer sync. conditions

Table B.1. Summary of Tests (Continued)

Test No.	Date	Test Type	Conditions	Details (Unbal. mom./ bias mass)	Comments
3b	4/28 1987	Vibratory (parameter)	•SJR sand •90% rel. den. •20 psi chamber press. •100 "# ecc. moment •558 lbs. bias mass •Variable frequency	0-37"	•Intermittent hammer synchronization •Pile did not drive beyond 37 " •Pile head cracked @ 37"; test terminated •Pile head repaired
3b, Cont'd	5/20 1987	Vibratory (parameter)	•SJR Sand •90% rel. den. •20 psi chamber press. •100 "# ecc. moment •1620 lbs. bias mass •Variable frequency	0-23"	•Motors on hammer never synchronized; Test terminated
3b, Cont'd	8/5 1987	Vibratory (parameter)	•SJR sand •90% rel. den. •20 psi chamber pres. •100 "# ecc. moment •Variable frequency, bias mass	0-28": 0 bias 28-63": 1620 lb. bias mass 63-65": 0 bias	•Would not drive w/o bias mass past 63" •Hammer occasionally desynchronized •Hammer was redesigned and rebuilt following this test
4a / 4b	9/15 1987	Vibratory (parameter)	•SJR sand •65% rel. den. •100"# ecc. moment •Variable chamber pressure, frequency, bias mass	8-44": 0 bias @10 psi 44-70": 1620 lb. bias @20 psi 70-74": 1620 lb. bias @15 psi	•Excellent hammer performance •Pile did not drive past 70" at 20 psi •Pressure was reduced to 15 psi to permit further driving and to assess effect of soil pressure reduction. See Note 6
5	10/8 1987	Vibratory (capacity)	•SJR sand •90% rel. den. •100"# ecc. moment •10 psi cham. pressure •1620 lb bias mass •20 Hz const. frequency	0-25": 0 bias mass 25-77": 1620 lb. bias mass	•No apparent problems •Compression and uplift tests conducted

Table B.1. Summary of Tests (Continued)

Test No.	Date	Test Type	Conditions	Details (Unbal. mom./ bias mass)	Comments
6	10/16 1987	Vibratory w/ Restrike (capacity)	•SJR sand •90% rel. den. •100"# ecc. moment •10 psi cham. pressure •1620 lb bias mass •20 Hz const. frequency •20" hammer stroke	0-26": 0 bias mass 26-75": 1620 lb. bias mass 75-77": restrike	•No apparent problems, although exceptionally high load transfer observed near pile entry port •Compression and uplift tests conducted •Videotape made of this complete test cycle
7	9/23 1987	Vibratory w/ Restrike (capacity)	•SJR sand •65% rel. den. •10 psi cham. pressure •100 "# ecc. moment •1620 lb. bias mass •20 Hz const. frequency •20" hammer stroke	0-20": 0 bias mass 20-75": 1620 lb. bias mass 75-78": restrike	•Compression and uplift tests conducted •No apparent problems
8	10/23 1987	Vibratory w/Restrike (capacity)	•SJR sand •K_o = 0.5 •90% rel. den. •20 psi vert./ 10 psi lateral cham. pressure •100"# ecc. moment •1620 lb. bias mass •20 Hz const. frequency •20" hammer stroke	0-25": 0 bias mass 25-75": 1620 lb. bias mass 75-77": restrike	•No apparent problems •Compression and uplift tests conducted
9	10/30 1987	Vibratory w/Restrike (capacity)	•SJR sand •90% rel den. •20 psi cham. pressure •100"# ecc. moment •1620 lb. bias mass •20 Hz const. frequency •20" hammer stroke	0-25": 0 bias mass 25-55": 1620 lb. bias mass 55-57": restrike	•No apparent problems •Refusal achieved by vibration at 55" •Compression and uplift tests conducted •Full-penetration load-movement curves synthesized from measured unit load transfer curves

Table B.1. Summary of Tests (Continued)

Test No.	Date	Test Type	Conditions	Details (Unbal. mom./ bias mass)	Comments
10a/ 12a	11/20 1987	Vibratory (parameter)	•BLS sand •90% Rel. Den. •10 psi cham. pressure •100"# ecc. moment •Variable bias mass •Variable frequency	0-40": 0 bias mass 40-69": 1620 lb. bias mass 69-78": 0 bias mass	•No apparent problems
10b/ 12b	11/25 1987	Vibratory (parameter)	•BLS sand •90% rel. den. •20 psi cham. pressure •100"# ecc. moment •Variable bias mass •Variable freqency	0-13": 0 bias mass 13-33": 0 bias mass 33-74": 1620 lb. bias mass	•No apparent problems •Refusal reached at 33" w/o bias mass and at 74" w/ bias mass
11a/ 13a	12/9 1987	Vibratory (capacity)	•BLS sand •65% rel. den. •10 psi cham. pressure •100"# ecc. moment •1620 lb bias mass •20 Hz frequency	0-25": 0 bias mass 25-77": 1620 lb. bias mass	•No apparent problems •Compression and uplift tests conducted •*This load test was a substitute for a parametric test that was originally planned but later judged to be unnecessary.*
11b/ 13b	12/3 1987	Vibratory (parameter)	•BLS sand •65% rel. den. •20 psi cham. pressure •100"# ecc. moment •Variable bias mass •Variable frequency	0-41": 0 bias mass 41-78": 1620 lb. bias mass	•No apparent problems •Bias mass clearly increased penetration rate
14	12/19 1987	Vibratory (capacity)	•BLS sand •90% rel. den. •10 psi cham. pressure •100"# ecc. moment •1620 lb. bias mass •20 Hz const. frequency	0-25": 0 bias mass 25-77": 1620 lb. bias mass	•No apparent problems •Compression and uplift tests conducted

Table B.1. Summary of Tests (Continued)

Test No.	Date	Test Type	Conditions	Details (Unbal. mom./ bias mass)	Comments
15	12/29 1987	Vibratory w/Restrike (capacity)	•BLS sand •90% rel. den. •10 psi cham. pressure •100"# ecc. moment •1620 lb. bias mass •20 Hz const. frequency •20" hammer stroke	0-25": 0 bias mass 25-75.5": 1620 lb. bias mass 75.5-77.5": restrike	•No apparent problems •Compression and uplift tests conducted
16	1/12 1988	Vibratory w/Restrike (capacity)	•BLS sand •65% rel. den. •10 psi cham. pressure •100"# ecc. moment •1620 lb. bias mass •20 Hz const. frequency •20" hammer stroke	0-27": 0 bias mass 27-77": 1620 lb. bias mass 77-79": restrike	•Pile drove very fast and coasted 3" after pump stopped •No apparent problems •Compression and uplift tests conducted
17	12/23 1987	Vibratory w/Restrike (capacity)	•BLS sand •90% rel. den. •20 psi cham. pressure •100"# ecc. moment •1620 lb. bias mass •20 Hz const. frequency •20" hammer stroke	0-20": 0 bias mass 20-75": 1620 lb. bias mass 75-77": restrike	•No apparent problems •Refusal achieved at penetration of 75" with vibratory driver •Compression and uplift tests conducted
18	6/2 - 6/3 1987	Impact (capacity)	•SJR Sand •90% rel. den. •10 psi cham. pressure •20" hammer stroke	0-79": driven	•Compression and uplift tests conducted •No reliable data for top strain gages and toe load cell during driving (otherwise, data OK)
19	8/25 1987	Impact (capacity)	•BLS sand •90% rel. den. •10 psi cham. pressure •20" hammer stroke	0-78.5": driven	•Compression and uplift tests conducted •No obviously bad data

Table B.1. Summary of Tests

Test No.	Date	Test Type	Conditions	Details (Unbal. mom./ bias mass)	Comments
20	6/19 1987	Impact (capacity)	•SJR sand •65% rel. den. •10 psi cham. pressure •20" hammer stroke	0-79": driven	•Compression and uplift tests conducted •No obviously bad data
21	6/11 1987	Impact (capacity)	•SJR sand •90% rel. den. •20 psi cham. pressure •20" hammer stroke	0-79": driven	•Compression and uplift tests conducted •No obviously bad data
22	7/1 1987	Impact (capacity)	•SJR sand •90% rel. den. •20 psi vert. cham. press. •10 psi lateral cham. press. •20" hammer stroke	0-79": driven	•Compression and uplift tests conducted •No obviously bad data

Notes: 1. "parameter" refers to a test in which the soil or driving parameters were varied in order to define optimum frequencies and bias mass.

2. "capacity" refers to a test in which the static capacity and load transfer characteristics were measured in addition to vibratory or impact response during insertion.

3. "SJR sand" is San Jacinto River (fine) sand.

4. "BLS sand" is commercial blasting (coarse) sand.

5. Pile was driven from 67 to 71 inches in 29 seconds, reducing from 0.2 ips at 67-inch penetration to 0.1 ips at 71-inch penetration. Driving was stopped for approximately 20 minutes, and an attempt was made to drive the pile further. No further penetration could be achieved.

6. After stopping driving at penetration of 70 inches for 10 minutes, an attempt was made to penetrate the pile further by sweeping through the same frequencies as were employed to penetrate the pile to 70 inches. No further movement could be generated with this procedure, so the chamber pressure was reduced to 15 psi, and penetration was successfully reinitiated.

7. In the impact tests the driving rate was approximately 23 blows per minute.

8. In the restrike events the driving rate was approximately 2 blows per minute.

APPENDIX C

Description of Test Chamber

This appendix describes the test chamber that was used to conduct all of the tests described in this report. The test chamber is termed a "long variable lateral pressure sand column," or LVLPSC. A conceptual schematic of a test arrangement is shown in Fig. C.1. The sand column into which the pile was inserted was 30.0 inches in diameter by 100.0 inches high. The boundaries of the sand column consisted of waffle-type, neoprene energy absorbers (2.0 inches thick) at the base of the column, which made the base semi-rigid, and rubber air pressure membranes at the top and lateral boundaries, which made those boundaries flexible (constant, controlled pressure boundaries). There existed an impermeable rubber membrane between the sand column and the base and lateral air membranes to provide watertightness to the sand column and permit the sand column to be saturated. The pressure membrane at the top of the LVLPSC was affixed to the underside of a steel plate that formed the top of the chamber. The top membrane was flat,with three holes passing through it: One for the pile port and two drainage ports for passage of water that was expelled from the chamber during insertion of the pile. The pore water pressures in the LVLPSC were always, therefore, hydrostatic, with the position of the head at the top of the chamber. There were eight lateral pressure membranes, each 12.5 inches high, of toroidal shape, and 33 inches in outside diameter.

The choice of the diameter of the pile and chamber represented a compromise between minimizing scale effects between maximum sand particle size (which was 2 mm in the case of the coarse sand) and pile size , by utilizing a minimum pile diameter-to-soil particle size ratio of 50, which resulted in the choice of the 4.0-inch-diameter pile. The diameter of the sand column was set at 7.5 times the diameter of the pile, which resulted in the 30-inch sand column diameter. With this column-to-pile diameter ratio, some boundary effects may have occurred in the chamber (21), although they would have been minimized with the flexible boundary that was employed.

A more detailed cross-section of the LVLPSC is shown in Fig. C.2. The chamber consisted of four 25-in.-high steel containment cylinders bolted end to end through flanges. This design was necessitated by the need to disassemble the long, slender chamber to remove the sand between tests and to facilitate deposition of sand. The other devices described below were all contained within these cylinders.

It is observed that soil saturation was provided by pumping deaired water down a saturation line to a metal diffusion ring containing several hundred small-diameter perforations at the base of the sand column, from which level the water was forced to rise under external pressure through the pores of the sand until the chamber was saturated (as evidenced by overflow through the drainage ports at the top of the chamber). A three to four hour saturation period was employed. Eight slotted vertical tubes were place at equal intervals around the perimeter of the sand column, inside the waterproof membrane (impermeable liner), to collect water that was flowing away from the penetrating pile, so as to produce radial drainage during pile insertion (and load testing).

The pressure in each of the eight lateral pressure membranes was controlled independently in order to produce a known , uniform lateral effective pressure in the sand at the lateral boundary of the sand column. This was accomplished by balancing the

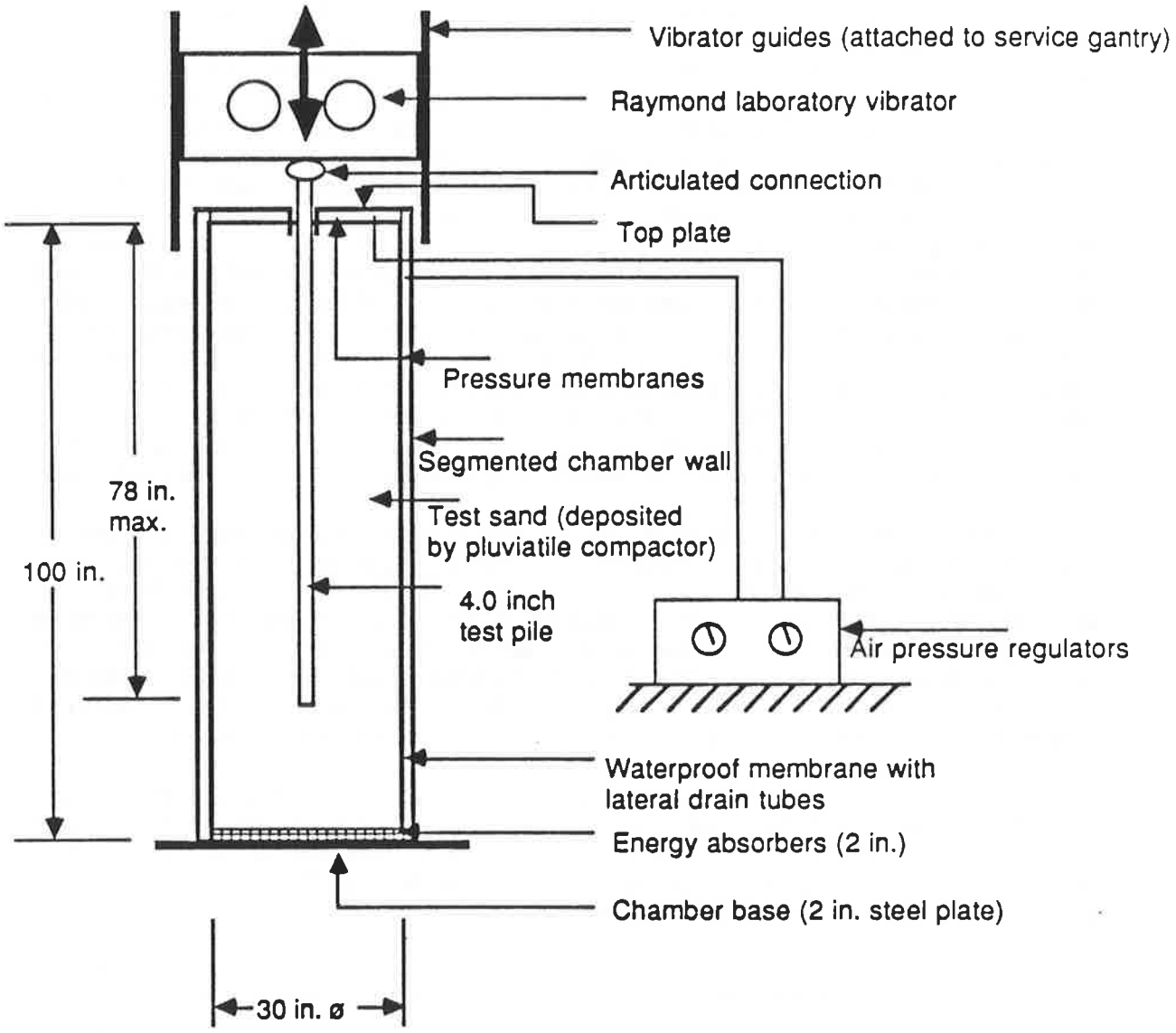

Fig. C.1. General Schematic of LVLPSC with Pile and Vibro-Driver

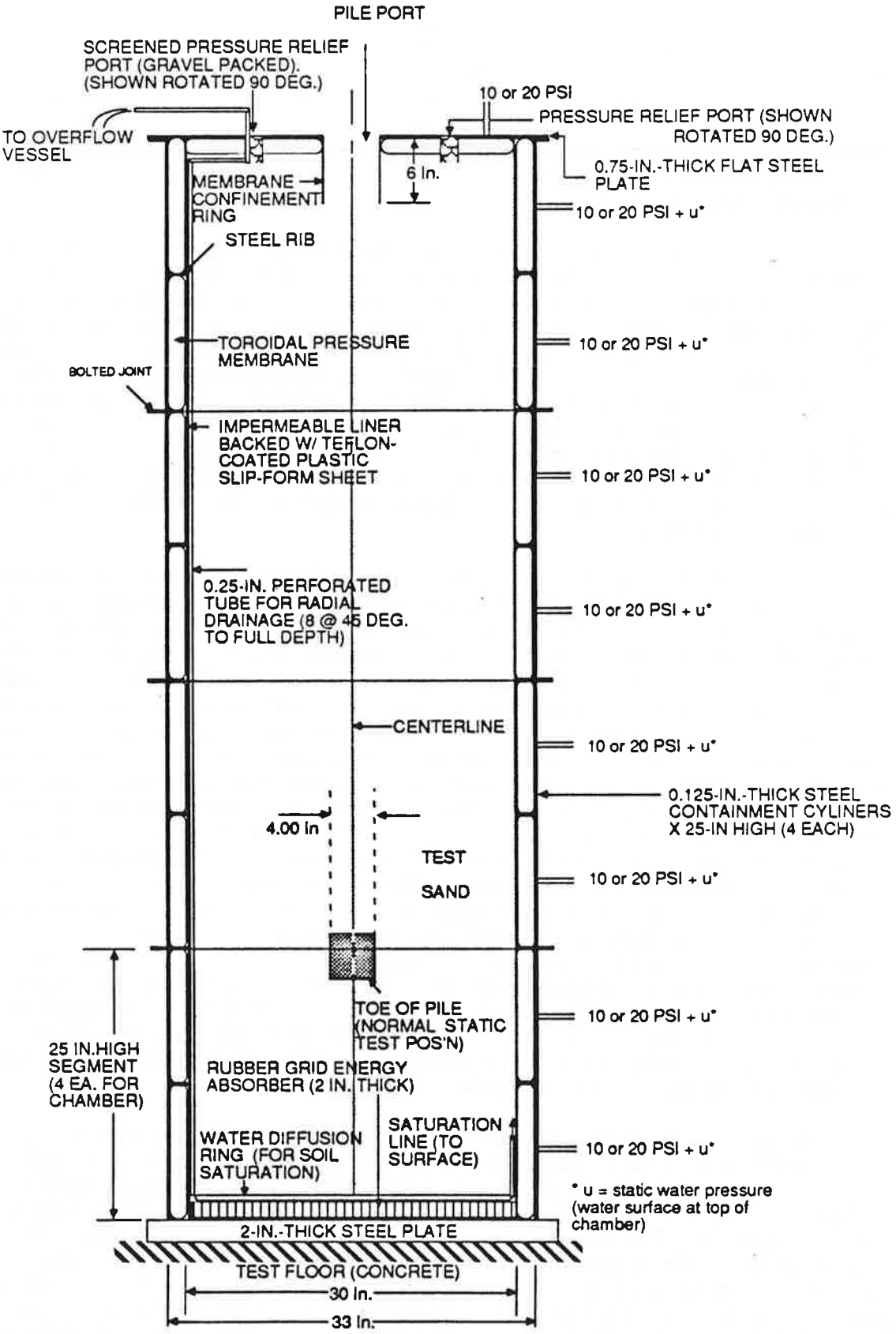

Fig. C.2. Detailed Schematic of LVLPSC, Showing Lateral and Vertical Pressure Membrane System

total lateral stress at the boundary, which increased with depth by the rate of increase in hydrostatic pore water pressure. An important detail is that the various lateral pressure membranes were all separated by steel rings, so that one membrane did not impinge upon another membrane that was pressurized to a different pressure and cause vertical distortion of the membranes. Since the pressure in the membrane situated under the top plate (which applied vertical pressure to the sand column) could also be varied independently of the lateral pressures, it was possible to vary the coefficient of lateral earth pressure in the sand column.

Further details are depicted in the schematic in Fig. C.3. The horizontal section shows that plastic sand forming jackets (lapped sections of sheet plastic) were placed inside the impermeable membrane. These jackets were supported laterally by the separation rings between the lateral pressure membranes. The purpose of the jackets was to contain the sand during placement and prohibit lateral strains that would be accompanied by changes in density of the sand. This procedure was necessitated because of the fact that during filling the lateral pressure membranes were not pressurized in order to ensure that passive conditions did not exist at any point in the sand, which would have also produced density changes. Once the chamber was filled, it was pressurized in steps so as to minimize the differential pressure between adjacent membranes, up to the desired values of total pressures. Soil deposition and density control procedures are described in Appendix J.

During filling, the forming jackets supported outward-driected radial normal stresses from the sand (assumed approximately equal to at-rest effective stresses). Once the chamber was filled and lateral stresses from the bladders were applied, the lateral body stresses were transferred to the air bladders, since the forming jackets were not capable of supporting compressive hoop stresses. Therefore the total lateral stresses in the sand at the boundary of the chamber were equal to the pressures in the bladders as measured by the pressure gages in the pressure manifold, shown schematically in Fig. C.3. These values of pressure remained constant throughout the remainder of a test. Because the bladder pressure was calculated to be equal to the desired lateral effective pressure plus the hydrostatic pore water pressure produced by a free water surface at the top of the sand column, the lateral effective stresses remained constant in the sand column at the boundary throughout a test, except possibly for brief periods of transient pore water pressure. The vertical effective stress at any point in the sand column was theoretically equal to the vertical stress applied by the top membrane plus the body stress produced by the buoyant soil within the column. However, in the analysis of data it was assumed that the vertical effective stress anywhere in the chamber is equal to the pressure in the top membrane, because the top membrane pressure is not applied at all points across the top of the sand column (absent at pile port and drains), so that the effect of the pressure voids on the top boundary approximately balances the slight increase with depth in the chamber in vertical effective pressure due to the body weight of the soil.

At the time of filling, the chamber was positioned inside the service frame, as shown in Fig. C.3. After pressurization of the membranes, the pores of the sand were flushed with carbon dioxide to displace nitrogen, which tends to form air bubbles in the soil pores. This was accomplished through the same line that was later used for soil column saturation. The soil column was then saturated by using pressure from the carbon dioxide bottle to pump water from the deaired water reservoir into the base of the LVLPSC. A separate air supply was used for the pressures in the top and lateral pressure membranes. Deaired water was produced in the deaired water reservoir by spraying tap water through a vacuum and then heating the water to 130°F prior to placing it in the chamber. This procedure was followed in order to produce as near

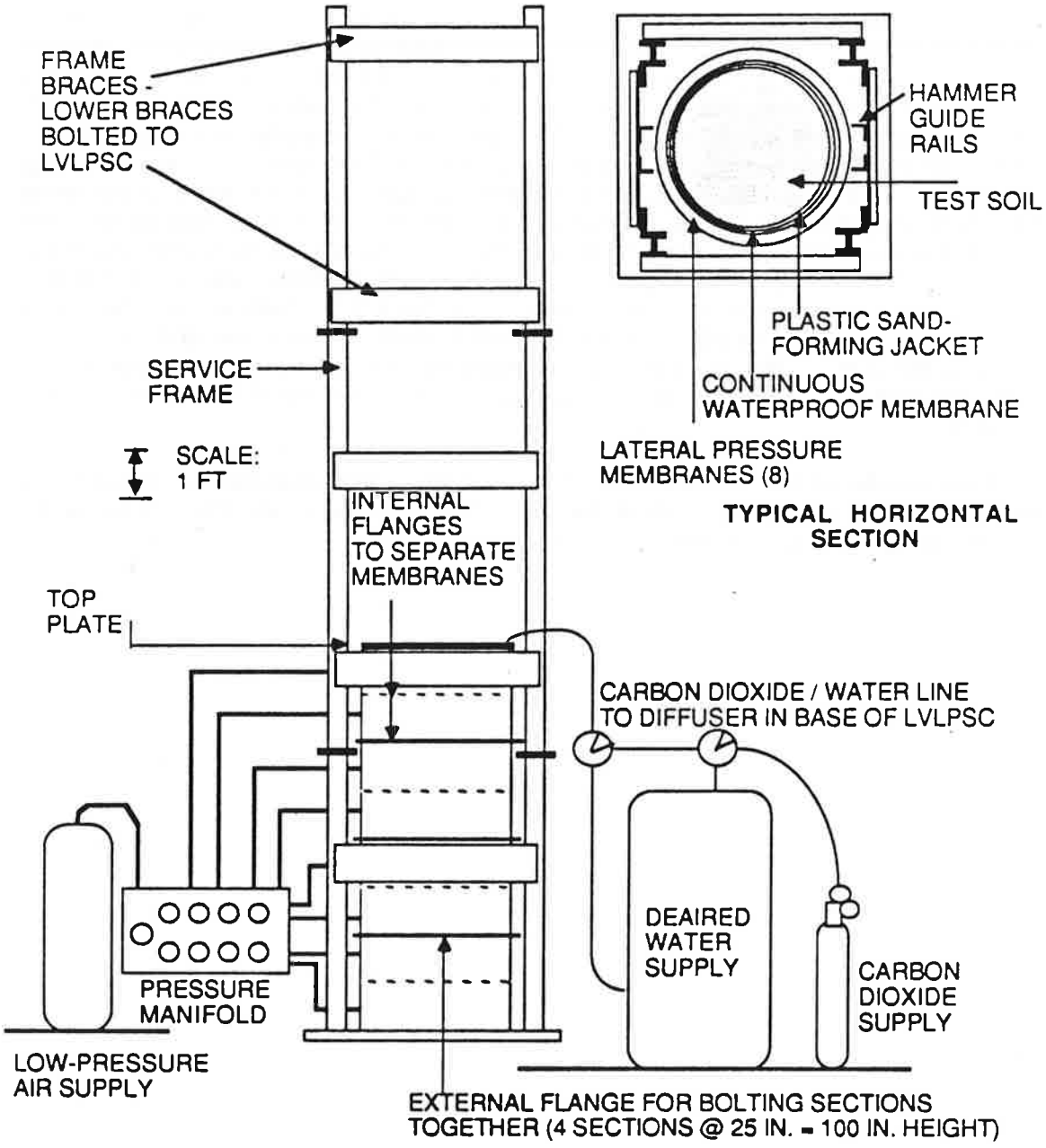

Fig. C.3. LVLPSC in Relation to Service Frame, Deaired Water Supply and Membrane Air Pressure Supply

100% saturation as possible, both in order to simulate actual in-situ conditions and to limit the compliance in the soil pores in order to facilitate high-quality pore water pressure measurements on the pile.

Figure C.4 depicts schematically the top plate and the piping for the internal lateral drainage system in the LVLPSC, which had to pass through the top plate. Header lines (hoses) connected to the vertical drains and carried the water out through the drainage ports into receptacles, where it was collected for volumetric measurement. The drainage ports were 2.0-in. ø pipes, 4.0 in. long, which protruded about 3 in. below the bottom of the top air membrane and penetrated the soil by about 3 in. initially. This "shaft" arrangement was necessary because the top surface of the sand could settle during a test, requiring the top air membrane to expand to remain in contact with the surface of the soil. The protruding shaft prevented the membrane from contacting the header lines and thereby restricting flow. A similar arrangement existed for the pile port, which was 5.0 in. in diameter to accommodate the 4.0-in.-diameter pile, leaving a 0.5-in. free space around the pile from which small amounts of water could also escape. The shaft protrusion on the pile port was provided to prevent the top membrane from engaging the pile and producing false indications of load transfer during insertion and load testing.

Photographs of the components of the LVLPSC, with appurtenant devices are shown in Fig. C.5, and a photograph of the assembled LVLPSC inside the service gantry with a test pile being placed in position is shown in Fig. C.6.

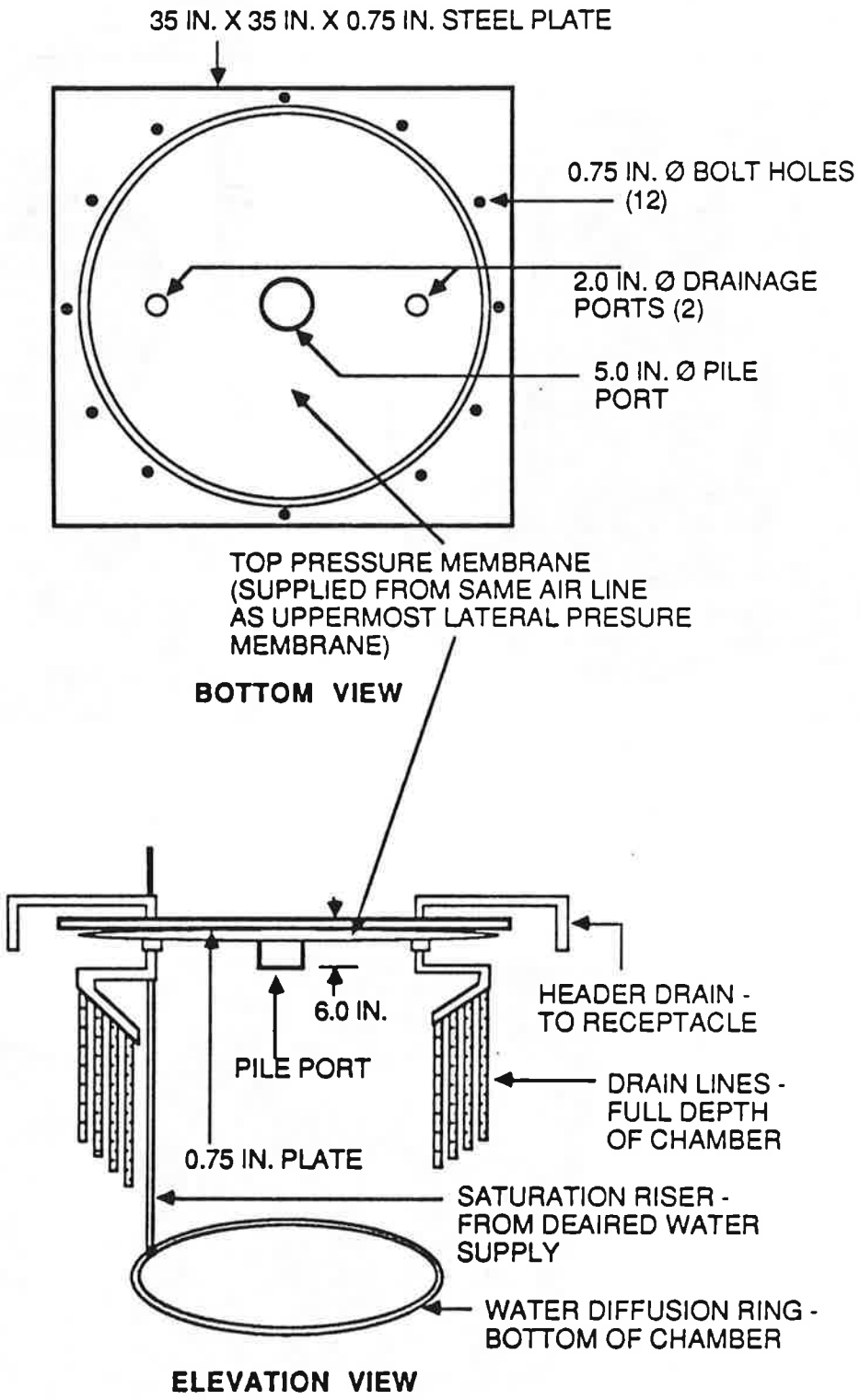

Fig. C. 4. Schematic Detail of Top Plate, Showing Pile and Drainage Ports and Drainage and Saturation Piping

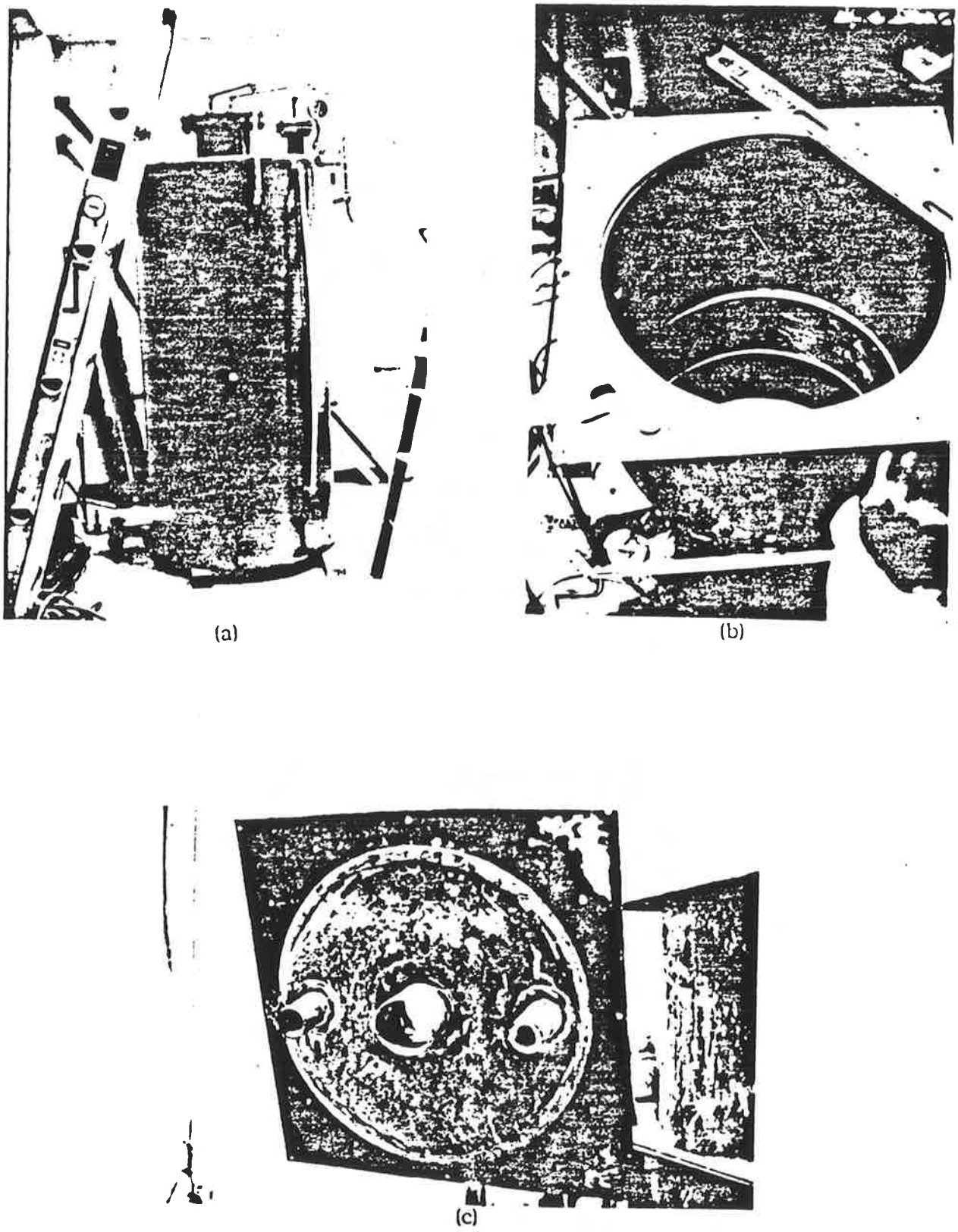

Fig. C.5. Photographs of (a) Deaired Water Tank, (b) Stacked LVLPSC Cells Showing Pressure Membranes, and (c) Top CapViewed from Below

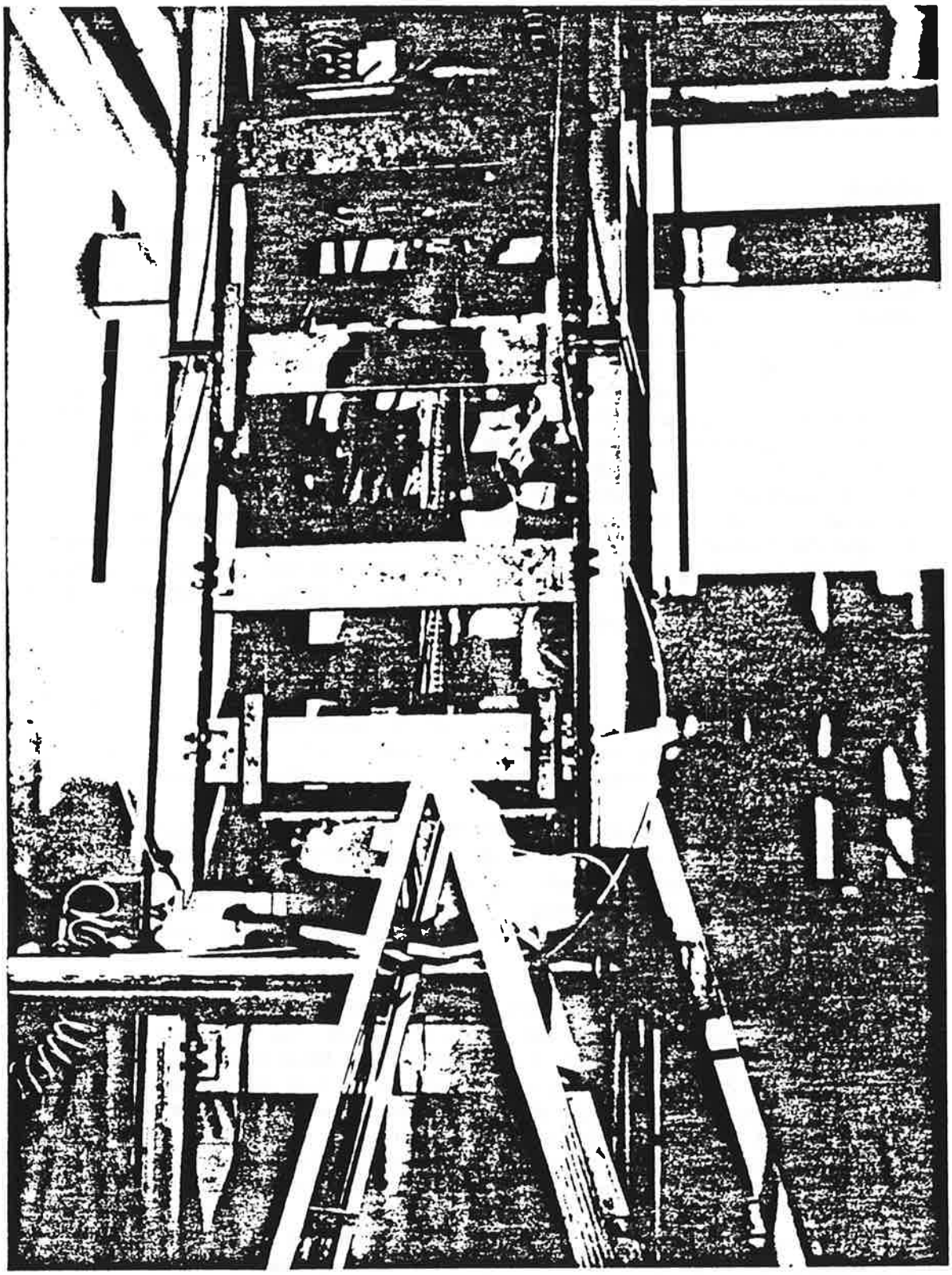

Fig. C. 6. Photograph of LVLPSC, Service Gantry and Test Pile

APPENDIX D

Description of Test Pile

General

This appendix describes the reusable test pile that was employed during the study. A longitudinal view of the pile is shown in Fig. D.1. The pile was a 4.00 in.-diameter steel tube with a 0.188-in.-thick wall. The original length of the pile was 90 inches; however, during the early parameter tests, in which full synchronization of the vibratory driver was not always achieved and in which the integral flange at the head of the pile was rigidly bolted to the base of the driver, fatigue cracks developed in the head of the pile, requiring that the top two inches of the tube be removed and the flange (which is an integral part of the pile) rewelded. The configuration shown in Fig. D.1 is the final configuration after the reduction of the pile's length, which is the configuration used in all of the capacity tests and in all parameter tests following the first attempt at Test 3b (4/28/87). To mitigate the possibility of future problems with fatigue of the pile head, vertical reinforcing strips were welded to the top of the pile as shown in Fig. D.1, and the method of coupling the pile to the driver was changed by the introduction of an articulated coupling between the pile head and the driver. The pile experienced no structural problems after that modification (which coincided with the solution of hammer synchronization problems).

Instrumentation

The pile contained considerable instrumentation, as described in this section. Except for the accelerometers, the instrumentation was placed permanently on the pile prior to the first trial test and remained on the pile throughout the study.

Pile-Wall Strain Gages. Seven levels of strain gages were placed in the pile wall, as shown schematically in Fig. D.1. Each level was a full-bridge circuit. The levels are denoted by the numerals "1-7," and the level marked "1" served as a force transducer during vibration and impact driving. The remaining six levels were read during the static load tests to develop load transfer curves but were not read during either vibro or impact driving.

At each gage level a linear strain gage was epoxy-bonded to the pile wall in each of two slots machined into the external side of the pile wall, situated 180° apart on the perimeter of the pile. A detail of a slot , which was filled with epoxy, and its gage is shown in Fig. D.2. Slot-mounting left the face of the pile geometrically unaltered from its uninstrumented state, which the investigators perceived to be important in the interpretation of the data from the tests. The two gages were wired as active gages in a Wheatstone bridge, as shown in Fig. D.3, permitting the cancellation of any bending stresses that might have been inadvertently applied to the pile and simultaneously doubling the sensitivity of the circuit to axial stresses. The dummies for this bridge were precision resistors placed directly on the external face of the test chamber so as to avoid differences in temperature with that of the active gages on the pile. Lead wires for the active gages were carried through the inside of the pile to a connection strip mated to the inside surface of the pile near the pile head, from which the leads were gathered and

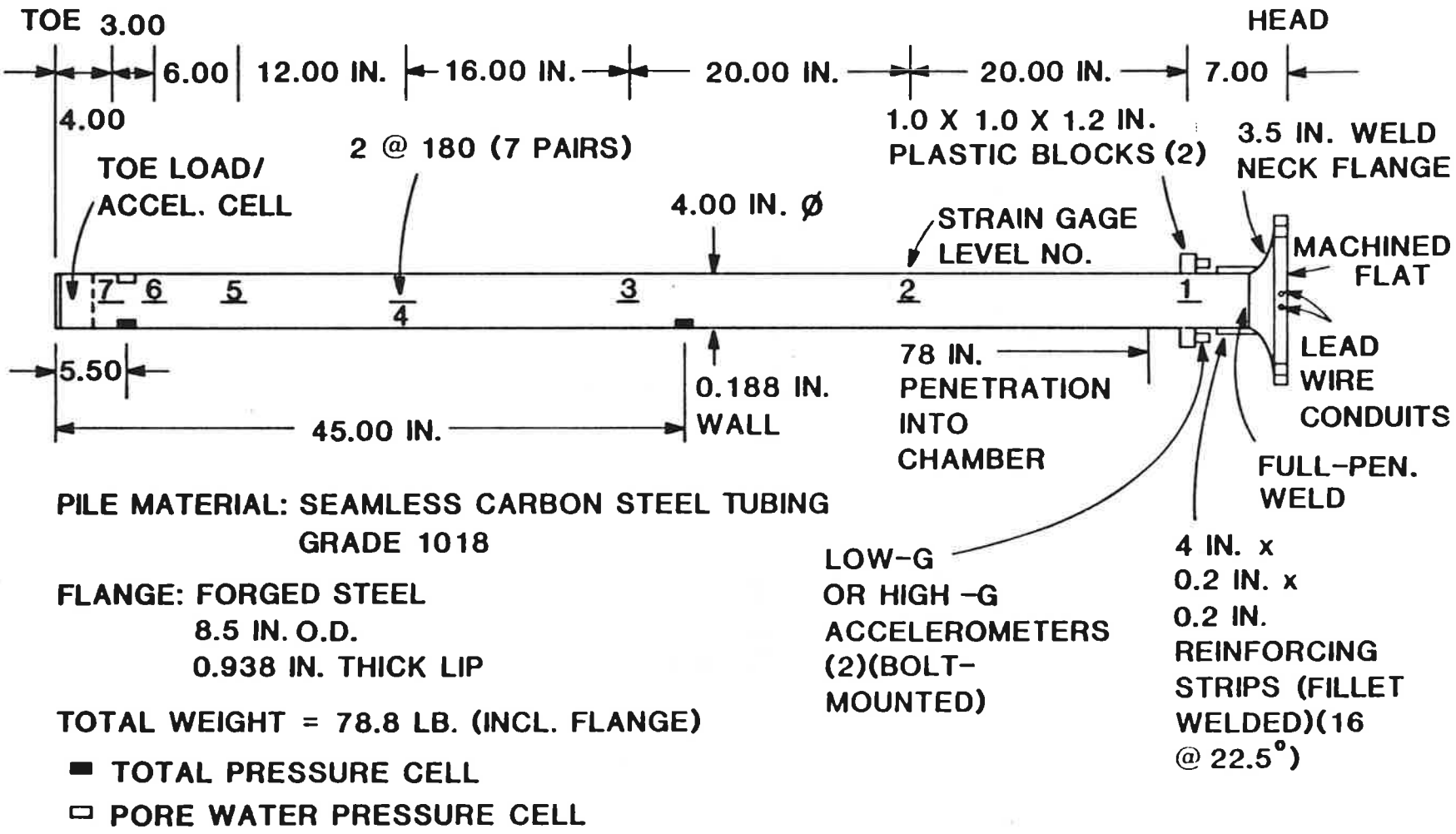

Fig. D.1. Schematic Longitudinal View of Reusable Test Pile

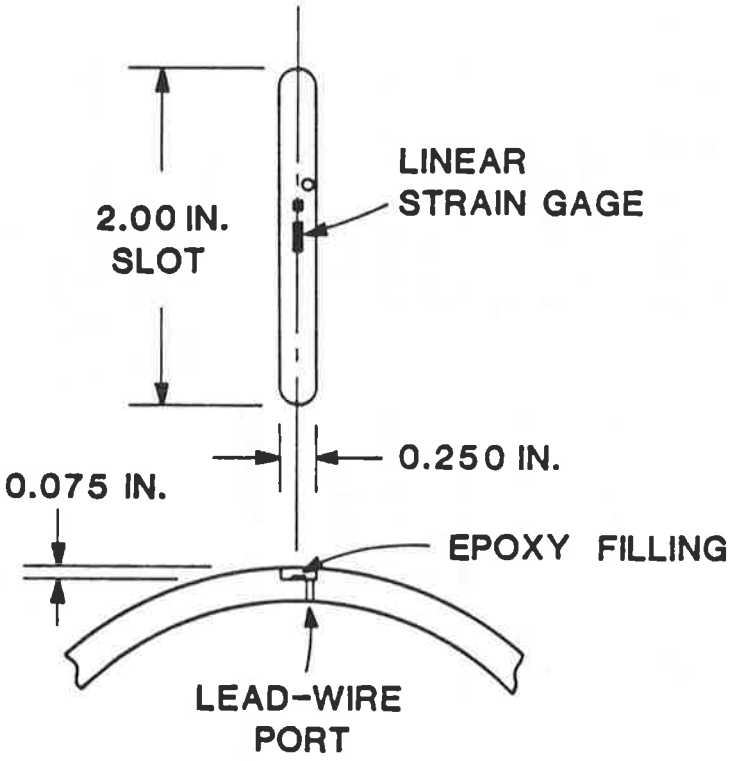

Fig. D.2. Pile-Wall Strain Gage Detail

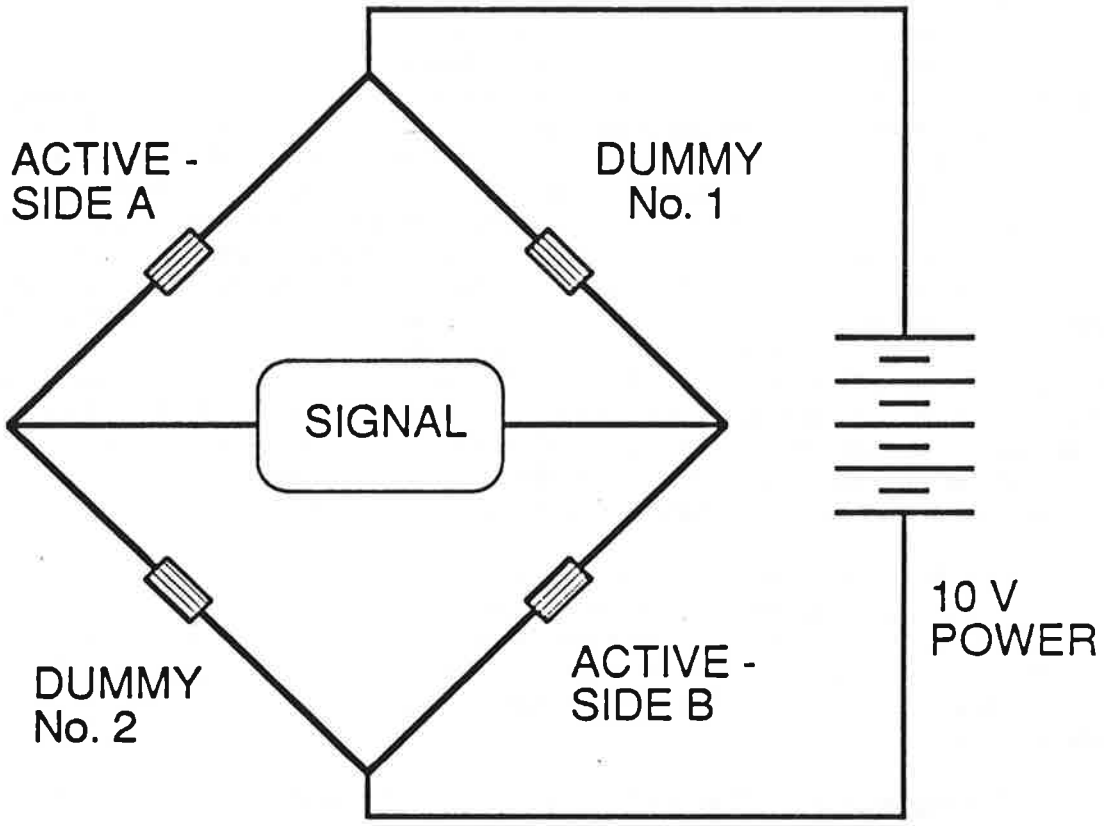

Gage Specifications:

Type: Micromeasurements CEA06062UW-350
Length: 0.22 in (overall); 0.12 in (sensing face)
Width: 0.12 in (overall); 0.065 in (sensing face)
Resistance: 350 ohms (within 0.3%)
Epoxy: AE 10-15

Fig. D.3. Pile-Wall Strain Gage Bridge Circuit Diagram

soldered into a plug that could be connected with a mating plug from the data acquisition system. The bridge circuits were completed outside the pile.

Total Pressure Cells. Two miniature total pressure cells were constructed and embedded in the wall of the test pile, with their sensing faces normal to the wall, as shown in Fig. D.1. The primary purpose of these cells was to measure lateral stresses against the side of the pile near the toe and near the mid-depth during the static load tests, when the pore water pressures could be closely approximated as hydrostatic, thus providing also a measure of the effective normal stresses on the pile shaft during static loading. The bottommost of these cells was also read during installation, both impact and vibratory, to obtain an indication of the time-dependent total lateral stresses against the side of the pile during the installation processes, and together with the pore water pressure cell situated near the pile toe, a measure of effective stress during installation. A detail of a total pressure cell is shown in Fig. D.4. The cell operated on a membrane principal, in which the membrane was a 0.600-in.-diameter by 0.008-in.-thick steel plate that was integrally tied to a rigid ring at its boundary. The membrane was instrumented with a single linear strain gage oriented so that its primary sensing direction was perpendicular to the direction of propagation of the stress wave in the pile. This procedure was successful in isolating the cell from the low-magnitude stress waves produced by vibratory driving, but some effect of the passage of stress waves produced by impact driving was registered by the cells. Therefore, the data from impact driving for the bottom-level total pressure cell were not analyzed extensively.

The total pressure cells were also read as full-bridges, with precision resistors mounted as described for the pile wall strain gages used in the adjacent arms and opposite arm of the bridge to complete the circuit. Lead wires were carried up the interior of the pile to the connection strip, as described for the pile-wall strain gages, and the exit lead s were bundled into the same plug that was used to accommodate the pile-wall strain gages.

The d_{50} size of the San Jacinto River test sand was approximately 0.4 mm, giving a sensitive-membrane-diameter-to-soil-grain-diameter ratio of about 38. Correspondingly, the d_{50} size of the Blasting test sand was approximately 1.15 mm, giving a ratio of about 13. These ratios affect, to some extent, the quality of the data, with the better-quality data expected for the larger ratio.

Pore Water Pressure Cell. A pore water pressure cell was mounted with its face normal to the wall of the test pile at the level of the lower total pressure cell, as shown in Fig. D.1.. The primary purpose of this cell was to confirm that the pore water pressure against the pile was hydrostatic during load testing. It was also read during vibratory driving to gain information on the variation of pore water pressures during installation and the role of pore water pressure development on dynamic soil resistance. A detail of this cell is shown in Fig. D.5. Its design and operation were identical to the design and operation of the total pressure cells except that the sensing face (membrane) was located below a small free-water saturation chamber that communicated with the pore of the soil through two finely perforated plastic disks separated by a segment of coarse filter fabric. The cell was saturated by passing deaired water under pressure through a tubular saturation line into the free-water chamber, which was vented to the atmosphere though the perforated disks. Flow of water though the disk openings indicted saturation of the cell, after which the saturation line was plugged. No desaturation of the cell was observed during trial vibration, the condition for which it was designed. It was not possible to observe whether desaturation occurred during impact driving; however,

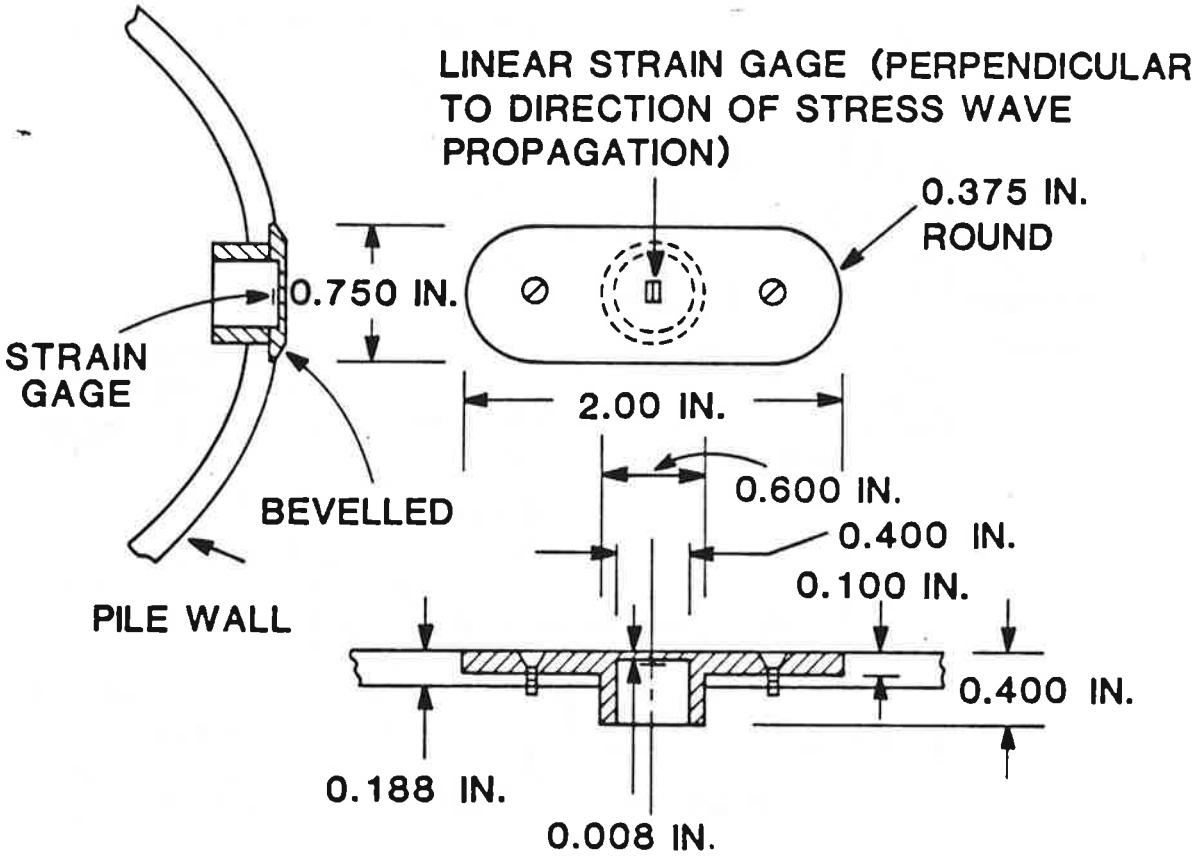

Fig. D.4. Total Pressure Cell Detail

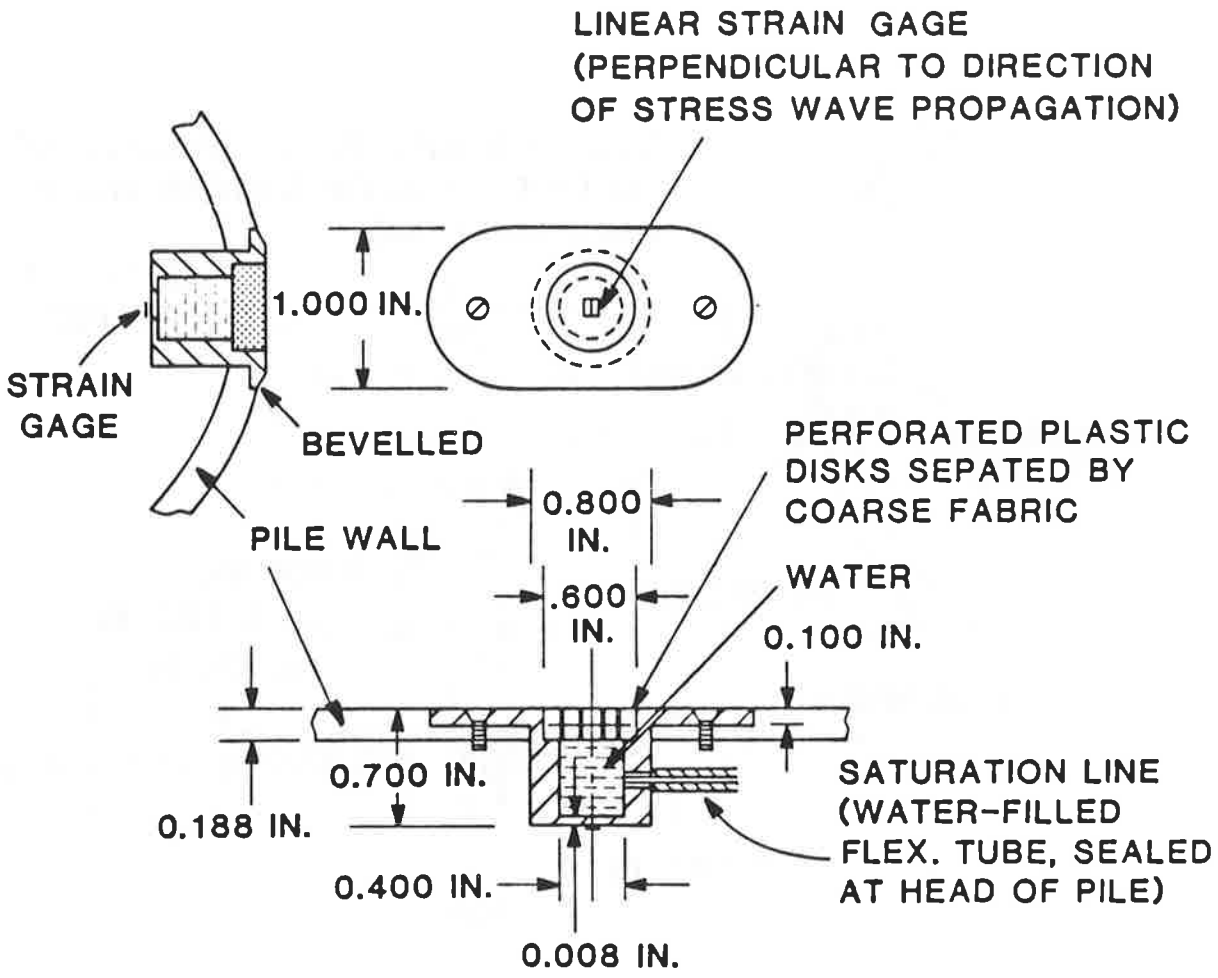

Fig. D.5. Pore Water Pressure Cell Detail

the pile was placed into the chamber in such a manner that the pore water pressure cell was submerged before driving commenced, such that desaturation was unlikely.

Toe Load /Acceleration Cell. A load cell was designed and constructed to permit direct measurement of the load at the toe of the pile. The decision to use this load cell had a major impact on the test program, because its use forced the closure of the pile to and precluded the testing of non-displacement piles. However, the fundamental information gained from its use (such as measurement of dynamic load transfer curves) was considered sufficient justification to warrant testing of closed-toed piles. The toe load cell was attached to the end of the test pile through a threaded connection. A detail of this cell is shown in Fig. D.6. Load was measured using the electronic resistance strain gage principle, with eight gages bonded with epoxy to a machined section of the cell wired in a full-bridge configuration. Four of the gages were mounted vertically and served as active gages; four were mounted horizontally and acted as temperature compensation gages. The Wheatstone bridge schematic, which required no external dummy resistors, is shown in Fig. D.7. Wire management and connection schemes were similar to those for the pile-wall strain gages.

Mounted on the top of the toe load cell, inside the pile, were two accelerometers. One was a low-g accelerometer (range, 0-50 g) for use in the vibratory tests, and one was a high-g accelerometer (range, 0-2500 g) for use in the impact tests or during restrike events after installation by the vibro-driver. The low-g accelerometer was protected to 2000 g and so was not damaged during impact events. Further details regarding these and other accelerometers used on the test pile are given in Table D.1. The purposes of the accelerometers were to provide a means of measuring power and energy at the toe of the pile, and velocity and displacement of the toe of the pile during dynamic events. Energy and power evaluation required simultaneous evaluation of the force and acceleration time histories at the toe. This information was useful in calibrating wave equation models, as explained in Appendix O, and in evaluating energy and power transmission through the pile to the pile toe in various soil conditions.

The complex geometry of the toe load cell cast some doubt on whether the accelerations measured by the accelerometers mounted atop the cell were representative of the accelerations on the pile wall. This concern prompted the calibration that is described in Appendix G.

Pile-Head Accelerometers. Pile-head accelerometers were mounted on plastic blocks, as shown in Fig. D.1, to permit measurement of acceleration at the head of the pile in order to determine energy or power being accepted at the pile head and to determine pile-head velocities. Low-g accelerometers were used during vibration tests. These accelerometers were exchanged for high-g (5000-g) accelerometers during restrike events and full-depth impact driving. Details of the accelerometers are given in Table D.1.

Photographic Views. Photographs of the test pile and the toe load/acceleration cell are provided as Figs. D.8 and D.9, respectively.

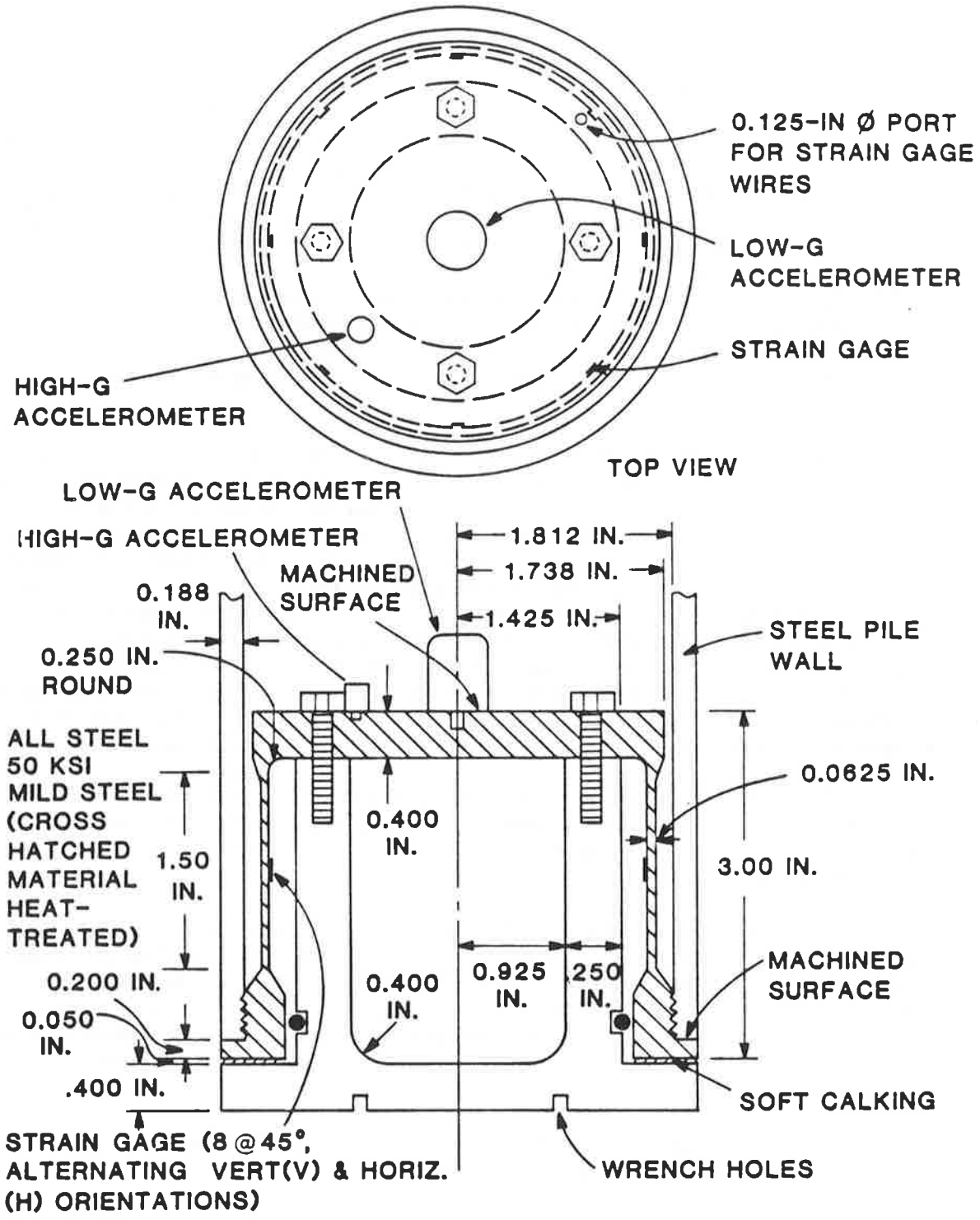

Fig. D.6. Toe Load / Accelerometer Cell Detail

Table D.1. Accelerometer Specifications

Accelerometer	Model[1]	Serial No.	Range[2] (g)	Sensitivity[3] (mv/g)
Pile Head (Pile-Wall)				
Vibratory	328M30	2028	±50	102.5
Loading	328M30	3773	±50	102.5
(Low-g)				
Impact	305A04	5305	±5000	0.965
Loading	305A04	5307	±5000	0.990
(High-g)				
Pile Toe (Cell)				
Vibratory	328M30	3709	±50	102.5
Loading				
(Low-g)				
Impact	305A05	3922	±2500	2.35
Loading				
(High-g)				

1. All accelerometers were of the piezoelectric type, manufactured by PCB Instruments, Inc.
2. 50-g instruments were protected to 2000 g, so were not damaged during restriking.
3. Sensitivity of data acquisition system was 0.01 mV, so no amplifiers other than the manufacturer's in-line signal conditioners were employed.

Note: Resonance frequency of all accelerometers exceeded 18 KHz.

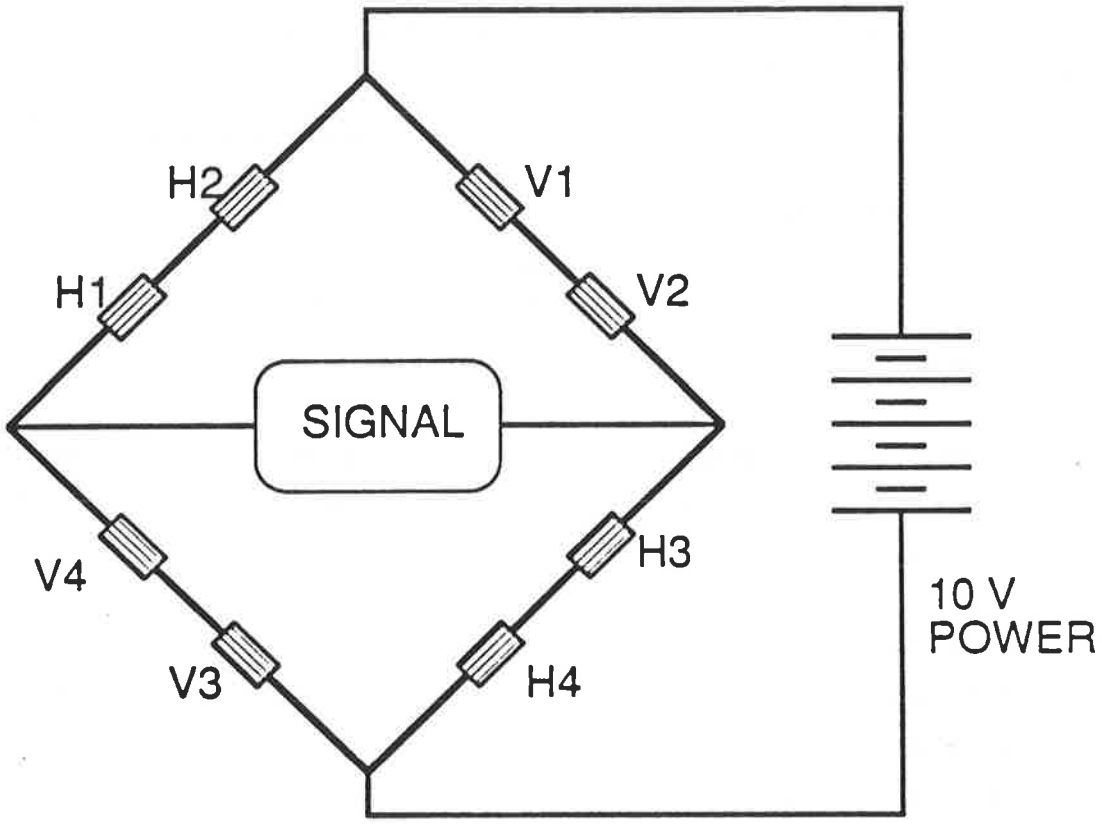

Gage Specifications:

Type: Micromeasurements CEA06062UW-350
Length: 0.22 in (overall); 0.12 in (sensing face)
Width: 0.12 in (overall); 0.065 in (sensing face)
Resistance: 350 ohms (within 0.3%)
Epoxy: AE 10-15

Fig. D.7. Toe Load Cell Bridge Circuit Diagram

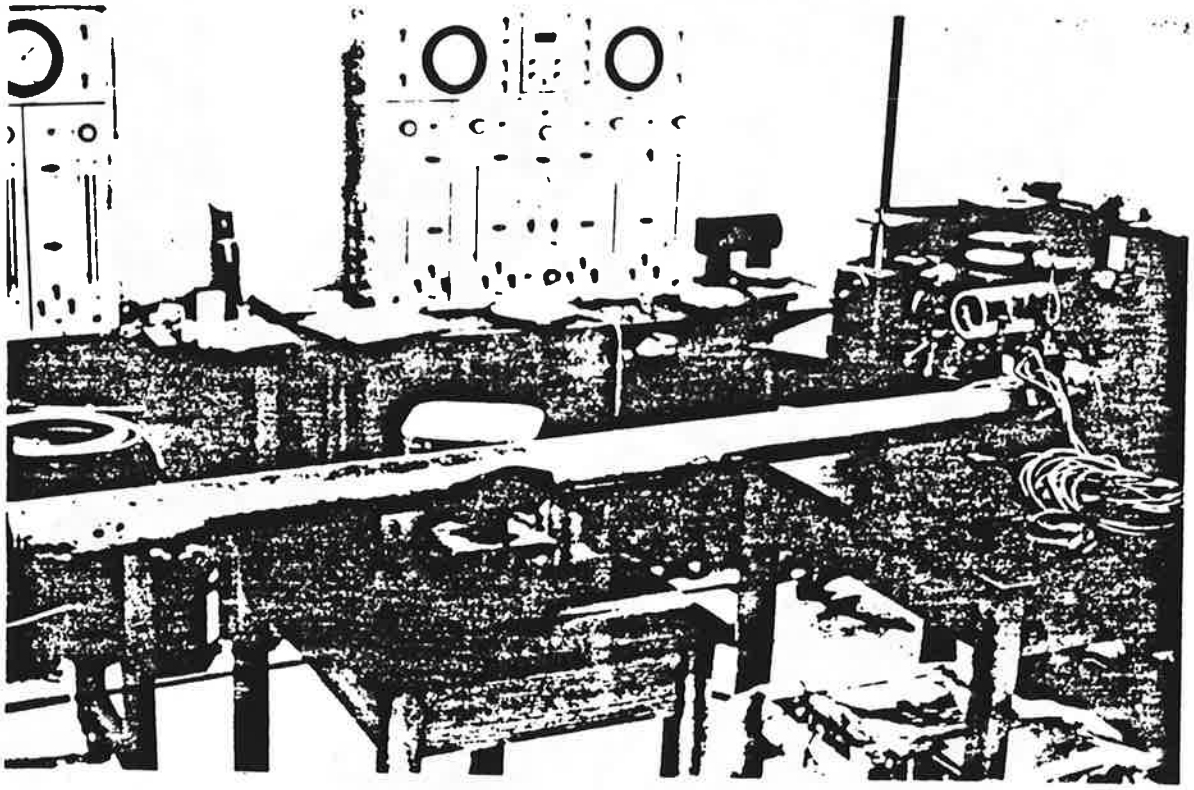

Fig. D.8. Photograph of Reusable Test Pile

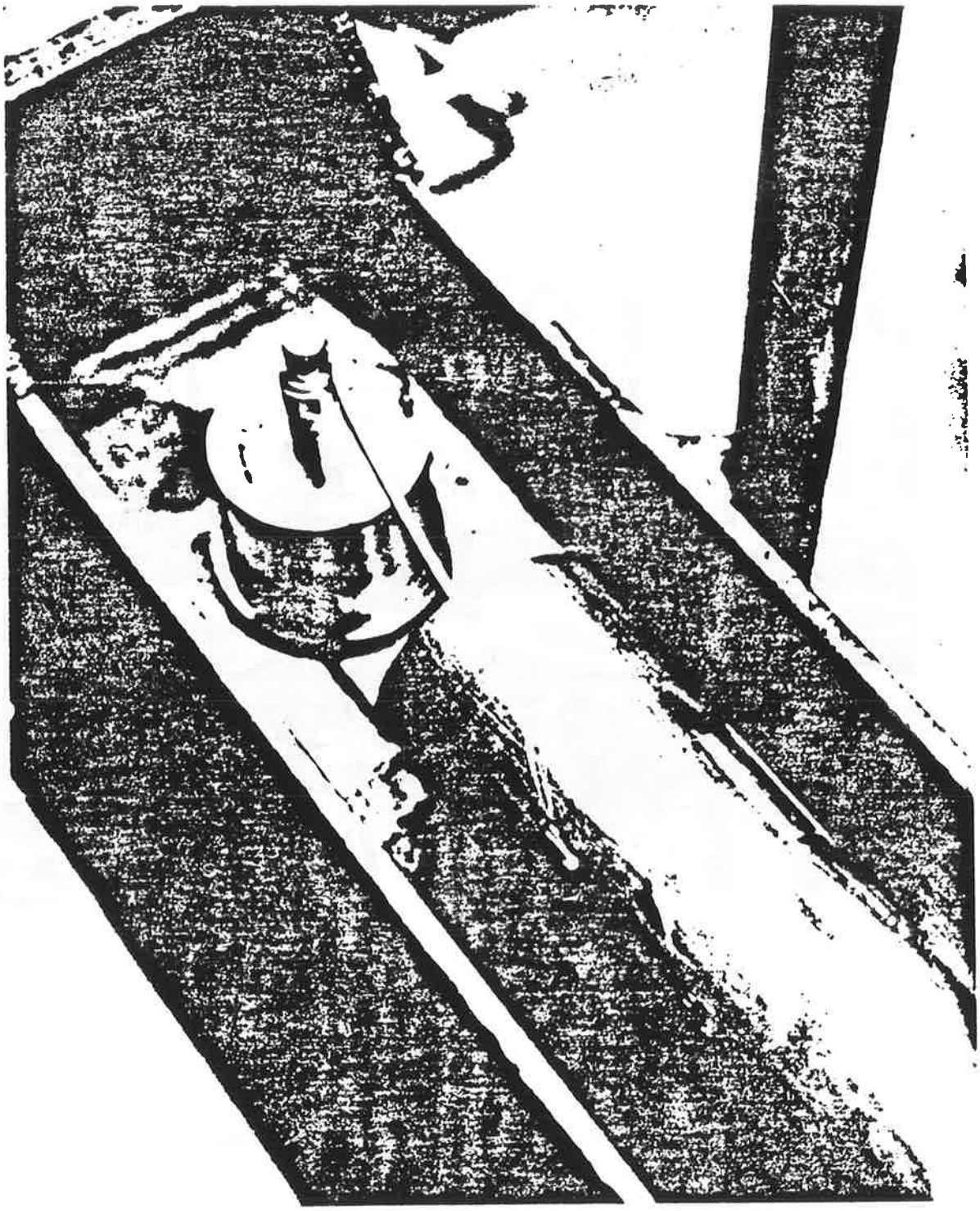

Fig. D.9. Photgraph of Toe Load / Accelerometer Cell Uncoupled from Pile

APPENDIX E

Description of Hammers

This appendix describes the two hammers that were used in the study. One hammer, the vibro-driver, was designed and constructed especially for this study. The other hammer, the impact hammer, was a device that was available in the University of Houston Geotechnical Laboratories prior to the start of the study and was used without modification.

Vibro-Driver Properties

A schematic of the laboratory vibro-driver is shown in Fig. E.1. This device, which operates on the principle of counterrotating masses that produce additive sinusoidal, vertical forces and that cancel (in theory) all horizontal forces, was designed by Raymond Technical Facilities, Inc., of Houston, Texas, and manufactured under contract by Hydradyne Hydraulics, Inc., also of Houston, Texas. The dynamic force is provided by unbalanced weights affixed to flywheels on the shafts of two self-synchronizing motors. The motors are powered by flowing hydraulic fluid provided by a 15 gpm hydraulic pump, also manufactured for this project by Hydradyne Hydraulics, Inc. The pump capacity was designed to provide a flow rate sufficient to produce a maximum frequency of 60 Hz in the driver, but the driver was not operated above about 35 Hz because it was found that the actual pump power requirements were higher than those assumed in design. This did not impact the objectives of the study, since optimum driving frequencies for the test pile were always found to be below 30 Hz.

The housing for the counterrotating masses was connected to slide rails that slid freely against mating rails in the service (guide) frame, which is shown schematically in Fig. E.2. The outer surface of the slide rails on the driver were teflon-coated and the mating surface on the guide frame was greased to reduce friction while the driver was in operation. A set of removable bias weights was placed directly above the vibrator to place a static biased compression force on the pile during vibro-driving. In order for this force to be essentially independent of the vibrational motion of the vibrator casing, the bias weights were isolated from the casing by a series of springs. Part of the purpose of the research was to assess the effect of the magnitude of bias weight on the performance of the driver, which required varying these weights from zero to the maximum value of 1620 lb. As the magnitude of bias weight was varied, so was the number of isolation springs between the casing and bias weights, so as to keep the natural frequency of the bias weight/spring system [$= (1/2\pi)(K/M_b)^{0.5}$, where M_b = mass of the bias weight and K = the combined constant of the springs in position] at approximately 1 Hz.

Initially, the vibro-driver casing was attached to the top of the pile by bolting the weldneck flange welded to the top of the pile to the base plate of the driver. In the early parameter tests it was discovered that the vibro-driver motors did not always remain synchronized, so that large horizontal forces developed. With the moment connection provided by the bolted flange, large flexural stresses were generated at the pile head that, in combination with the axial stresses produced rapid fatigue failure at the pile head, resulting in cracking of the steel near the points at which the flange had been welded to the pile. Two remedies to the problem were developed. First, the vibro-driver was redesigned, as described later in this appendix, and second, a swivel-head

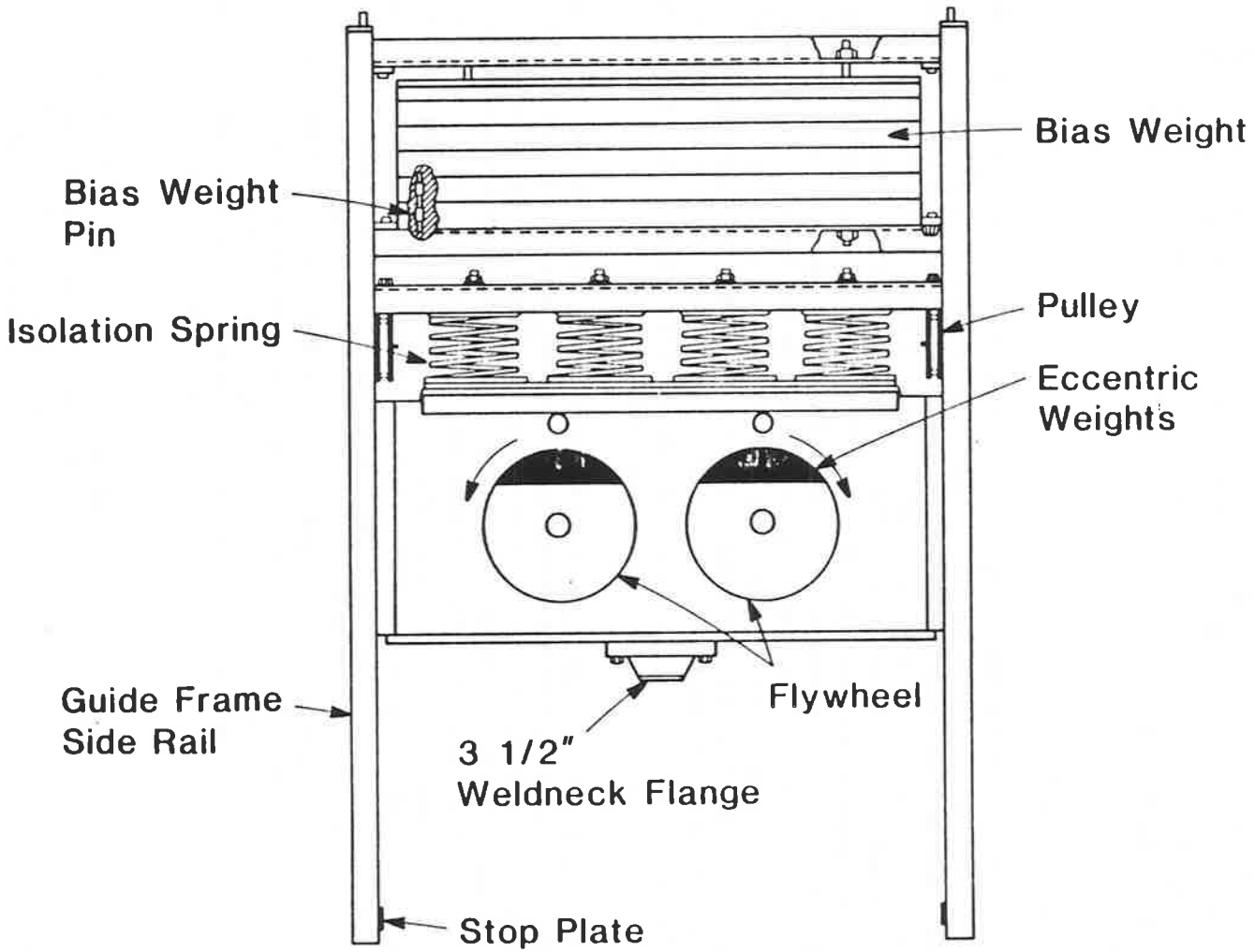

Fig. E.1. Schematic of Laboratory Vibro-Driver

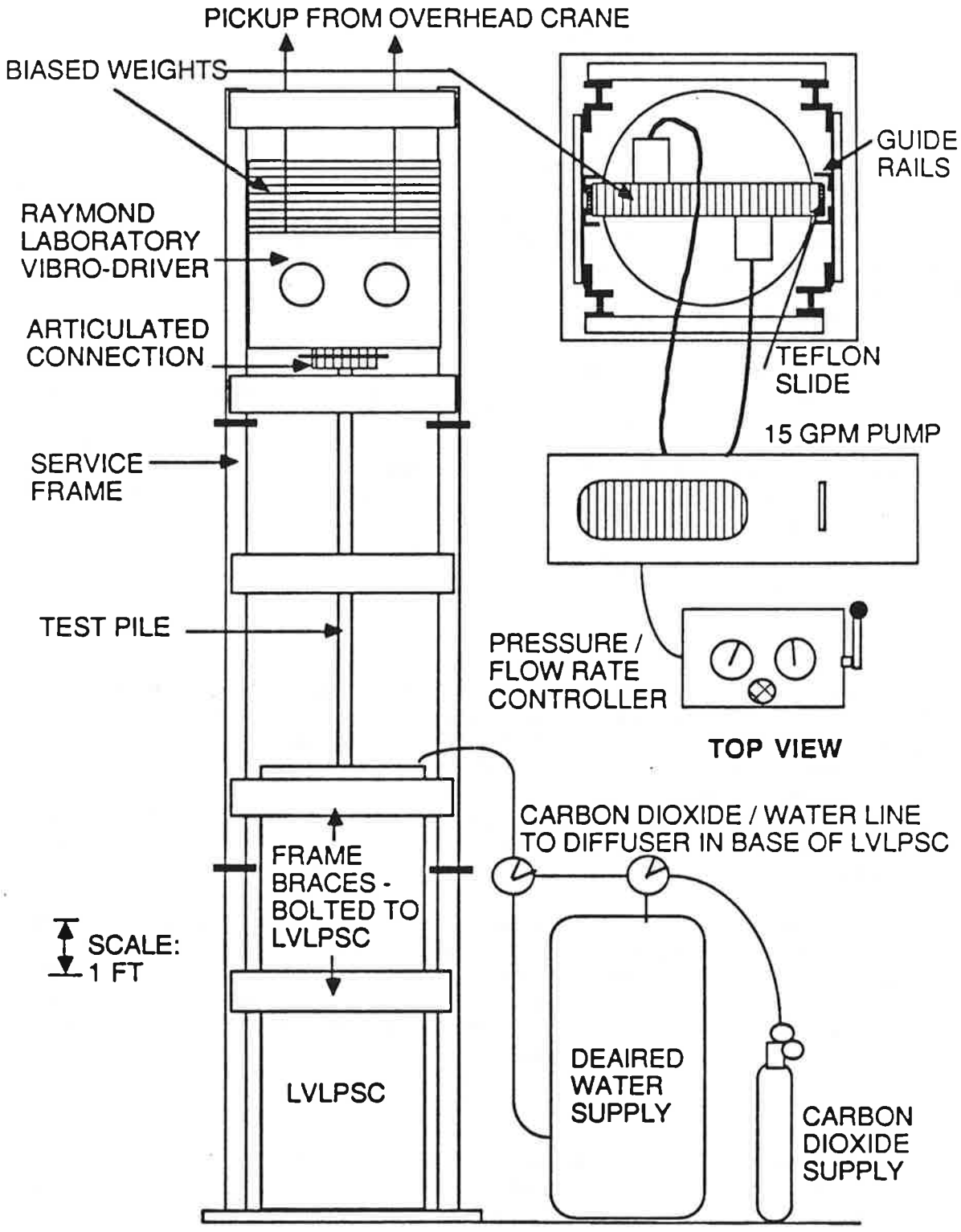

Fig. E.2. Schematic of Laboratory Vibro-Driver, Hydraulic Pump, LVLPSC, Test Pile and Service Frame in Operation at Beginning of a Test

(pinned) connection was developed between the driver and the pile. This connection is shown in line drawing form and photographically in Fig. E.3. It is bolted between the flange on the pile head and the center of the base plate on the driver, provides for free rotation about an axis parallel to the axes on the driver motors and operates with less than 0.001 in. double amplitude axial slack.

Design details, as provide by Raymond Technical Facilities, Inc., are reproduced in Figs. E.4 - E.8 and in Table E.1. The system was designed so that the two hydraulic motors would be self-synchronizing. In operation they were found to be difficult to synchronize initially and to frequently desynchronize during operation. This was unacceptable performance for the study being conducted, and Raymond Technical Facilities redesigned the vibro-driver to synchronize fully at all times. This was accomplished by rebuilding the two flywheels so that they interconnected through a system of gears, at their outer edges, which meshed to a very low tolerance. A detail of the redesigned flywheels is given in Fig. E.9.

The theoretical performance curves for the vibro-driver is shown in Fig. E.10. The eccentric moment is defined as the product of the unbalanced mass on each flywheel times and its radial distance from the center of the motor shaft times two (for two motors and two masses). Four different sets of unbalanced weights were constructed that permitted the application of the four discrete values of eccentric moment shown in Fig. E.10. The theoretical force (single amplitude) generated by the counterrotating masses, F_c, is given by

$$F_c = [2\pi f]^2 \frac{M_o e}{g} \qquad (E.1)$$

where $M_o e$ is the combined eccentric moment produced by the pair of unbalanced masses (not by each mass), f is the operating frequency in Hz and g is the acceleration of gravity (386 in/sec/sec). The values of biased weight, eccentric moment and frequency were varied during the "parameter" tests (Table B.1). All of the "capacity" tests (Table B.1) were conducted with full biased weight (1620 lbs. plus 38b lbs. carriage weight), 100 in-lb. eccentric moment. 780 lb. vibratory body weight and f = 20 Hz. The combination of the eccentric moment and frequency produced (theoretically) an unbalanced vertical force at the axes of the motors of 4.1 k. Structurally, the driver could not operate with $F_c > 13$ k.

Photos of the driver in operation and of the hydraulic pump (with controls) are shown in Figs. E.11 and E.12, respectively. The driver and pump were connected through ordinary flexible hydraulic hoses: one pressurized hose and one unpressurized (return-line) hose per hydraulic motor. A flow divider was employed at the point of connection of the pressurized hoses with the pump to produce as nearly equal fluid flow through each of the two motors as possible.

Impact Hammer Properties

A simple single-acting air hammer was used for the impact tests and for restriking the piles driven with the vibro-driver. A schematic of this impact hammer is shown in Fig. E.13, and a schematic of the entire driving system is shown in Fig. E.14. The anvil of the impact hammer was bolted directly to the flange on the head of the test pile. The hammer operates as follows:

a. The solenoid valve is closed by an actuator mounted on the valve upon command from an electronic signal from a controller operated by the research team, allowing air under regulated pressure of 20 psi to flow from a reservoir into the 3-in. hose and into the chamber of the hammer, lifting the ram. The pressure above the ram remains atmospheric throughout the cycle because the top of the hammer cylinder is open.

b. At the full lift height of the ram (set according to the targeted level of impact energy) a tube affixed to the ram breaks a light beam at the top of the cylinder casing, which sends a trigger signal to the actuator on the solenoid valve to open the valve and to reduce the regulated pressure in the inlet line, essentially instantaneously, making the 3-in. hose an exhaust line.

c. The ram then falls freely, impacting a hammer cushion (2.5 in. of plywood sheets) that is situated on top of the anvil at the base of the cylinder. This impact is transferred to the head of the pile.

In normal operation (both impact driving and restrike), the beam-breaker tube was set to produce a 21-in. actual drop (20-in. nominal drop) during this study. Since the ram weighs 460 lb., this resulted in a theoretical energy of 0.805 ft-k per blow. Fluid mechanics studies of the air compression in the cylinder indicated that compression of air produced only a 3% loss of energy. The machined inside surface of the cylinder is lubricated on every blow through an in-line mister, and the ram has teflon bushings on its perimeter to prevent metal drag. To minimize transmission of energy of impact into the hammer casing and thus maximize the transmission of energy into the pile, the anvil at the base of the cylinder is not rigidly connected to the cylinder casing but is connected by means of springs located around the perimeter of the casing. The laboratory impact hammer is therefore a high-efficiency device.

The controller can be operated automatically, in which the rate of driving is controlled by a prescribed time lag between the receipt of the trigger signal to open the valve and the generation of a new signal to close it. During the impact tests, the rate was set at approximately 23 blows per minute. The controller can also be operated manually, which was the mode of operation during the restrike tests. The time between restrike blows was set at 30 to 60 seconds to allow observation of accelerometer and strain gage signals between blows and thus verify correct operation of the instrumentation.

The valve actuator provides the power to open and close the solenoid valve pneumatically, such that air under pressure must also be supplied to it, separate from the air line used to lift the ram. In the system that was used in this study a 200 cubic foot air reservoir with an initial pressure of 100 psi was used. Pressurized air was supplied by this reservoir to both the ram cylinder and the valve actuator, but at different line pressures. The line pressure to the cylinder inlet, as stated earlier, was 20 psi, while the line pressure to the valve actuator was 70 psi. While the pressure in the reservoir dropped during impact driving, sufficient air volume was always available to keep the reservoir pressure above 70 psi, so that no difficulty occurred in operating the valve actuator.

A new cushion was used for each impact test, although very little visible damage could be observed in the retired cushions. A reusable cushion was employed for the restrike tests because relatively few total blows were involved. This cushion showed no sign of permanent compression or damage.

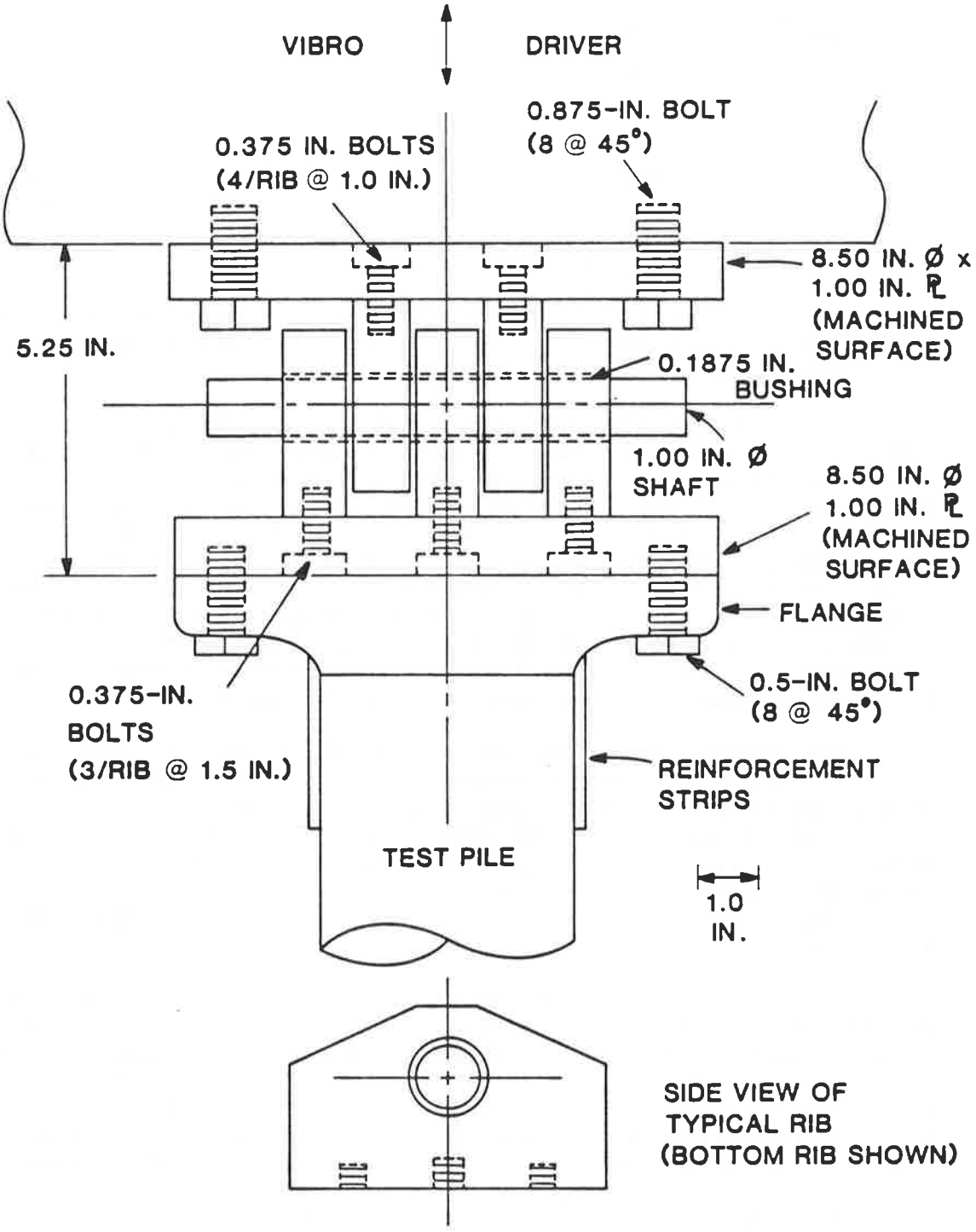

Fig. E. 3a. Detail of Articulated Swivel Connection Between Vibro-Driver and Pile

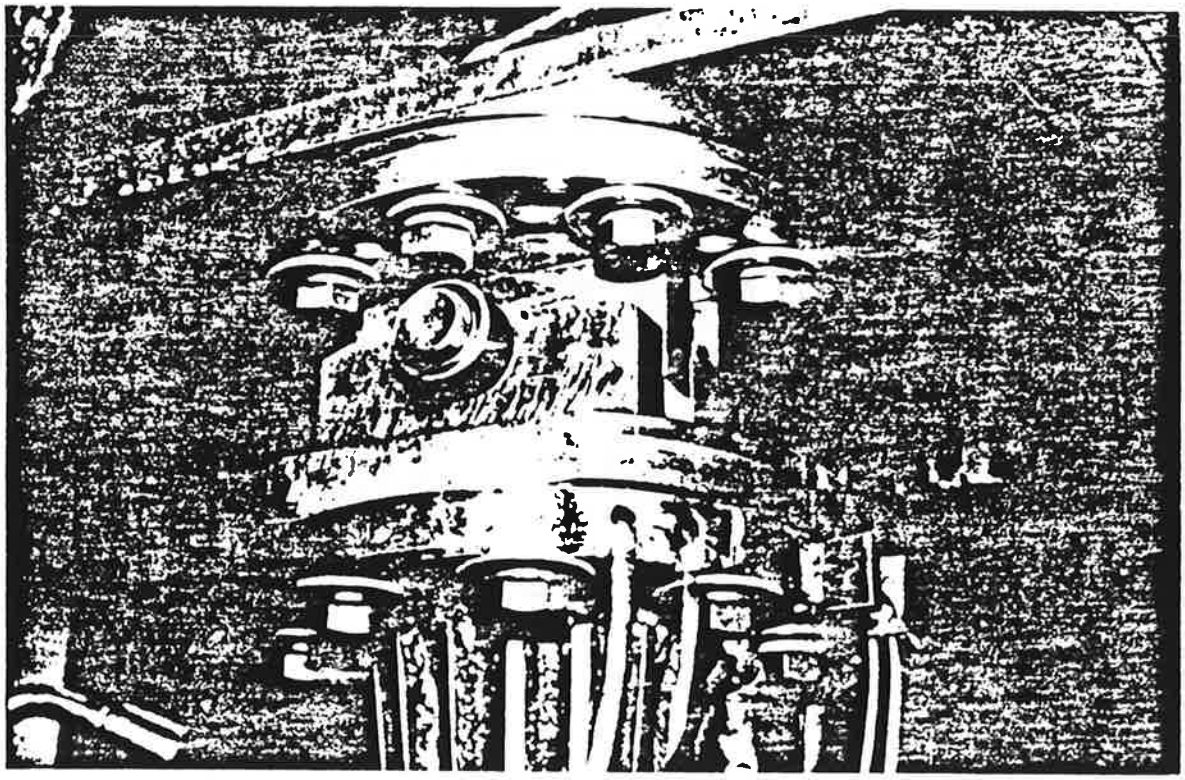

Fig. E. 3b. Photograph of Articulated Swivel Connection Between Vibro-Driver and Pile

NCHRP Note:

Page 37 was missing from the original, bound report

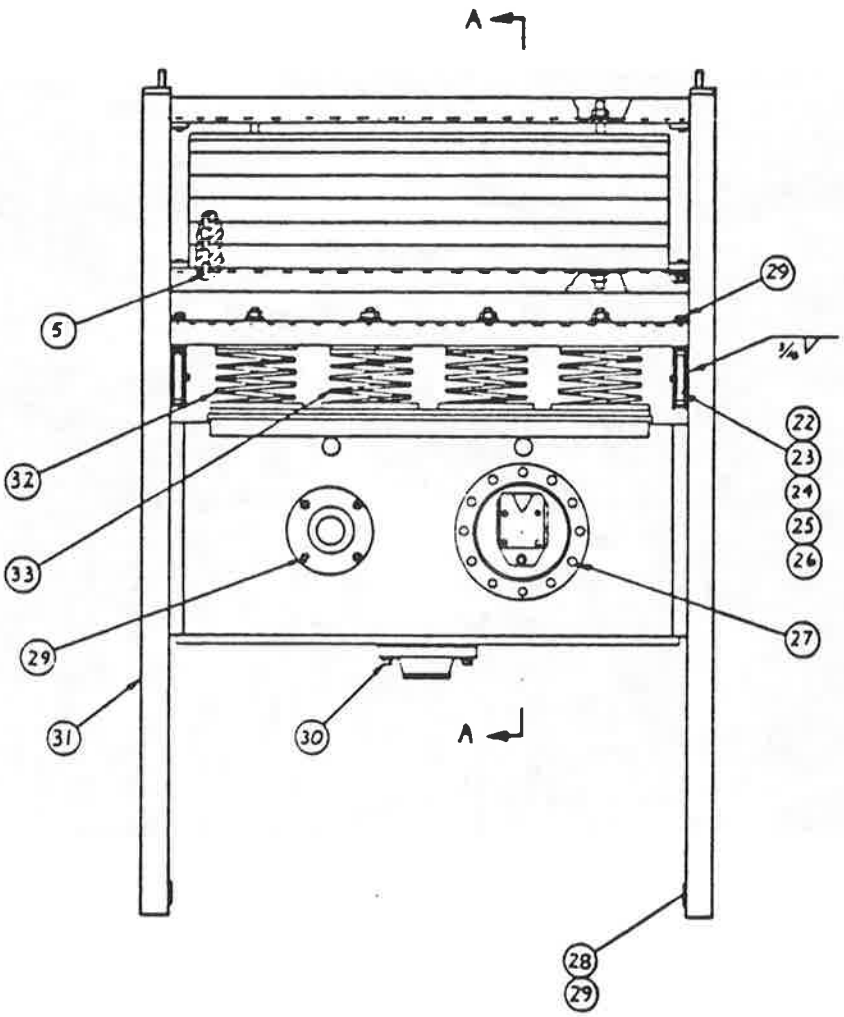

Fig. E.4. Detail of Vibro-Driver: Overall Elevation

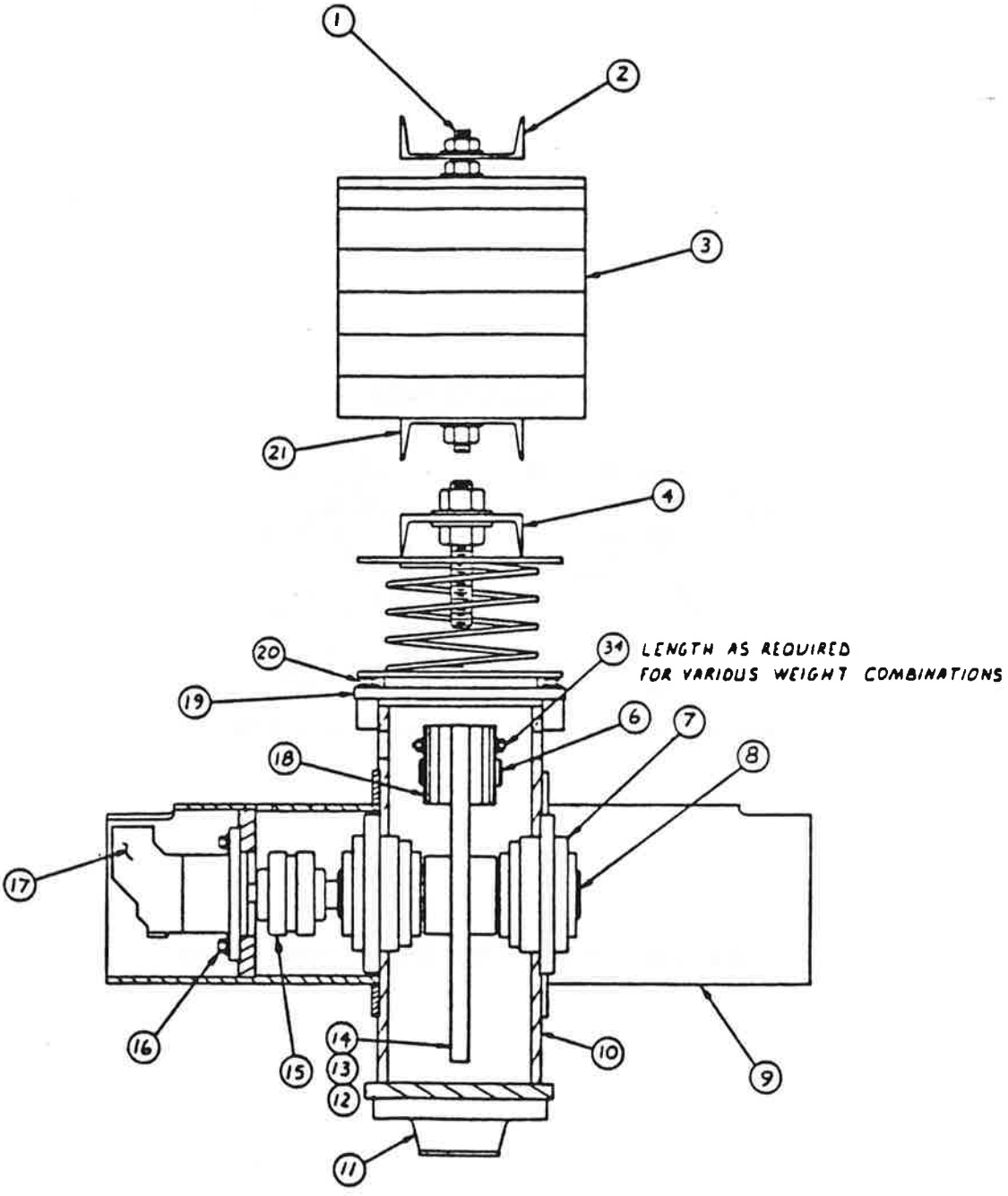

Fig. E.5. Detail of Vibro-Driver: Cutaway View (Section A-A from Fig. E.4)

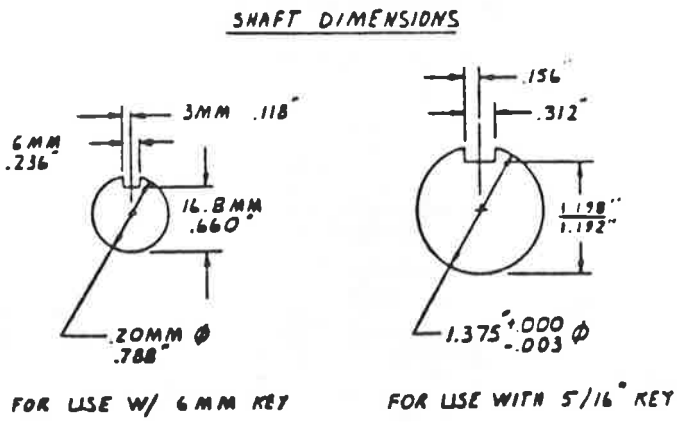

Fig. E.6. Detail of Vibro-Driver: Motor Shafts

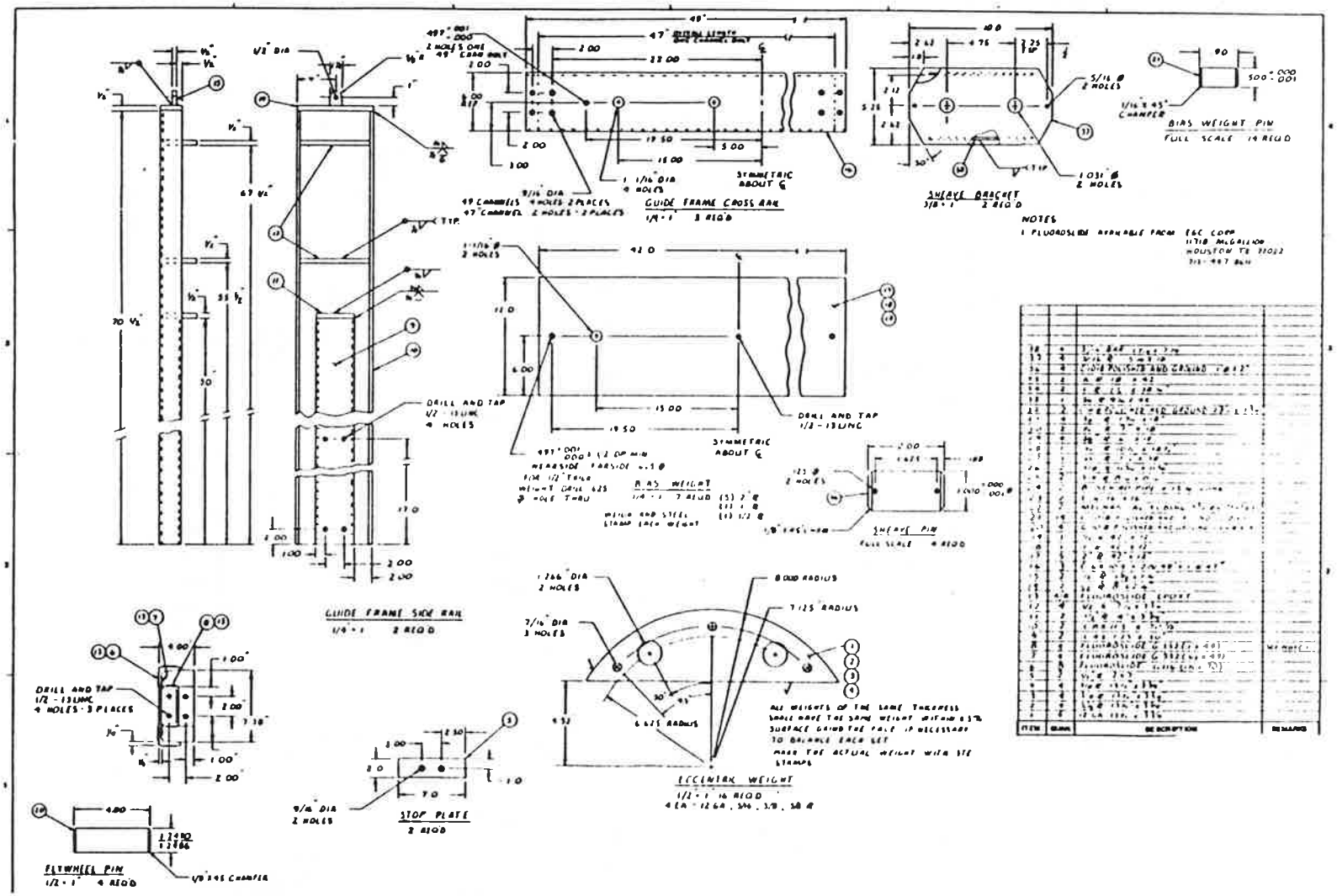

Fig. E. 7. Detail of Vibro-Driver: Individual Components (I)

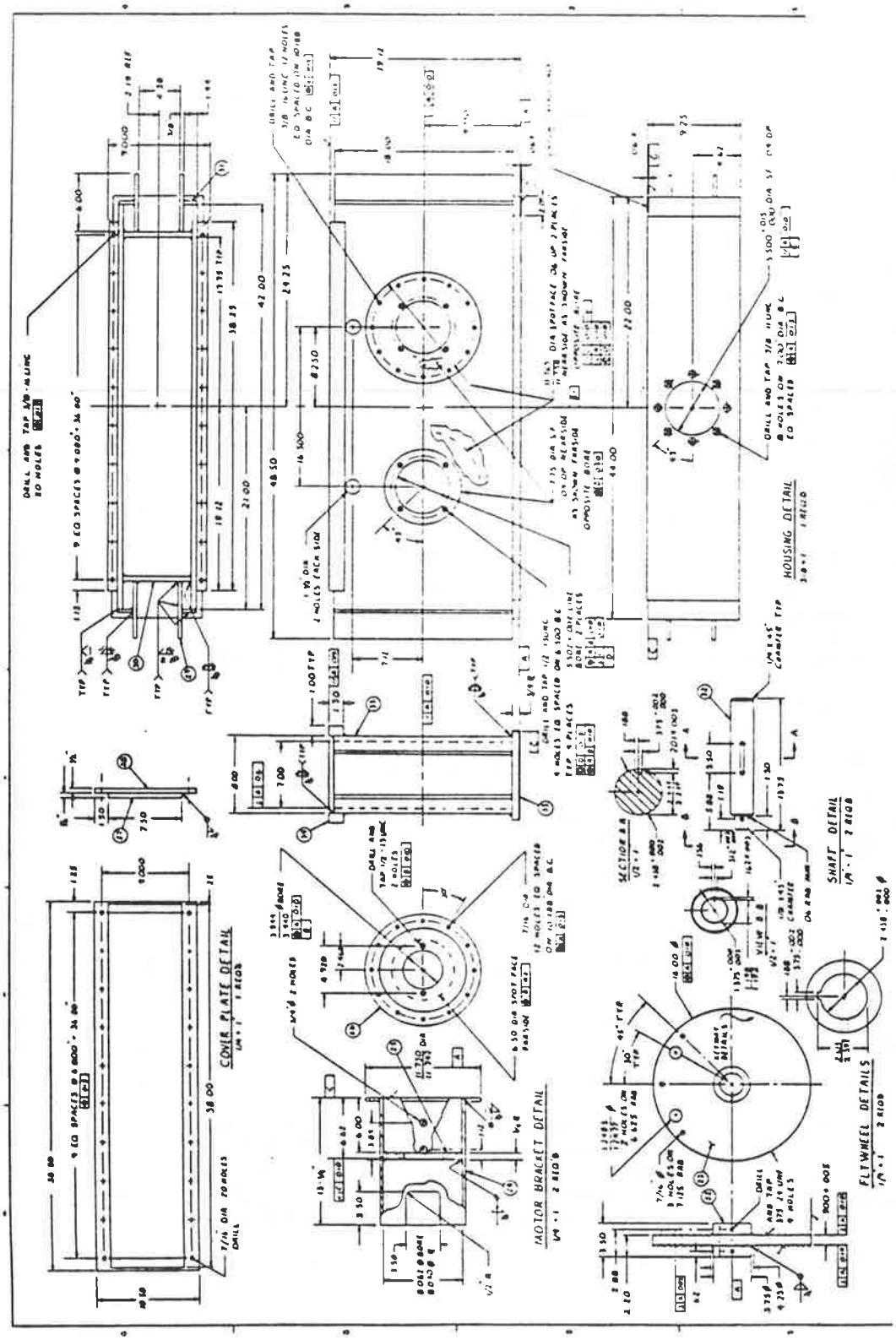

Fig. E. 8. Detail of Vibro-Driver: Individual Components (II)

Table E.1. Parts List for Laboratory Vibro-Driver

Item No.	No. Req'd	Description
1	2	0.75" IO UNC Allthread, 16" Lg. W/ 3 Nuts & Washers
2	1	Guide Frame Cross Rails, 47" Lg.
3	7	Bias Weights , Total Wgt, 1620 Lb.
4	1	Guide Frame Cross Rail
5	4	Bias Weight Pin
6	4	Flywheel Pin
7	7	Didge Flange Bearing, #42933
8	2	Shaft
9	2	Motor Bracket
10	1	Housing
11	1	3.5" 150 Lb. Weldneck Flange
12	8	0.375" - 24 UNF X 0.50" Lg. Set Screw
13	2	0.375" Sq. Key, 3.25" Lg.
14	2	Flywheel
15	2	Wood Sure Flex Coupling, Type 6J
16	4	0.5" - 13UNC X 1.5" Hex. Head Bolt w/ F. W. & L. W.
17	2	Sundstrand Hydraulic Motor, Model F11-10
18	16	Eccentric Weight
19	1	Cover Plate
20	20	0.375" - 16 UNC X 2" Hex. Head Bolt w/ F. W. & L. W.
21	1	Guide Frame Cross Rail w/ 0.5" Holes
22	4	0.25" - 20 UNC X 2" Bolt w/ F. W., L. W. & Nut
23	4	Crosby Sheave #4, 1 Bronze Bushed, 1" ø
24	2	Sheave Housing
25	4	Sheave Pin
26	8	0.125" X 2" Cotter Pin
27	24	0.375" - 16 UNC X 1" Hex Head Bolt w/F. W. & L. W.
28	2	Stop Plate
29	40	0.50" - 13 UNCX X 1" Hex Head Bolt w/ F. W. & L. W.
30	8	0.625" - 11 UNC X 2" Hex Head Bolt w/ F. W. & L. W.
31	2	Guide Frame Side Rail
32	2	Amber Booth Isolator #SW-6A-300
33	2	Amber Booth Isolator #Sw-6A-800
34	36	0.375" - 16 UNC Bolt w/ 2 F. W. & Lock Nut, 6 Ea. 2", 2.5", 3", 3.5", 4" and 4.5" Lg.

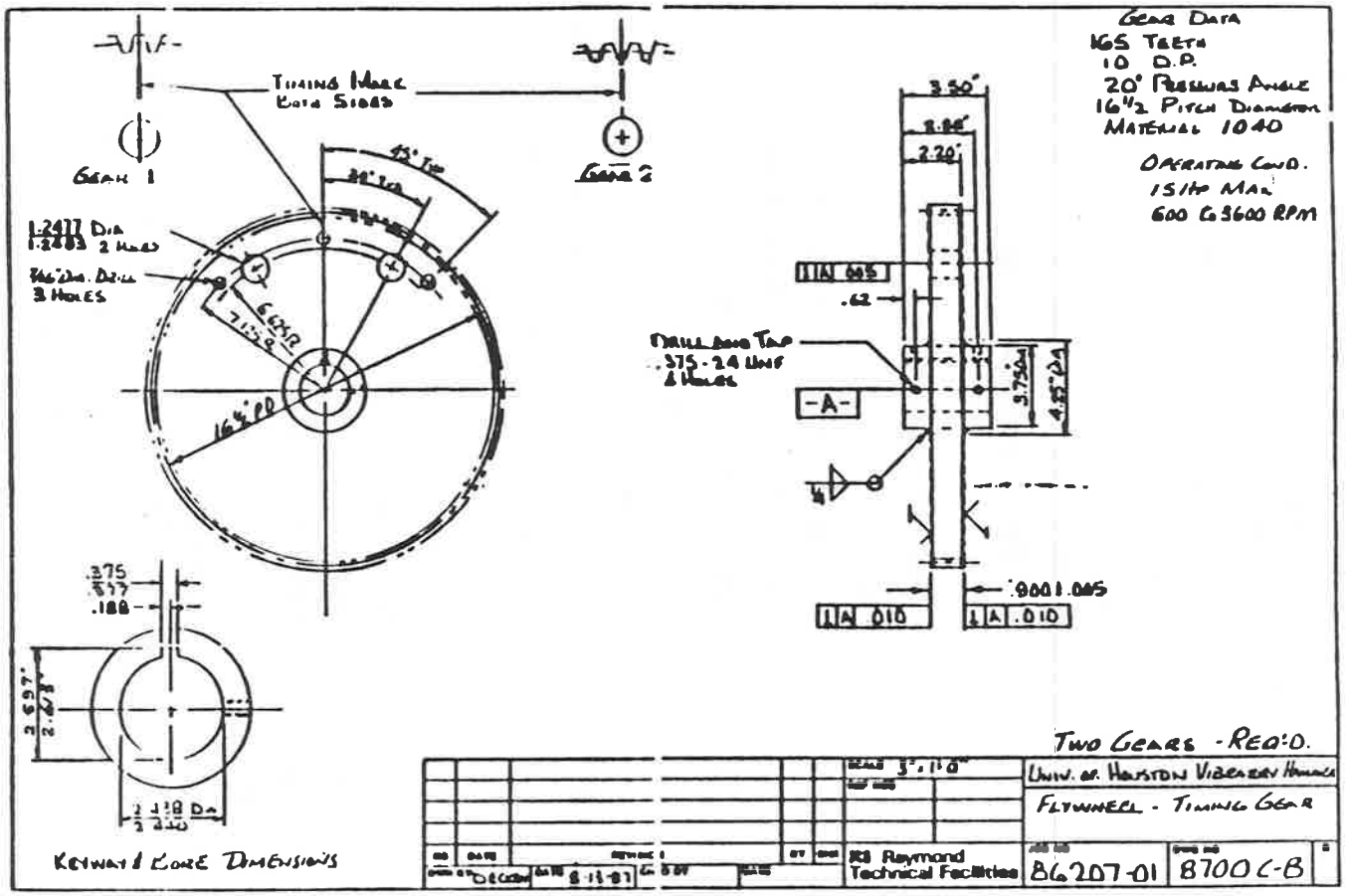

Fig. E.9. Detail of Flywheel Modifications for Vibro-Driver to Assure Motor Synchronization

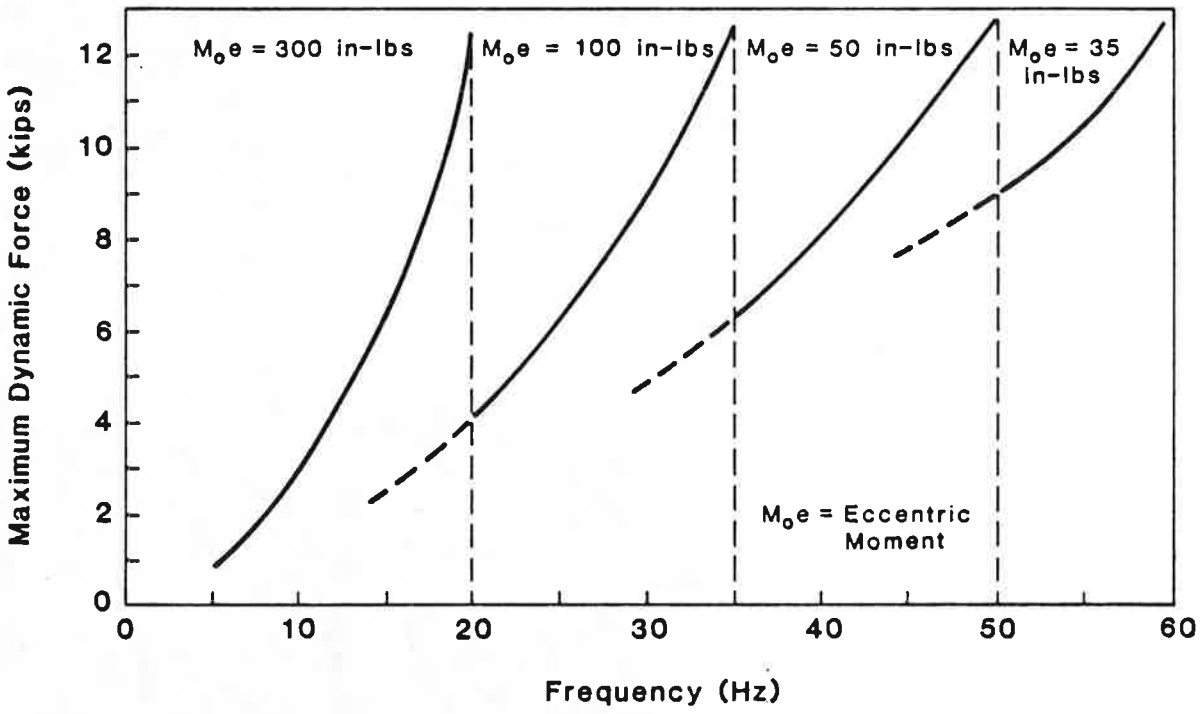

Fig. E. 10. Theoretical Performance Curves for Laboratory Vibro-Driver

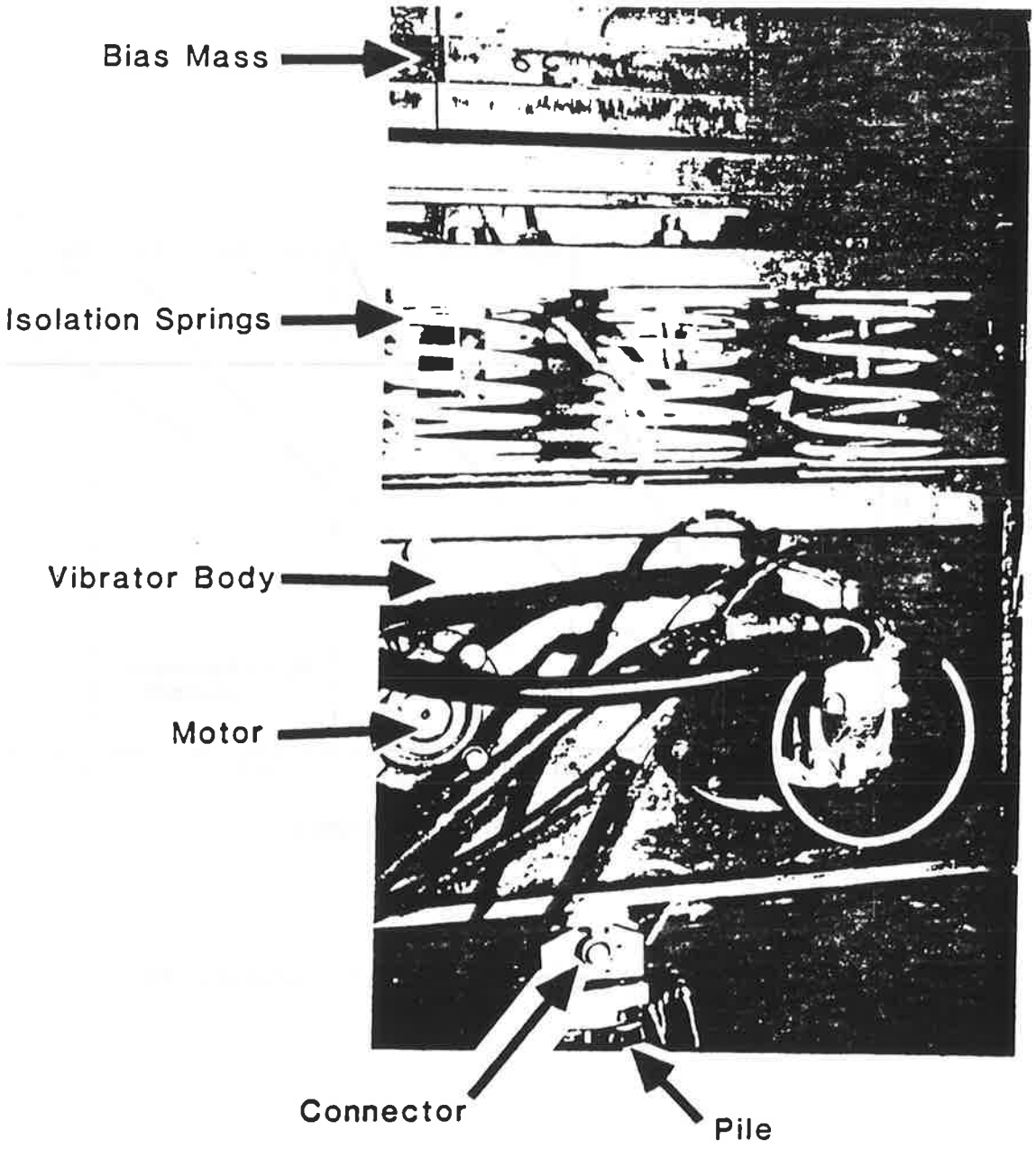

Fig. E. 11. Photograph of Vibro-Driver in Operation During Test 14

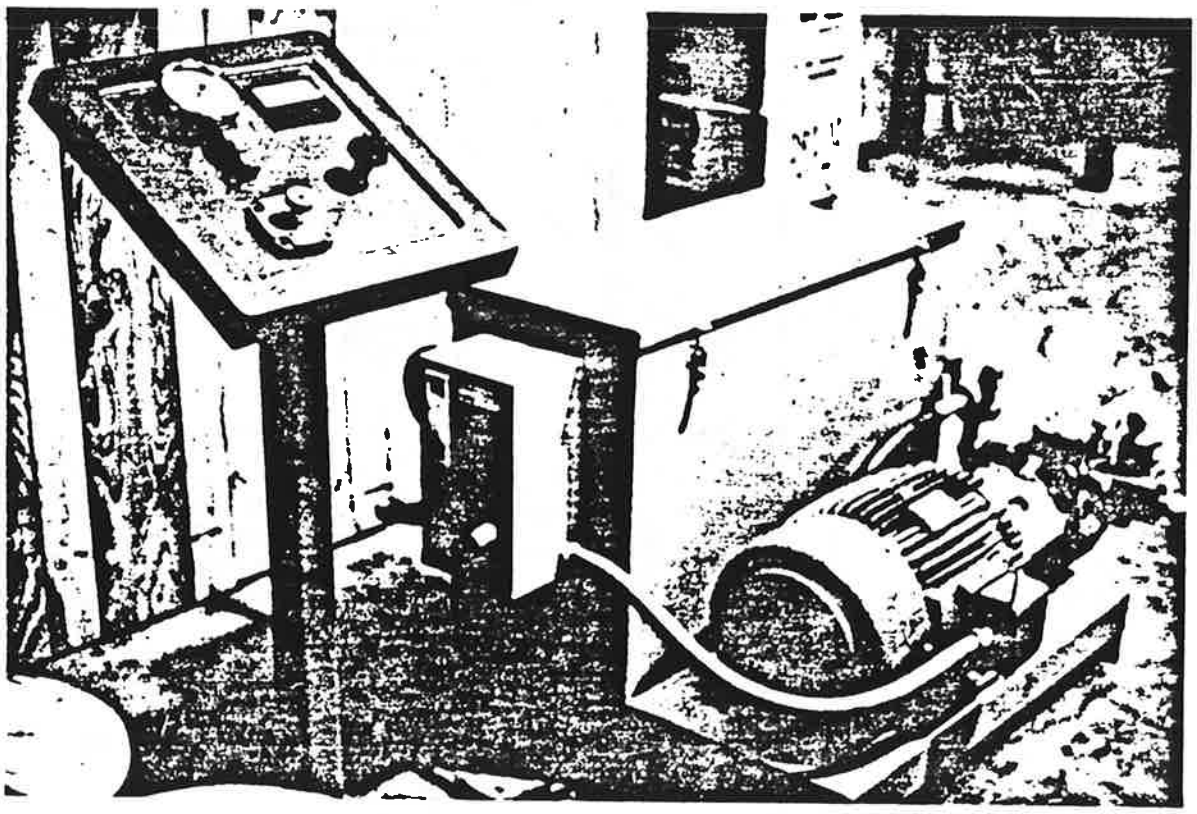

Fig. E. 12. Photograph of Hydraulic Pump and Controls

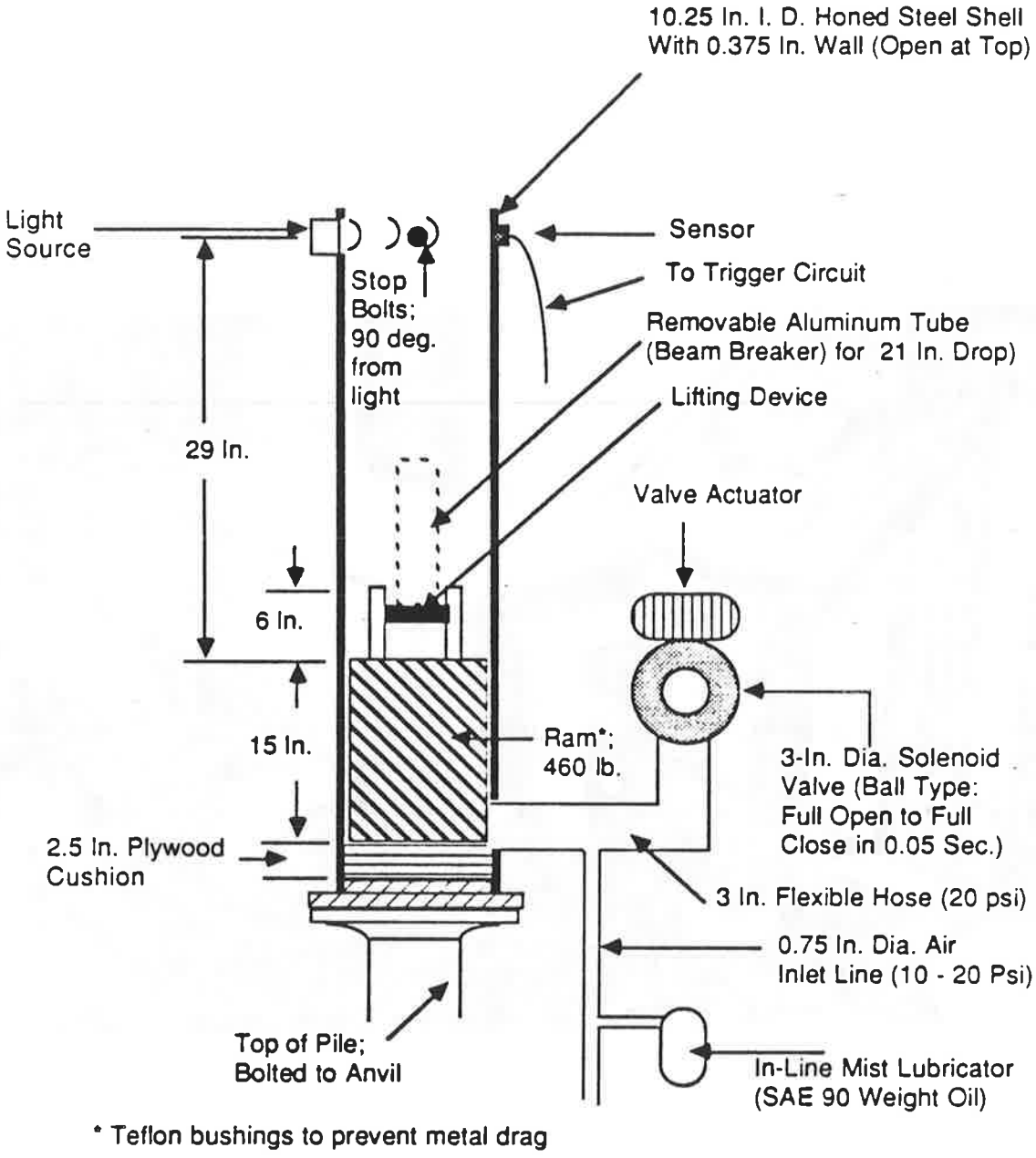

Fig. E. 13. Schematic of Impact Hammer

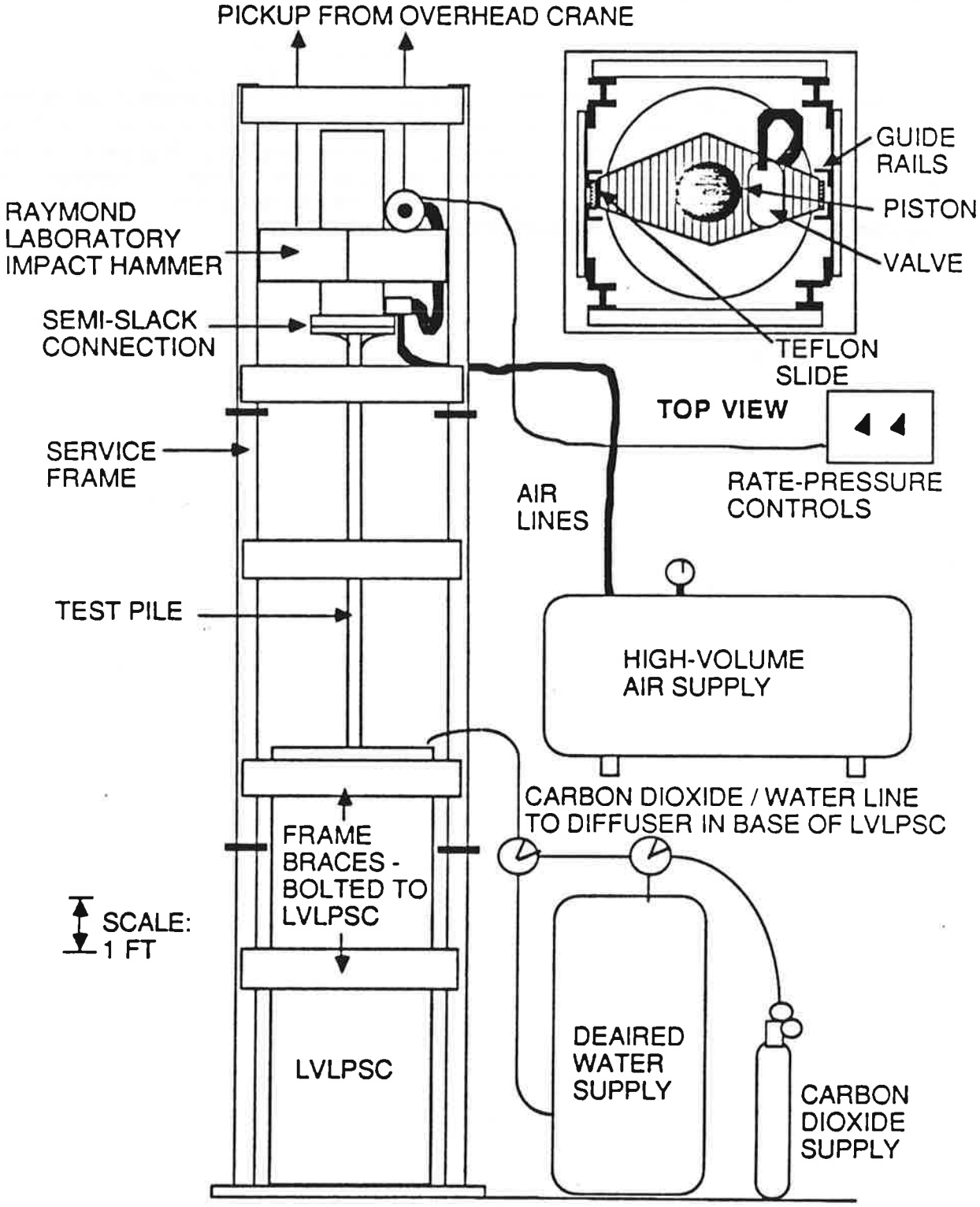

Fig. E. 14. Schematic of Impact Hammer , LVLPSC, Test Pile, High-Volume Air Supply Reservoir and Service Frame in Operation at Beginning of a Test

Vibro-Driver-Pile Interaction

The peak compressive pile-head forces measured during vibro-driving in the capacity tests exceeded the 4.1 k unbalanced force amplitude developed by the counterrotating unbalanced masses. This effect was caused by the superposition of the bias weight (2.0 k) and the inertial force produced by the body of the vibrator (= 0.78 k X $(a/g)_{vibrator}$. This system of forces is illustrated in the free body diagram shown in Fig. E. 15. The peak pile-head force (developed near the bottom of the downstroke) plus the inertial force of the pile are in turn balanced by the peak soil shaft and toe resistances, assuming that the pile behaves as a rigid body during vibro-driving.

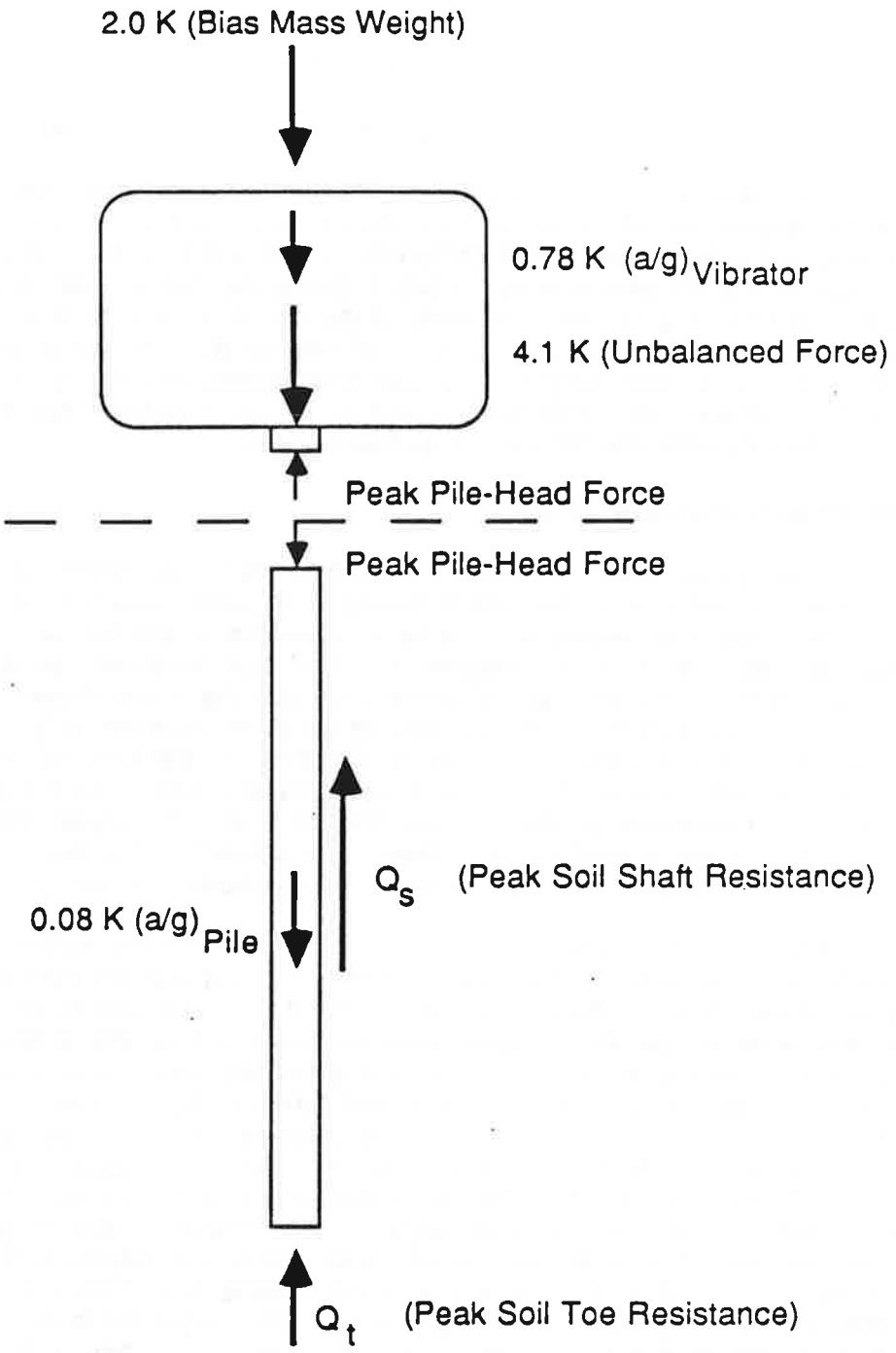

Fig. E.15. Free-Body Diagram of Vibro-Driver and Pile at Bottom of Stroke with Force Values for Capacity Tests

APPENDIX F

Description of Data Acquisition Systems

Two separate data acquisition systems were used for the "capacity" test series: One for acquisition of dynamic data during pile installation (vibration, impact and restrike) and one for the static compression and uplift tests. Only data for rate of penetration and frequency were recorded during the "parameter" tests. These data, which consisted of optical measurements of the rate of movement of marked points on the shaft of the pile past the upper surface of the top plate of the chamber and spectral analysis of the average output of the pile-head accelerometers to ascertain frequency, were recorded manually. The dynamic and static data acquisition systems that were used for the capacity tests are described separately below.

Dynamic Data Acquisition System

The dynamic data acquisition system is shown in schematic form in Fig. F.1. During any installation event, the following data were recorded on an eight-channel analog magnetic tape recorder: Pile-head acceleration, pile-toe acceleration, pile-head force, pile-toe force, total pressure (bottom cell location), pore water pressure (bottom cell location) and rate of penetration (on the voice channel). Acoustic time marks were placed on the voice channel, on which an observer indicated the passage of various depth marks past the top of the top plate of the LVLPSC, which allowed for accurate determination of the rate of penetration and which tied the data on the other channels to a particular penetration into the chamber. The eighth channel on the tape was used for flutter control and was therefore not available for data. The tape recorder was run continuously during the period of pile installation for any given capacity test.

The resulting data tapes are recordings of voltage outputs for the various instruments on the channels that are indicated in Fig. F.1 and are valid for a tape speed of 7.5 inches per second. These tapes are archived for further use by others. The voltages that are recorded on those tapes must be multiplied by the appropriate instrument calibration factor (Appendix G) to obtain engineering units. It is also pointed out that the input voltage to all of the electrical resistance instruments was 10.00 Volts for all of the capacity tests, which must be considered when converting the voltages to engineering units using the factors from Appendix G. The output of electrical resistance instruments recorded on the tape has been amplified by a factor of 200. However, amplification of 200:1 was also employed in the calibration tests reported in Appendix G, so that correction of the calibration factors shown in Appendix G for amplification differences between calibration and capacity testing is not necessary. Piezoelectric devices are read directly without amplification. The output for those devices need only been multiplied by the appropriate calibration factor from Appendix G.

Wave forms from impact tests were expected to be very complex because the test pile was very short, permitting rapid return of reflected waves from the pile toe and (of lesser magnitude) from the boundaries of the chamber during impact tests and restrike events. Since high-speed, real-time digitizing equipment was not available, it was decided to record the dynamic data on analog tape and to digitize off line at a rate that was appropriate to replicate the analog signals. This was accomplished two channels at a time by the digitizing circuits contained by an A/D unit that was coupled to the spectrum analyzer (Fig. F.1). Digitized data were stored in the memory of the spectrum analyzer

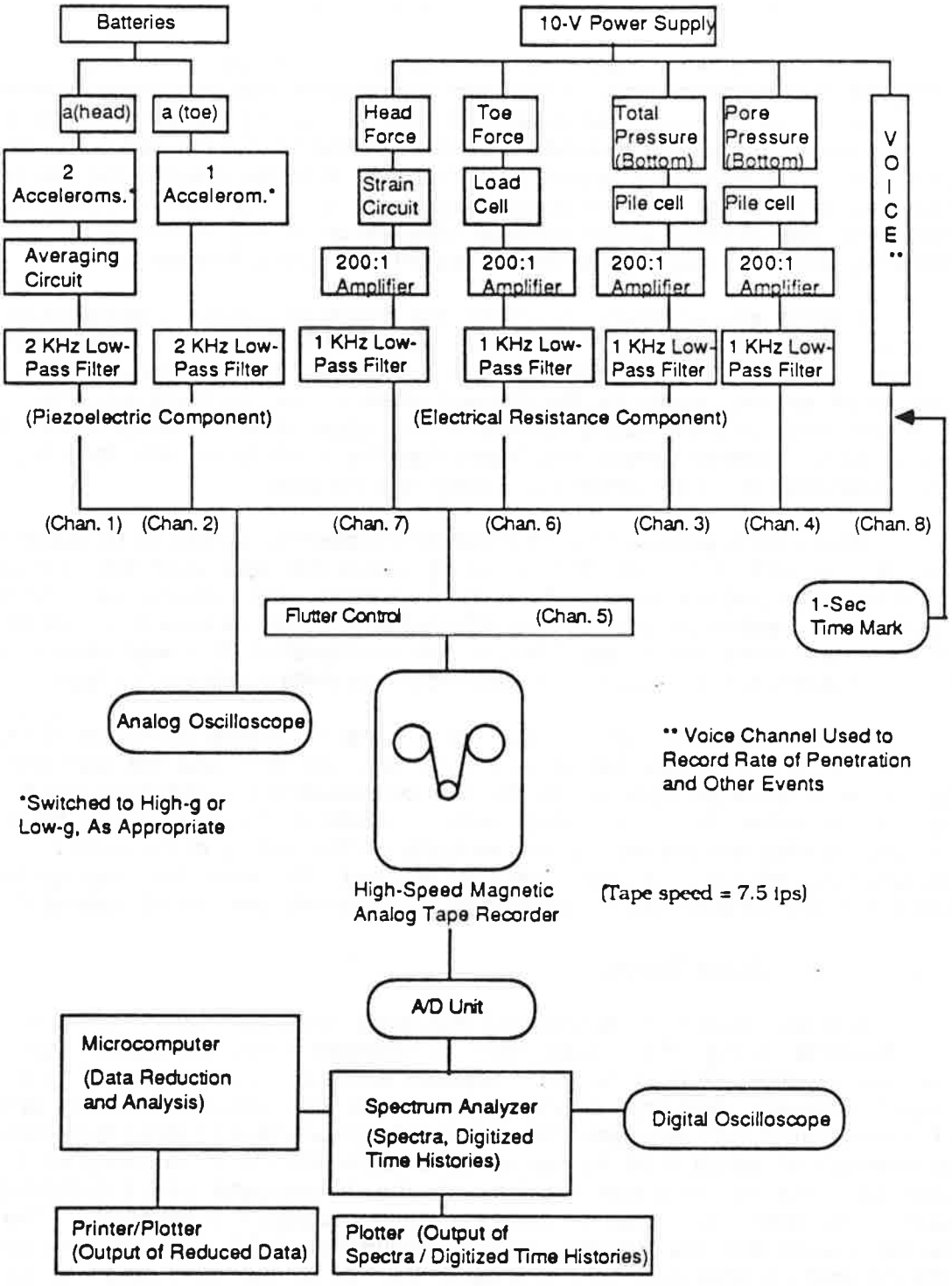

Fig. F.1. Schematic of Data Acquisition System for Impact and Vibratory Data

for further processing by the spectrum analyzer (either Fourier analyses or simple multiplication by calibration factors) after which they were output to a pen plotter or to a microcomputer for further reduction and/or analysis.

Immediately after a test, digitized data were reviewed for apparent correctness using the digital oscilloscope. The digital oscilloscope was also used to monitor the frequency of the pile-head acceleration in real time during vibratory driving after the average output of the two pile-head accelerometers had been converted to its fast Fourier transform. This monitoring system permitted very accurate determination of pile-head frequency and additionally gave precise information regarding the synchronization of the motors on the vibratory driver (through observation of the harmonics of the driving frequency and the decay of their magnitudes with increasing frequency).

Filtering was employed to remove the effects of frequency components of any signals that are of no importance in the analysis of the tests. Low-pass filters were employed on all of the instruments, using a 2 KHz rolloff for the accelerometers and a 1 KHz rolloff for the circuits for the pile-wall strain gages, pressure cell and load cell. The tape recorder itself had a nominal 5 KHz upper limit frequency response. Any signals with frequency components higher than the rolloff levels described above have been discounted in the presentation and analysis of the data.

Phase shifts produced by the piezoelectric devices, as well as by components of the data acquisition system (the averaging circuit that was used with the pile-head accelerometers and the various filters)was a concern. The dynamic calibrations of the accelerometer and strain gage circuits reported in Appendix G were therefore conducted with the averaging circuit and filters in the configuration that was used during the testing program, and a discussion of observed phase shifts is provided in Appendix G.

Although not explicitly shown in Fig. F.1, each electrical resistance strain gage - type circuit (including pile-wall strain gages, pressure cells and toe load cell) was a full Wheatstone bridge (Appendix D) that was connected to a shunting resistor to balance each circuit individually prior to each tests. All instruments were zeroed by balancing the circuits while the pile was resting vertically on the surface of the sand at the top of the LVLPSC, without a hammer resting on its head. Therefore, the readings that were taken during installation are readings relative the initially unstressed state of the pile.

Static Data Acquisition System

The data acquisition system that was used during the static load tests is shown schematically in Fig. F.2. Data from 12 channels (plus the power supply) were acquired on command from the microcomputer, which was manually keyed by one of the project engineers. Readings of amplified data from all channels were made at intervals of penetration of 0.01 inch (prior to a pile-head displacement of about 0.25 inches) and at intervals of about 0.02 inches of penetration thereafter, resulting in 60 to 70 readings in the loading phase of a test. Keying the computer sent a command to the scanner to read each channel serially (requiring about 0.5 seconds). The digital voltmeter used with the scanner permitted acquisition of 5.5 digits of significant data. The digitized voltages were sent to a buffer from which they were read immediately by the microcomputer. Physically, all of the system shown within the dashed boundary in Fig. F.2 was contained in one unit.

The computer then performed simple mathematical operations (multiplying the voltage on each channel by the appropriate calibration factor) and wrote the resulting

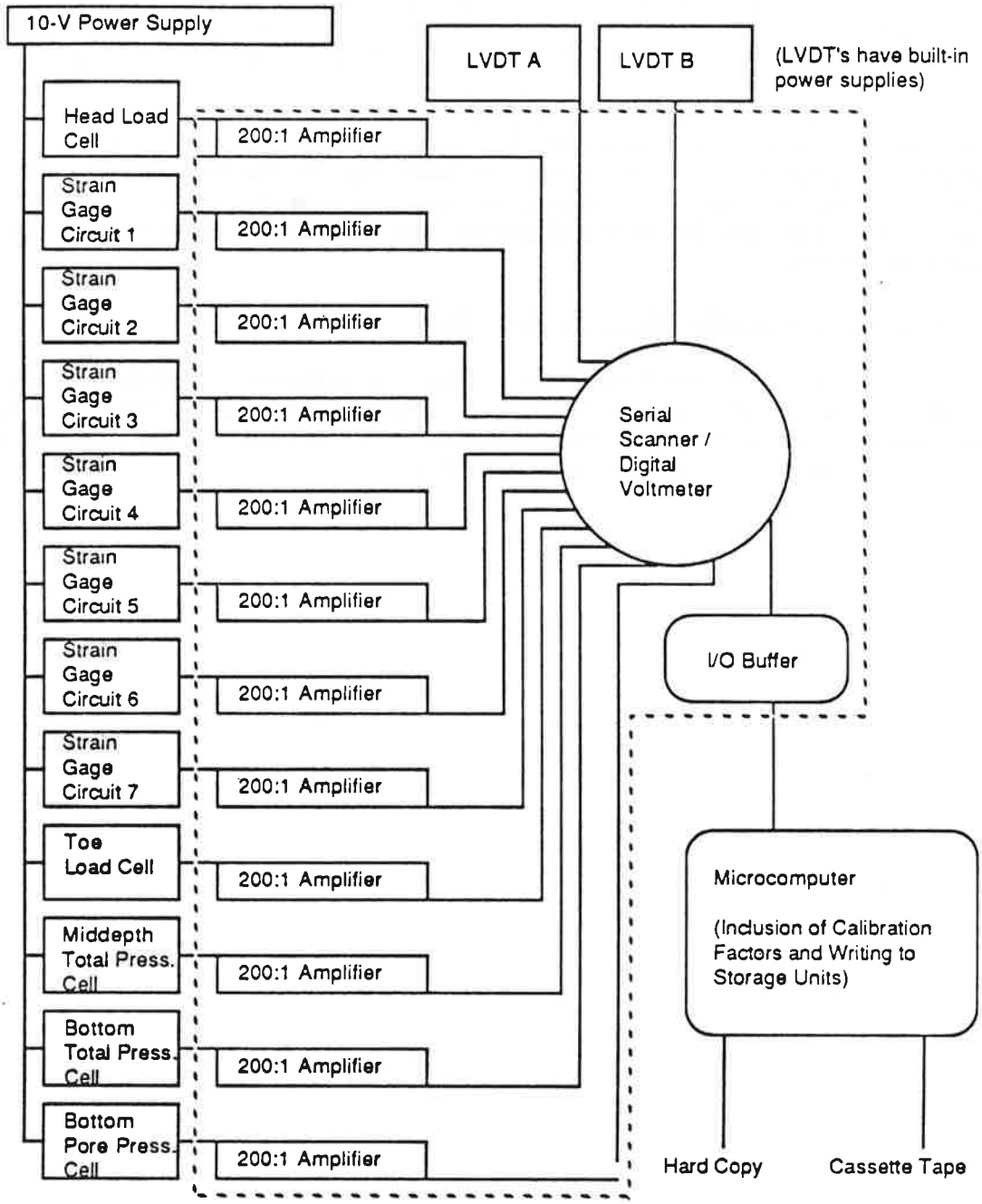

Fig. F.2. Schematic of Data Acquisition System for Static Load Tests

output (in engineering units) to both paper tape and a magnetic tape cassette. The hard copies (paper tapes) have been archived as permanent records of the static tests. The cassettes were re-read in delayed time by the microcomputer and transferred to a second microcomputer (the one used with the dynamic data acquisition system) for development of load transfer curves, load-movement curves and similar finished information.

As with the dynamic data acquisition system, the various strain gage circuits in the static system were balanced while the pile was stress free (sitting vertically on the top of the chamber). These zero conditions were used for the static load tests (i. e., no rebalancing was done once pile installation started), so that the stresses reported for the static load tests contain the effects of any residual stresses that were induced in the pile during installation.

Photographic View of Data Acquisition Systems

A photographic view of the main components of both the dynamic and static data acquisition systems is provided in Fig. F.3. The dynamic system (tape recorder and spectrum analyzer) is shown in the foreground, and the static system (scanner system and microcomputer) is shown in the background.

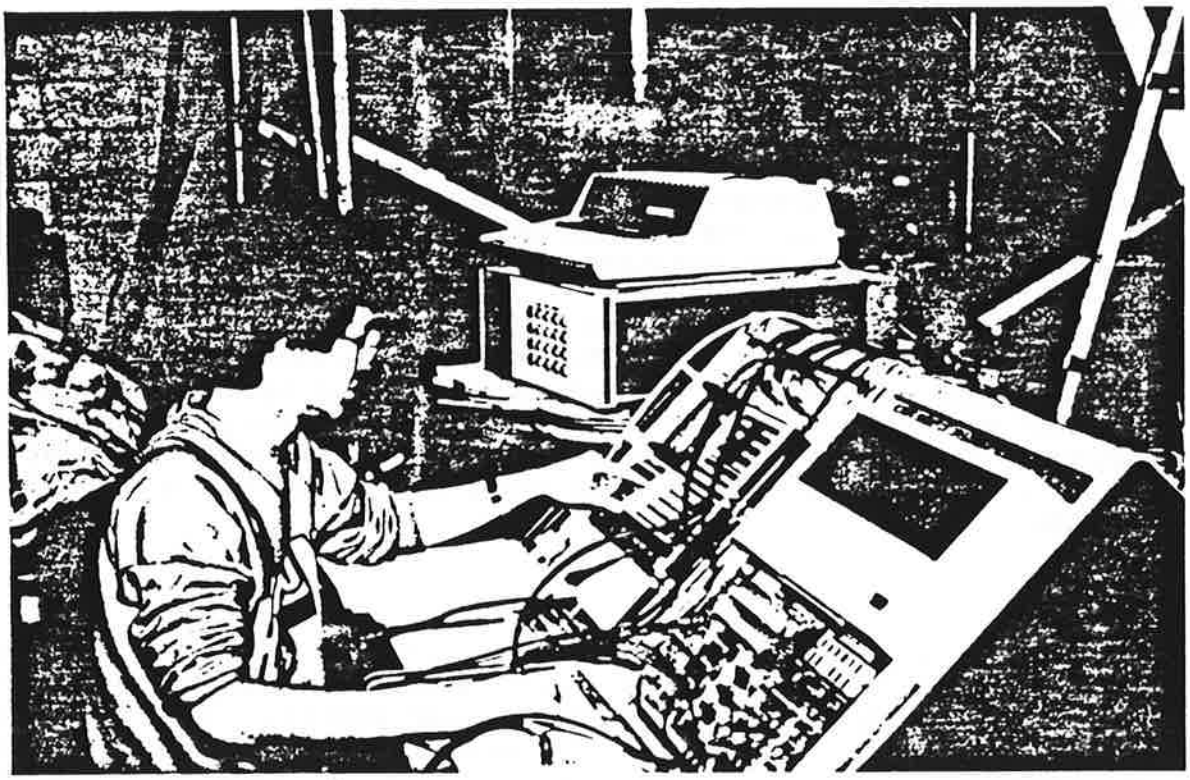

Fig. F.3. Photograph of Data Acquisition Systems (Magnetic Tape Recorder and Spectrum Analyzer in Foreground; Scanner/Digital Voltmeter and Microcomputer in Background)

APPENDIX G

Calibration Procedures

This appendix describes the calibration of the vibrator frequency to the flow rate of hydraulic fluid, the load cell used in the static tests and in the further calibration of the toe load cell and strain gages, the strain gage circuits along the pile, the toe load cell, the lateral pressure transducers in the pile and dynamic calibrations pertaining to magnitude, phase and cross-sensitivity of the instruments.

Frequency of Vibro-Driver

The frequency of the vibro-driver during a chamber test was controlled primarily by adjusting and monitoring the flow rate in the hydraulic pump. [Backup frequency monitoring was accomplished during operation by mounting a low-g accelerometer on the casing of the driver and monitoring it directly with the spectrum analyzer, in which the accelerometer output was displayed in the frequency domain.] During analysis of the data, the pile-head force records were examined to obtain the precise frequency actually obtained during the test.

The flow-rate calibration is summarized in Fig. G.1. The flow rate from the hydraulic pump was monitored with its flow meter and the frequency of the motors on the vibro-driver were monitored with tachometers., yielding the result that is shown. Eccentric moments on the driver flywheels were varied during this calibration to determine whether they had any effect. They did not. The linear relationship is expected for the system that was designed, which serves to inspire confidence in the driver's operation.

Load Cell

A commercial load cell was used to calibrate the test pile statically and to apply the compression and uplift loads in the static load tests. This instrument was a Lebow Associates, Inc., Model 3652-50K, 50,000 lb static load cell. This load cell was calibrated against a testing machine in the University of Houston materials laboratory that has an NBS traceable calibration. This calibration was performed twice, once at the beginning of the study (Dec. 15, 1986), before any pile calibration was conducted, and once at the end of the study (Jan. 15, 1988), after the last static load test. These two calibrations gave identical results., shown in Fig. G.2.

Axial Strain Gage and Lateral Pressure Transducer Bridges

The pile was calibrated in compression to a load of 41,000 lb on three separate occasions: Dec. 21, 1986 (prior to the first test), Aug. 4, 1987 (during the testing program), and Jan. 21, 1988 (after testing was completed). The second calibration was carried out after the pile head had cracked during an early test in which the pile head had been bolted rigidly to the driver, the upper two inches of the pile removed (to remove the structurally failed section) and the new head reinforced with vertical, welded steel strips. Small differences were observed in the calibration constant at the topmost level of strain gages between the first and second calibrations. Otherwise, calibration constants at all levels remained essentially uniform from the beginning of the tests until their completion.

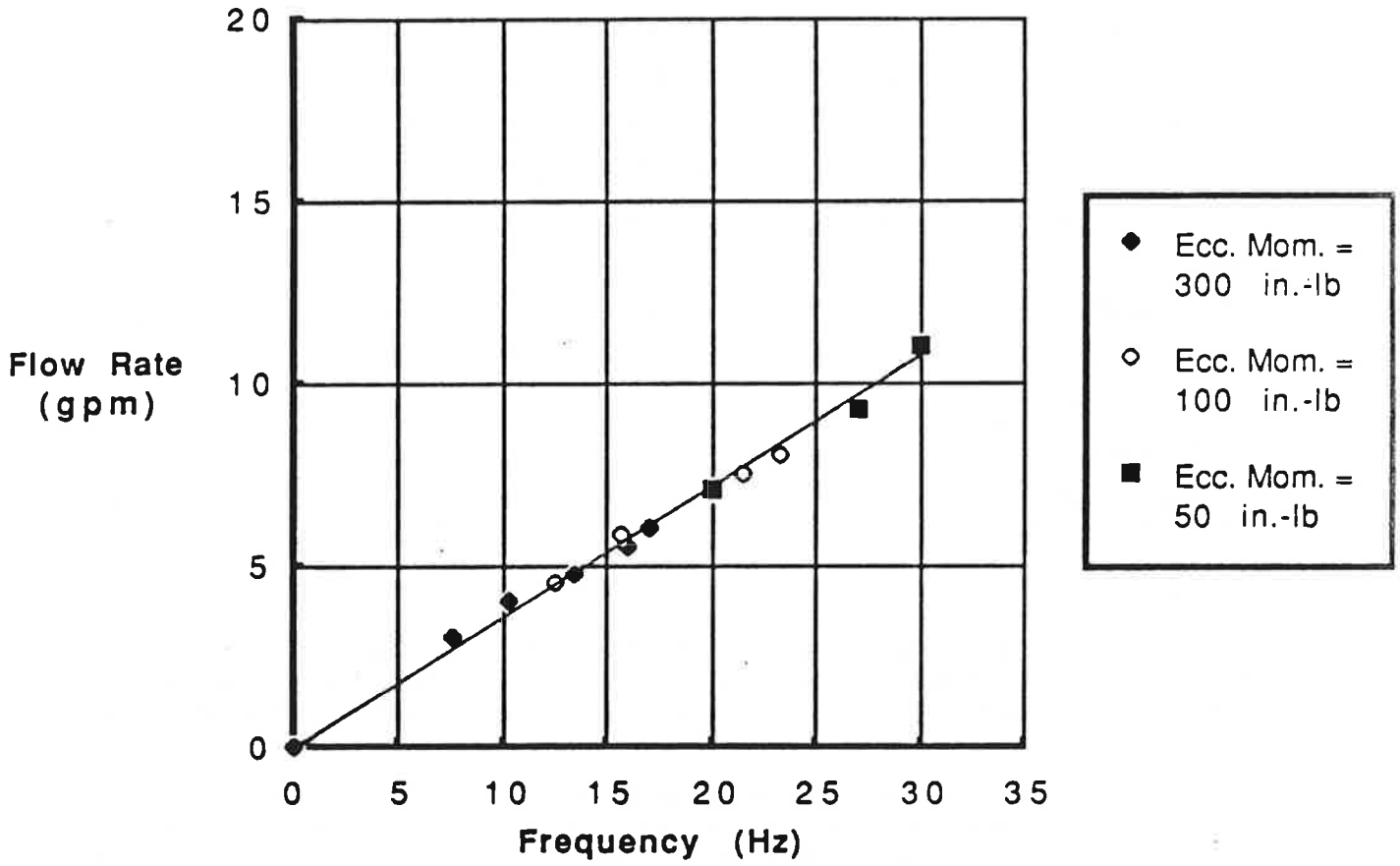

G.1. Flow Rate Vs. Frequency for Laboratory Vibro-Driver

Table G.1. Calibration Constants for Pile Strain Gage Bridges, Pressure Transducers and Toe Load Cell

Instrument	Date of Calibration Test			
	12/21/86	8/4/87	10/21/87	2/27/88
SG Level 1	62,101	63,910	63,810	-
SG Level 2	61,177	62,050	61,690	-
SG Level 3	61,223	60,890	61,212	-
SG Level 4	62,239	62,850	61,969	-
SG Level 5	61,661	62,290	61,146	-
SG Level 6	63,624	64,100	62,736	-
SG Level 7	63,931	62,440	60,431	-
Toe Load Cell	14,297	14,530	14,237	-
Top Total Pressure Cell	45.35	41.60	-	38.40
Bottom Total Pressure Cell	35.18	29.30	-	29.32
Bottom Pore Pressure Cell	42.74	38.80	-	38.80

Notes:

1. Calibration constants for SG (strain gage) and Load Cell instruments are expressed in pounds per millivolt output per volt of excitation. Calibration constants for Pressure Cell Instruments are expressed in psi per millivolt output per volt of excitation.

2. Because of the damage inflicted on the pile head using the fixed attachment fixture between the vibro-driver and the pile head, which occurred between the 12/21/86 calibration and the 8/4/87 calibration, the strain gage circuits (SG) and pressure cells had to be rewired. Differences in calibration constants between the first two calibrations reflect the difference in resistance due to changed wire lengths required by the rewiring.

3. In the calibration tests and the record tests bridge completion in all circuits except the Toe Load Cell was accomplished by means of steel-mounted dummy gages placed on the side of the LVLPSC. The SG circuits were full-bridge circuits, with the dummy gages in the arms of the bridge opposite the active gages; the Pressure Cell circuits were half-bridge circuits, with the dummy gage in an arm of the bridge adjacent to the active gage to provide temperature compensation. The remaining half bridge consisted of precision resistors placed adjacent to the data acquisition devices.

The calibration process was as follows: The pile was placed in a compression loading device (a wide-flange steel section configured to rest on the tips of its flanges on the floor, with reaction plates welded on its ends). A hydraulic jack situated at the head of the pile then applied a compression load of 45,000 lbs, which was then released. This process was repeated from three to five times, in order to exercise the pile and mitigate the effects of residual stresses from manufacture and welding. The pile was then loaded in increments to 41,000 lb, and each strain gage bridge was read using the static data acquisition system and bridge completion circuit that was used in the chamber tests, along with the Lebow load cell, which was placed at the head of the pile, between the pile and the jack, and the power supply. A swivel-head device was placed between the jack and the load cell to minimize moments applied to the pile during calibration. The pile was not calibrated in tension. It was assumed that the calibration constants determined from compression loading also applied to tension (uplift) loading.

The lateral pore water and total pressure transducers were also calibrated statically, while the pile was unloaded. The calibration consisted of a fluid pressure test, in which a small cylindrical water reservoir was clamped to the pile directly over the transducer being tested. The water in the calibration cylinder communicated directly with the sensing face of each transducer. [The pore water pressure transducers had been saturated prior to this time.] Pressure was applied to the water column by an air-over-water device in a triaxial test panel and read by means of a calibrated pressure transducer in the triaxial panel. The calibration procedure consisted of exercising the lateral pressure transducer three to five times to a pressure of 60 psi and releasing the pressure. Records of pressure vs. pile transducer output were then made incrementally during loading and unloading of the transducer.

Essentially no zero shift or hysteresis was observed in either the pile axial strain gage or lateral pressure transducer output during any of the calibrations. The calibration constants that were obtained in each of the calibration tests are shown in Table G.1, and graphical displays for the 8/4/87 calibrations, which were used in the reduction of all test data, are shown in Figs. G.3 - G.13.

Dynamic Calibration for Magnitude and Phase of Toe Acceleration and Load

Because of the complex structure of the toe load cell and the fact that the piezoelectric accelerometers used in the tests are known to experience phase shifts, special calibration studies, described in this section, were conducted.

Amplitude of Toe Acceleration. First, as depicted in Fig. G.14, the test pile was freely suspended in a horizontal position, and the pile-head accelerometers were remounted on the wall of the pile at the level of the toe accelerometer. The pile was then struck lightly at the head, as indicated in Fig. G.14., to simulate blows from the impact hammer. This test, which produced a standing wave in the pile having a frequency of approximately 500 Hz, was conducted to ascertain whether the magnitude of the acceleration indicated by the high-g accelerometer, mounted atop the toe load cell, was equivalent to the actual acceleration in the wall of the pile at the toe during impact driving. Some doubt existed regarding the correspondence of the acceleration indicated by the toe accelerometer during impact driving to the true acceleration of the pile toe because the toe load cell itself is flexible and can potentially magnify pile accelerations at high frequencies. A comparison of the time history records of the two types of accelerometers is shown in the upper trace of Fig. G.15. The high-g toe accelerometer, as mounted, gave peak accelerations that were consistently higher than the average of

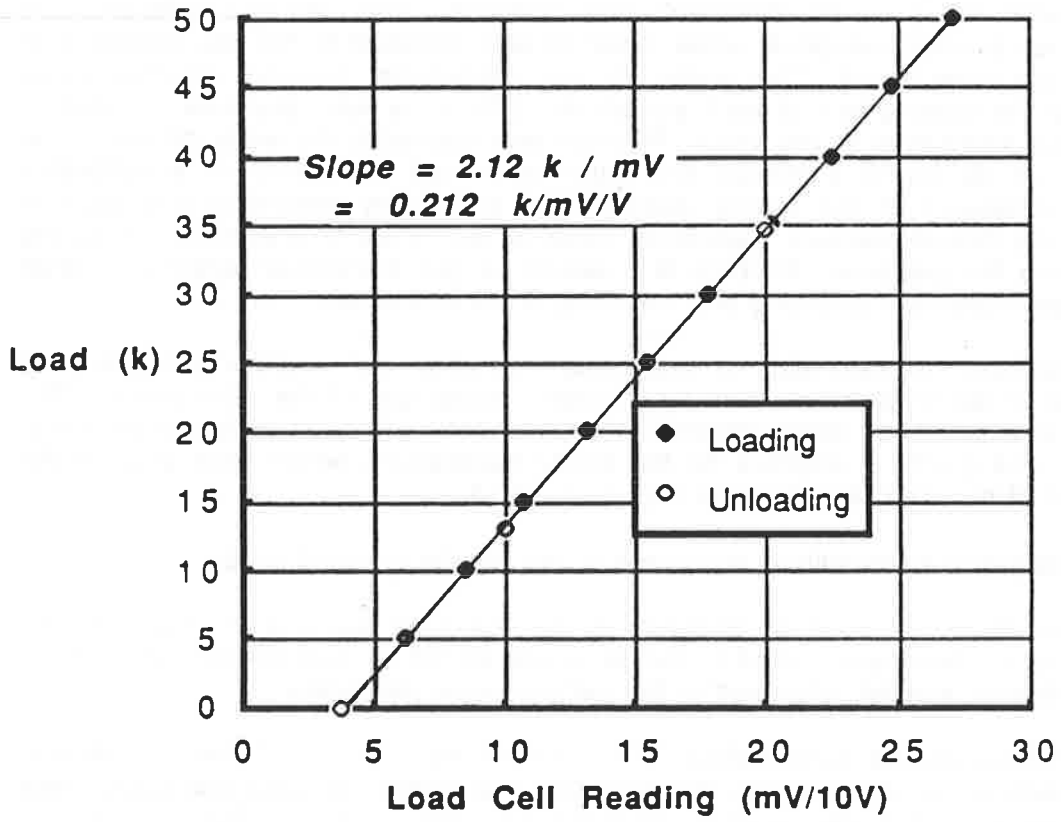

Fig. G. 2. Applied Load Vs. Load Cell Reading
(Lebow Load Cell Read Through HP 3497A/HP-85 Data Acquisition System)

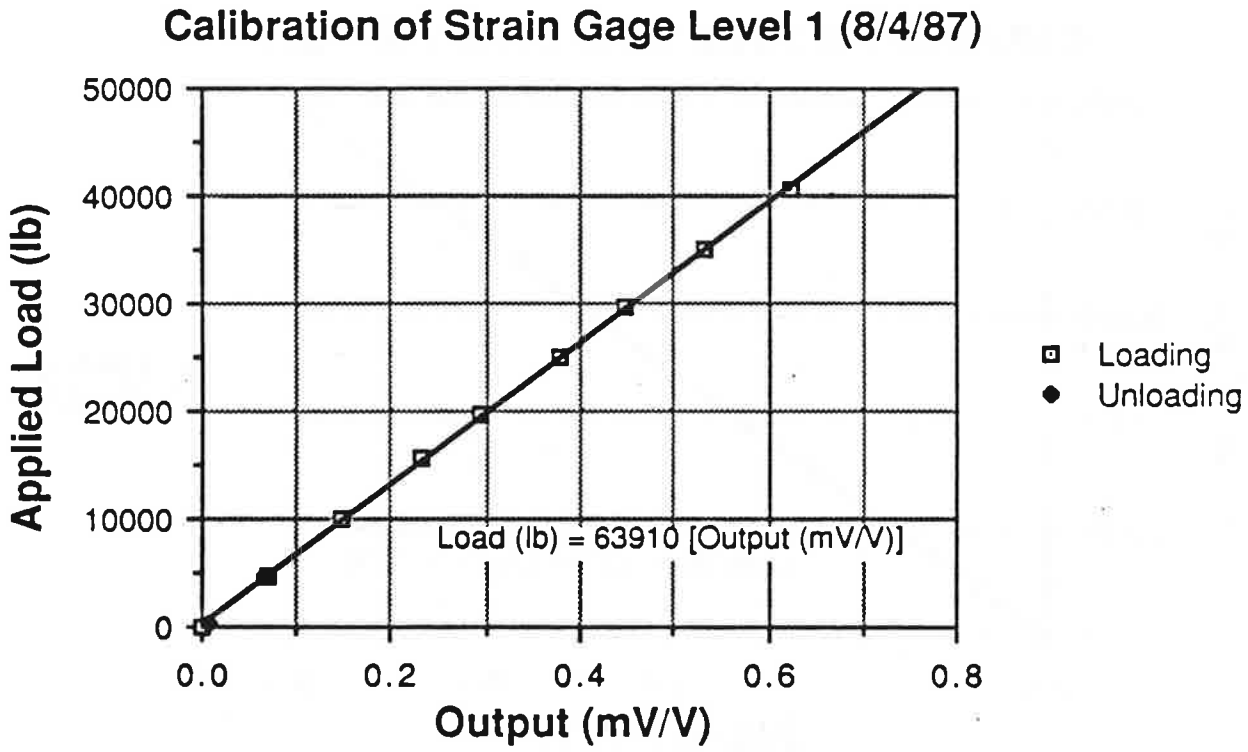

Fig. G.3. Load Vs. Output, SG Level 1 (8/4/87)

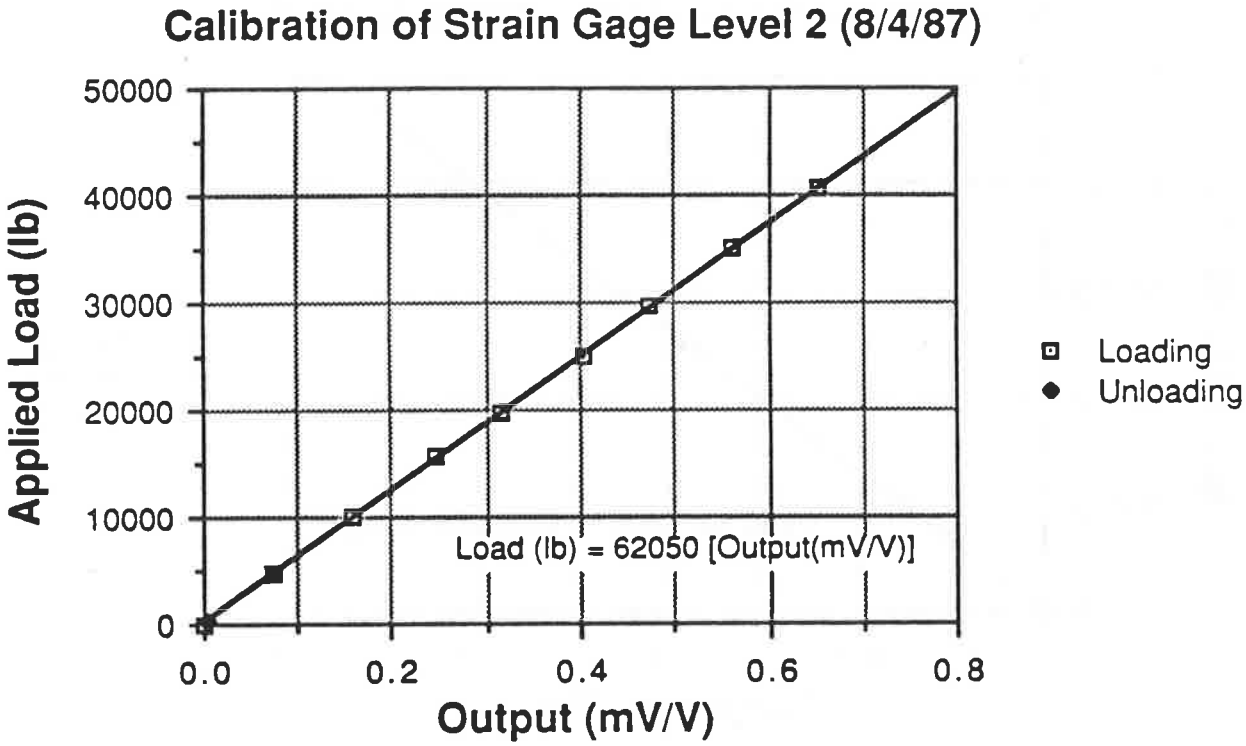

4. Load Vs. Output, SG Level 2 (8/4/87)

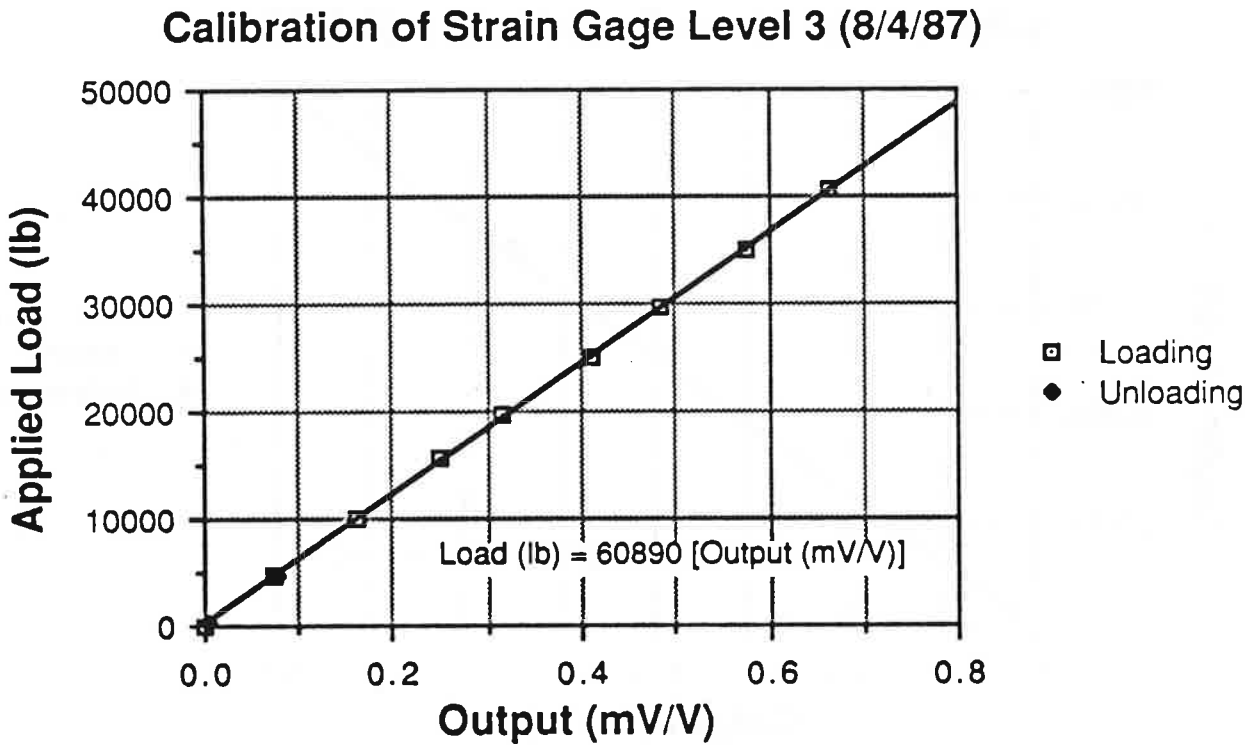

Fig. G.5. Load Vs. Output, SG Level 3 (8/4/87)

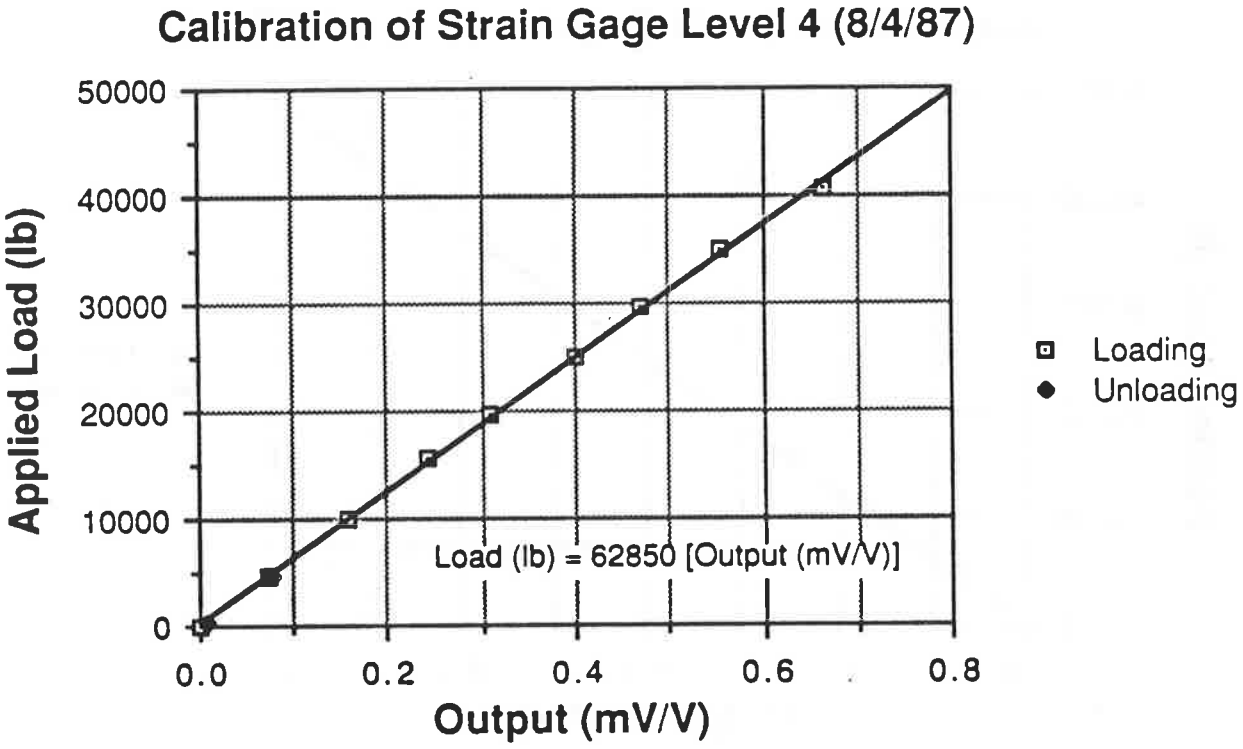

Fig. G.6. Load Vs. Output, SG Level 4 (8/4/87)

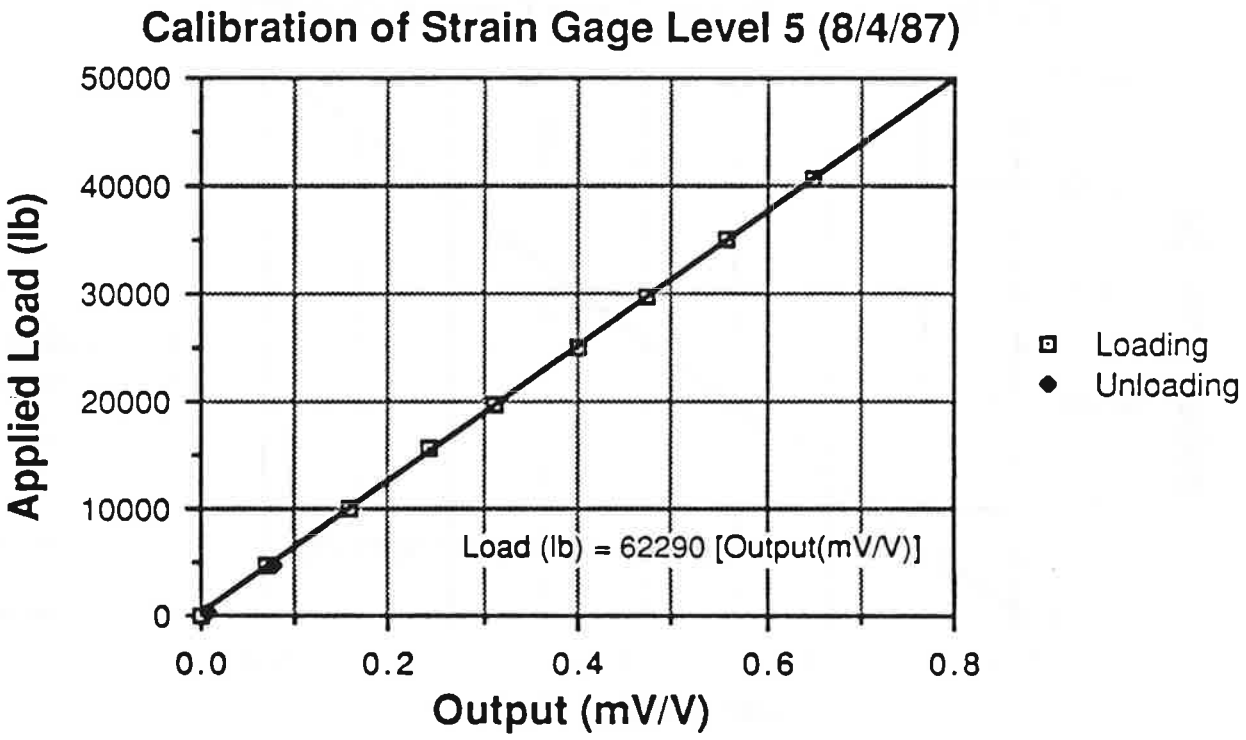

Fig. G.7. Load Vs. Output, SG Level 5 (8/4/87)

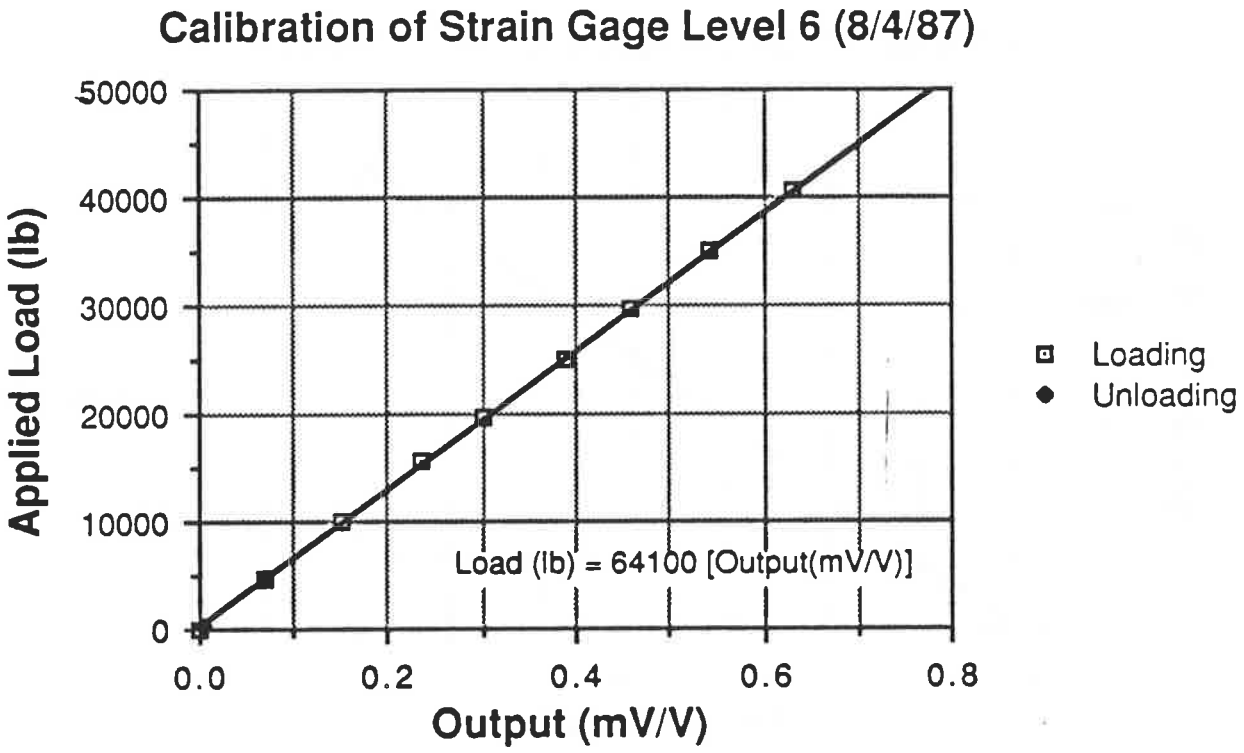

Fig. G.8. Load Vs. Output, SG Level 6 (8/4/87)

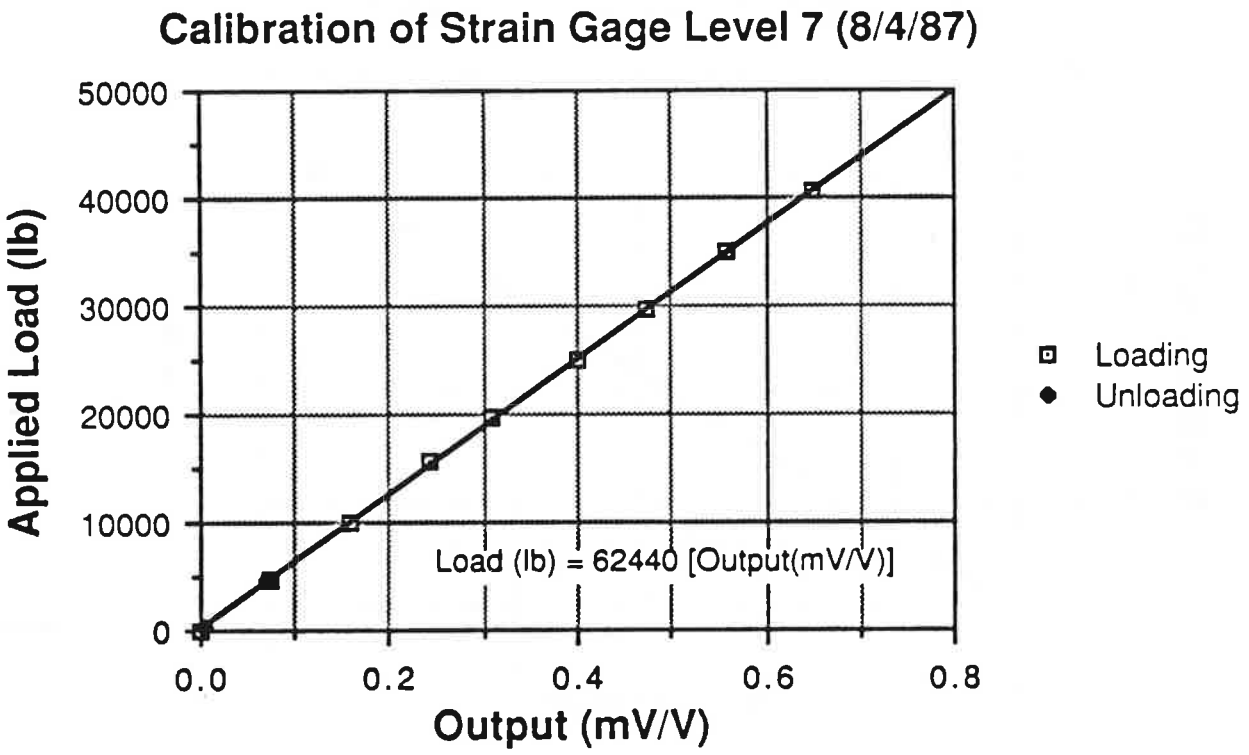

Fig. G.9. Load Vs. Output, SG Level 7 (8/4/87)

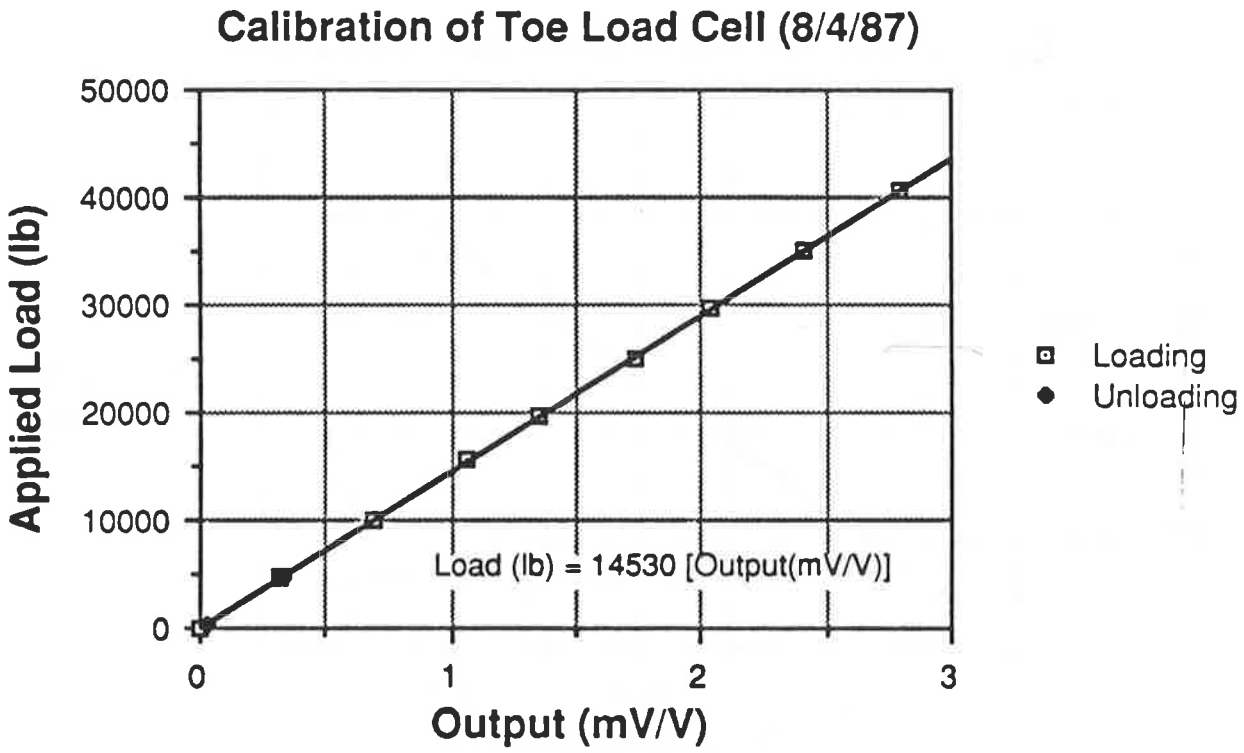

Fig. G. 10. Applied Load (Lebow Load Cell) Vs. Pile Toe Load Cell Output (8/4/87)

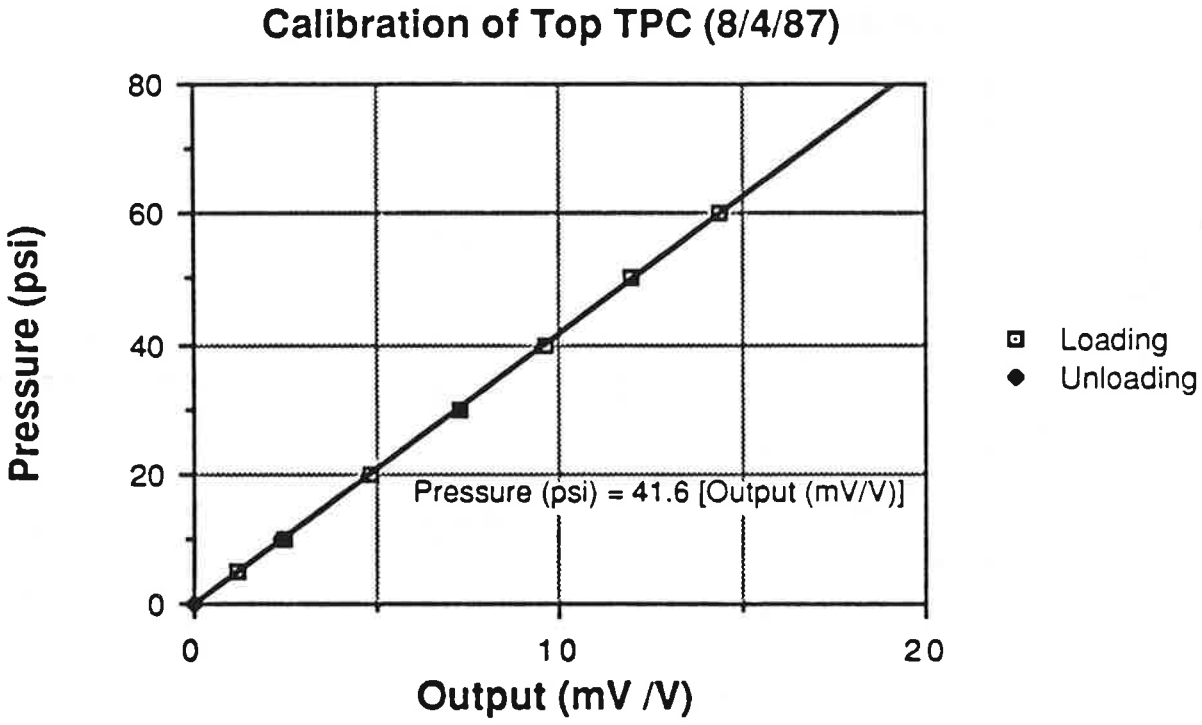

Fig. G. 11. Applied Pressure Vs. Top Total Pressure Cell Output (8/4/87)

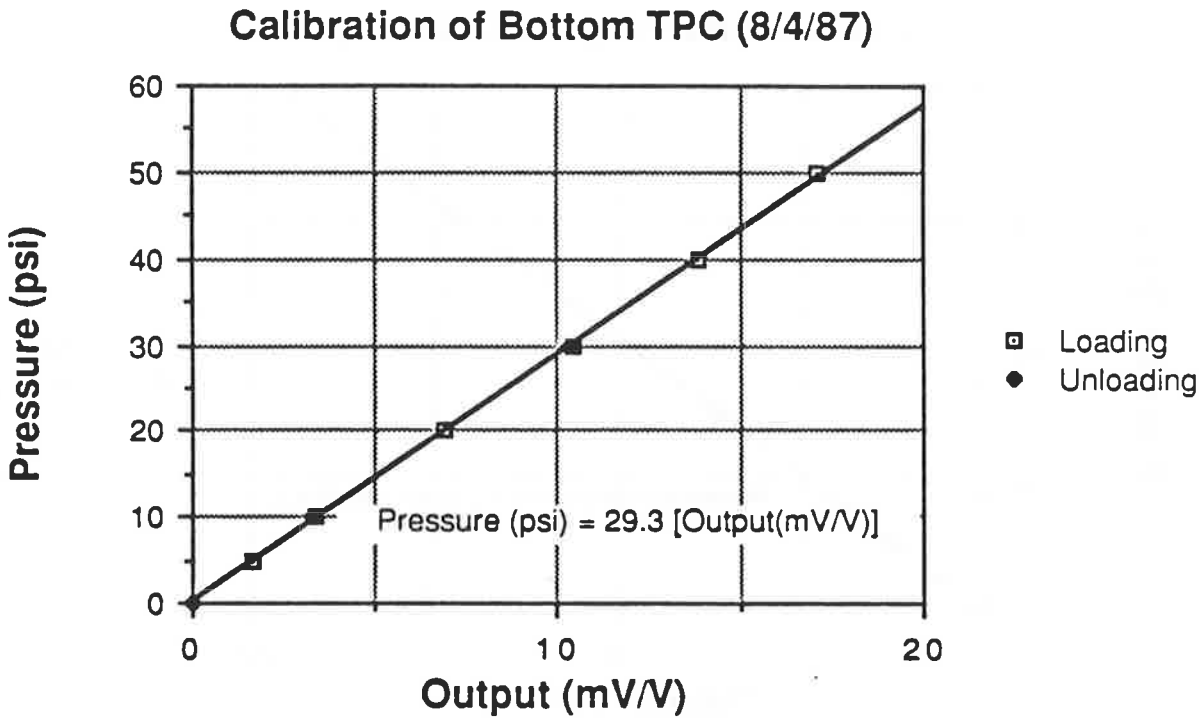

Fig. G. 12. Applied Pressure Vs. Bottom Total Pressure Cell Output (8/4/87)

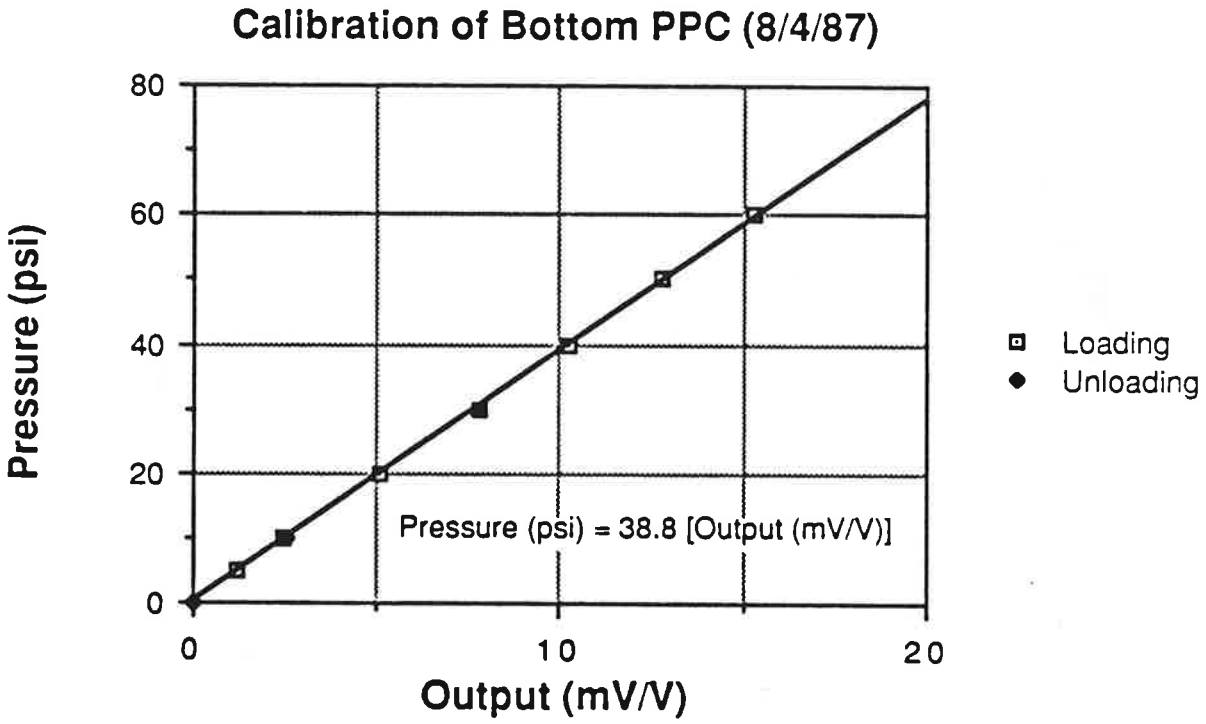

Fig. G. 13. Applied Pressure Vs. Bottom Pore Pressure Cell Output (8/4/87)

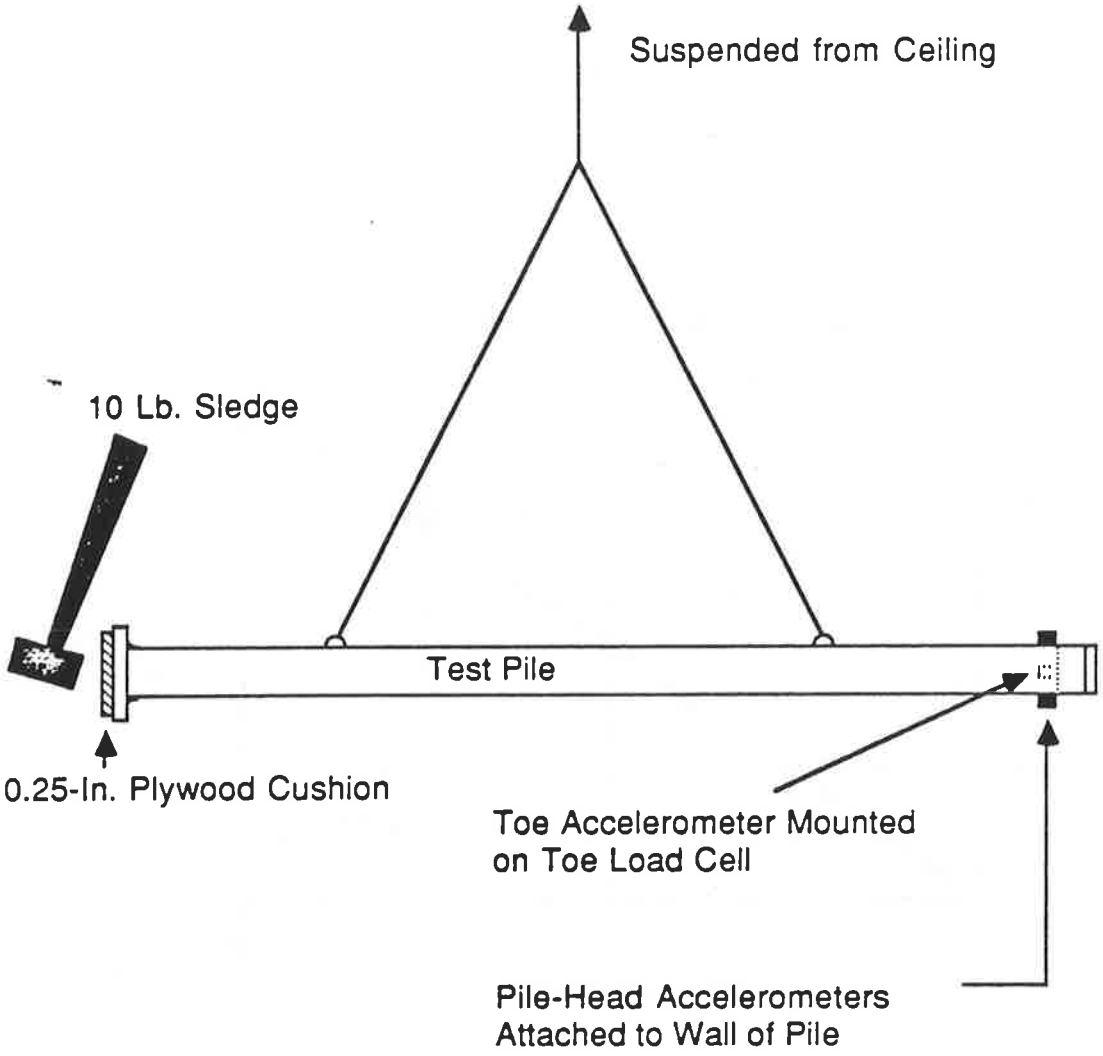

Data Analyzed for Average of Five Consecutive Blows of Sledge

Correlation Factor for Toe Accelerometer = 0.76
(Multiplication Factor Used in Reduction of Data for
Toe Accelerometer)

Fig. G. 14. Schematic of Calibration Test For Toe Acceleration Magnitude

those measured on the pile wall. A calibration factor (multiplier) of 0.76 for the toe accelerometer was found to be necessary to bring that accelerometer into approximate compliance with the wall accelerometers, as indicated in the lower trace of Fig. G.15. That factor was used to correct all of the toe acceleration data for the impact, restrike and vibro-driving tests.

Phase Between Head and Toe Accelerations. Because piezoelectric accelerometer circuits can experience phase shifts, particularly when employed using electronic averaging circuits, as was done in the tests reported here, it was also decided to determine the phase between the low-g pile-head accelerometers and the low-g pile-toe accelerometer that were acquired during vibratory installation. This particular phase shift is important because the toe and head acceleration (and force) information was used to determine unit load transfer relationships during vibrational installation. Since the true phase is known to be approximately 2.9° at 20 Hz based on the known distance between the head and toe instruments and the wavespeed of 16,800 ft/sec for steel, any phase difference in excess of that value would be considered to be due to electronic effects and not to physical effects in the pile. Therefore, 2.9° was subtracted from the phase measured in this test to obtain a phase correction for toe acceleration data during vibration. In the data reduction procedures the time history for the toe acceleration was then shifted relative to the head acceleration by that amount.

The testing arrangement is shown in Fig. G.16., in which an available 4 Hz (nominal) vibrator was used to excite the pile. Time histories of both the pile-head (average) and pile-toe accelerometers are shown in Fig. G.17, and the corresponding phase and magnitude spectra are shown in Fig. G.18. At 3.9 Hz, the phase is 5°. At 20 Hz the phase is then 25.6°, such that the toe accelerometer data must be shifted forward in time 22.7° relative to the recorded position in the time domain at a frequency of 20 Hz (that is, 3.15 msec).

No formal assessment was made of the phase shift in acceleration at the toe during impact driving., since such shifts were not needed in the data analysis.

Phase Between Head and Toe Forces. A similar concern existed regarding potential phase relations in the forces measured at the head and toe. Therefore, a third dynamic calibration was employed in which the pile was impacted with a small falling weight while standing in the vertical position, as shown in Fig. G.19. The resulting time histories are shown in Fig. G.20, and the phase relation from spectral analysis of the average of seven blows is shown in Fig. G.21. In this test the predominant frequency was about 850 Hz, at which a phase shift of 39.5° is observed. Transforming this phase shift to the corresponding phase shift at 20 Hz, one arrives at (20/850) (39.5) = 1°, which is insignificant. Consequently, no phase corrections were made for toe force.

Procedure for Handling Phase Between Velocity and Force at Head or Toe. No formal calibrations were made of the phase between force and acceleration at either the head or the toe. When the integrated acceleration (velocity) acquired during each of the chamber tests was multiplied by pile impedance at either the head or the toe and the resulting time histories compared with the corresponding measured force time histories during the initial part of an impact blow, however, the resulting curves did not exactly overlay each other (even after the toe acceleration had been shifted relative to head acceleration by 22.7°), indicating that a small electronic phase shift existed between force and acceleration at the toe and head levels. This shift was accounted for in the development of pile force and velocity relations for display in the report and for comparisons with the wave equation solutions for the impact and restrike tests by manually

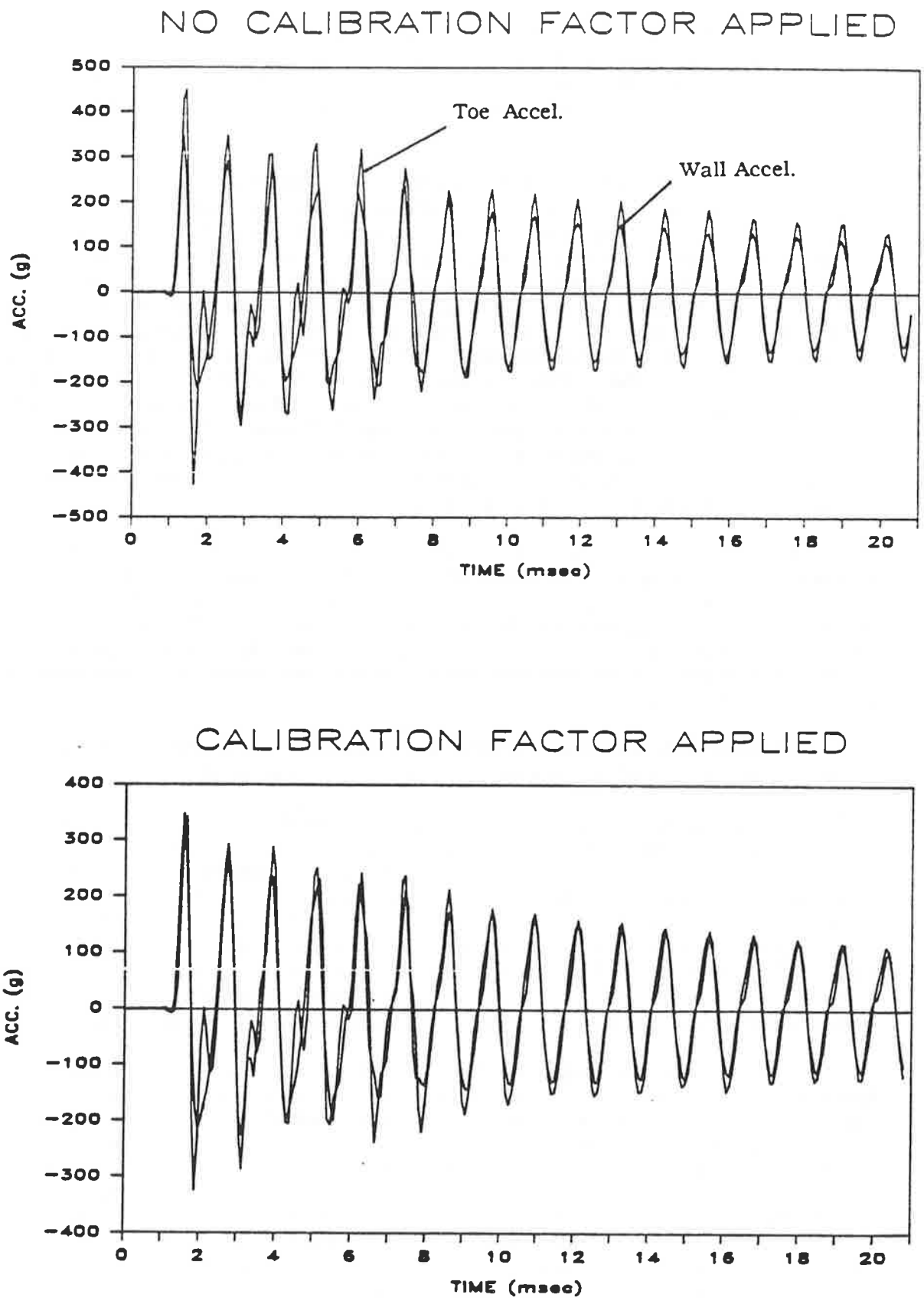

Fig. G. 15. Time Histories of Pile Wall (Average) and Toe Load CellAcceleration ; Uncorrected and Corrected

shifting the velocity time histories so that their initial branches overlaid the initial branches of the force time histories, as stress wave theory requires. This shift, in terms of time, was noted, and a corresponding shift was made in the integrated acceleration records for purposes of computing energy (which requires that velocity and force be multiplied together timewise and integrated across time). No corresponding shifts were made in the vibratory test data because of the low frequencies involved (approximately 20 Hz).

Investigation of Cross-Sensitivity of Lateral Pressure Transducers

Since the total and pore water pressure transducers on the piles contain thin-plate sensing faces that are not completely isolated from the pile wall, it is possible that the stress wave in the pile will cause a false reading in a pressure transducer as it passes the transducer's location. The design of the transducer was such that the active gage on the sensing face was a linear gage that was oriented with its grid perpendicular to the direction of wave motion in the pile in order to minimize this "cross-sensitivity" problem. To check the cross-sensitivity, the following scheme was used. Following Test 19, on Aug. 25, 1987, while the chamber was still pressurized and saturated, the pile was struck with five blows of the impact hammer, and the pore water pressure was monitored. A maximum excursion of pressure of about 0.9 psi was recorded during each of these blows. The chamber was then drained of all water, the pile was struck again and the pore water pressure time history recorded. The results of this striking were inconsistent, but indicated pore water pressures induced during driving never exceeded 0.2 psi, with an average of under 0.1 psi. One would expect that the readings in the drained soil would be essentially zero, although some small positive value (perhaps 0.1 psi) might be recorded due to compression of air in the soil pores. Based on this study, it was decided not to correct pore water pressure readings that were acquired during either impact driving or vibro-driving. Since the total pressure transducers were of similar design, it was also considered reasonable not to correct their readings, either.

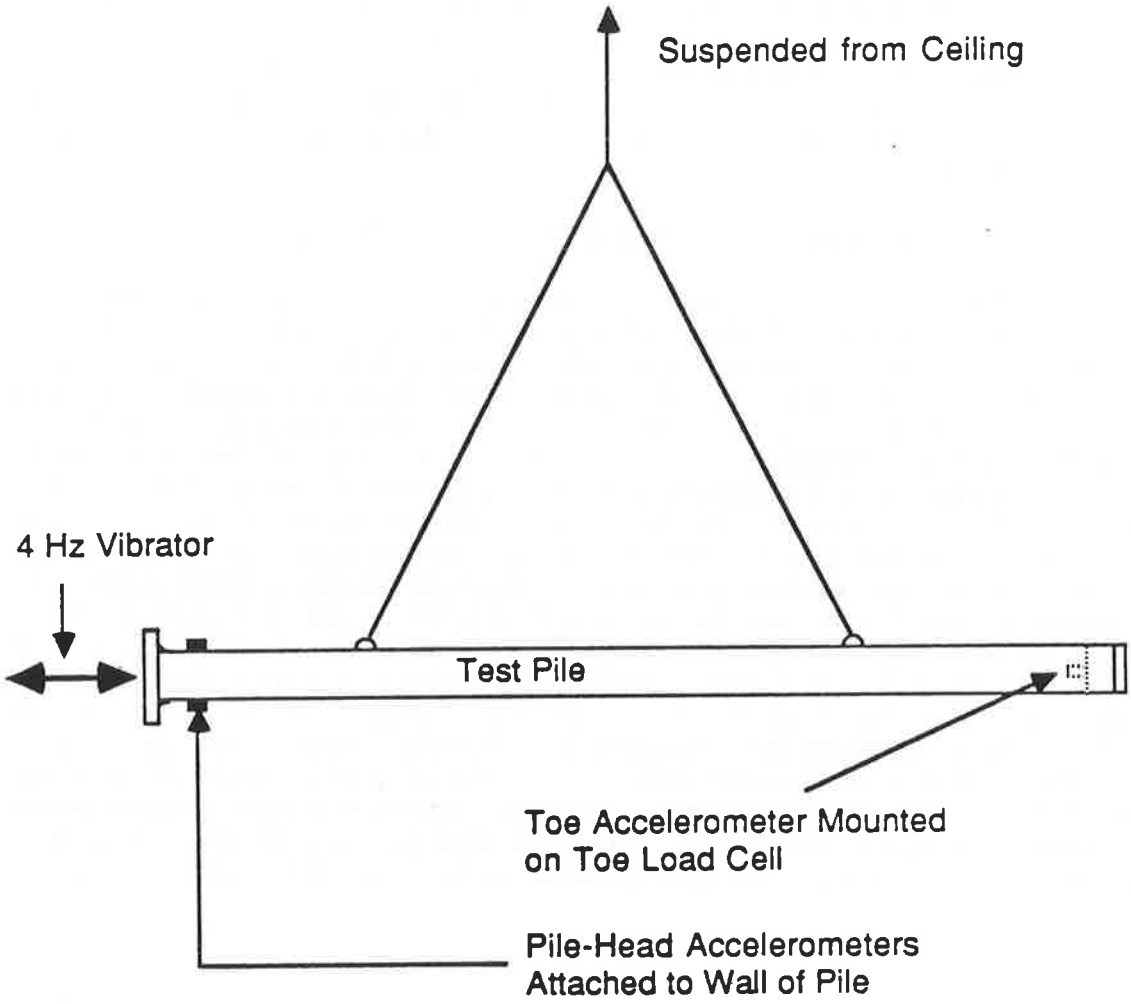

Fig. G. 16. Schematic of Calibration Test for Phase Lag Between Indicated Head and Toe Accelerations

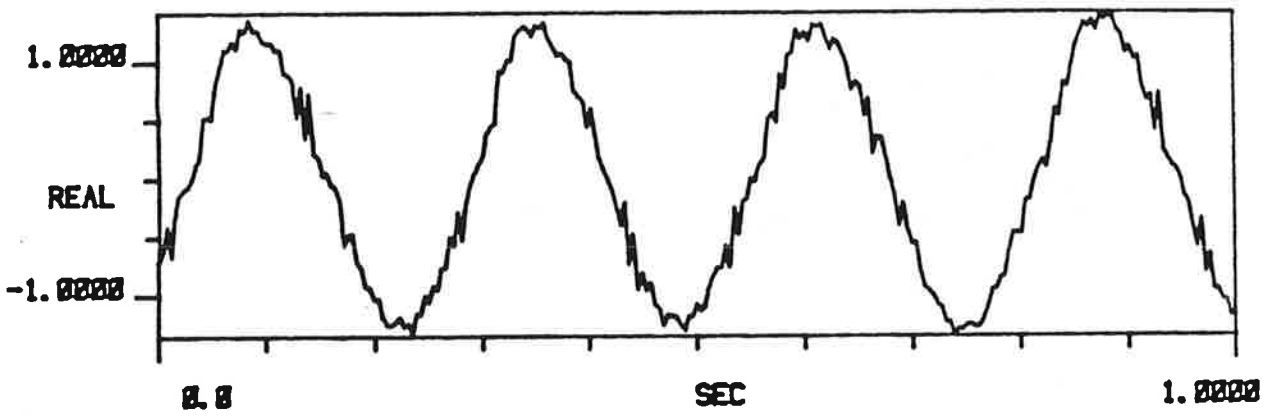

Pile-Head Acceleration (g)
(Unfiltered)

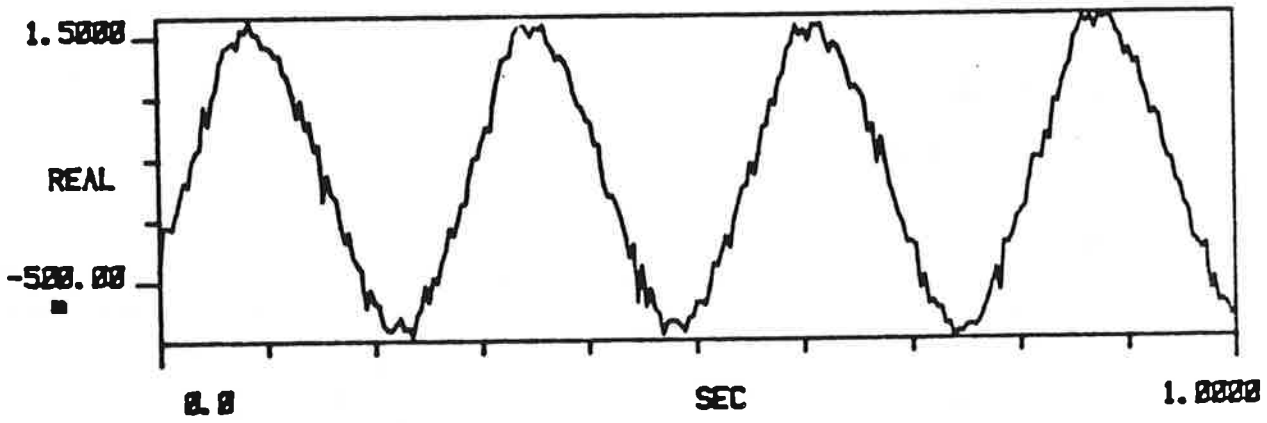

Pile-Toe Acceleration (g)
(Unfiltered)

Fig. G. 17. Typical Time Histories of Pile-Head (Average) and Pile-Toe Accelerations; Phase Calibration Test

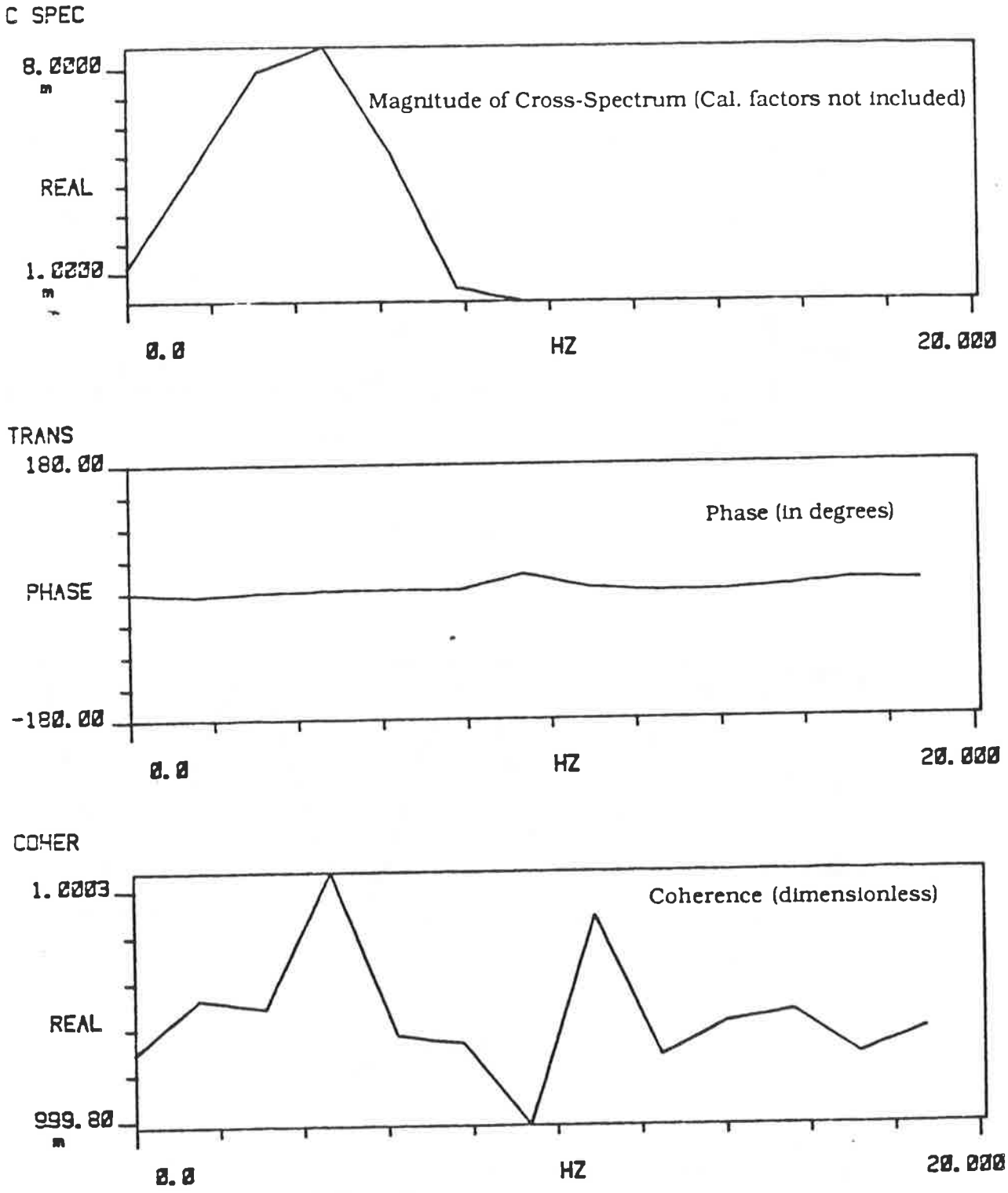

Fig. G. 18. Spectral Magnitude and Phase Relationships Between Head (Average) and Toe Accelerometers; Phase Calibration Test

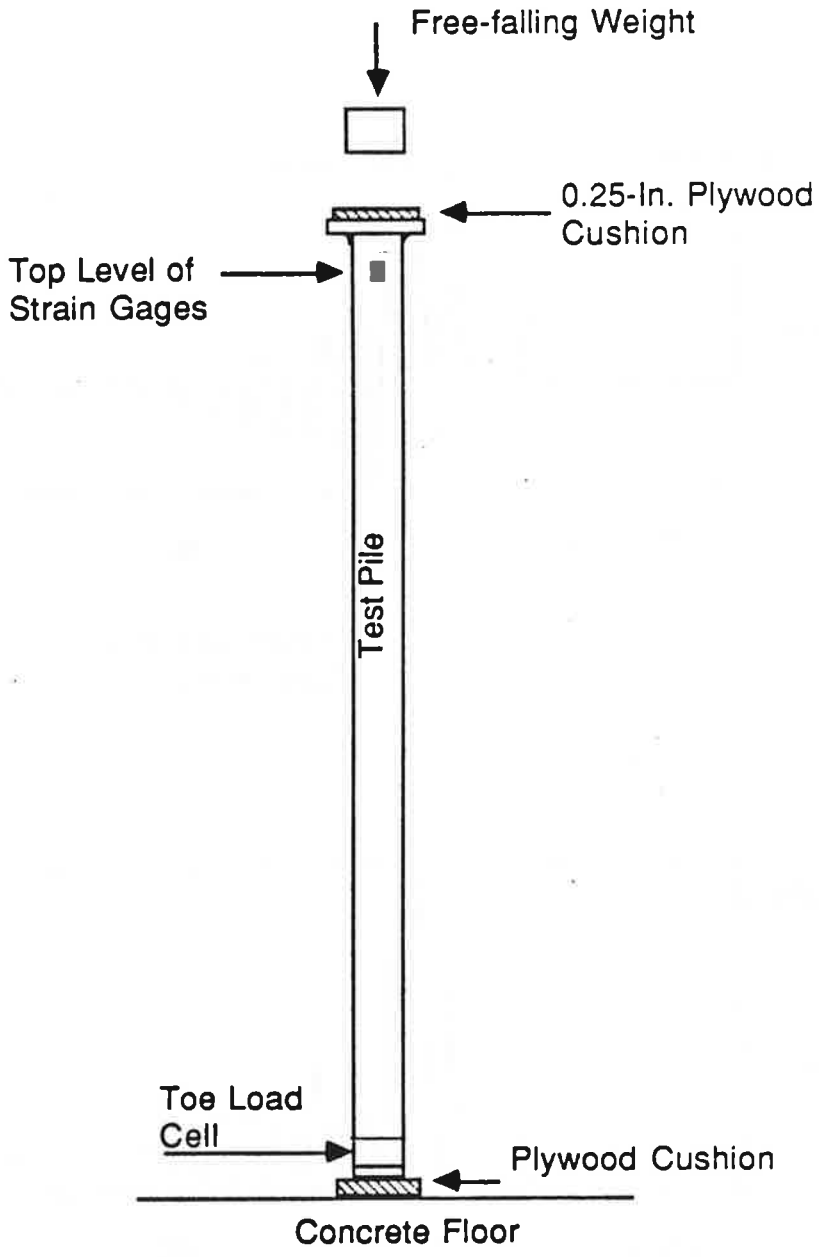

Phase Determined from Spectrum Analysis of Average of Seven Consecutive Blows from Falling Weight

Fig. G. 19. Schematic of Calibration Test for Phase Lag Between Head and Toe Forces

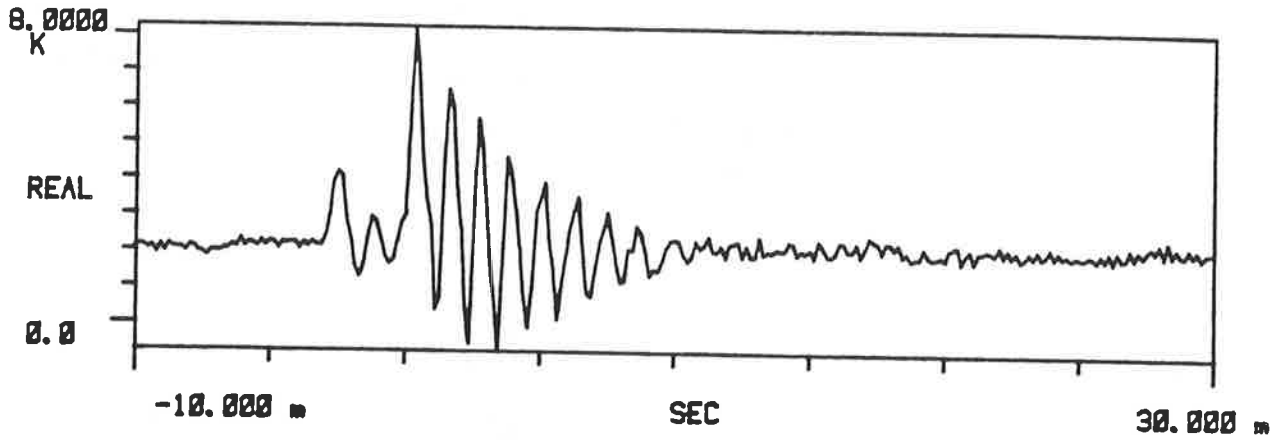

Pile-Head Force
(Unfiltered)

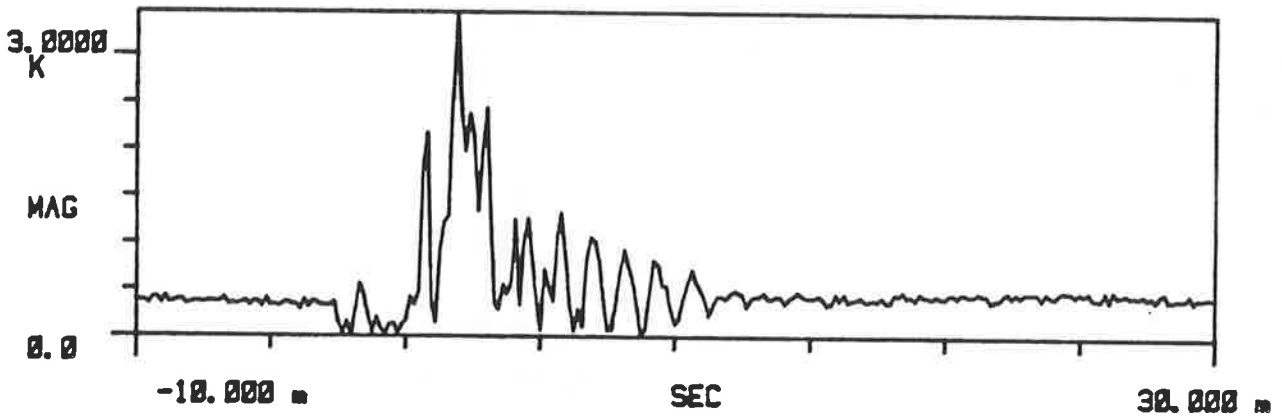

Pile-Toe Force
(Unfiltered)

Fig. G. 20. TypicalTime Histories of Pile-Head and Pile-Toe Forces; Phase Calibration Test

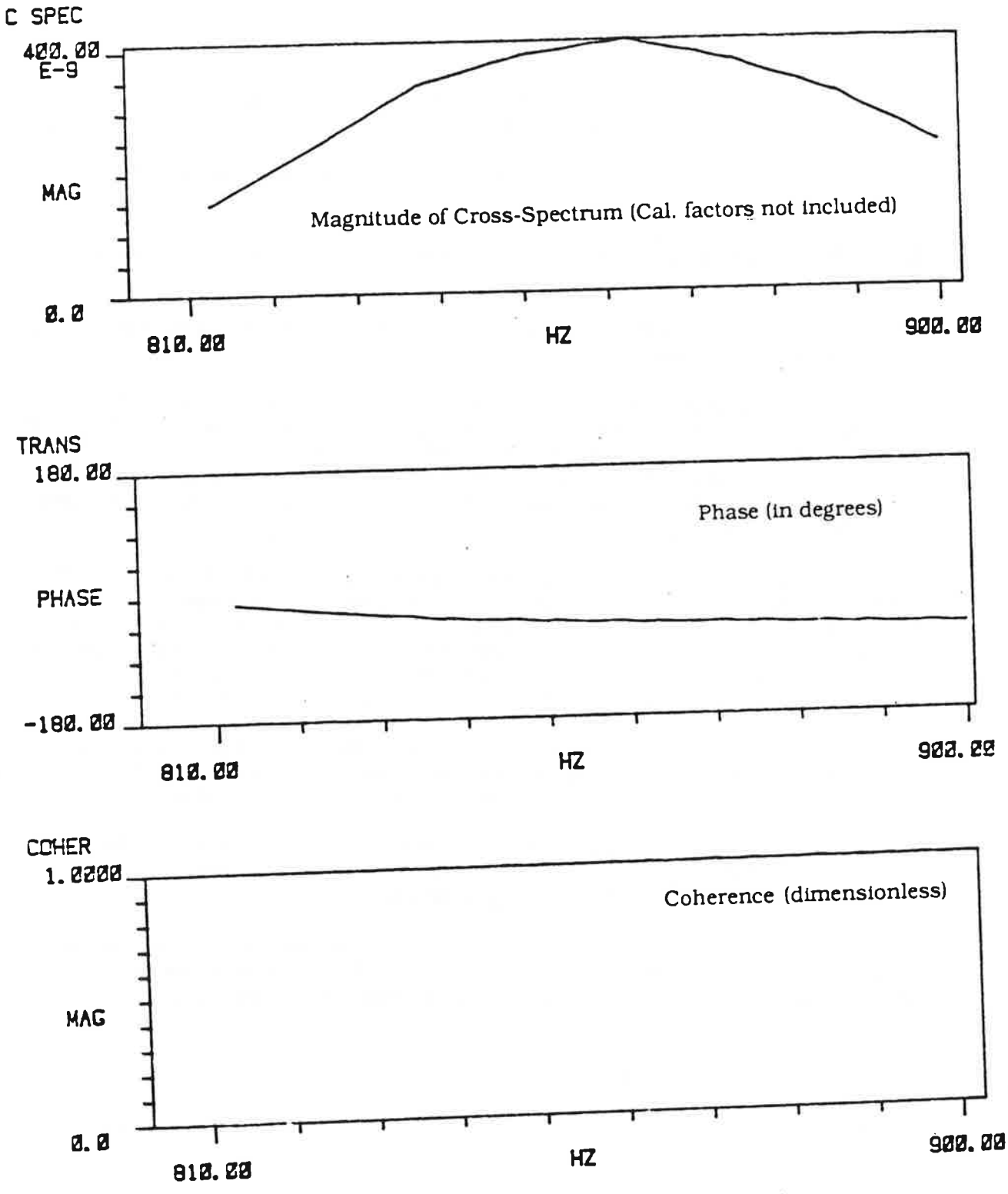

Fig. G. 21. Spectral Magnitude and Phase Relationships Between Head and Toe Forces; Phase Calibration Test

APPENDIX H

Computation of Pile Energy and Power and Methodology for Developing Dynamic Unit Load Transfer Curves

This appendix describes certain procedures that were employed in reducing dynamic data.

Pile-Head and Pile-Toe Energy and Power from Analog Force and Acceleration Time Histories

Energy. The following procedure was used in pile-head and pile-toe energy computations (impact events):

1. Digital time histories were developed from electronically filtered analog records of head and toe force and acceleration for several consecutive blows (10, if availble; less if 10 blows were not acquired, as in some restrike events), using a digitization time step of 78 μsec over a time window of 40 msec to ensure that the whole blow was captured. The average records for these blows were then obtained by averaging values for each time step.

2. A segment of each average digitized signal, containing the main portion of the signal to be processed, was selected by first locating the peak value in the strain gage (force) record and then including the previous 1.5 msec and the subsequent 20 msec, for a total of 21.5 msec. This window ensures that adequate record lengths are utilized for energy computations. Separate windows were employed for the head and toe records, and identical windows were used for the force and acceleration data at one location.

3. Any zero offset in the pile-head strain gage signal was removed by subtracting the average of the 50 discrete force values immediately preceding the time window. No zero offset correction was made in the pile-toe force readings.

4. The pile-head and toe force and accelerometer signals were filtered using electronic filters during recording. Those filters had a 1 KHz rolloff frequency. No further filtering was employed during signal processing.

5. Next, a correction was applied to the filtered pile-head acceleration signal in order to ensure that the conditions of zero velocity and displacement equal to the observed pile set are met at the end of the time window considered in the analysis. This correction takes the form:

$$a_m(t) = a(t) - (b + c\ t)$$

where

$a_m(t)$ = corrected acceleration signal;

$a(t)$ = uncorrected acceleration signal;

$b = a_{av} - 0.5\ c\ T$;

$c = 12/T^2\ \{ S / T - v_{av} + 0.5\ a_{av}\ T \}$;

S = permanent pile set per blow in range of interest;

T = total period of the signal (21.5 millisec);

a_{av} = average of acceleration signal over $T = \{1 /T \} \int_0^T a(t)\ dt$; and

v_{av} = average of velocity signal, obained from integration of original signal over $T = \{ 1 / T \} \int_0^T v(t)\ dt$, where $v(t) = \int_0^t a(t)\ dt$.

A similar correction was made to the toe accelerometer signal.

6. Next, the blow energy is computed as follows, where $a_m(t)$ is the corrected pile-head or toe acceleration signal and $F_m(t)$ is the corrected pile-head or toe force signal:

(a) Compute velocity for each time step (time t) by

$$v_m(t) = \int_0^t a_m(t)\ dt$$

using the trapezoidal rule for numerical evaluation. (Note: This step leads to the velocity time histories that have been reported. The force time histories are simply the graphs of corrected force versus time.)

(b) Compute the product $E(t) = v_m(t)\ F_m(t)$.

(c) Compute pile-head energy E_T from $E_T = \Delta t\ \Sigma_{over\ T}\ E(t)$, where Δt is the integration time step (normally 78 μsec).

Power. Power computations for vibratory pile tests were made in a similar manner, except that uncorrected digitized force and acceleration time history records were used, and a time window (T) equivalent to 10 cycles of head or toe force were used in the computations. Mathematically, the power for a given time window T can be expressed as

$$P_T = T^{-1} \int_0^T v(t)\ F(t)\ dt = T^{-1} E_T,$$

where integration is conducted using the trapezoidal rule using a time increment of 0.98 msec (512 data points per integration).

Dynamic f-w and q-w Curves

The dynamic unit load transfer curves shown in Chapter 2 were determined from the digitized time histories of force and acceleration. Three to four cycles of load were selected from selected analog records, and the pile-head and pile-toe force records and the pile-head acceleration record were igitized (512 points for each record). The pile-head acceleration record was integrated once, as described above. If necessary, the resulting digitized velocity record was shifted one or two time steps so that the pile-head force and velocity records began to rise on the first cycle at the same time. The pile-head velocity record was then integrated again to obtain a pile-head displacement record $w_m(t)$ by

$$w_m(t) = \int_{t_1}^{t2} v_m(t)\ dt$$

using the trapezoidal rule for numerical evaluation and 512 time steps.

It was assumed that the pile, during vibratory installation, behaved as a rigid body, so that the value of $w_m(t)$ was assumed to apply all along the pile at any given instant of time. At this same instant of time the value of digitized toe force divided by toe area (12.57 square inches) was taken to be q(t). Corresponding values of $w_m(t)$ and q(t) were then graphed as unit load transfer curves that occurred during vibration.

The value of unit shaft resistance f(t) corresponding to w(t) was computed from the digitized head and toe force records ($Q_{head}(t)$ and $Q_{toe}(t)$], respectively) and the digitized head acceleration $a_m(t)$ record from

$$f(t) = [Q_{head}(t) - a_m(t)(W) - Q_{toe}(t)] \ / \text{ Shaft area of penetrating part of pile,}$$

where W = weight of the pile. The digitized function f(t), which represents the mean unit shaft resistance along the pile at time t, was then plotted versus $w_m(t)$.

It is noted that the dynamic f-w and q-w curves contain the effects of any residual stresses that may have been present during the period for which the curves were derived.

The beginning point of a plot was selected to occur at a time near the top of a stroke (pile-head in upmost position during a vibration cycle).

APPENDIX I

Sand Properties

This appendix describes laboratory tests that were used to characterize the properties of the soils tested in the pile testing chamber (the LVLPSC). Triaxial compression, interface shear, permeability and torsional resonant column tests were conducted in the laboratory for the San Jacinto River Sand (SJR) and Blasting Sand (BLS) in the medium dense and dense states. Although these tests do not necessarily represent the stress paths to which the sand was subjected in the LVLPSC, they provide appropriate index information on the mechanical properties of the sands selected for testing.

It was assumed that the most important characteristic of the grain-size distribution of the test sands was the fineness or coarseness of the sand, as measured by the effective grain size, d_{10}, and that grading (poorly graded versus well graded) was of lesser importance. Considering the number of variables that were investigated in the study and the limited resources that were available, the effect of soil grading was not investigated. All laboratory tests reported in this appendix, which represent the soil conditions in the test chamber, were specifically for poorly graded soils.

It was also assumed that the penetrations of piles of interest to transportation facility designers is in the order of 50 to 100 feet. In selecting effective pressures in the chamber tests, it was assumed that the ground stresses for such penetrations could be simulated within a reasonable approximation by applying a uniform, isotropic effective stress within the chamber equal to the ground stress that would occur at the middepth of the pile if K_o in the deposit being simulated were 1.0. Assuming that the water table (piezometric surface) is at the ground surface and using representative unit weights of sand (115 - 120 pcf), one arrives at the conclusion that the in-situ isotropic effective stress levels of interest are in the range of 10 to 20 psi. Most of the pile tests in the chamber were conducted with initial isotropic effective pressures of 10 and 20 psi. However, it was also realized that the insertion of the pile would increase the mean effective stress in the soil mass in the vicinity of the pile wall and that static loading could increase the level of mean effective stress below the pile toe considerably above the initial, in-situ value. Therefore, laboratory strength tests were conducted with isotropic, effective confining stresses of 10 to 50 psi. Analysis of the data in Appendices M and Q suggest that this confinement pressure range was appropriate, such that further, high-pressure laboratory soil testing was deemed unnecessary.

Several pile tests were conducted in the LVLPSC with $K_o = 0.5$ (anisotropic, initial, in-situ stresses in the soil), in which the 10 to 20 psi pressure range was maintained for the horizontal effective pressures; however, no corresponding laboratory strength tests were conducted under an anisotropic state of initial effective stress.

Grain-Size Distribution

Three grain-size distribution tests were conducted for each of the two test sands, and the average results are shown in Fig. I.1. For the San Jacinto River Sand the effective grain size, d_{10}, is 0.2 mm, and the coefficient of uniformity C_u is 1.74. From visual observations the typical shape of the grains was subrounded, and the soil is classified according to the Unified Soil Classification System as "SP," or a poorly graded

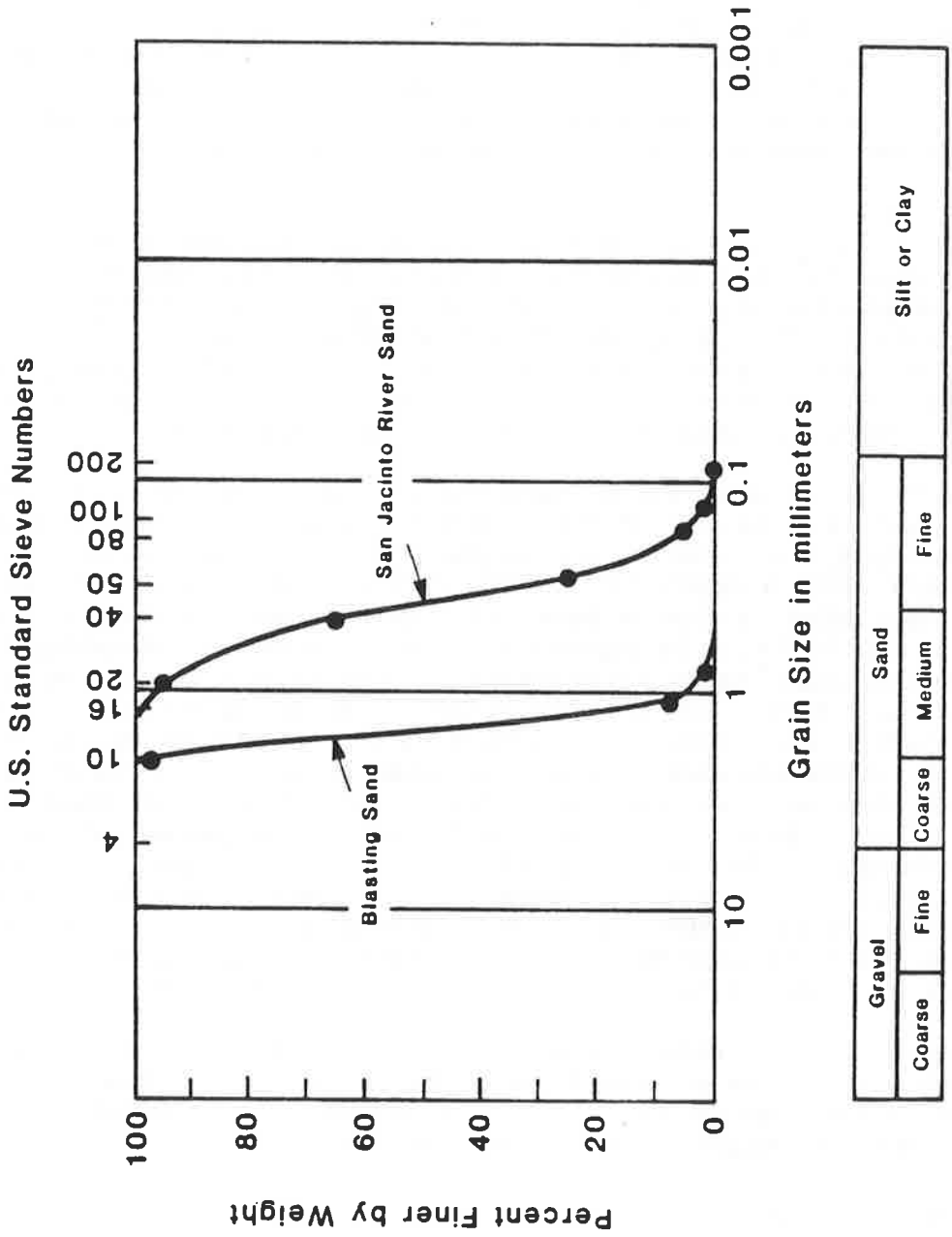

Fig. 1.1. Grain Size Distribution for Sands Selected for the Study

fine sand. For the Blasting Sand d_{10} = 1.2 mm, and C_u = 1.42. The grain shapes were angular to subangular, and the Unified classification is "SP," or a poorly graded coarse to medium sand. Both sands were siliceous in mineralogy, and both can be classified as "clean," since essentially no material finer than the No. 200 sieve size was present in either sand.

Minimum and Maximum Density

Volume-change characteristics of the sand are considered to be one of the main factors influencing the driveability and the behavior of the pile-soil system under load. The volume-change characteristics are complex functions of the effective stress state and initial density of the sand. It was also assumed that the relative density of most natural sand deposits into which piles will be vibrated will exceed 50%. For that reason it was decided to deposit the test soils in the LVLPSC at target relative densities of 60 and 85%. In order to determine the actual density required for the attainment of these values of relative density, it was necessary to conduct tests for minimum and maximum index density as defined by ASTM standards D 4253 and D 4254 (22). Each density index was obtained as an average of three independent test results on samples taken randomly from the stockpile of the test material. The maximum and minimum index densities for the San Jacinto River Sand were 110.4 and 94.2 pcf, respectively, (corresponding to a minimum void ratio of 0.50 and a maximum void ratio of 0.76), and the corresponding index densities for Blasting Sand were 102.6 and 90.2 pcf, respectively (corresponding to a minimum void ratio of 0.61 and a maximum void ratio of 0.83).

It was discovered during laboratory triaxial testing that, when either soil was deposited at a relative density of 60%, application of isotropic effective pressure of 10 to 20 psi produced an increase in relative density to approximately 65%. Therefore, while the soils were deposited , both in the chamber and in triaxial molds, at a relative density very near 60%, the actual relative density at the initiation of shearing in the laboratory tests on the soil or at the beginning of pile driving in the test chamber was approximately 65%. Reported relative densities in this appendix are for nominal relative density at deposition (60%), while the pile test results are reported in terms of the nominal relative density after pressurization (65%).

Permeability

Constant-head permeability tests were conducted on both soils deposited in the relative density range of interest. Tests were conducted by depositing oven-dry soil by raining through air into cylinders 3 inches in diameter by 6 inches high and then saturating the samples very slowly with deaired water by gravity to simulate the procedures that were used to deposit and saturate the sand in the LVLPSC. (Deposition procedures are reviewed in Appendix J.) Flow during the permeability test was from top to bottom of the specimens, parallel to the direction of the particle velocity vector during deposition. The results are reported in Table I.1 and represent steady-state flow rates. It is observed that the Blasting Sand (the coarser of the two test sands) is about twice as permeable as the San Jacinto River Sand.

Table I.1. Permeabilities of Test Sands

Sand	Relative Density (%)	Coefficient of Permeability (cm/sec)
San Jacinto River (fine)	91	0.9×10^{-2}
	64	1.0×10^{-2}
Blasting (medium to coarse)	88	2.1×10^{-2}
	60	2.3×10^{-2}

Triaxial Compression

Consolidated-undrained triaxial compression tests were conducted on saturated samples of dense (85% nominal relative density) and medium dense (60% nominal relative density, as deposited) SJR and BLS Sands. These tests were conducted to provide information on stress-strain properties and shear strength, as characterized by the angle of internal friction, of both sands. The samples were prepared by raining of oven-dry sand, as per the permeability tests. After gravity saturation (and verification of saturation by measurement of the B-parameter), the 1.5-inch-diameter by 3.0-inch-high specimens were consolidated isotropically and then loaded to failure by increasing the major (vertical) principal effective stress at a constant displacement rate of 0.23 mm/minute. During the application of load (principal stress difference), volume change was measured by recording the amount of water that flowed into or out of the specimen from a calibrated burette that communicated with the pores of the specimen.

The stress-strain and volume-strain curves are presented in Figs. I.2 - I.5. Volumetric changes are expressed as volumetric strain (change in volume / initial volume, as a per cent). The specimen of dense BLS Sand at an isotropic, effective confining pressure of 20 psi was subjected to two unloading cycles to determine the plastic strain and reloading modulus (Fig. I.5). While the specimen had only a small strain recovery, the reload modulus appeared to be reasonably constant with increasing value of plastic strain and to exceed by a factor of about two the modulus obtained upon initial loading. The same specimen was also tested to 16% axial strain to determine the large-strain residual shear strength, and the peak strength was found to be reduced by 15% at this value of major principal strain. A similar high-strain test was conducted on a dense specimen of SJR Sand (Fig. I.3), with the result that more high-strain degradation (peak strength reduced by 38% at 16% strain) was observed than in the BLS Sand. Both sands are seen to dilate consistently in the dense state under triaxial compression loading conditions.

The results for the medium dense sands (relative density of 60%, Figs. I.2 and I.4) indicate that the soils contract initially upon shearing, with the magnitude of contraction depending on the value of the confining pressure, and then dilate after shearing failure begins. The specimens of SJR Sand tended to dilate more than corresponding specimens of BLS Sand at this density state.

Graphs of mean effective normal stress versus principal stress difference ("p'-q diagrams") at peak principal stress difference are presented in Fig. I.6. The angle of internal friction ϕ can be derived from the slopes of these relations from the simple equation

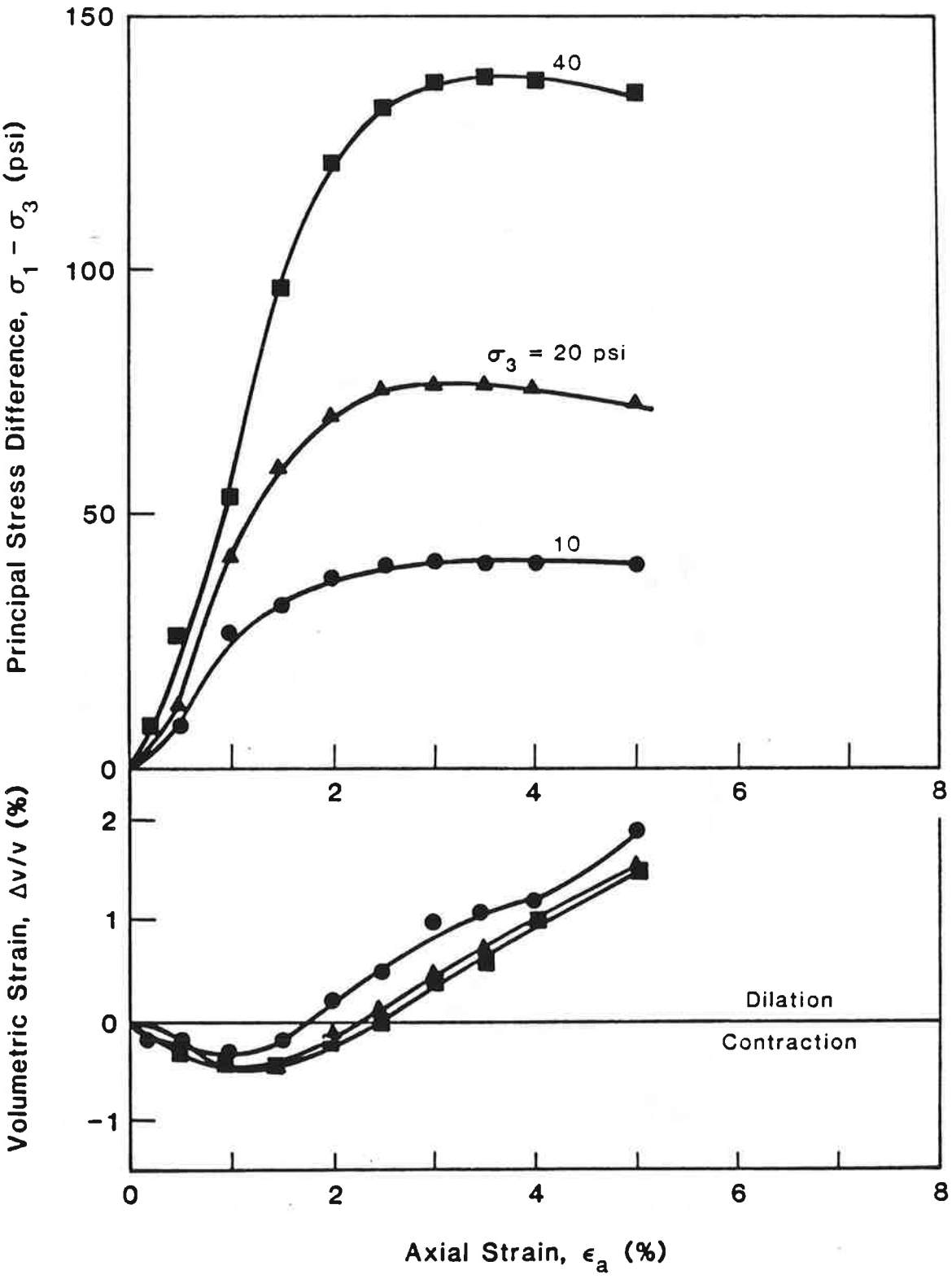

Fig. I.2. Results of Consolidated-Drained Triaxial Compression Tests for San Jacinto River Sand at 60% Relative Density

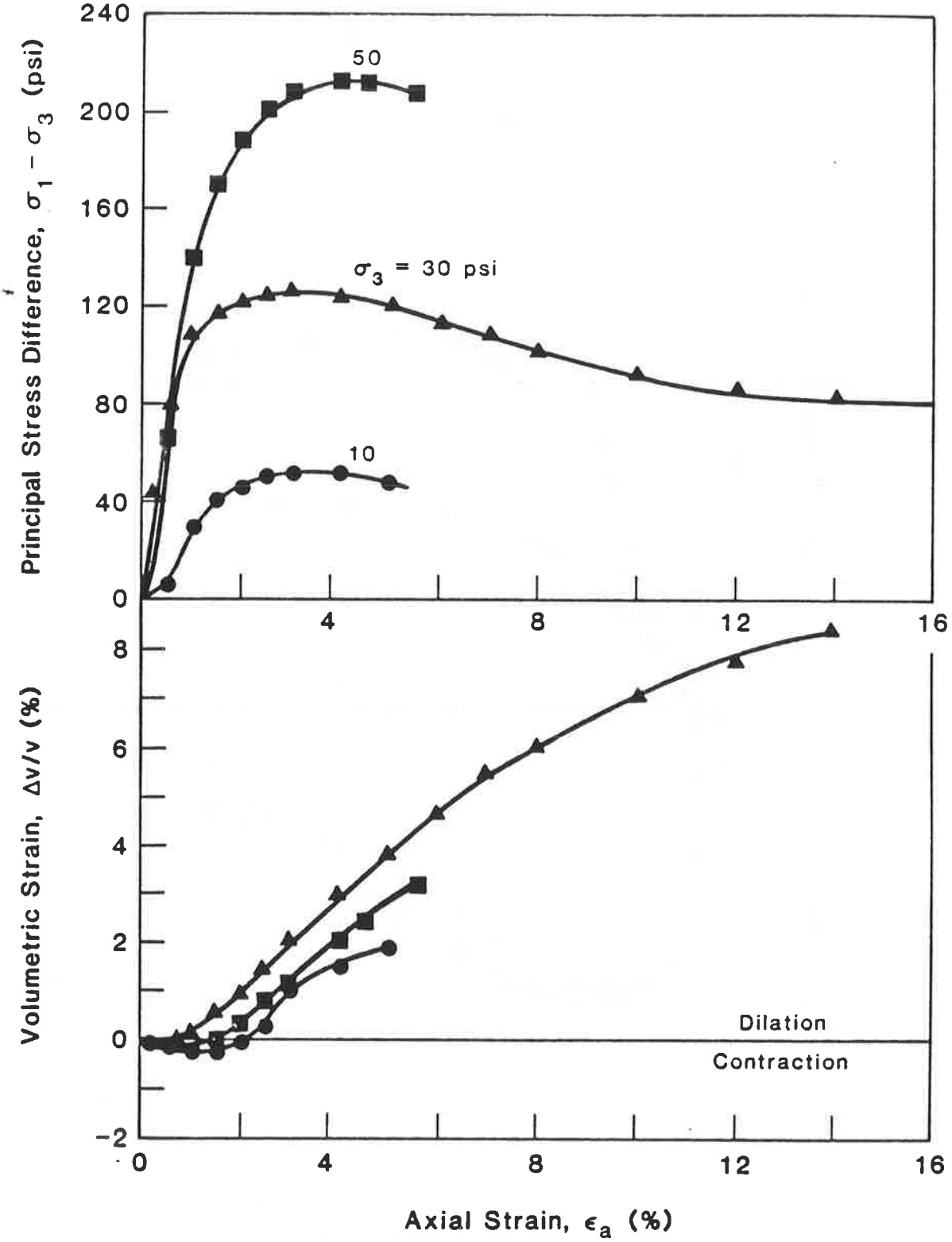

Fig. I.3. Results of Consolidated-Drained Triaxial Compression Tests for San Jacinto River Sand at 85% Relative Density

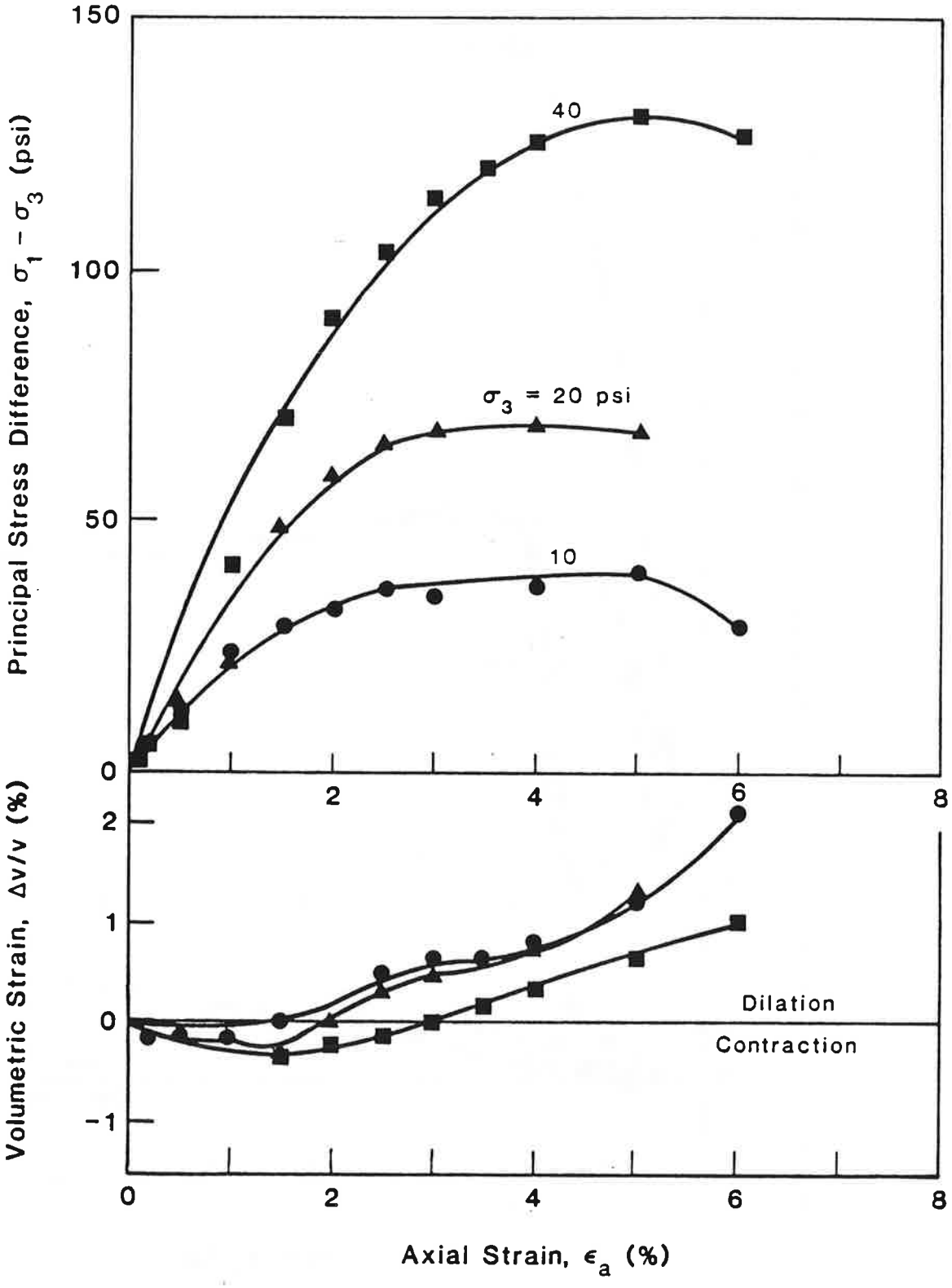

Fig. I.4. Results of Consolidated-Drained Triaxial Compression Tests for Blasting Sand at 60% Relative Density

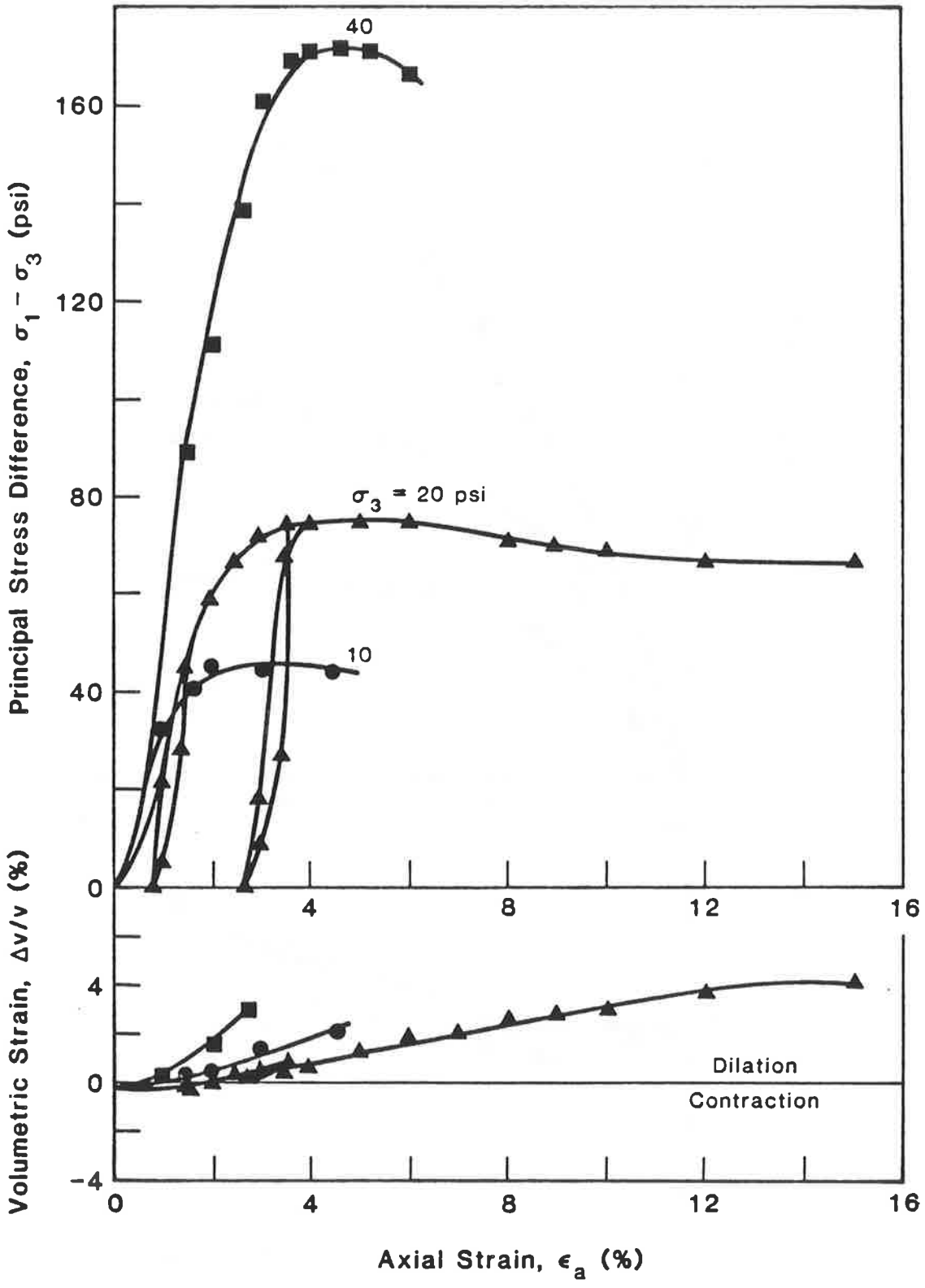

Fig. I.5. Results of Consolidated-Drained Triaxial Compression Tests for Blasting Sand at 85% Relative Density

$$\phi = \sin^{-1} [\tan \xi] \qquad (I.1)$$

where ξ is the slope of the appropriate line in Fig. I.6. The range of angle of internal friction is 38.5° to 43.6 °.

Interface Shear

It was also considered important to investigate the interface shear strength properties of the sand and the material comprising the outer wall of the pile. In order to study this effect, interface shear tests were conducted in a direct shear apparatus. Sand was deposited by raining the soil in a dry state at relative densities of 60% and 85% onto a prepared flat steel plate in the bottom half of a circular direct shear box 3 inches in diameter, following which the top of the sand surface was vibrated lightly to ensure that the relative density at the sand-steel interface was equivalent to that in the sand mass within the shear box. In order to represent the the pile surface closely, the steel plate was made of the same material as the pile and was given the same finish as that on the pile by lightly machining it with an end mill and rubbing it with an emery cloth prior to depositing the sand. After placement, the sand was saturated and tested in a consolidated-undrained mode under normal interface stresses of 10, 30 and 50 psi. Results of the tests, in terms of both shear stress-displacement and volume-change-displacement relations, are given in Figs. I.7 - I.10. The SJR Sand contracts at the interface at medium density (60%) but dilates at high density (85%) (Figs. I.7 and I.8), while the BLS Sand contracts at medium density but undergoes relatively minor volume change at high density, except at the 50 psi normal effective stress, where it contracts slightly. This type of interface behavior suggests that the test pile will exhibit somewhat different load transfer characteristics when installed in the two types of sand in the LVLPSC.

Interface frictional failure envelopes are shown in Fig. I.11. The interface friction angle is seen to be largest for dense SJR Sand (30°) and smallest for medium dense BLS Sand (25°). It is noted that these values are all considerably lower than the angles of internal friction obtained from triaxial compression tests for peak principal stress difference and are somewhat lower than angles of internal friction that can be inferred for high-strain conditions in the triaxial compression tests.

Resonant Column

Several torsional resonant column tests were performed on samples of SJR and BLS Sands at the medium dense state (nominal relative density = 65%). The results of these tests provide an indication of the stiffness and material damping of the sand at very low strain amplitudes (for example, near the boundaries of the test chamber). The test specimens were similar in size to the triaxial compression samples and were also prepared by raining. However, they were tested in a dry condition to preclude the buildup of pore water pressures during application of the vibratory torsional moments to the specimens. Variations in the shear modulus of the sand with shear strain amplitude are shown in Fig. I.12, and the measured equivalent single-degree-of-freedom damping ratios are tabulated in Table I.2.

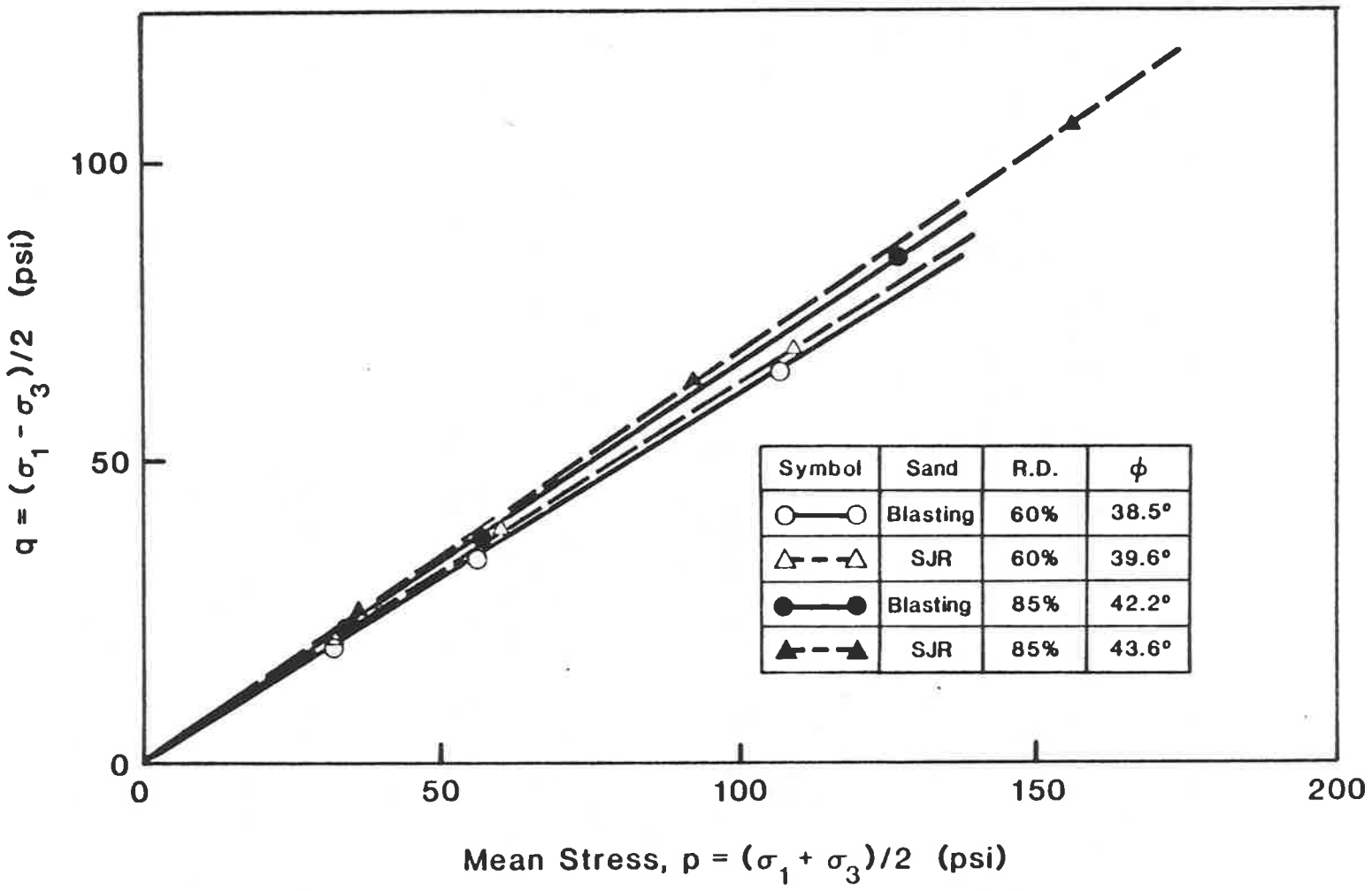

Fig. I.6. Failure Envelopes for Triaxial Compression Tests on p' - q Diagram

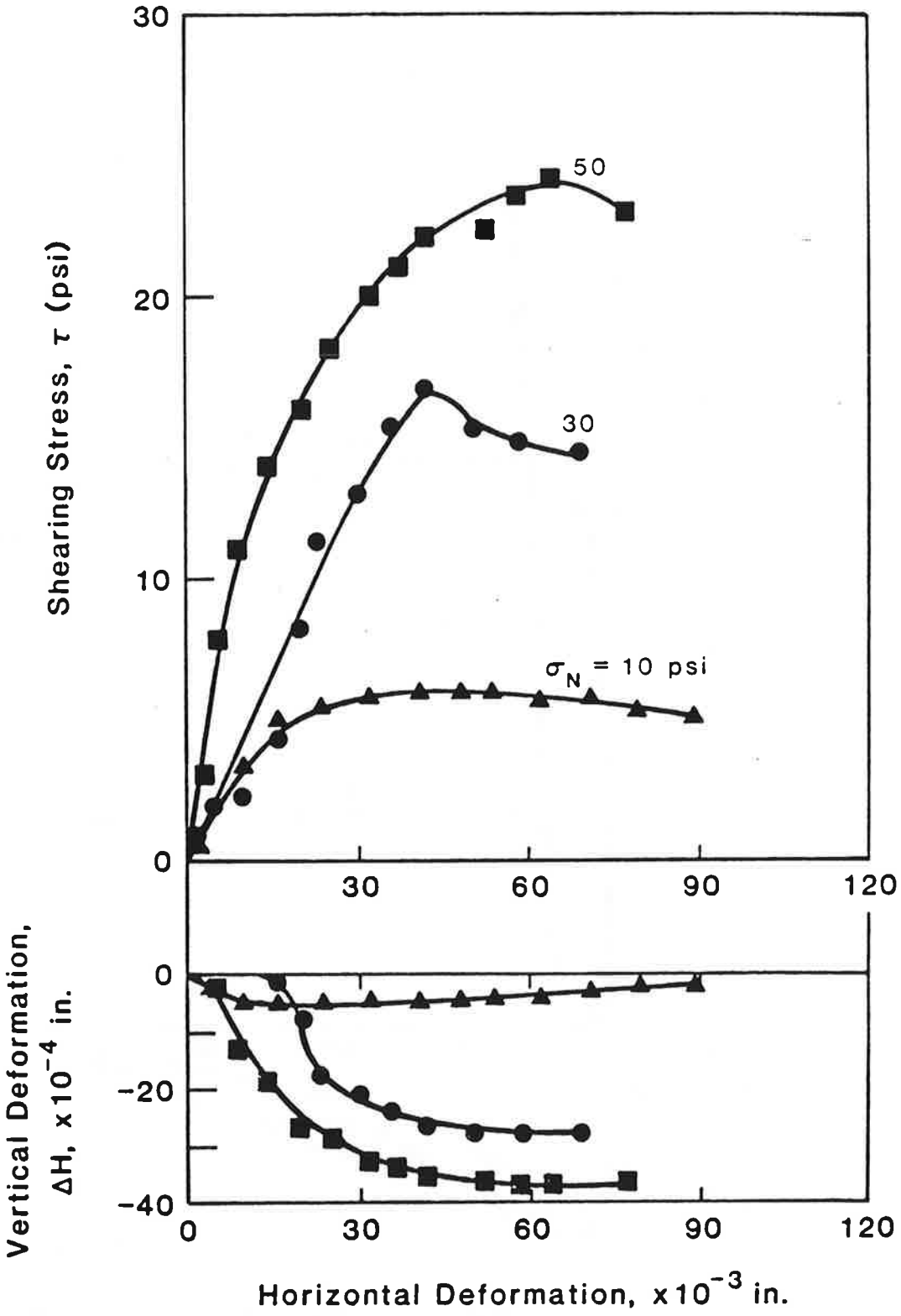

Fig. I.7. Results of Direct Interface Shear Tests for San Jacinto River Sand at 60% Relative Density

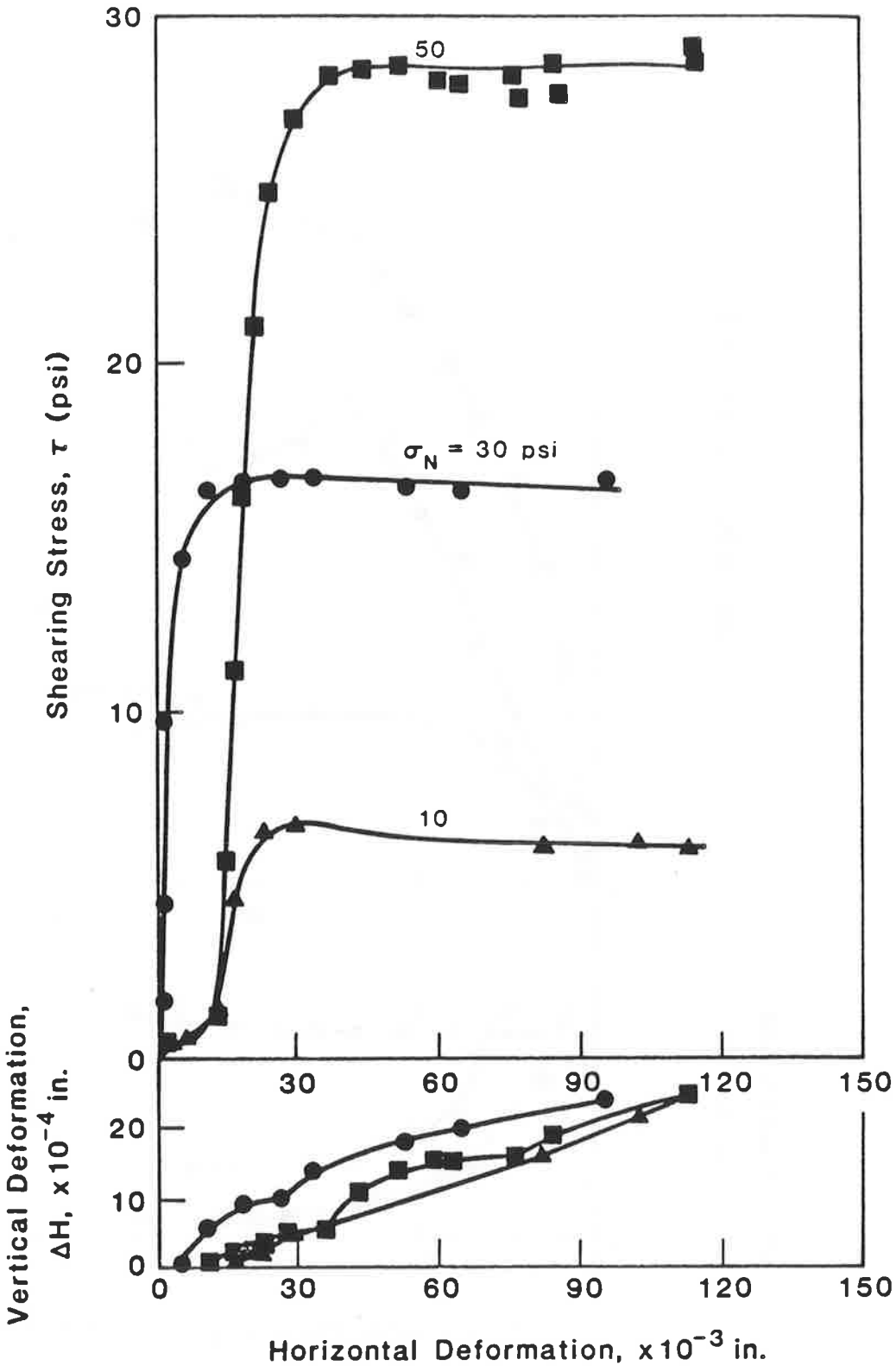

Fig. I.8. Results of Direct Interface Shear Tests for San Jacinto River Sand at 85% Relative Density

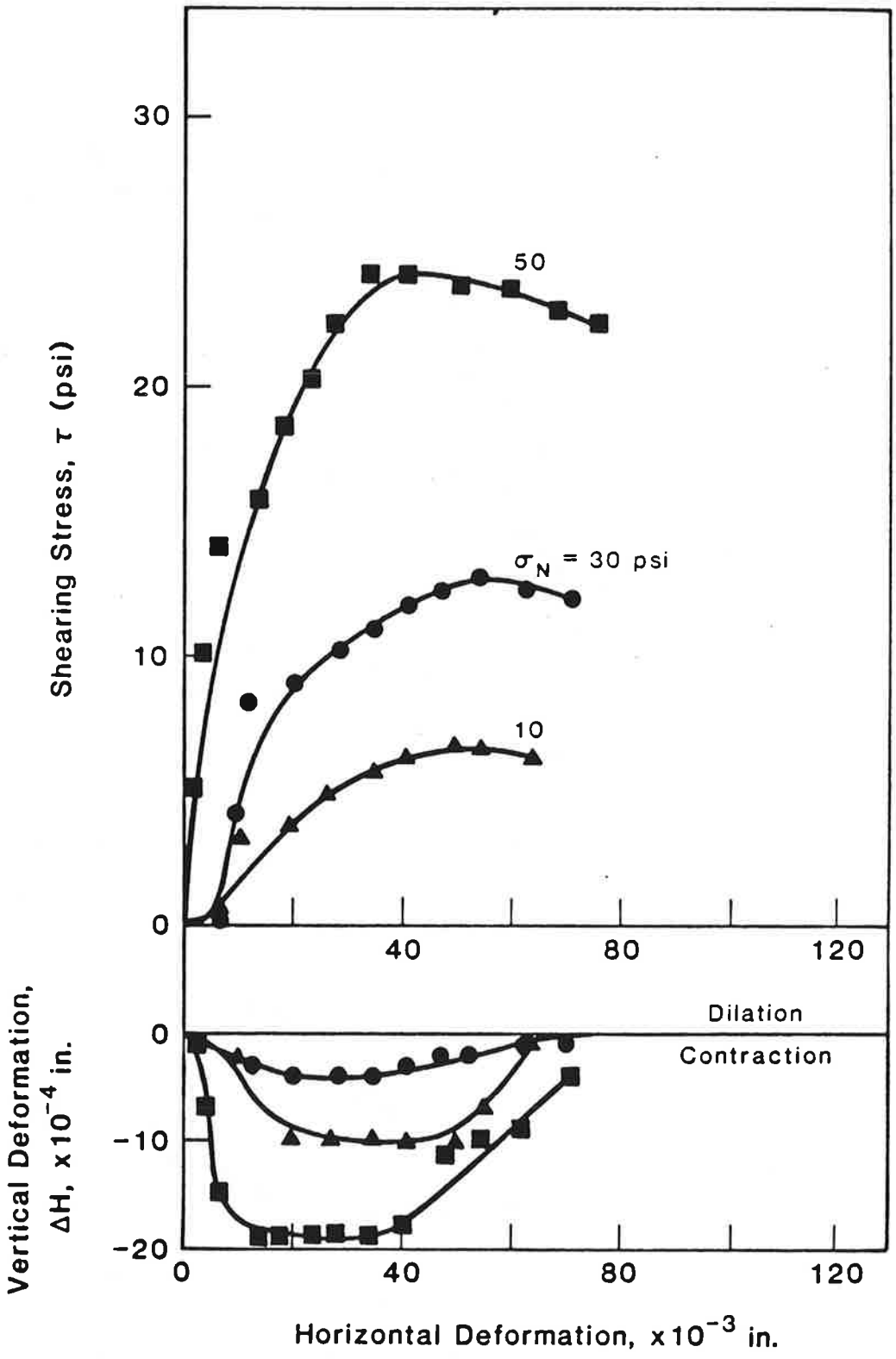

Fig. I.9. Results of Direct Interface Shear Tests for Blasting Sand at 60% Relative Density

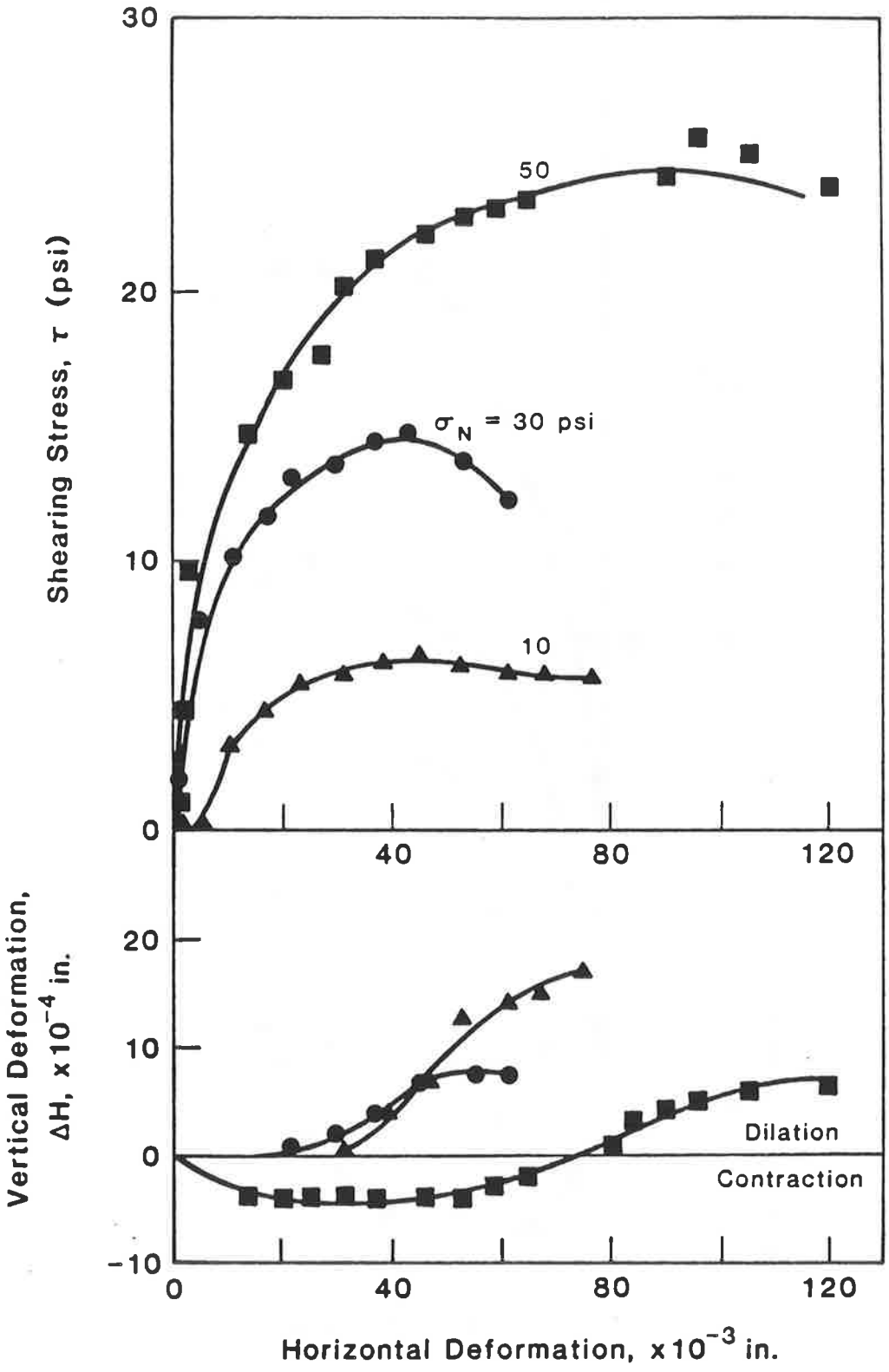

Fig. I.10. Results of Direct Interface Shear Tests for Blasting Sand at 85% Relative Density

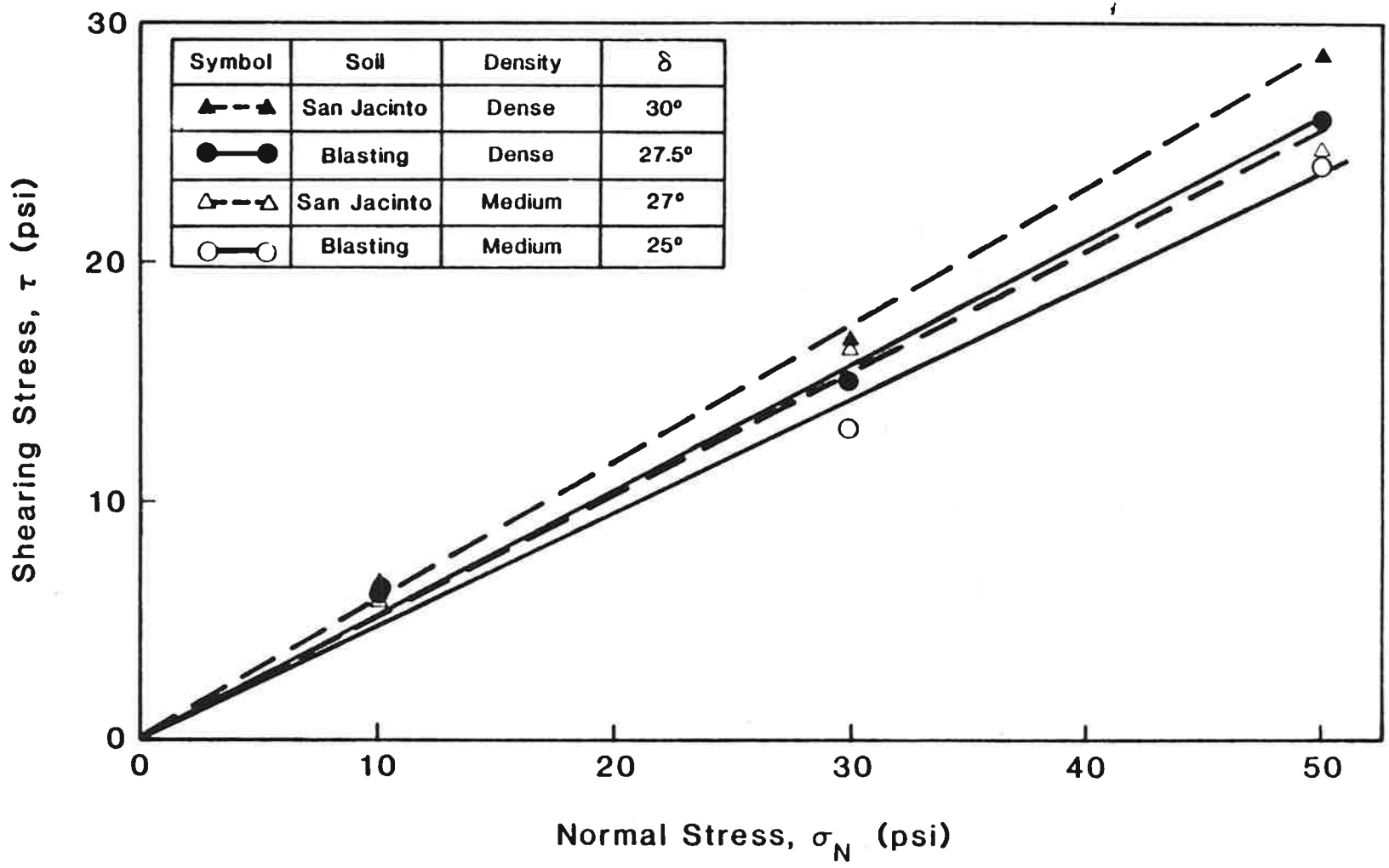

Fig. I.11. Failure Envelopes for Direct Interface Shear Tests

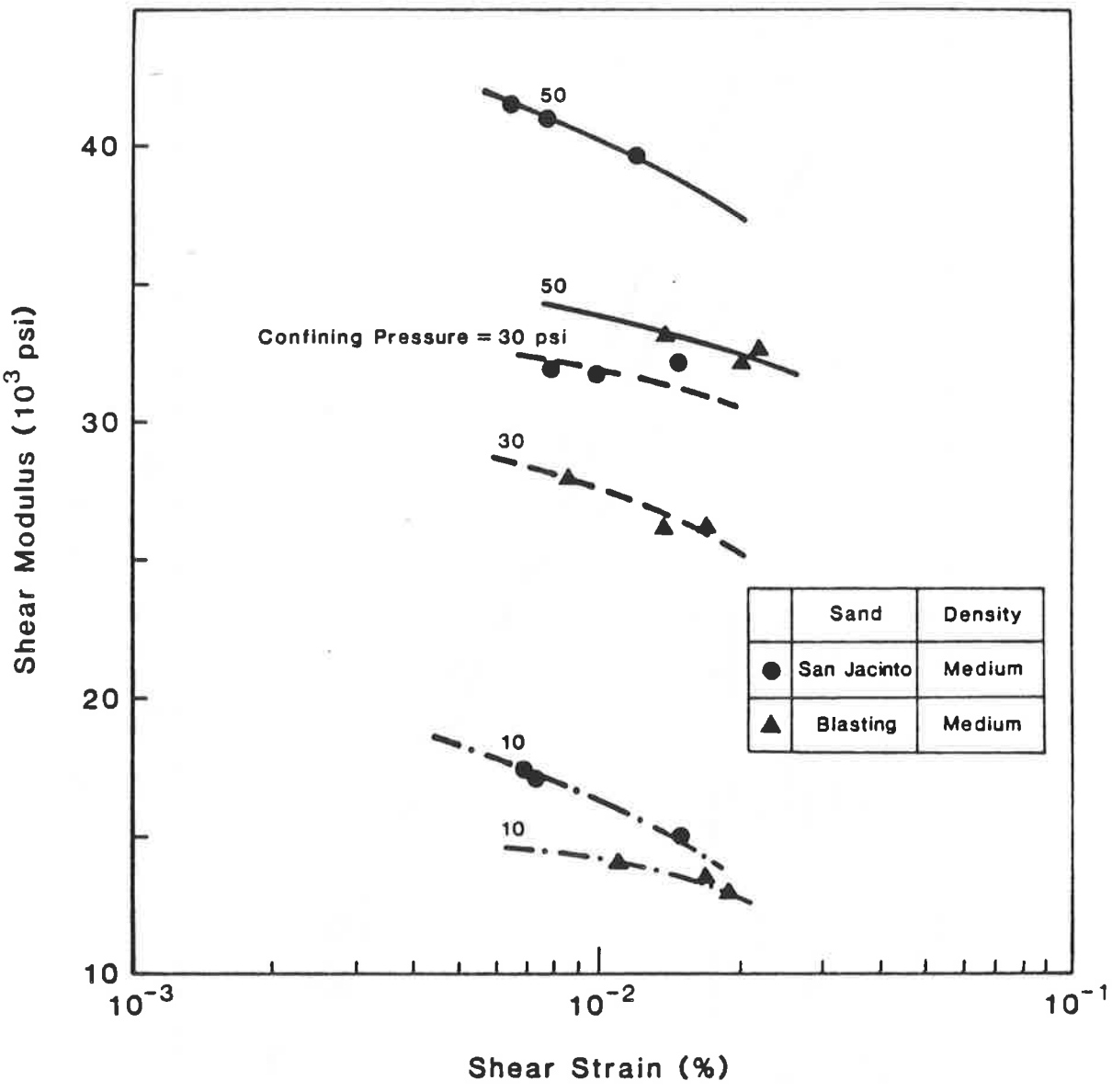

Fig. I. 12. Dynamic Shear Moduli vs. Shear Strain Amplitude (Single) as Functions of Sand Type and Confining Pressure from Torsional Resonant Column Tests

Table I.2. Damping Ratios of Medium Dense Sands from Resonant Column Tests

Sand	Confining Pressure (psi)		
	10	30	50
San Jacinto River			
	$\gamma = 7X10^{-3} - 1.5X10^{-2}$	$\gamma = 8X10^{-3} - 1.5X10^{-2}$	$\gamma = 6X10^{-3} - 1.2X10^{-2}$
	D = 2.2 - 3.3	D = 1.0 - 1.8	D = 1.0 - 2.5
Blasting			
	$\gamma = 1X10^{-2} - 1.9X10^{-2}$	$\gamma = 9X10^{-3} - 1.7X10^{-2}$	$\gamma = 1X10^{-2} - 2.2X10^{-2}$
	D = 1.8 - 3.7	D = 0.0 - 1.4	D = 1.1 - 1.2

Notes: γ = shear strain amplitude in percent; D = damping ratio in percent of critical

At equivalent confining pressures and shear strain amplitudes the shear modulus of the BLS Sand is much lower than that of the SJR Sand, with differences increasing with increasing confining pressure. The damping ratios for both sands appear to be similar for equivalent ranges of shear strain amplitude and confining pressure. For both sands damping ratio tends to decrease slightly with increasing confining pressure.

APPENDIX J

Sand Deposition Procedures

Placement Devices

A significant detail in the testing program was the preparation of the soil in the test chamber (LVLPSC). It was judged that the soil densities in the test chamber, which simulate in-situ conditions, of greatest practical interest would be those in the medium dense to very dense range (relative density of approximately 60% to 90%), since naturally occurring sands are relatively rare at relative densities of less than 50 to 60%, and pile foundations would not normally be needed in soils with relative densities exceeding 90%. Experience indicated that the most appropriate means of preparing multiple specimens of the approximately 40 cubic feet required to fill the test chamber was to place them into the chamber by raining through air ("pluviatile compaction").

The first step in developing the deposition procedures for the test chamber was to construct small-scale model rainers and to vary their properties until they were capable of producing sands at each end of the scale of target densities (approximately 60% and 90%) in a reproducible manner. The small-scale rainers that were developed in this subtask are shown in Fig. J.1. They consisted of a funnel, a pair of #10 sieves placed at various distances below the mouth of the funnel and at various distances from each other, and a sheath, which directed the falling sand and which excluded currents of air from passing through the falling column of sand. These rainers were used in the preparation of the laboratory test specimens described in Appendix I.

Full-scale rainers were then developed from the designs shown on Fig. J.1. A schematic diagram of the full-scale rainer that was developed for deposition of both sands in all states (except for the medium dense Blasting Sand) is shown in Fig. J.2. In place of the funnel on the laboratory rainers, a pan hopper with a bottom-discharge shutter was used in the full-scale rainer. The shutter consisted of matching metal sheets with corresponding hole patters, as shown in Fig. J.2. The top sheet was designed so that it could slide laterally. As the hopper was filled the holes in the top sheet were out of line with those on the bottom (stationary) sheet. To deposit the sand, the top sheet was slid laterally until the holes aligned and the sand fell onto the top sieve. The holes in the stationary sheet were machined in such a way as to produce minimum turbulence of the falling sand particles as they exited the shutter (i. e., they were slightly crimped perpendicular to the sheet in the direction of sand flow).

The length of the skirt on the rainer (the sheath below the shutter, containing the sieves) and the positions of the sieves within the skirts were varied, as indicated for the model rainers in Fig. J.1, to produce sands of differing densities. The base of the skirt was kept at the top of the sand level during deposition by suspending the rainer from an overhead pulley that was continuously raised during deposition of a lift, which was nominally three inches thick. A photograph of sand placement with this rainer is shown in Fig. J.3.

Attainment of the medium dense state by pluviatile compaction with Blasting Sand could not be accomplished with the rainer shown in Fig. J. 2; therefore, it was necessary to construct a second rainer for depositing sand under those conditions. That rainer is shown schematically in Fig. J.4. It consisted of a shutter, as shown, which was

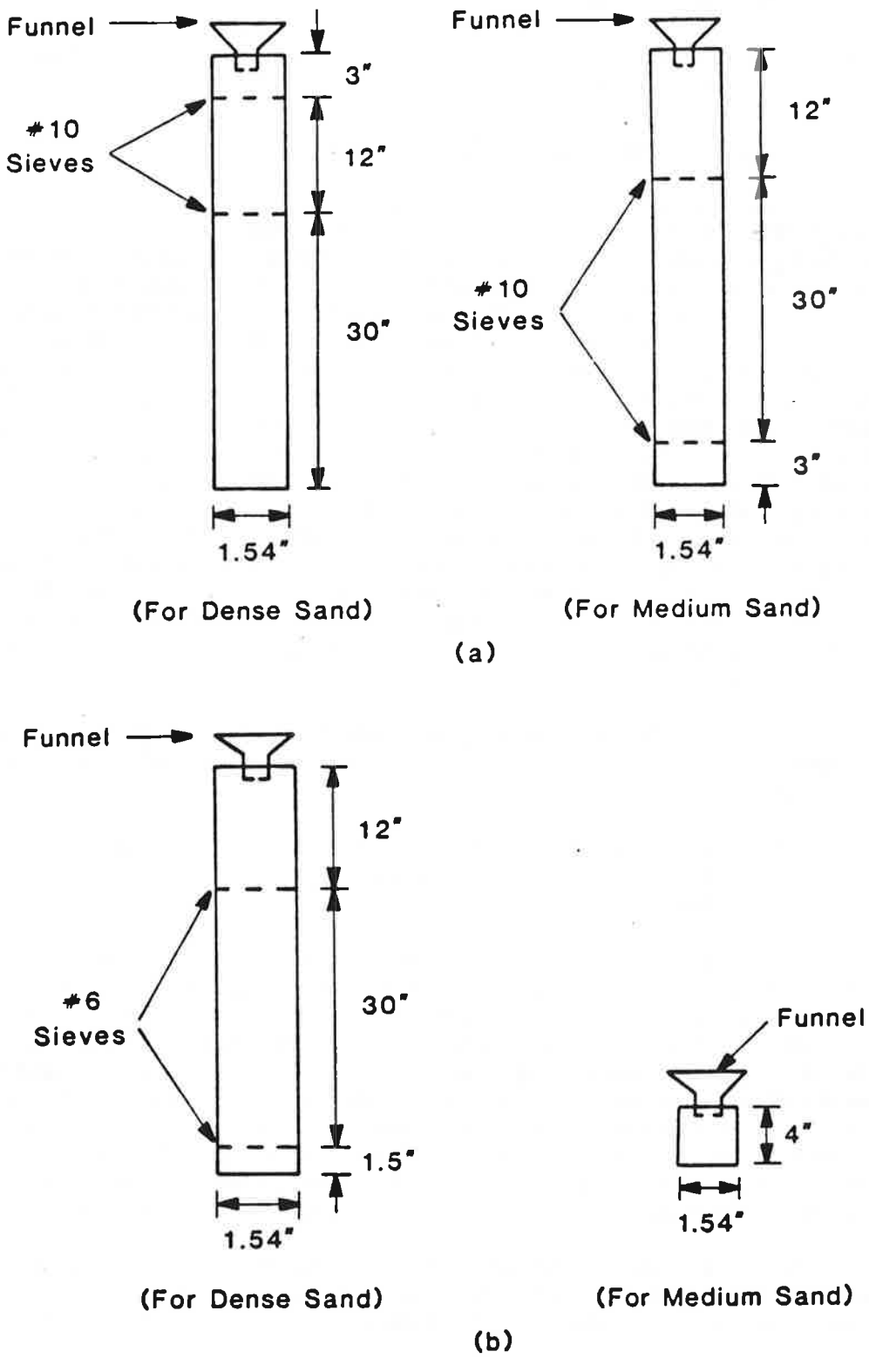

Fig. J.1. Model Rainers for Sands: (a) for San Jacinto River Sand; (b) for Blasting Sand

activated by torsional motion. No sieves were used, and the sand was dropped through a distance of three inches directly from the shutter to the surface of the newly deposited sand. As with the rainer shown in Fig. J.2, this rainer was suspended from an overhead pulley and raised continuously during the placement of a lift of sand.

Sand Placement and Removal Procedures

Using the raining devices described in the preceding section, each of the four cells in the LVLPSC was filled with dry sand, beginning with the bottom cell and concluding with the top cell. A given cell was not bolted into place in the column until the labor crew was ready to begin filling that cell. At the base of the bottom cell was place the energy absorbers described in Appendix C, followed by the water diffusion ring and riser, prior to beginning the raining process. Plastic forming jackets that could resist tensile hoop stresses but not compressive hoop stresses were used to provide lateral confinement to the sand and were put into place in a given cell just prior to beginning the filling of that cell. Once the topmost cell had been filled with dry sand, the top cap of the chamber was bolted into place. The chamber was then pressurized to the required levels of total stress to produce the effective stresses required for the particular test for which the chamber was being prepared. That is, the vertical total stress applied at the top of the chamber was equal to the target effective stress, but the total stresses in the lateral pressure membranes were set equal to the target effective stress plus the pressure produced by the head of water in the pores of the soil in the chamber. The pores of the dry sand were then purged with carbon dioxide; finally, the chamber was saturated with deaired water, through the riser and diffusion ring, as described in Appendix C.

Approximately one crew-day was required to fill and pressurize the chamber, and approximately one-half day was required to purge the pores of the soil and saturate the soil column.

The instrumented test pile was then placed into the top of the chamber through the pile port to the elevation of the bottom of the pile-port guide tube (Fig. C.2), and the test was conducted.

Following the completion of a given test, the free pore water was drained back through the diffuser ring into the holding tank for the deaired water. The chamber was then depressurized and the pile extracted vertically. The top cap of the chamber was then removed, and the moist sand was removed from the top cell by vacuuming or by shovelling. This process was repeated with the remaining cells as the sand was removed from the chamber in the reverse sequence from which it was placed. The moist sand was then placed in a forced-air convection oven for drying. The oven-dry sand was then placed back into the stockpile bin for reuse in future tests. The drying process, which occurred in a small bakery-type oven, required about two days for 40 cubic feet of the Blasting Sand and about three days for the 40 cubic feet of San Jacinto River Sand.

The grain-size distribution of the sand was checked against the initial distributions (Fig. I.1) periodically during the testing program to observe whether reuse resulted in degradation of the sand particles. None could be observed.

Verification of Density

Preliminary studies with the full-sized rainers indicated that they give slightly higher densities in the chamber than the corresponding laboratory rainers (Fig. J.2).

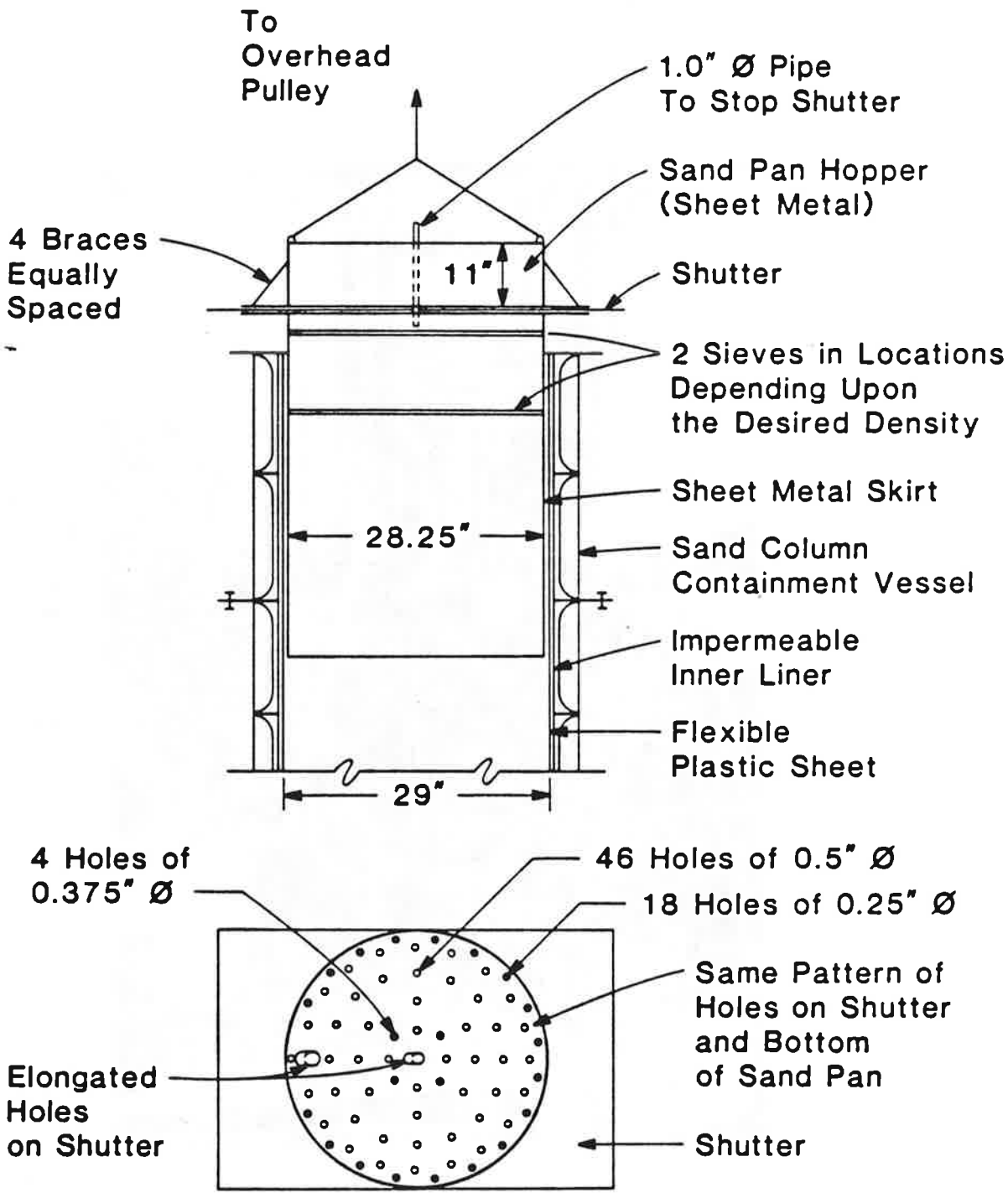

Fig. J. 2. Schematic Diagram of Full-Scale Rainer Used on All Tests Except Those for Medium Blasting Sand

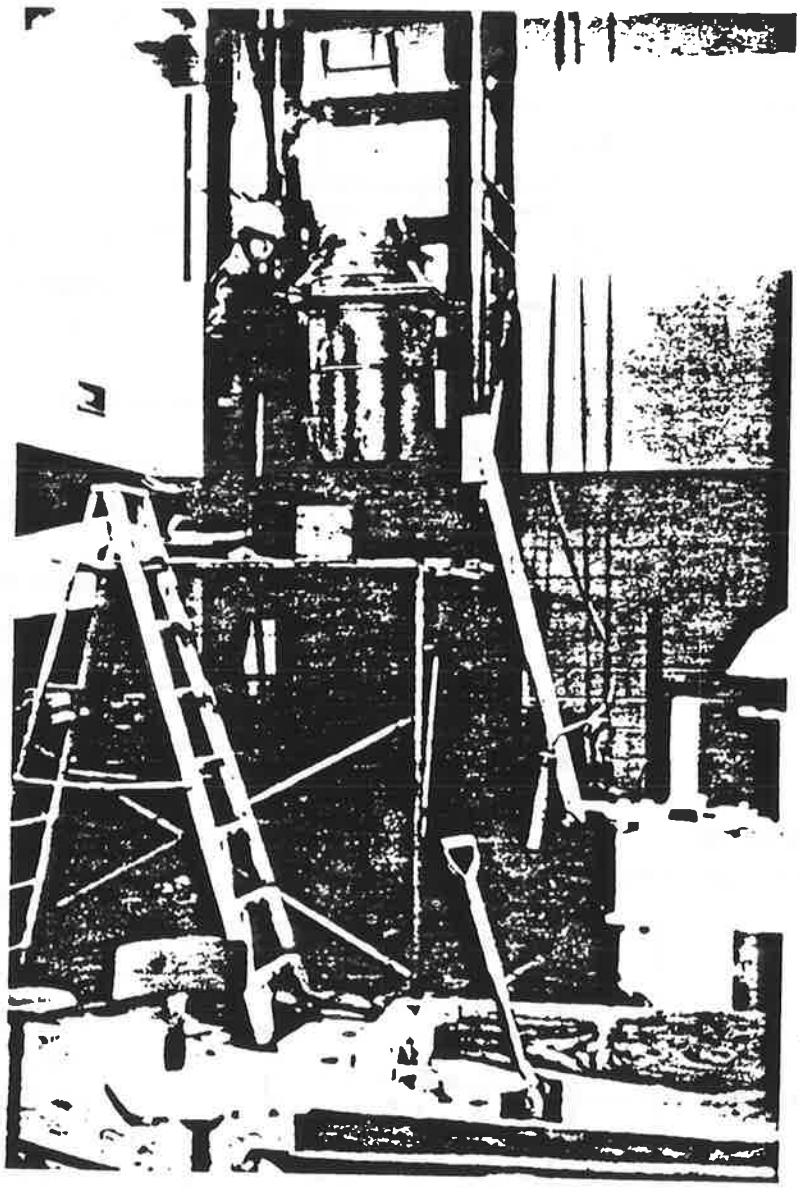

Fig. J.3. Photograph of Rainer Placing Sand in Chamber

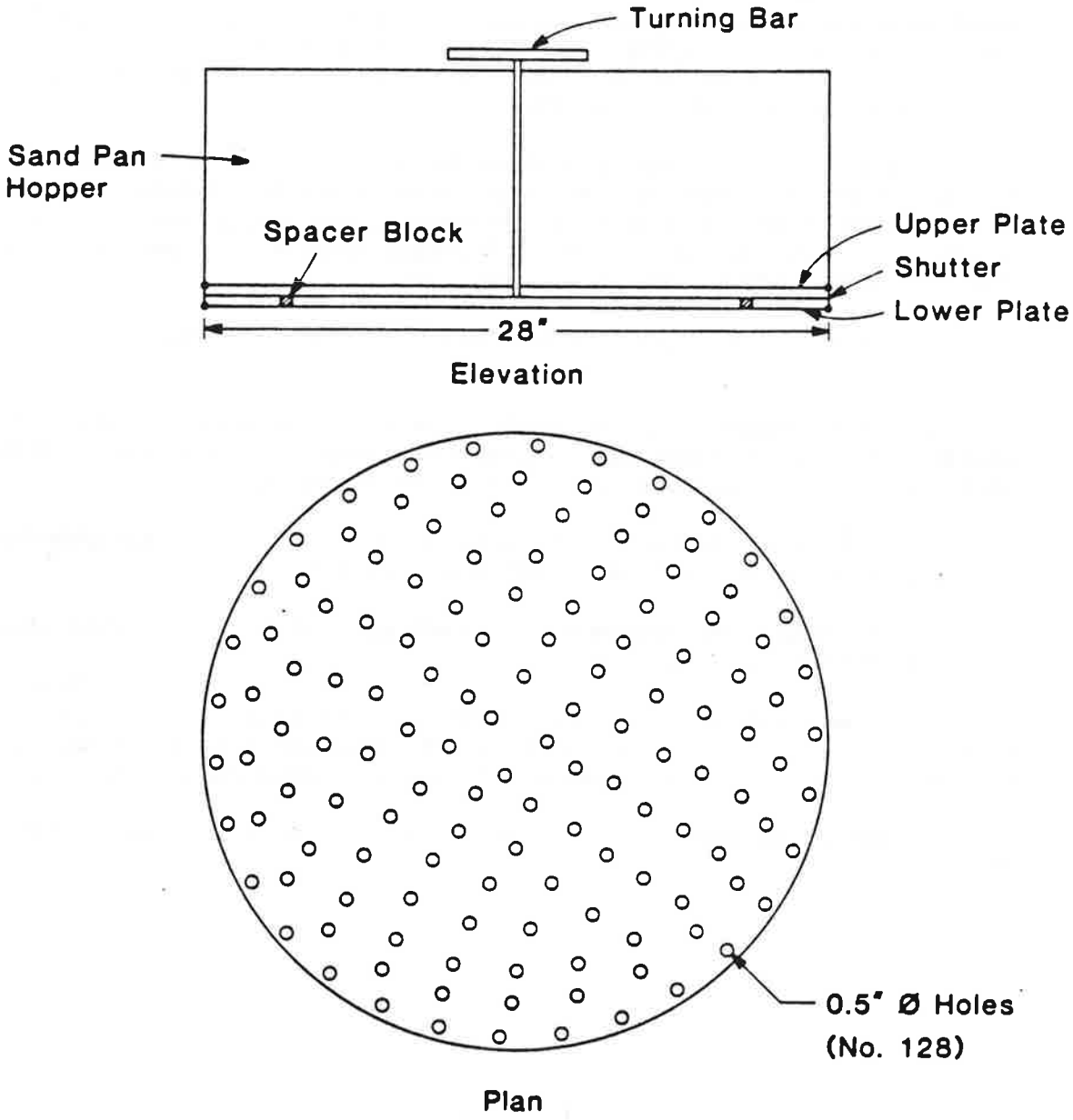

Fig. J. 4. Schematic Diagram of Full-Scale Rainer Used for Medium Blasting Sand

Therefore, while the soils were deposited at relative densities of approximately 60% and 85% for laboratory testing, the corresponding relative densities attained in the chamber were approximately 65% and 90%. Since the process of isotropic pressurization in the triaxial tests raised the relative densities of the looser specimens from about 60% to about 65%, the deposited relative density of 65% in the chamber to represent the medium dense case is probably more representative of the actual relative density after pressurization of the chamber than would have occurred had the soil been deposited in the chamber at a relative density of 60%.

The primary control exercised on the production of a column of sand of a given density was the close adherence to the prescribed deposition process (use of proper rainer, oven-dry sand and constant lift thickness). However, gravimetric checks were also made of the densities of the sands as they were placed in the chamber for every test. This was accomplished through the following process:

a. Twelve sampling points were established within the chamber, as indicated in Fig. J.5;

b. After placement of the fourth lift in each cell, aluminum sampling cans (standard laboratory moisture sample cans), two inches in diameter and 1.5 inches in height, were placed on the sand surface and the next lift placed;

c. A thin-walled tube was then pushed into the sand over each sampling can, the overburden soil removed , and the sampling can recovered;

d. The void within the tube was filled with sand using the appropriate laboratory rainer, and the tube was withdrawn;

e. The weight of the dry soil within the sampling can (which had a known volume) was measured, the dry unit weight calculated and the relative density determined based on the know minimum and maximum index densities (Appendix I).

Results of the gravimetric tests on the density samples are given in Tables J.1 and J.2.

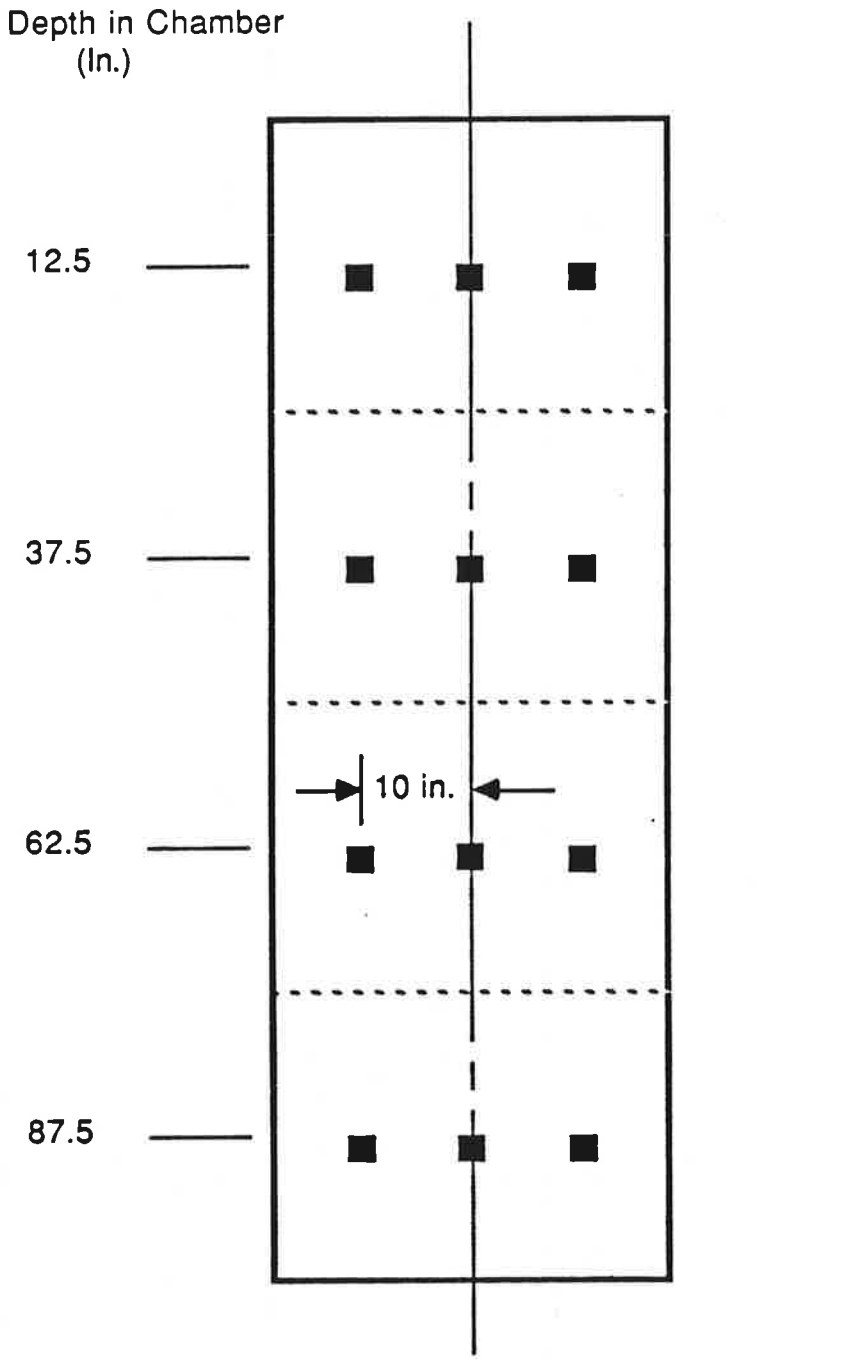

Fig. J.5. Location of Gravimetric Sampling Points in Chamber

Table J.1. Measured Values of Relative Density (%) of Dry Sand As Placed in the LVLPSC; Tests on San Jacinto River (Fine) Sand

Depth in Chamber (In.)	Test No.													
	1A/ 1B	2A/ 2B	3A	3B	4A/ 4B	5	6	7	8	9	18	20	21	22
12.5	85.5	67.7	85.8	90.1	65.3	89.2	93.7	66.1	92.2	87.9	95.4	67.2	91.7	94.4
37.5	86.5	63.4	86.6	88.5	69.1	90.5	91.6	64.7	91.3	89.6	89.0	64.0	90.7	90.0
62.5	83.3	70.3	83.9	91.5	66.1	87.4	90.2	71.6	90.2	90.3	93.4	61.6	92.4	90.1
87.5	86.2	65.3	84.2	91.8	71.4	86.4	89.8	65.8	89.0	90.7	93.5	66.7	91.2	92.2
Avg.	85.3	66.7	95.3	90.5	68.0	88.4	91.3	67.0	90.7	89.6	92.8	64.9	91.5	91.7
Target Value	90	65	90	90	65	90	90	65	90	90	90	65	90	90

Maximum dry unit weight = 110.4 pcf
Minimum dry unit weight = 94.2 pcf

Each value is an average of three gravimetric samples.

Table J.2. Measured Values of Relative Density (%) of Dry Sand As Placed in the LVLPSC; Tests on Blasting (Coarse) Sand

Depth In Chamber (In.)	Test No. 10A/ 12A	10B/ 12B	11A/ 13A	11B/ 13B	14	15	16	17	19
12.5	97.1	96.3	72.0	59.5	96.6	98.2	67.5	96.9	95.1
37.5	99.8	99.6	70.6	61.0	94.1	96.2	64.1	95.5	91.2
62.5	97.1	98.4	69.8	64.5	96.1	97.2	67.8	98.0	92.1
87.5	98.8	96.6	72.3	70.6	95.6	98.2	62.3	96.0	98.6
Avg.	98.2	97.7	71.2	63.9	95.6	97.5	65.4	96.6	94.8
Target Value	90	90	65	65	90	90	65	90	90

Maximum dry unit weight = 102.6 pcf
Minimum dry unit weight = 90.17 pcf

Each value is an average of three gravimetric samples.

APPENDIX K

Observations

In the course of the pile-testing program, significant observations were made that do not fall into any specific technical category relative to the objectives of the project but that of interest, nonetheless. These observations are addressed in this appendix. For example, difficulties were encountered with the original designs of the testing equipment, which eventually warranted modification. Future research of this type should benefit from these observations.

Radial Drainage

Before any driving tests were conducted for record, two trial driving tests (one impact-driving and the other vibro-driving) were performed to check the testing procedure and the data acquisition system. Both trial tests were conducted in the chamber with full saturation and with water drainage at the top only. This procedure for drainage had no apparent effect on the impact-driving test. In the vibro-driving test, however, it was observed that the pile penetrated dense SJR sand at 10 psi effective confining pressure at a rate of about 10 inches/second with a driving frequency of around 15 Hz and an eccentric vibrator moment of 50 in-lbs. When the vibrator was stopped, the pile continued to penetrate until the vibrator hit a safety stop. A significant amount of water and some sand was expelled from the drainage ports at the top of the chamber, continuing for several minutes after the driver was stopped. It was concluded that liquefaction of the sand had occurred as the pile penetrated the LVLPSC and produced positive pore water pressures. The liquefaction of the soil, which contributed to the unreasonably fast driving rate and water/soil expulsion, was caused by allowing water to drain only vertically upward, producing an upward drainage gradient that was large enough to cause the soil in the chamber to become quick. A modification of the internal drainage system in the LVLPSC was developed, in which the water was forced to drain primarily radially, as described in Appendix C . Reconsideration of the drainage path also led to the conclusion that radial drainage more closely simulates in-situ conditions than does vertical drainage. The radial drainage system was employed in all of the tests reported herein.

Connection Between Pile and Driver

During the early stages of the testing program (before 4/28/87), the pile was connected to the vibro-driver by bolting the integral weldneck flange of the pile directly to the base plate of the driver. It was discovered that large flexural stresses were generated at the pile head with this type of rigid pile-head fixity. These stresses were magnified by unbalanced horizontal forces in the vibrator that had developed early in the testing program due to problems with synchronization of the two motors of the vibro-driver. This situation apparently led to rapid fatigue failure, which resulted in cracking of the steel near the point at which the flange had been welded to the pile. A new articulated connection was developed and used thereafter, and the pile was repaired by cutting off the cracked section and rewelding the flange. The modified connection was a swivel-head (pinned) fixture (described in detail in Appendix E) that was bolted between the flange of the pile head and the center of the base plate of the driver. The

pinned connection was oriented in such a way that no bending moment was introduced in the plane of the vibro-driver flywheels, in which it was believed that the largest flexural stresses were being generated. No structural distress was observed in the test pile after this modification.

Synchronization of motors

As mentioned above, difficulty was experienced with the operation of the vibratory driver during the early part of the testing program, primarily in the ability of the two hydraulic motors to synchronize to produce a monochromatic frequency input and minimize lateral vibrations. The problem was remedied by rebuilding the flywheel system such that two flywheels on which the unbalanced masses were mounted interconnected through a system of gears, at their outer edges, which meshed to a very low tolerance. The new system decreased the driver efficiency very slightly as evidenced by the fact that the flow rates that were calibrated to driving frequencies with the original system were slightly higher to achieve the corresponding frequencies in the new system. The original and modified designs are presented in detail in Appendix E.

Transducer Performance

It was observed that the readings of the lateral total pressure transducers during static and dynamic testing were sometimes unreasonable, particularly in the BLS Sand. It was believed that this behavior was caused by uneven distribution of pressure exerted by sand grains on the small area of the sensing surface of the transducers. Readings from the pore water pressure transducer were comparatively better, however, because water exerted uniform pressure on the sensing surface of the transducer. It was not possible to correct this problem with the resources available.

There existed a concern that the lateral pressure transducers were sensitive to the application of axial stress in the pile, despite the design precautions taken to minimize this effect (Appendix D). A cross-sensitivity calibration was therefore conducted on the total pressure transducers (reported in Appendix G) to develop a perception of whether false lateral pressure readings were being generated by either static axial stresses or dynamic stress waves. It was concluded, after dynamic calibration, that the cross-sensitivity problem was very minimal even in impact-driving conditions, such that corrections for this effect were not necessary and were not made.

Placement of Bias Mass

Because of limited vertical clearance of the overhead crane in the room in which all driving tests were carried out, the pile was first driven into the chamber to a penetration of about 25 inches with only the bias mass carriage weight acting above the isolation springs on the driver for all the vibro-driving capacity tests. Additional bias masses could then be placed using the crane, and the pile was then driven to final penetration (usually, 76 to 78 inches). It was believed that this 25-inch "spudding" of the pile had no measurable effect on the results of the capacity tests, either during driving or during static loading.

Water Expulsion

As documented in Appendix C, receptacles were used to collect any water expelled from the radial drains in the LVLPSC during driving. This expulsion was the result of volume changes in the soil and development of pore water pressures produced by

shearing of the soil that occurred due to the insertion of the pile. The amount of water expelled was recorded, as was the settlement of soil surface within the LVLPSC at the conclusion of each test, as reported in Chapter 2. These data give qualitative information regarding the disturbance produced in the soil by the insertion of the pile for a given set of chamber and hammer conditions. The results are not quantitative because it was possible for volume changes to be accommodated partially by radial expansion or contraction of the lateral membranes in the chamber (Appendix C).

APPENDIX L

Computation of Theoretical Power

This appendix describes the equations that are used to compute the theoretical power of a simple, counterrotating vibrator. The assessment of such theoretical power is necessary in the application of the design procedures outlined in Chapter 2.

It is desirable to develop a definition of vibrator power that is independent of the impedance that is offered by the pile to which it is attached. In the following development only the dynamic and static forces acting upon a freestanding vibrator and vertical displacements and velocities of the vibrator are considered. Under such physical conditions the theoretical power is defined in principle from Eq. L.1.

$$P_t = \frac{1}{T} \int_0^T F(t)\ v(t)\ dt \quad , \tag{L.1}$$

in which P_t = theoretical power,

T = period of vibration,

t = time,

$F(t)$ = net force acting on the vibrator (function of time), and

$v(t)$ = vertical velocity of the vibrator (function of time).

The net force produced by the counterrotating masses and the presence of the bias mass, F(t), and the vibrational velocity, v(t), may be derived from a simple single - degree-of-freedom system model shown in Fig. L.1. The spring constant k may be assumed to represent the stiffness of the spring or springs located between the primary mass of the vibrator and any bias mass that may be present. The vibrator itself consists of a primary mass (M) and the combined masses of the unbalanced rotators (m). The unbalanced, or eccentric, masses each have mass m/2 and rotate with an eccentricity e in opposite directions with angular velocity ω. The free-body diagrams of the system are shown in Fig. L.2. The horizontal components of force always balance each other, so that only the vertical components need be considered. From Fig. L.2a the equation of motion for an eccentric mass undergoing harmonic excitation can be written as:

$$F_z = \frac{m}{2} \frac{d^2}{dz^2} [\, z(t) + e \sin \omega t \,] = \frac{m}{2} [\, a(t) - e\, \omega^2 \sin \omega t \,] \tag{L.2}$$

In Eq. L.2 z is vertical displacement and a is vertical acceleration. From Fig. L.2b the equation of motion for the entire vibrator can be written as:

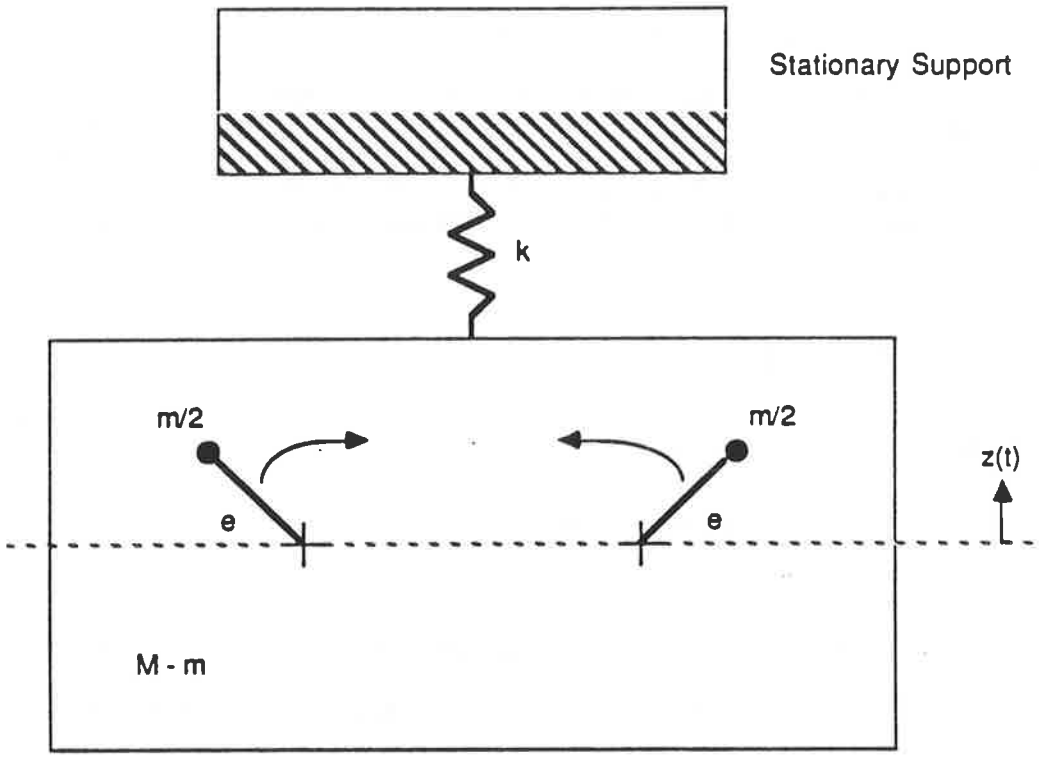

Fig. L.1. Single-Degree-of-Freedom System Model of Vibro-Driver

$$-2F_z - k\,z(t) = (M - m)\,a(t) \qquad \text{(L.3)}$$

Combining Eqs. L.2 and L.3 yields

$$M\,a(t) + k\,z(t) = m\,e\,\omega^2 \sin \omega t \qquad \text{(L.4)}$$

The steady state response solution of Eq. L.4 is

$$z(t) = Z \sin \omega t \qquad \text{(L.5)}$$

where Z is the amplitude of dynamic motion of the driver, which can be expressed as

$$Z = \frac{m\,e\,\omega^2}{M\,(\omega_n^2 - \omega^2)} \qquad \text{(L.5a)}$$

in which ω_n is the natural frequency of the primary mass and spring system, $(k/M)^{0.5}$.

The velocity and acceleration can then be expressed as

$$v(t) = Z\,\omega \cos \omega t \qquad \text{(L.6)}$$

$$a(t) = -Z\,\omega^2 \sin \omega t \qquad \text{(L.7)}$$

and, from Eq. L.4, the time-dependent vibrational force exerted on the spring kz(t) is

$$k\,z(t) = me\omega^2 \sin \omega t - M\,a(t) = (me\omega^2 + MZ\omega^2) \sin \omega t \qquad \text{(L.8)}$$

If bias mass exists above the spring, such that the natural frequency of the bias mass-spring system is much lower than the natural frequency of the primary mass-spring system, an additional time-independent downward bias force W (equal to the weight of the bias mass) is always exerted on the spring, such that the net force F(t) on the spring is the sum of the static bias and the dynamic forces:

$$F(t) = W + (me\omega^2 + MZ\omega^2) \sin \omega t \qquad \text{(L.9)}$$

Substituting Eqs. L.6 and L.9 into Eq. L.1 yields

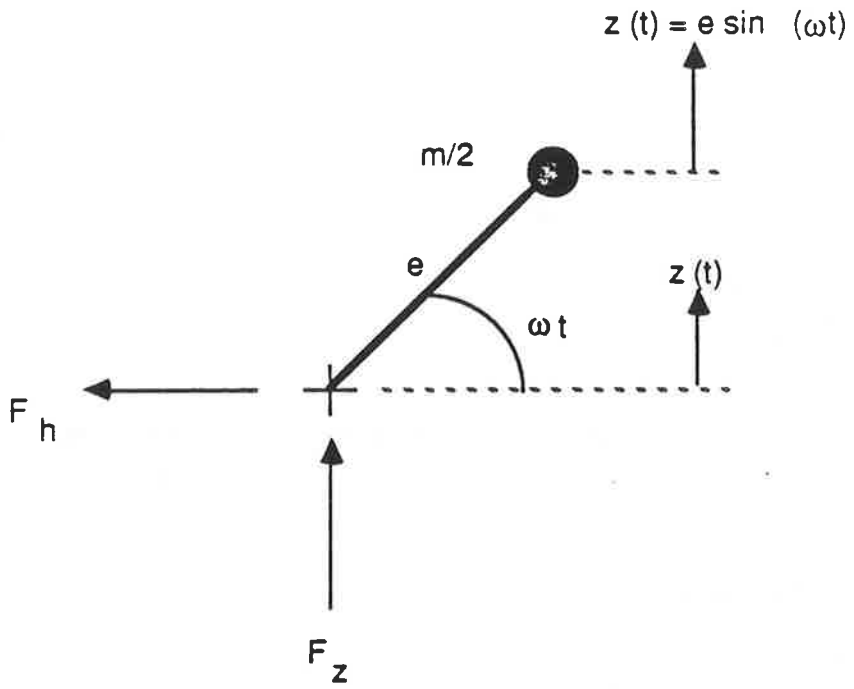

Fig. L.2a. Free-Body Diagram of One Eccentric Mass

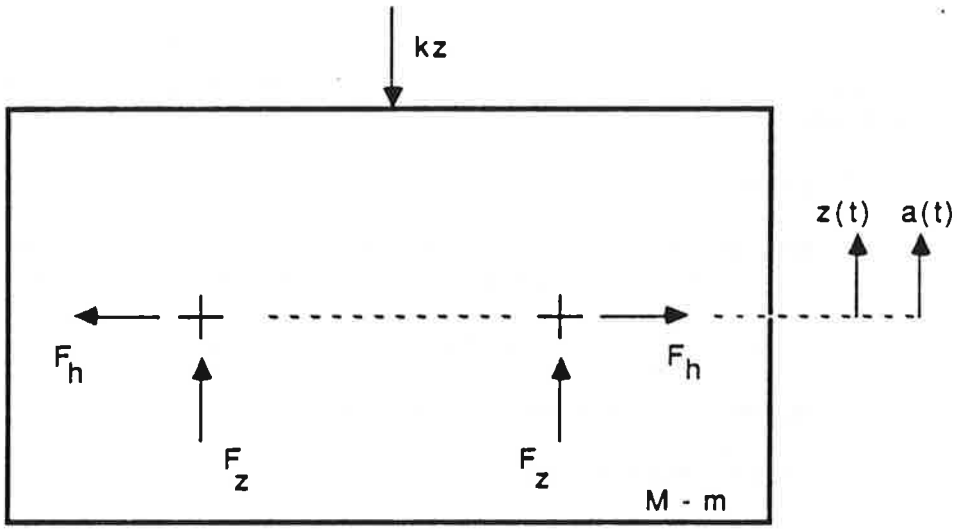

Fig. L.2b. Free-Body Diagram of Vibro-Driver

$$P_t = \frac{1}{T} \int_0^T [\, W + (me\omega^2 + MZ\omega^2) \sin \omega t \,]\; Z\, \omega \cos \omega t \, dt$$

$$= [\, 4W + 2\,(me\omega^2 + MZ\omega^2)\,]\, Z\, f, \qquad \text{where} \qquad \text{(L.10)}$$

$$f = \frac{1}{T} = \frac{\omega}{2\pi} \qquad \text{(L.11)}$$

In practice, the following steps would be followed to compute the theoretical power of a vibrator.

1. Determine

   M, the mass of the vibrator (excluding bias mass), which is equal to the vibrator weight divided by the acceleration of gravity;

   m, the combined mass of the rotating eccentric (unbalanced) weights;

   e, the eccentricity of the rotating weights;

   W, the weight of the bias mass;

   k, the combined spring constant of the springs separating the bias mass from the vibrator masss; and

   f, the frequency of vibration.

   Units should be consistent among all parameters.

2. Compute ω from Eq. L.11.

3. Compute $\omega_n = (k/M)^{0.5}$.

4. Compute Z from Eq. L.5a.

5. Finally, compute the theoretical power, P_t, from Eq. L.10.

APPENDIX M

Time Histories of Force, Velocity, Acceleration, Pore Water and Total Lateral Pressures at One-Half and Full Pile Penetration for Vibro-Driving Tests

This appendix documents the performance of the pile during insertion with the vibro-driver by presenting representative graphs of half-second time histories of acceleration, velocity, force, pore and total pressure signals measured on the pile during vibro-driving at penetrations into the chamber of about one-half of full pile penetration (about ten pile diameters) and near full penetration (about eighteen pile diameters) for each "capacity" test. All signals presented are direct, uncorrected output from the indicated instruments, except for the velocity signals, which were obtained by numerically integrating the measured average acceleration signal at the pile head and the single acceleration signal at the pile toe. The signals presented have been filtered and/or amplified as indicated in Appendix F. For each record, except as described below, the pile was in motion (had not met refusal).

Time histories are arranged in Figs. M.1a - M.22d at each penetration and for each test in the following order: pile-head and pile-toe acceleration, pile-head velocity and force, pile-toe velocity and force, and total and pore water pressure signals obtained from the pressure transducers at the bottom of the pile (Appendix D). For Tests 9 and 17 data were recorded when the pile was at a state of refusal (was not penetrating while under vibratory load), and additional time histories are included for those tests for that condition.

The sign convention for the signals is as follows. Positive acceleration corresponds to the acceleration at the bottom of the downstroke and so is actually deceleration; positive velocity corresponds to downward movement of the pile; positive force corresponds to compression in the pile; positive pressure corresponds to pressure greater than atmospheric (i. e., is "gage pressure").

It is observed that acceleration signals for BLS Sand are generally more noisy than those for the SJR Sand, which may be due to more severe grain-to-grain slips by the larger and more angular sand grains of the BLS Sand. Total pressure signals are noisy, and unreasonable in some cases, especially for BLS Sand, presumably because of the fact that sand grains were large relative to the size of the sensing face of the transducer and perhaps failed to exert pressure evenly on the relatively small sensor faces. No electrical problems could be detected that would otherwise explain the noisy traces.

In Tests 9, 14, 15 and 17 (densest sand), a slightly negative toe force was observed that remained essentially constant over about one-forth to one-third of a cycle, which was followed by a high peak compressive force in the remainder of the cycle. This behavior indicated that the toe was being lifted off the soil, with some suction being generated beneath the toe, and later thrust back against the soil to give very high peak toe forces. In the other tests, especially for sand at the medium-dense state, near-sinusoidal toe force signals with lower amplitudes than those in the above tests were recorded, which suggests a different mechanism of toe penetration. All velocity signals were generally sinusoidal with excursions of approximately one foot per second about the zero velocity line.

In dense sand (relative density = 90%), the pore water pressure on the pile shaft near the pile toe exhibited steady state sinusoidal behavior with mean values very close to the geostatic pore water pressure in the chamber at half and full penetration and with excursions of from 0.5 to 2.0 psi about the mean. In the medium-dense sand, the pore water pressure was usually in the transient state of increasing as the pile was penetrating (or dissipating if the vibrator was in the process of being shut down). This phenomenon of pore pressure buildup against the pile wall may partially explain the relatively higher rates of penetration of the pile in the medium-dense sand compared to those in dense sand, where no ambient pore pressure change was indicated during vibro-driving.

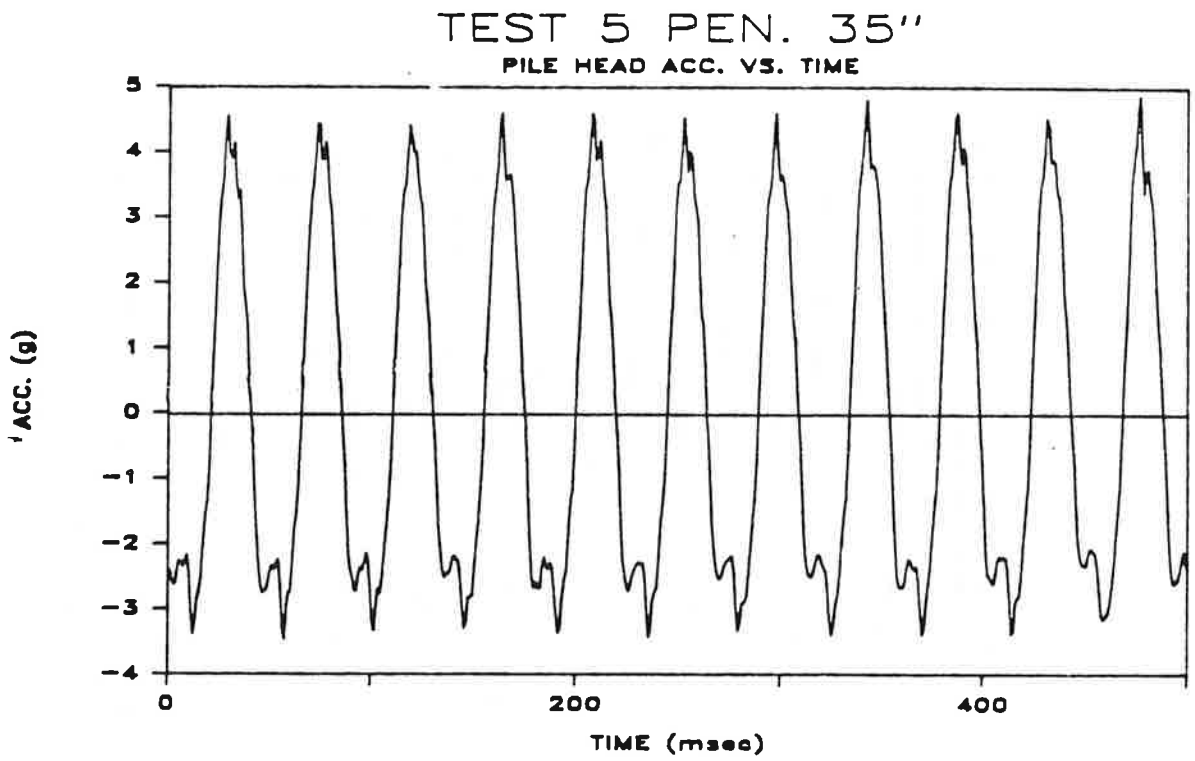

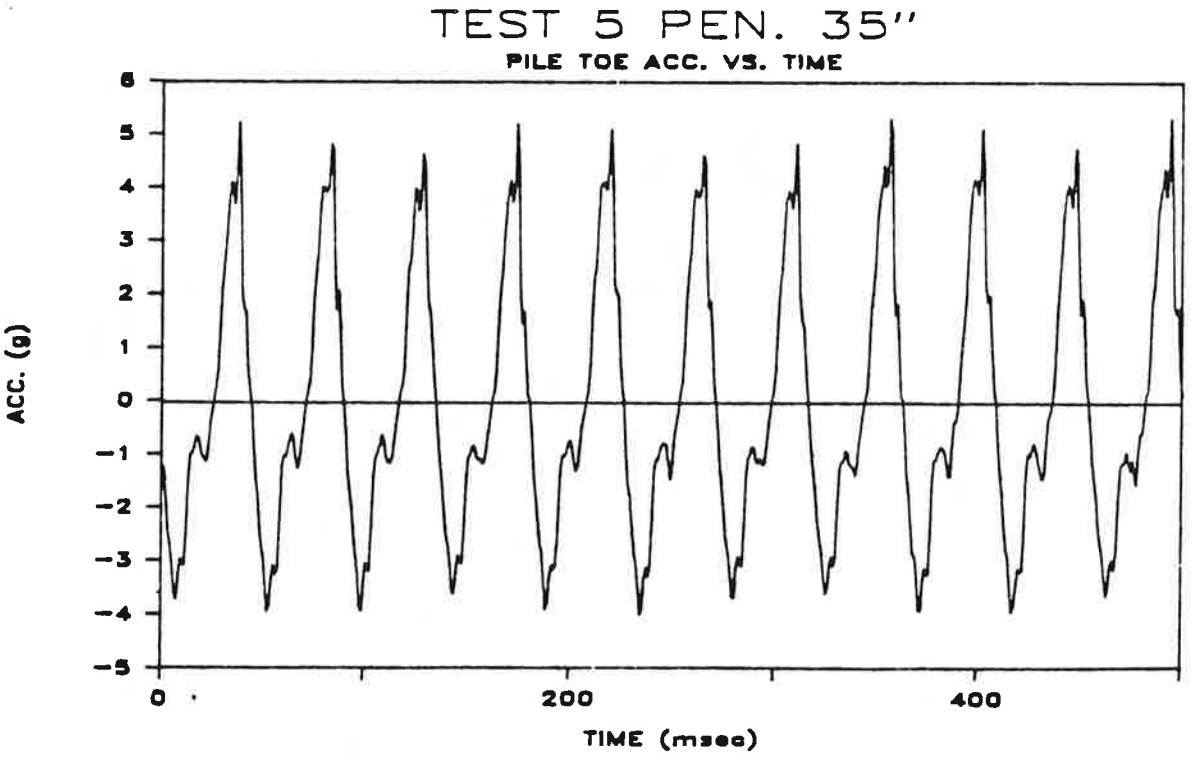

Fig. M.1a. Pile-Head and Toe Acceleration Vs. Time; Penetration = 35 Inches; Test 5

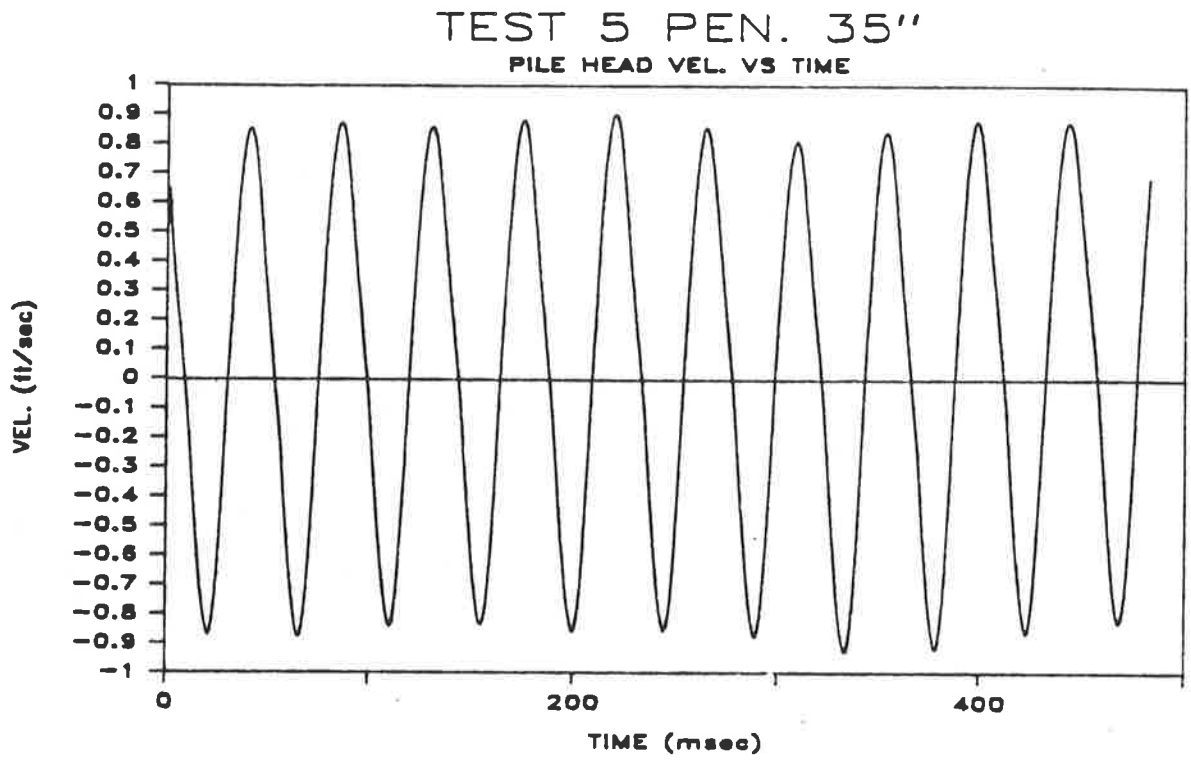

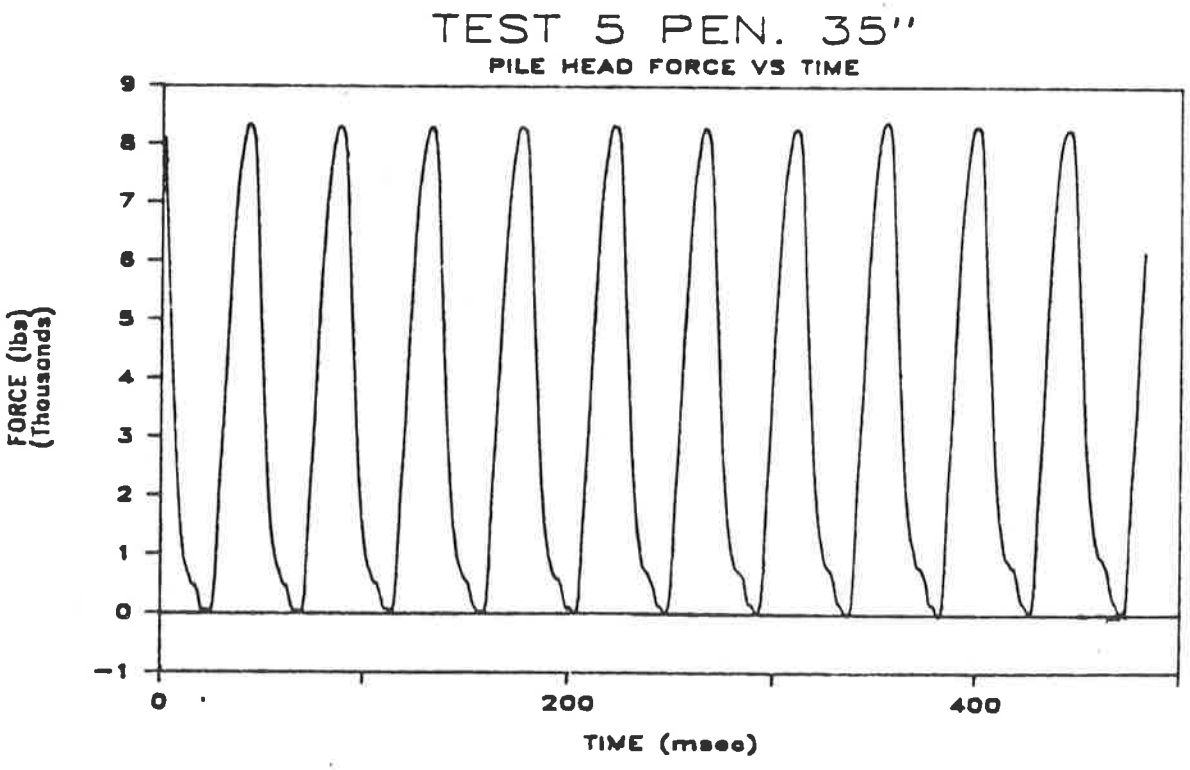

Fig. M.1b. Pile-Head Velocity and ForceVs. Time; Penetration = 35 Inches; Test 5

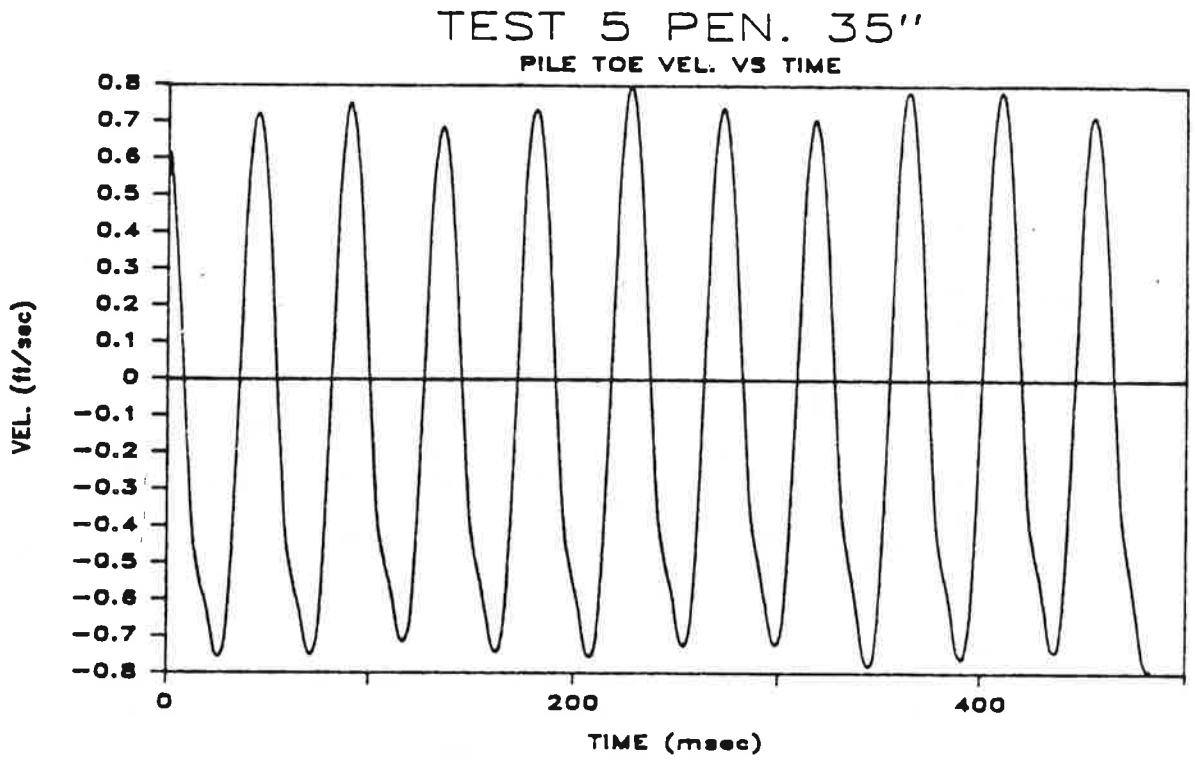

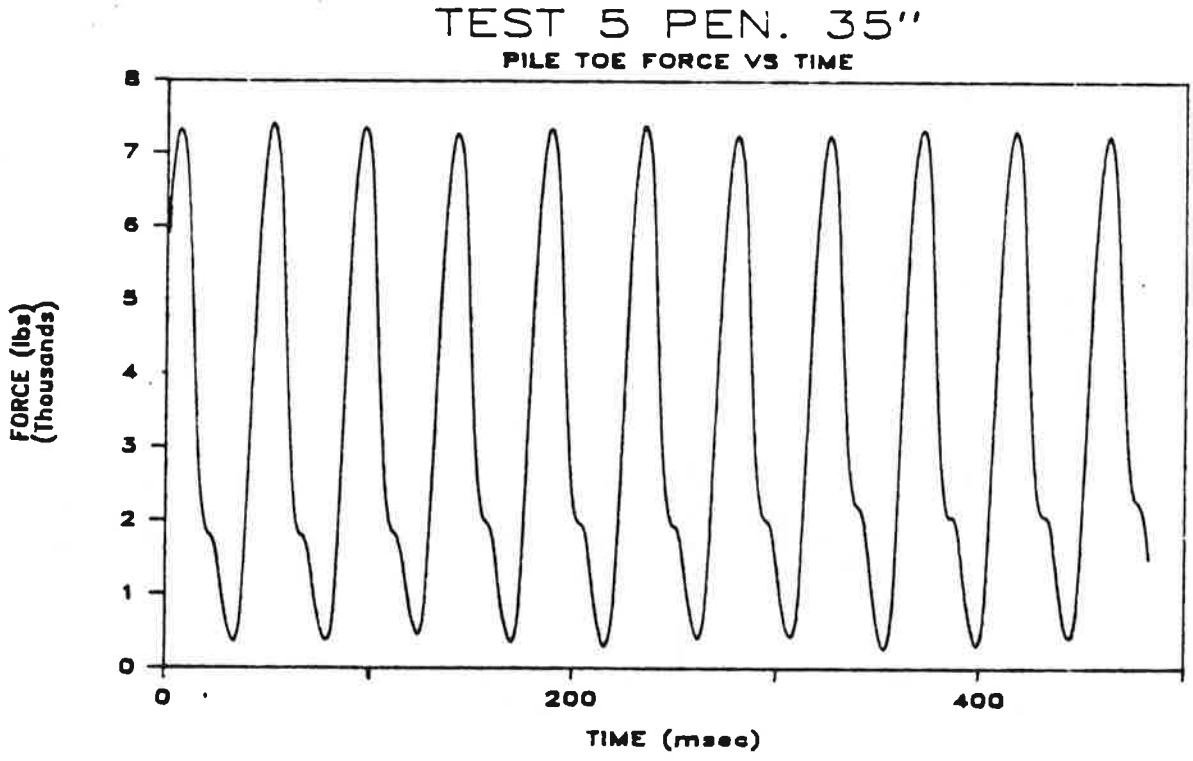

Fig. M.1c. Pile-Toe Velocity and Force Vs. Time; Penetration = 35 Inches; Test 5

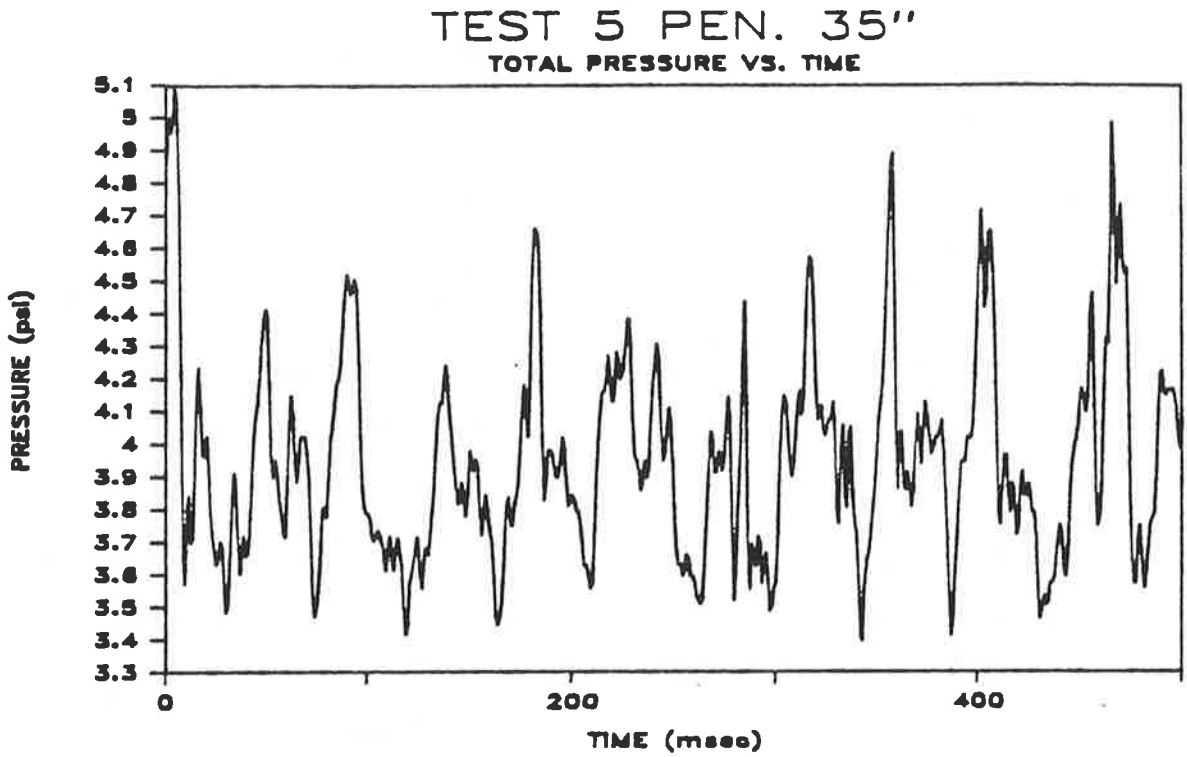

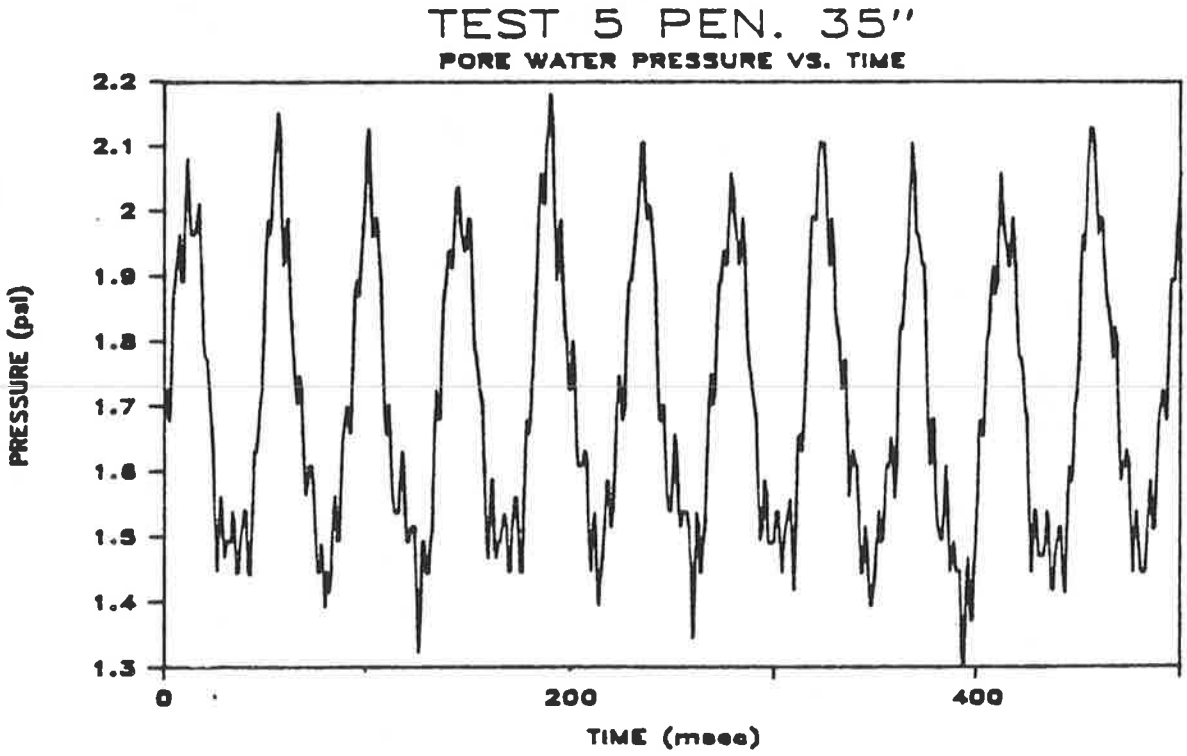

Fig. M.1d. Total and Pore Water Pressure Vs. Time at Bottom of Pile Shaft; Penetration = 35 Inches; Test 5

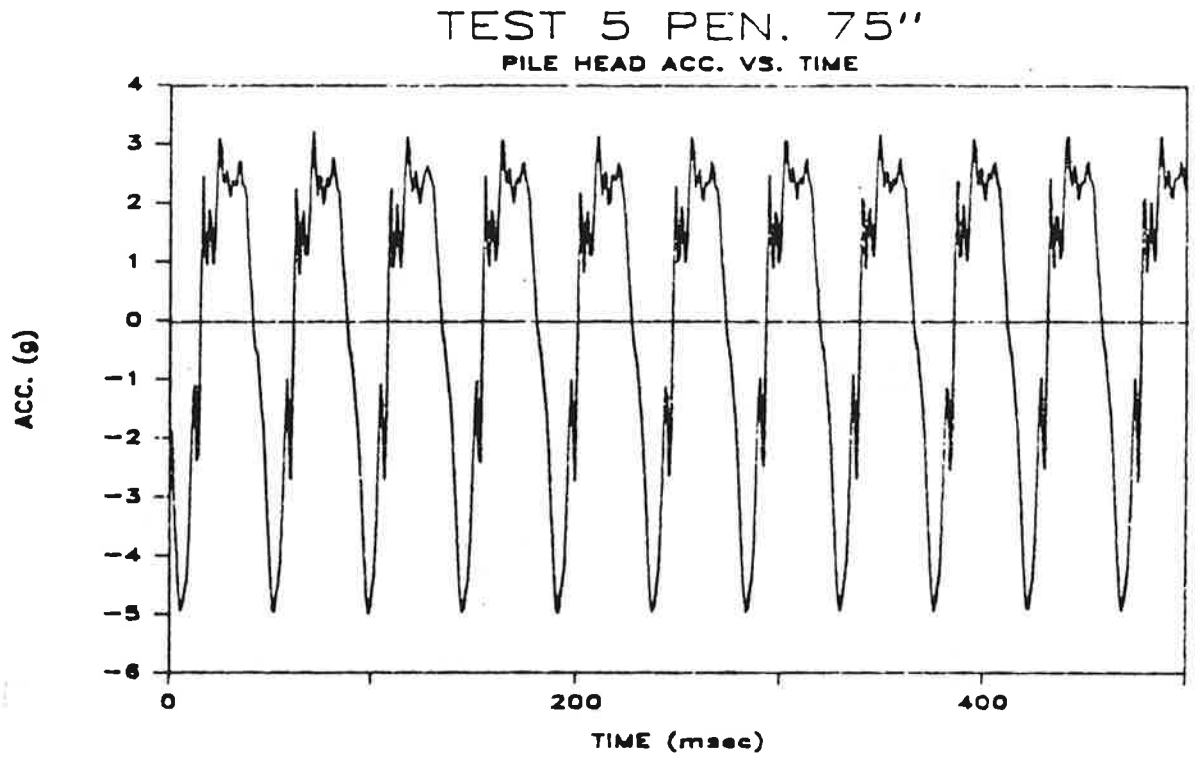

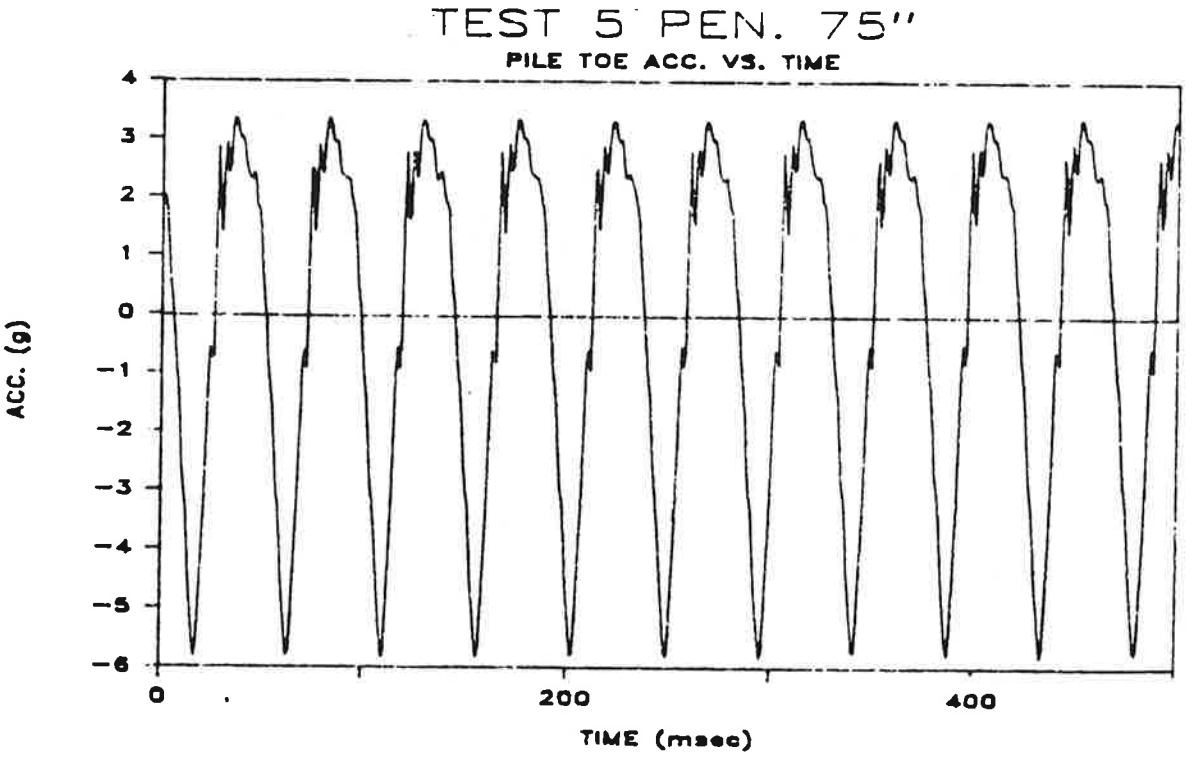

Fig. M.2a. Pile-Head and Toe Acceleration Vs. Time; Penetration = 75 Inches; Test 5

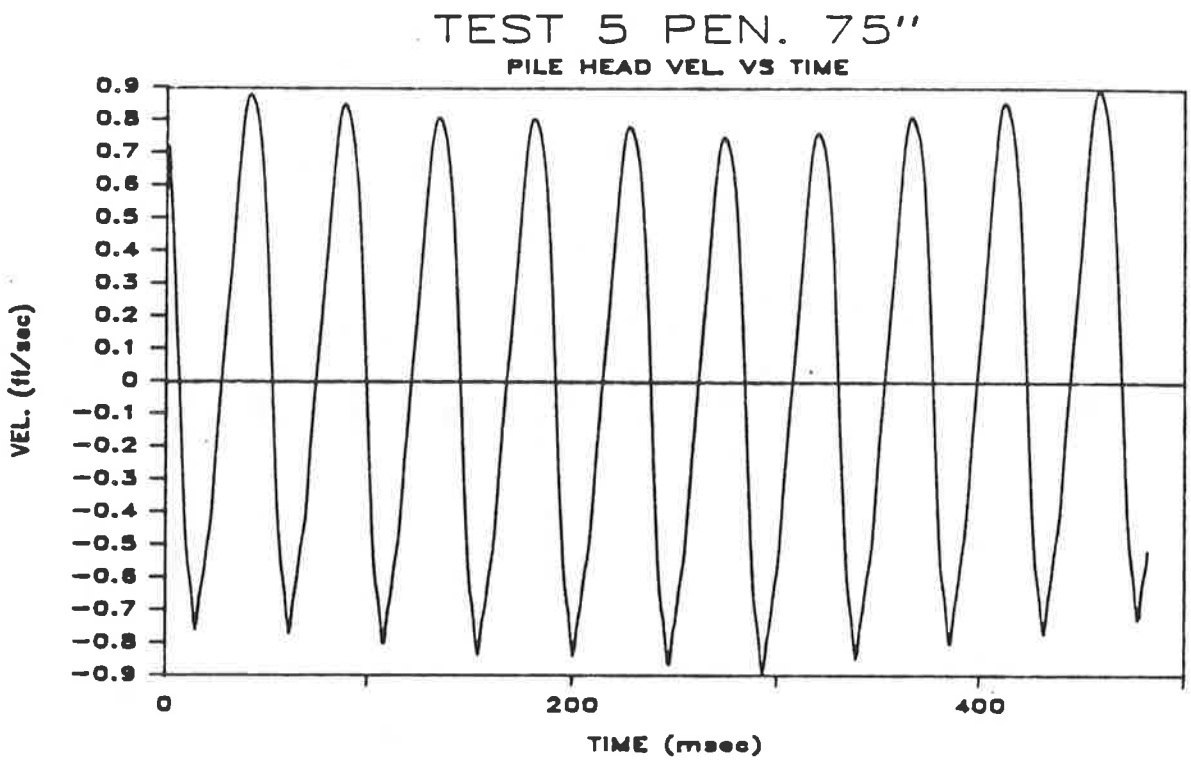

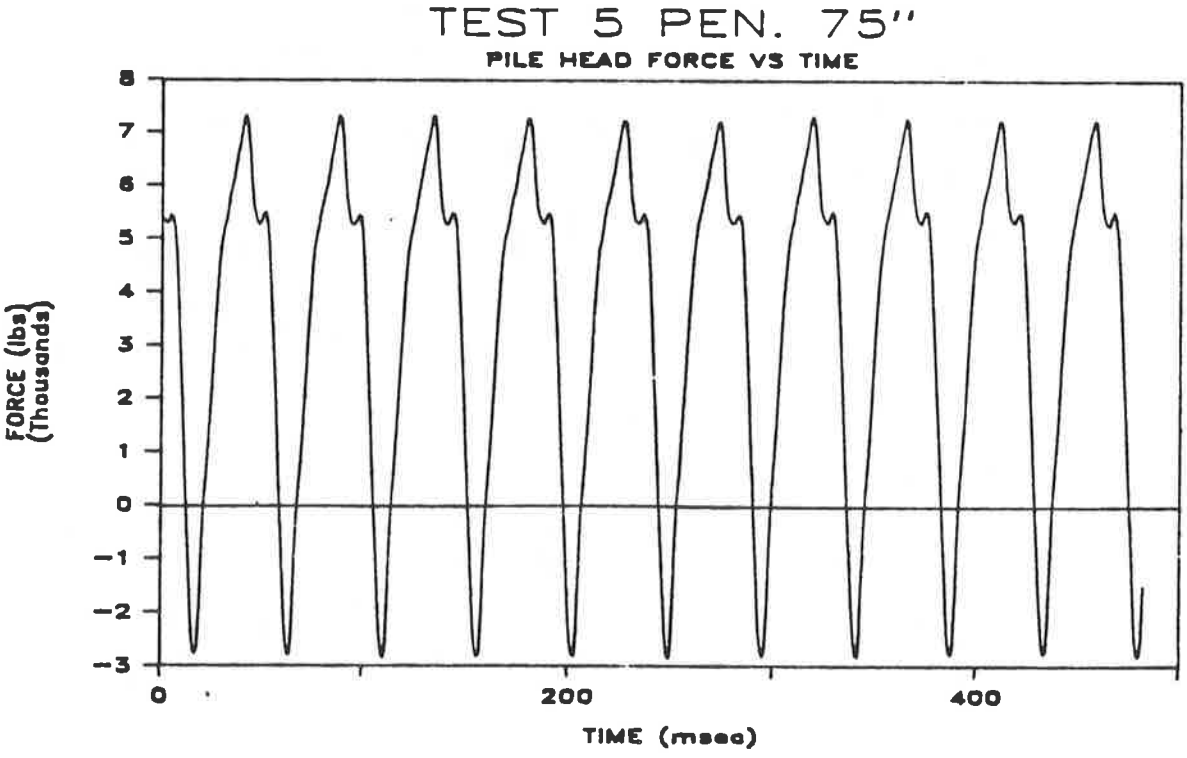

Fig. M.2b. Pile-Head Velocity and ForceVs. Time; Penetration = 75 Inches; Test 5

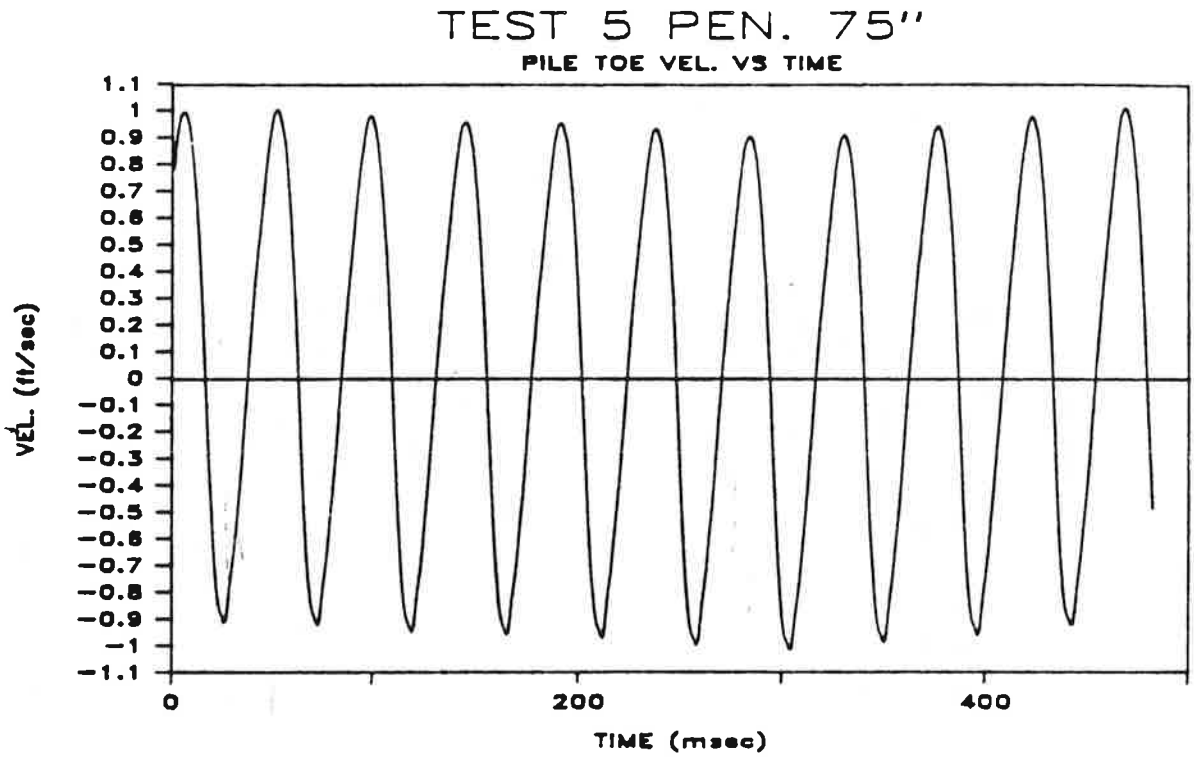

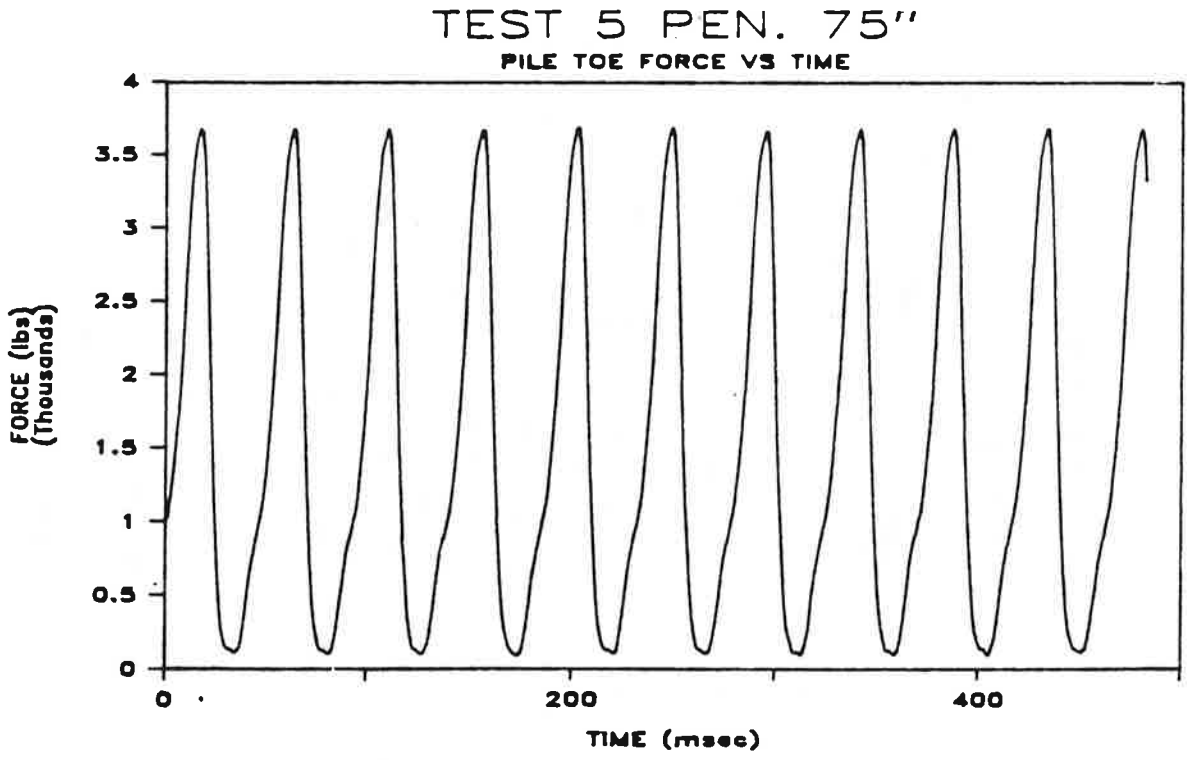

Fig. M.2c. Pile-Toe Velocity and Force Vs. Time; Penetration = 75 Inches; Test 5

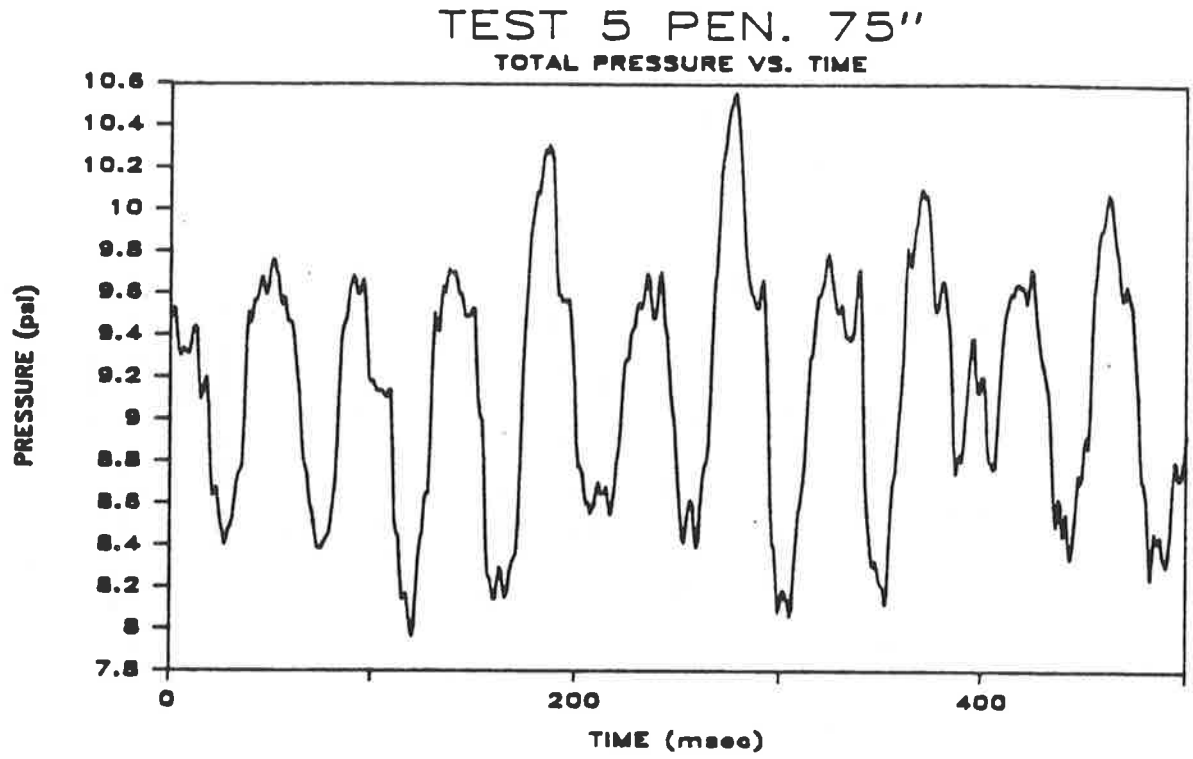

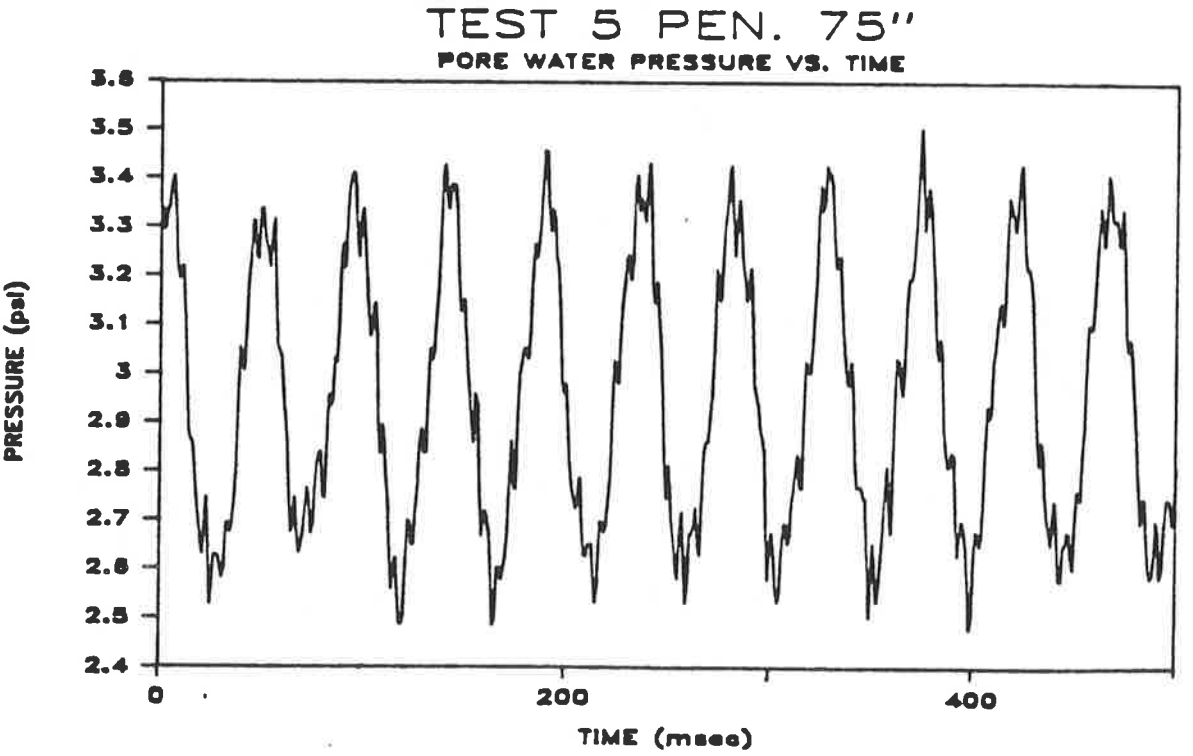

Fig. M.2d. Total and Pore Water Pressure Vs. Time at Bottom of Pile Shaft; Penetration = 75 Inches; Test 5

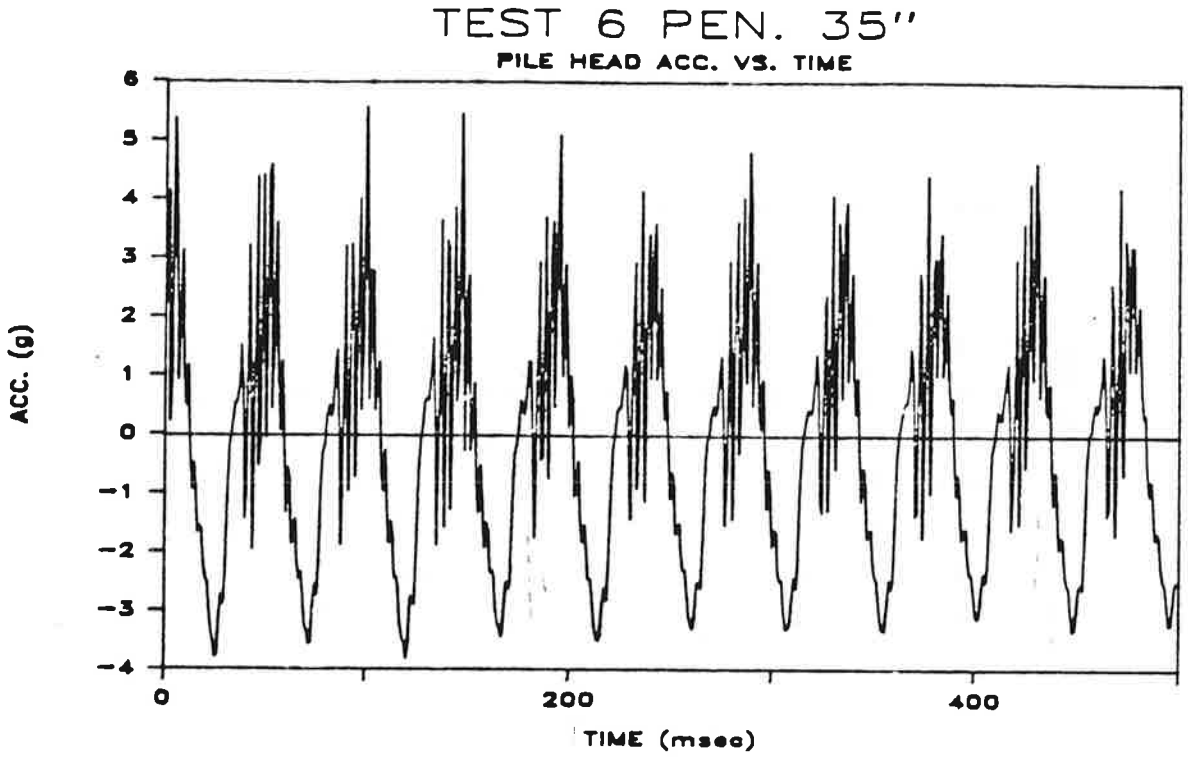

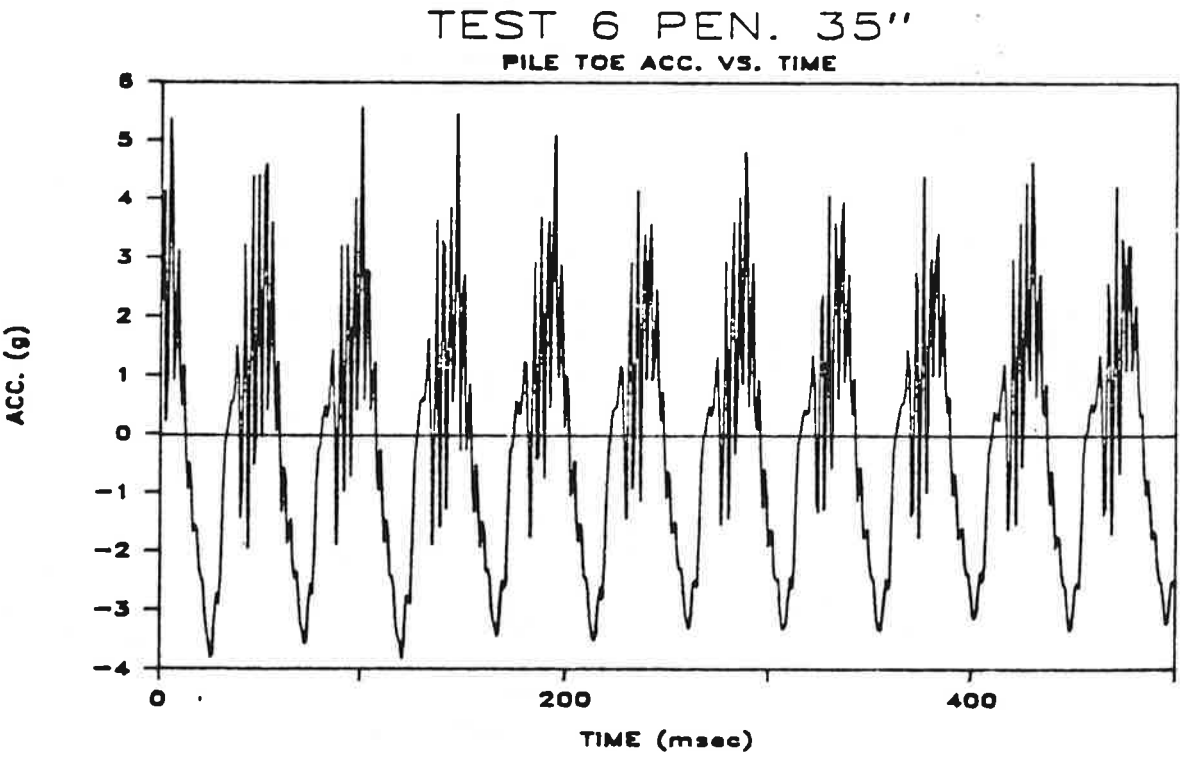

Fig. M.3a. Pile-Head and Toe Acceleration Vs. Time; Penetration = 35 Inches; Test 6

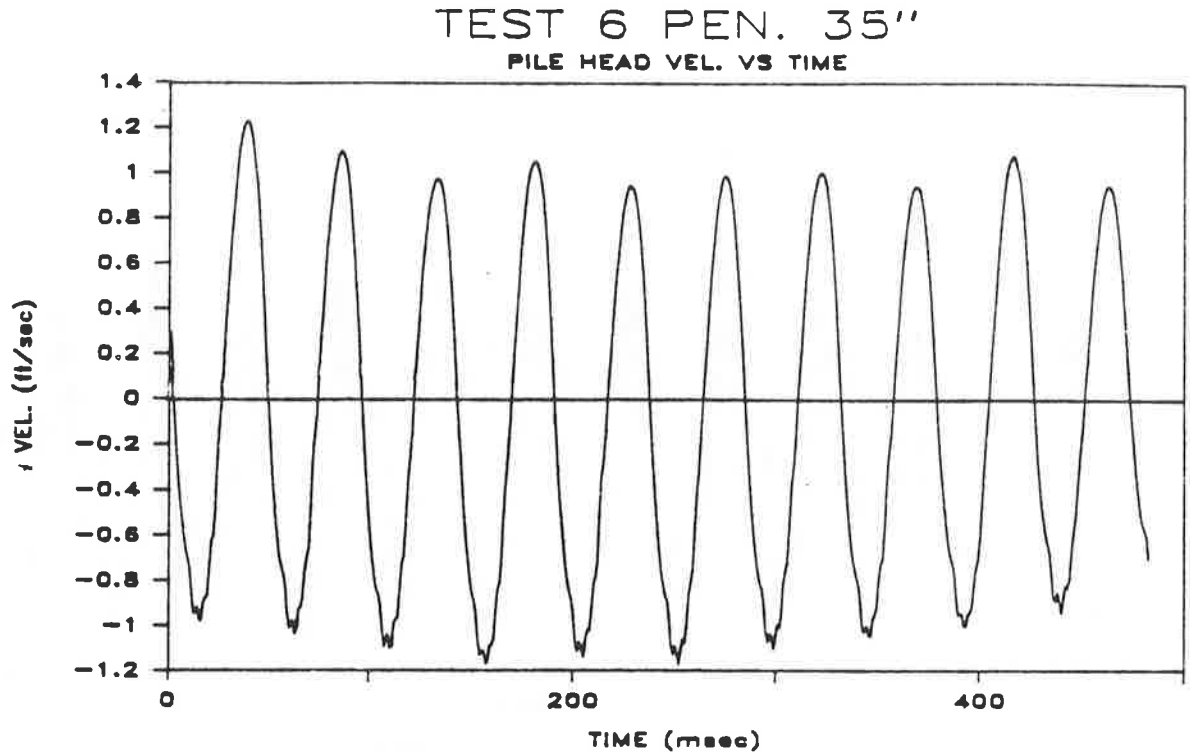

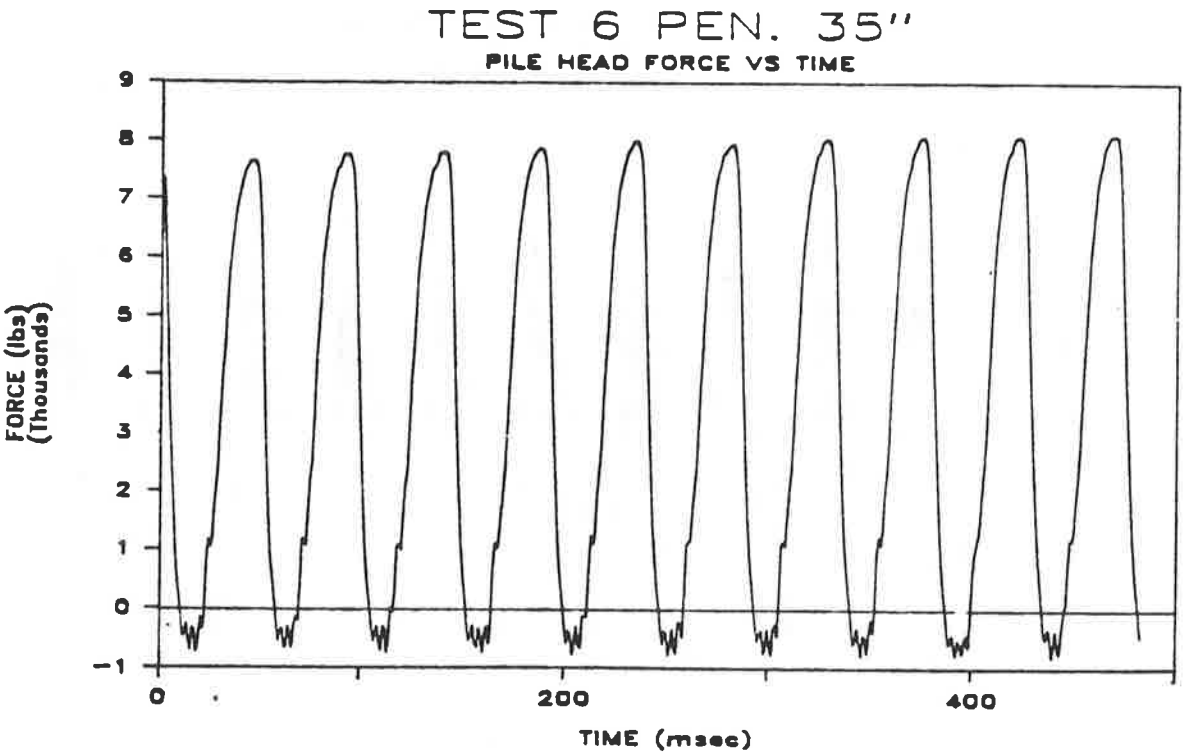

Fig. M.3b. Pile-Head Velocity and ForceVs. Time; Penetration = 35 Inches; Test 6

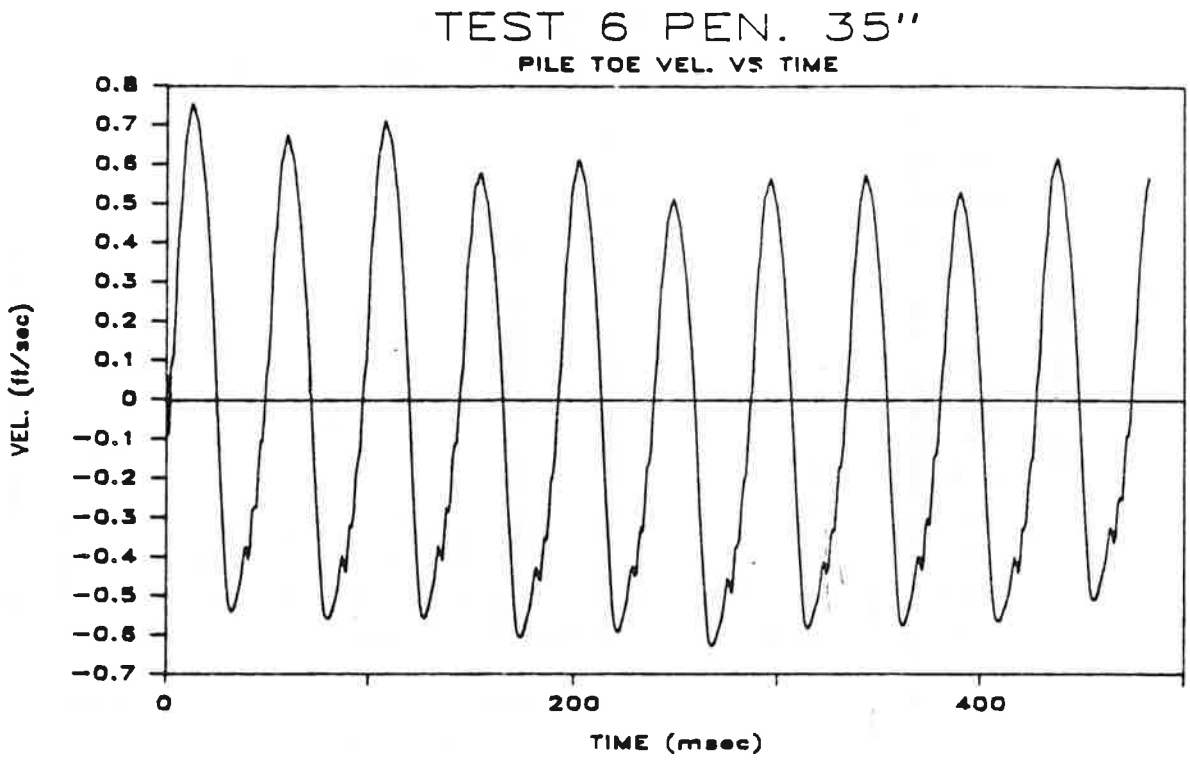

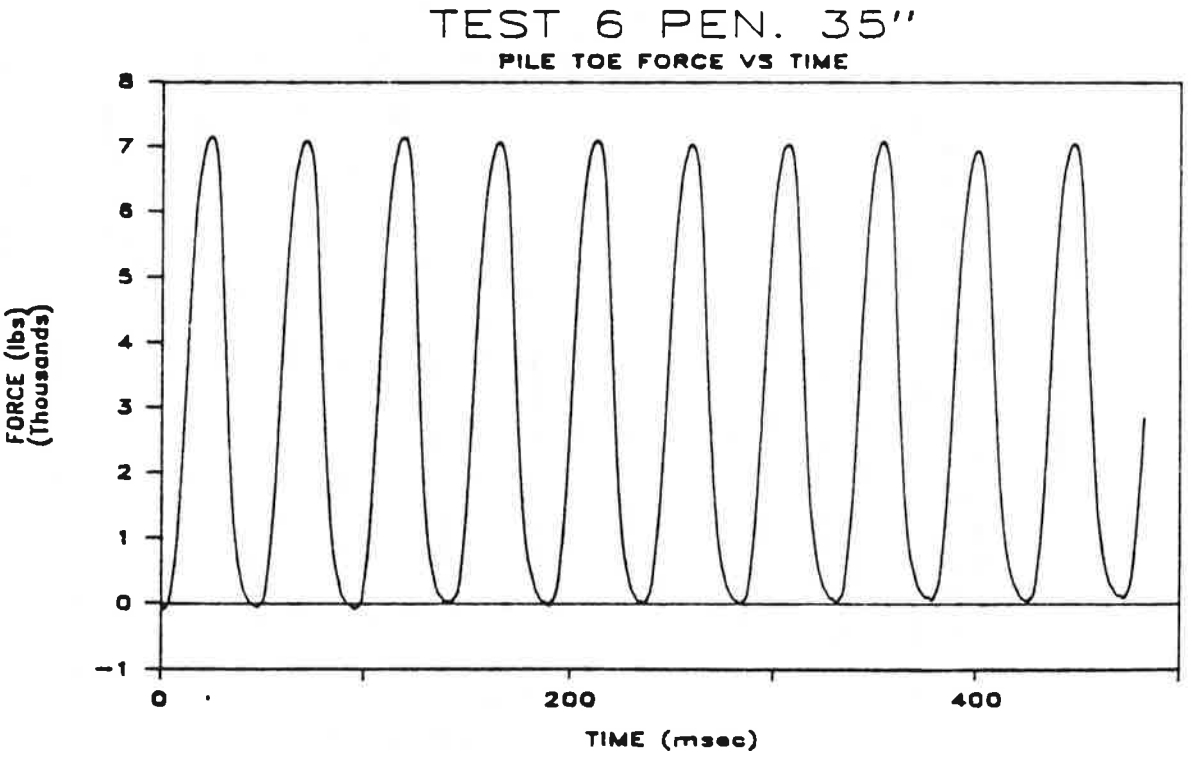

Fig. M.3c. Pile-Toe Velocity and Force Vs. Time; Penetration = 35 Inches; Test 6

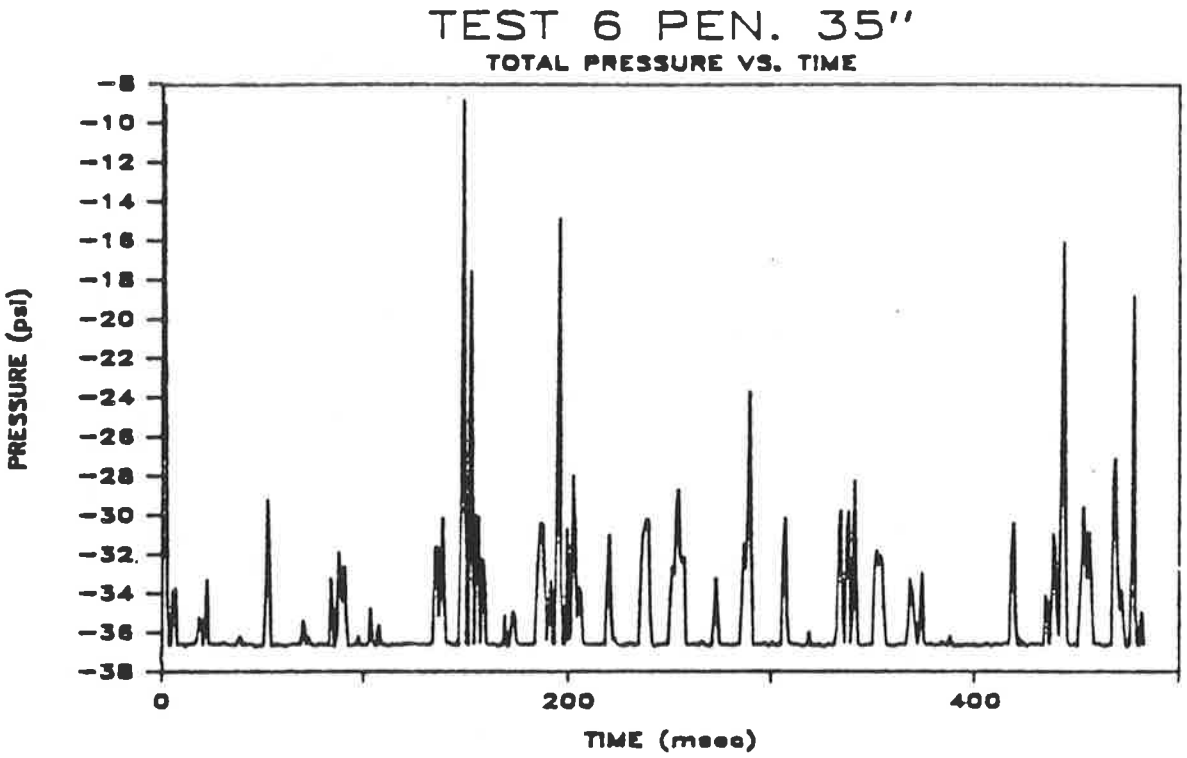

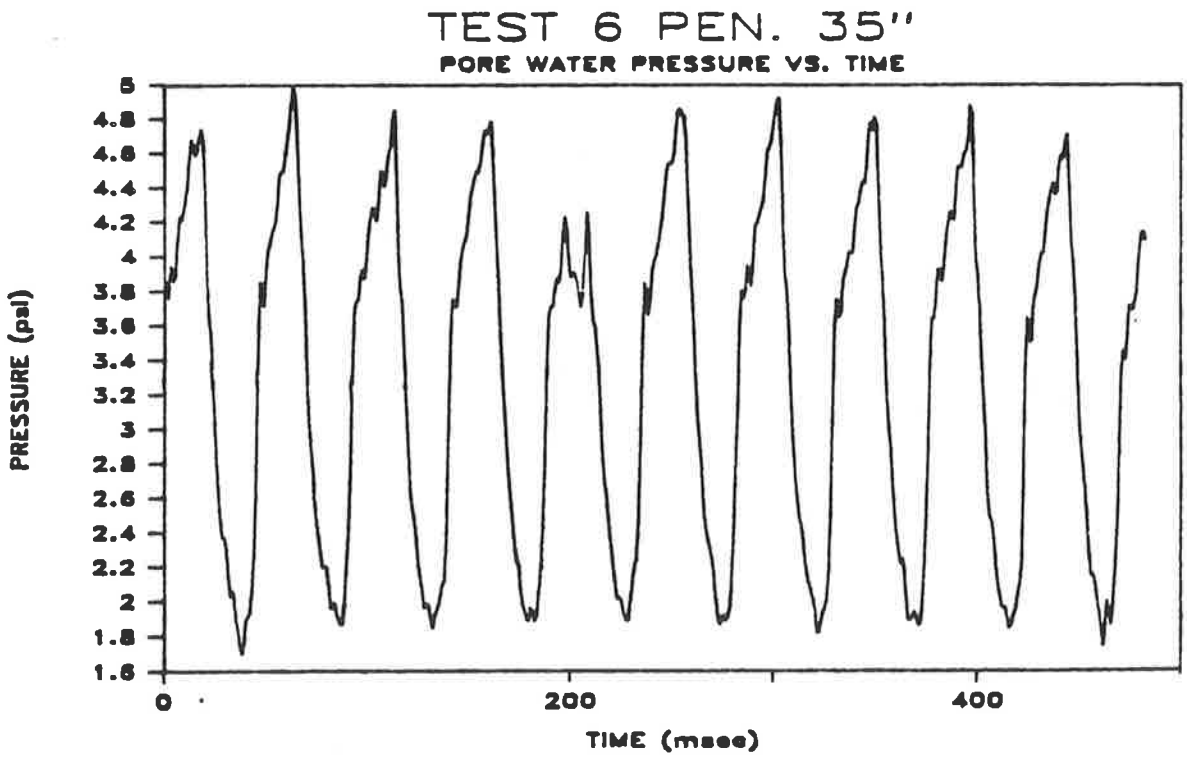

Fig. M.3d. Total and Pore Water Pressure Vs. Time at Bottom of Pile Shaft; Penetration = 35 Inches; Test 6

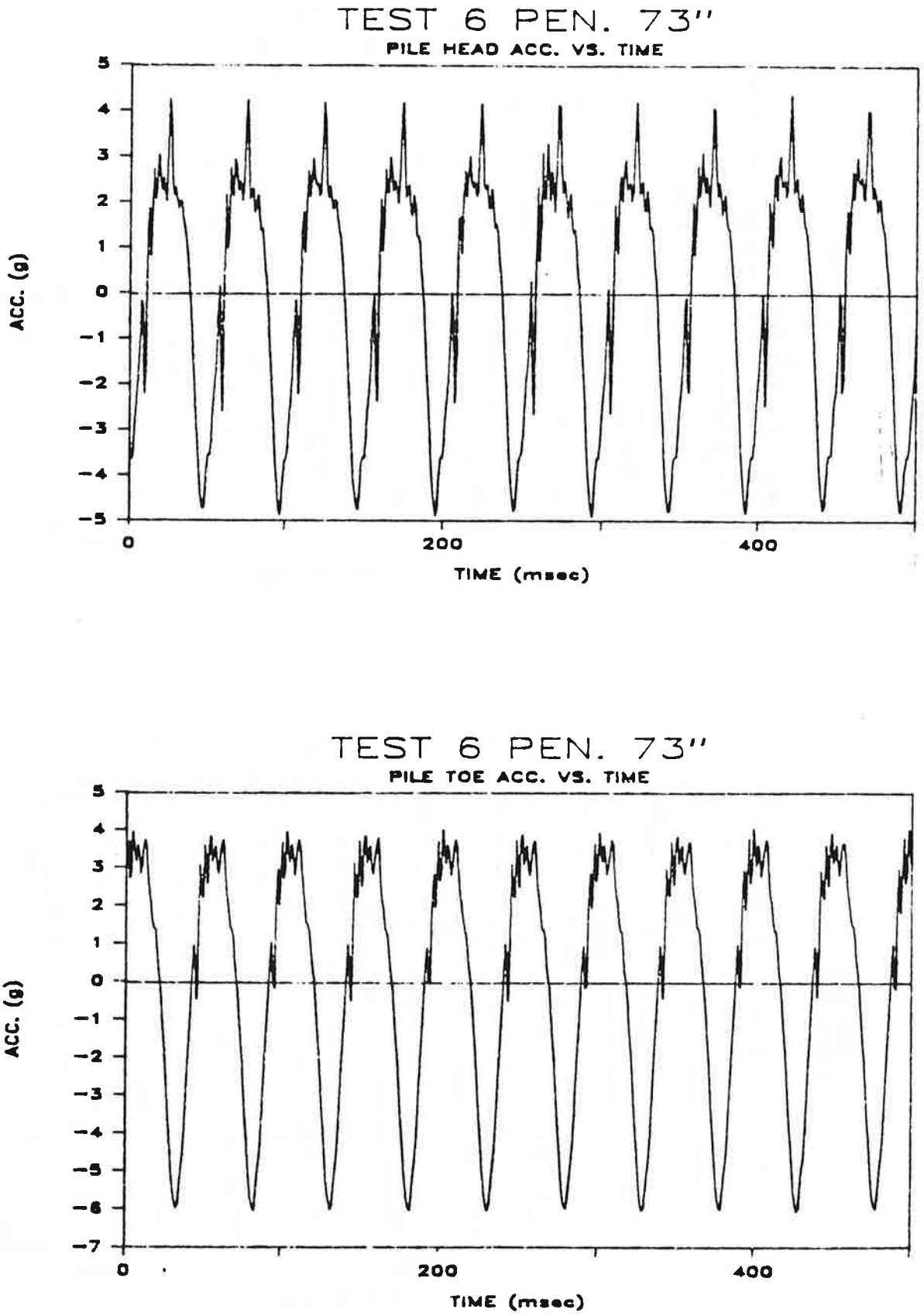

Fig. M.4a. Pile-Head and Toe Acceleration Vs. Time; Penetration = 73 Inches; Test 6

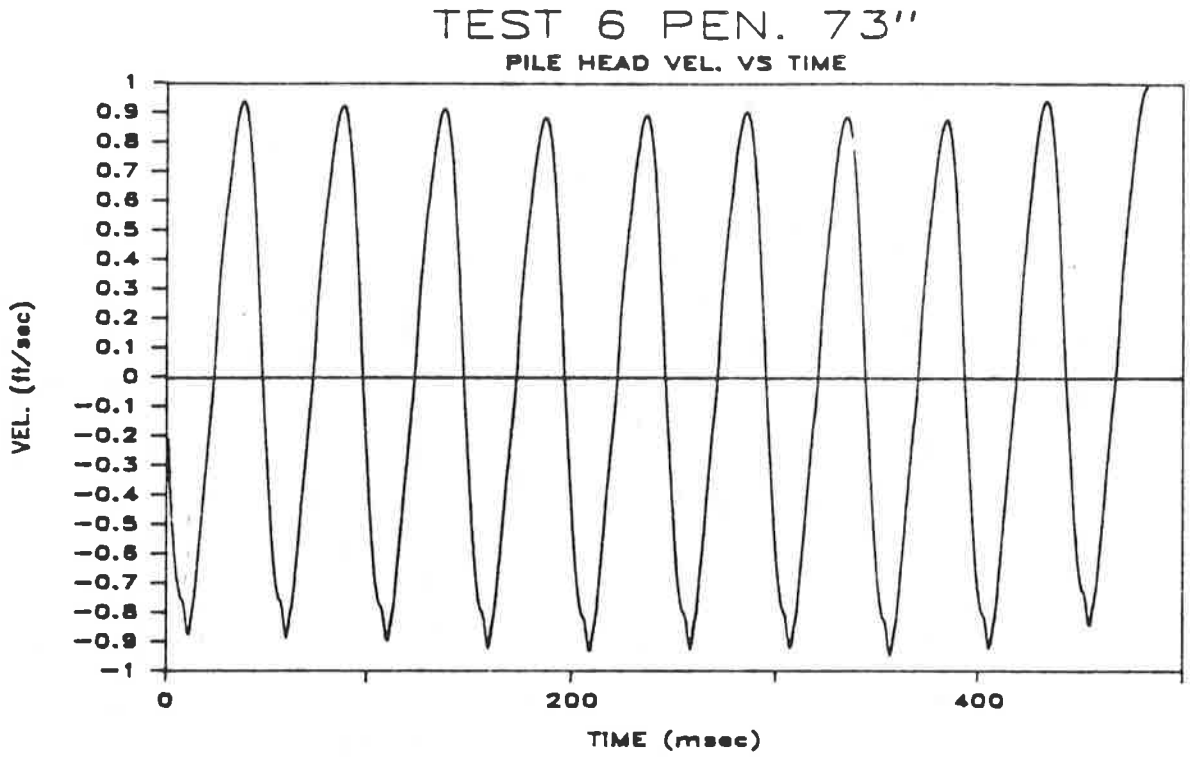

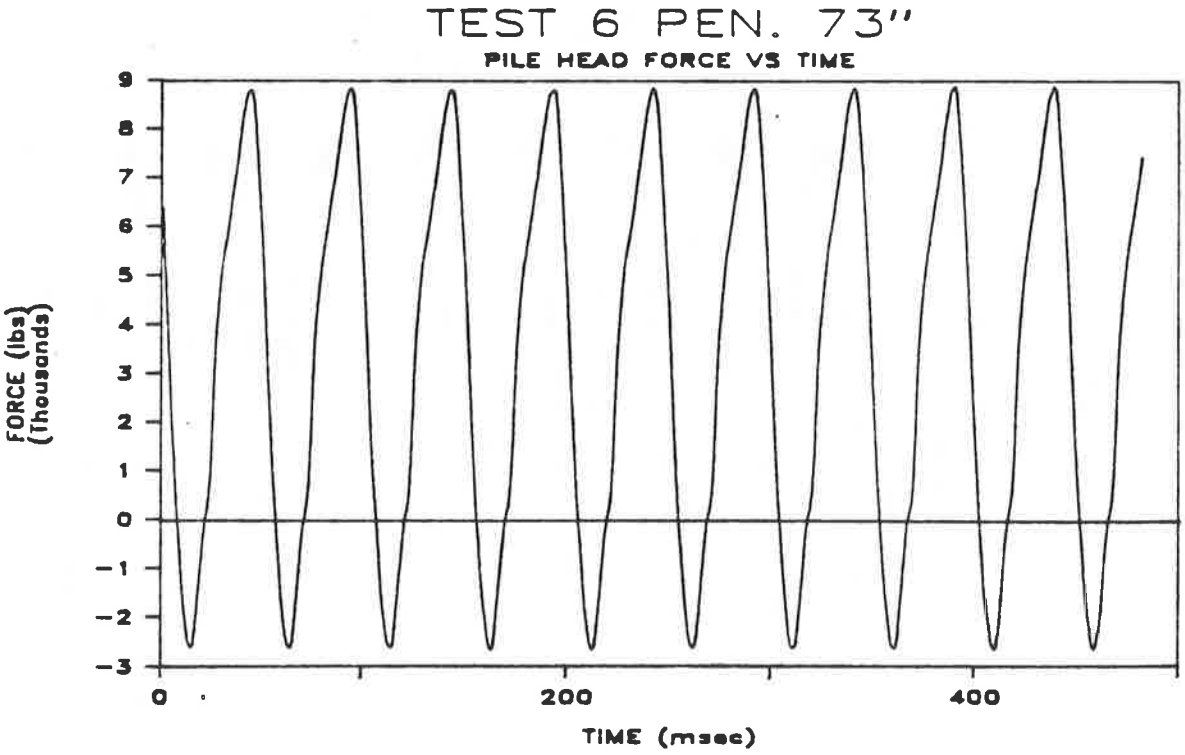

Fig. M.4b. Pile-Head Velocity and ForceVs. Time; Penetration = 73 Inches; Test 6

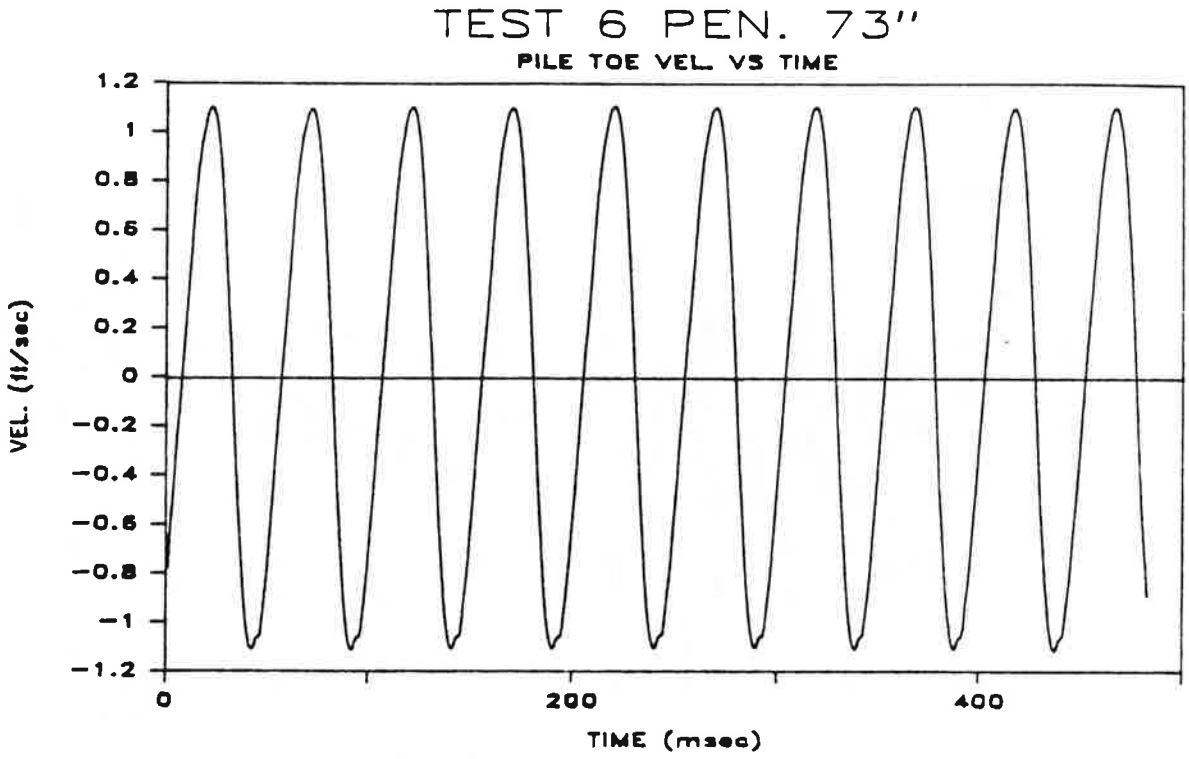

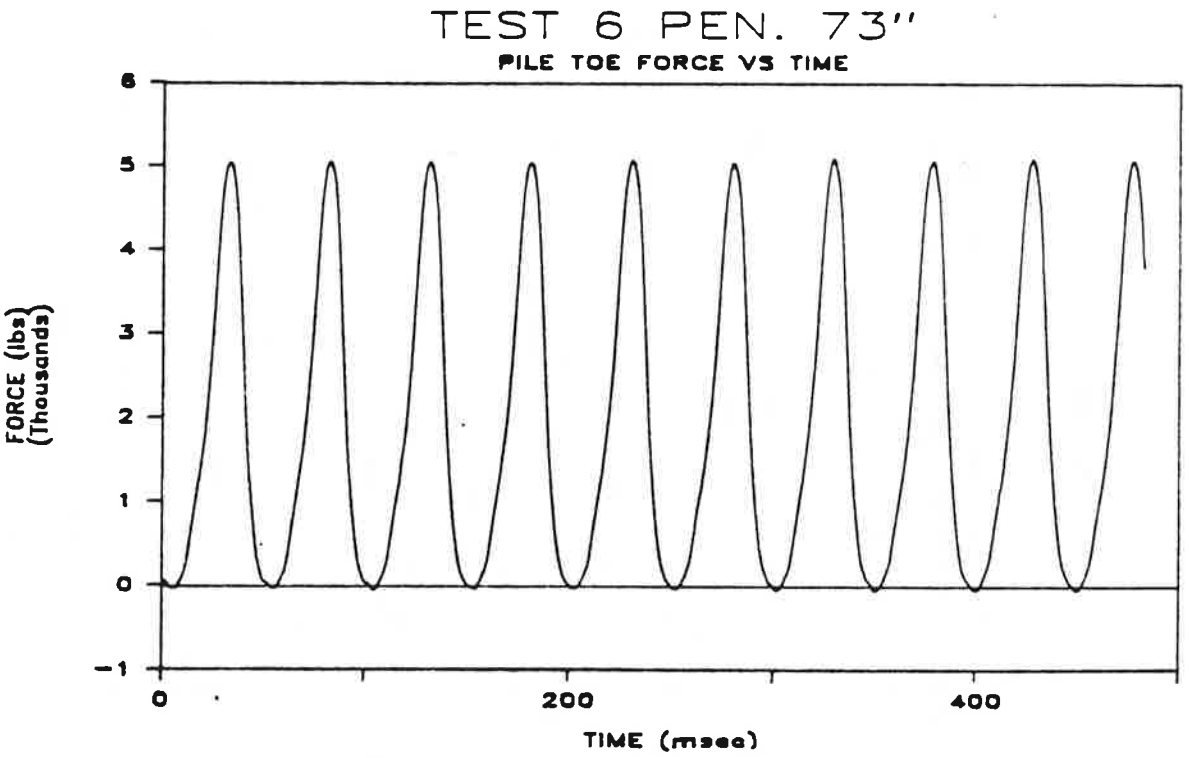

Fig. M.4c. Pile-Toe Velocity and Force Vs. Time; Penetration = 73 Inches; Test 6

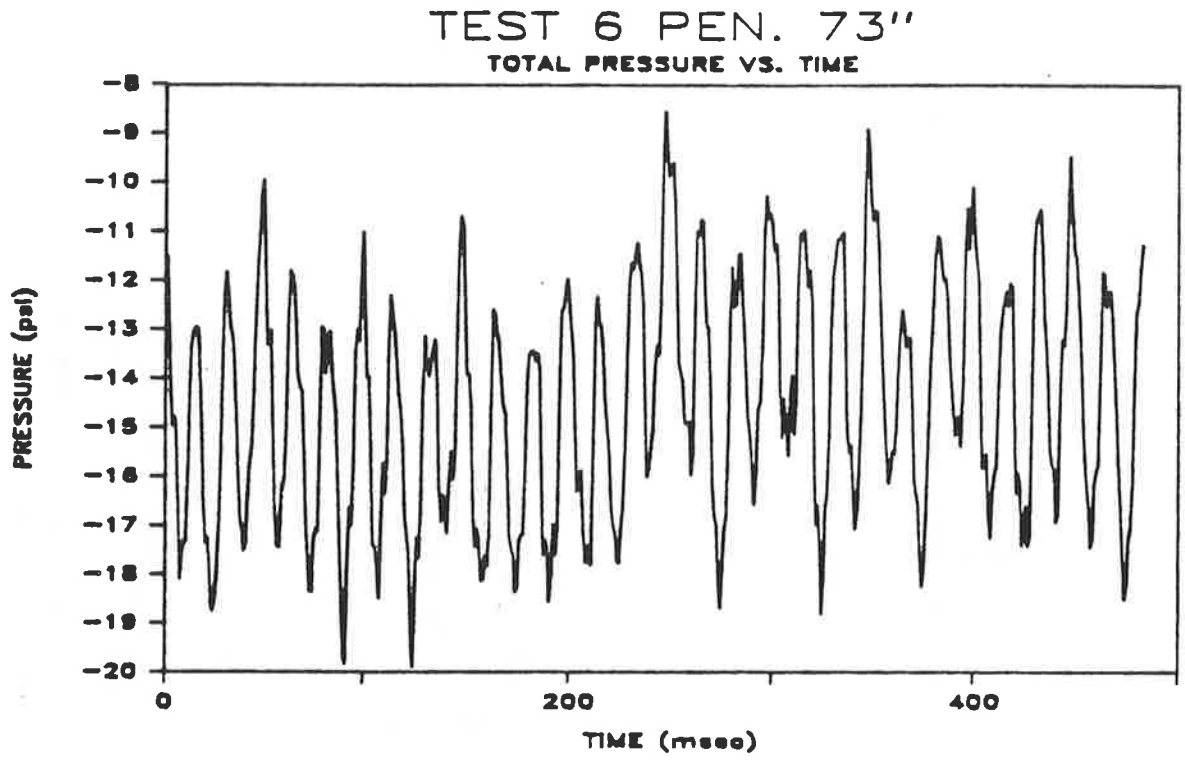

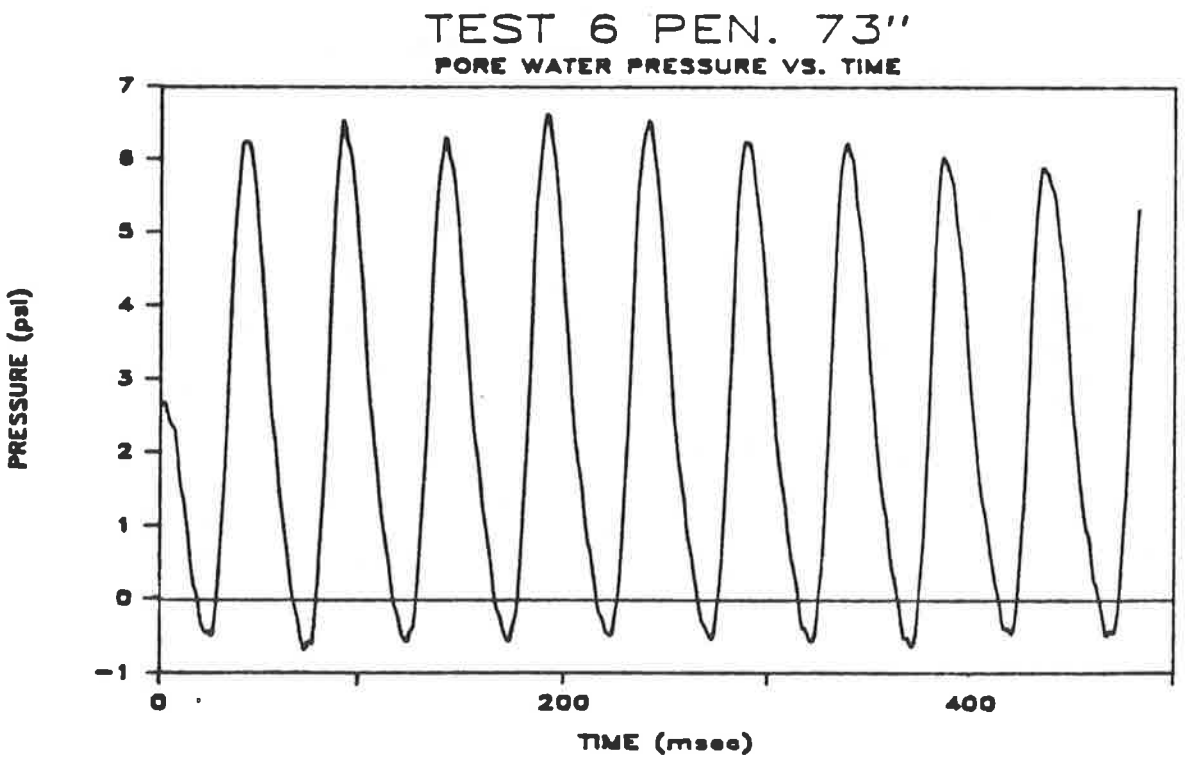

Fig. M.4d. Total and Pore Water Pressure Vs. Time at Bottom of Pile Shaft; Penetration = 73 Inches; Test 6

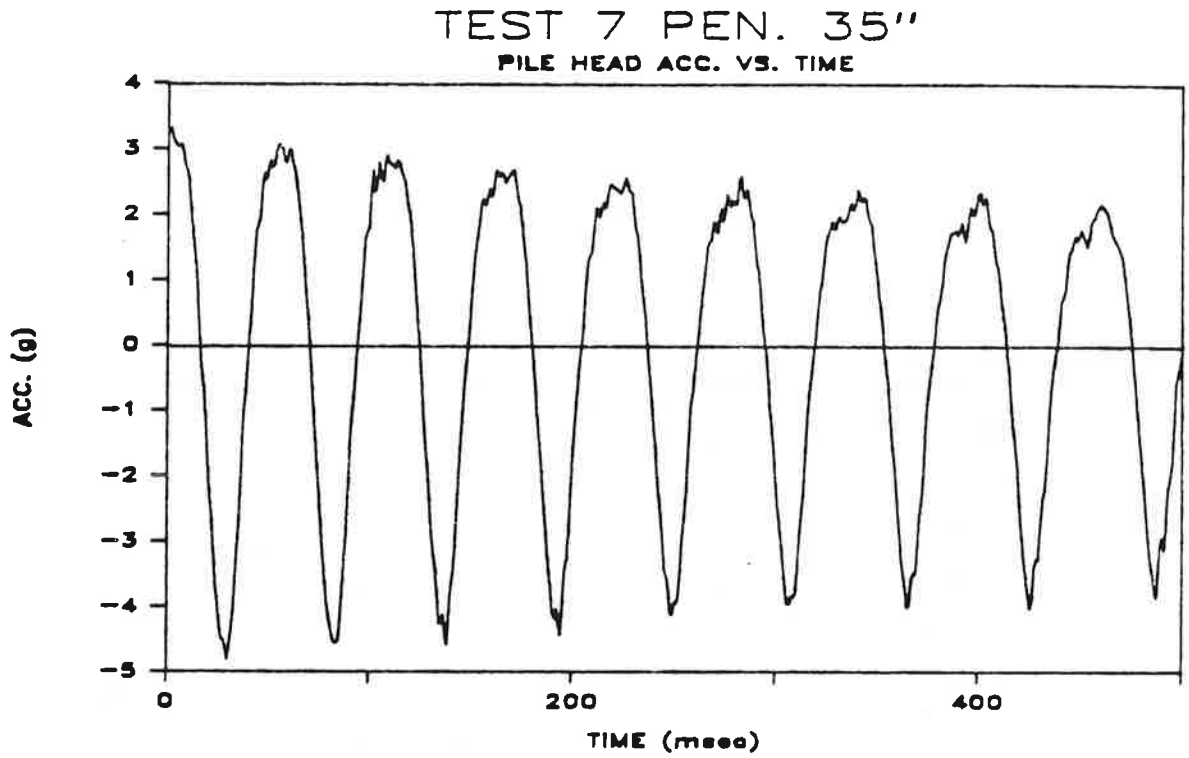

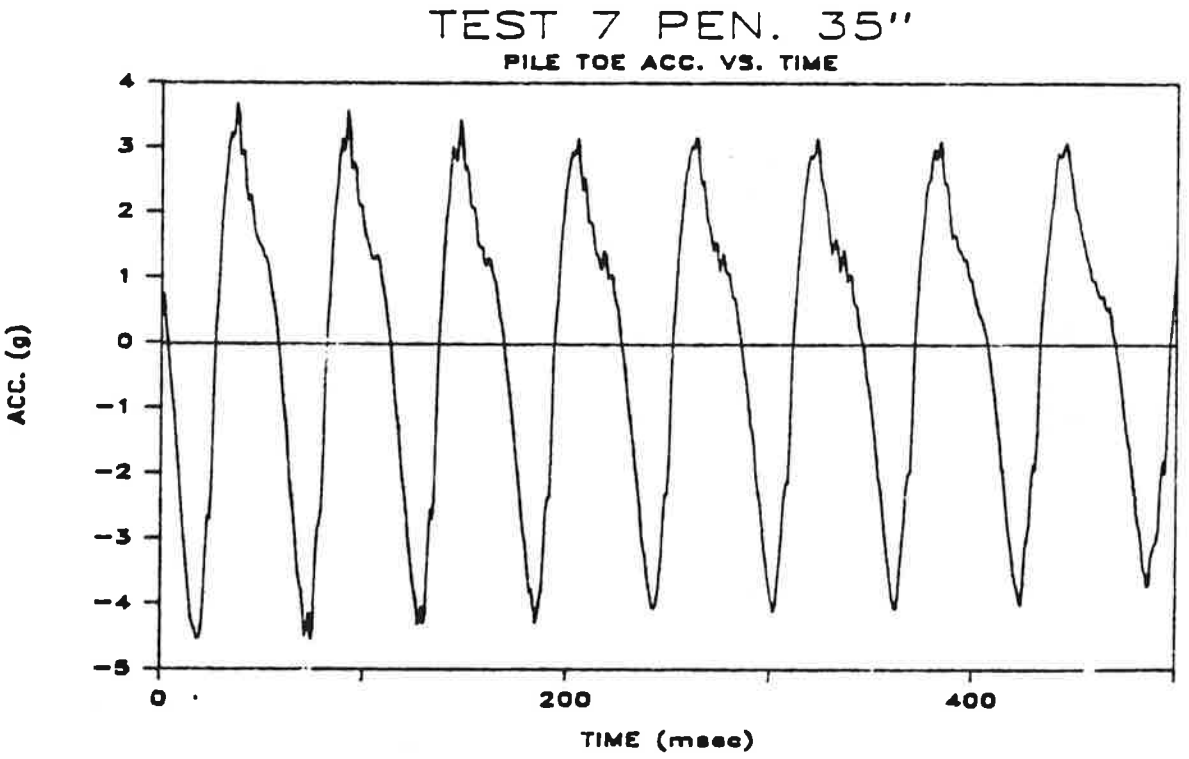

Fig. M.5a. Pile-Head and Toe Acceleration Vs. Time; Penetration = 35 Inches; Test 7

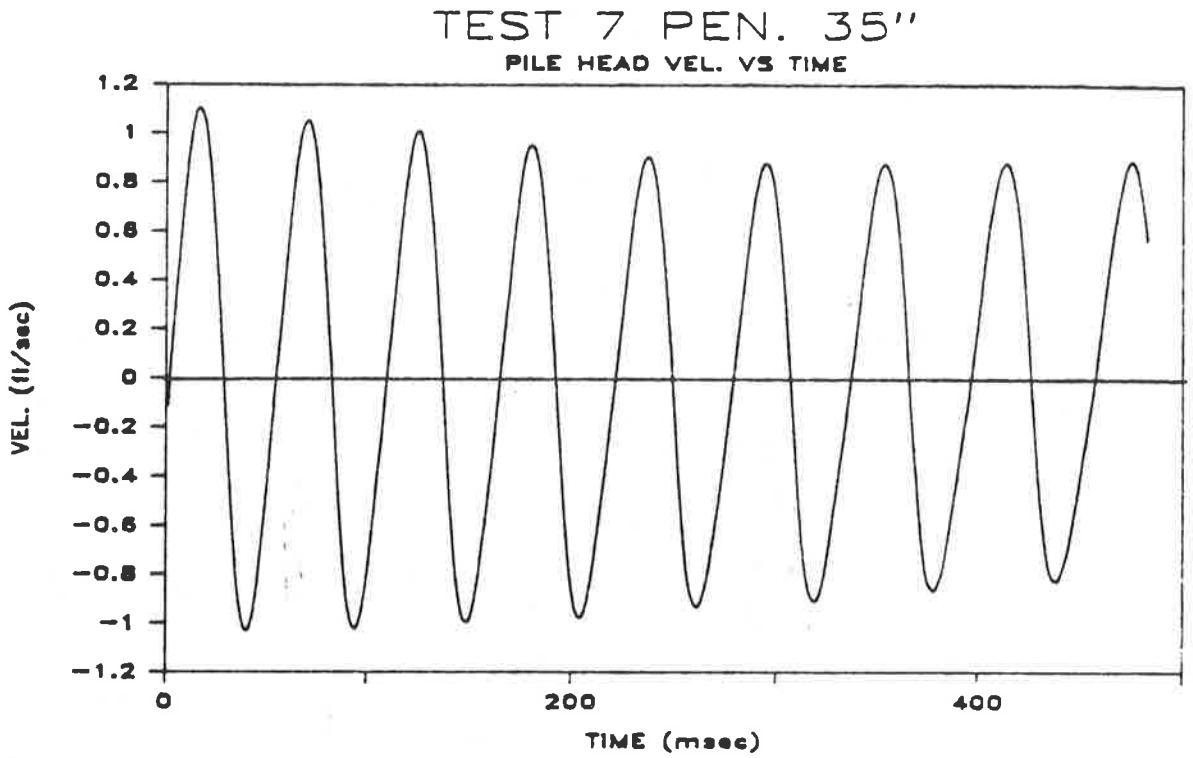

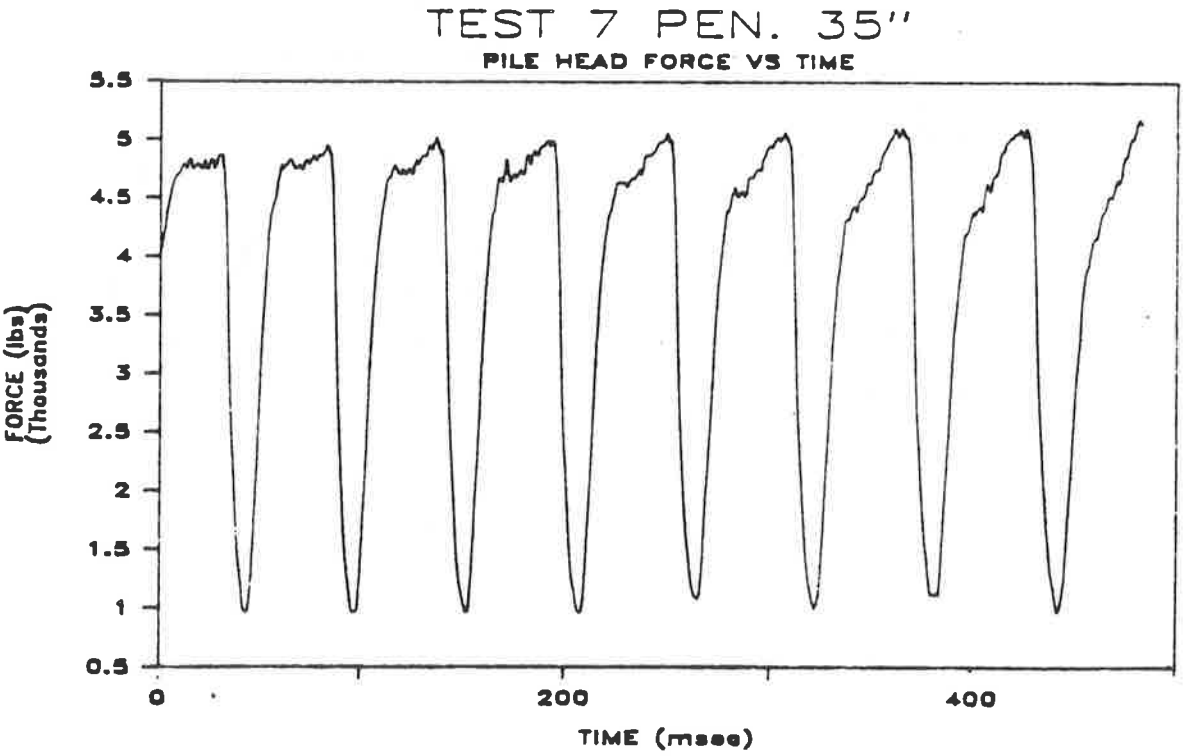

Fig. M.5b. Pile-Head Velocity and ForceVs. Time; Penetration = 35 Inches; Test 7

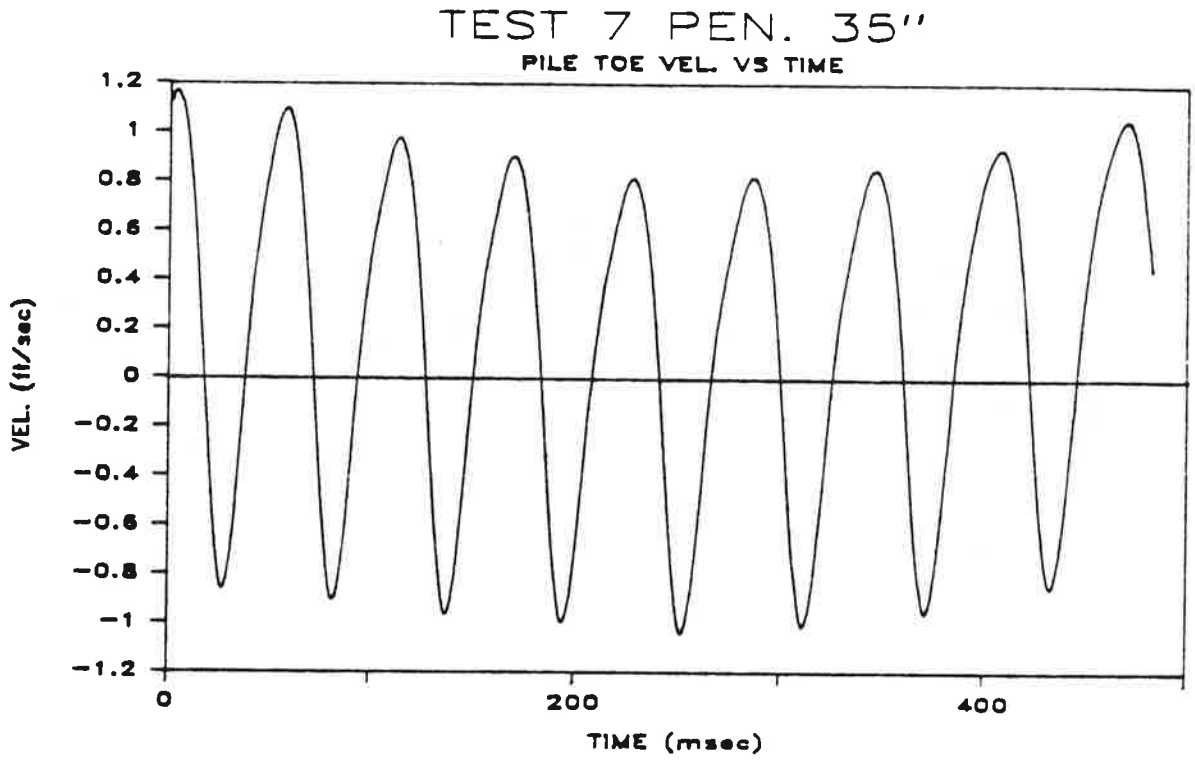

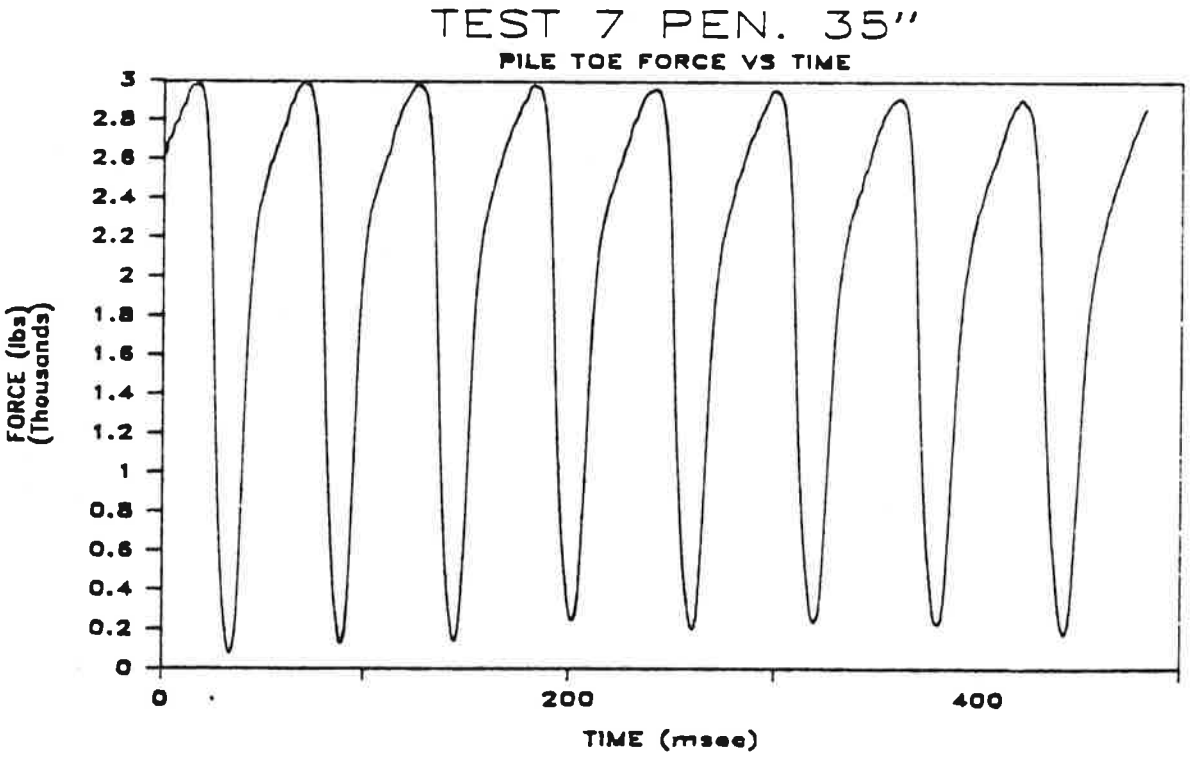

Fig. M.5c. Pile-Toe Velocity and Force Vs. Time; Penetration = 35 Inches; Test 7

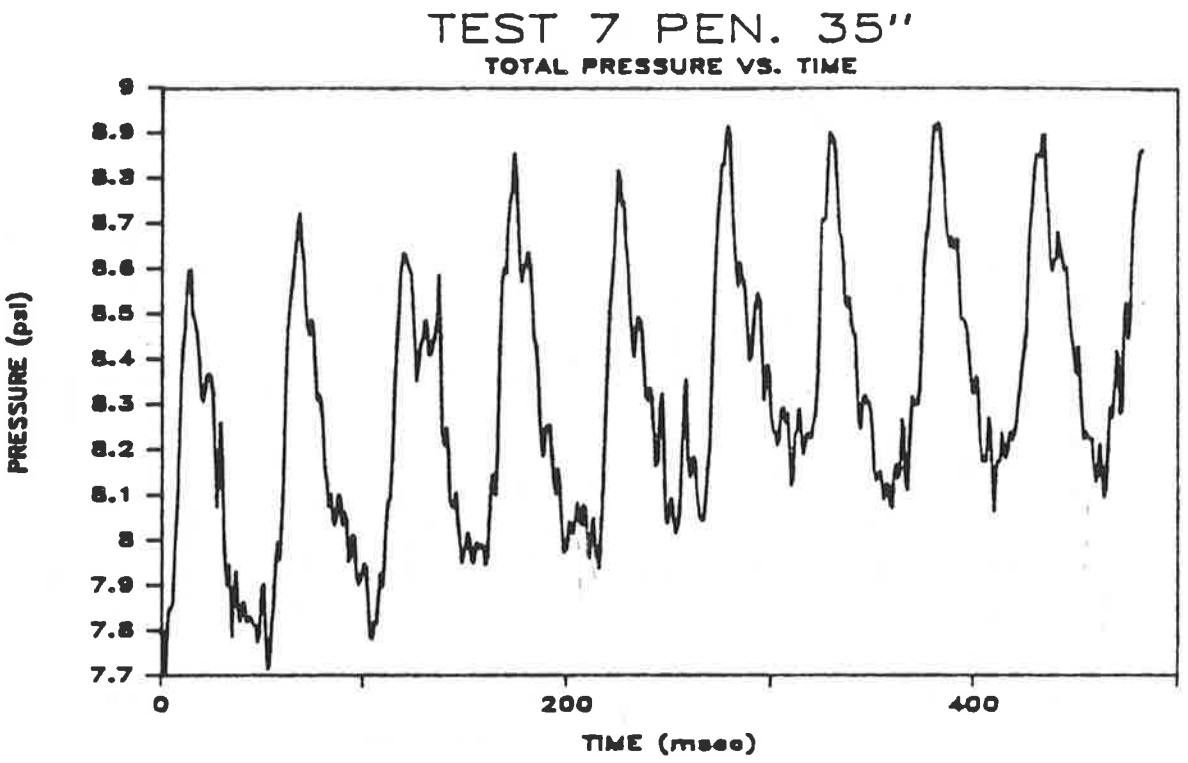

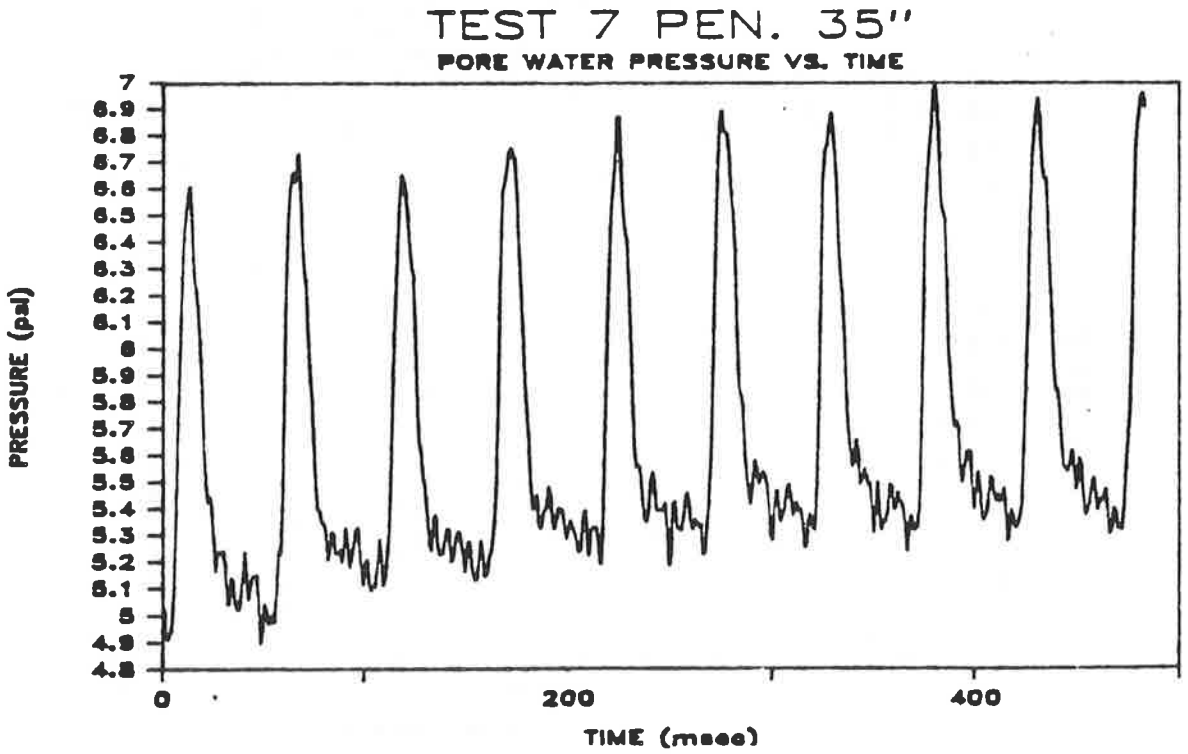

Fig. M.5d. Total and Pore Water Pressure Vs. Time at Bottom of Pile Shaft; Penetration = 35 Inches; Test 7

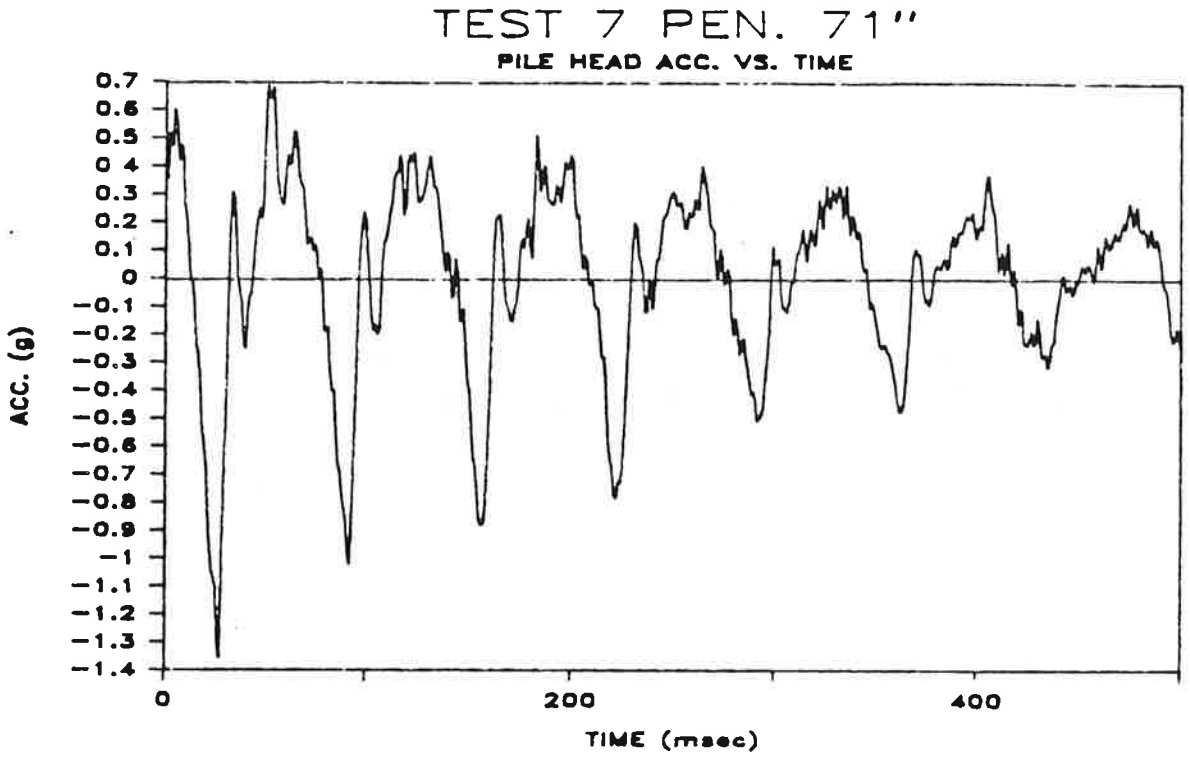

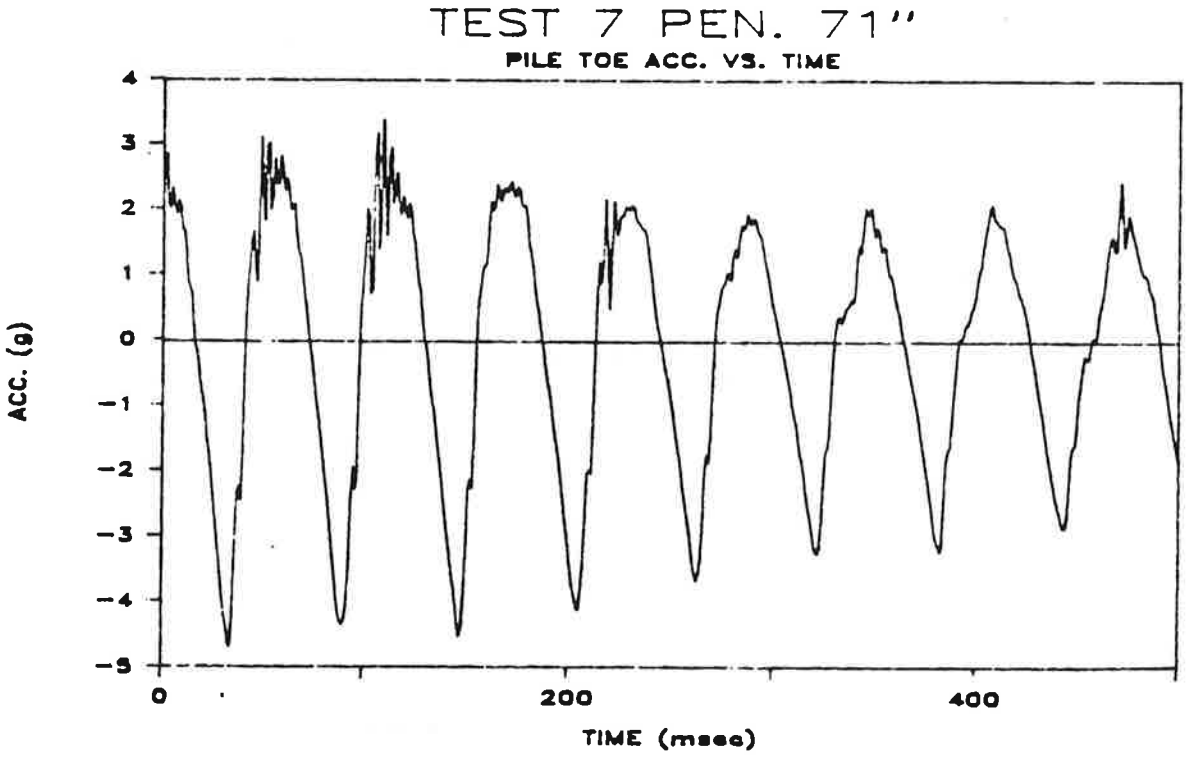

Fig. M.6a. Pile-Head and Toe Acceleration Vs. Time; Penetration = 71 Inches; Test 7

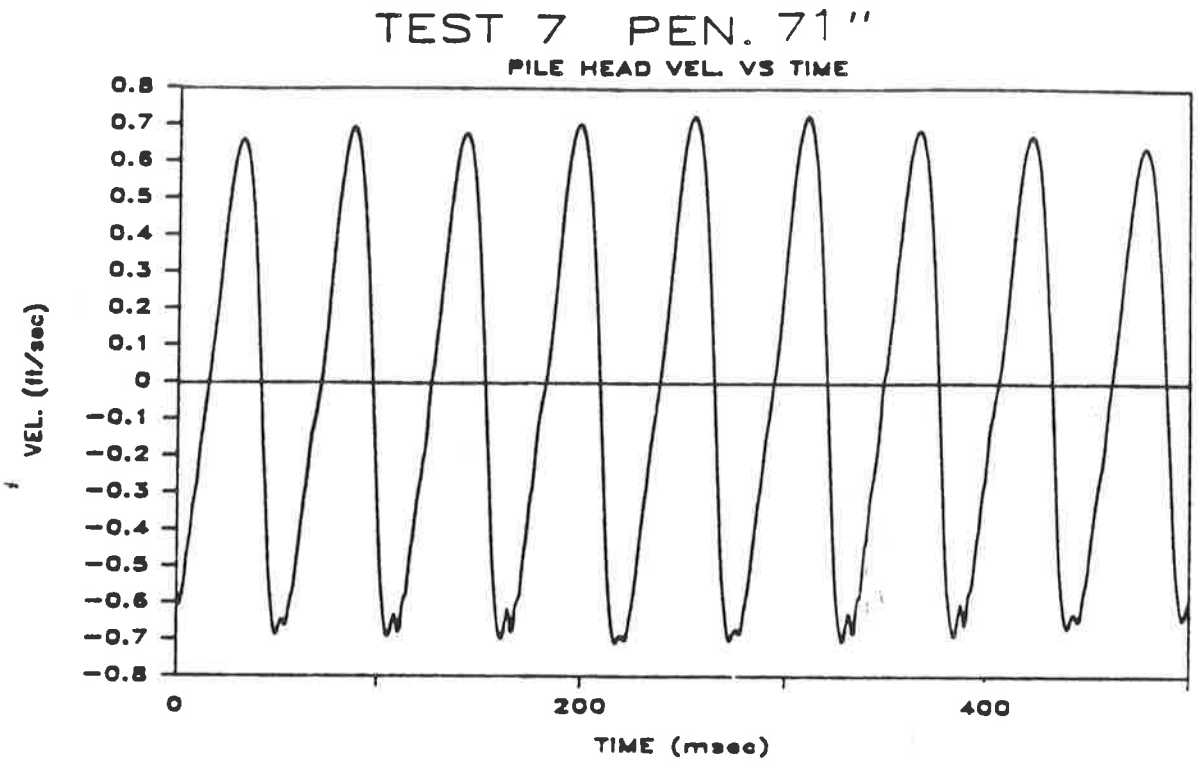

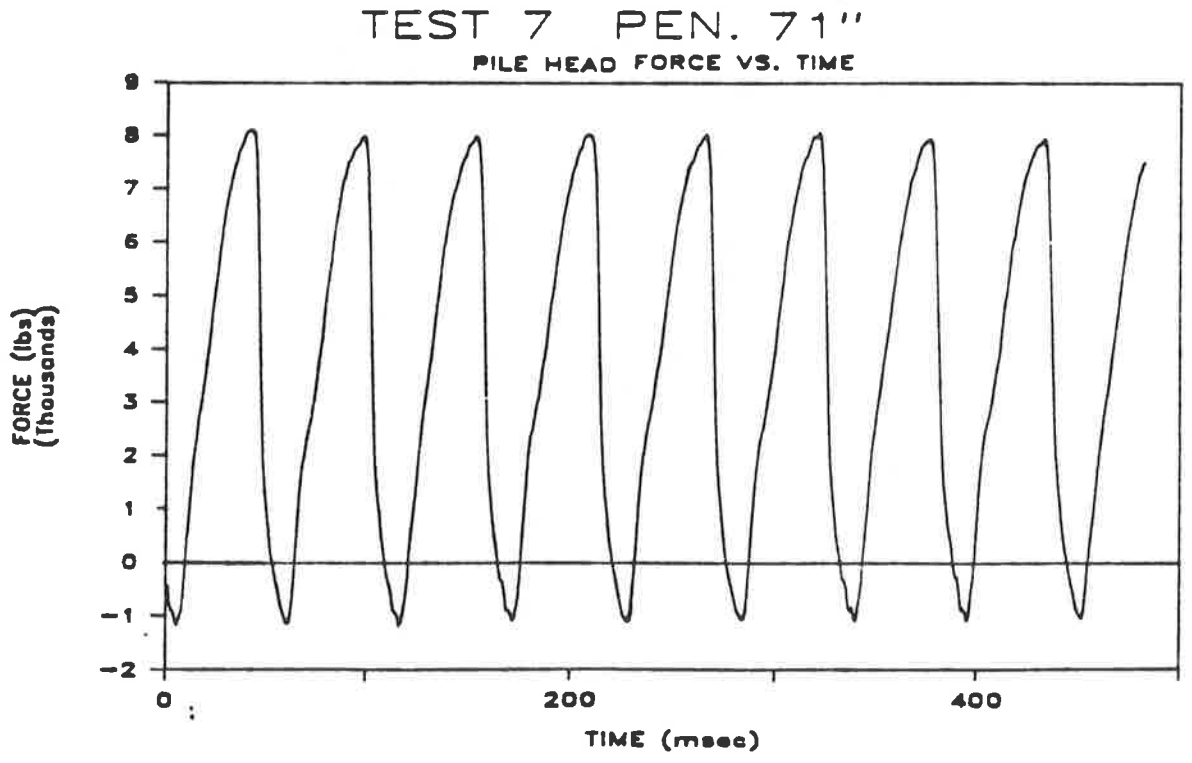

Fig. M.6b. Pile-Head Velocity and ForceVs. Time; Penetration = 71 Inches; Test 7

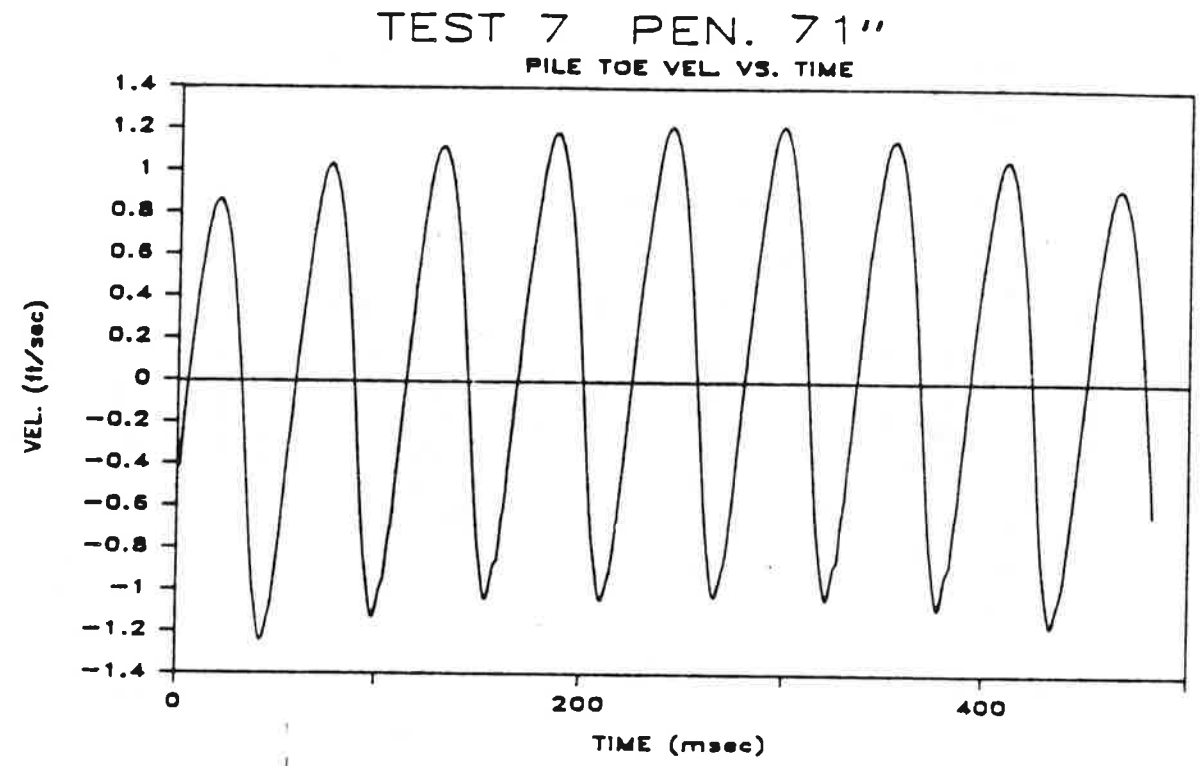

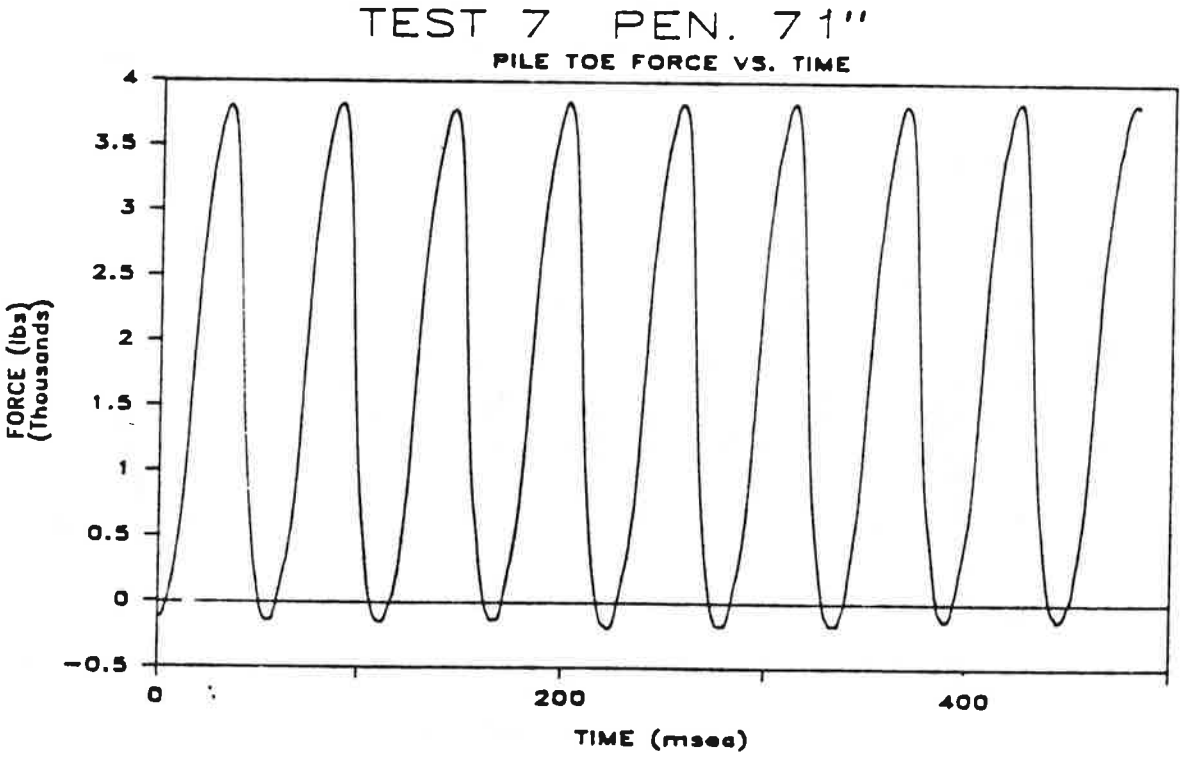

Fig. M.6c. Pile-Toe Velocity and Force Vs. Time; Penetration = 71 Inches; Test 7

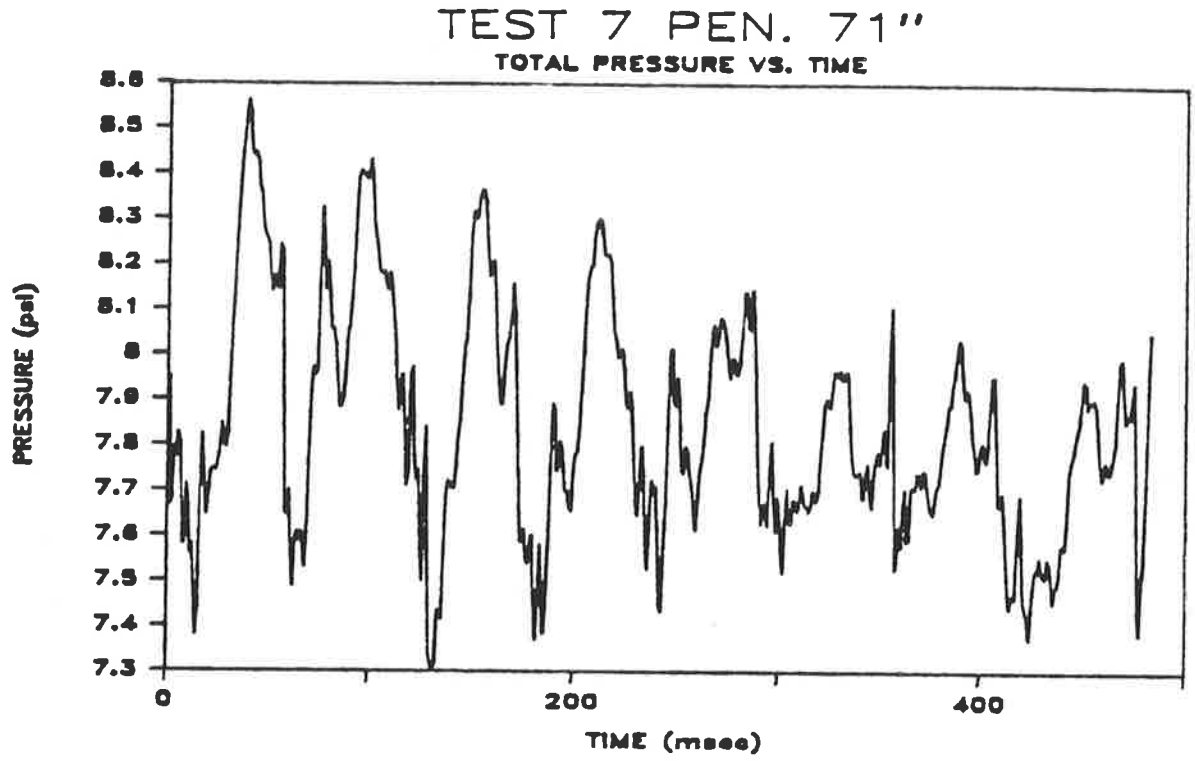

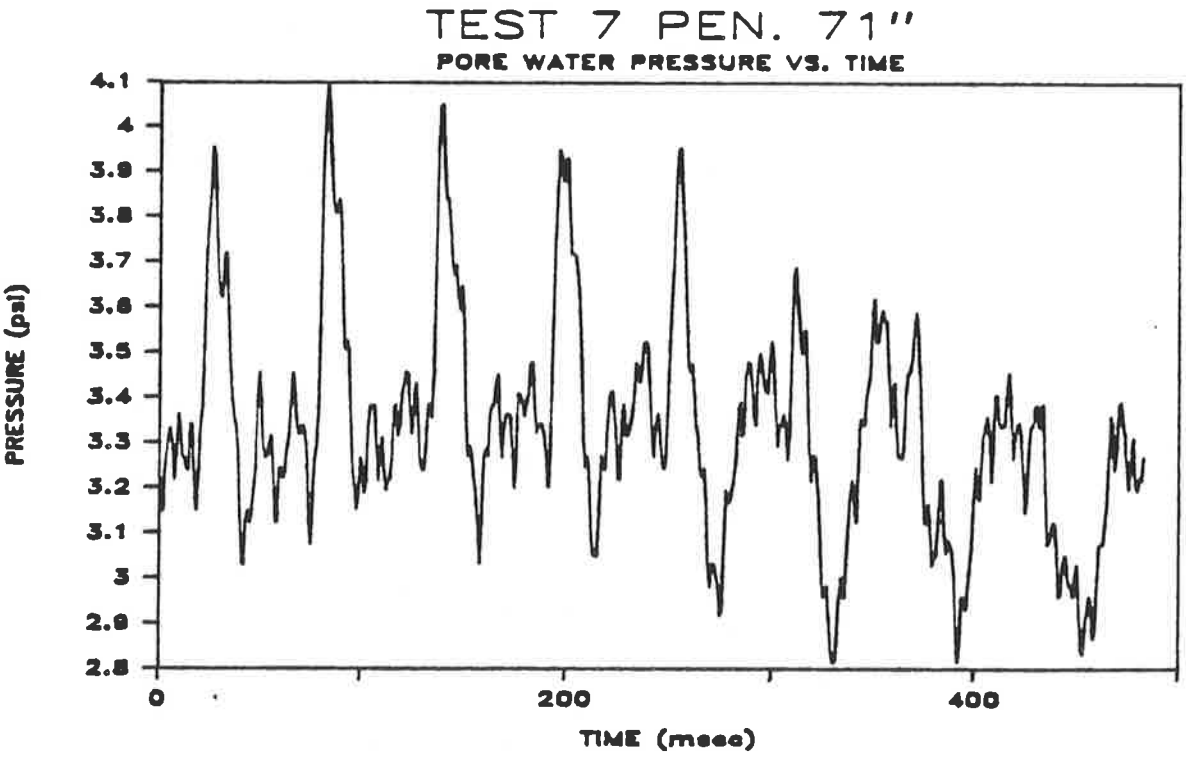

Fig. M.6d. Total and Pore Water Pressure Vs. Time at Bottom of Pile Shaft; Penetration = 71 Inches; Test 7

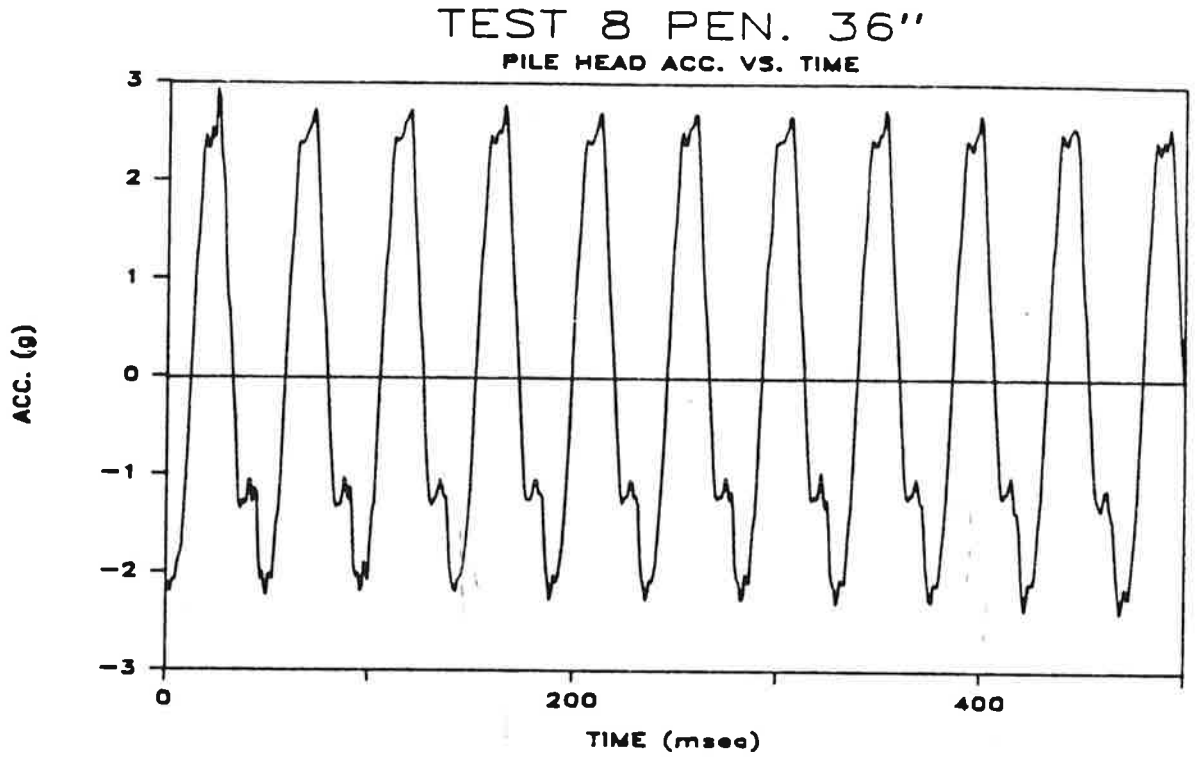

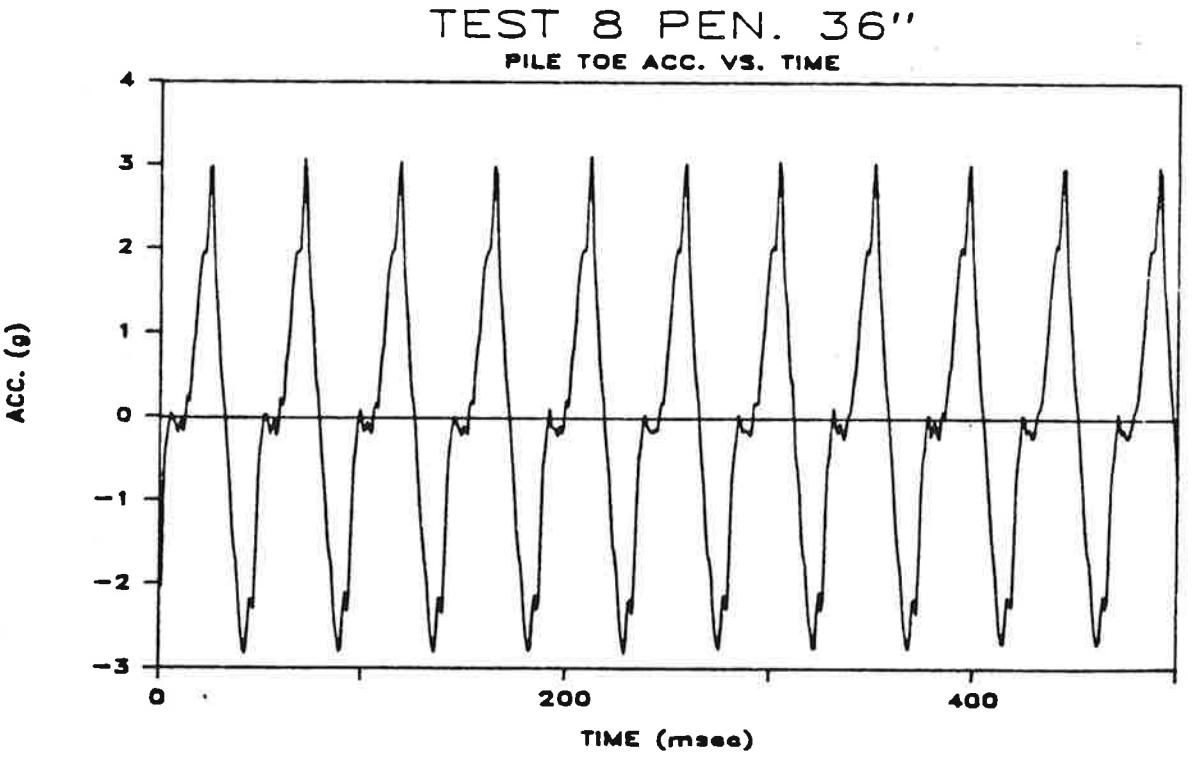

Fig. M.7a. Pile-Head and Toe Acceleration Vs. Time; Penetration = 36Inches; Test 8

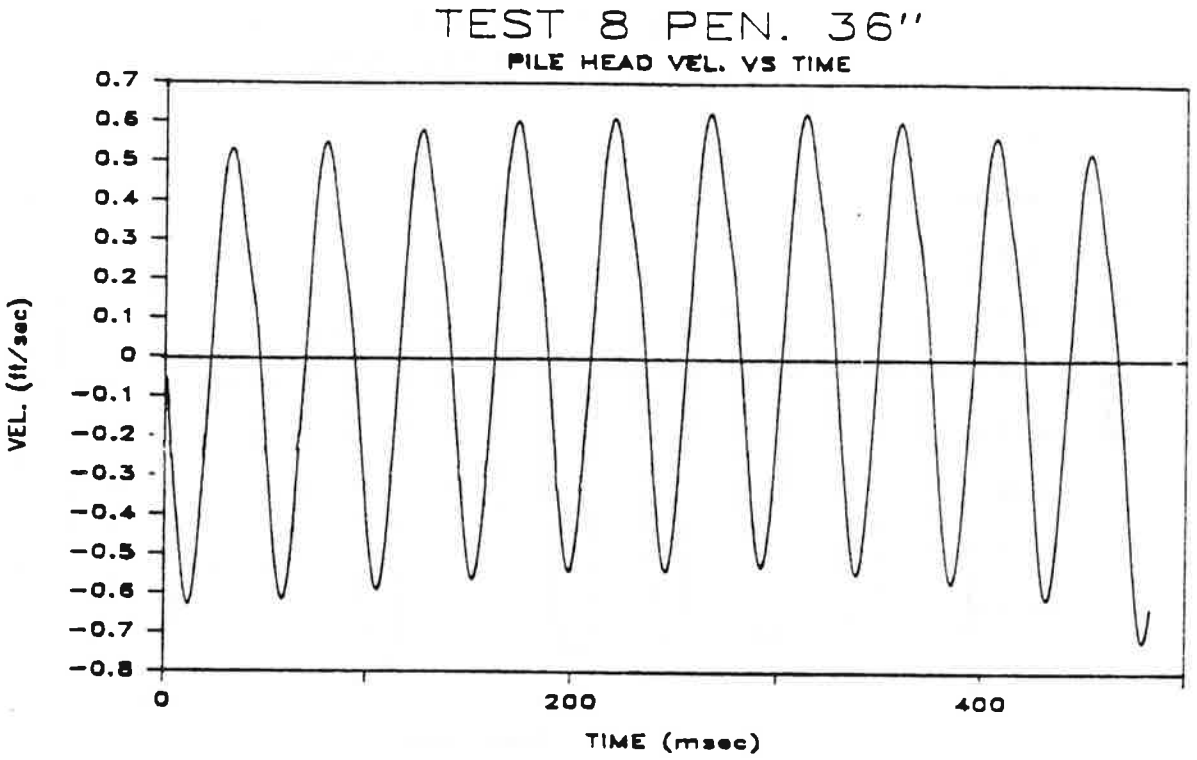

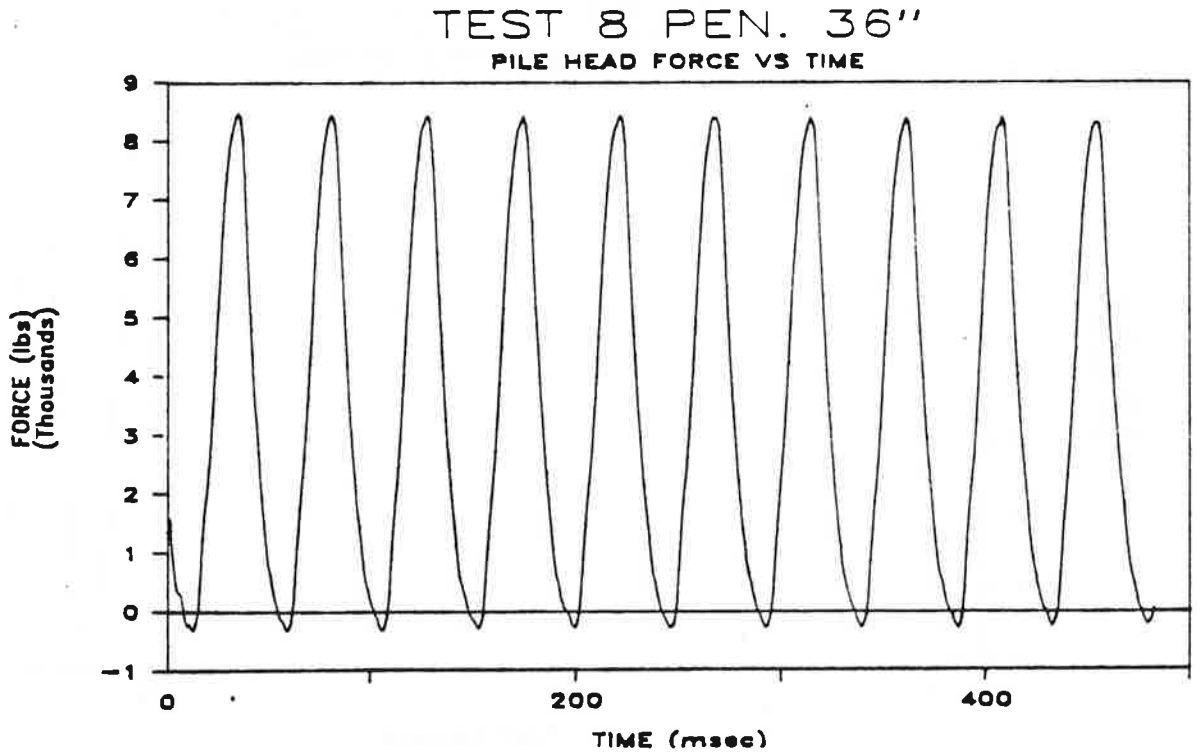

Fig. M.7b. Pile-Head Velocity and ForceVs. Time; Penetration = 36 Inches; Test 8

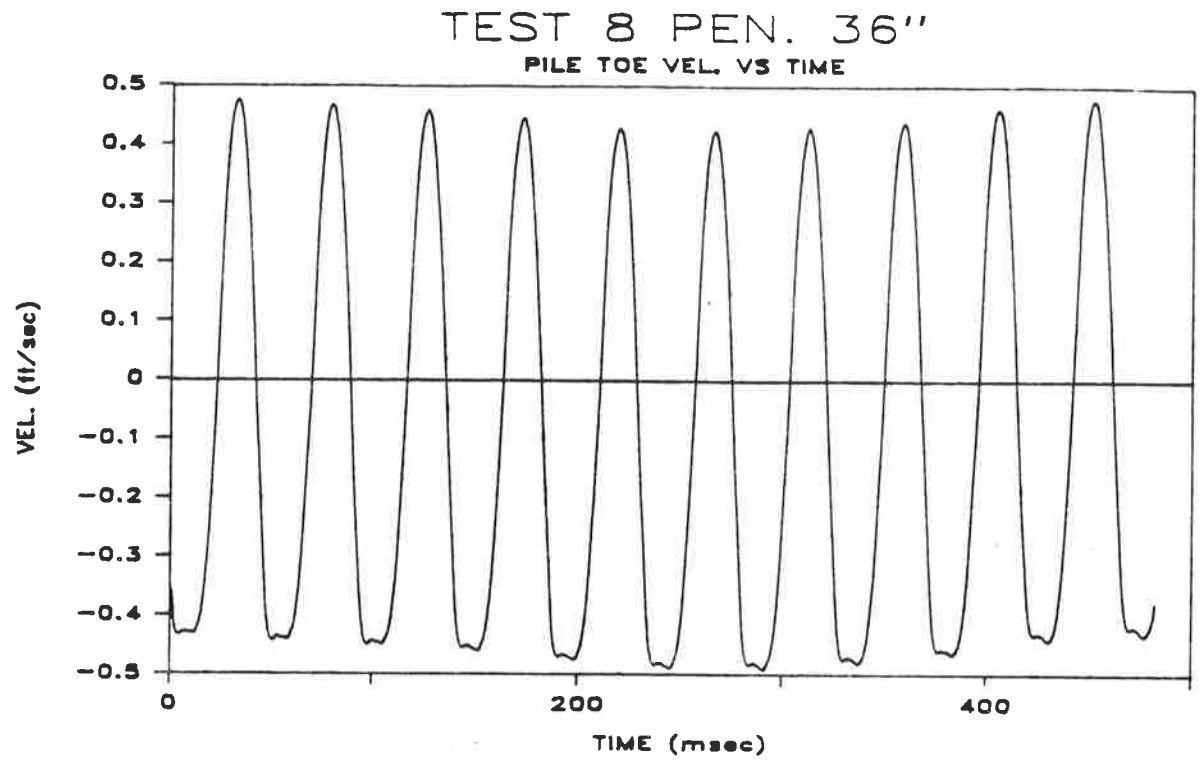

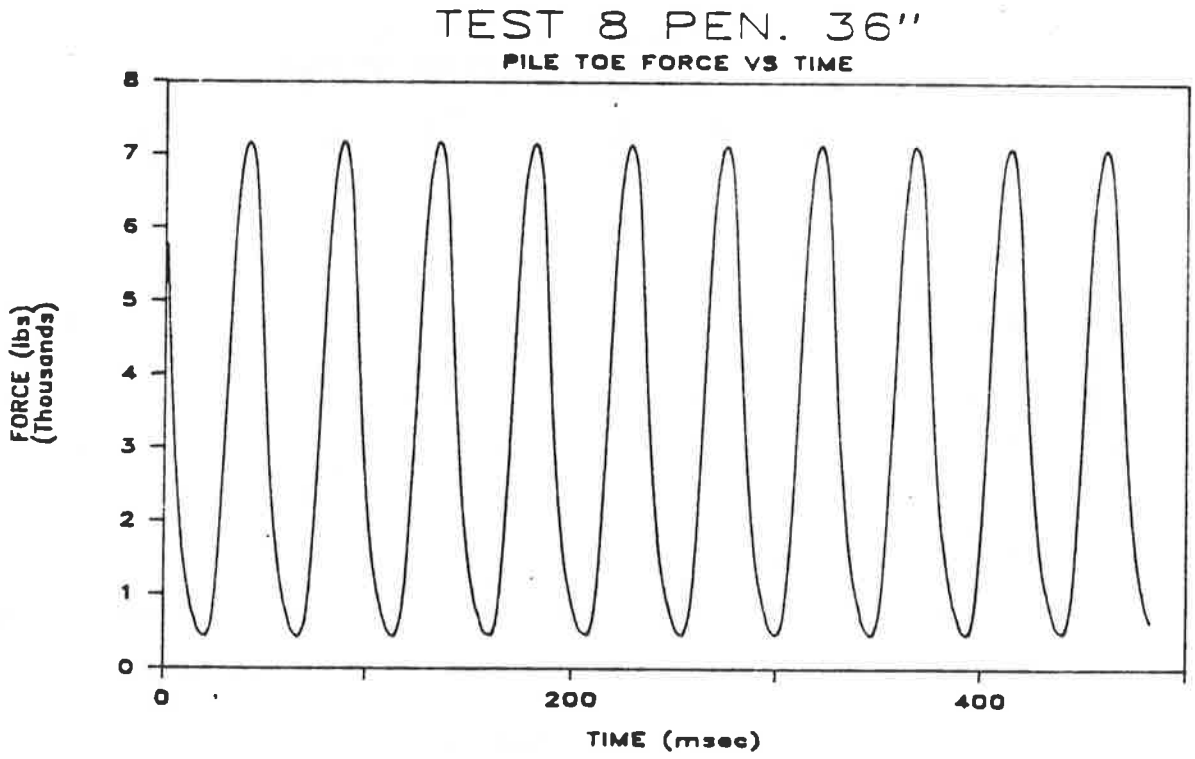

Fig. M.7c. Pile-Toe Velocity and Force Vs. Time; Penetration = 36 Inches; Test 8

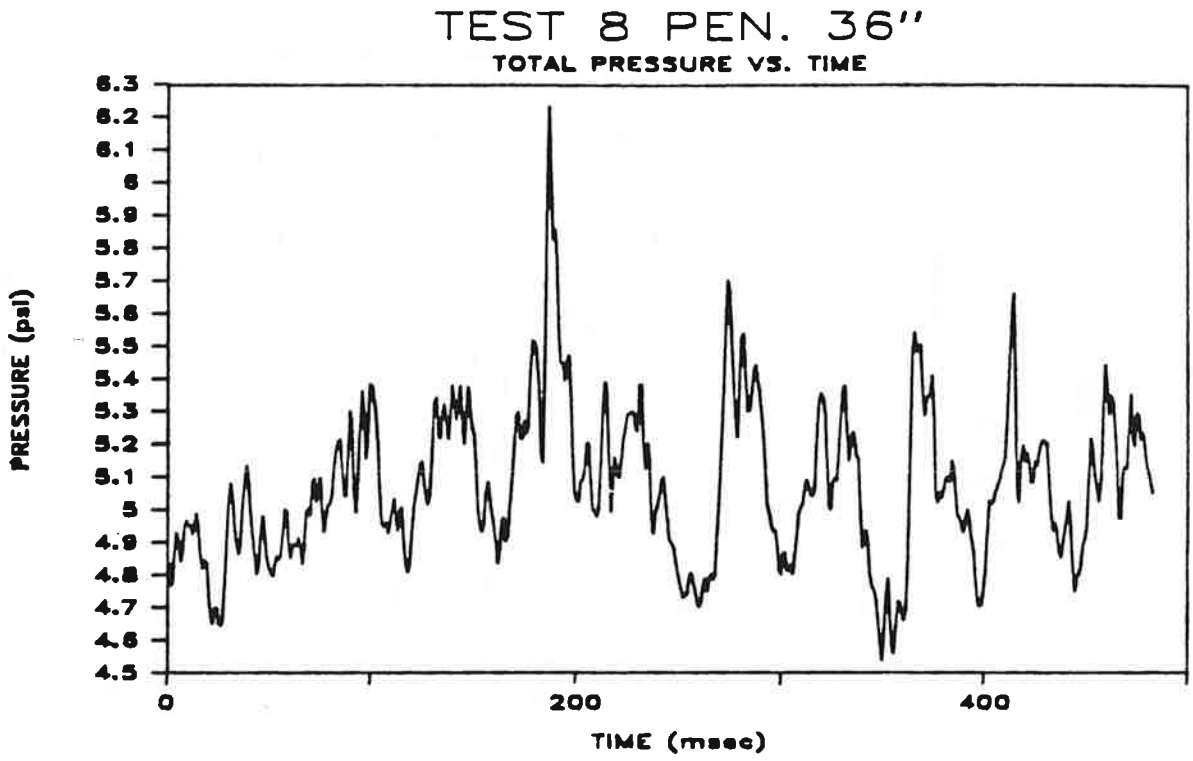

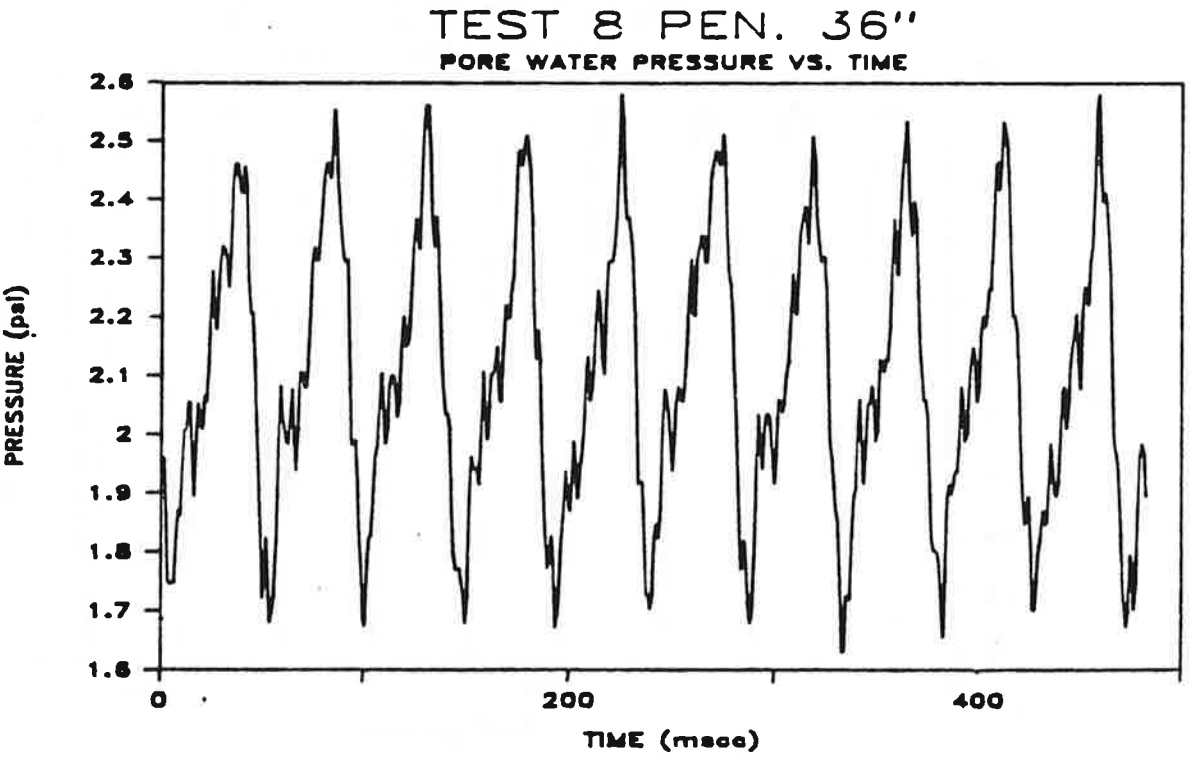

Fig. M.7d. Total and Pore Water Pressure Vs. Time at Bottom of Pile Shaft; Penetration = 36 Inches; Test 8

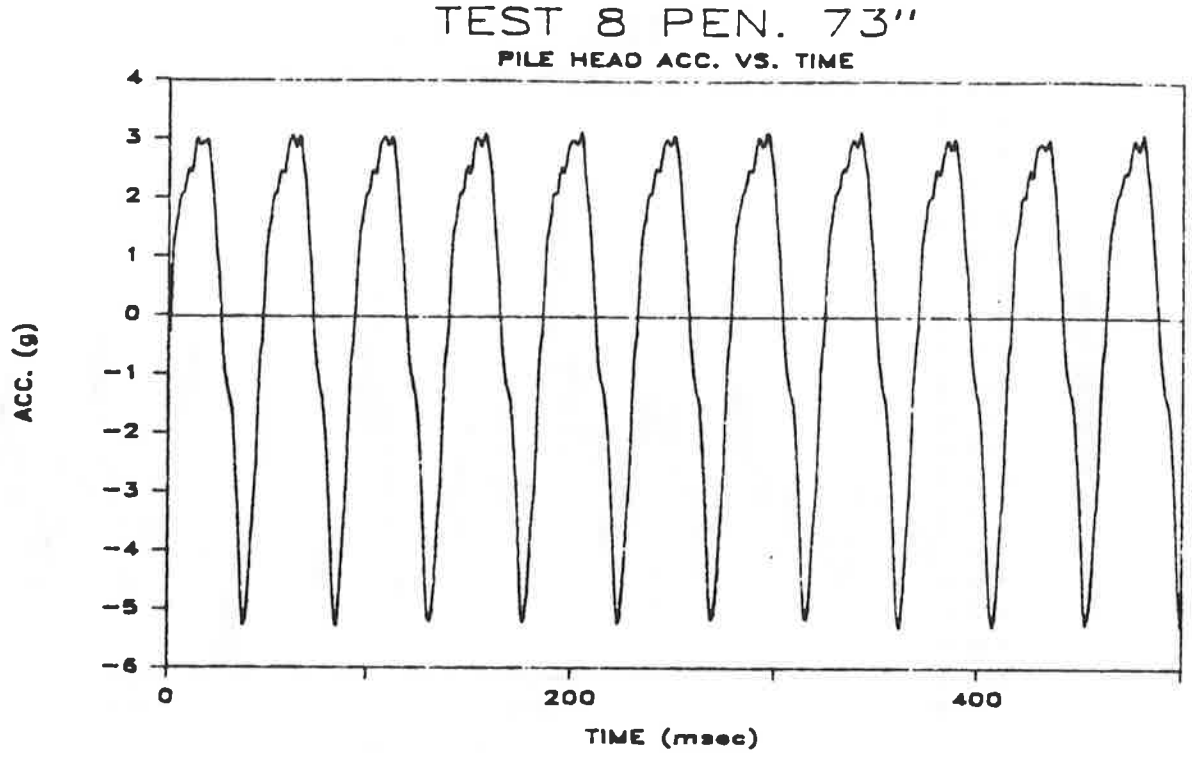

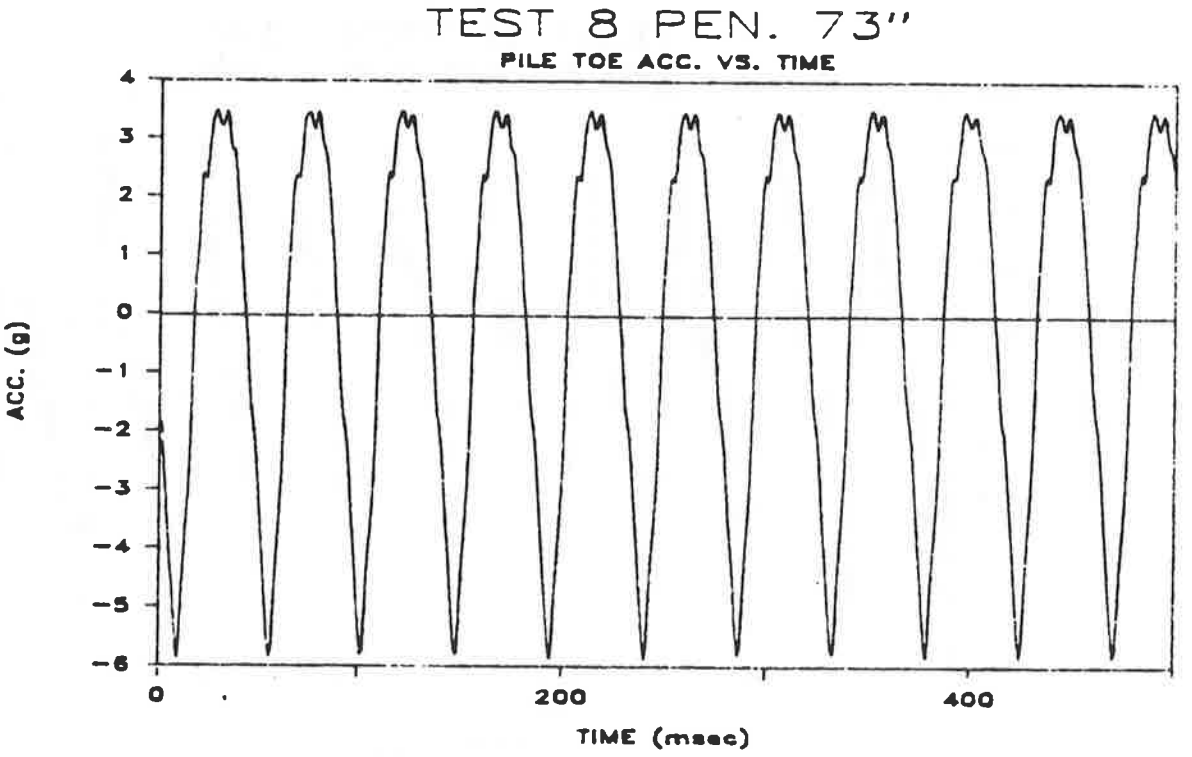

Fig. M.8a. Pile-Head and Toe Acceleration Vs. Time; Penetration = 73 Inches; Test 8

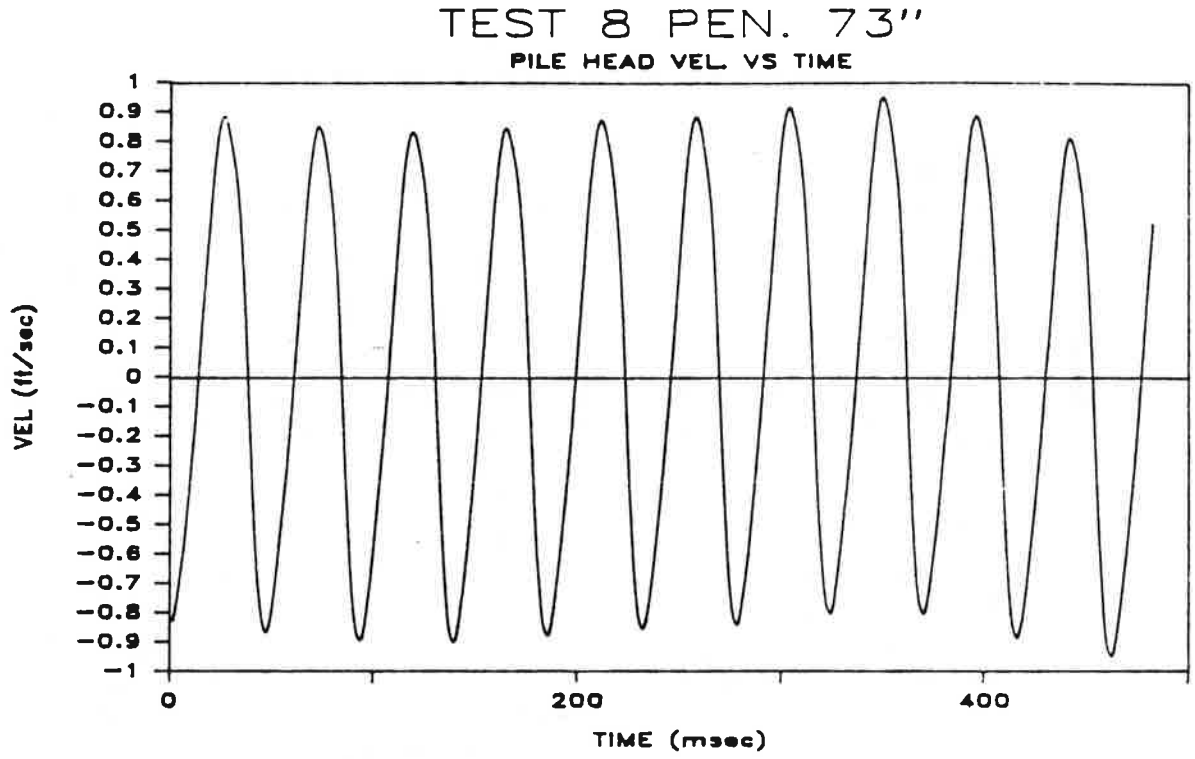

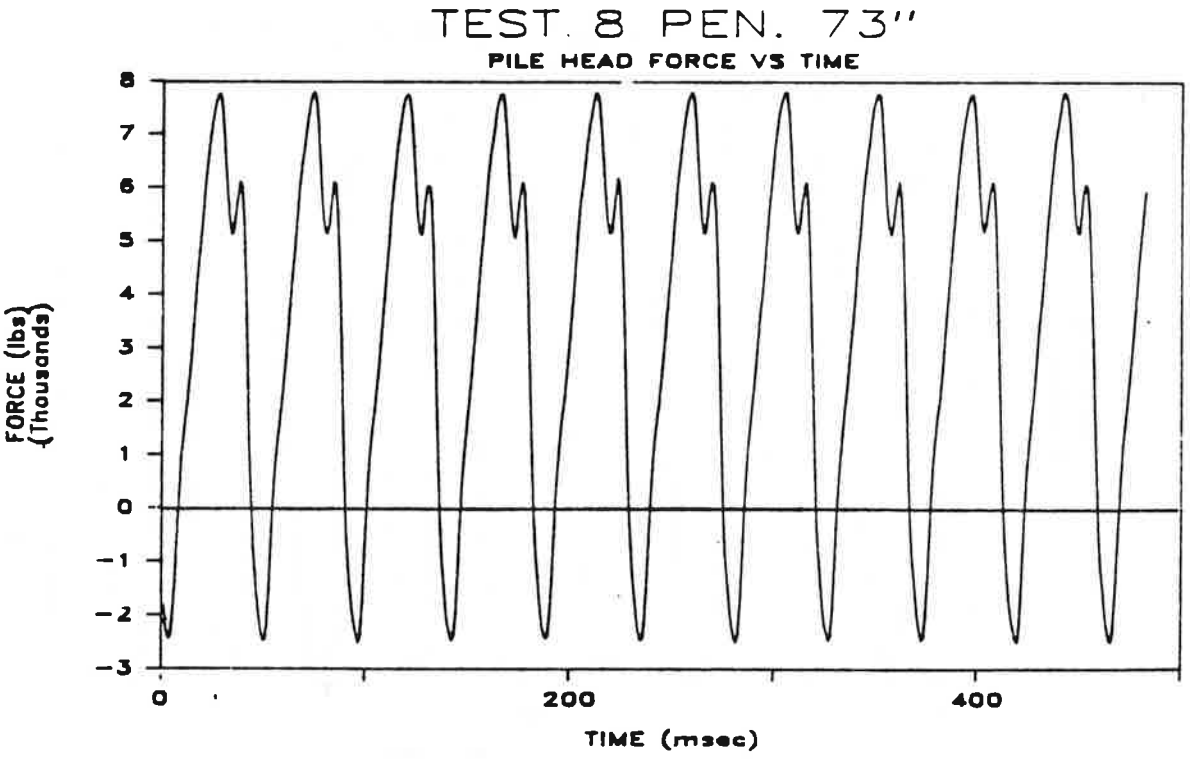

Fig. M.8b. Pile-Head Velocity and ForceVs. Time; Penetration = 73 Inches; Test 8

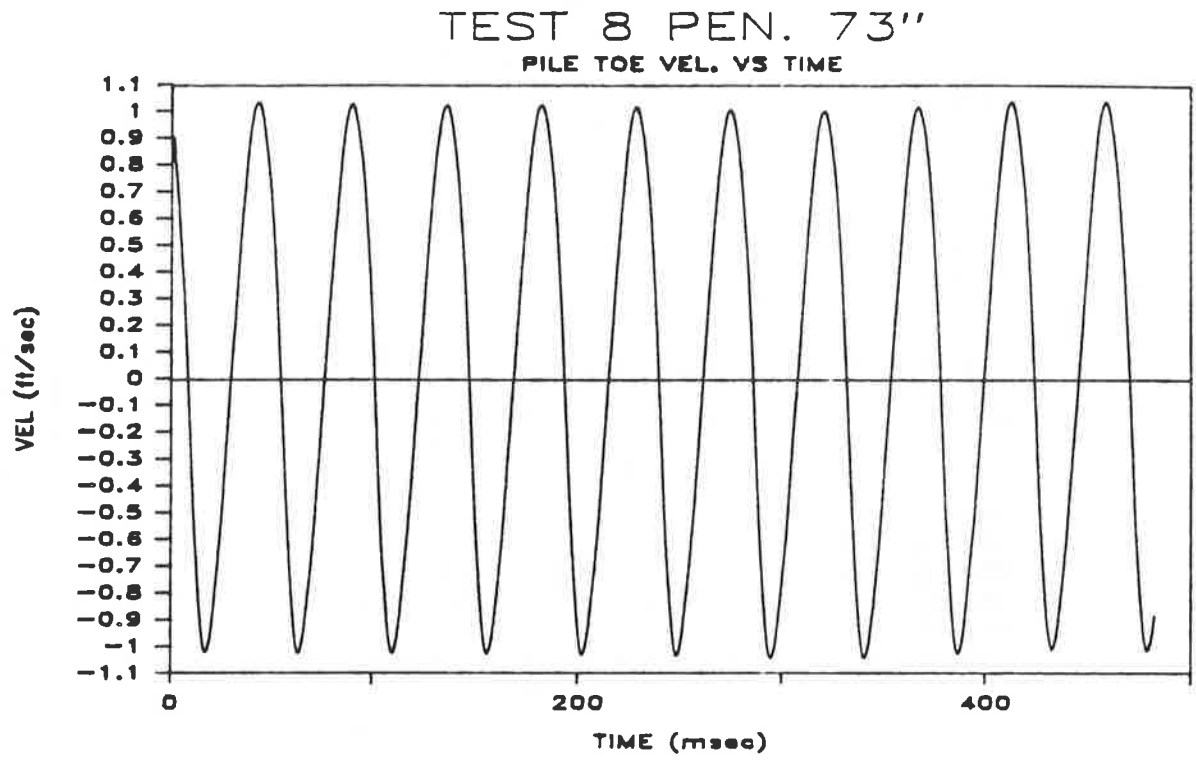

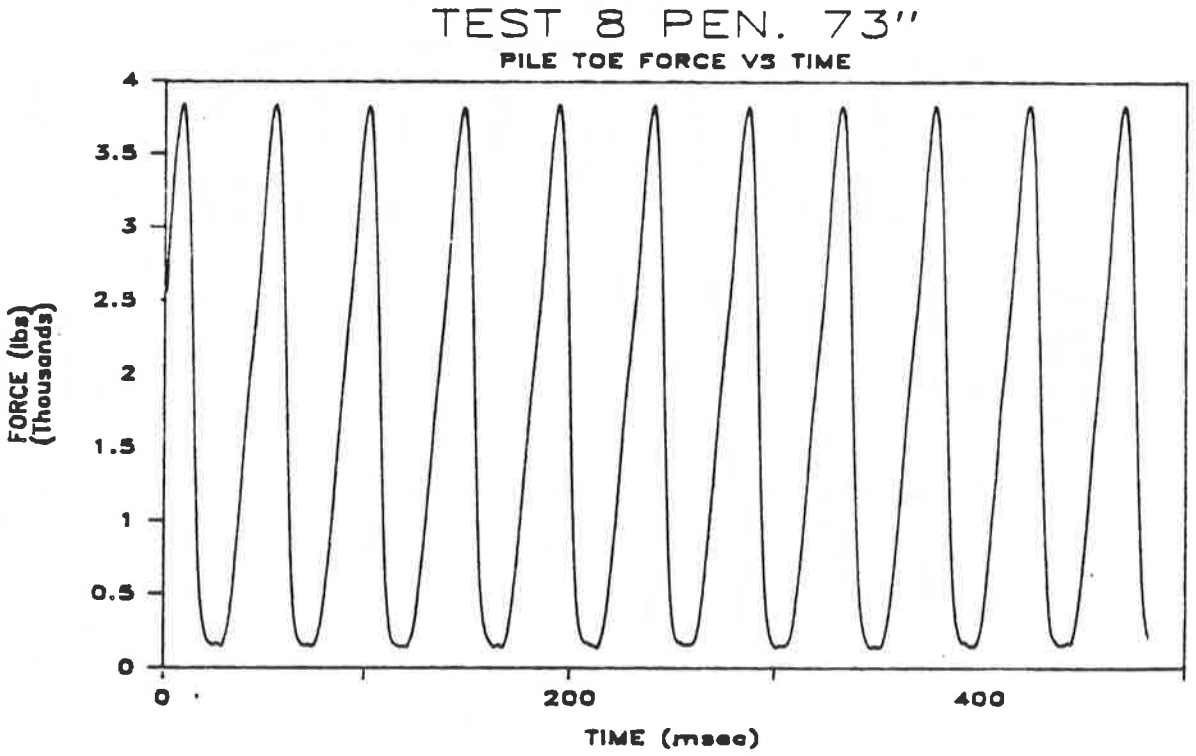

Fig. M.8c. Pile-Toe Velocity and Force Vs. Time; Penetration = 73 Inches; Test 8

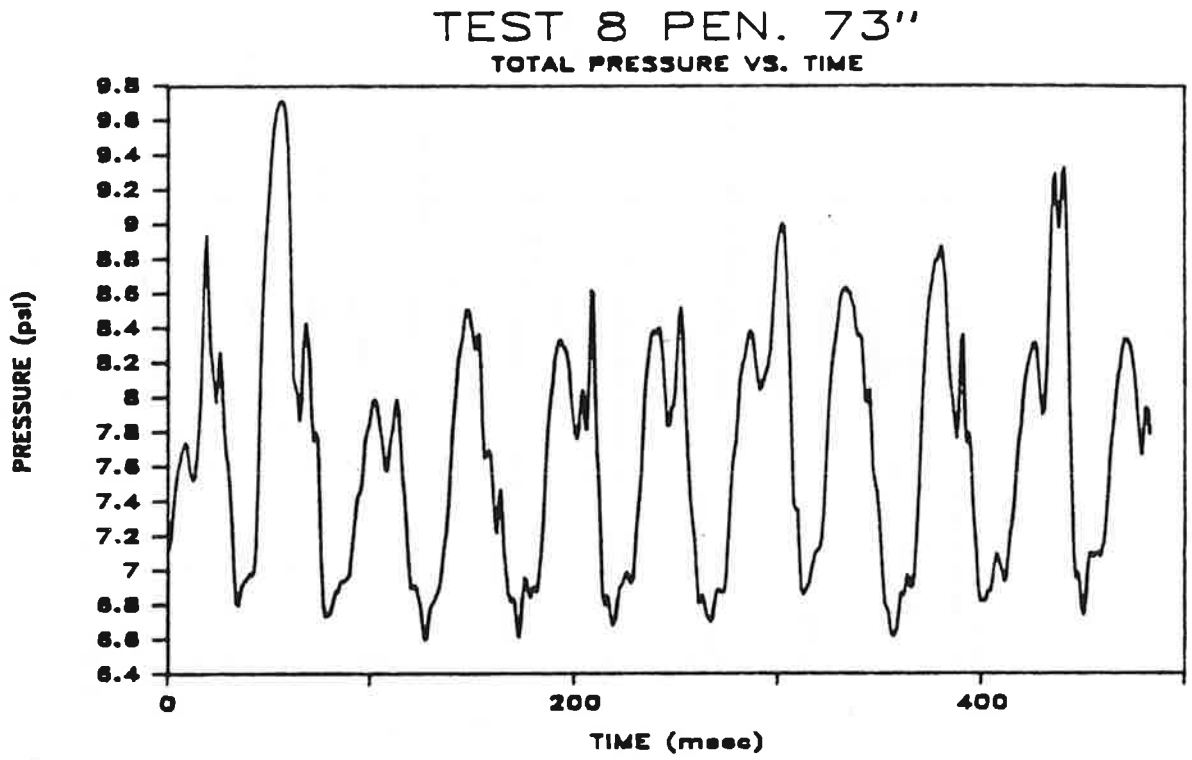

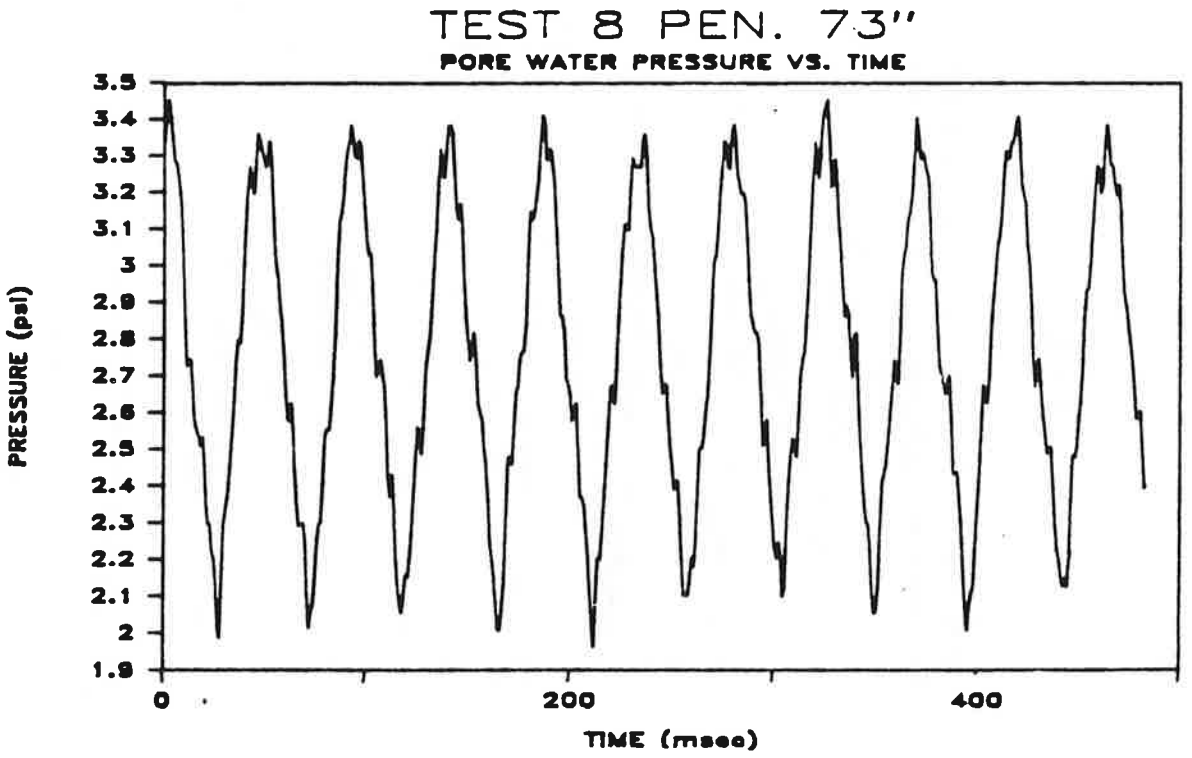

Fig. M.8d. Total and Pore Water Pressure Vs. Time at Bottom of Pile Shaft; Penetration = 73 Inches; Test 8

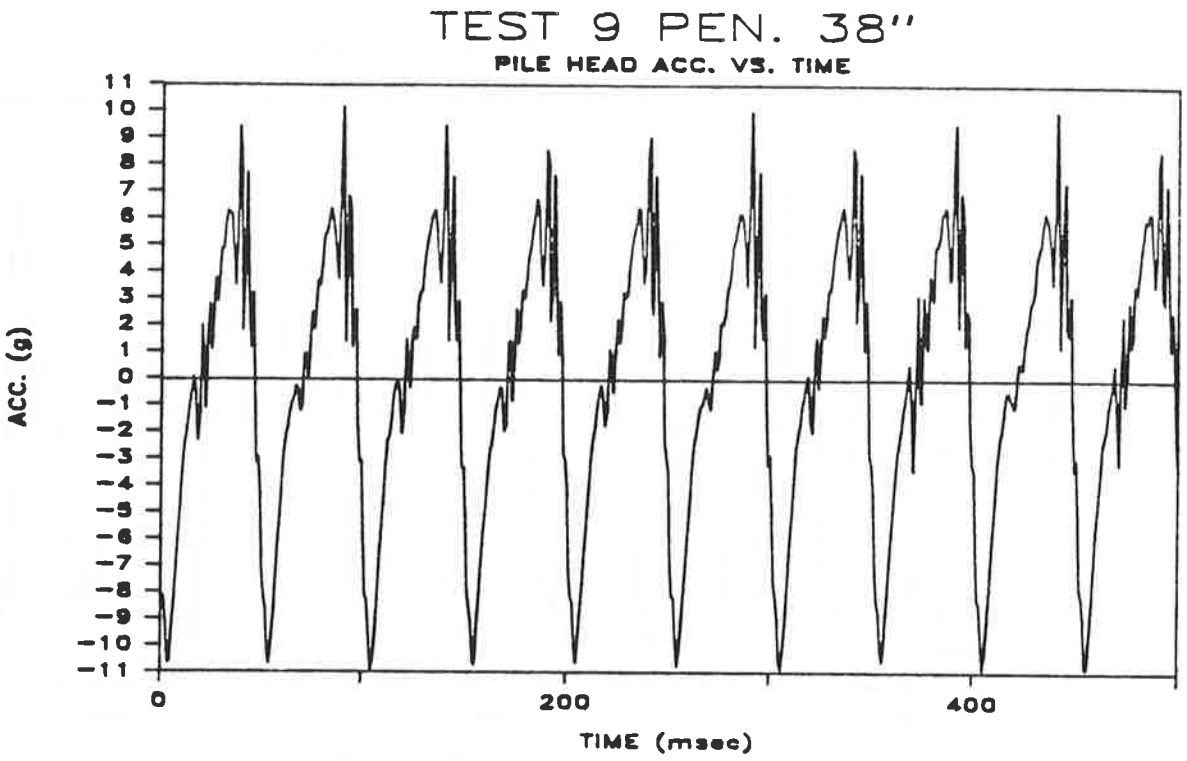

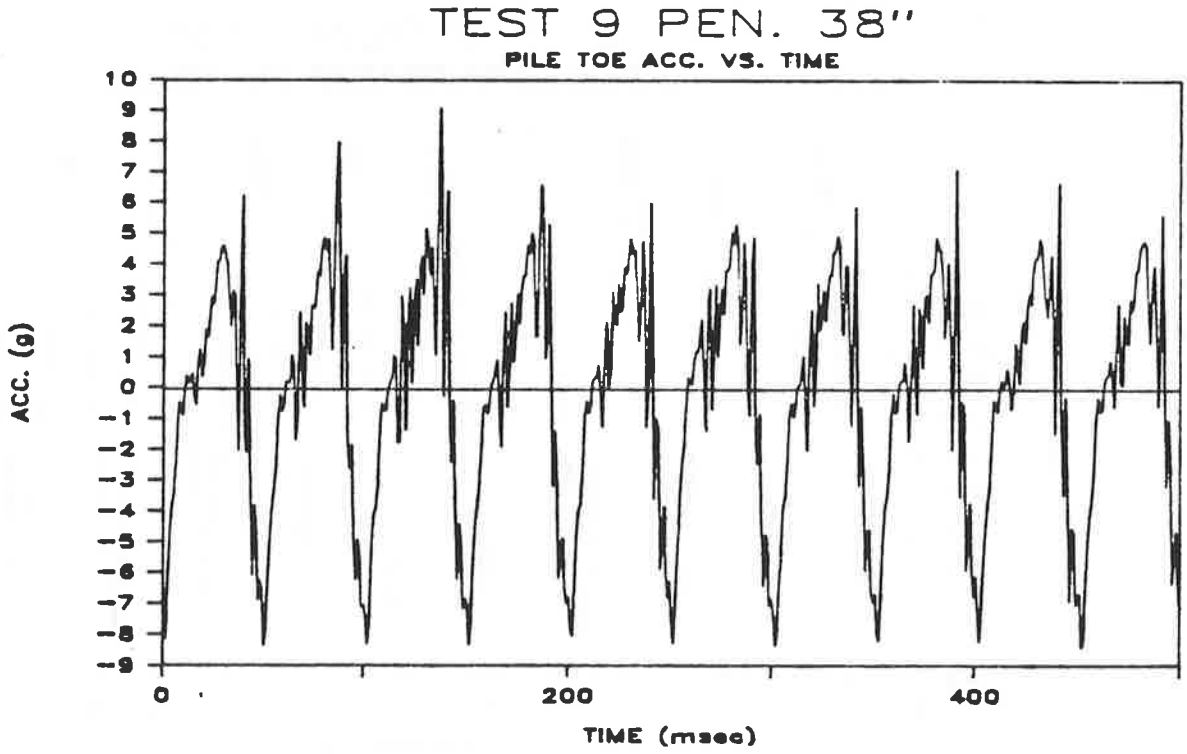

Fig. M.9a. Pile-Head and Toe Acceleration Vs. Time; Penetration = 38 Inches; Test 9

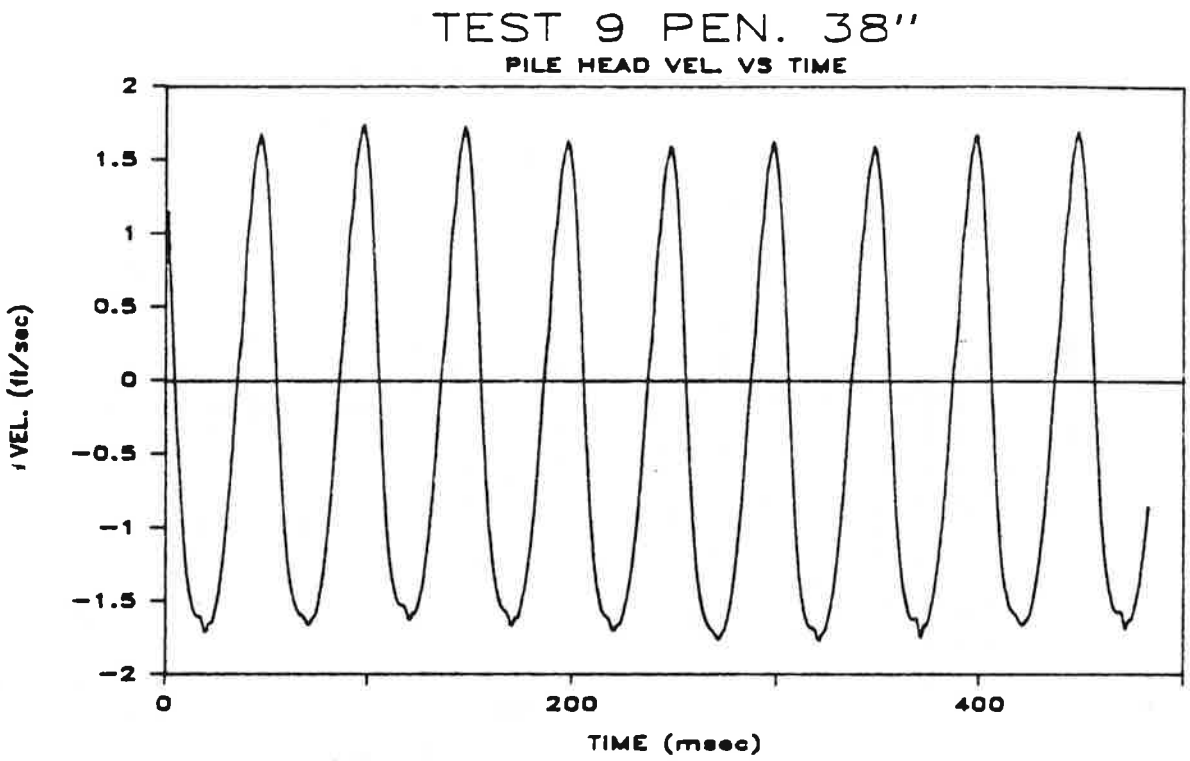

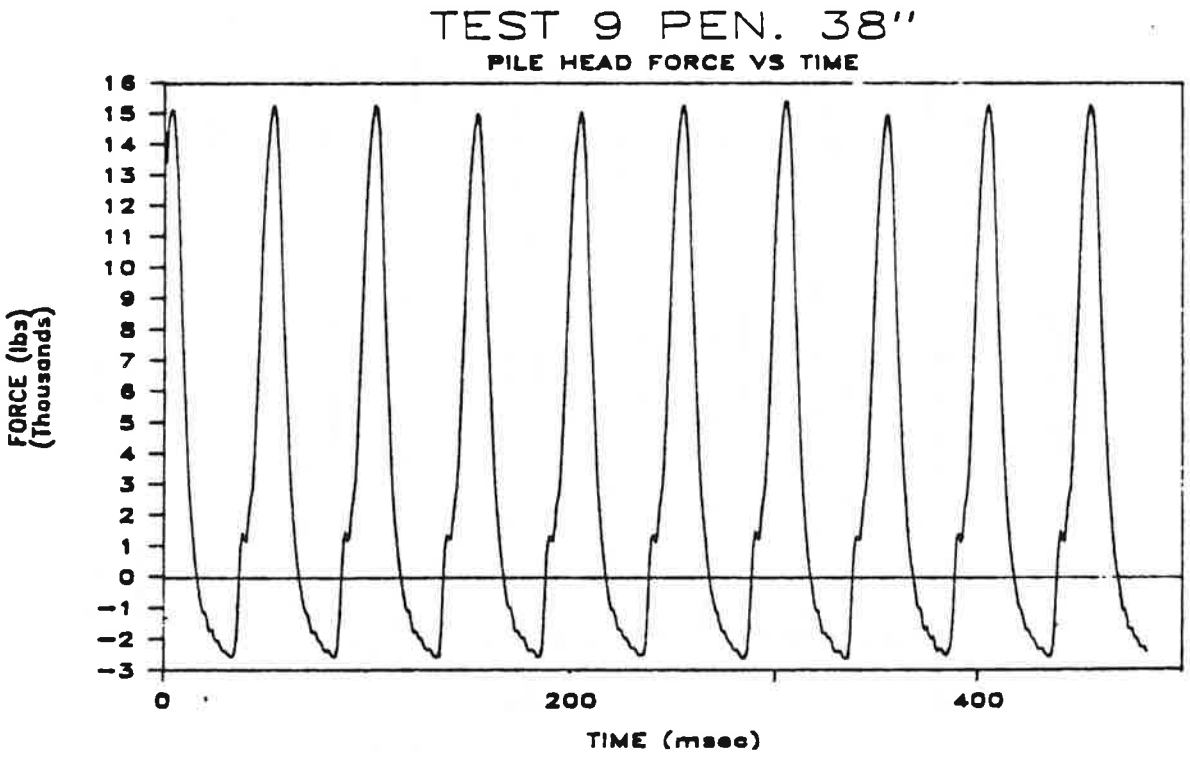

Fig. M.9b. Pile-Head Velocity and ForceVs. Time; Penetration = 38 Inches; Test 9

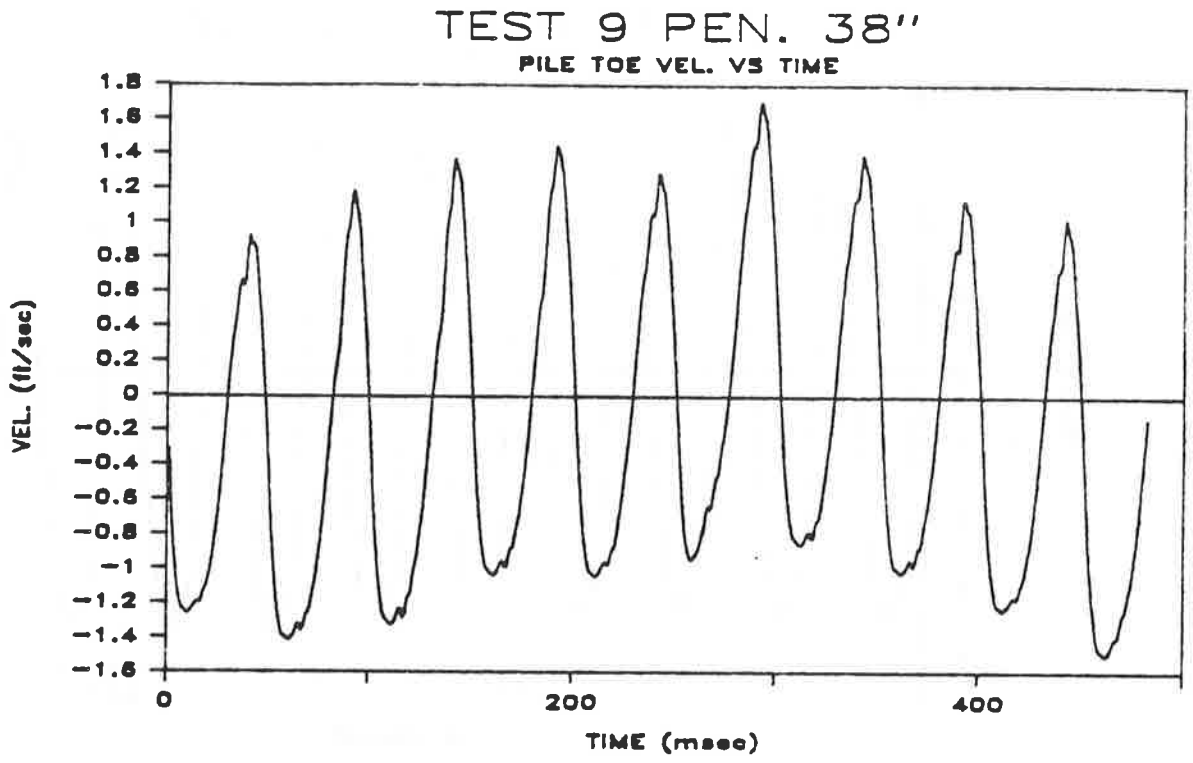

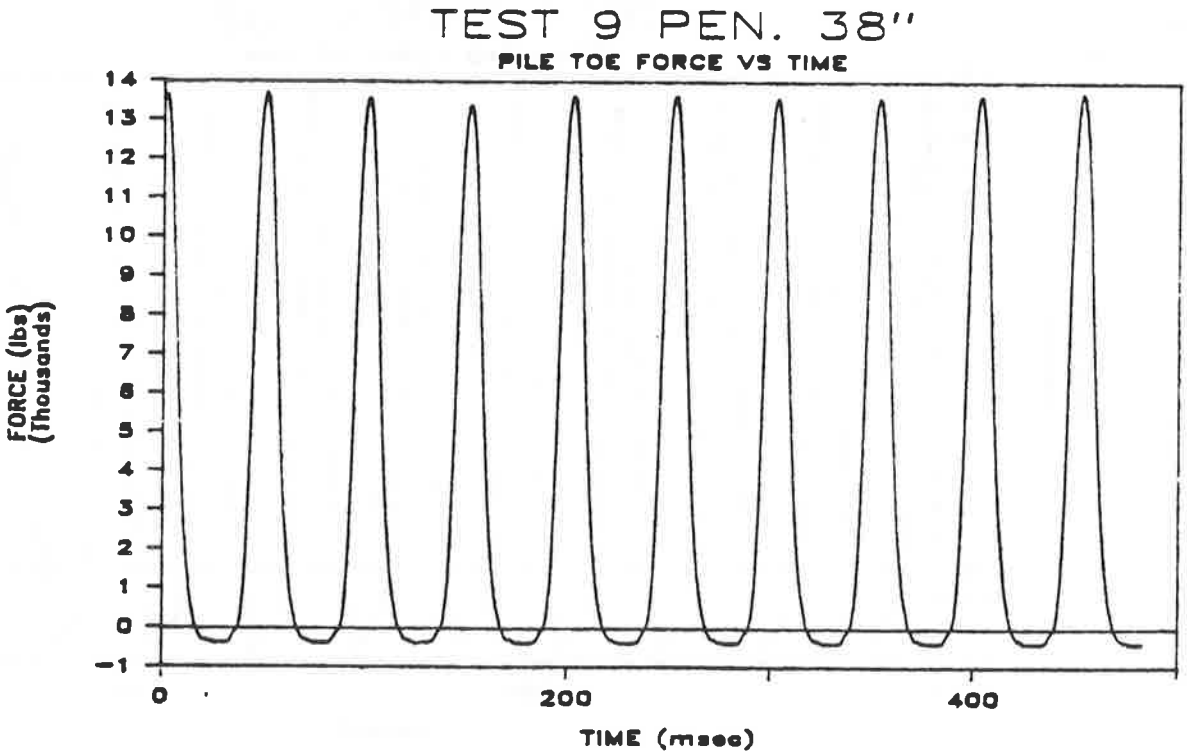

Fig. M.9c. Pile-Toe Velocity and Force Vs. Time; Penetration = 38 Inches; Test 9

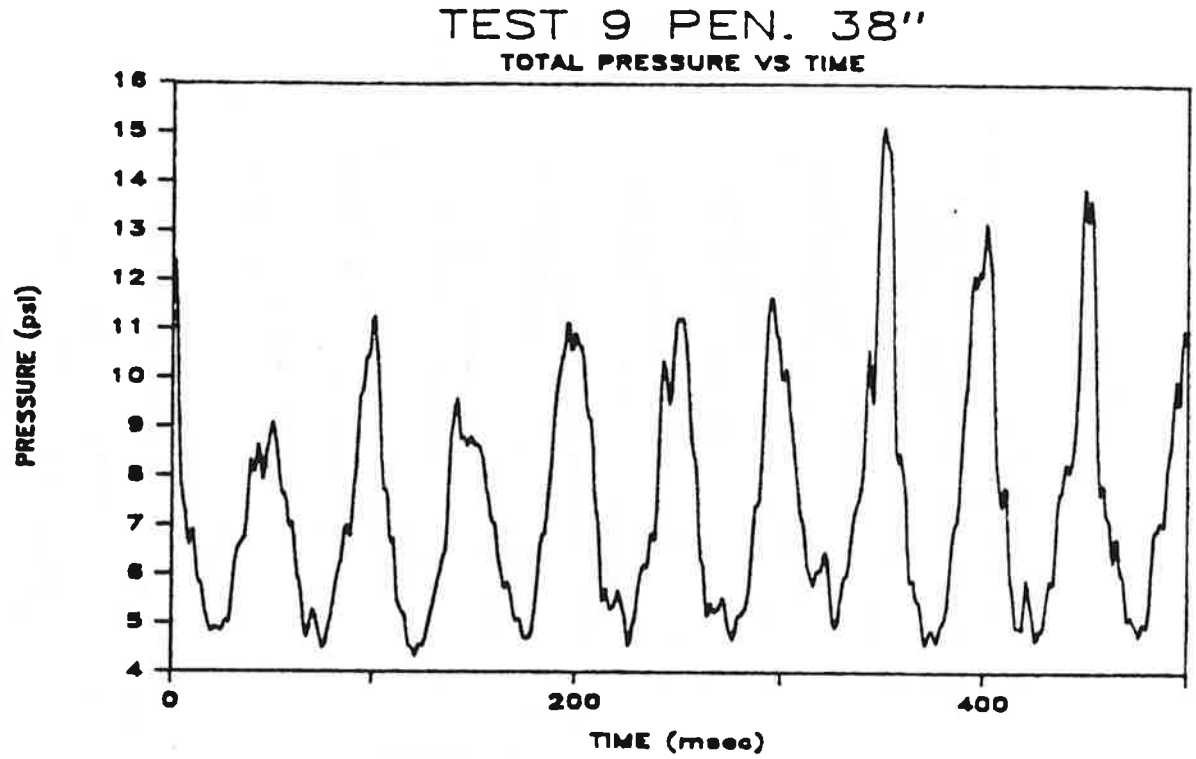

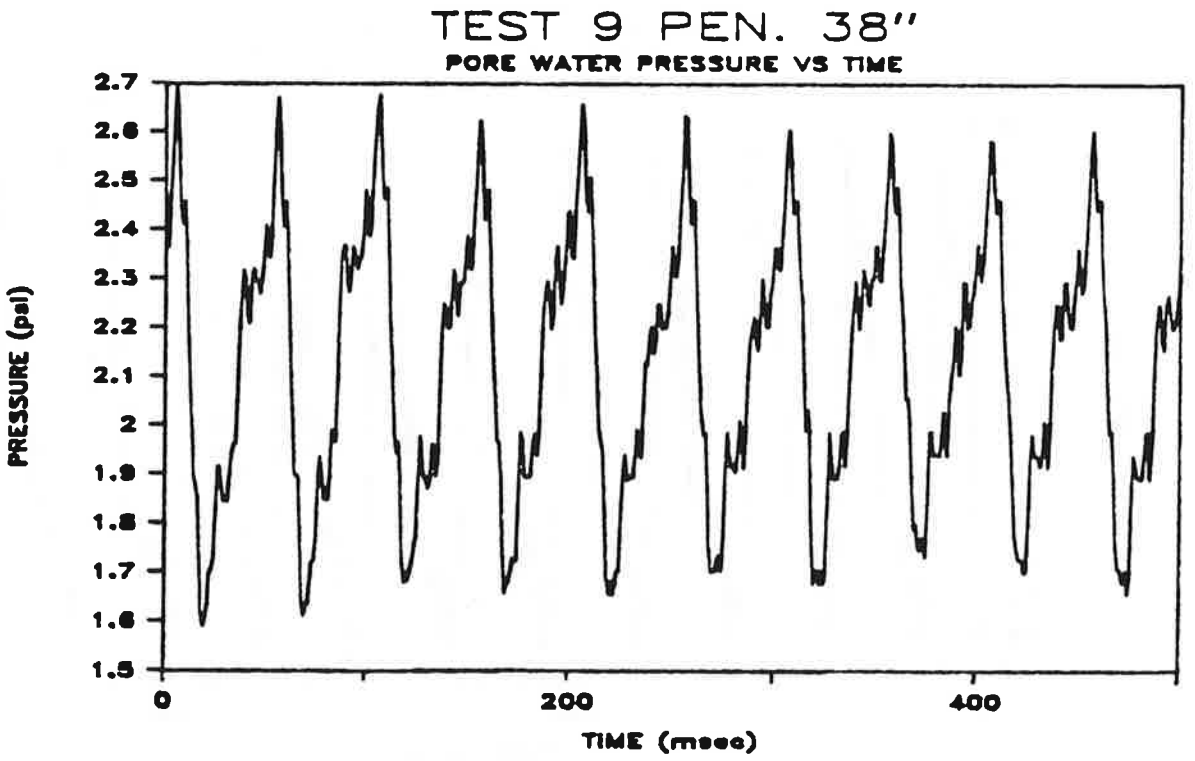

Fig. M.9d. Total and Pore Water Pressure Vs. Time at Bottom of Pile Shaft; Penetration = 38 Inches; Test 9

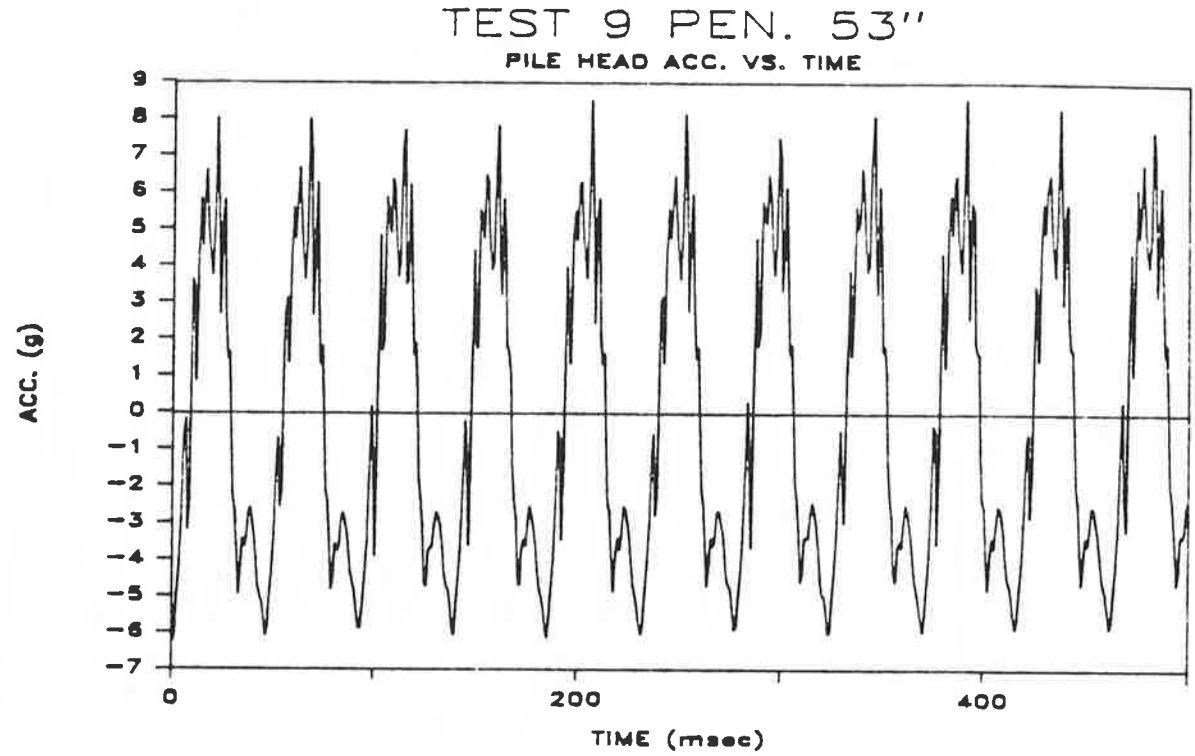

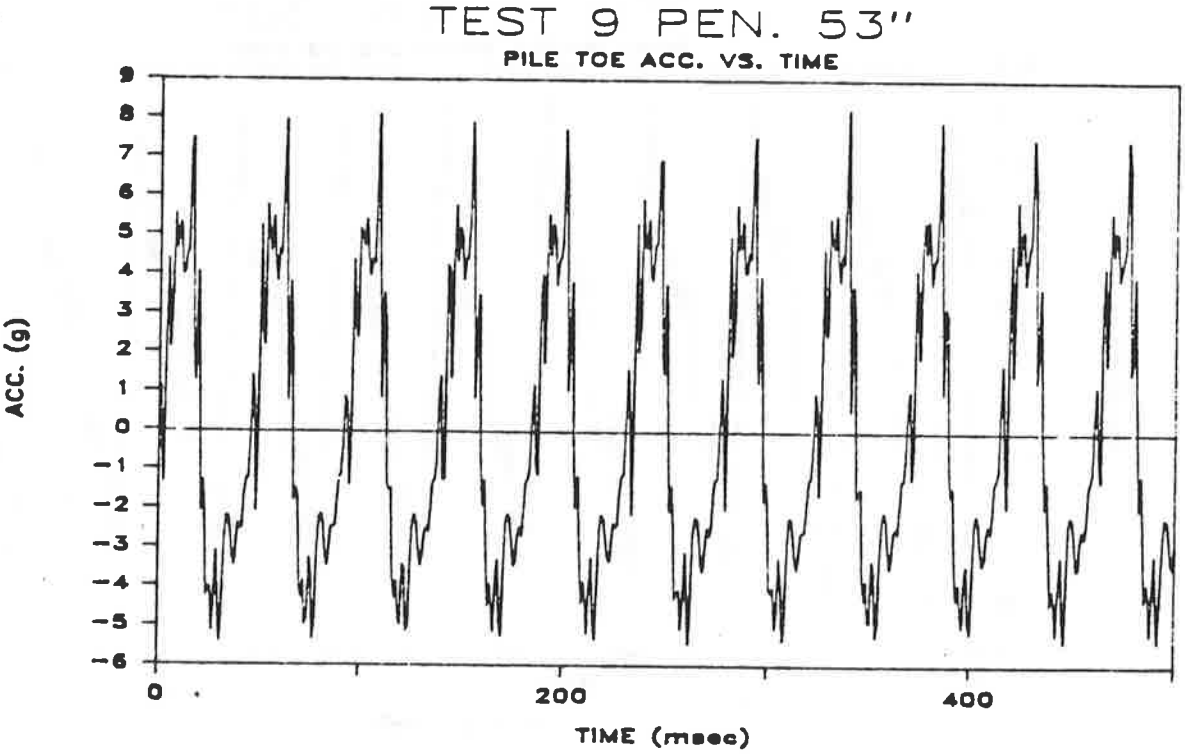

Fig. M.10a. Pile-Head and Toe Acceleration Vs. Time; Penetration = 53 Inches; Test 9

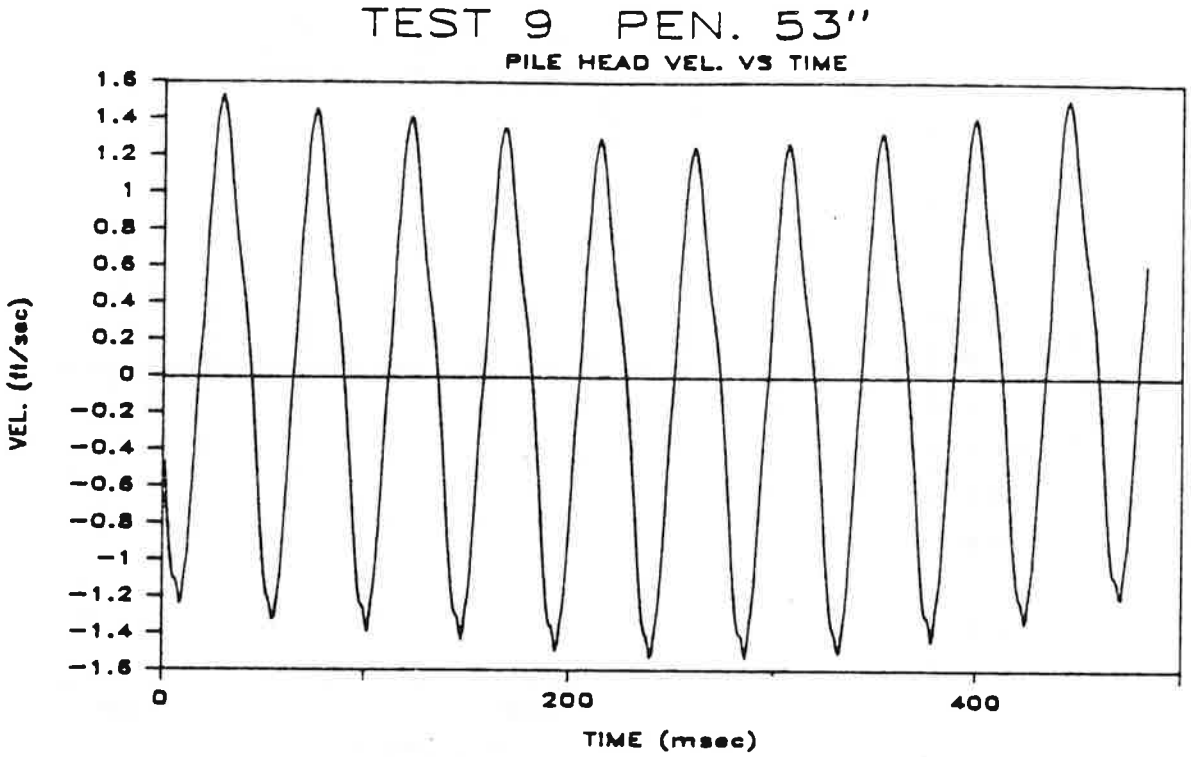

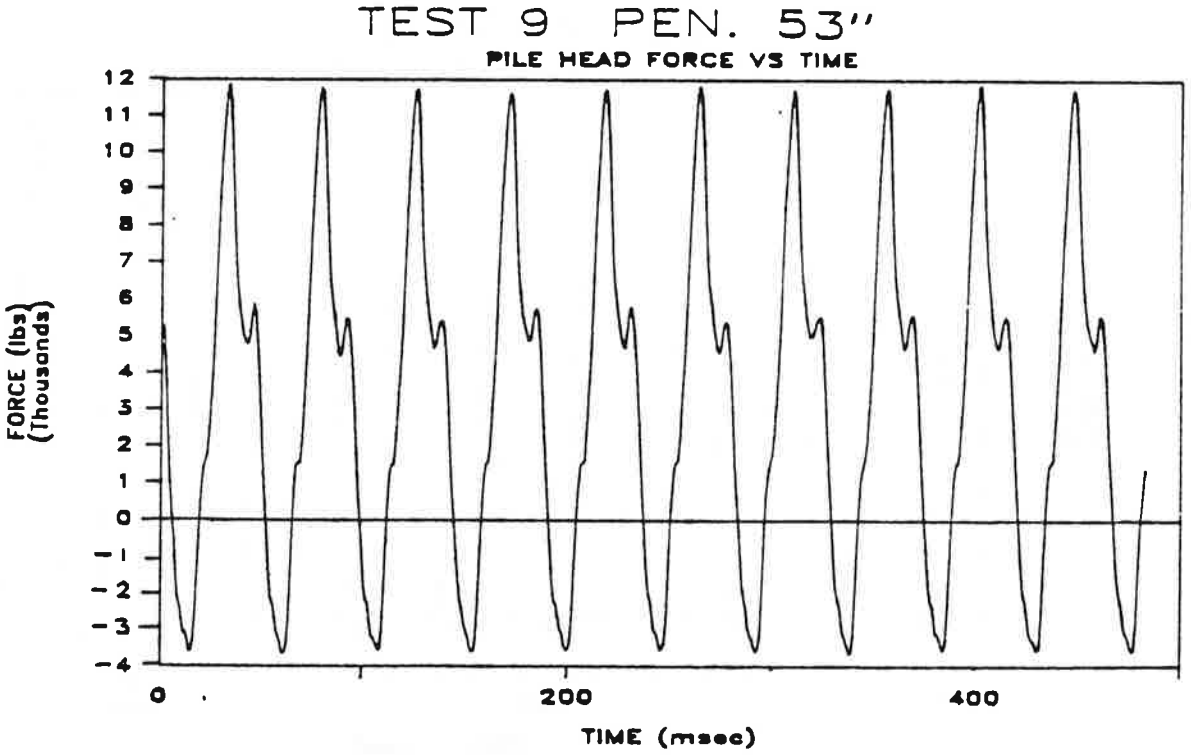

Fig. M.10b. Pile-Head Velocity and ForceVs. Time; Penetration = 53 Inches; Test 9

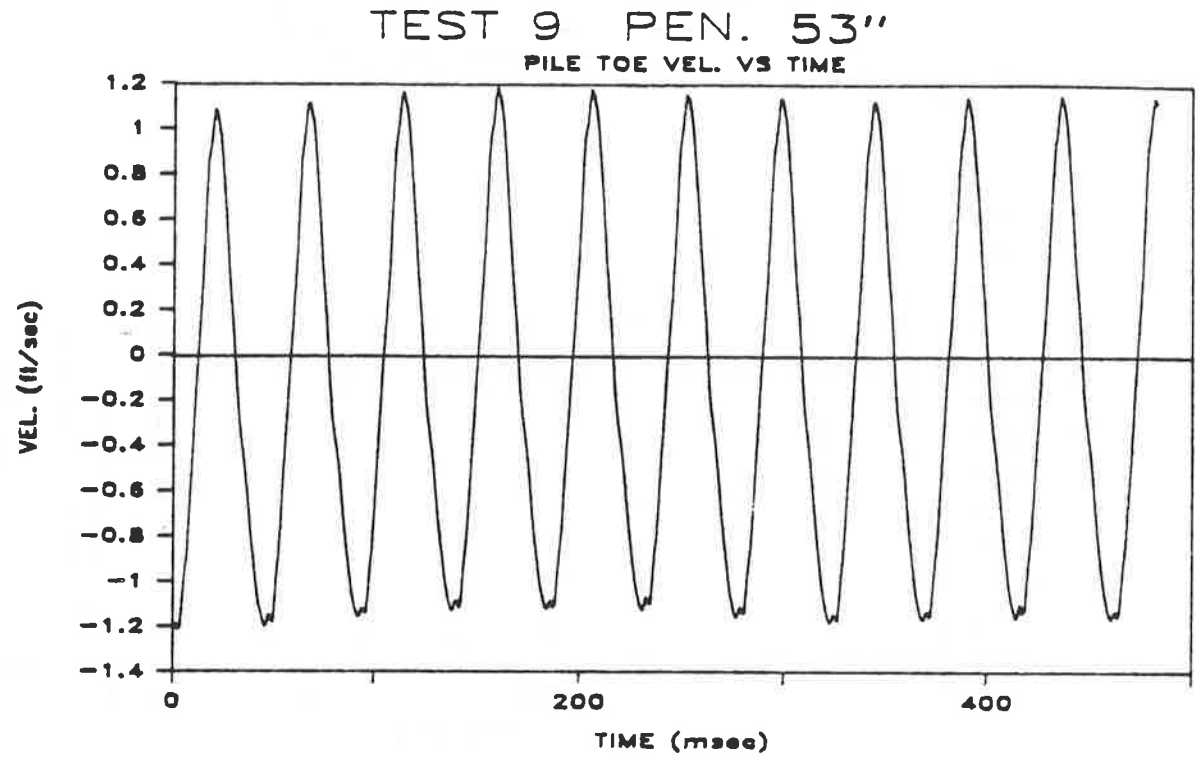

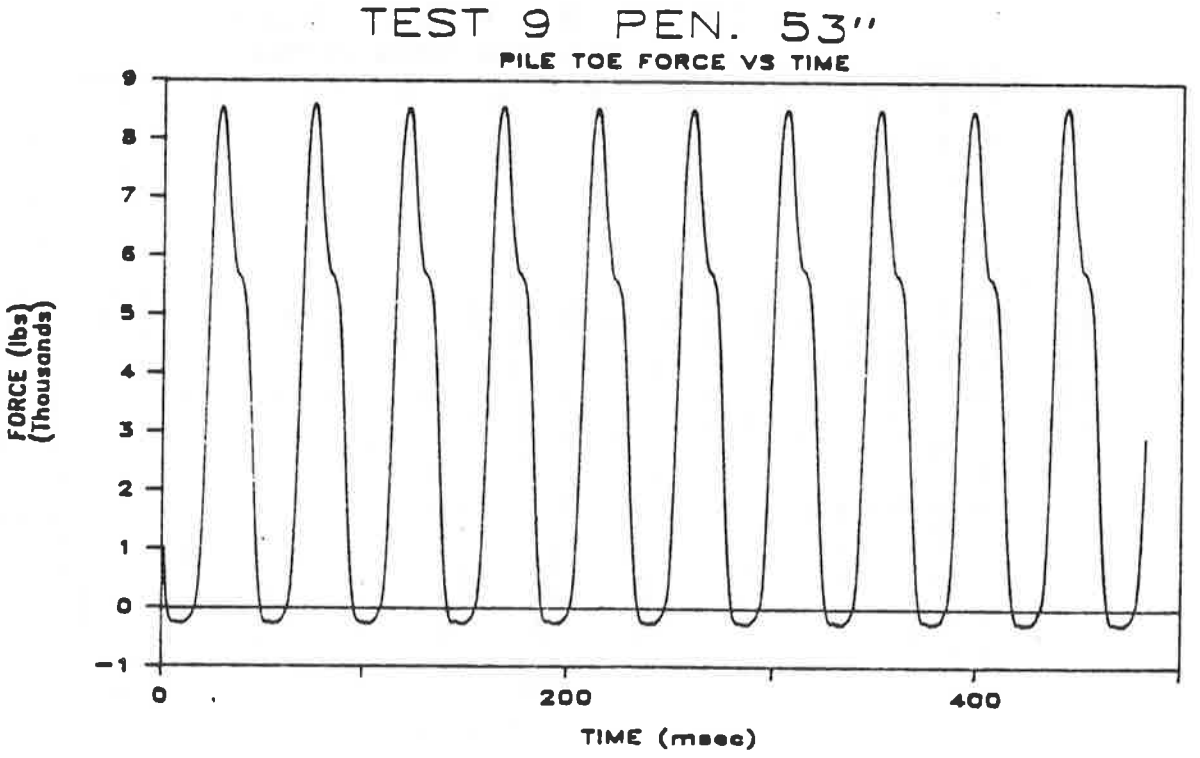

Fig. M.10c. Pile-Toe Velocity and Force Vs. Time; Penetration = 53 Inches; Test 9

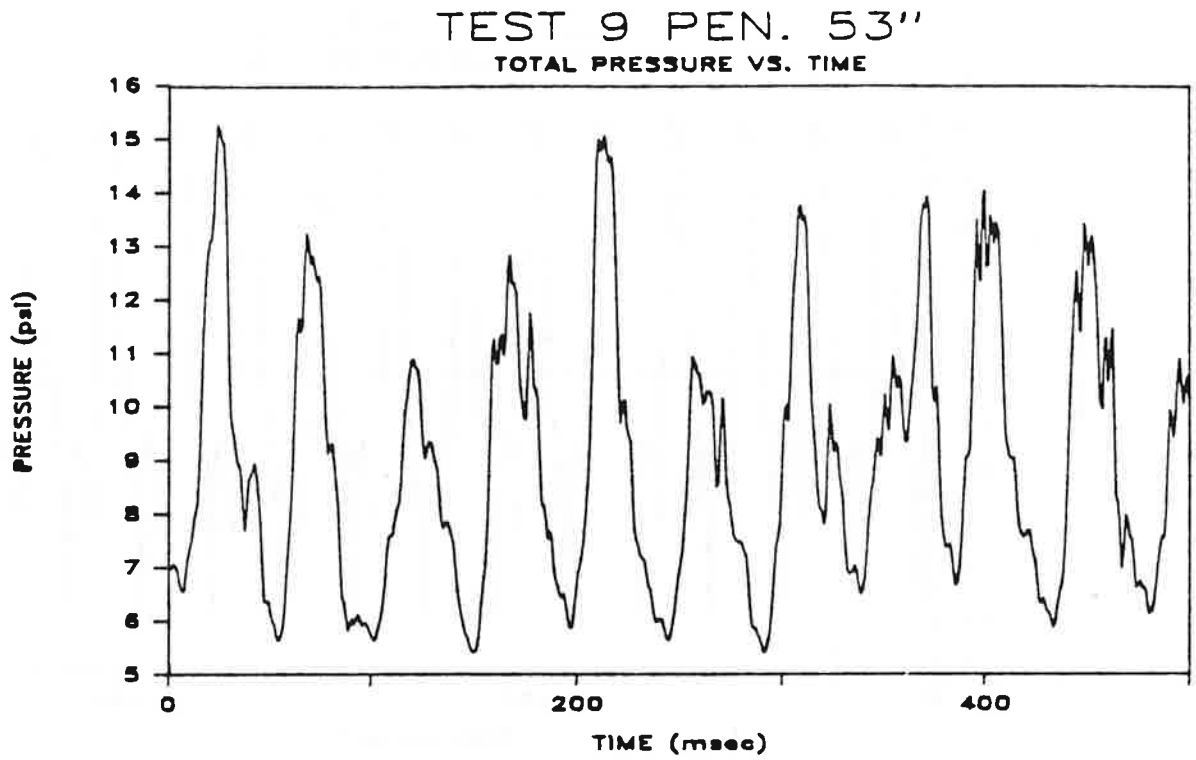

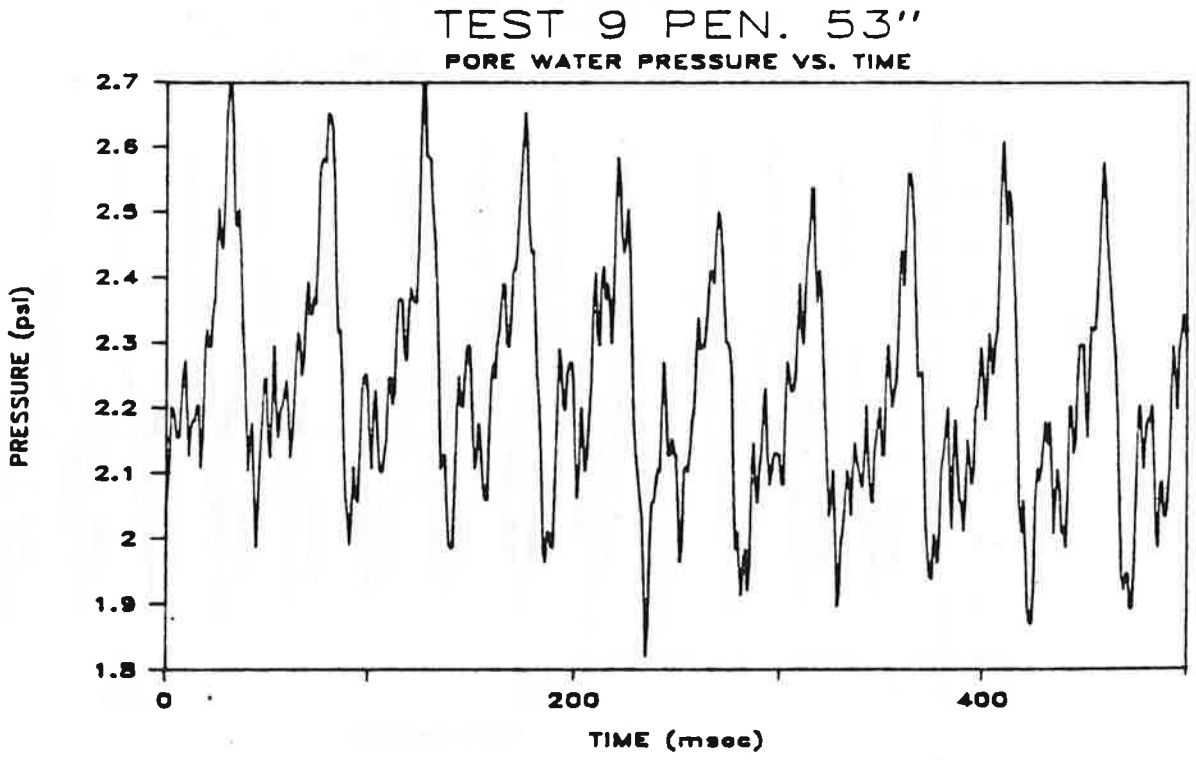

Fig. M.10d. Total and Pore Water Pressure Vs. Time at Bottom of Pile Shaft; Penetration = 53 Inches; Test 9

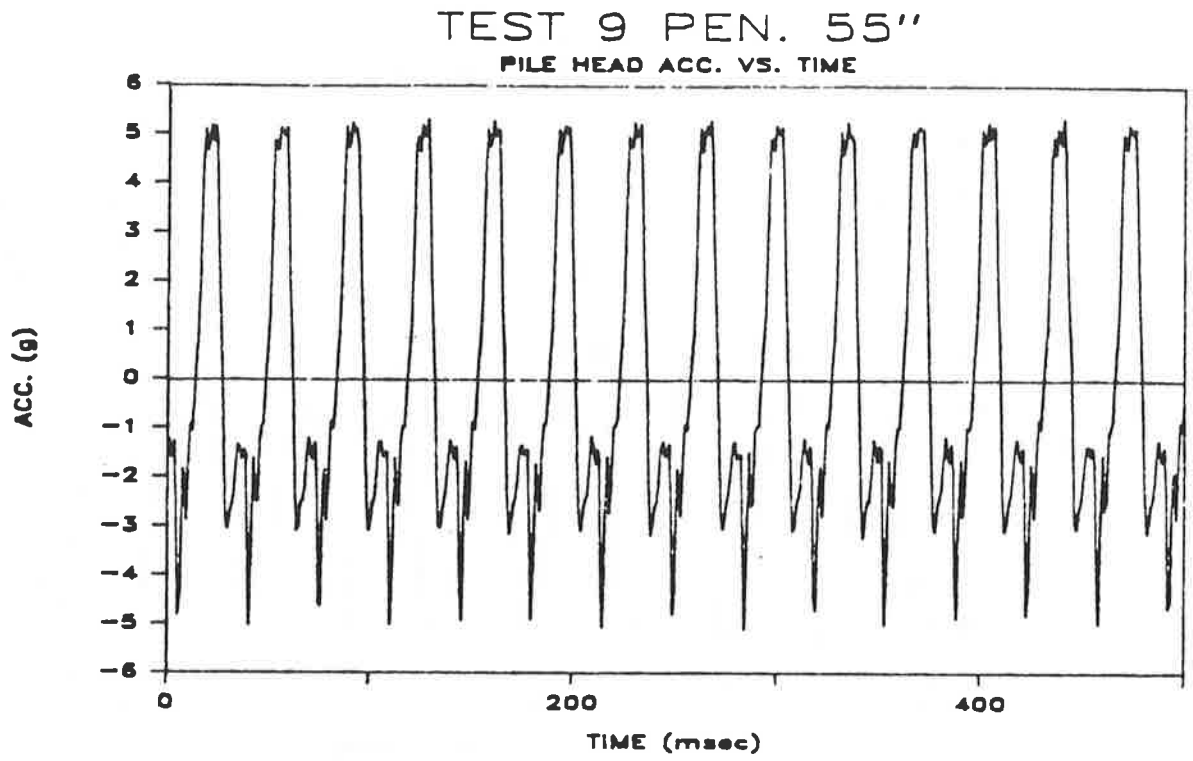

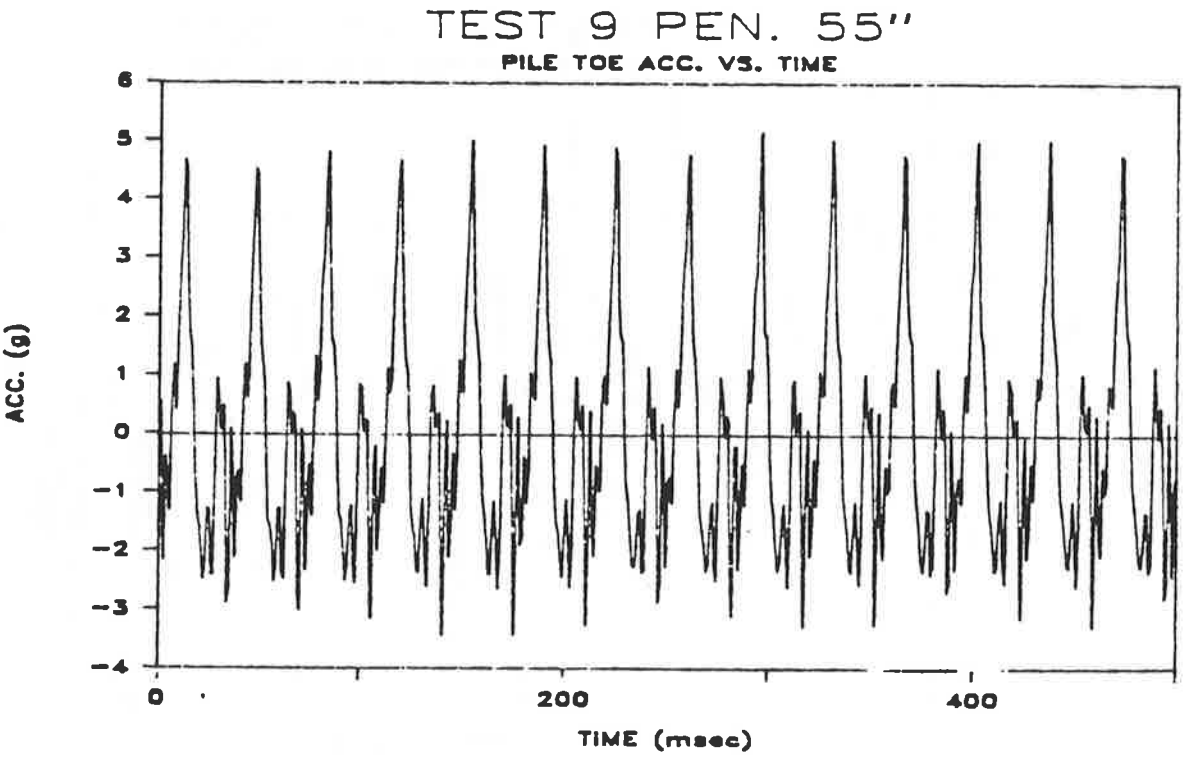

Fig. M.11a. Pile-Head and Toe Acceleration Vs. Time; Penetration = 55 Inches; Test 9 (Refusal)

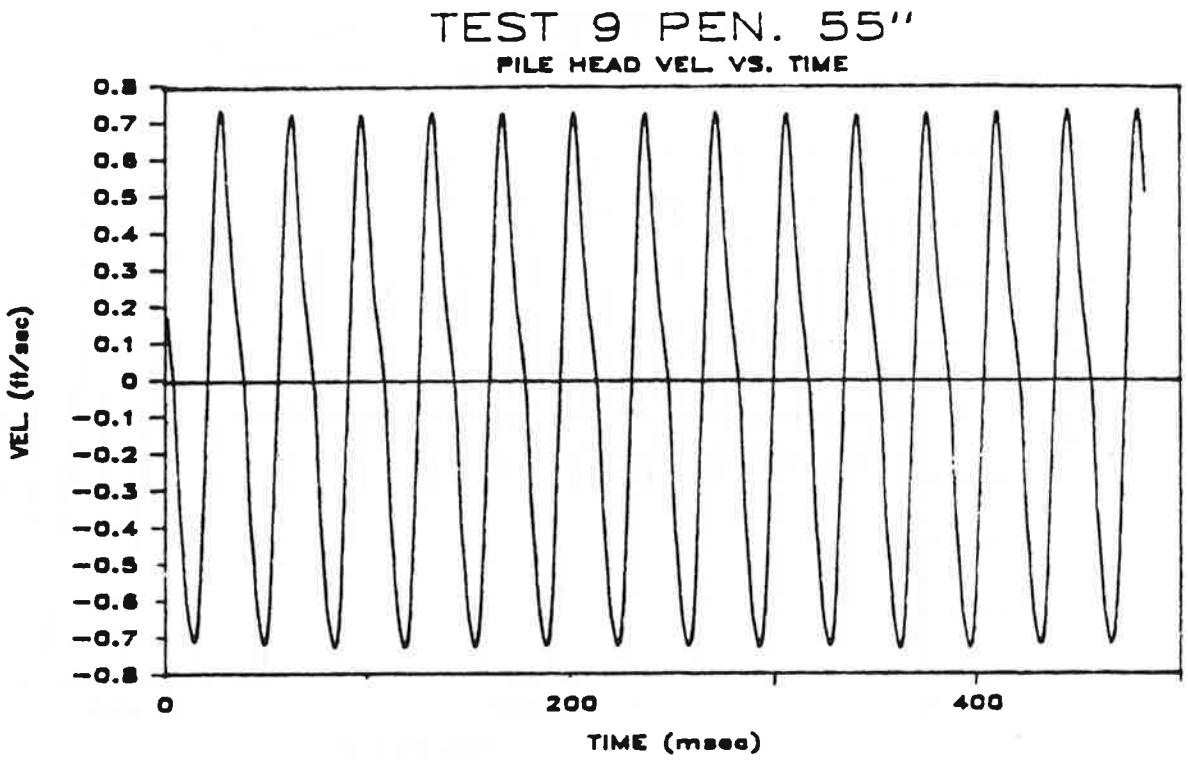

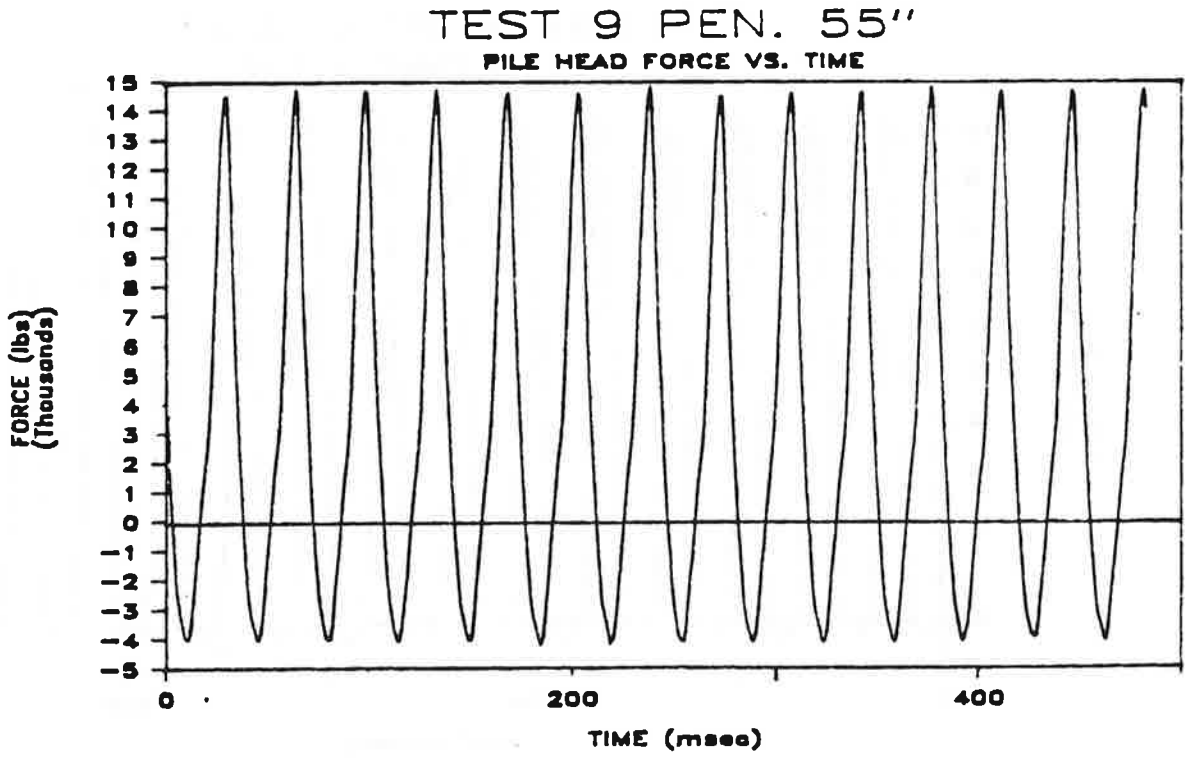

Fig. M.11b. Pile-Head Velocity and ForceVs. Time; Penetration = 55 Inches; Test 9 (Refusal)

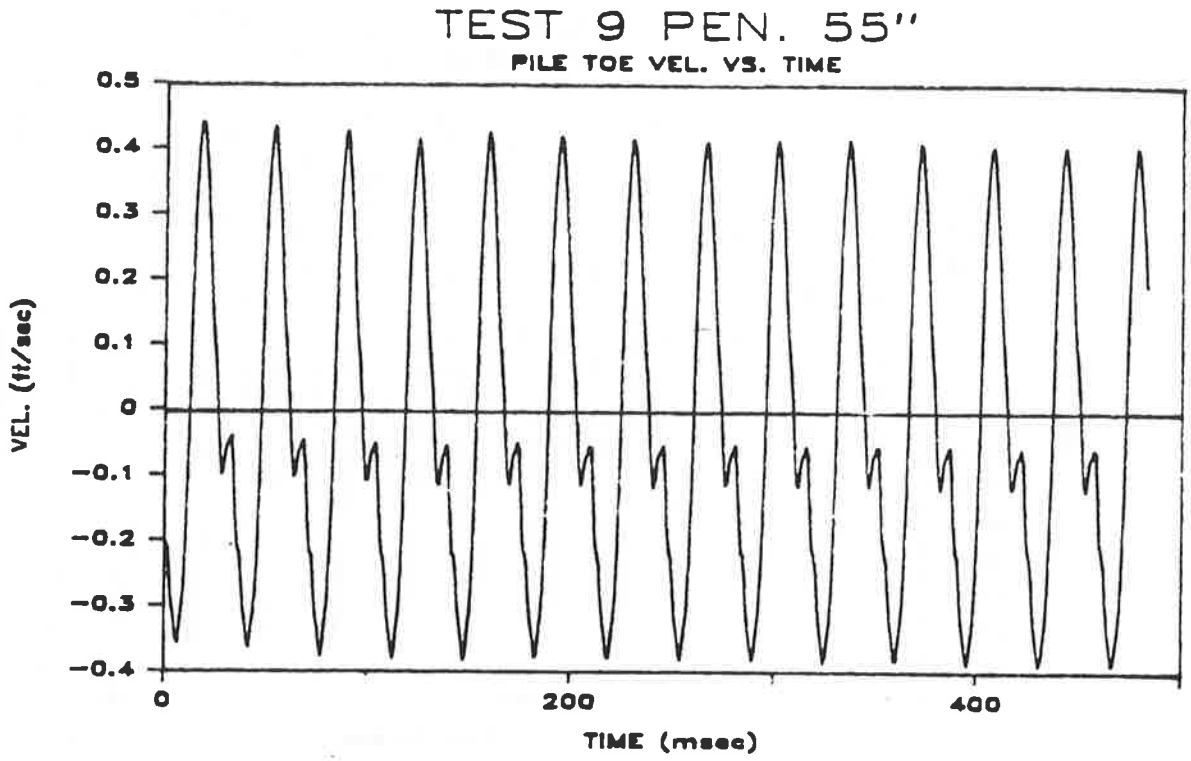

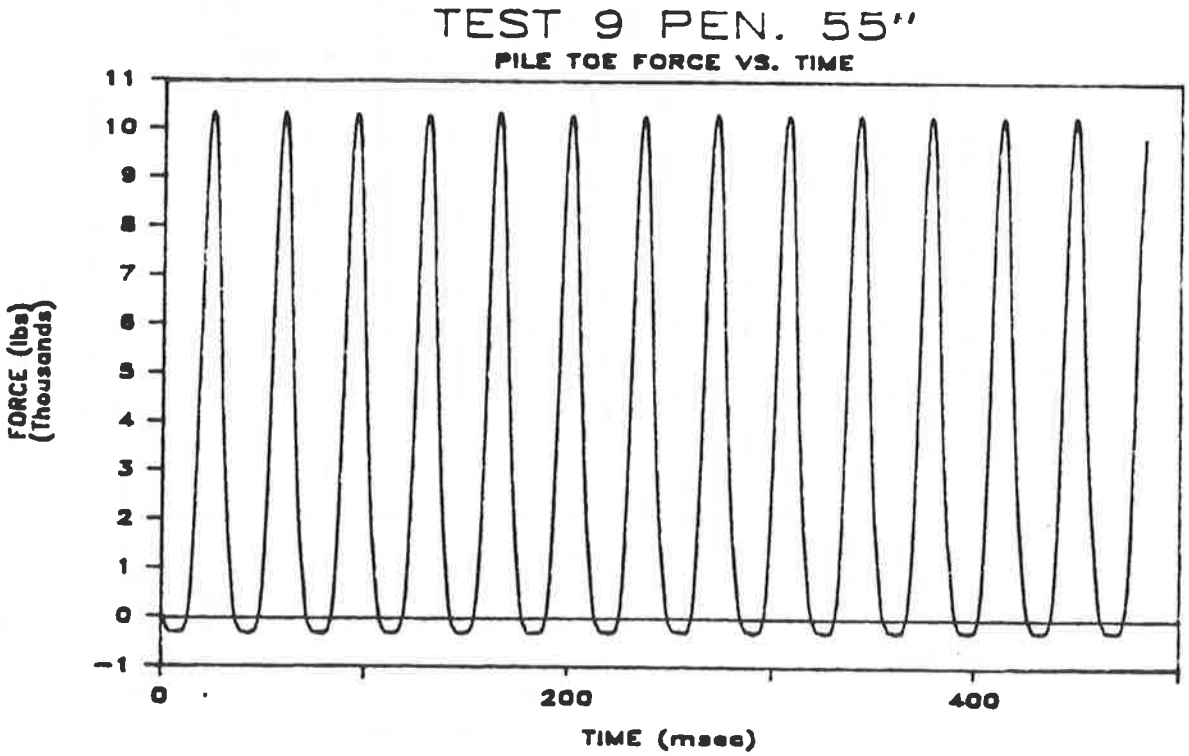

Fig. M.11c. Pile-Toe Velocity and Force Vs. Time; Penetration = 55 Inches; Test 9 (Refusal)

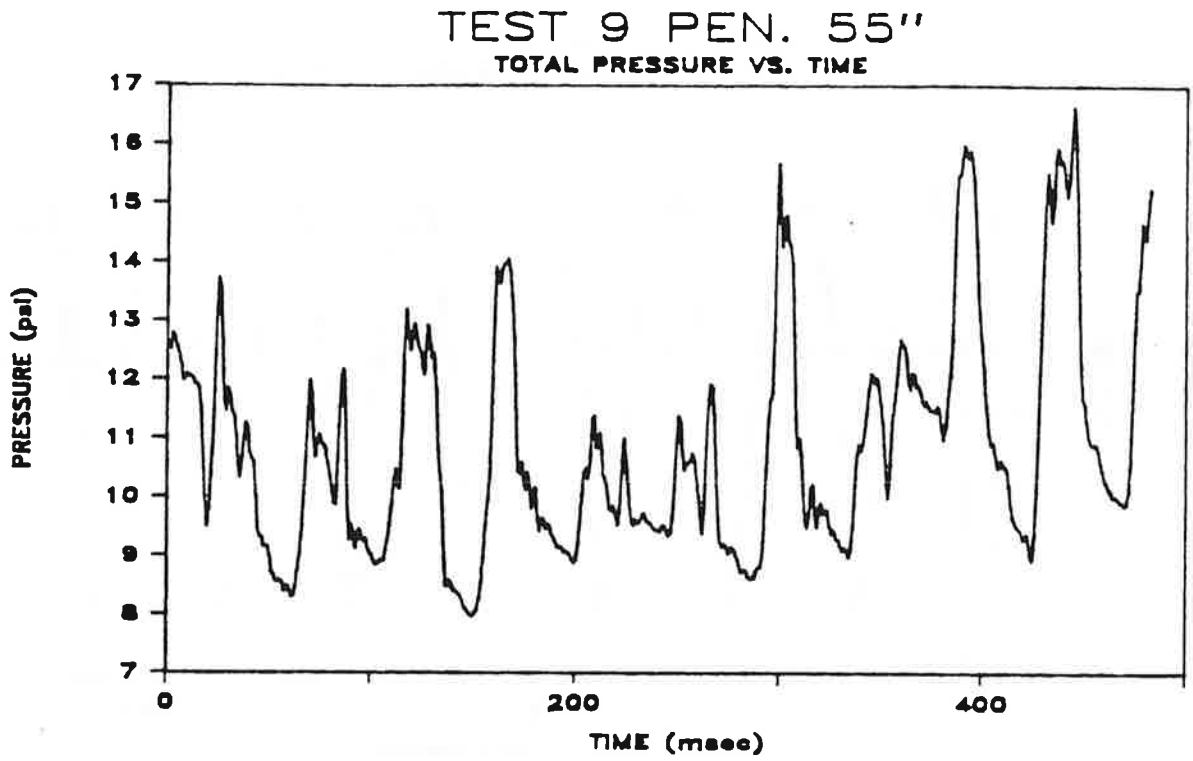

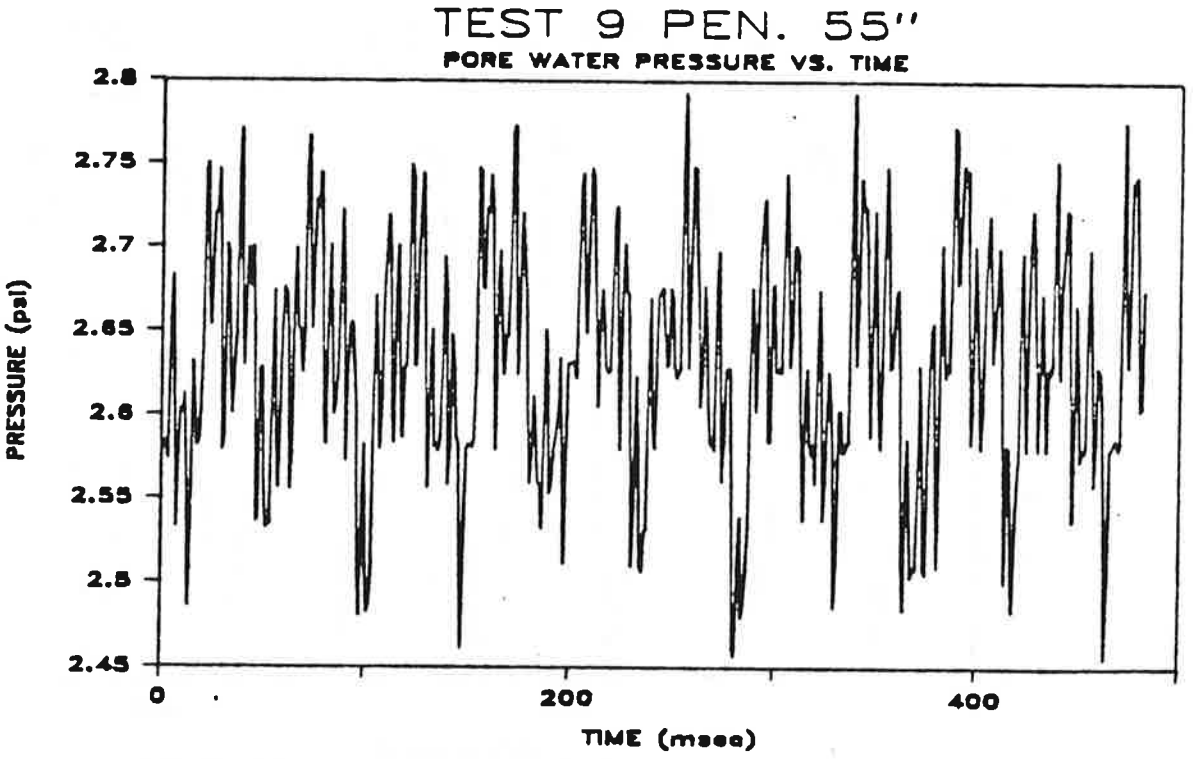

Fig. M.11d. Total and Pore Water Pressure Vs. Time at Bottom of Pile Shaft; Penetration = 55 Inches; Test 9 (Refusal)

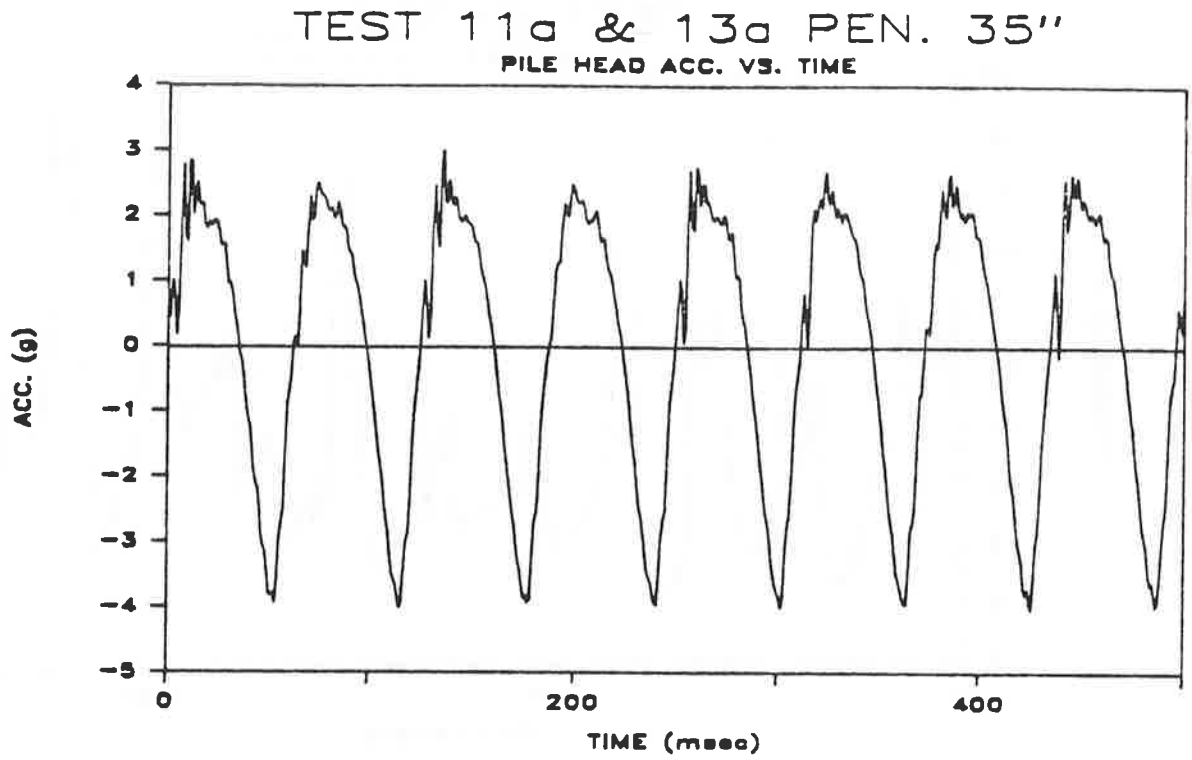

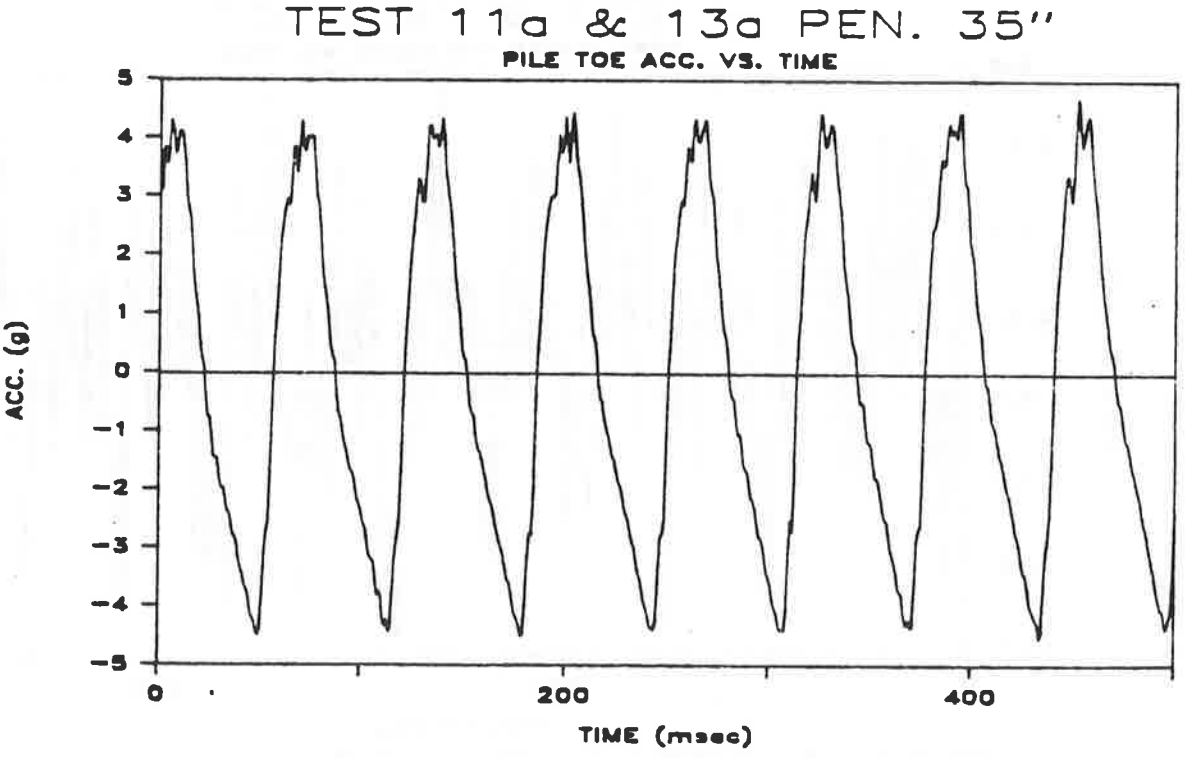

Fig. M.12a. Pile-Head and Toe Acceleration Vs. Time; Penetration = 35 Inches; Test 11a/13a

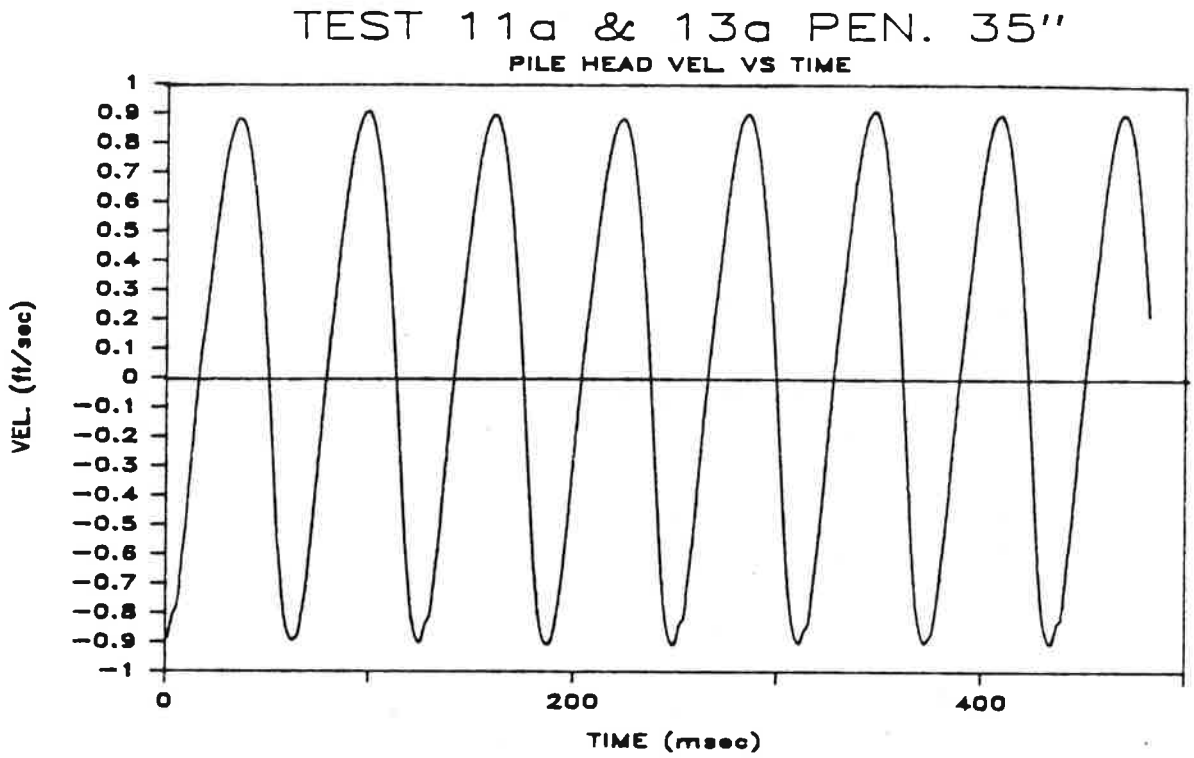

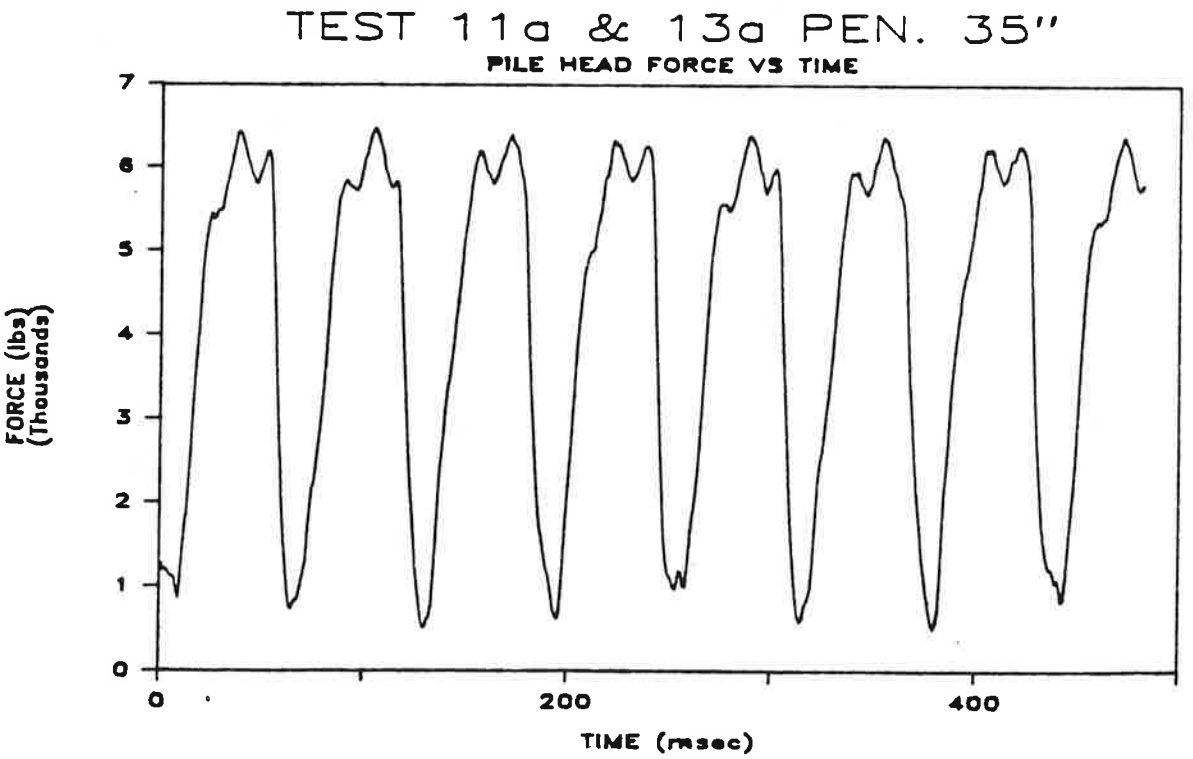

Fig. M.12b. Pile-Head Velocity and ForceVs. Time; Penetration = 35 Inches; Test 11a/13a

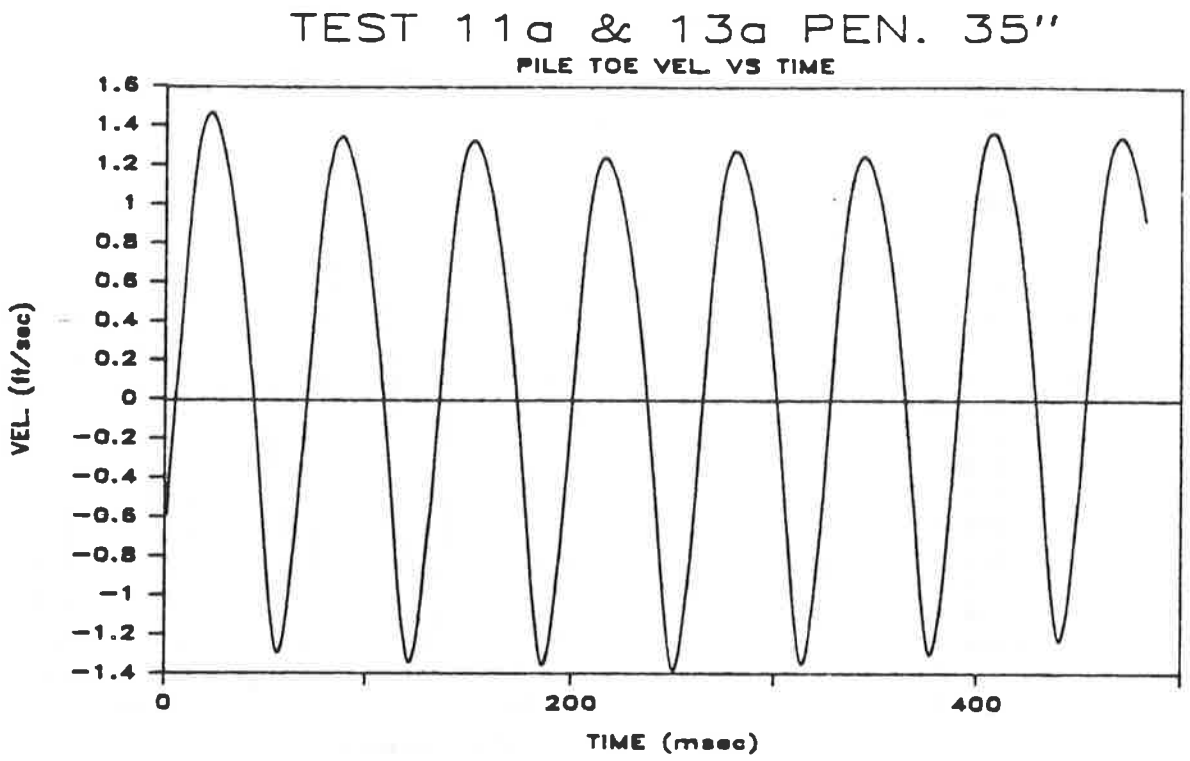

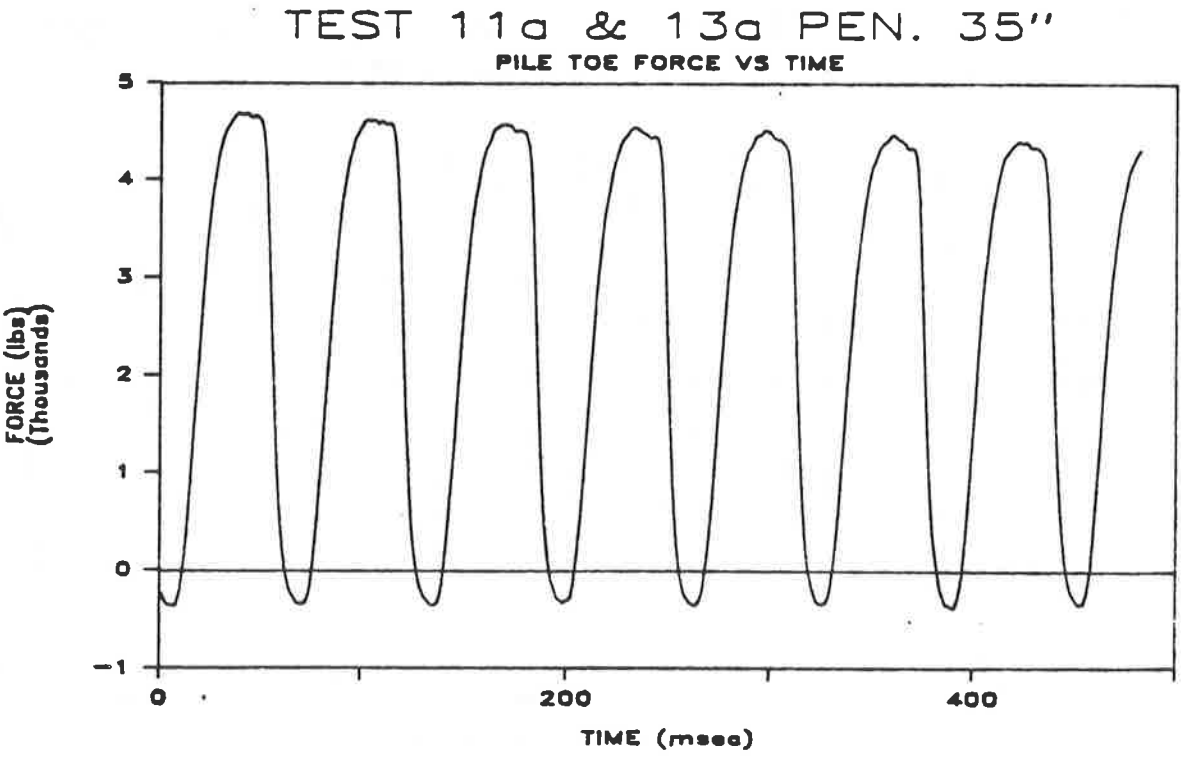

Fig. M.12c. Pile-Toe Velocity and Force Vs. Time; Penetration = 35 Inches; Test 11a/13a

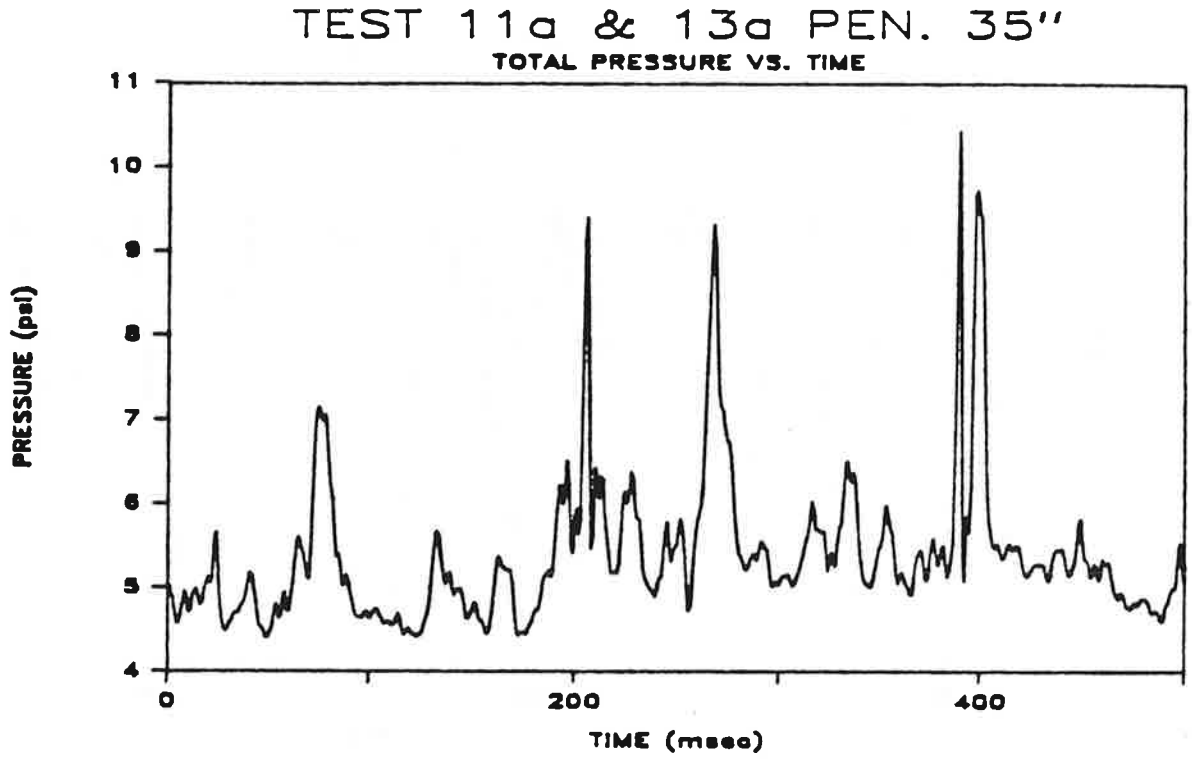

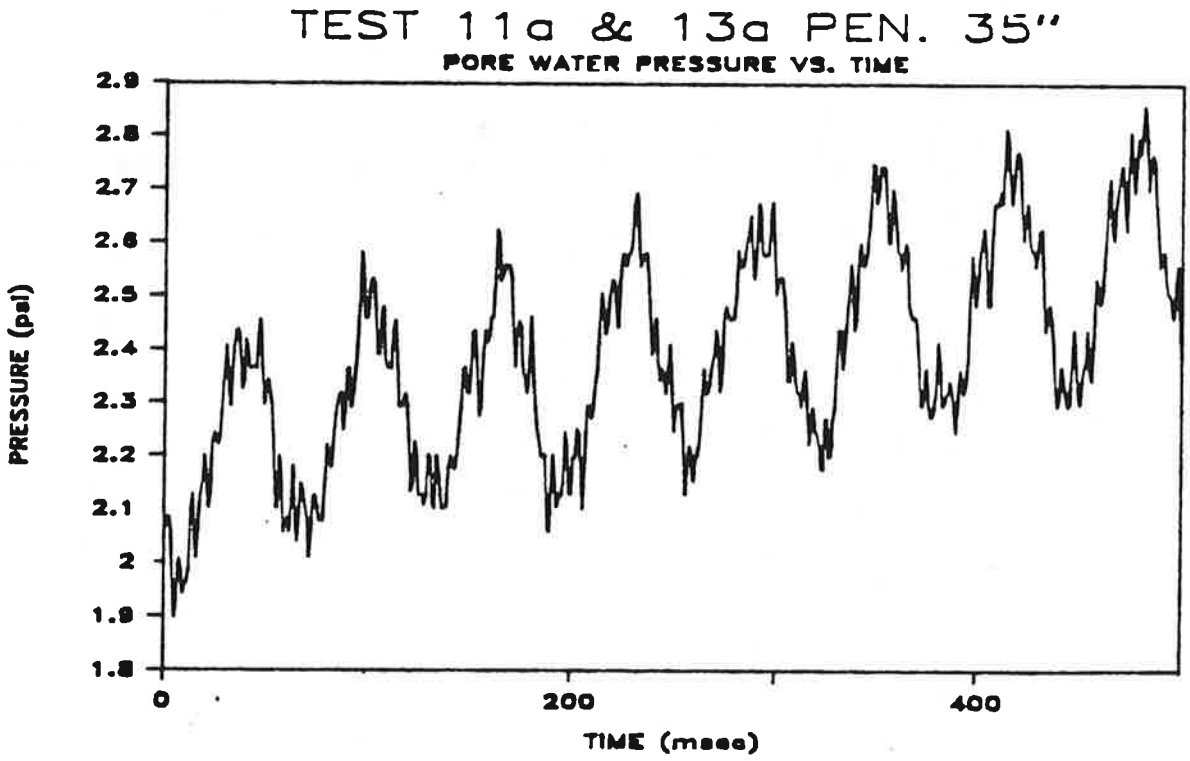

Fig. M.12d. Total and Pore Water Pressure Vs. Time at Bottom of Pile Shaft; Penetration = 35 Inches; Test 11a/13a

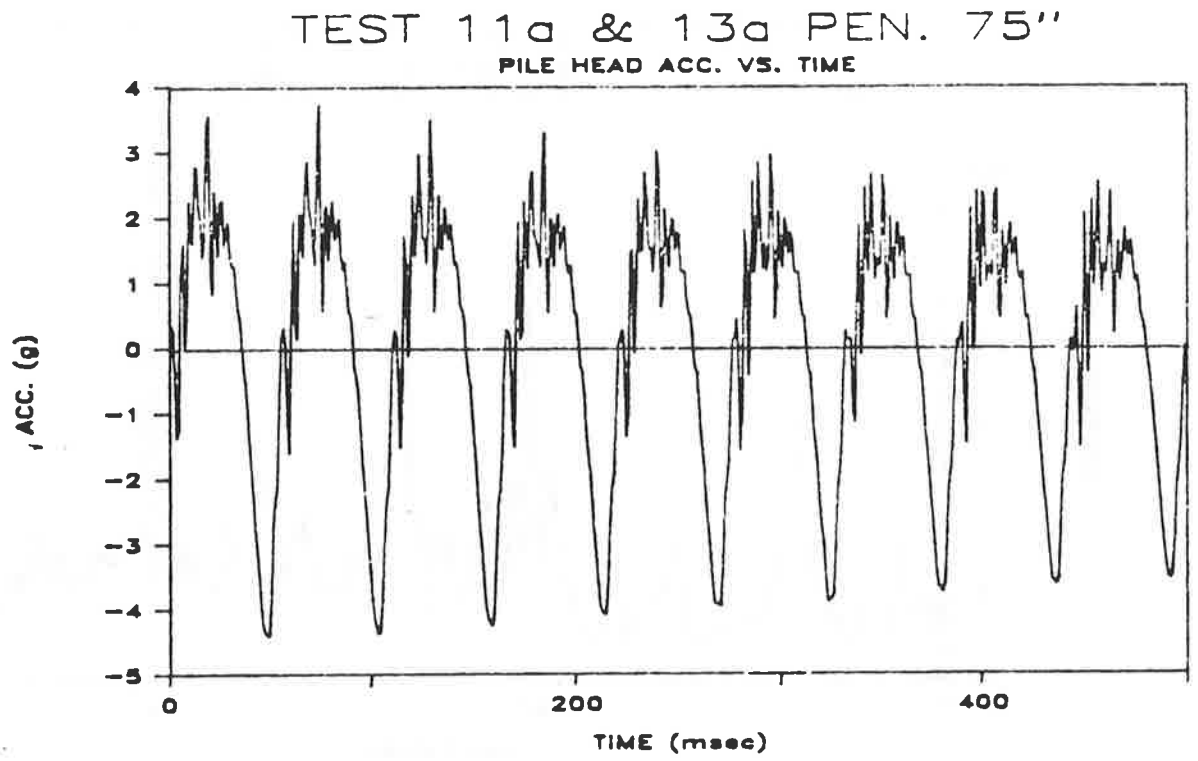

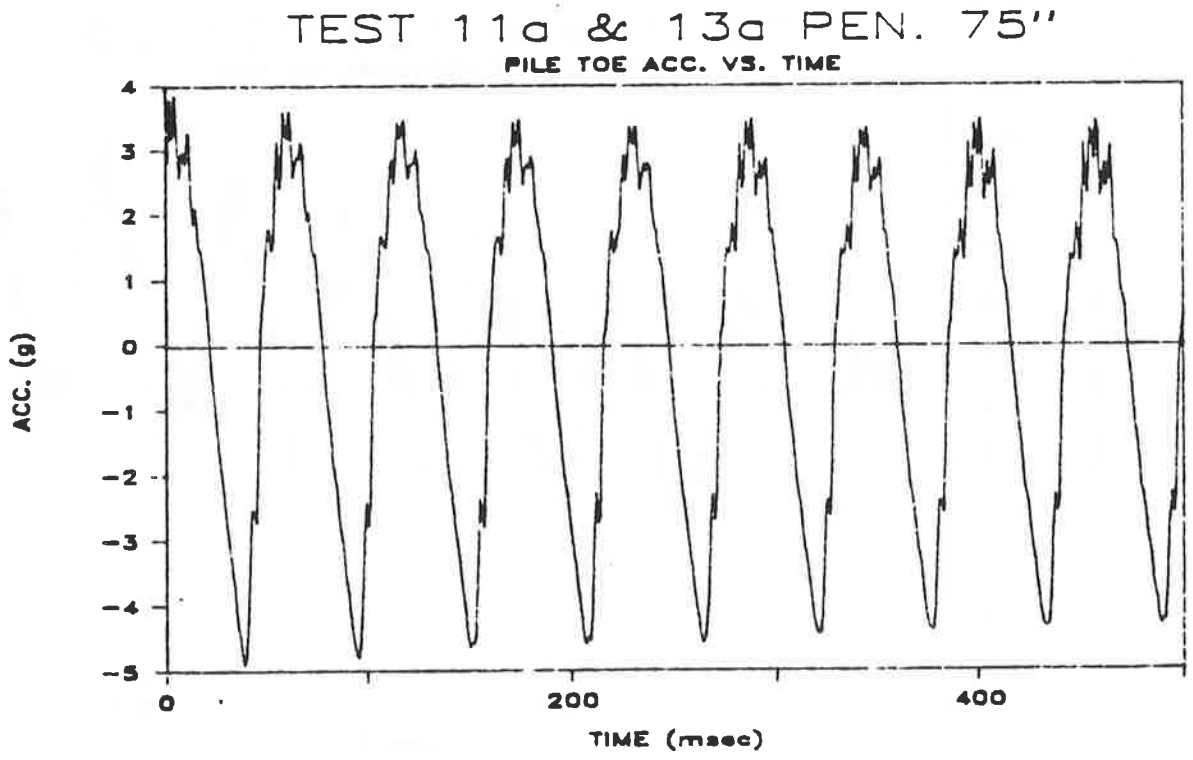

Fig. M.13a. Pile-Head and Toe Acceleration Vs. Time; Penetration = 75 Inches; Test 11a/13a

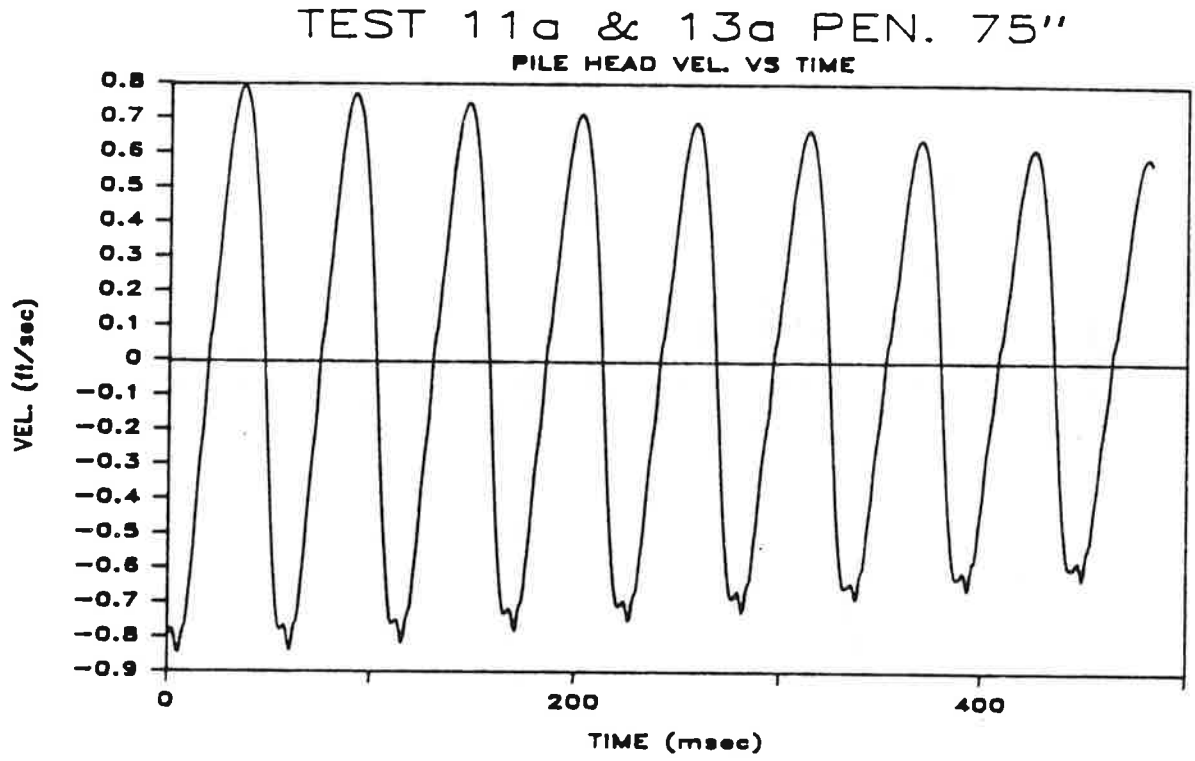

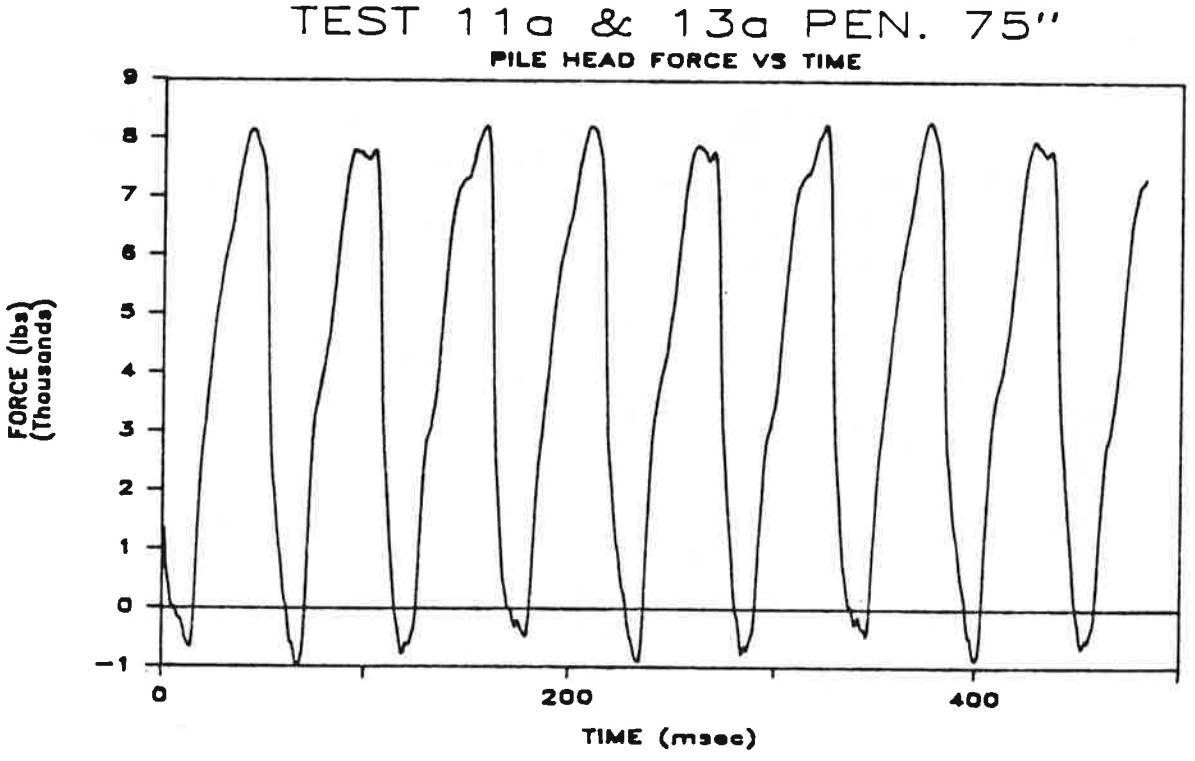

Fig. M.13b. Pile-Head Velocity and ForceVs. Time; Penetration = 75 Inches; Test 11a/13a

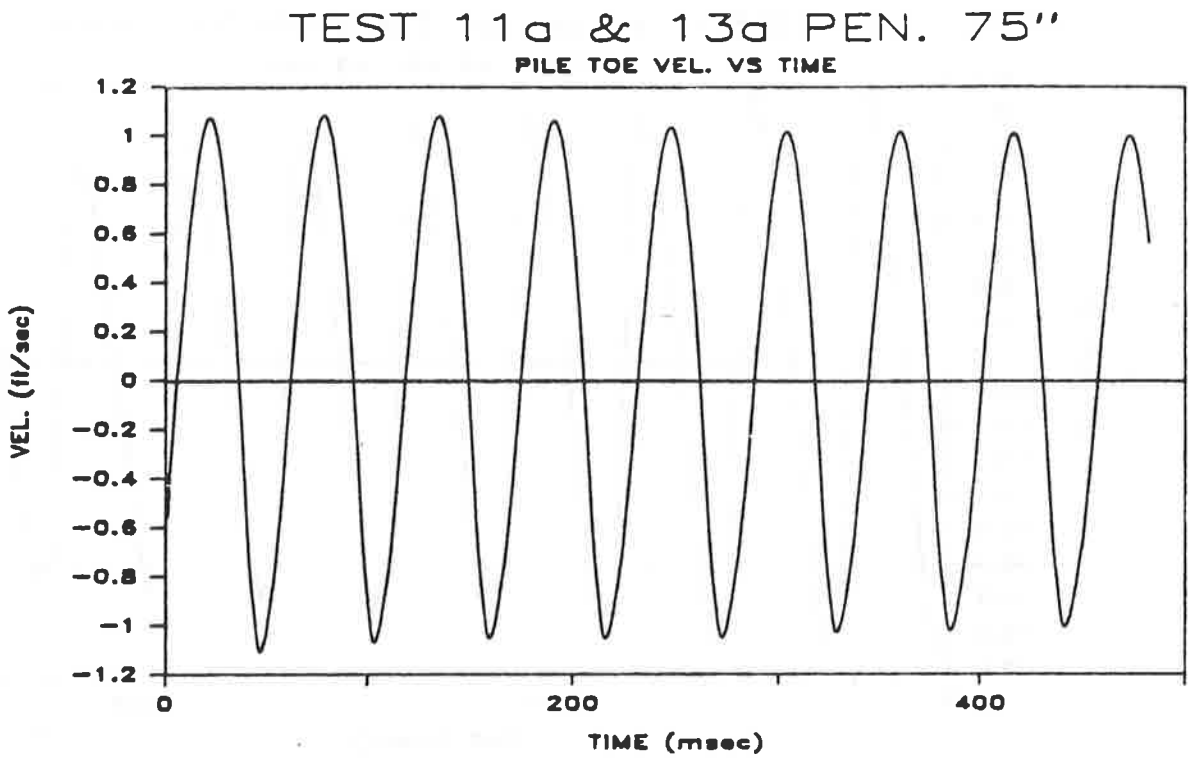

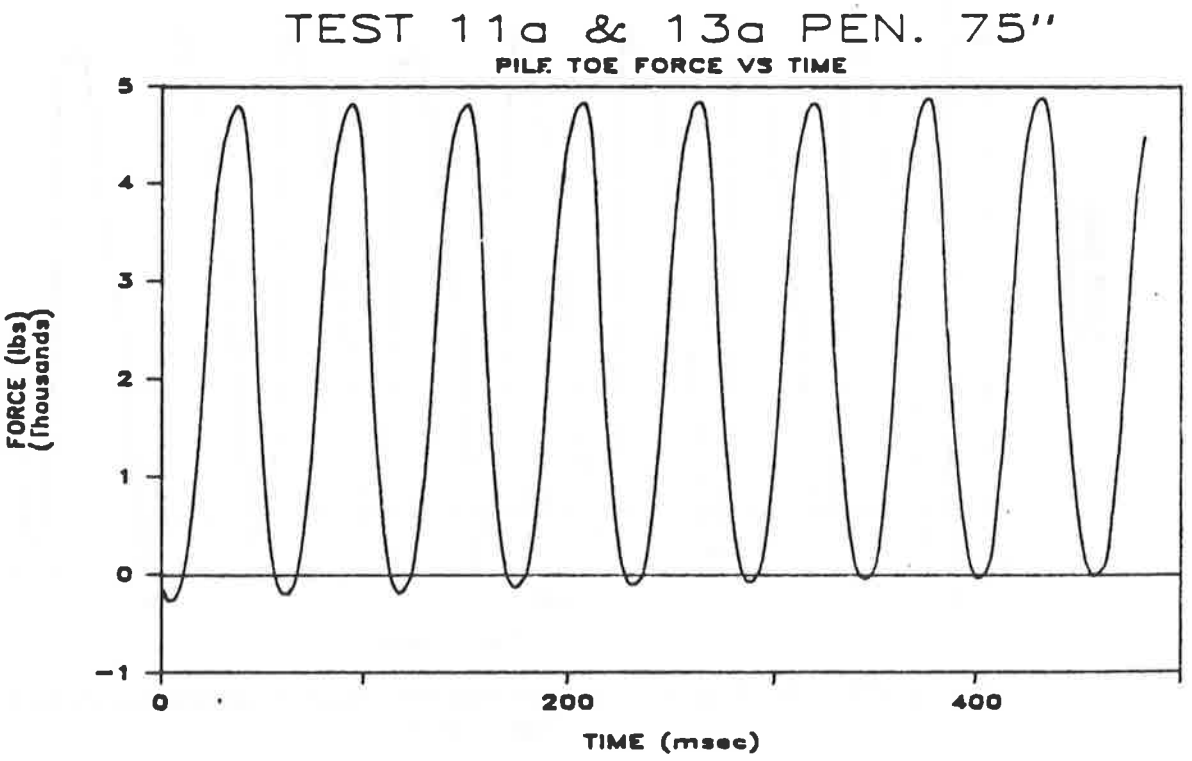

Fig. M.13c. Pile-Toe Velocity and Force Vs. Time; Penetration = 75 Inches; Test 11a/13a

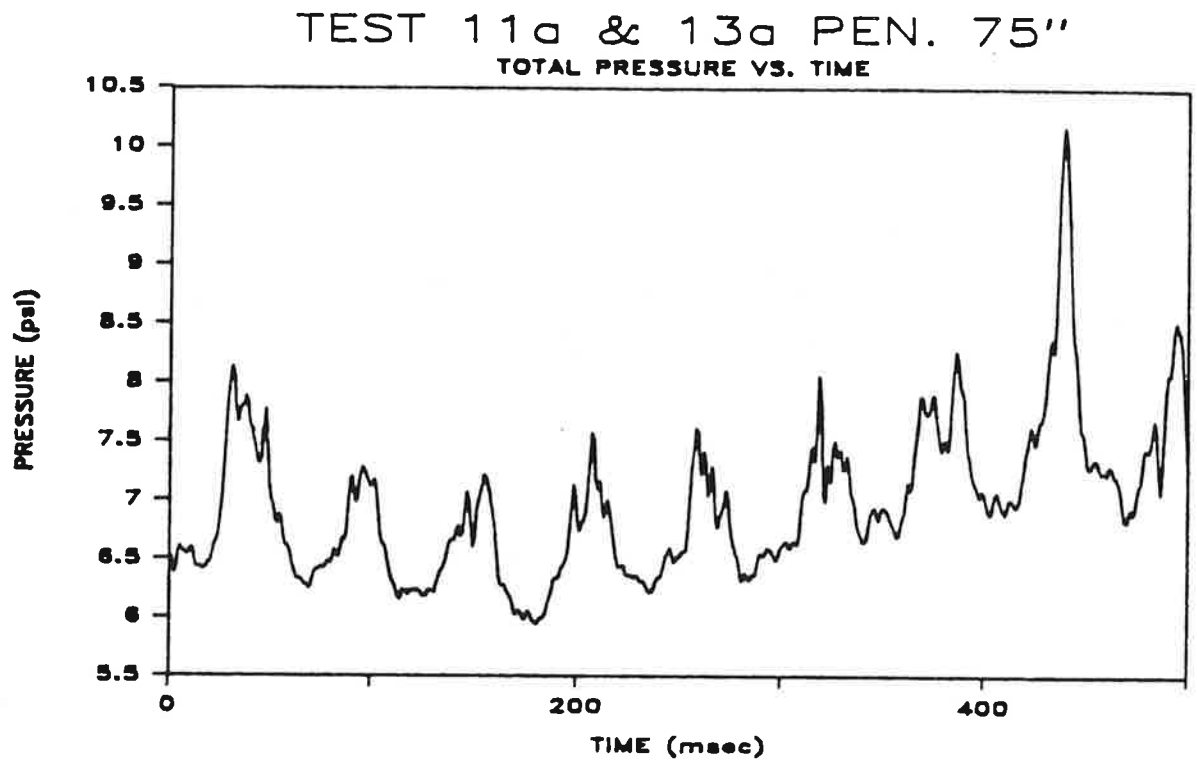

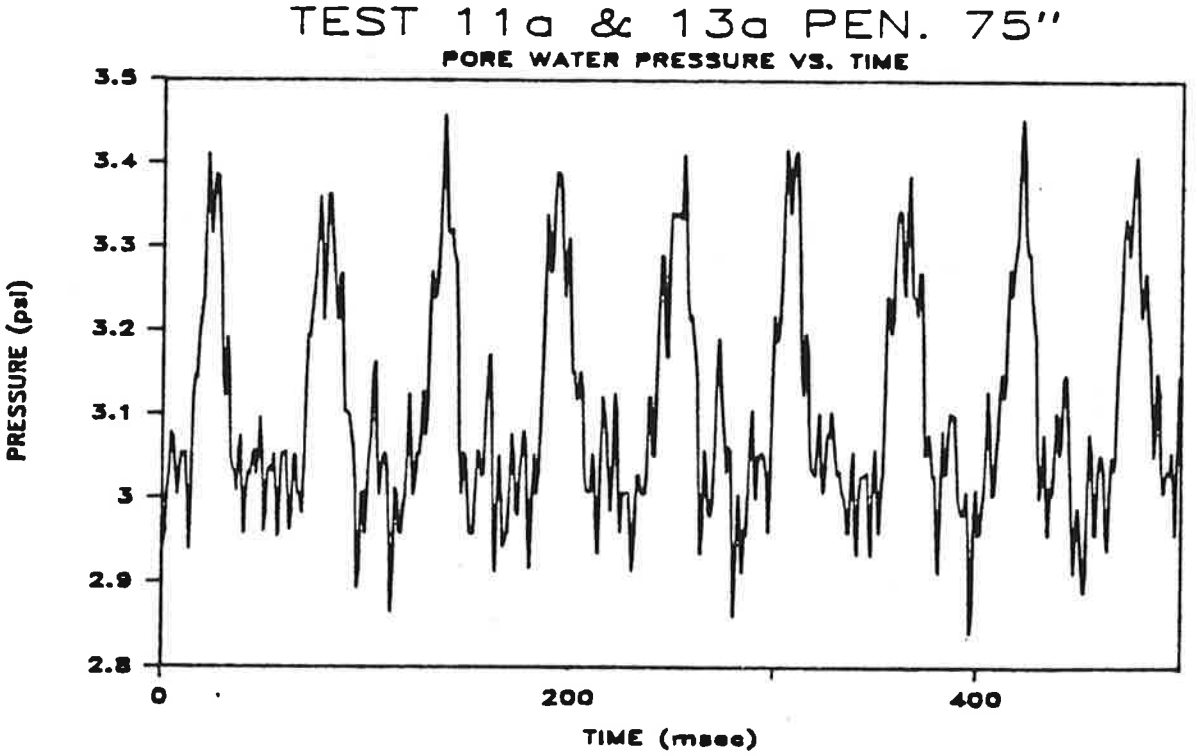

Fig. M.13d. Total and Pore Water Pressure Vs. Time at Bottom of Pile Shaft; Penetration = 75 Inches; Test 11a/13a

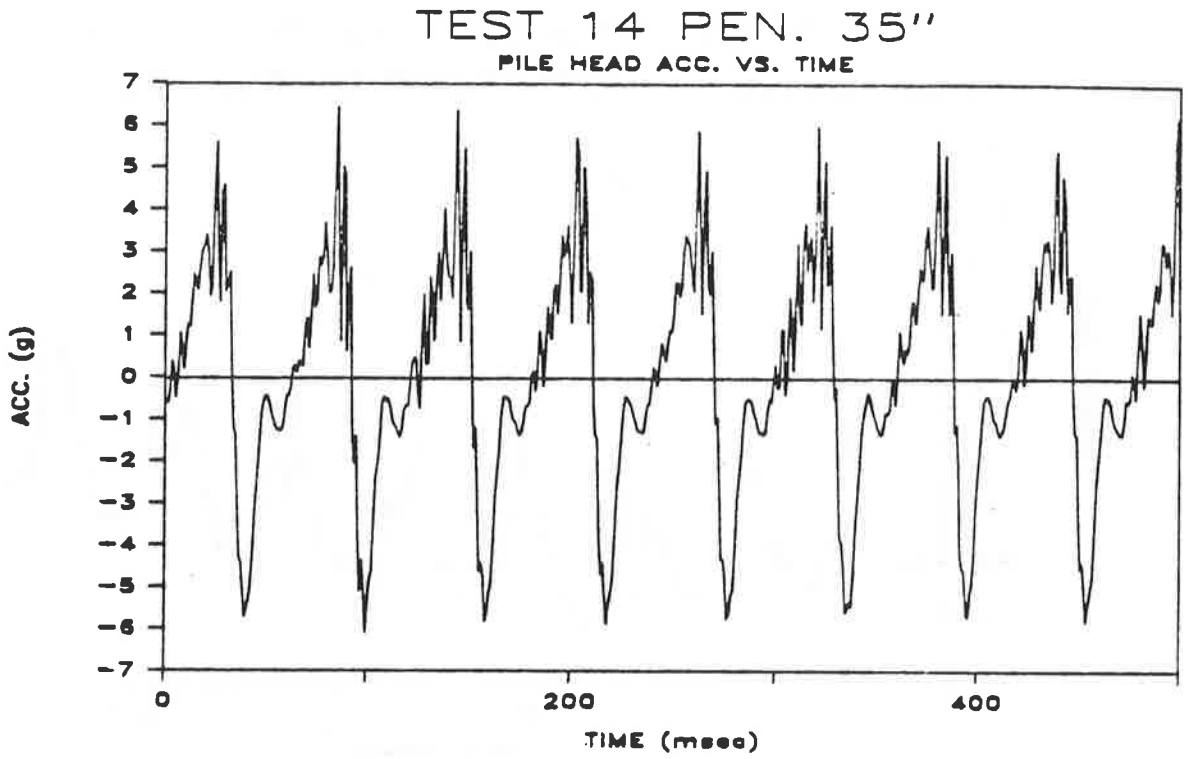

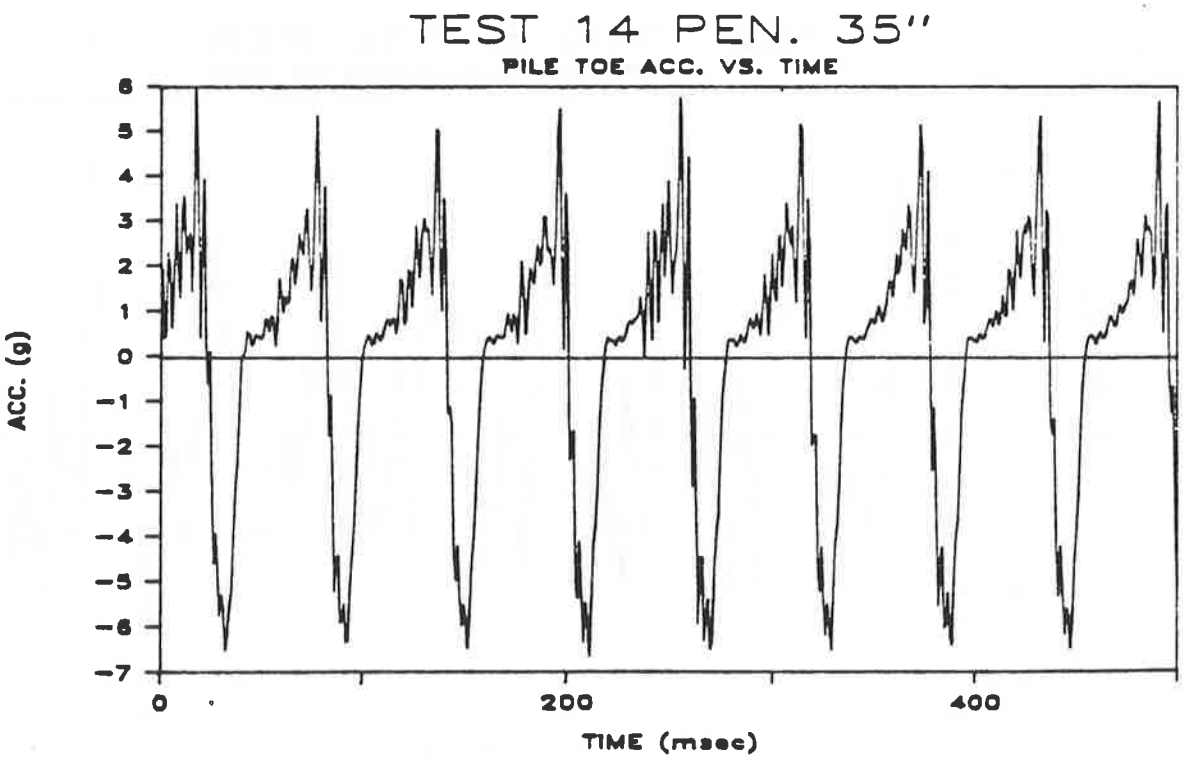

Fig. M.14a. Pile-Head and Toe Acceleration Vs. Time; Penetration = 35 Inches; Test 14

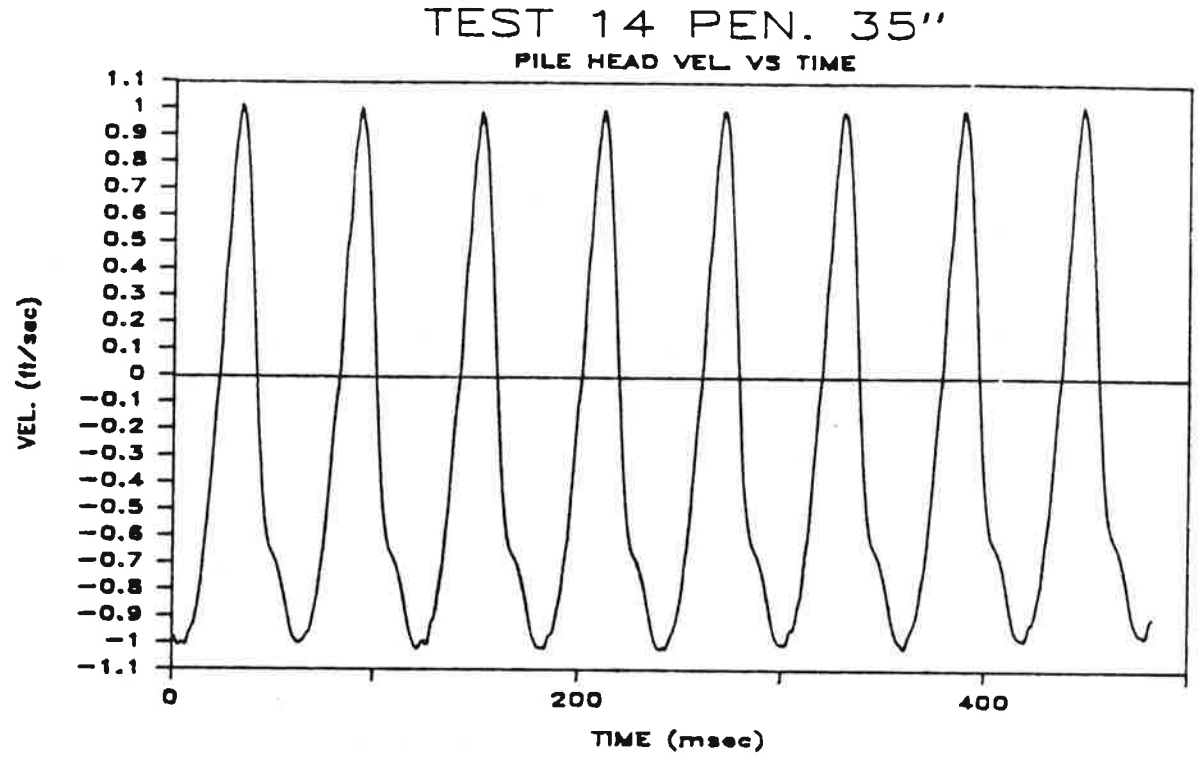

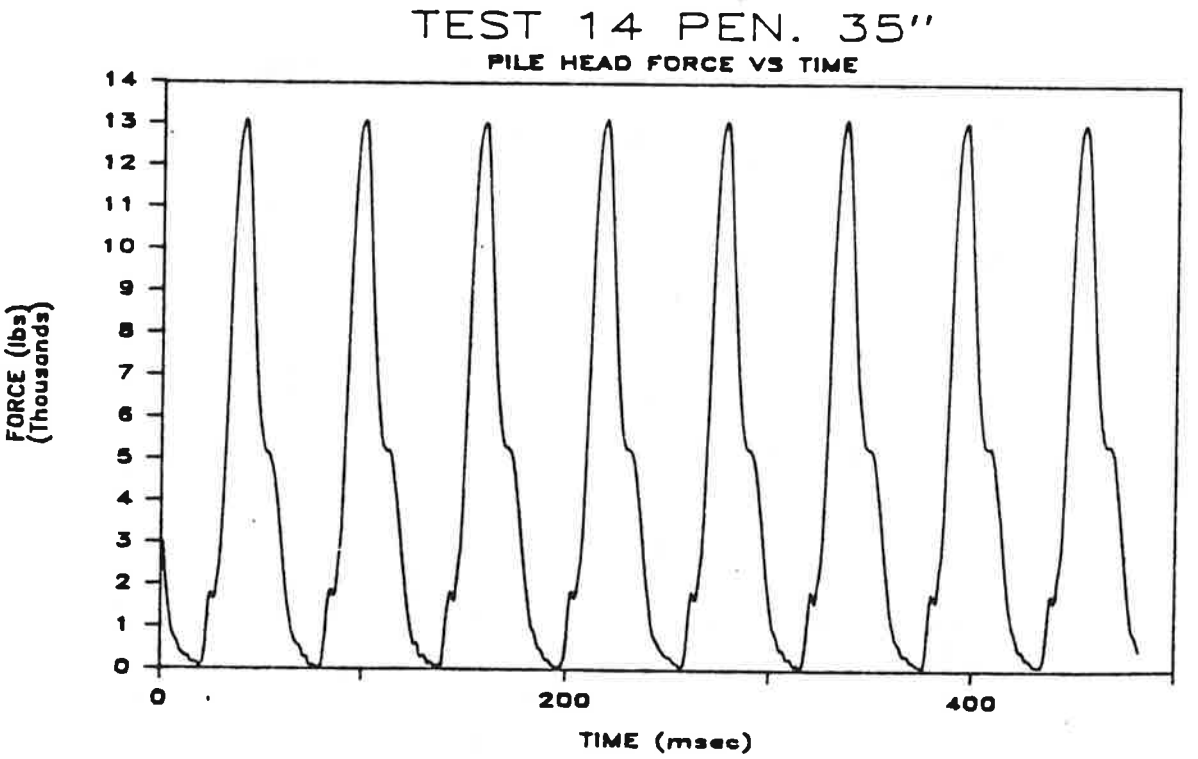

Fig. M.14b. Pile-Head Velocity and ForceVs. Time; Penetration = 35 Inches; Test 14

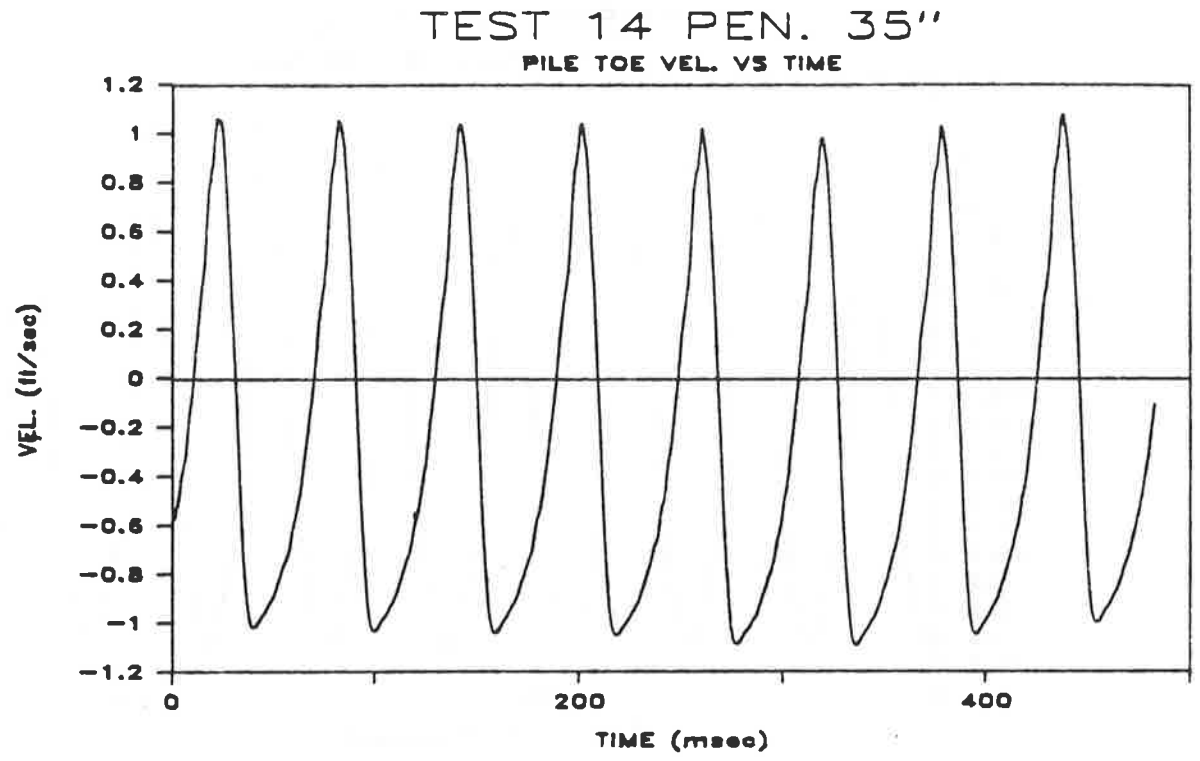

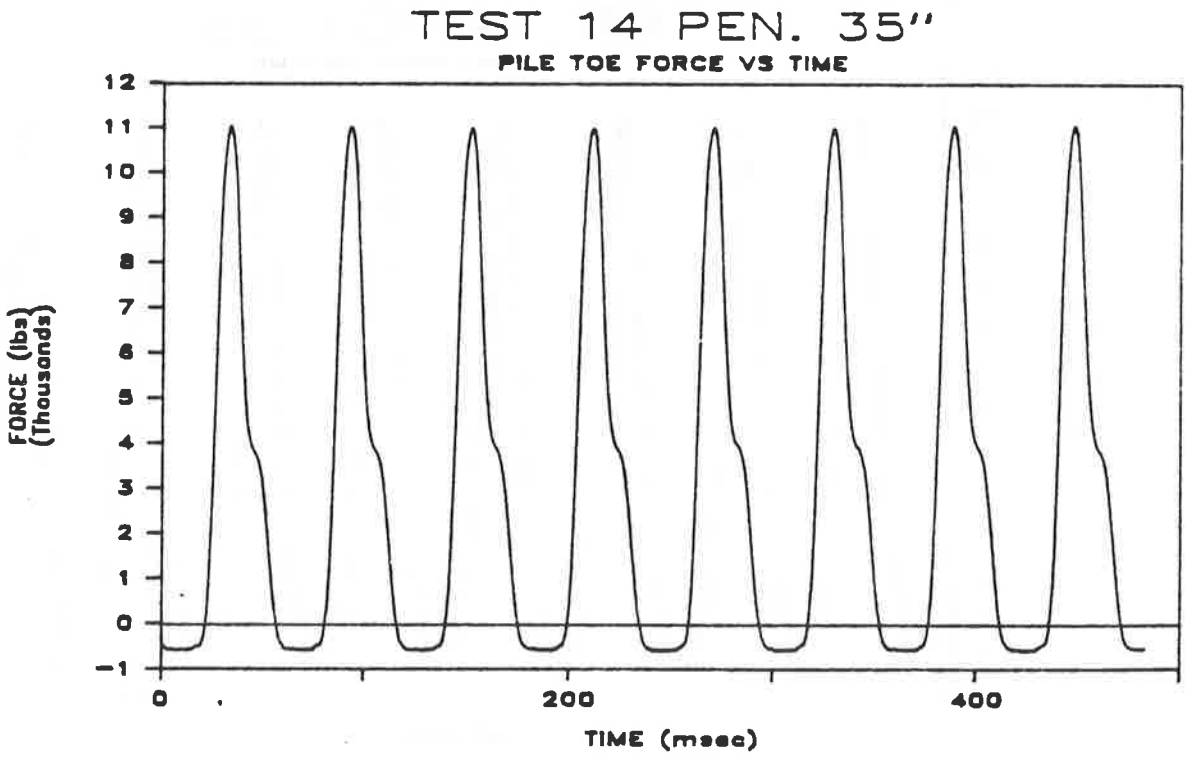

Fig. M.14c. Pile-Toe Velocity and Force Vs. Time; Penetration = 35 Inches; Test 14

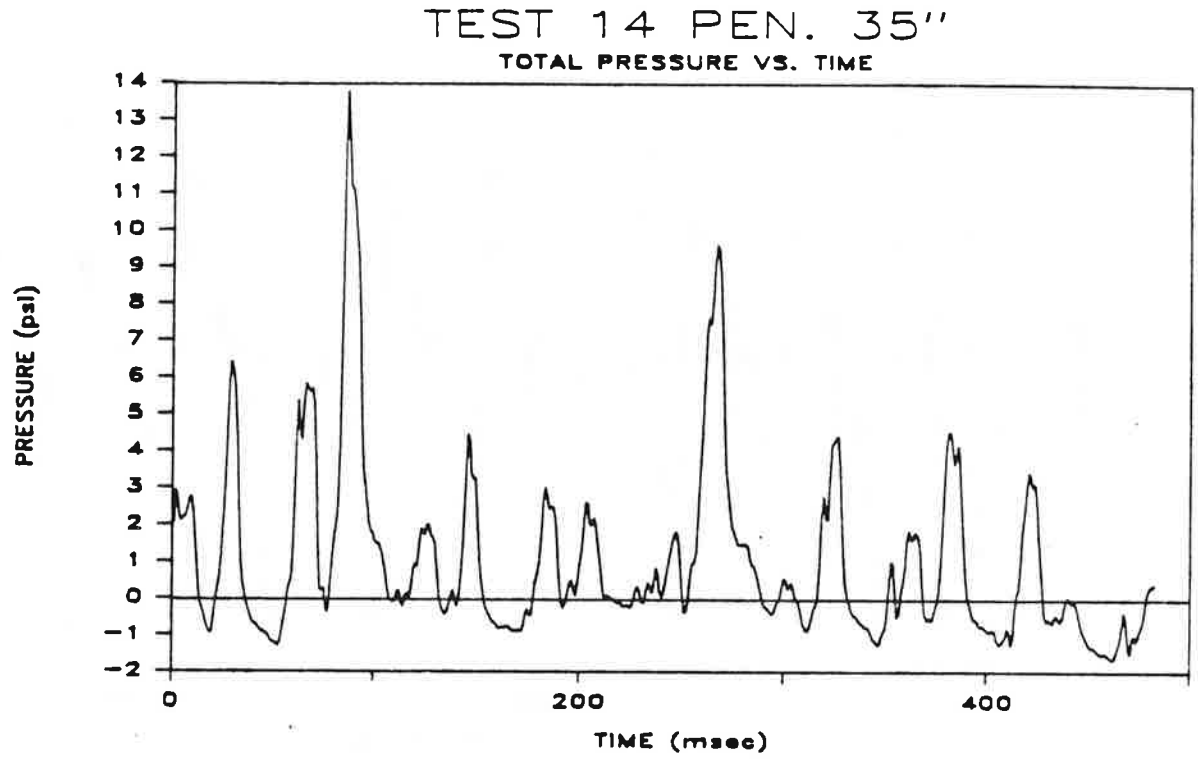

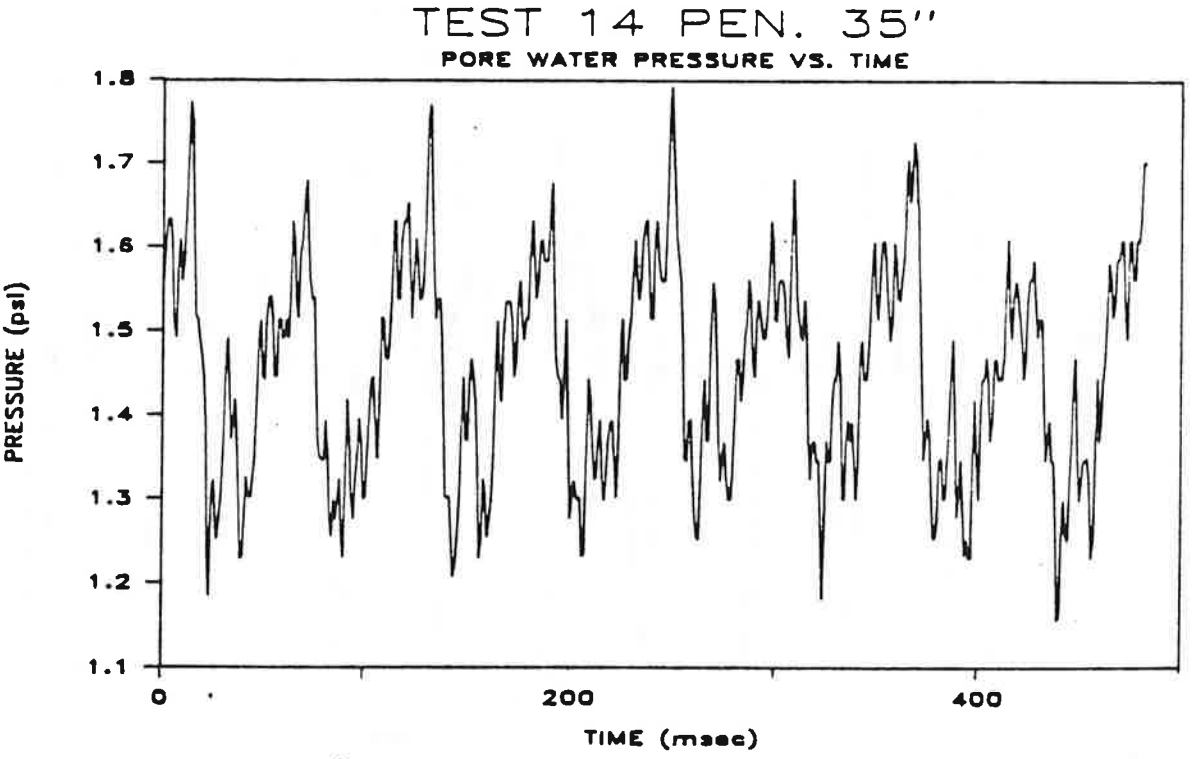

Fig. M.14d. Total and Pore Water Pressure Vs. Time at Bottom of Pile Shaft; Penetration = 35 Inches; Test 14

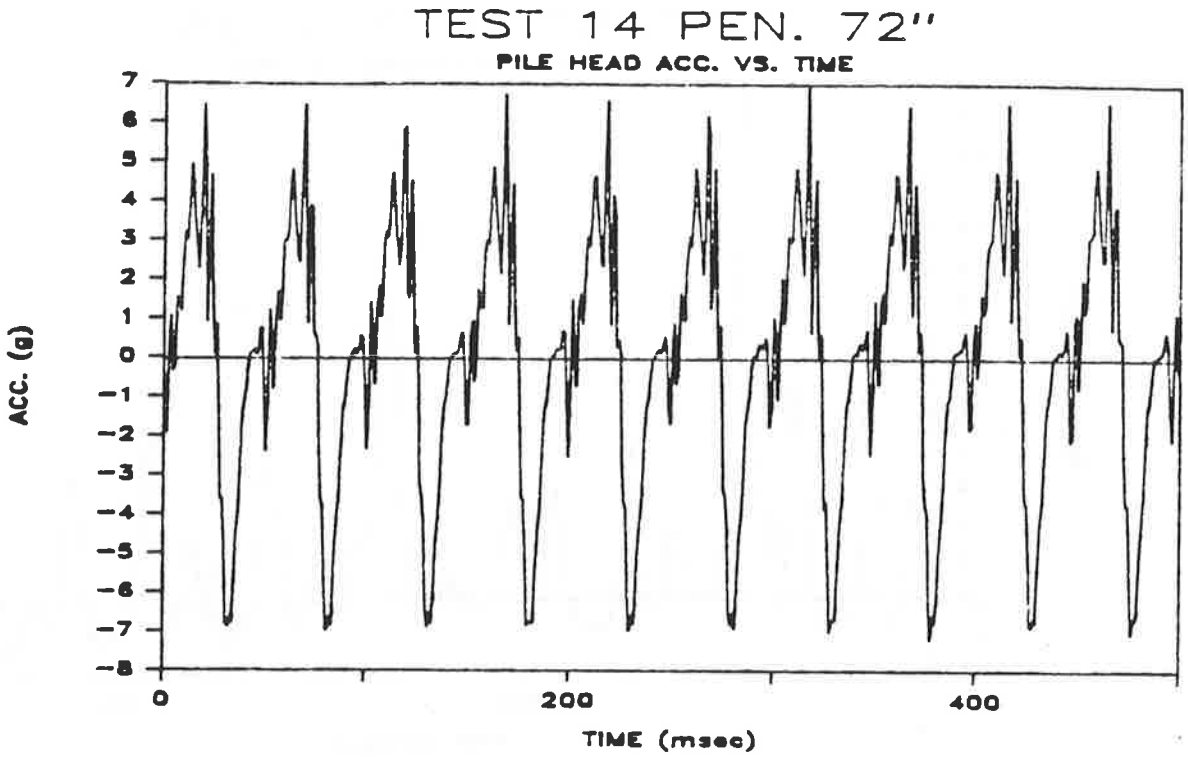

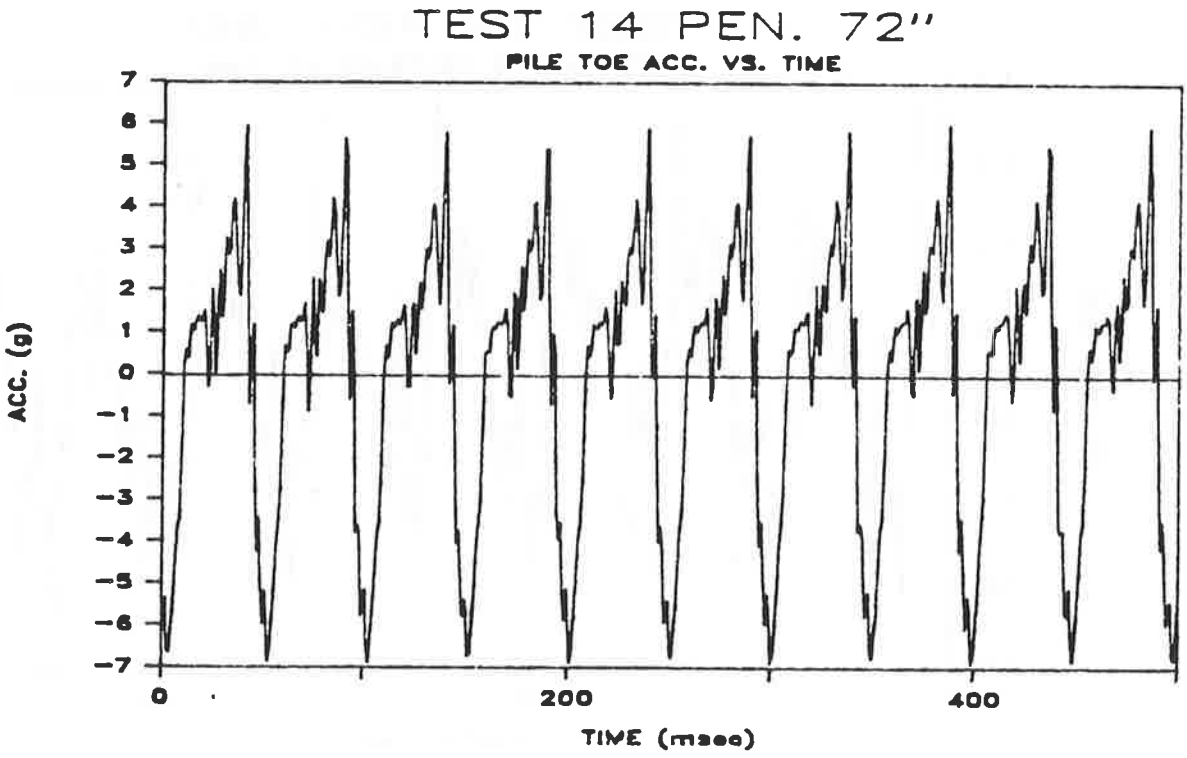

Fig. M.15a. Pile-Head and Toe Acceleration Vs. Time; Penetration = 72 Inches; Test 14

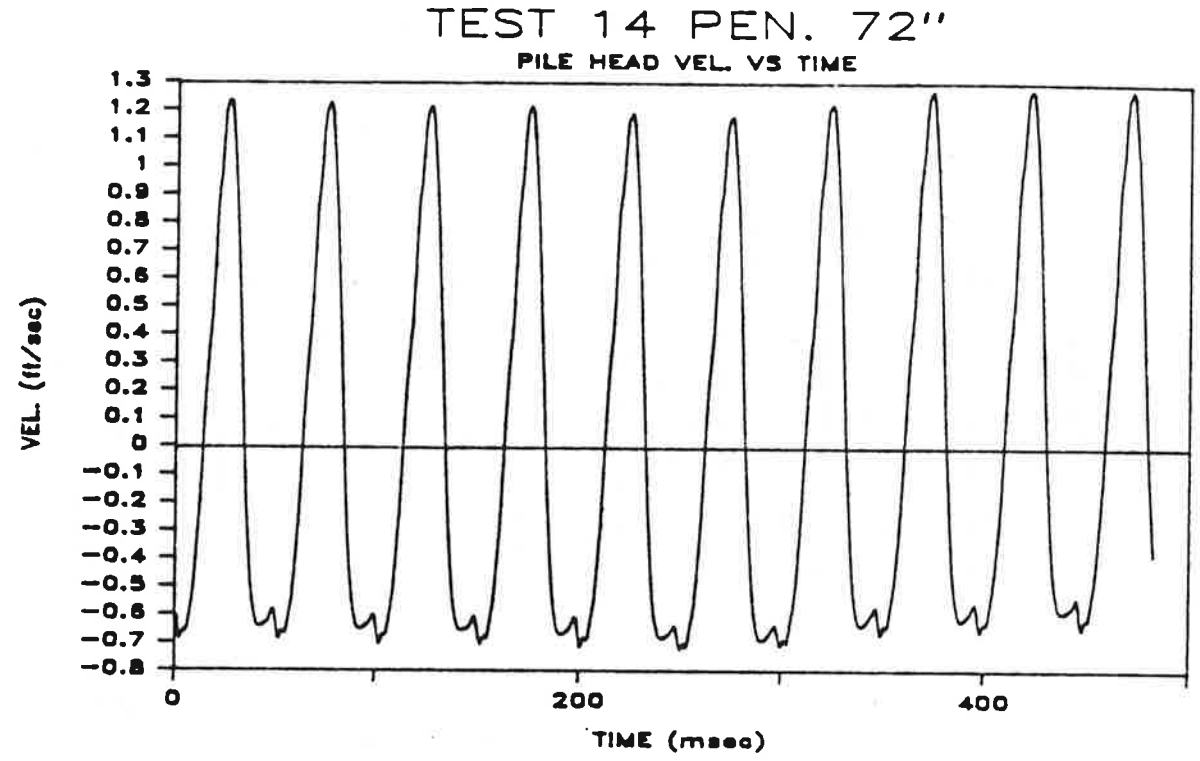

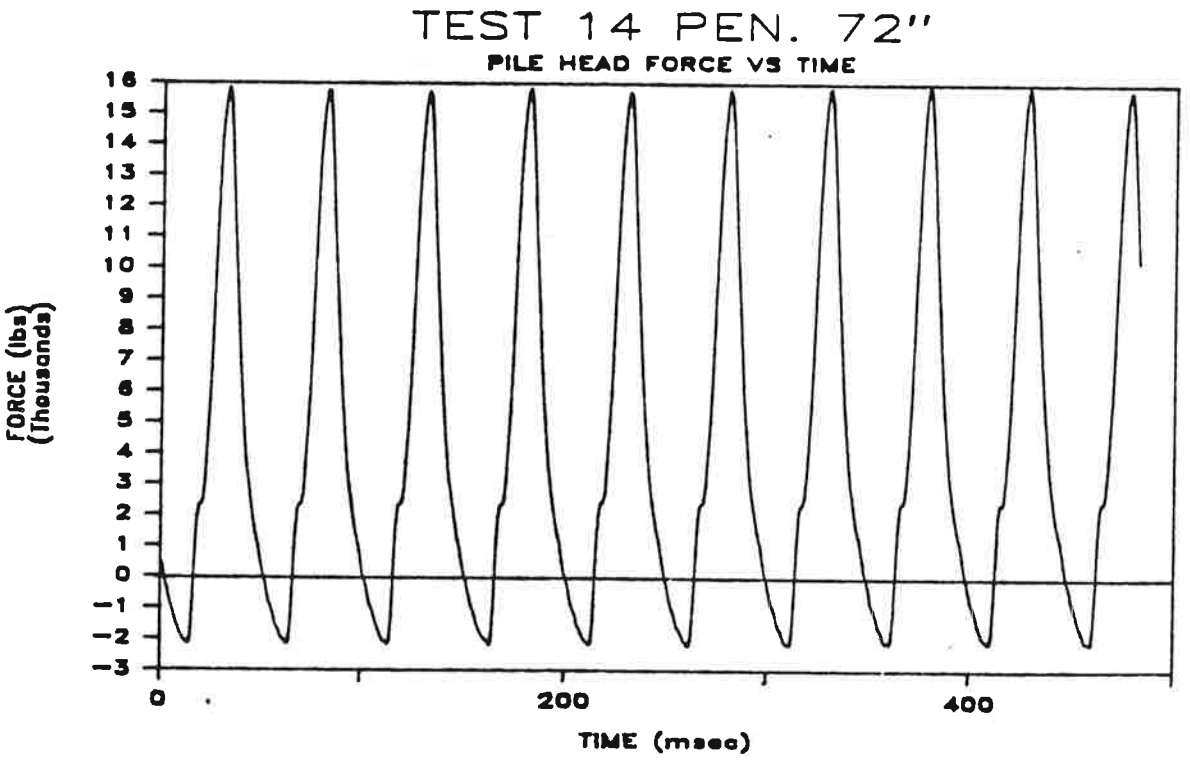

Fig. M.15b. Pile-Head Velocity and ForceVs. Time; Penetration = 72 Inches; Test 14

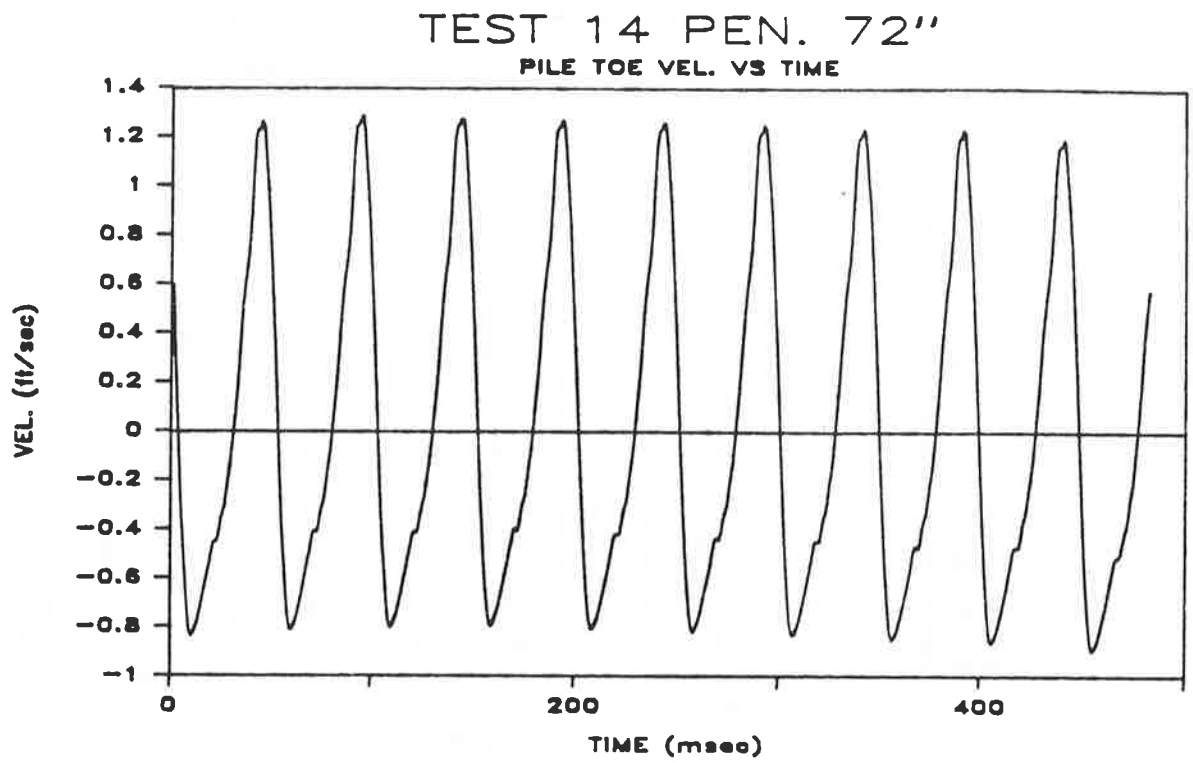

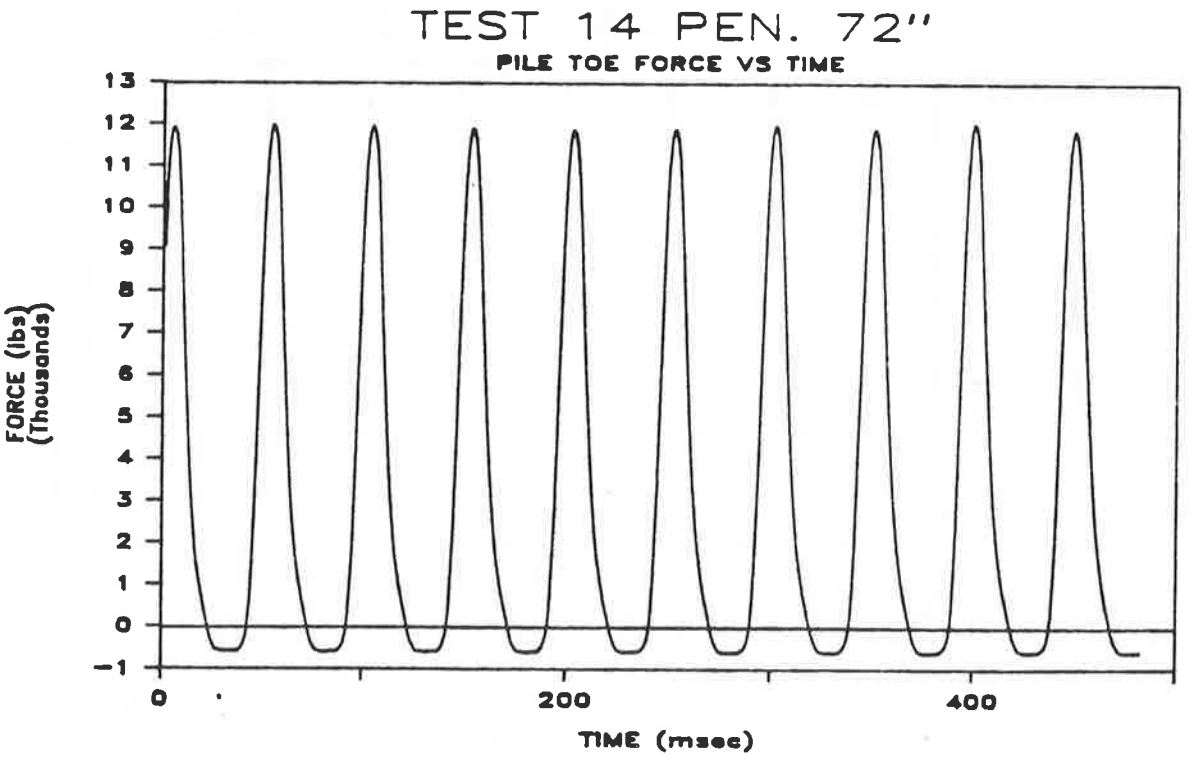

Fig. M.15c. Pile-Toe Velocity and Force Vs. Time; Penetration = 72 Inches; Test 14

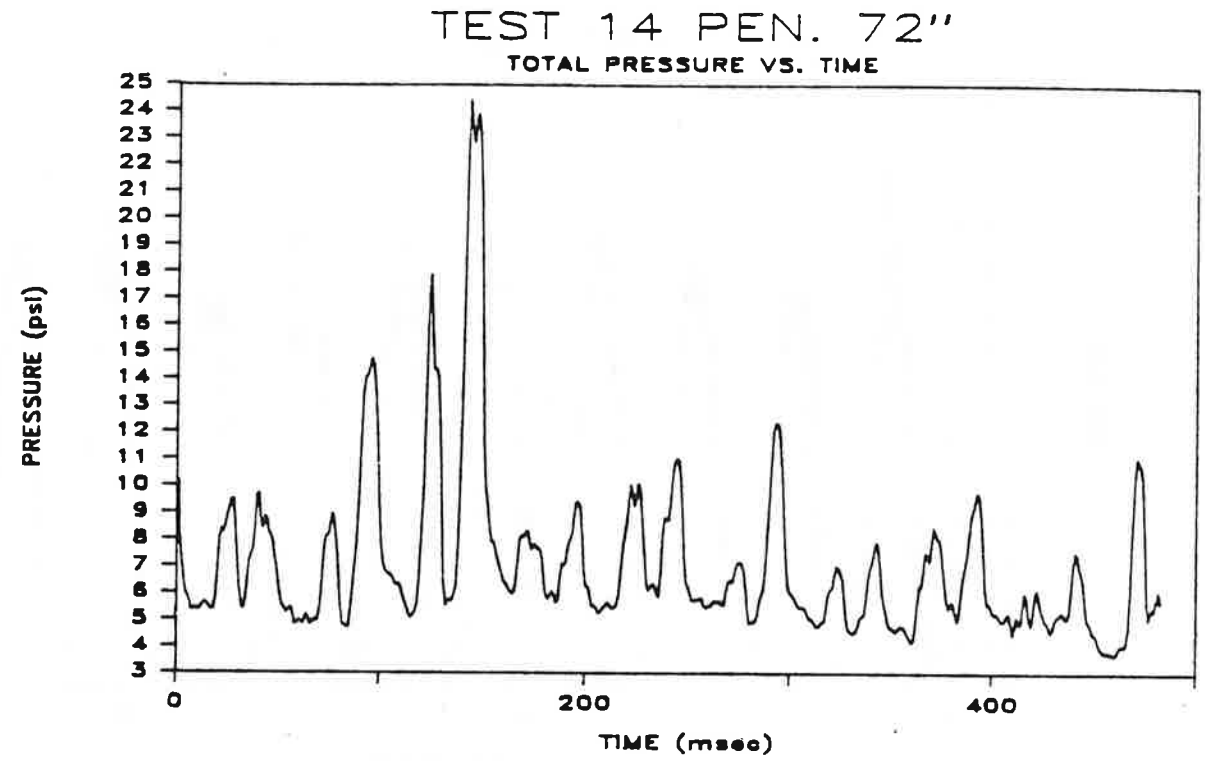

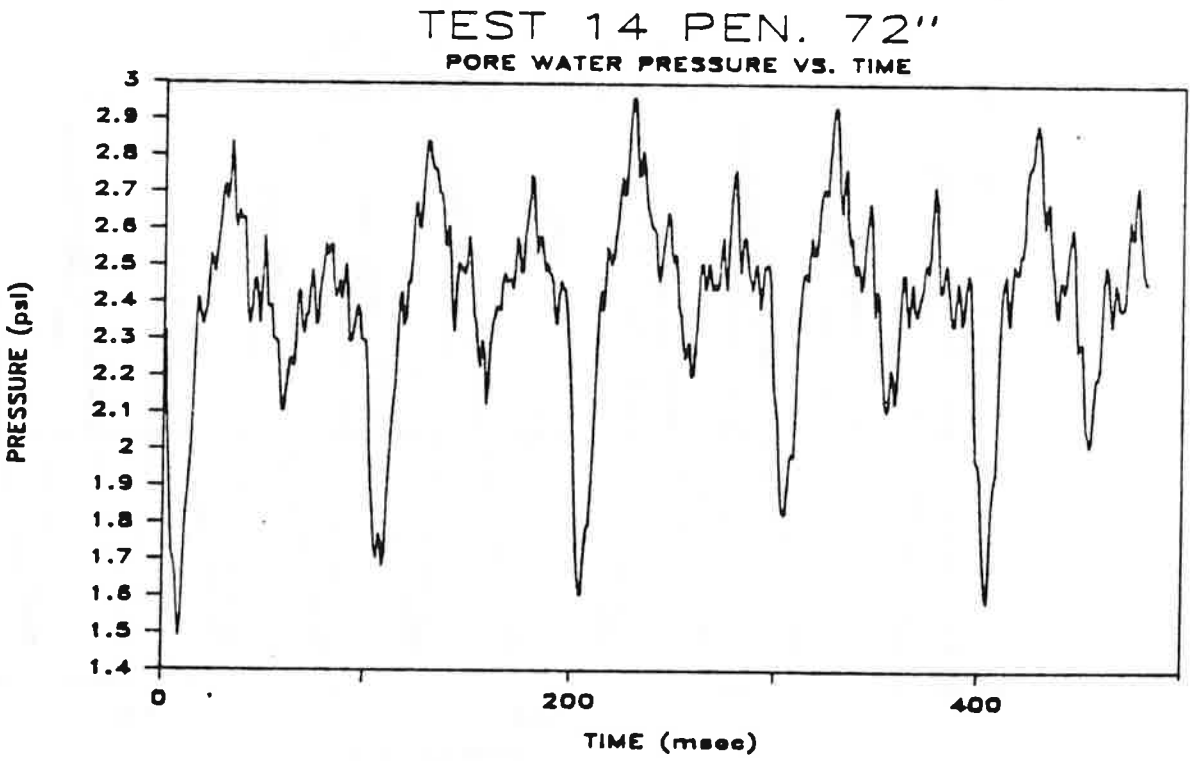

Fig. M.15d. Total and Pore Water Pressure Vs. Time at Bottom of Pile Shaft; Penetration = 72 Inches; Test 14

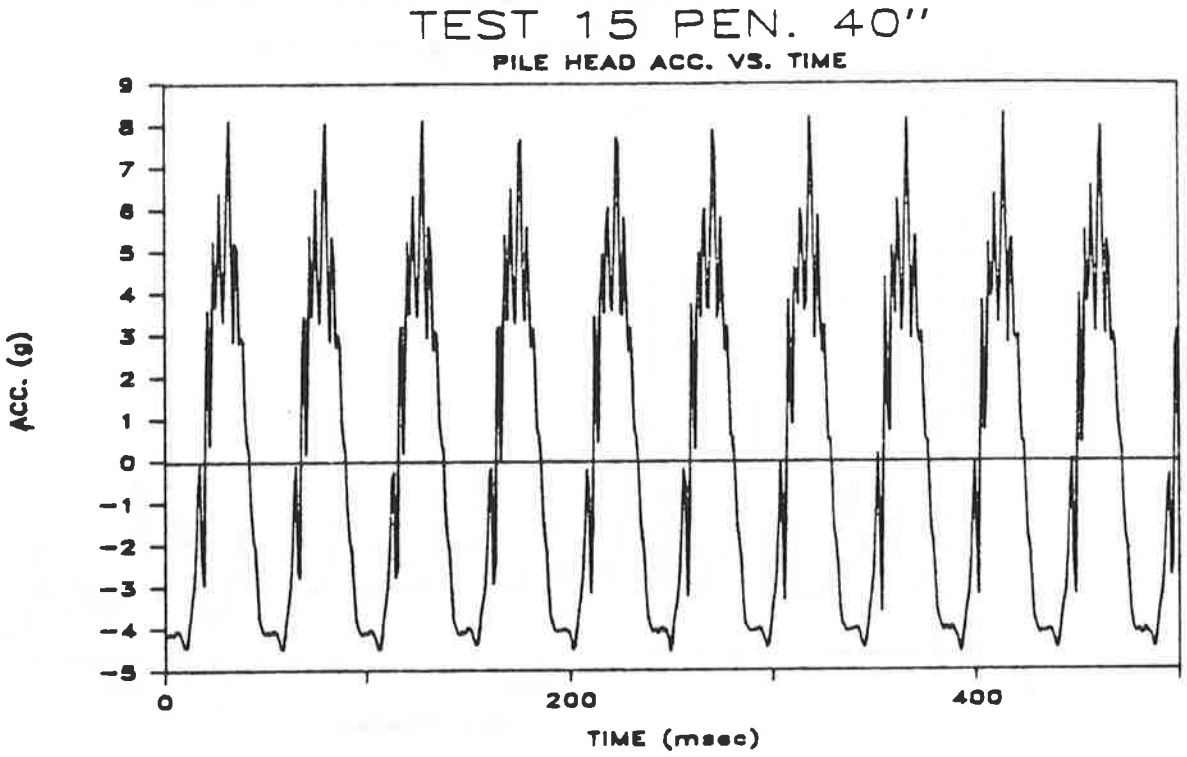

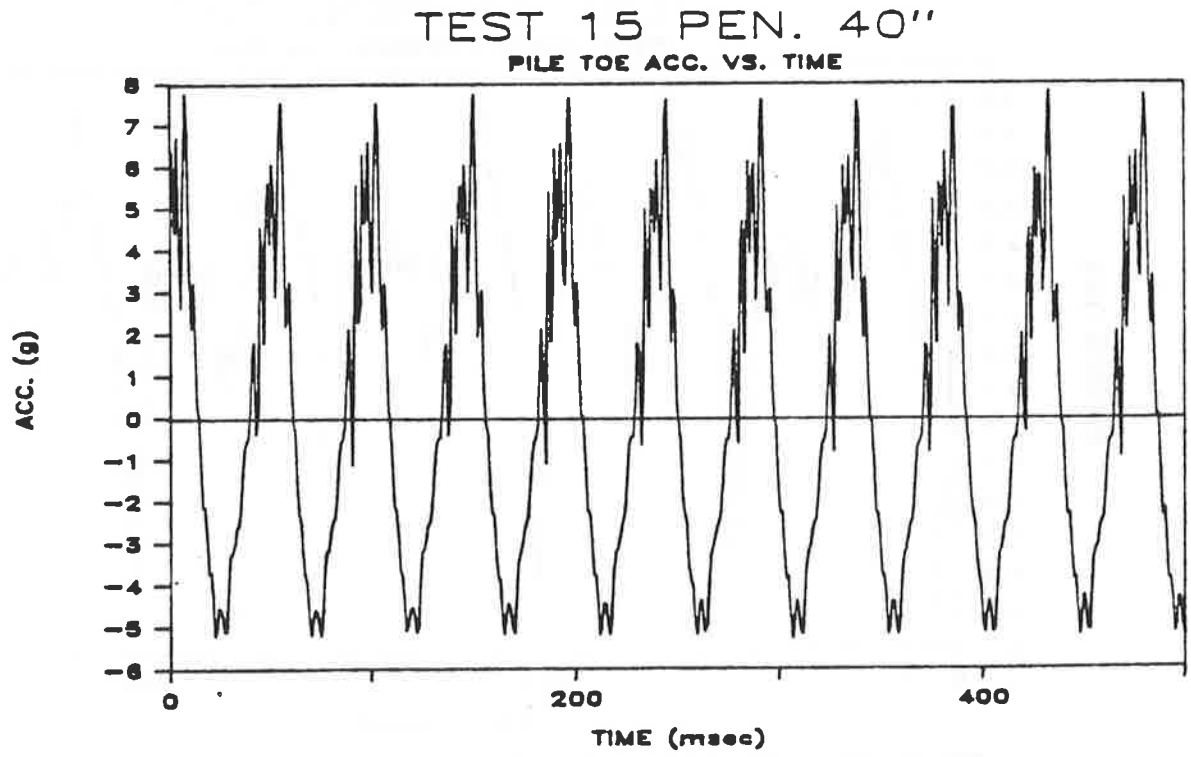

Fig. M.16a. Pile-Head and Toe Acceleration Vs. Time; Penetration = 40 Inches; Test 15

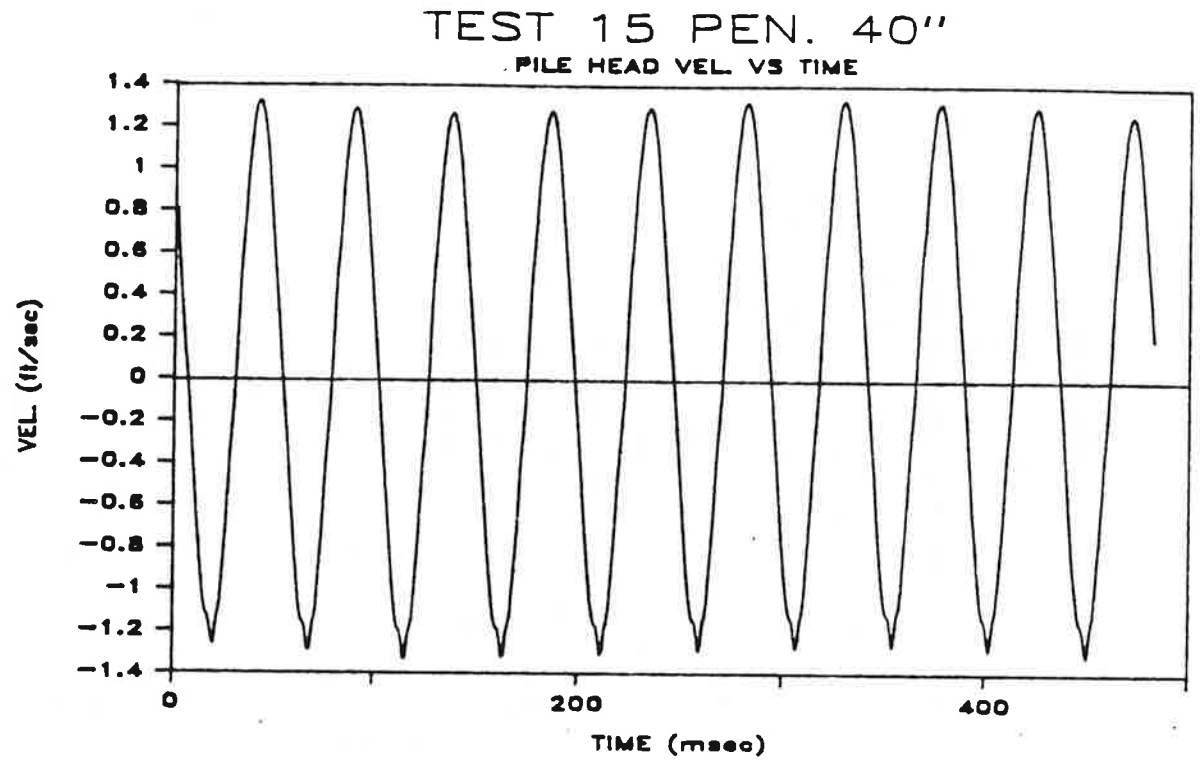

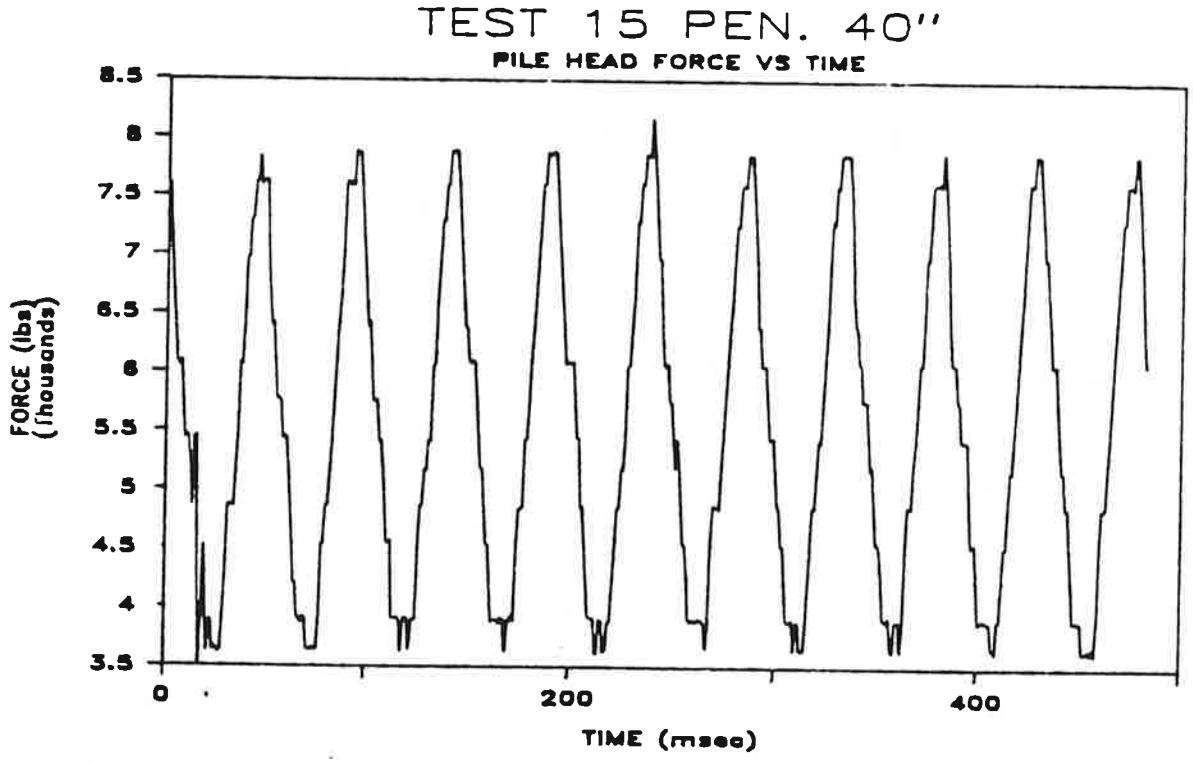

Fig. M.16b. Pile-Head Velocity and ForceVs. Time; Penetration = 40 Inches; Test 15

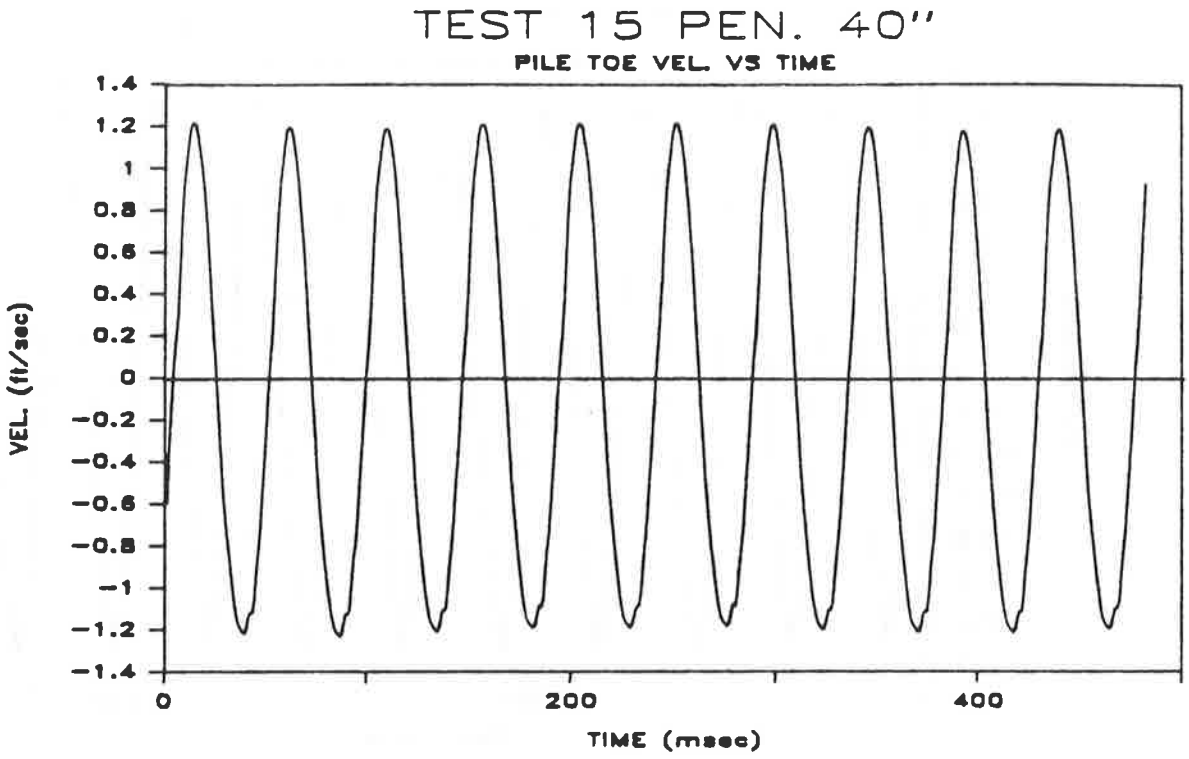

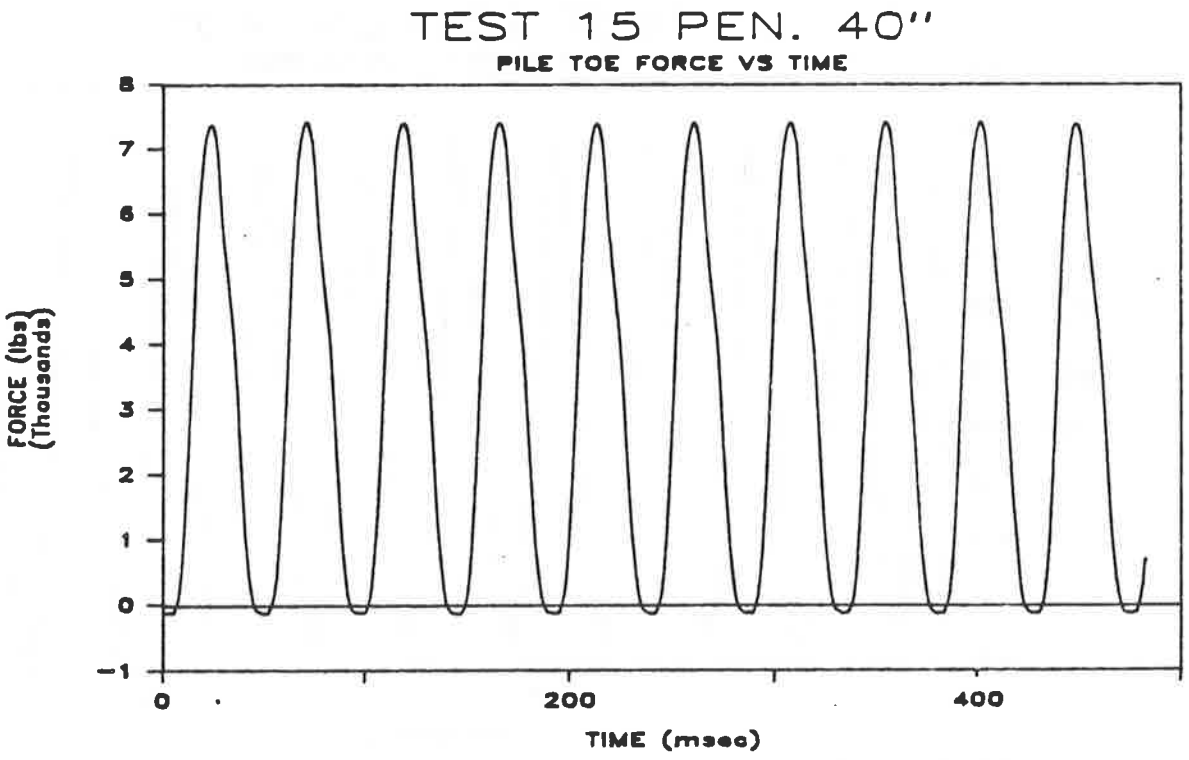

Fig. M.16c. Pile-Toe Velocity and Force Vs. Time; Penetration = 40 Inches; Test 15

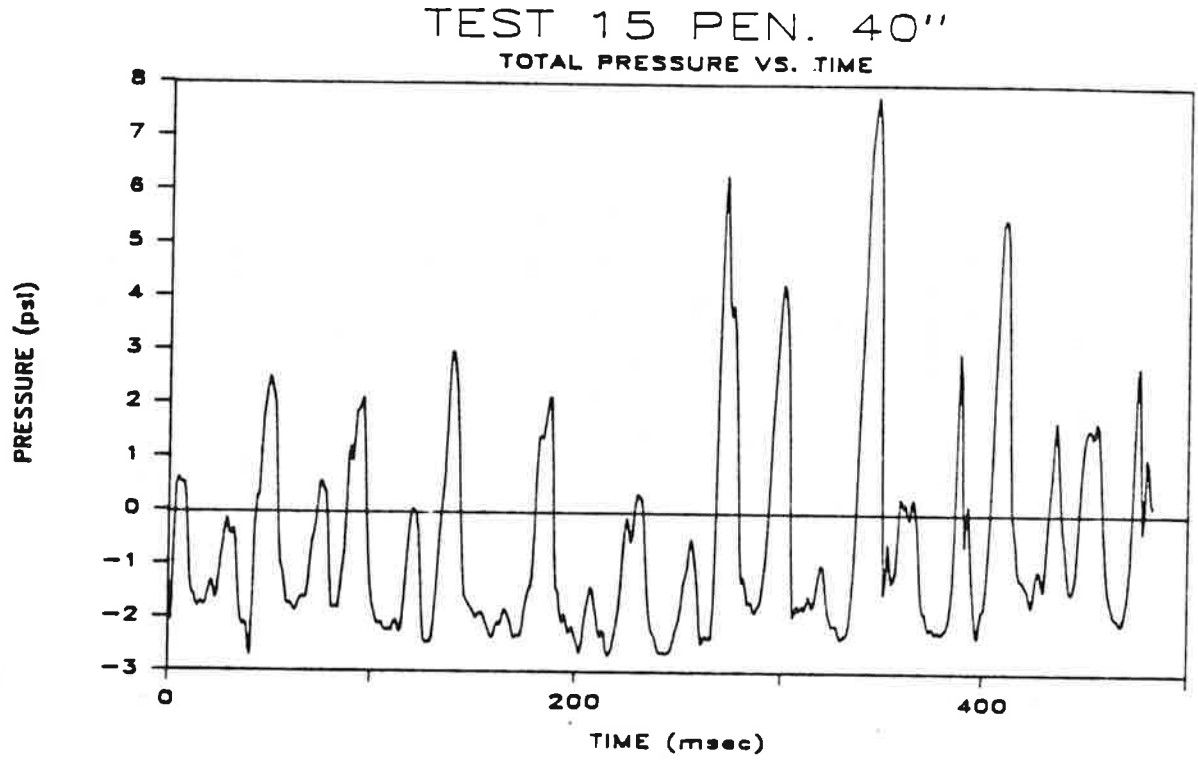

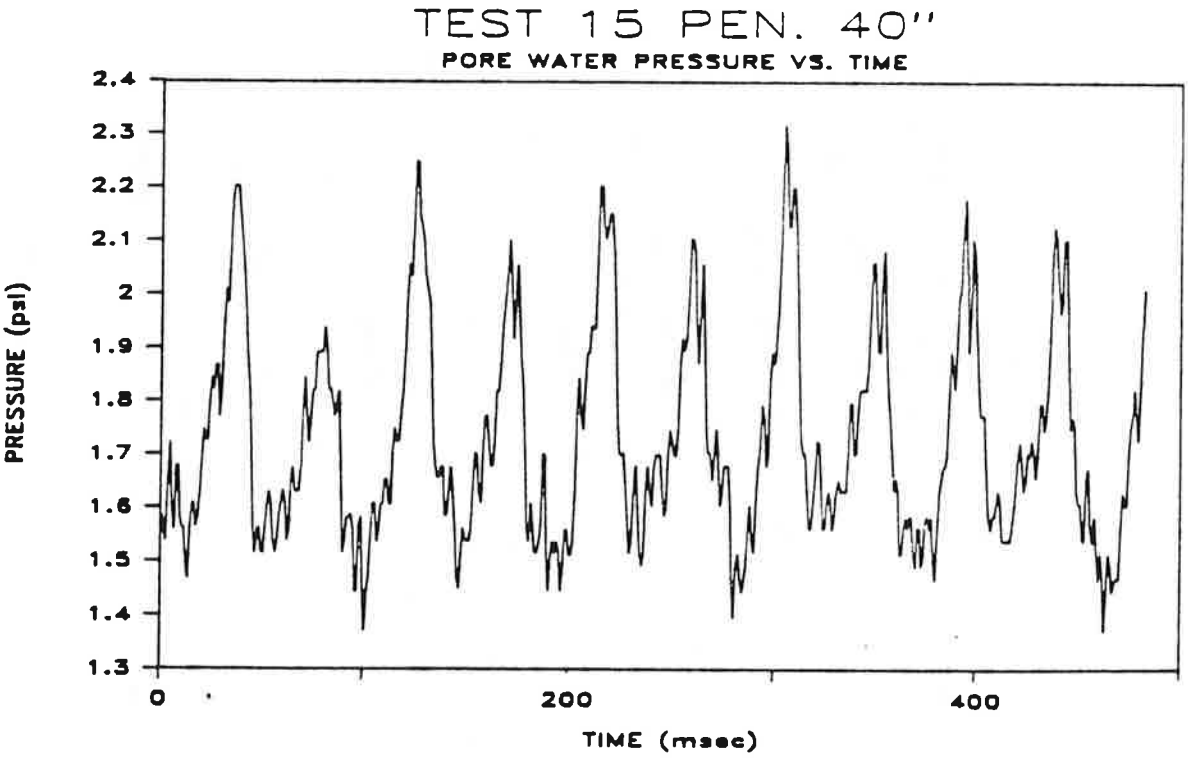

Fig. M.16d. Total and Pore Water Pressure Vs. Time at Bottom of Pile Shaft; Penetration = 40 Inches; Test 15

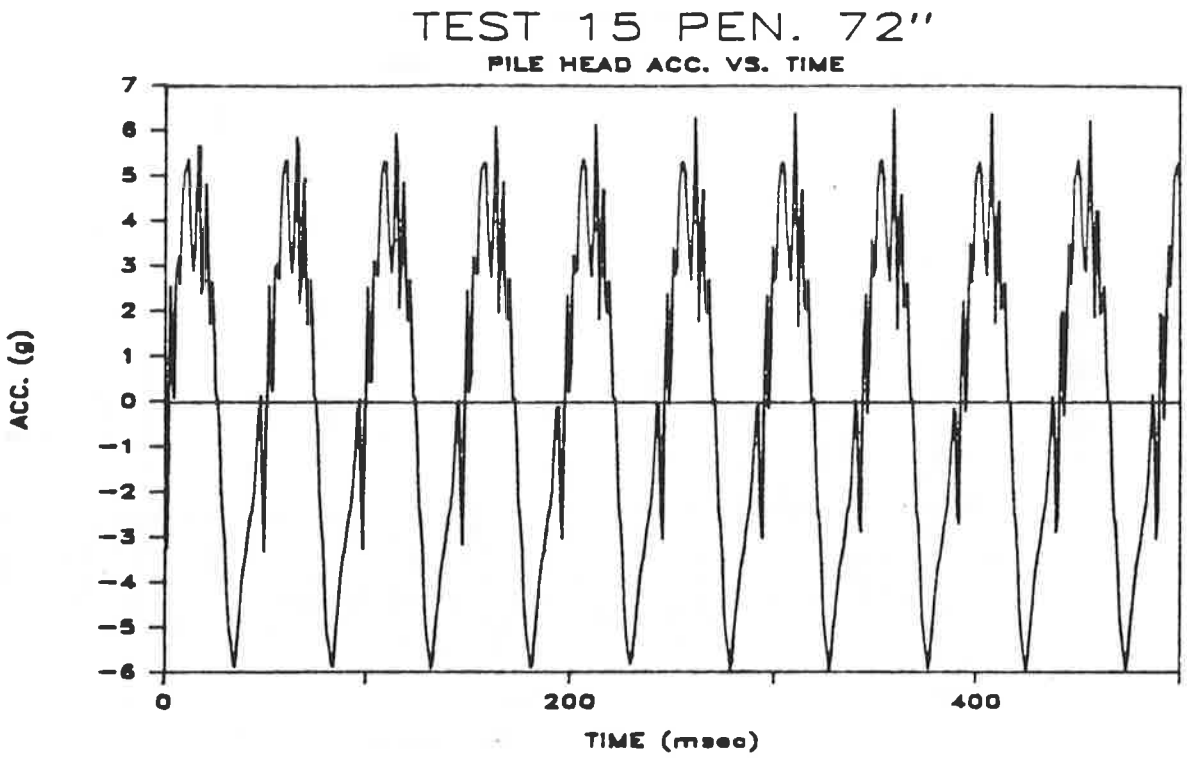

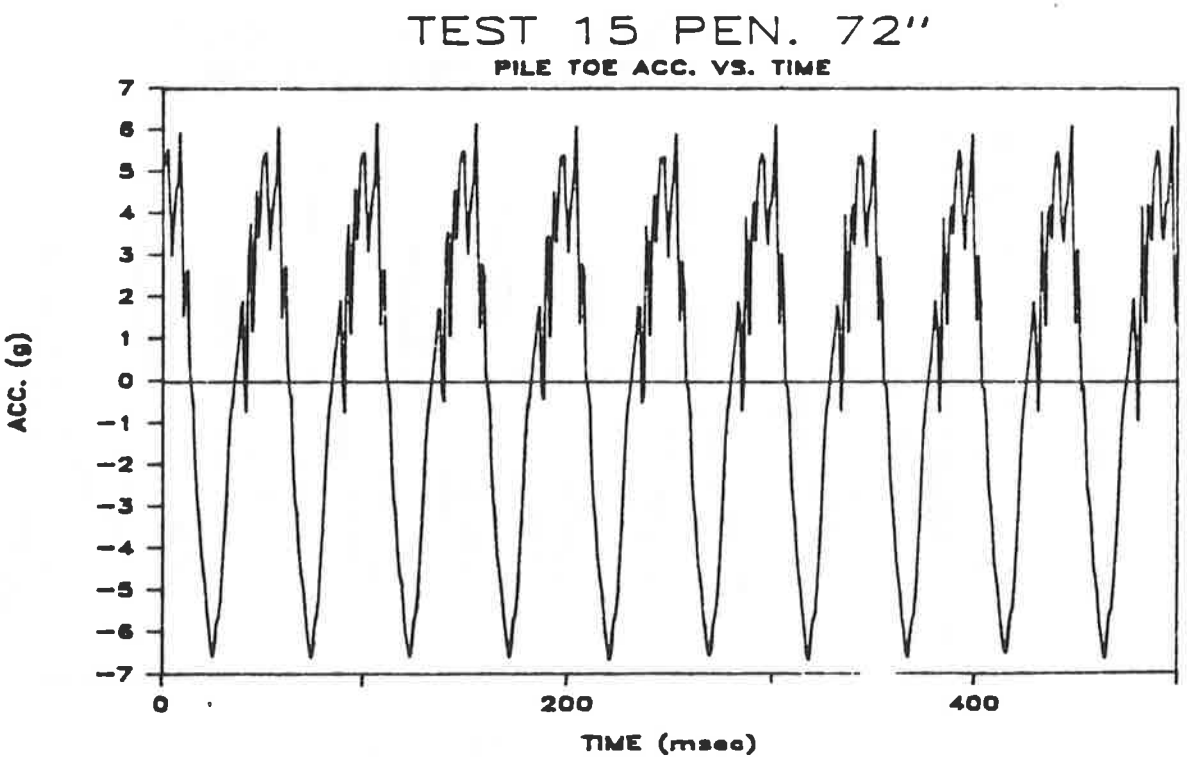

Fig. M.17a. Pile-Head and Toe Acceleration Vs. Time; Penetration = 72 Inches; Test 15

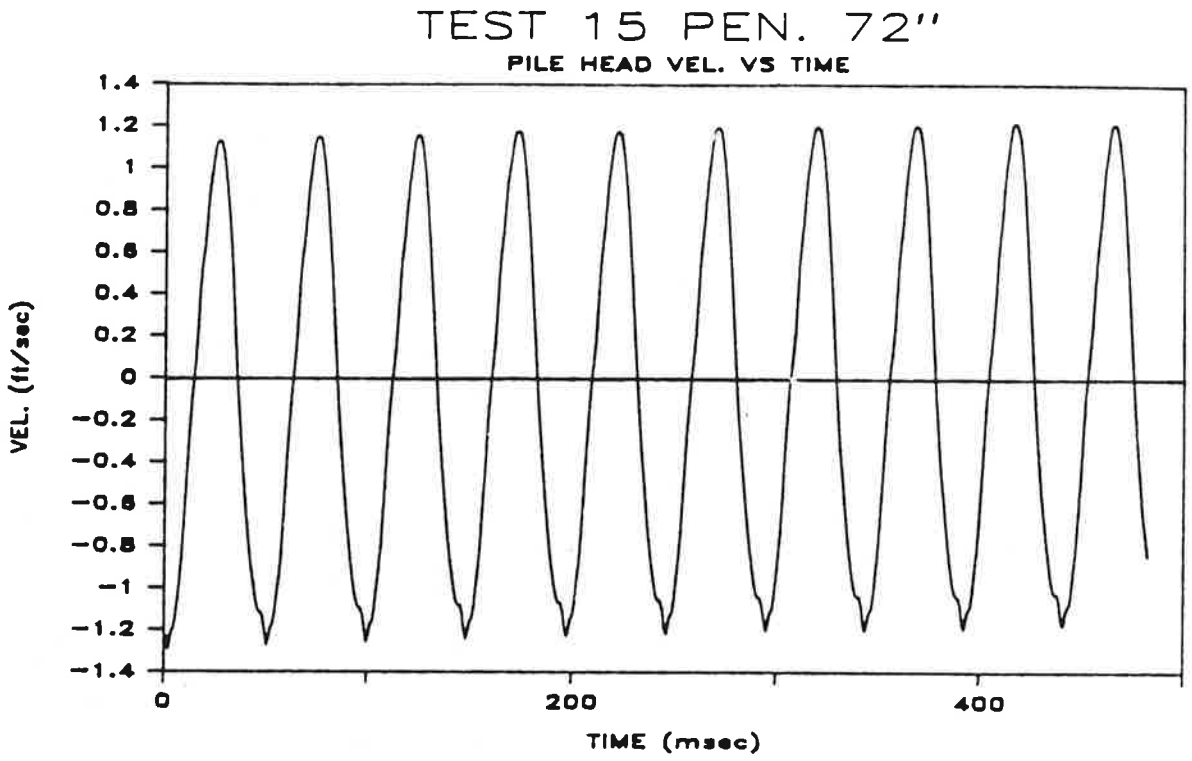

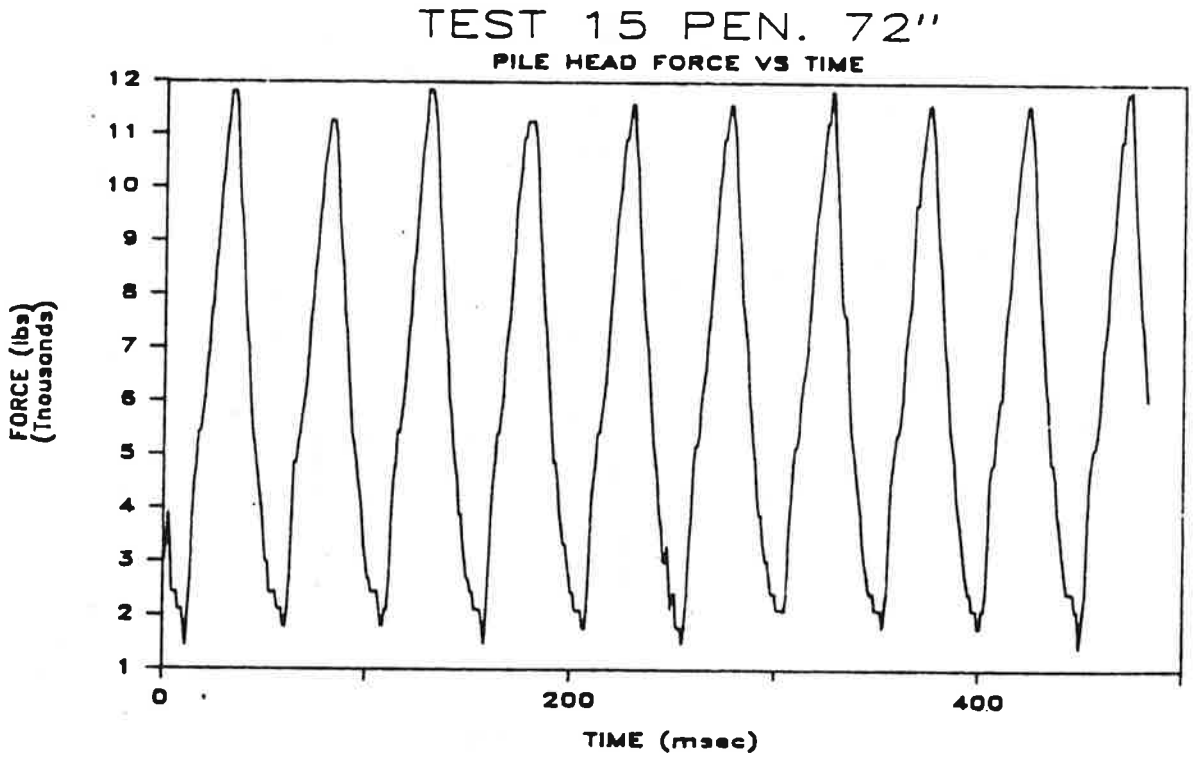

Fig. M.17b. Pile-Head Velocity and ForceVs. Time; Penetration = 72 Inches; Test 15

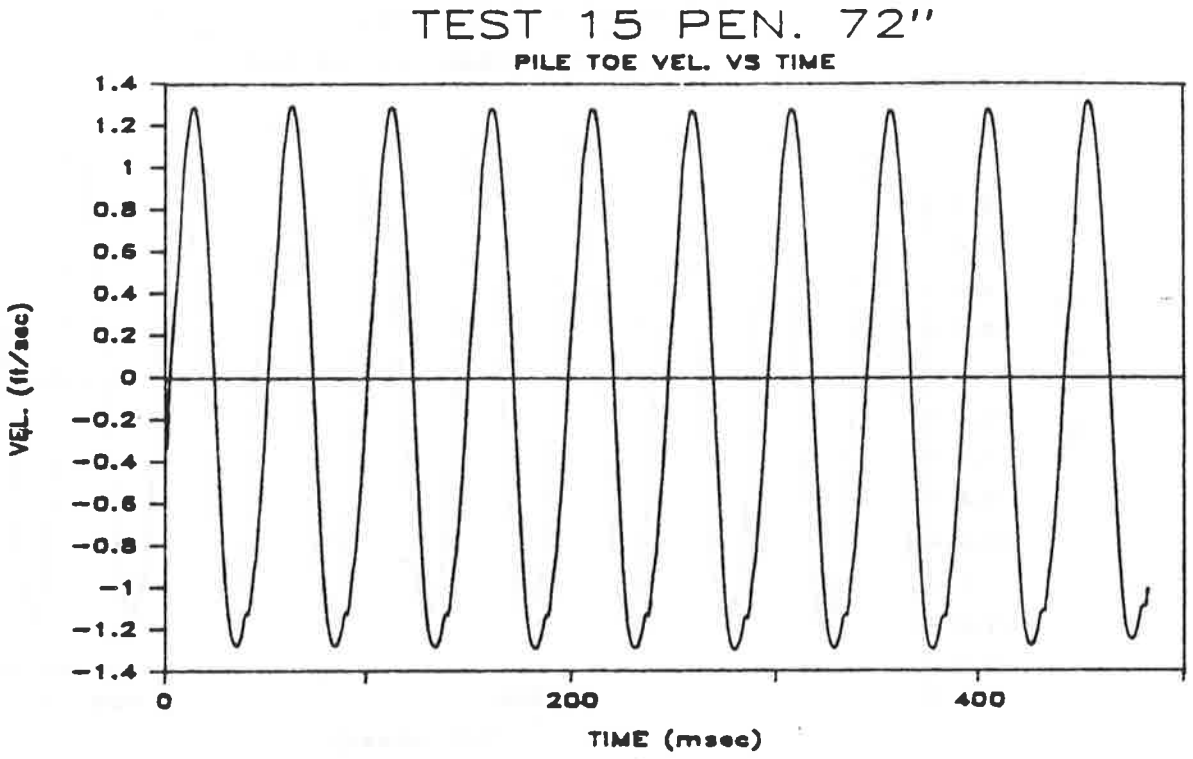

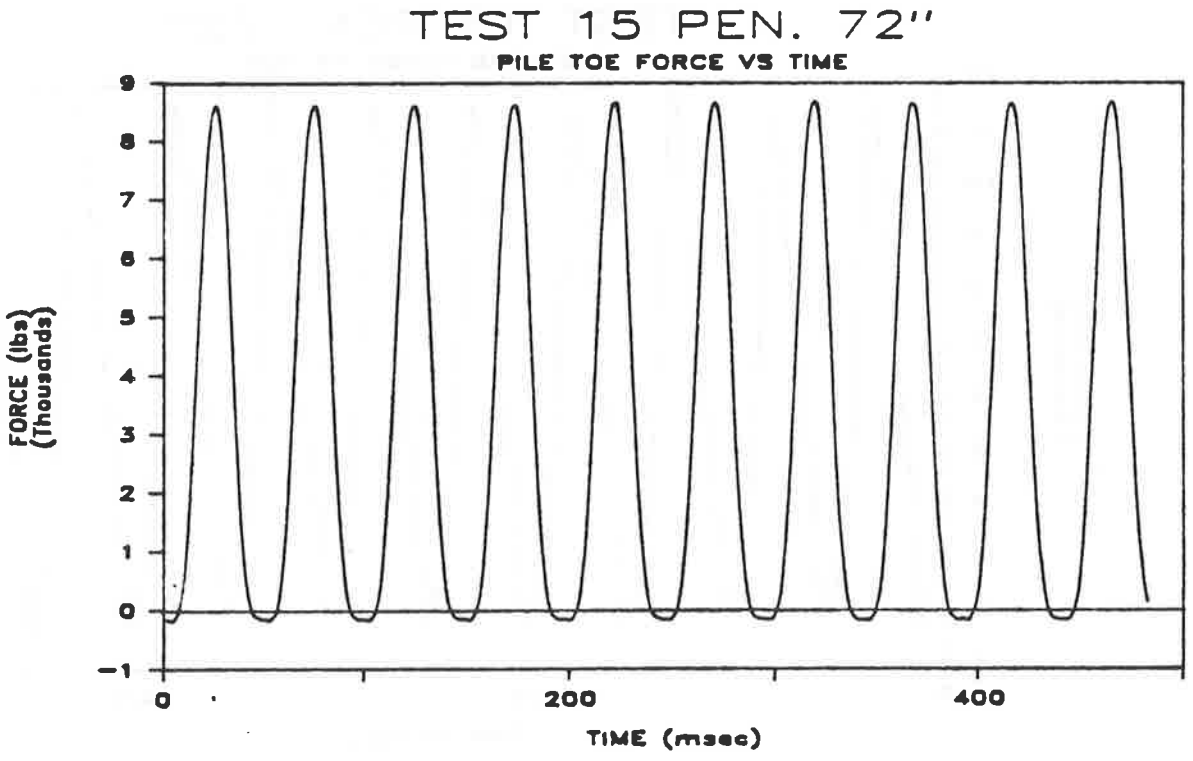

Fig. M.17c. Pile-Toe Velocity and Force Vs. Time; Penetration = 72 Inches; Test 15

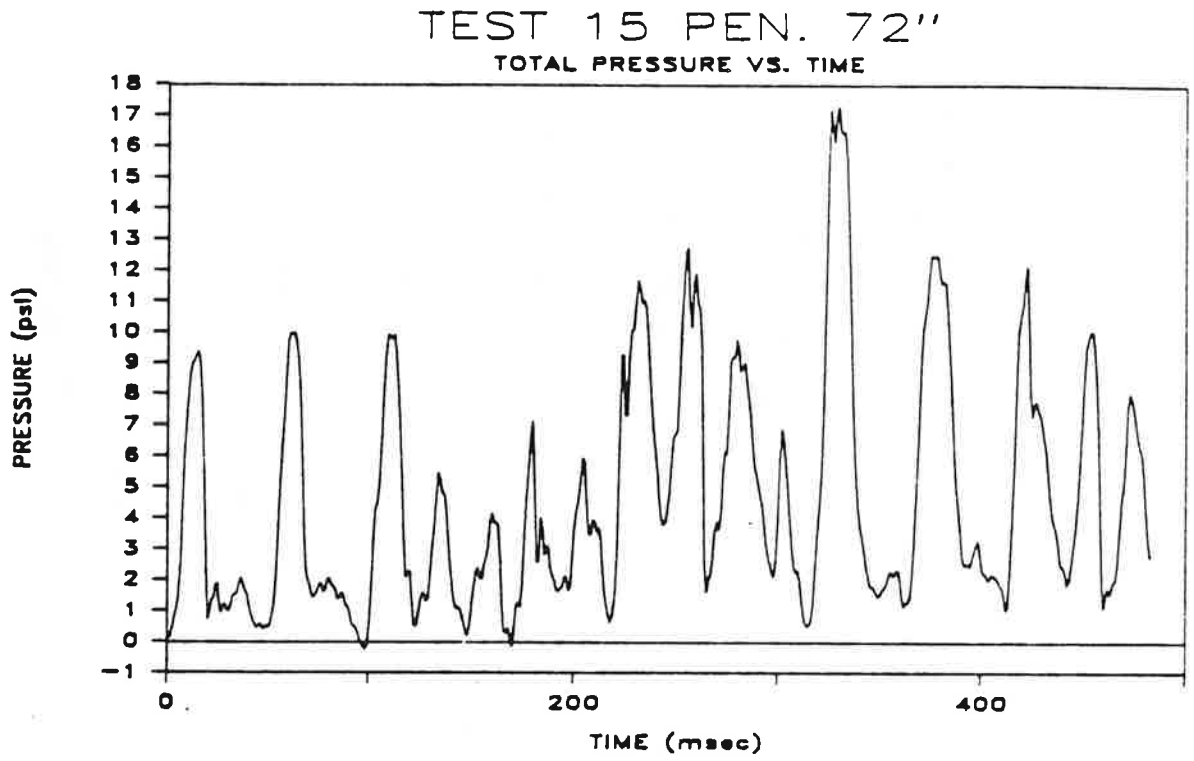

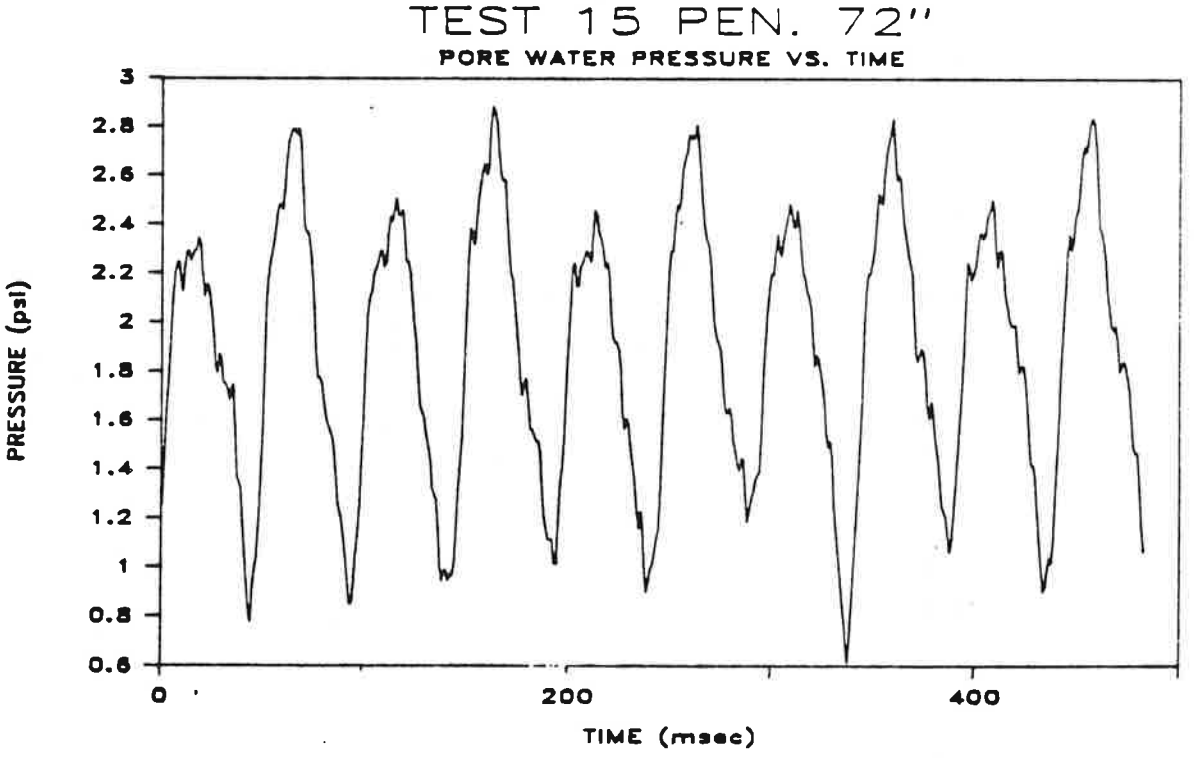

Fig. M.17d. Total and Pore Water Pressure Vs. Time at Bottom of Pile Shaft; Penetration = 72 Inches; Test 15

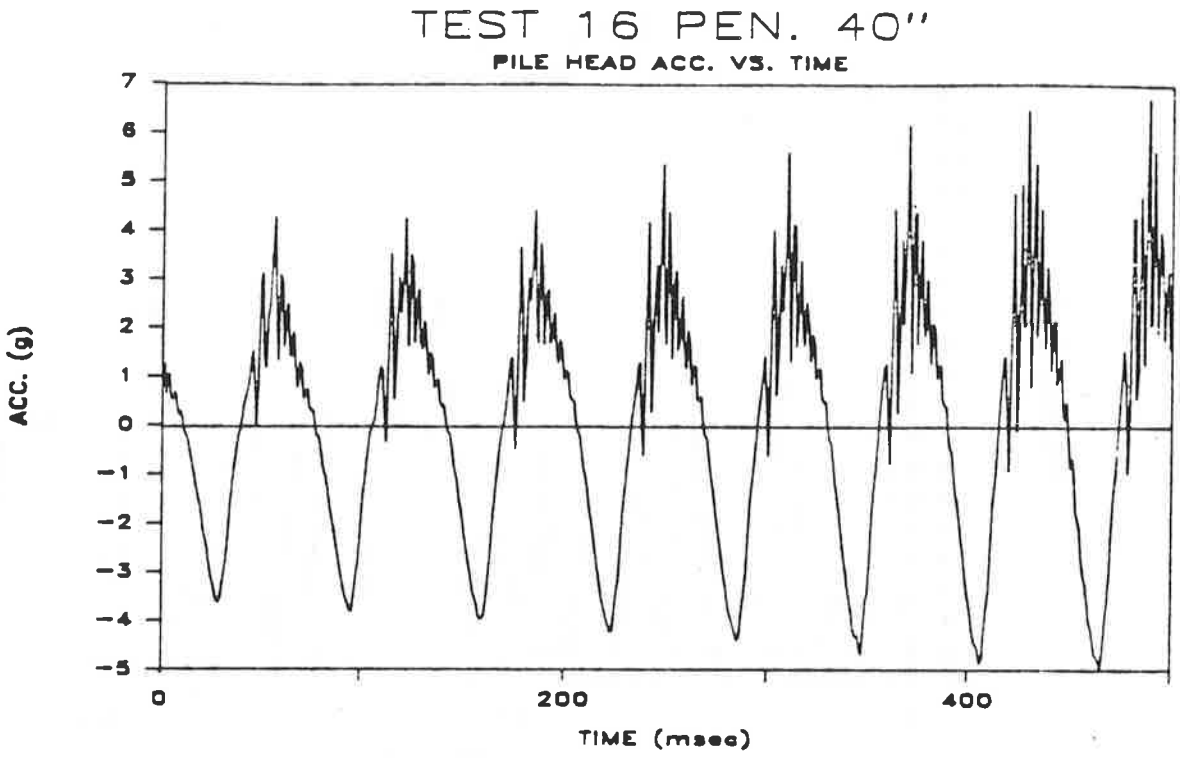

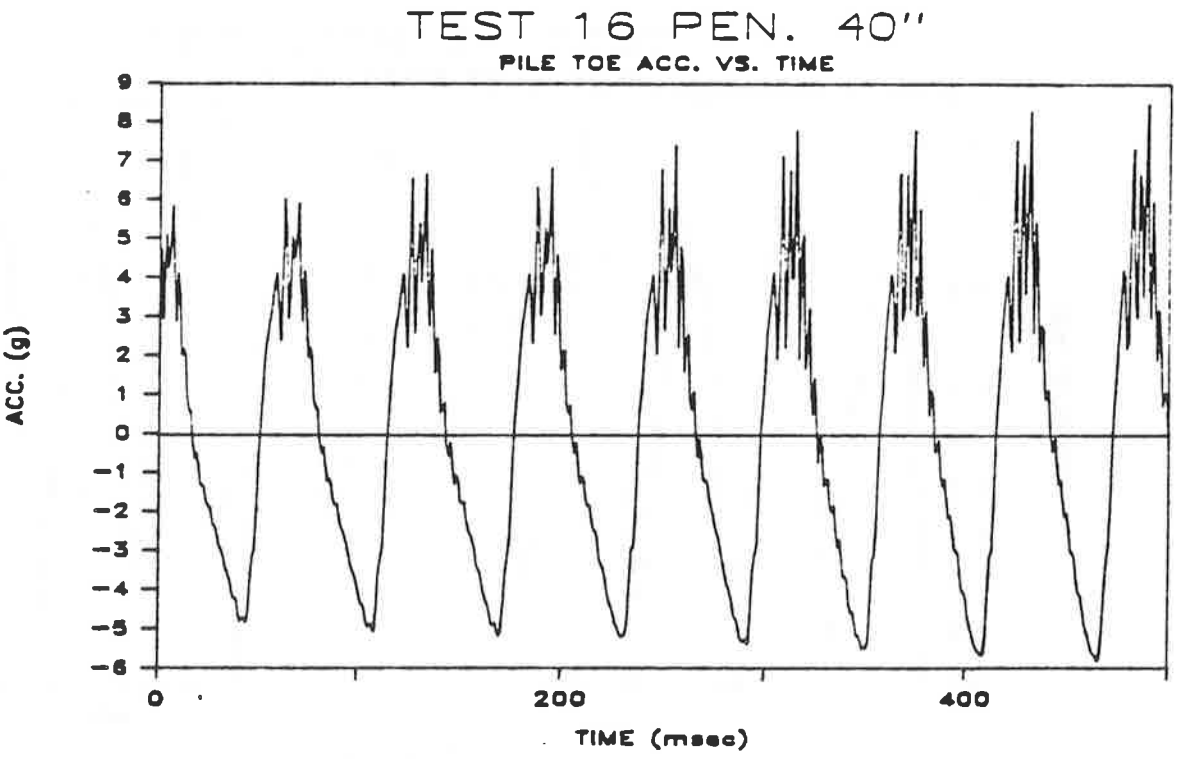

Fig. M.18a. Pile-Head and Toe Acceleration Vs. Time; Penetration = 40 Inches; Test 16

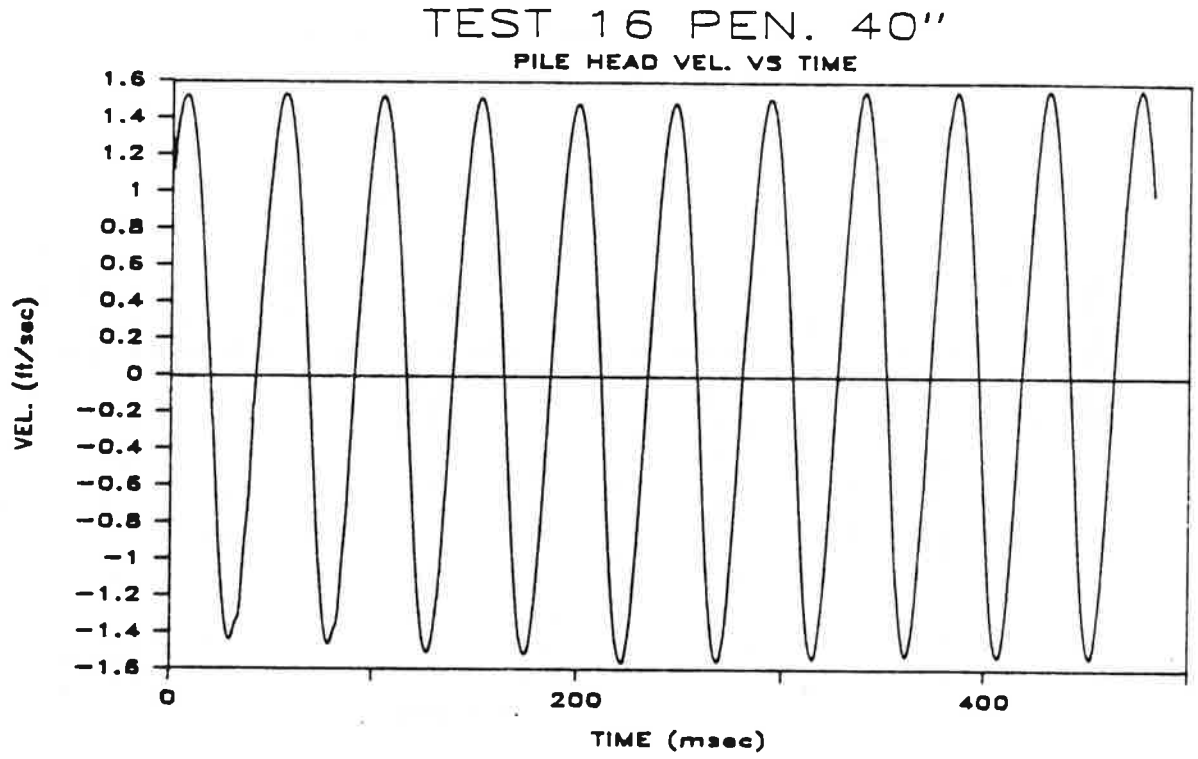

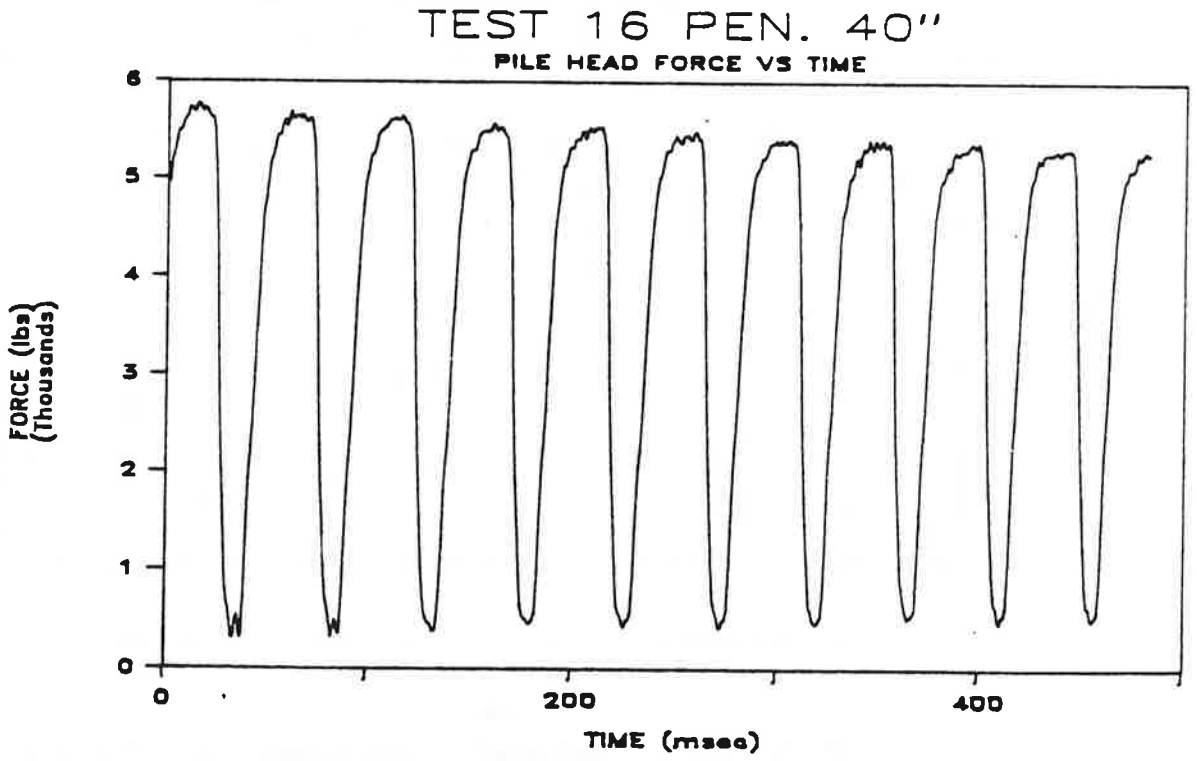

Fig. M.18b. Pile-Head Velocity and ForceVs. Time; Penetration = 40 Inches; Test 16

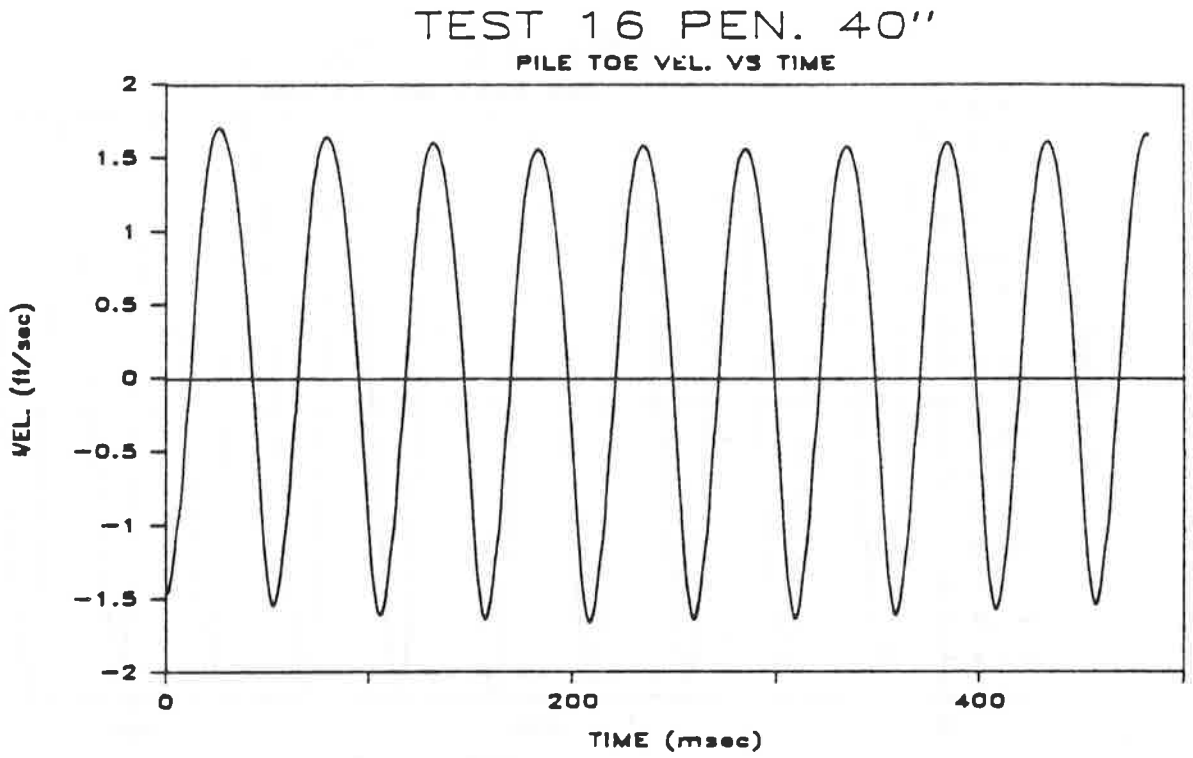

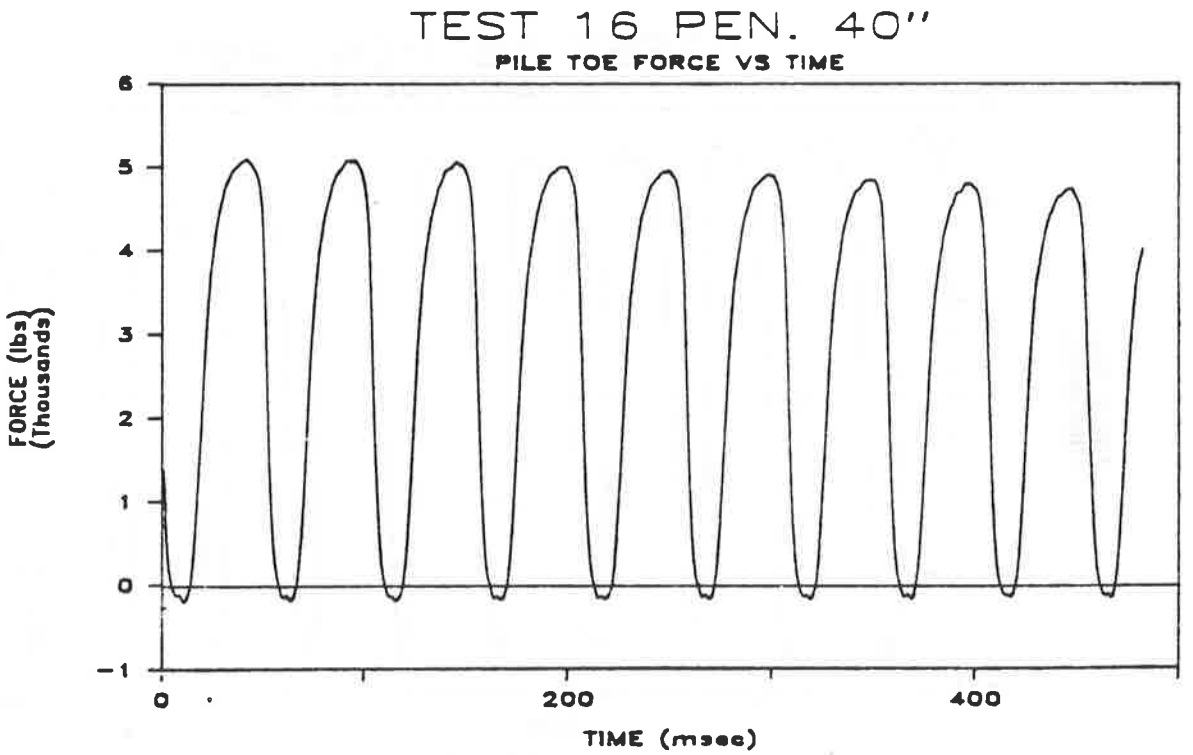

Fig. M.18c. Pile-Toe Velocity and Force Vs. Time; Penetration = 40 Inches; Test 16

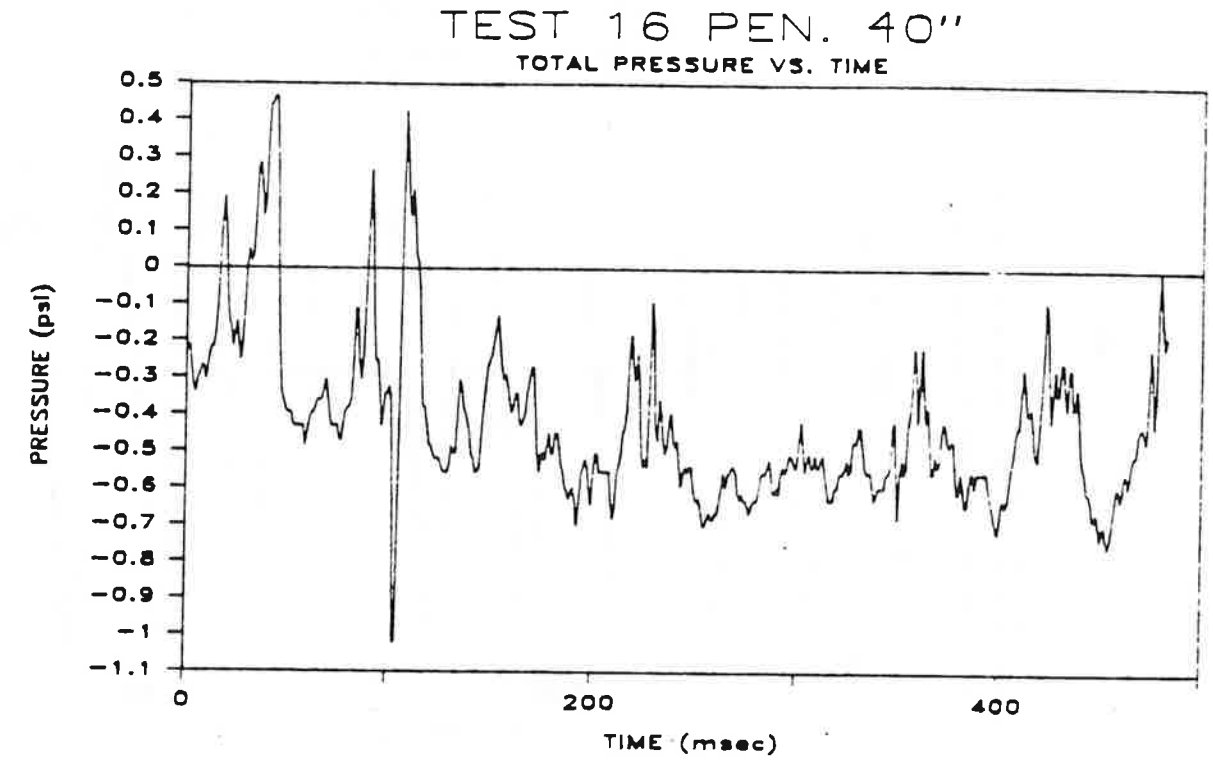

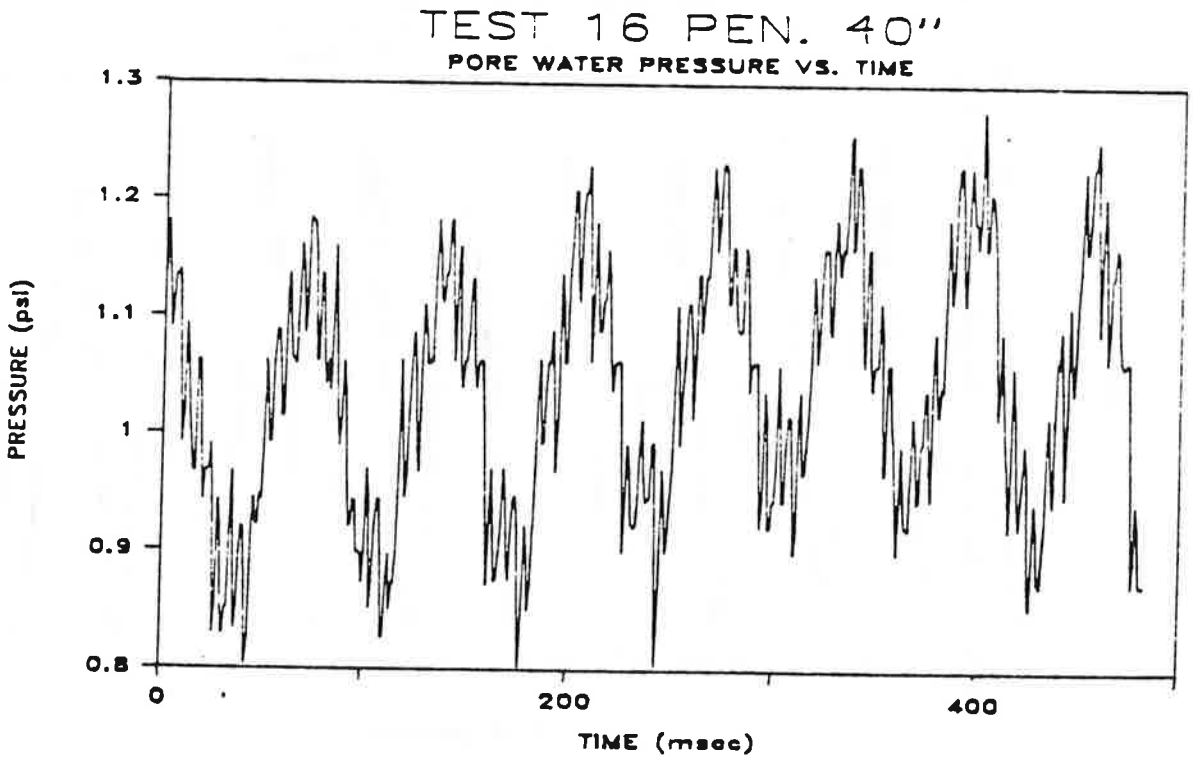

Fig. M.18d. Total and Pore Water Pressure Vs. Time at Bottom of Pile Shaft; Penetration = 40 Inches; Test 16

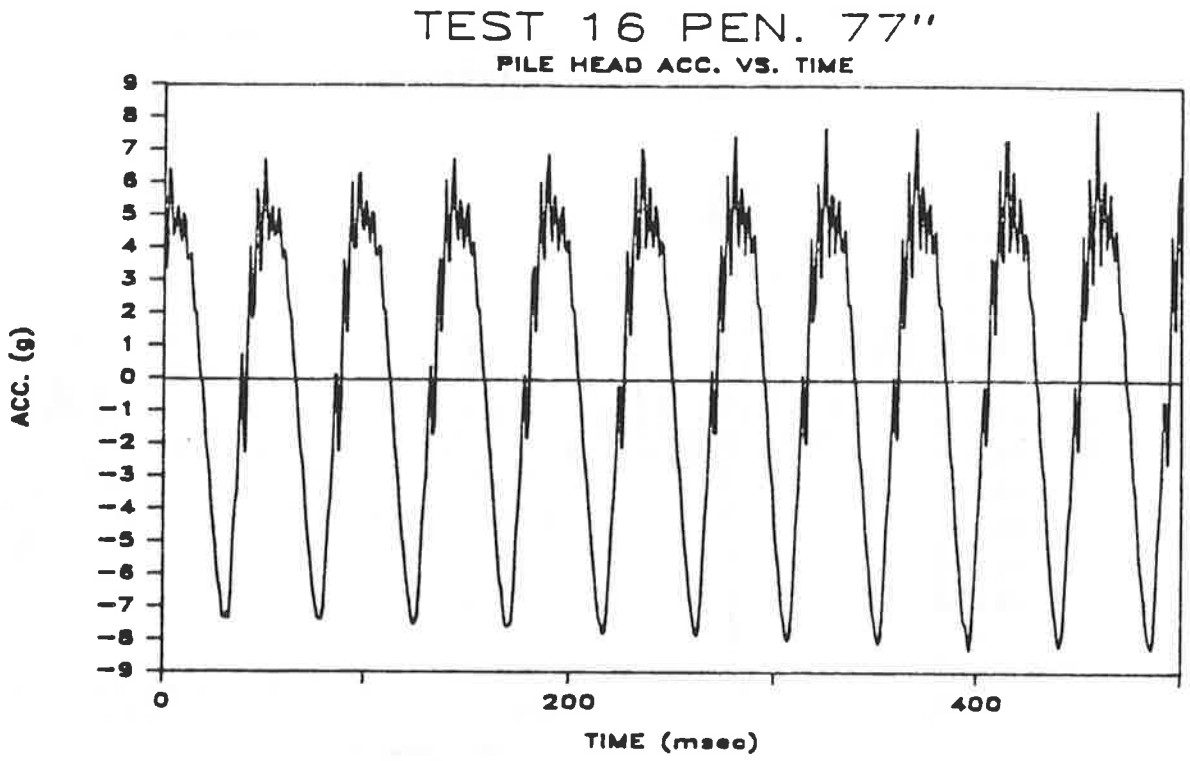

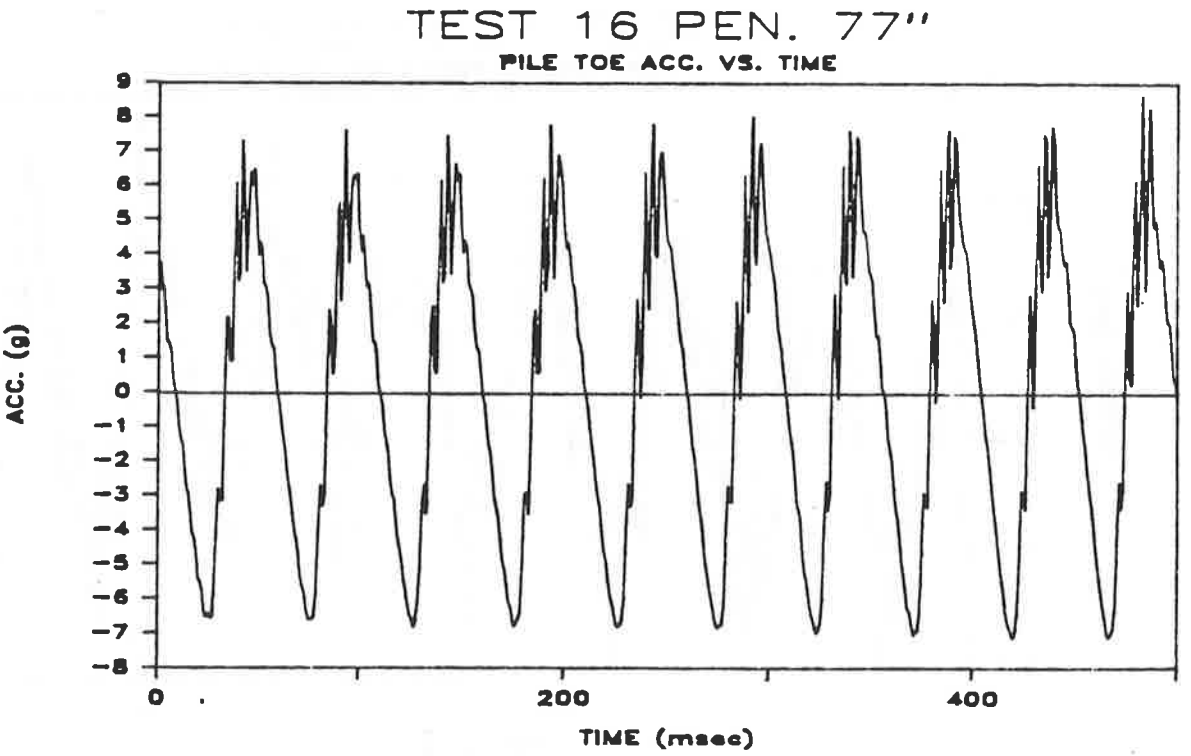

Fig. M.19a. Pile-Head and Toe Acceleration Vs. Time; Penetration = 77 Inches; Test 16

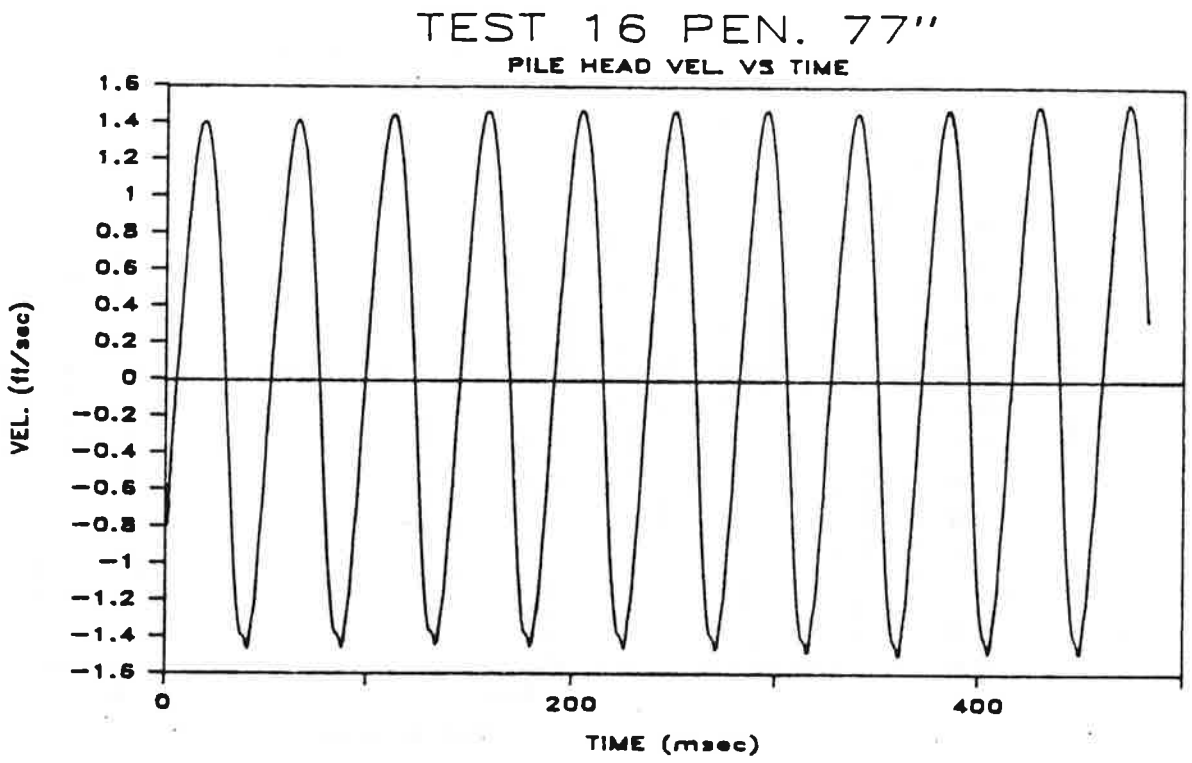

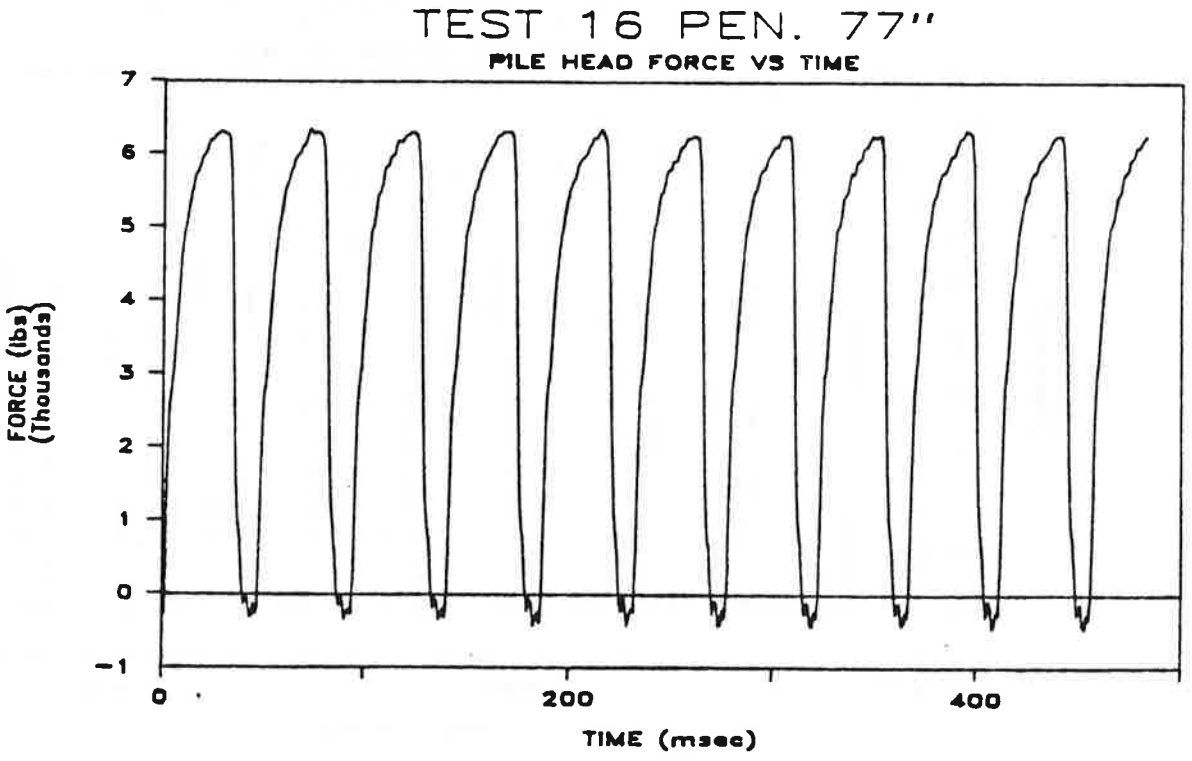

Fig. M.19b. Pile-Head Velocity and ForceVs. Time; Penetration = 77 Inches; Test 16

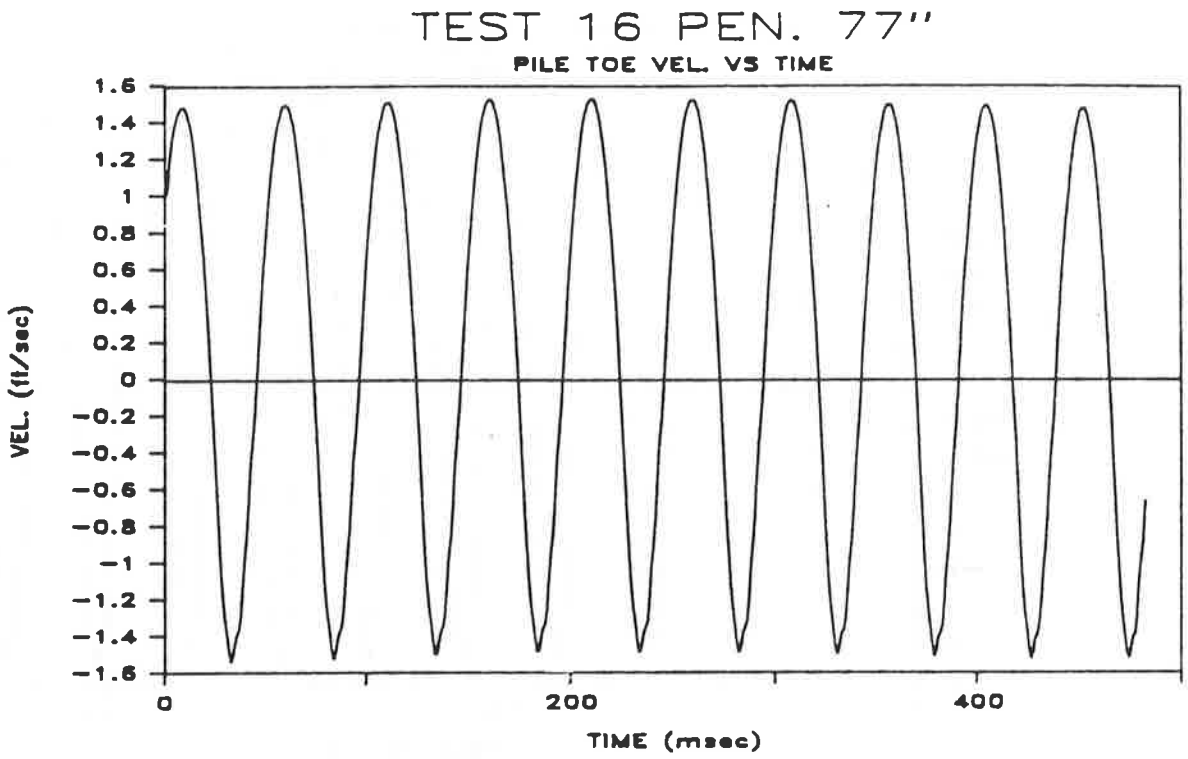

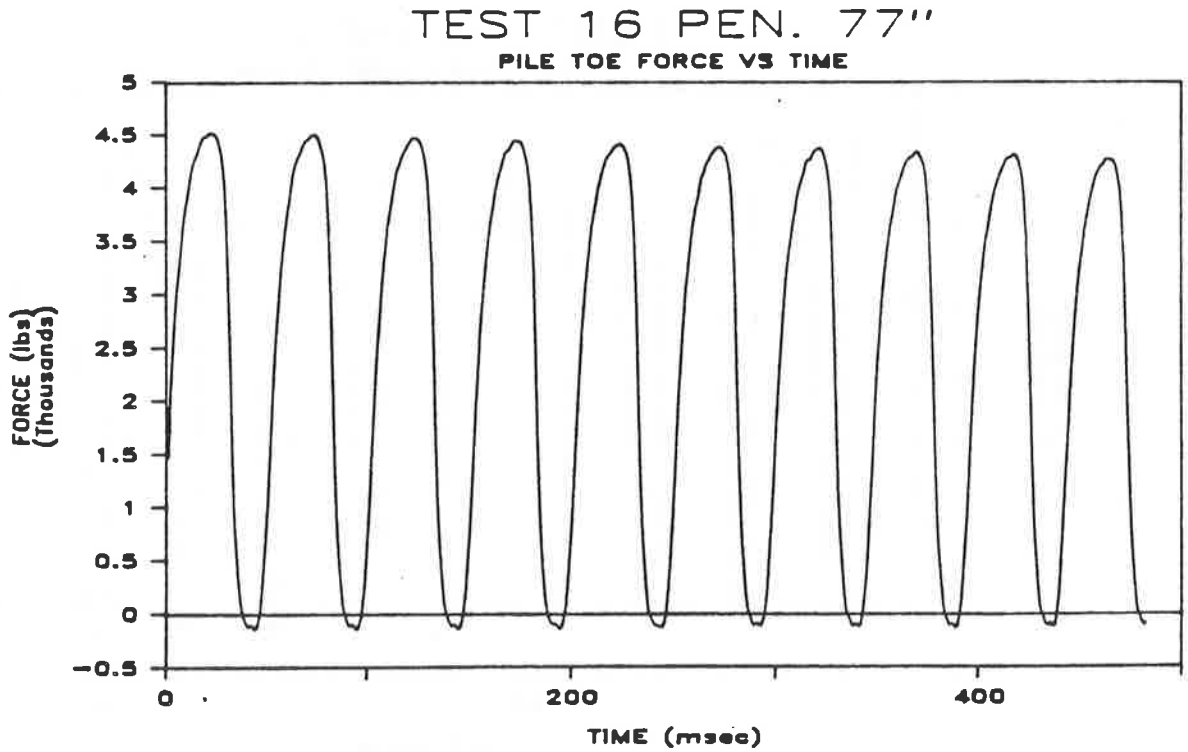

Fig. M.19c. Pile-Toe Velocity and Force Vs. Time; Penetration = 77 Inches; Test 16

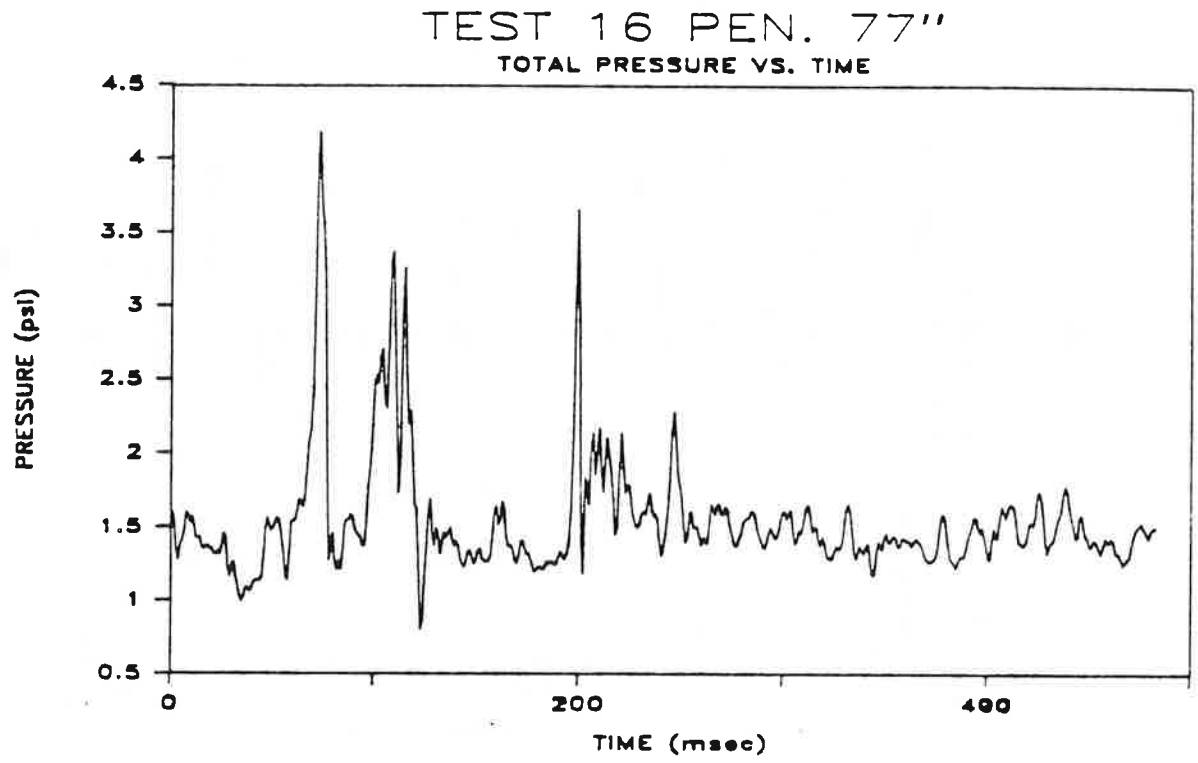

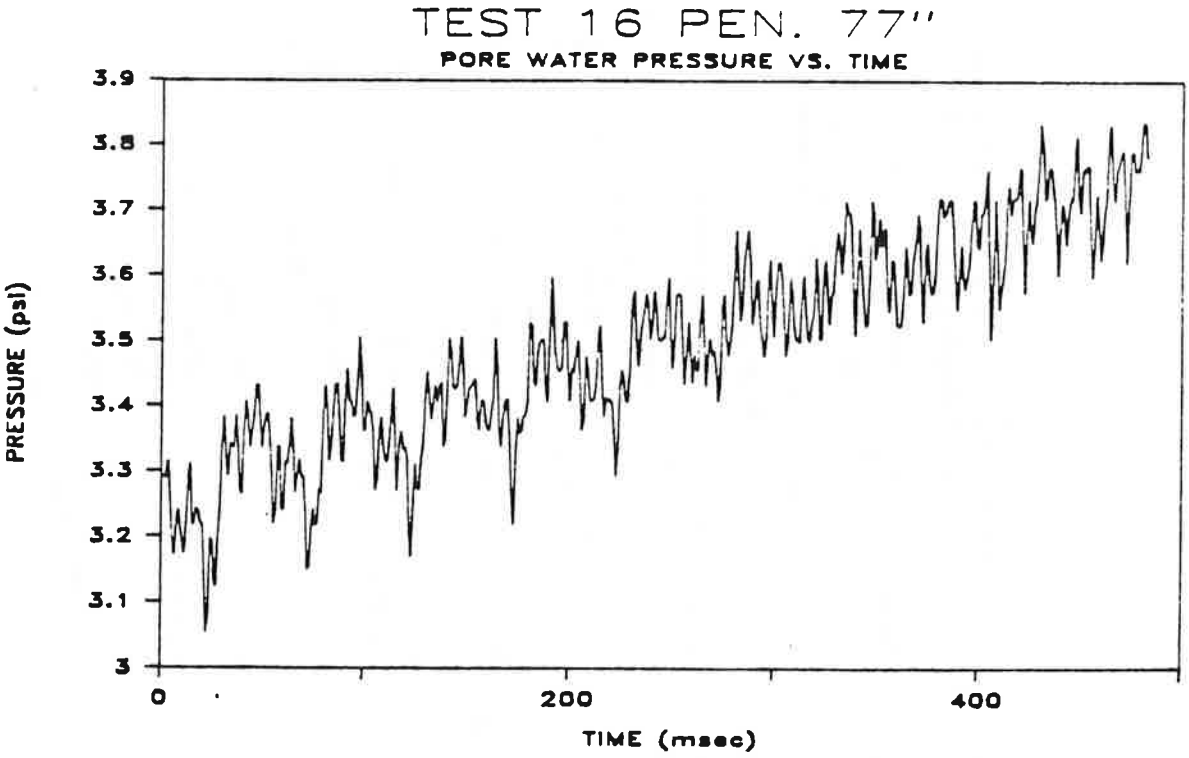

Fig. M.19d. Total and Pore Water Pressure Vs. Time at Bottom of Pile Shaft; Penetration = 77 Inches; Test 16

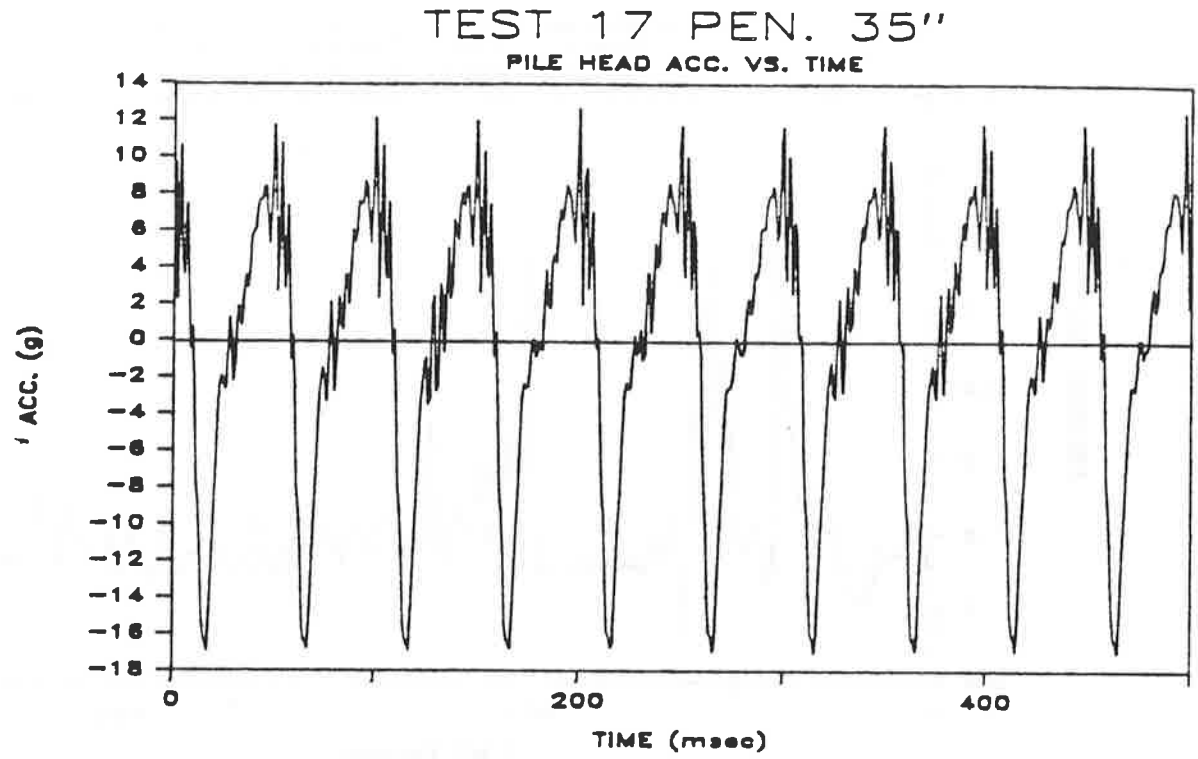

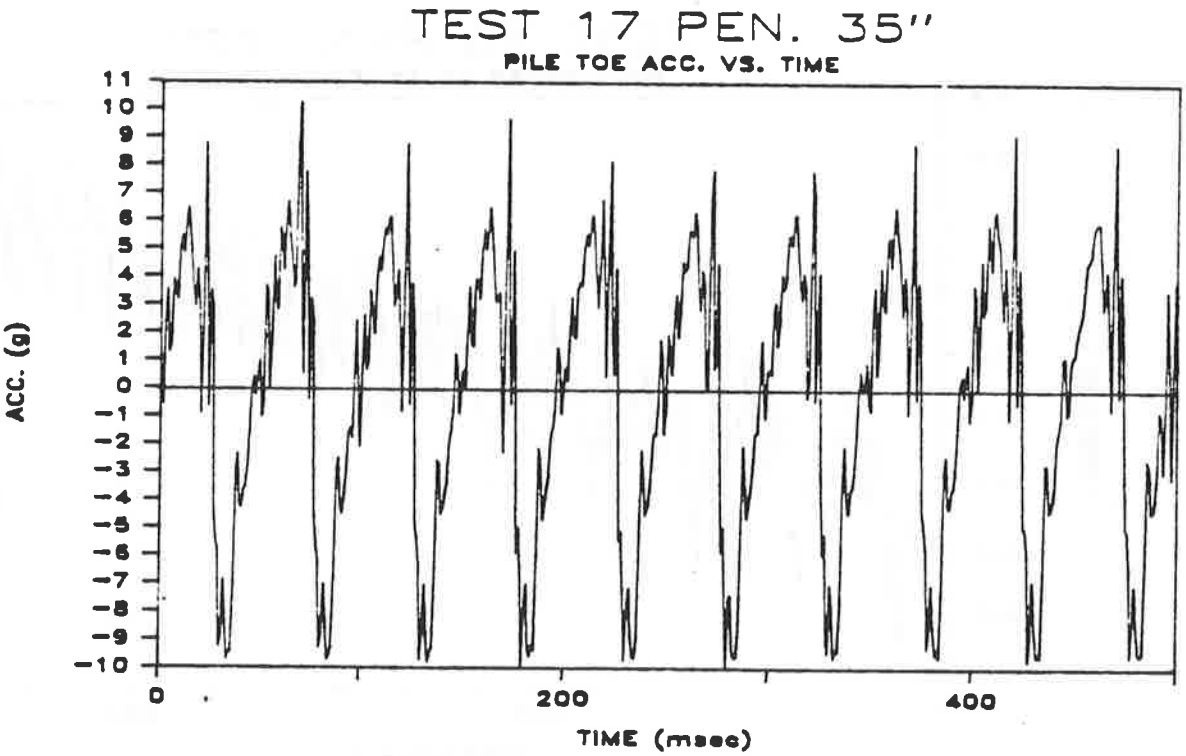

Fig. M.20a. Pile-Head and Toe Acceleration Vs. Time; Penetration = 35 Inches; Test 17

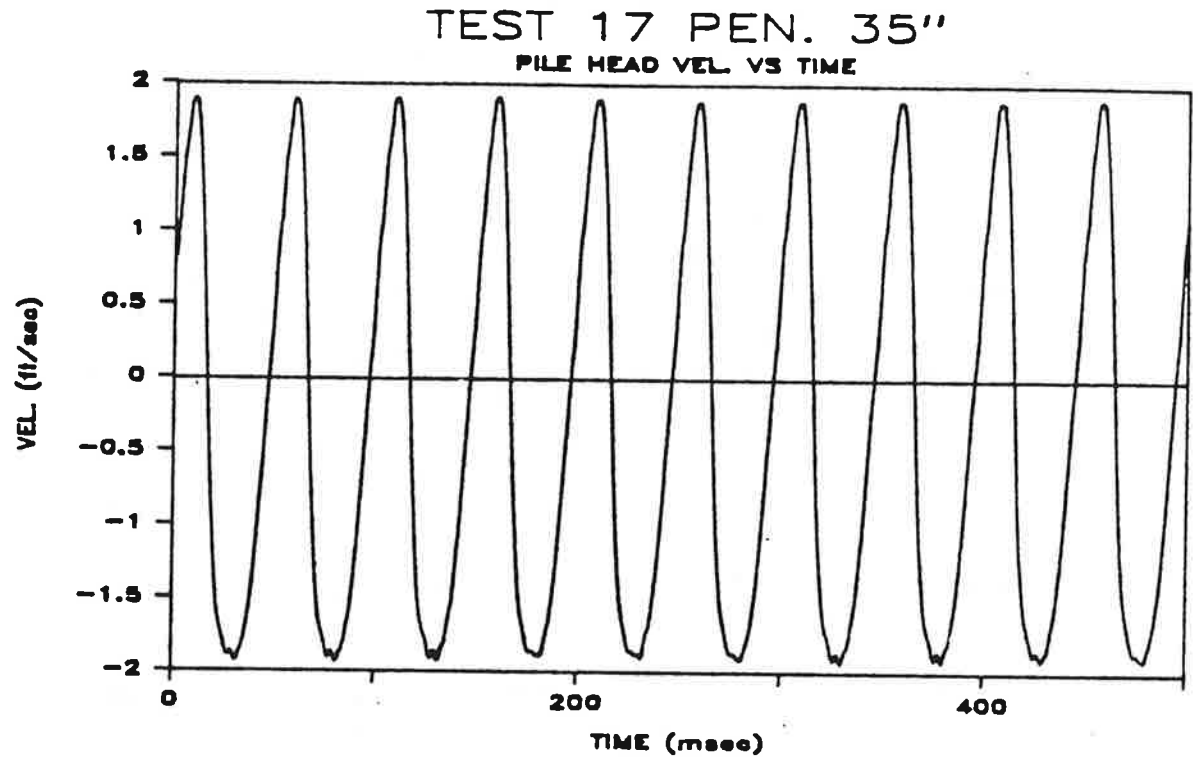

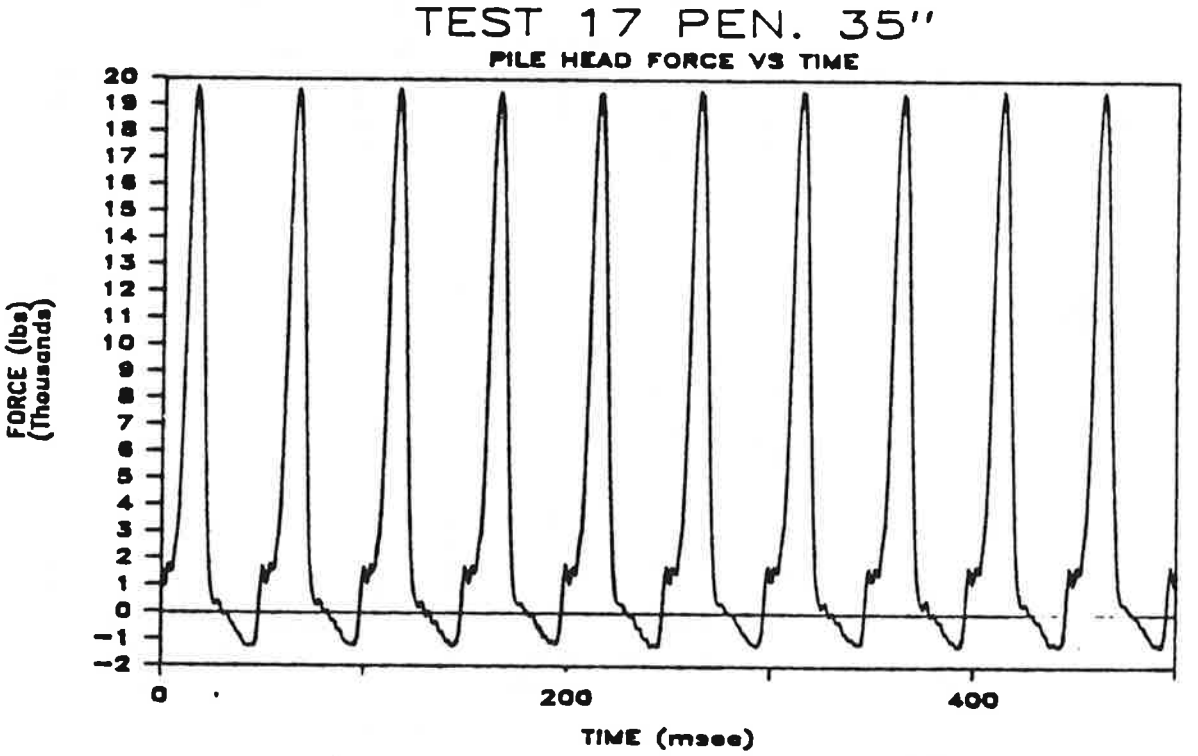

Fig. M.20b. Pile-Head Velocity and ForceVs. Time; Penetration = 35 Inches; Test 17

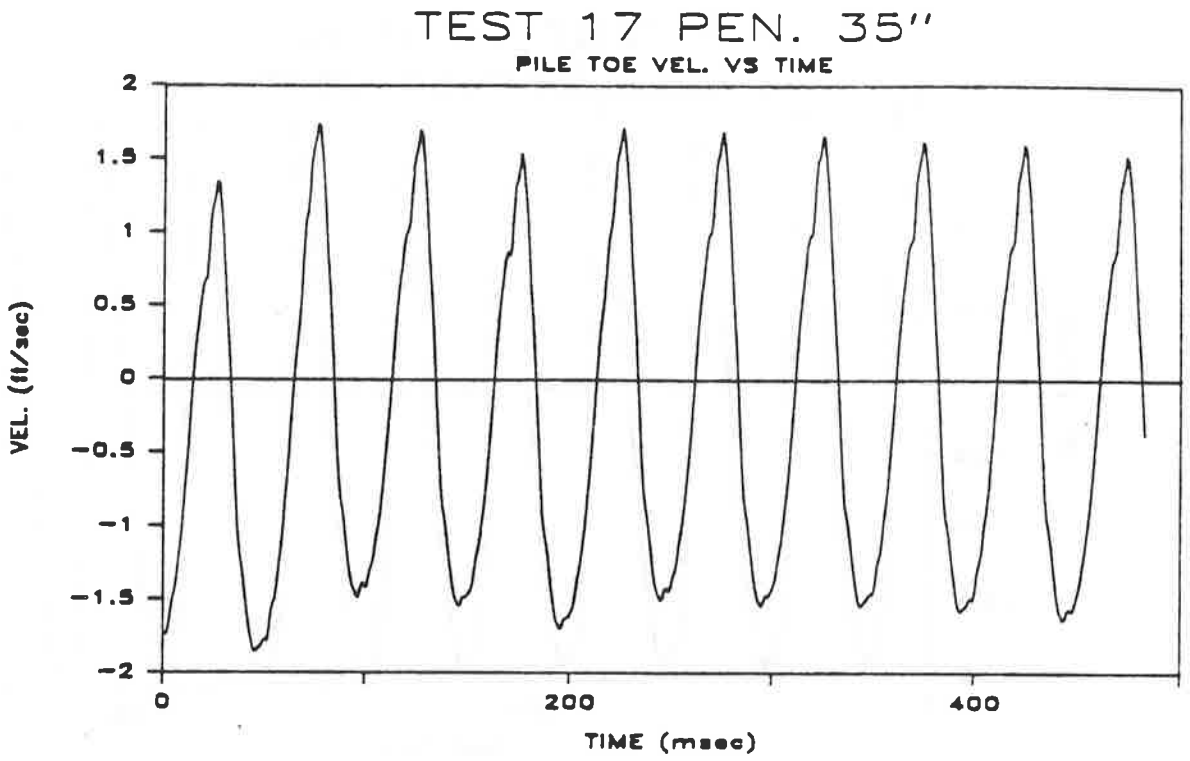

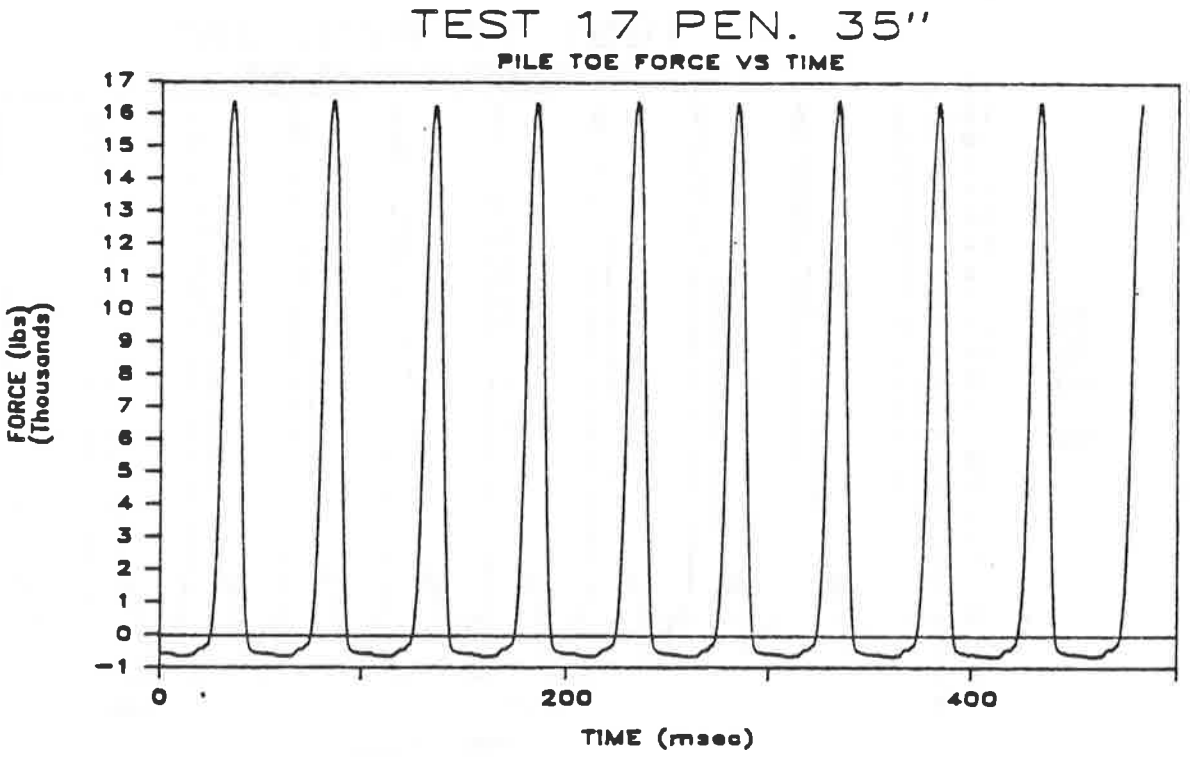

Fig. M.20c. Pile-Toe Velocity and Force Vs. Time; Penetration = 35 Inches; Test 17

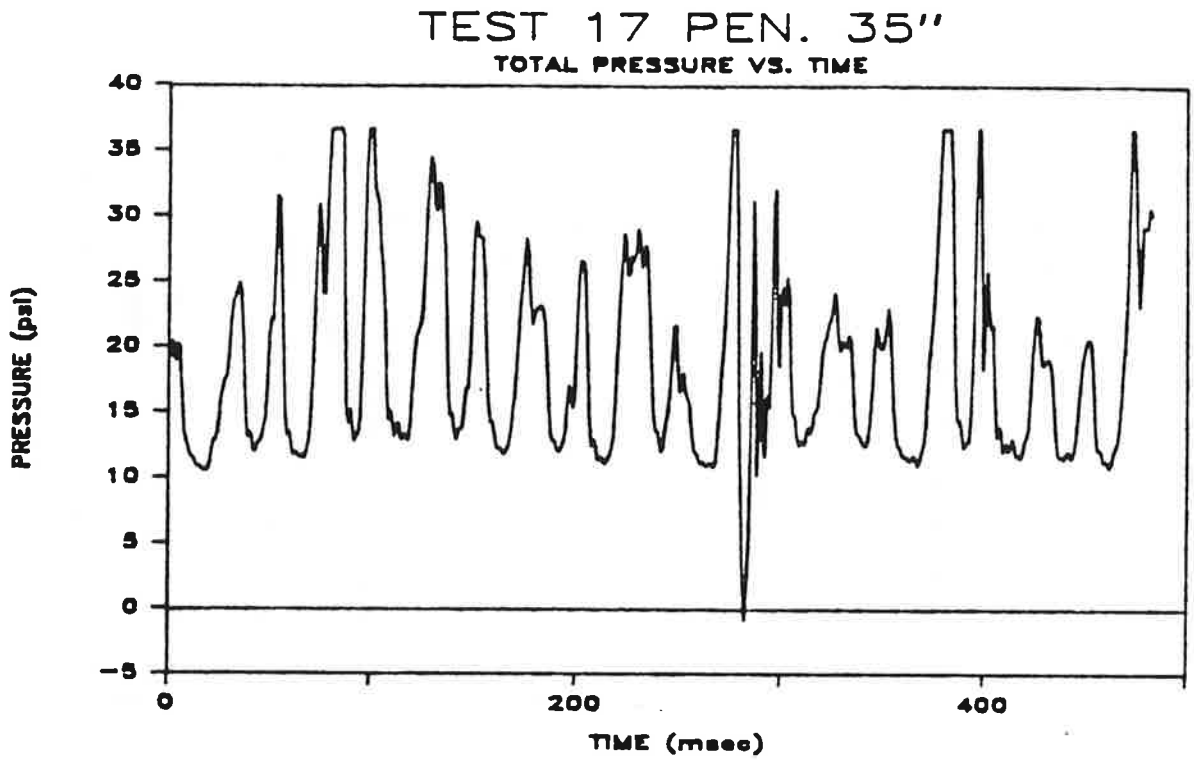

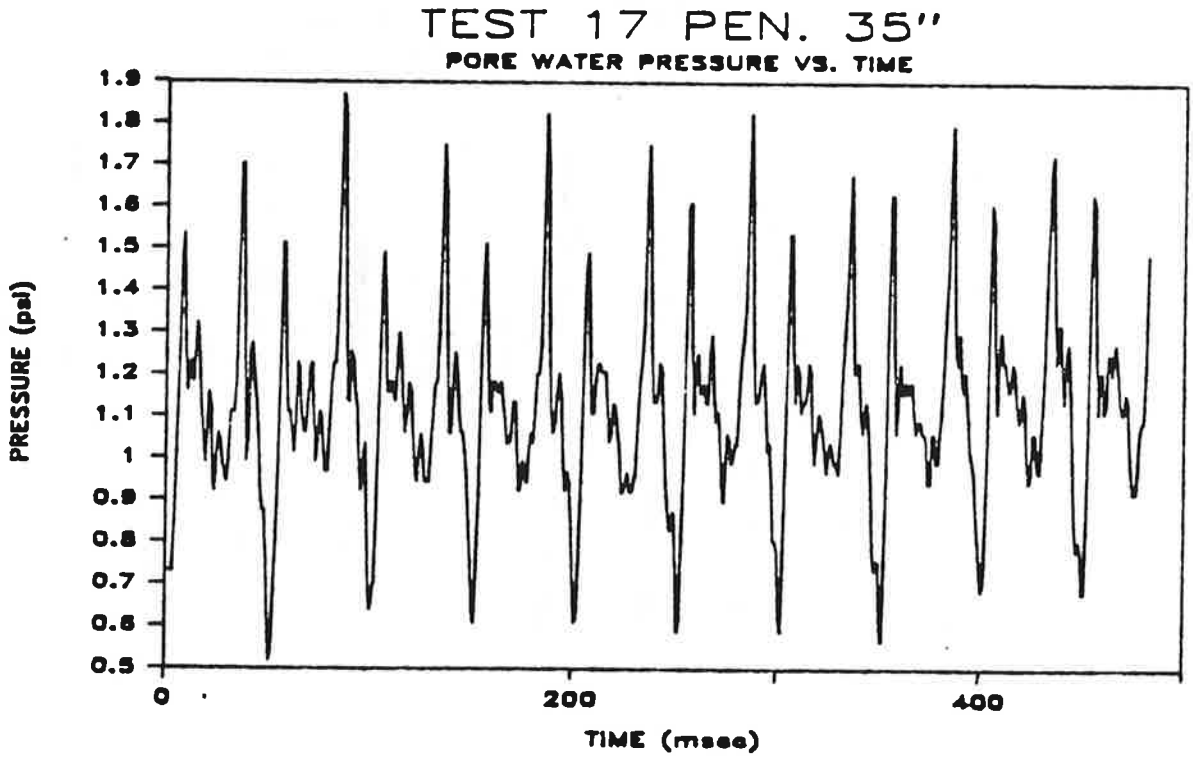

Fig. M.20d. Total and Pore Water Pressure Vs. Time at Bottom of Pile Shaft; Penetration = 35 Inches; Test 17

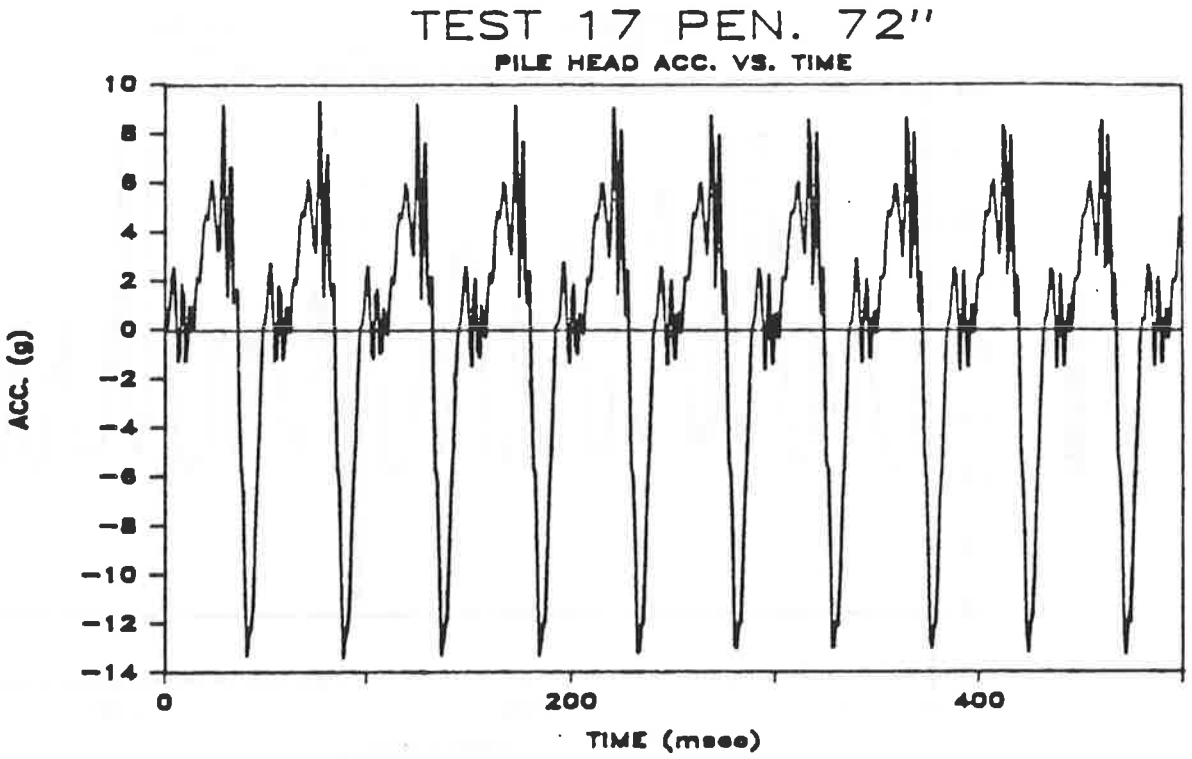

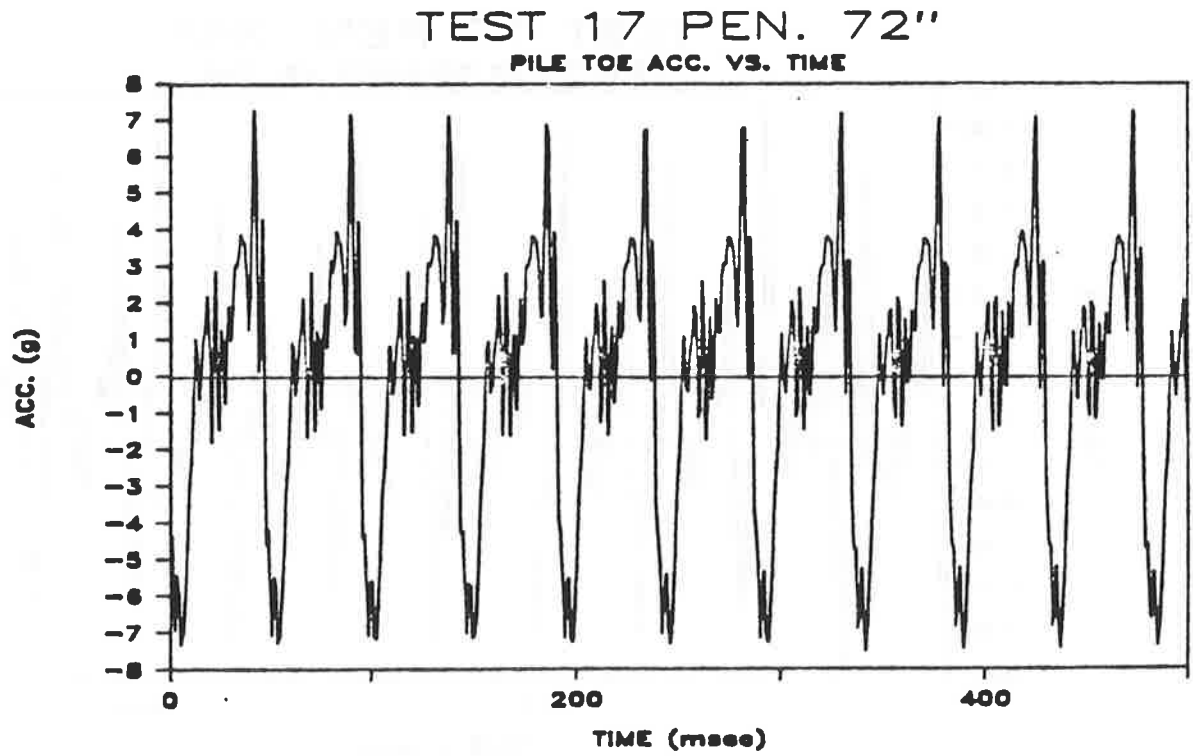

Fig. M.21a. Pile-Head and Toe Acceleration Vs. Time; Penetration = 72 Inches; Test 17

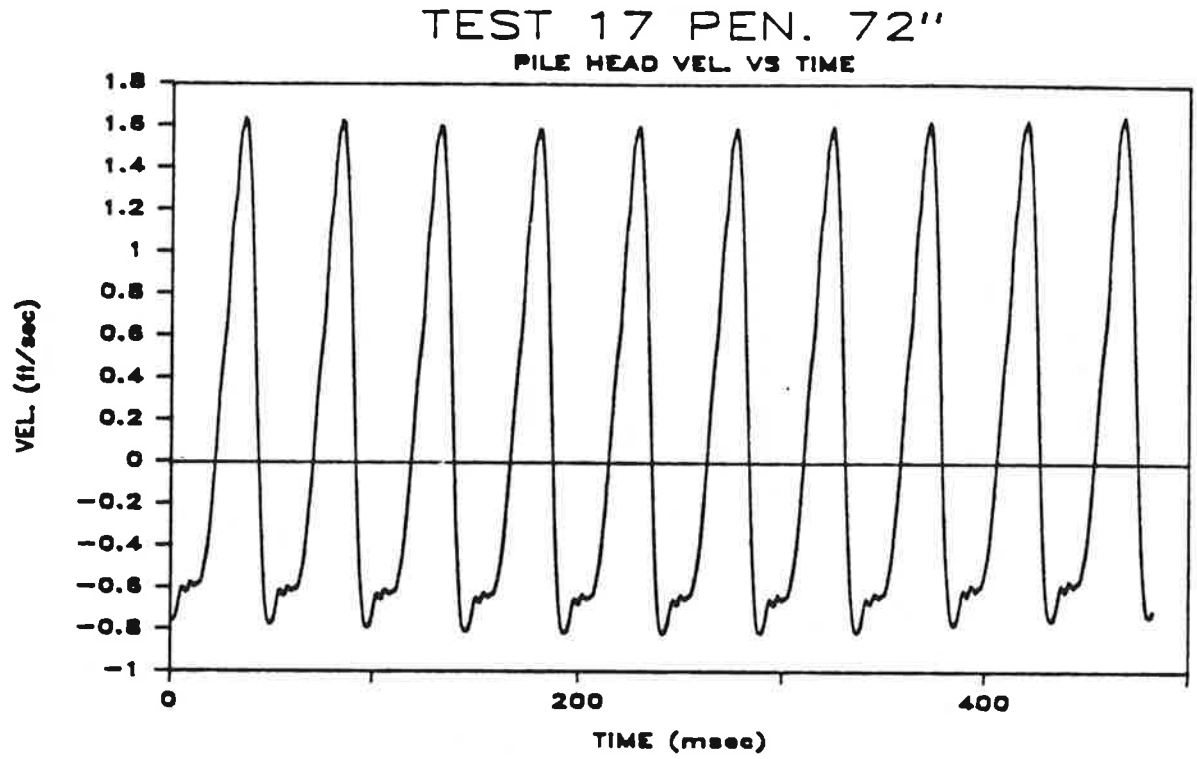

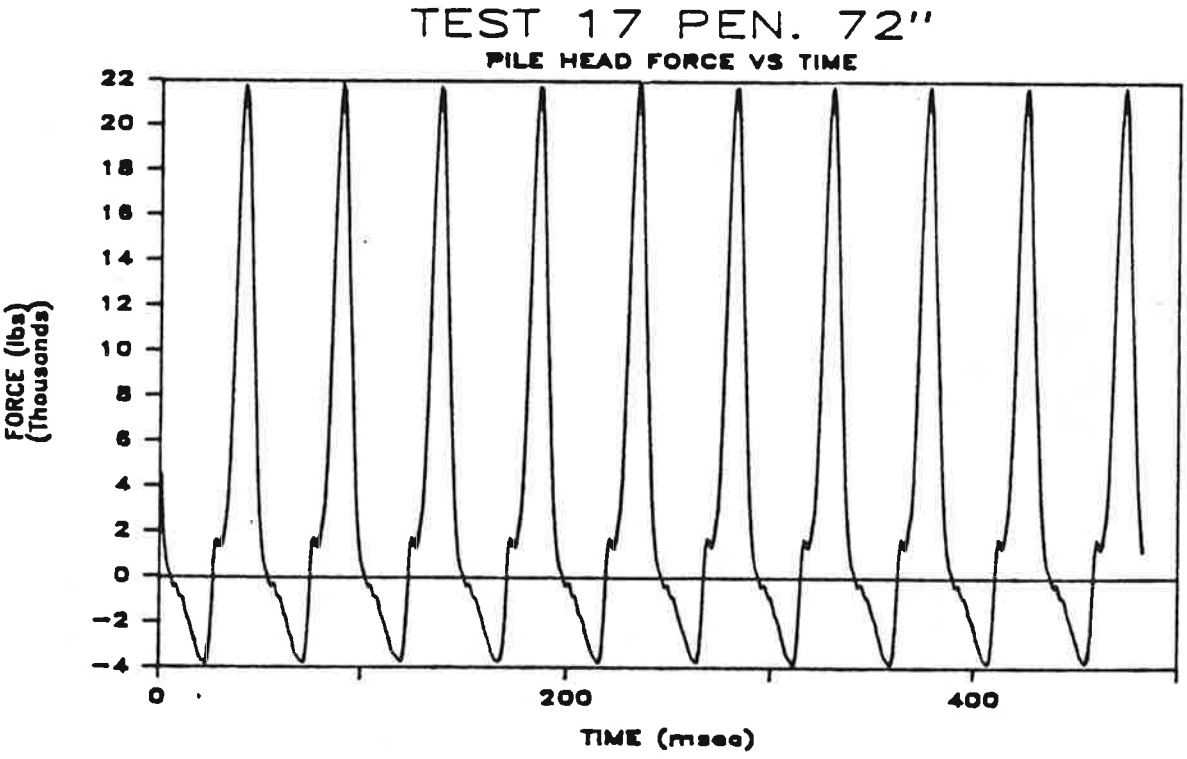

Fig. M.21b. Pile-Head Velocity and ForceVs. Time; Penetration = 72 Inches; Test 17

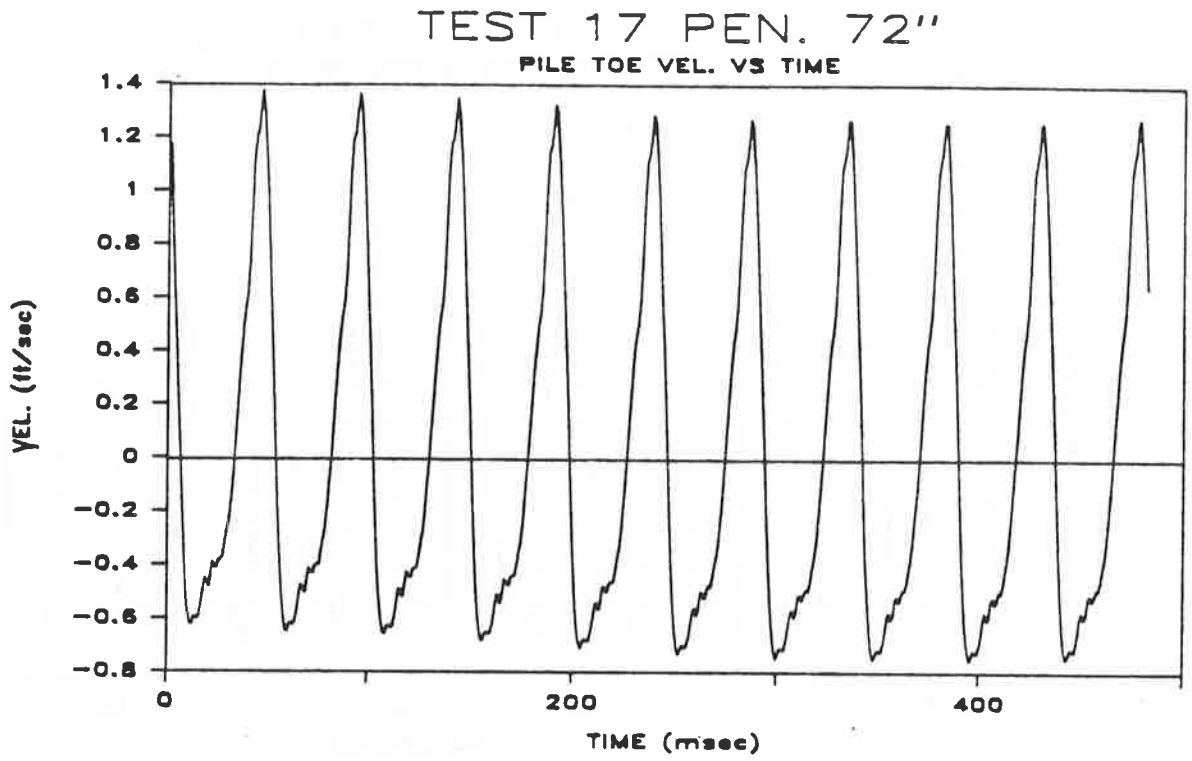

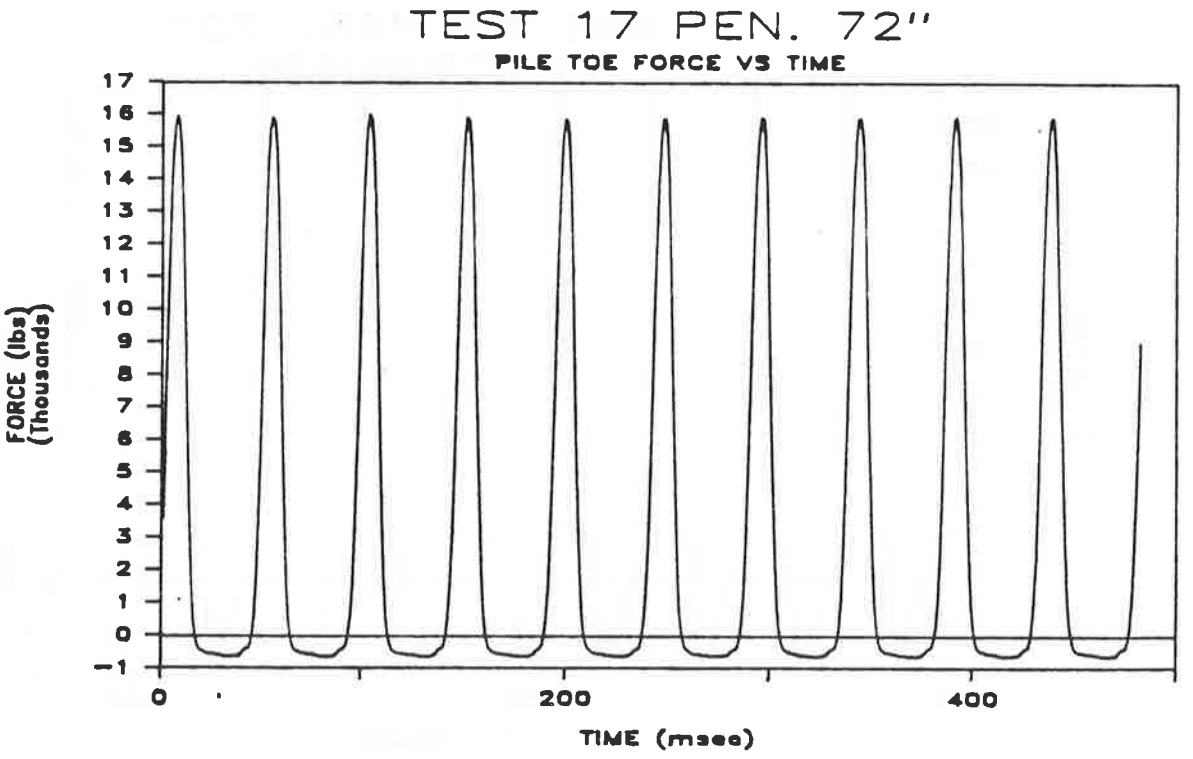

Fig. M.21c. Pile-Toe Velocity and Force Vs. Time; Penetration = 72 Inches; Test 17

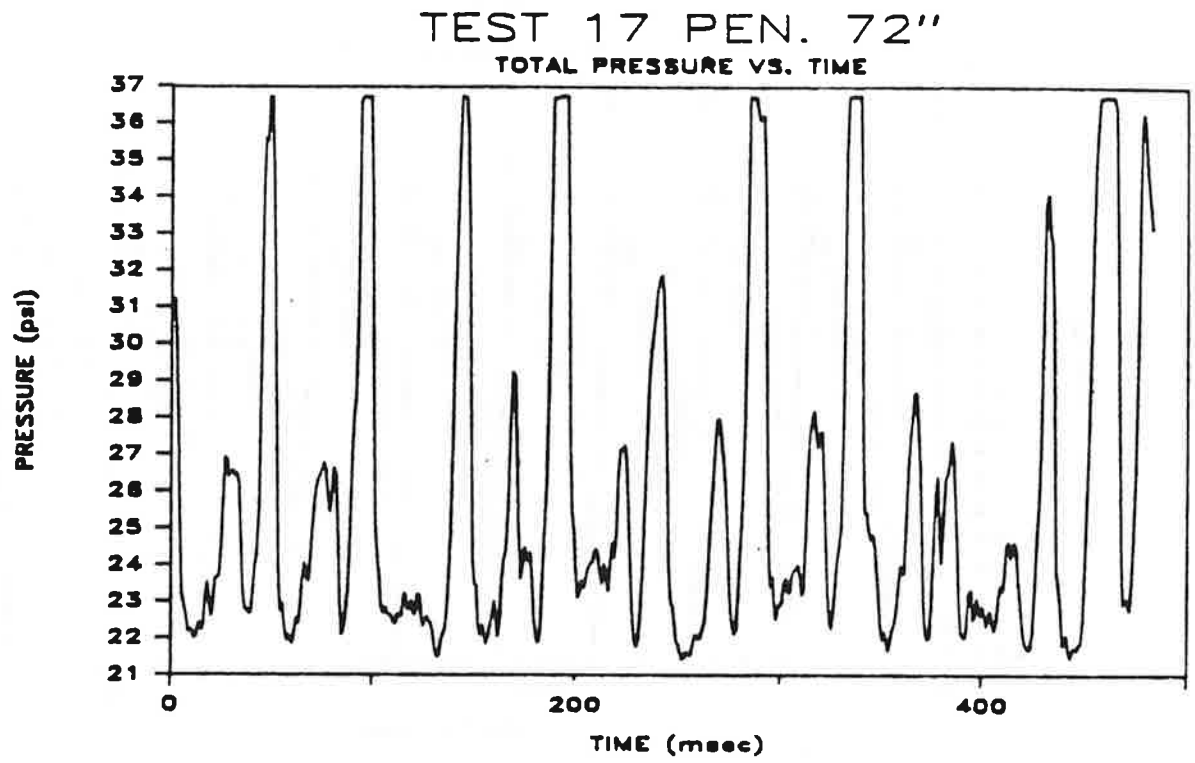

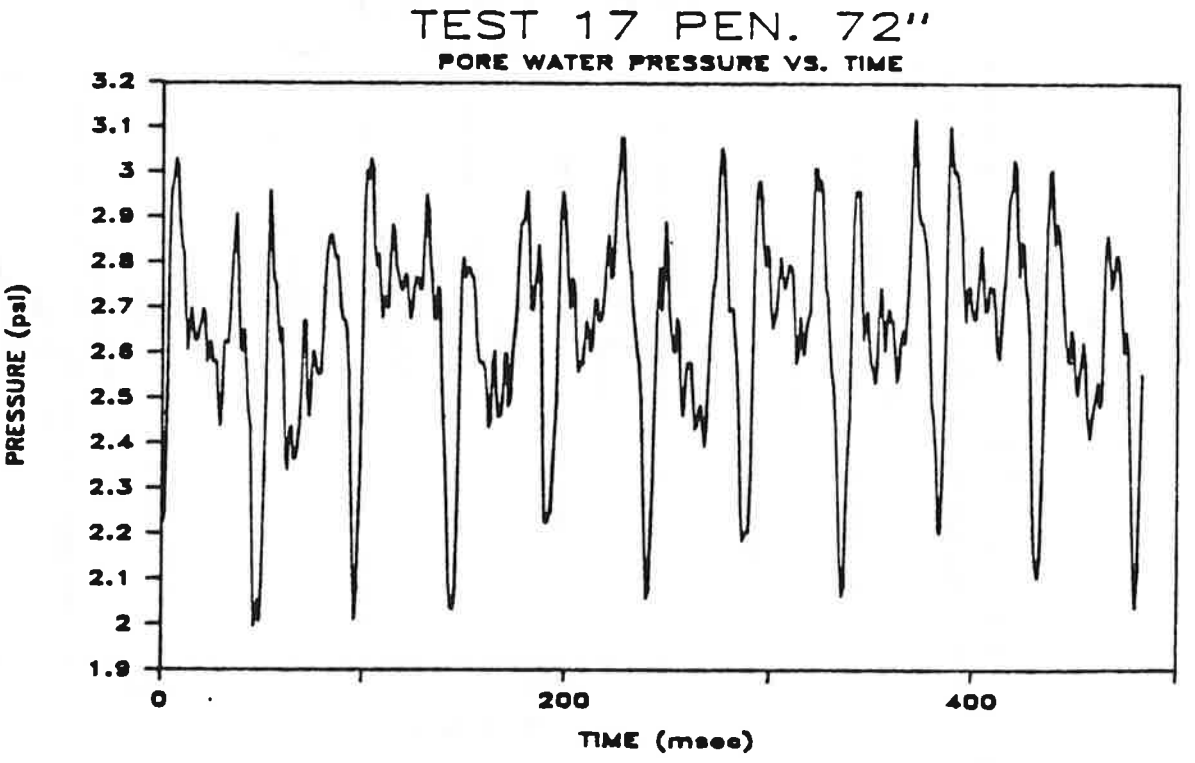

Fig. M.21d. Total and Pore Water Pressure Vs. Time at Bottom of Pile Shaft; Penetration = 72 Inches; Test 17

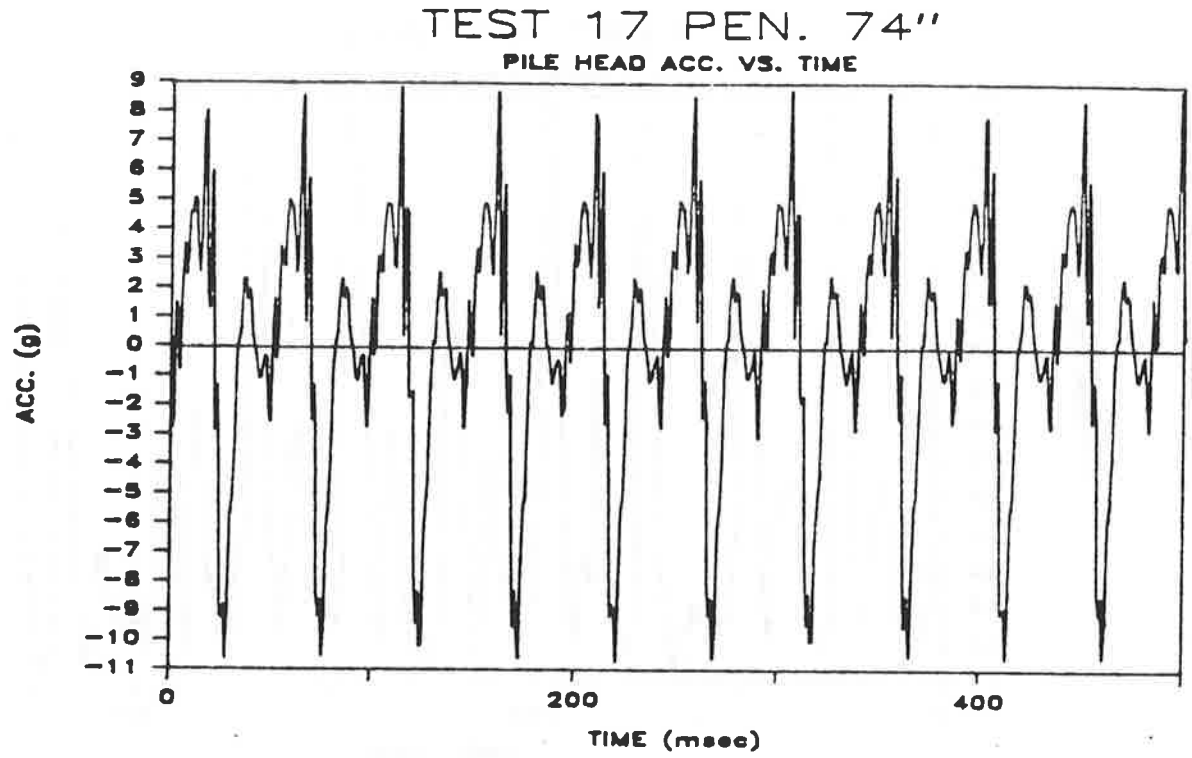

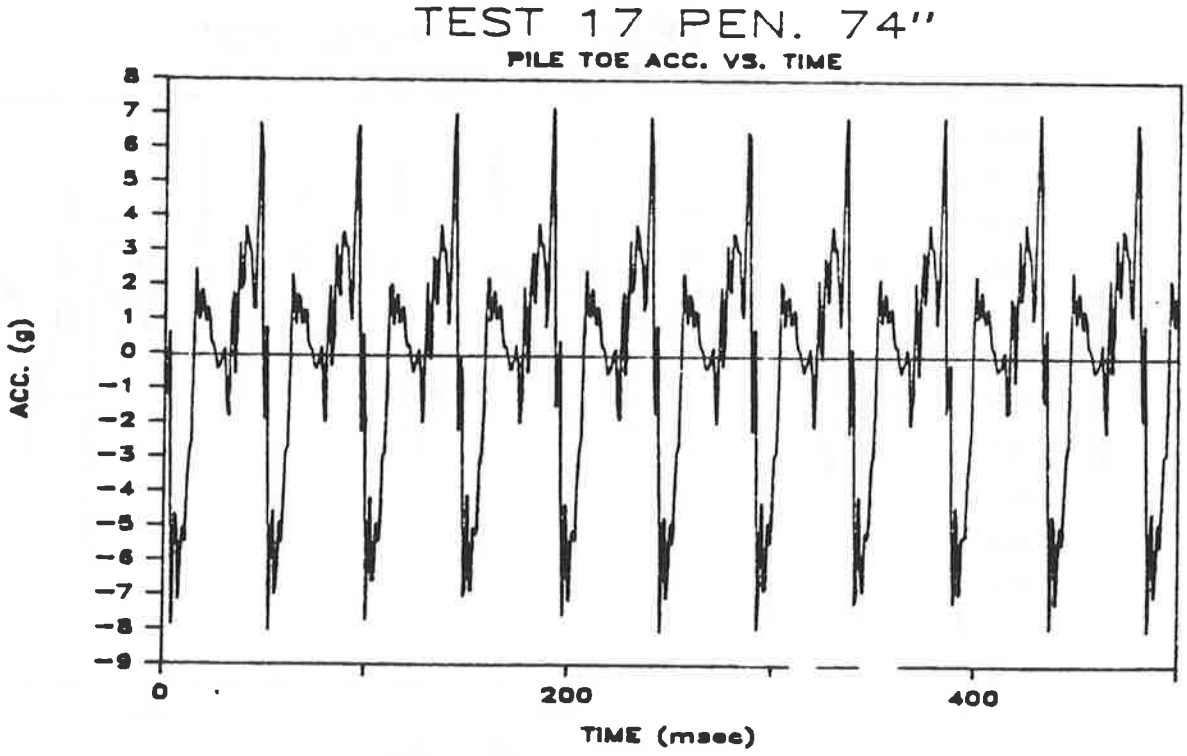

Fig. M.22a. Pile-Head and Toe Acceleration Vs. Time; Penetration = 74 Inches; Test 17 (Refusal)

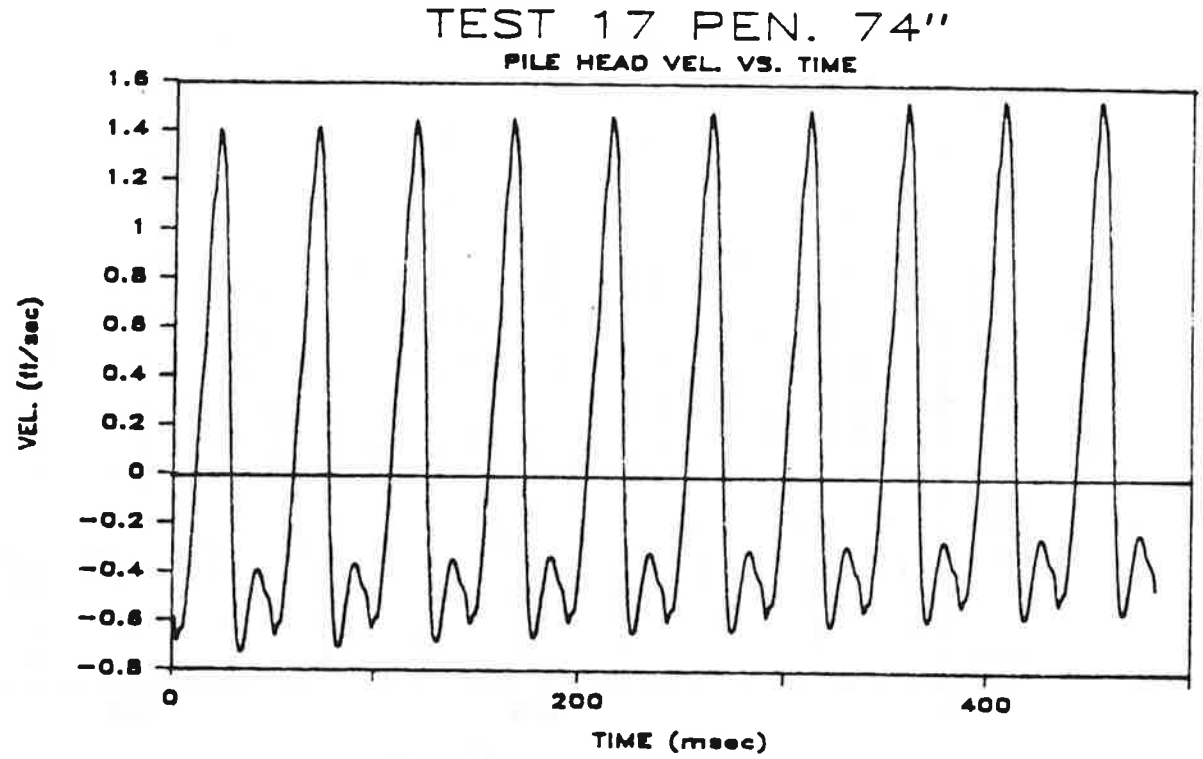

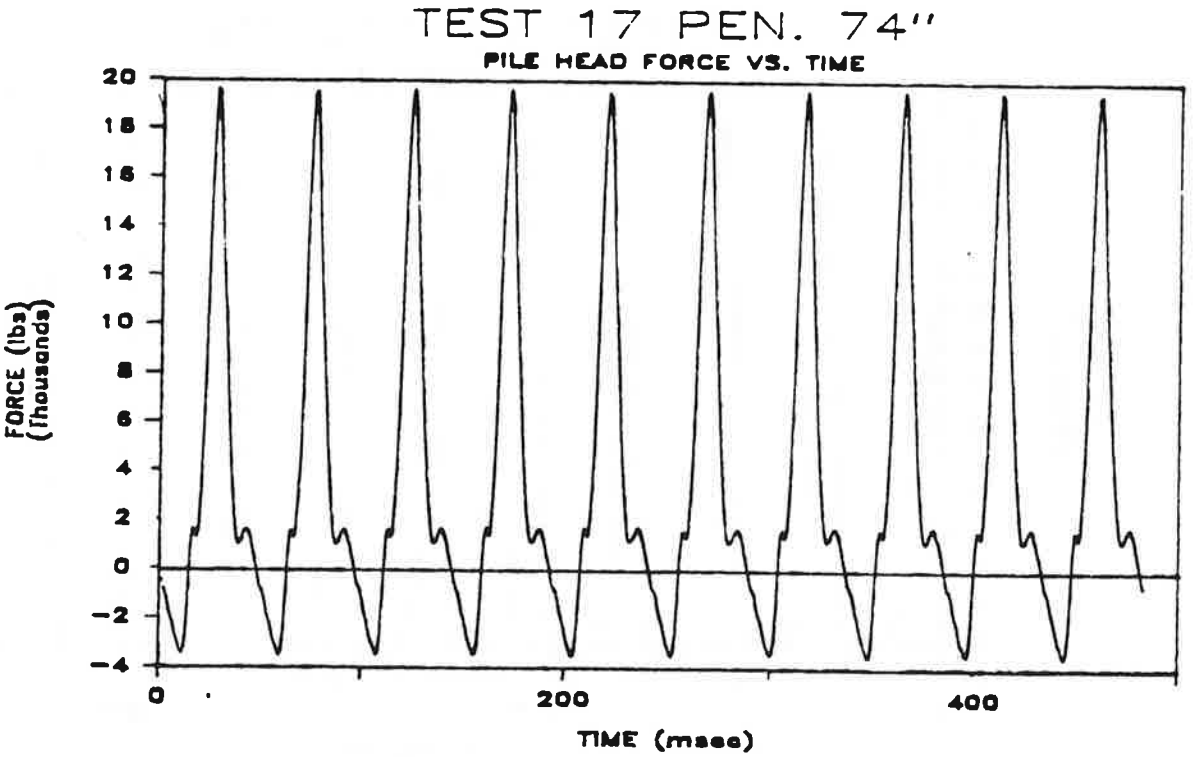

Fig. M.22b. Pile-Head Velocity and ForceVs. Time; Penetration = 74 Inches; Test 17 (Refusal)

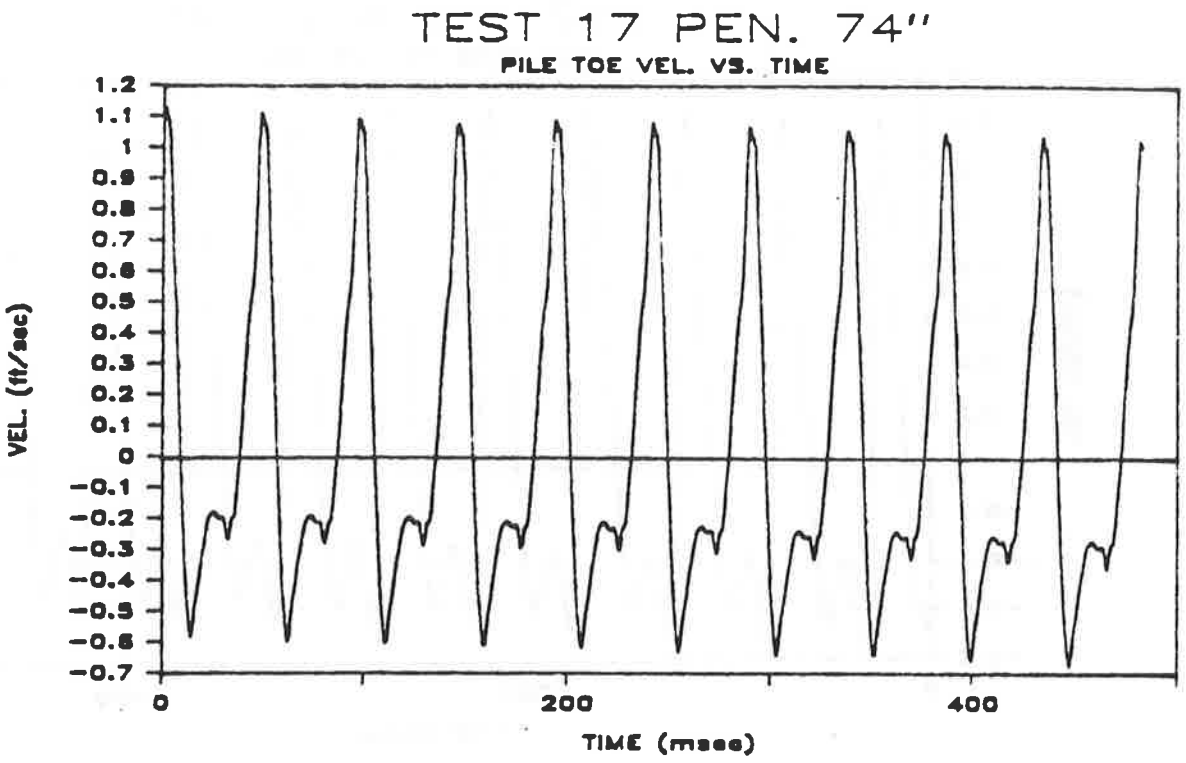

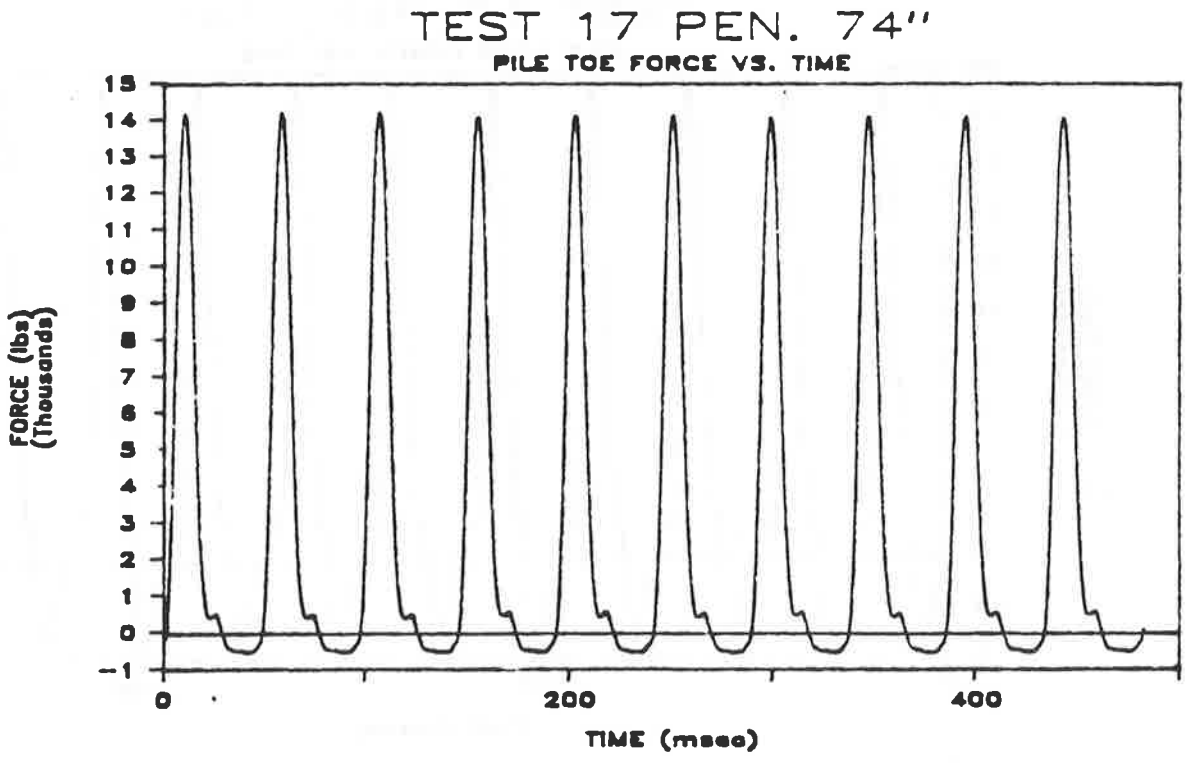

Fig. M.22c. Pile-Toe Velocity and Force Vs. Time; Penetration = 74 Inches; Test 17 (Refusal)

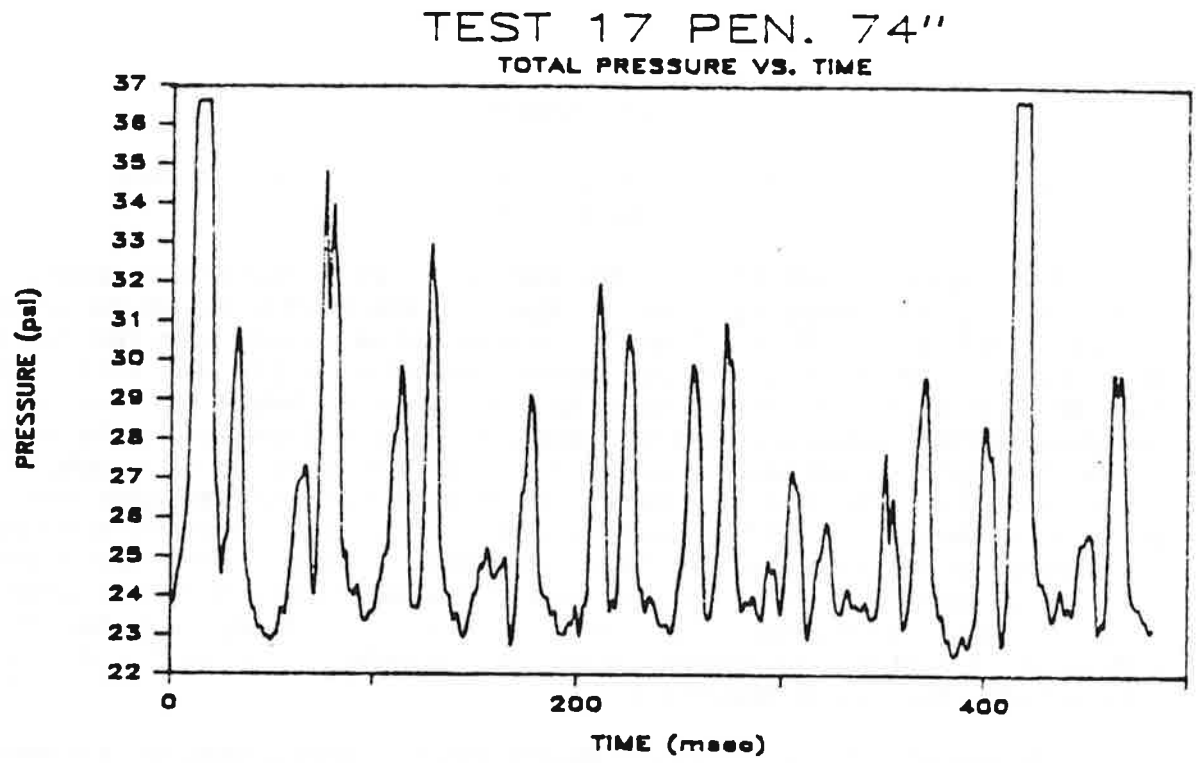

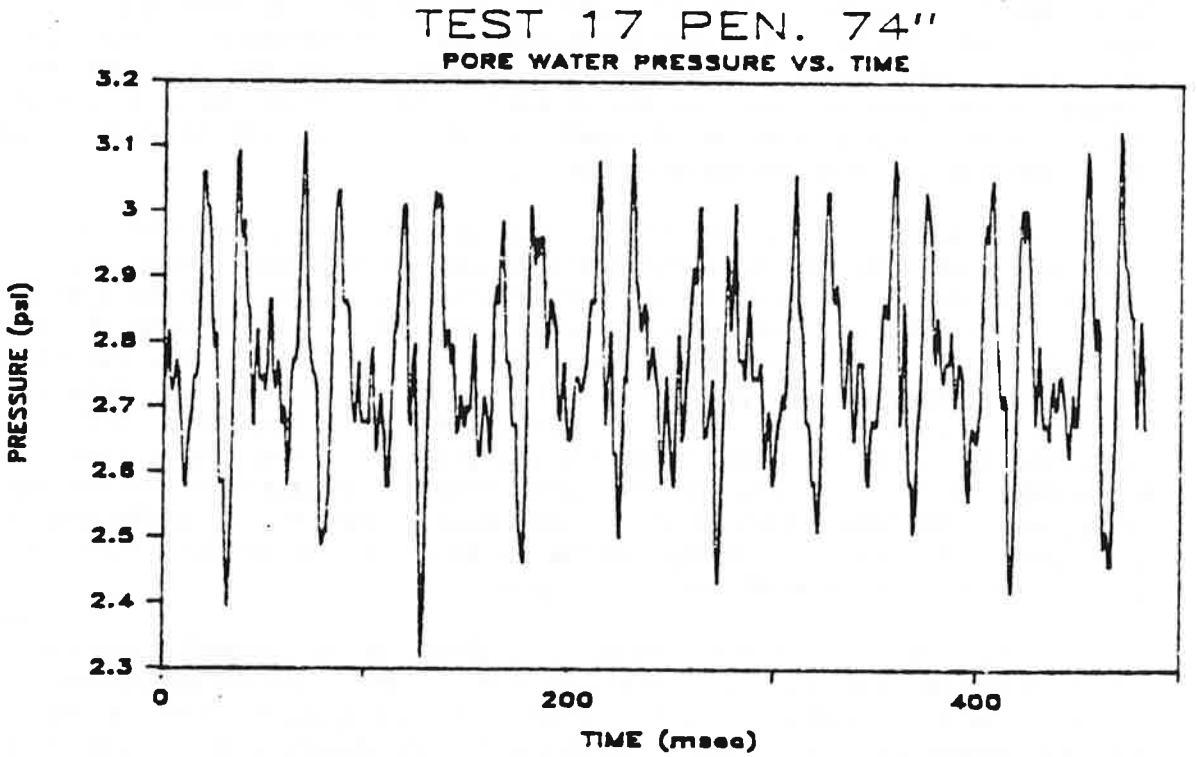

Fig. M.22d. Total and Pore Water Pressure Vs. Time at Bottom of Pile Shaft; Penetration = 74 Inches; Test 17 (Refusal)

APPENDIX N

Force and Velocity Time Histories at Full Penetration for Impact and Restrike Tests

Time histories of pile-head and pile toe-force superimposed on time histories of pile-head and pile-toe velocities for the average of several blows of the impact hammer are shown in Figs. N.1 - N.11. These figures represent all capacity tests that involved only impact driving of the pile or that involved restriking the pile after the pile had been driven to within one-half diameter of full penetration by vibration. The forces that are shown in these figures are those that have been determined directly from the output of the strain gages at the head of the pile or the load cell at the toe of the pile. The velocities were obtained from integration of the average accelerometer signal from the pile-head accelerometers and from the single high-g accelerometer at the toe of the pile, as described for the computation of energy in Appendix H. (Appendix D describes these instruments; Appendix G describes instrument calibration procedures; and Appendix F describes the signal conditioning that was employed.) The velocity traces have been shifted to account for the phase lag in the averaging circuit for the pile-head accelerometers described in Appendix G.

The purpose of developing these records was to provide a basis for determining whether vibrated-and-restruck piles (Figs. N.1 - N.7) exhibited dynamic characteristics significantly different from impact-driven piles (Figs. N.8 - N.11) when being struck with an impact hammer. Because the application of the first blow, or first several blows in the denser sand at high chamber pressure, produced very little permanent set, only the final three to ten blows were included in the averaged records. An exception to this rule is Test 16 (Appendix B), for which all three restrike blows were averaged. The blows for which the average traces presented in this appendix are given relative to the entire suite of blows that was applied to the pile can be obtained by comparing the blow numbers on the respective figures with the driving records (impact-driven piles) or number of blows for each inch of restrike driving (vibro-driven-and-restruck piles) shown in Chapter 2.

Wave propagation theory indicates that in an infinitely long pile that is not supported by soil, the force time history should correspond to the velocity time history provided that the velocity is multiplied by the mechanical impedance of the pile, which is characterized by the term AE/c, where A = the cross-sectional area of the pile material (2.251 square inches for the test pile used in this study), E = the Young's modulus of elasticity of the pile (29 X 10^6 psi (steel) for the test pile used in this study), and c = the compression wave velocity of the material out of which the pile is made (201,000 inches per second for the test pile). In a real pile of finite length interacting with the supporting soil, the wave forms will deviate from one another at some point in the time history when p-waves reflected from the toe of the pile or p-waves produced by transfer of energy into the soil along the shaft through shearing at the shaft-soil interface return to the head of the pile.

In Figs. N.1 - N.11 the time scale is direct, in milliseconds; however, the magnitude of a quantity shown as 2L/c is also shown on the graphs for the pile-head time histories. In this expression L is the length of the pile (distance from the pile-head force and acceleration transducers to the toe of the pile; Appendix D). Therefore, 2L/c represents the time required for a wave to travel down to the toe of the pile and be

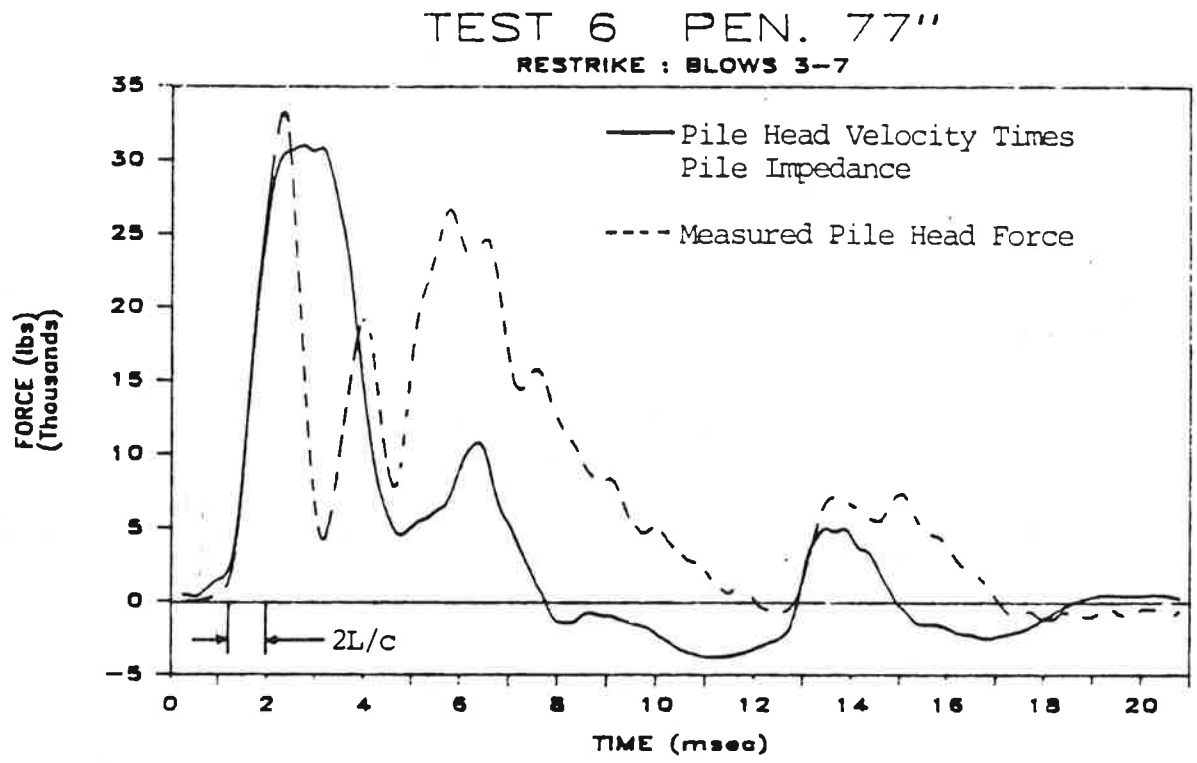

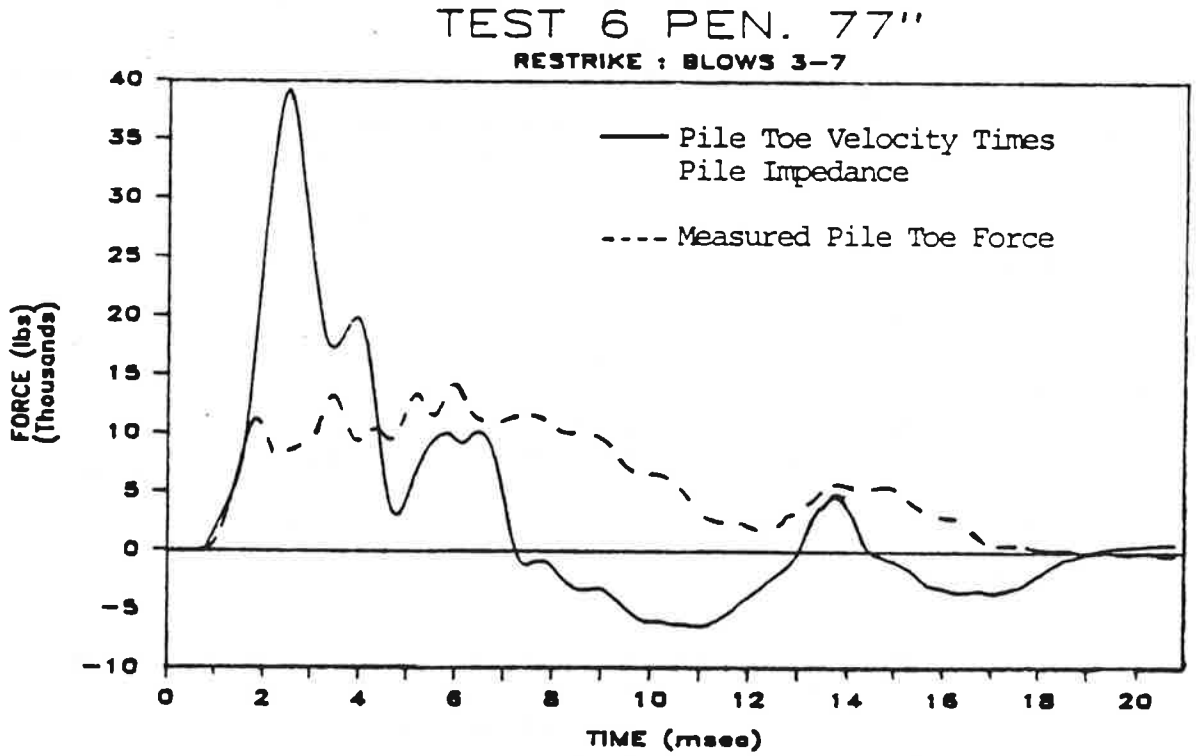

Fig. N.1. Measured Head and Toe Force and Velocity-Impedance Time Histories; Restrike at Full Penetration; Test No. 6 (SJR Sand; 90% Rel. Den.; 10 psi Press.)

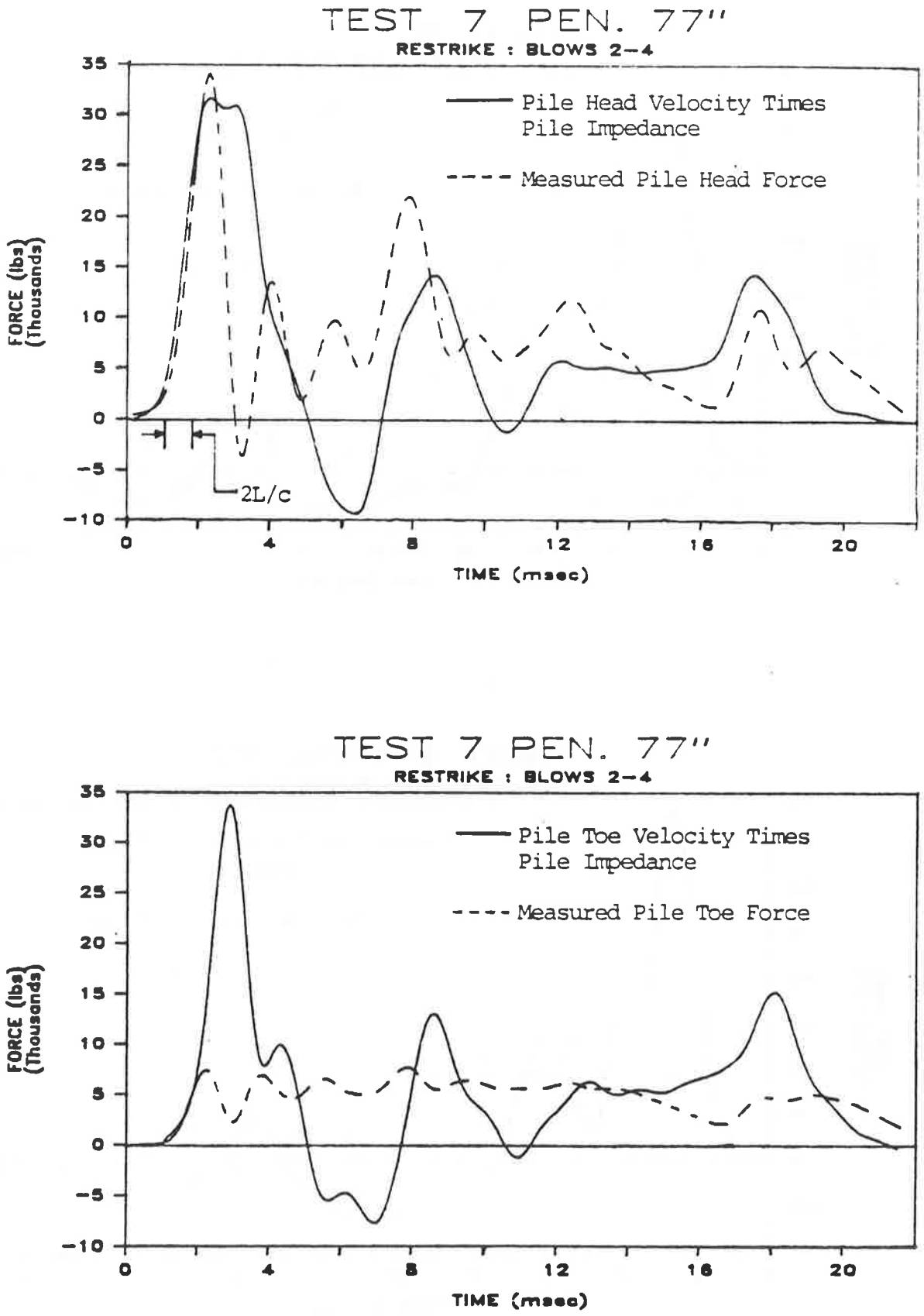

Fig. N.2. Measured Head and Toe Force and Velocity-Impedance Time Histories; Restrike at Full Penetration; Test No. 7 (SJR Sand; 65% Rel. Den.; 10 psi Press.)

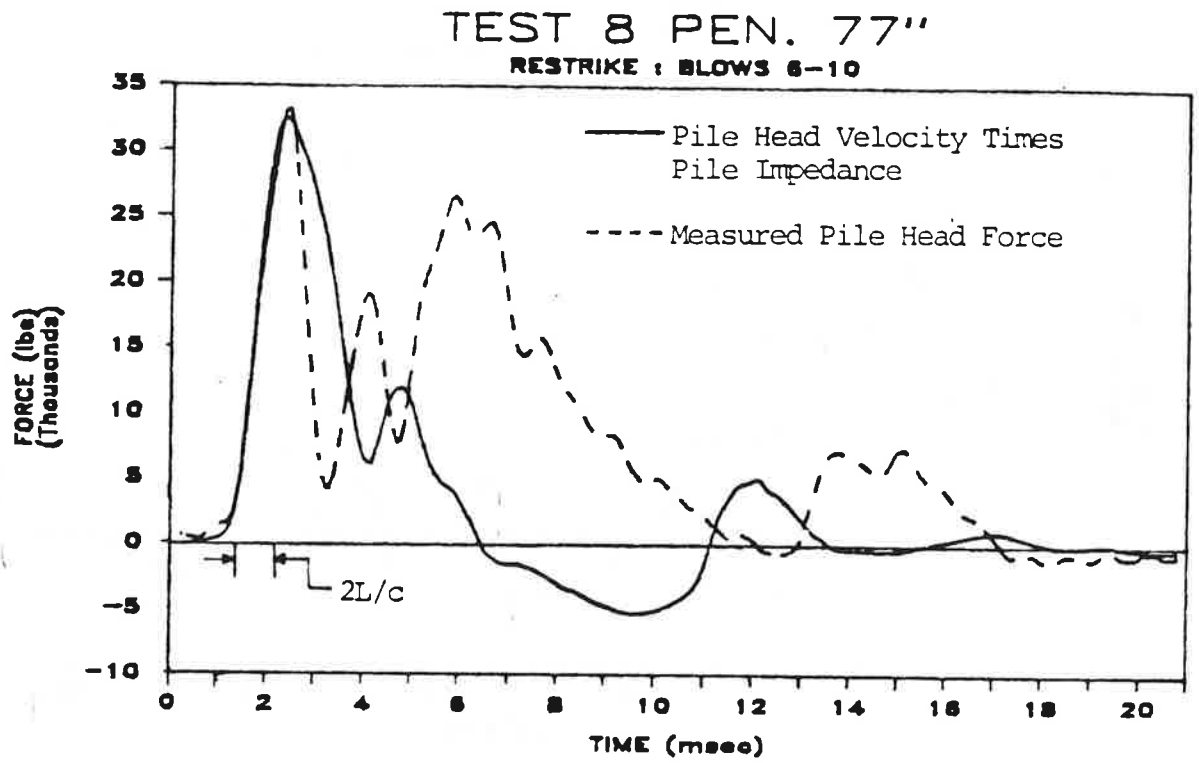

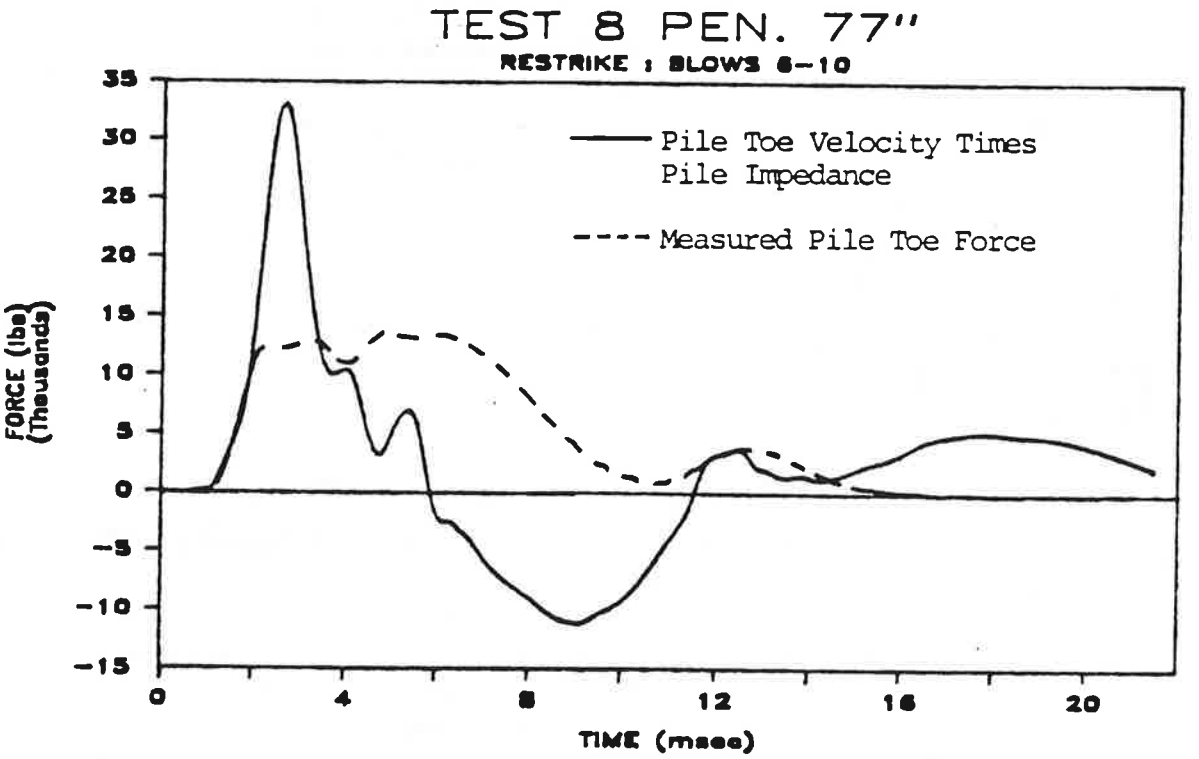

Fig. N.3. Measured Head and Toe Force and Velocity-Impedance Time Histories; Restrike at Full Penetration; Test No. 8 (SJR Sand; 90% Rel. Den.; 10 psi Lat. Press.)

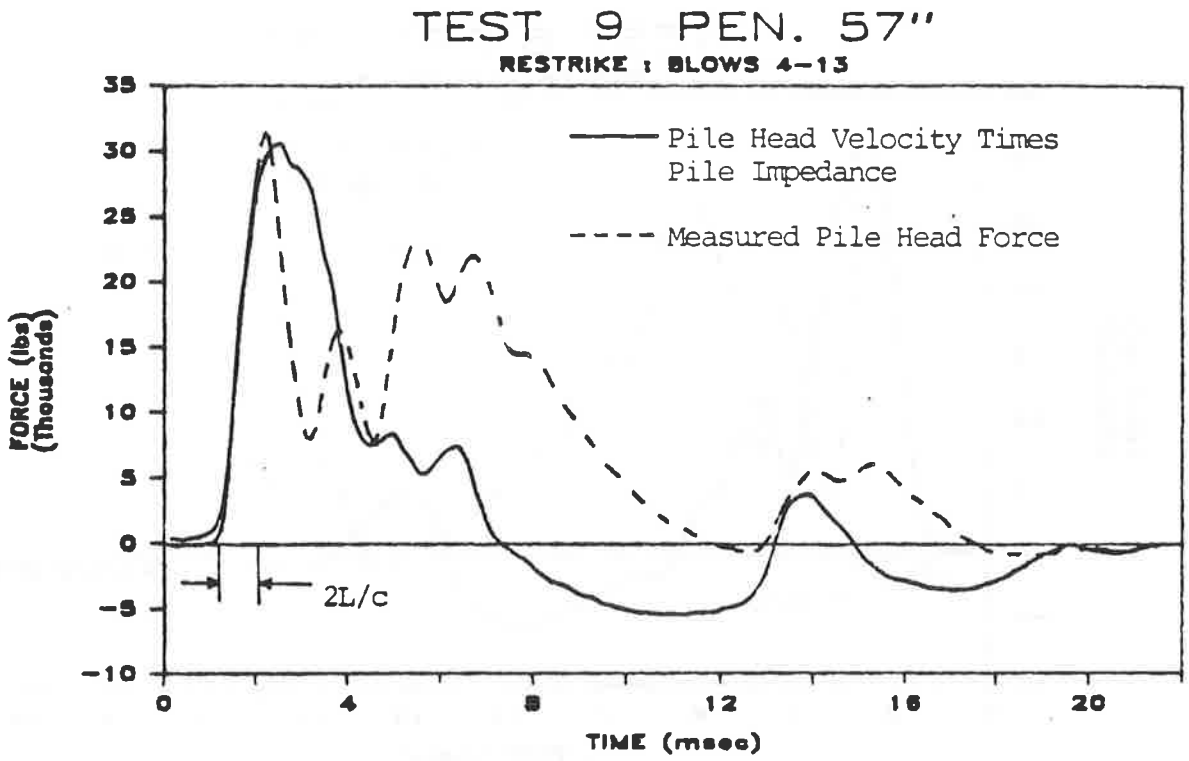

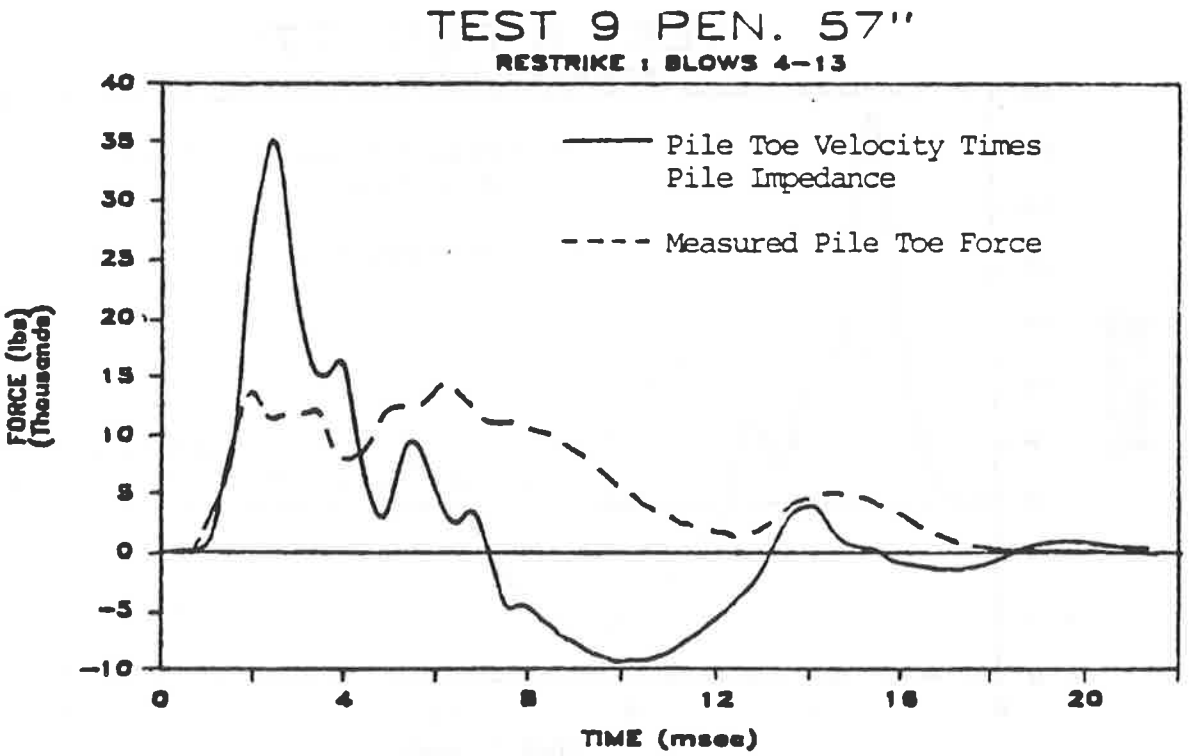

Fig. N.4. Measured Head and Toe Force and Velocity-Impedance Time Histories; Restrike at Full Penetration; Test No. 9 (SJR Sand; 90% Rel. Den.; 20 psi Press.)

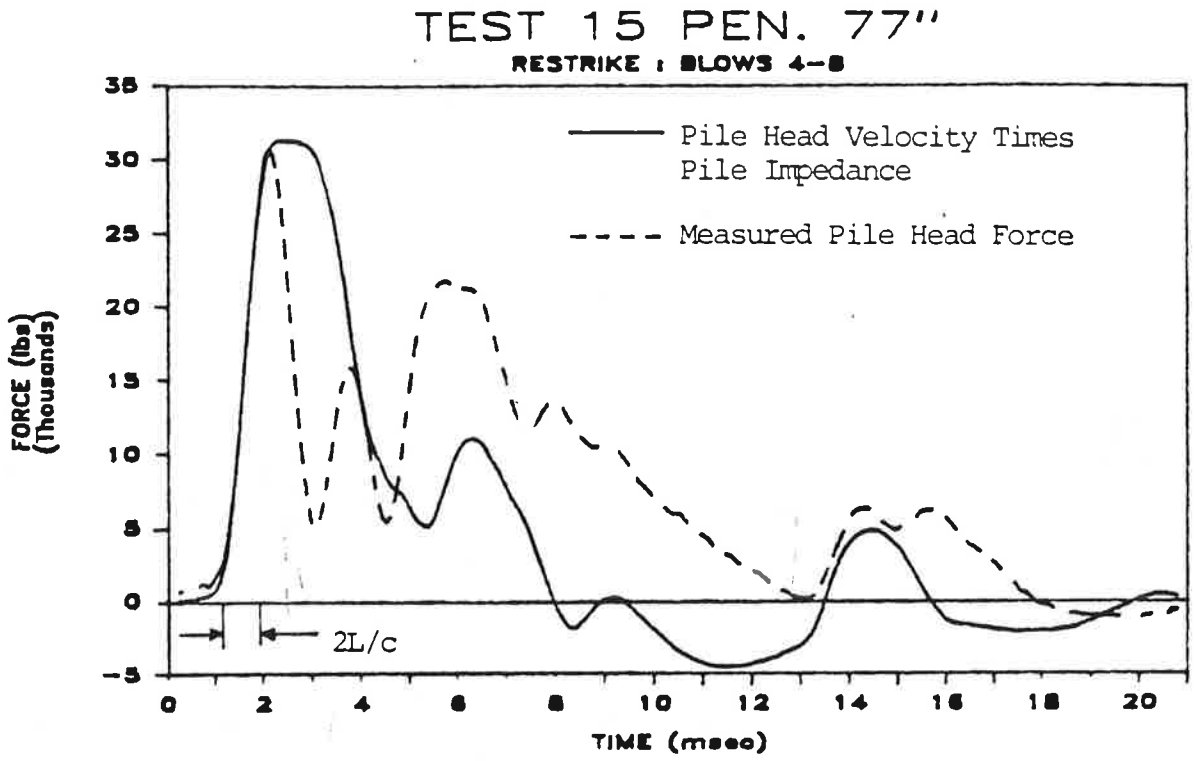

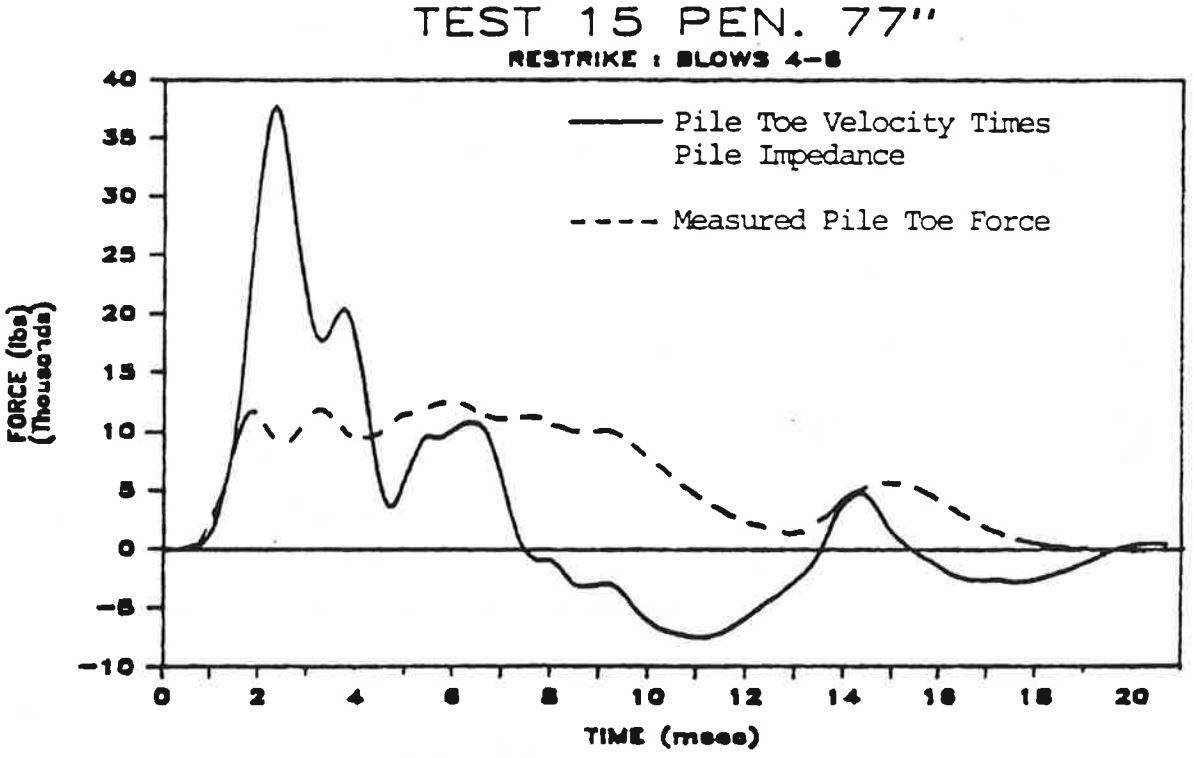

Fig. N.5. Measured Head and Toe Force and Velocity-Impedance Time Histories; Restrike at Full Penetration; Test No. 15 (BLS Sand; 90% Rel. Den.; 10 psi Press.)

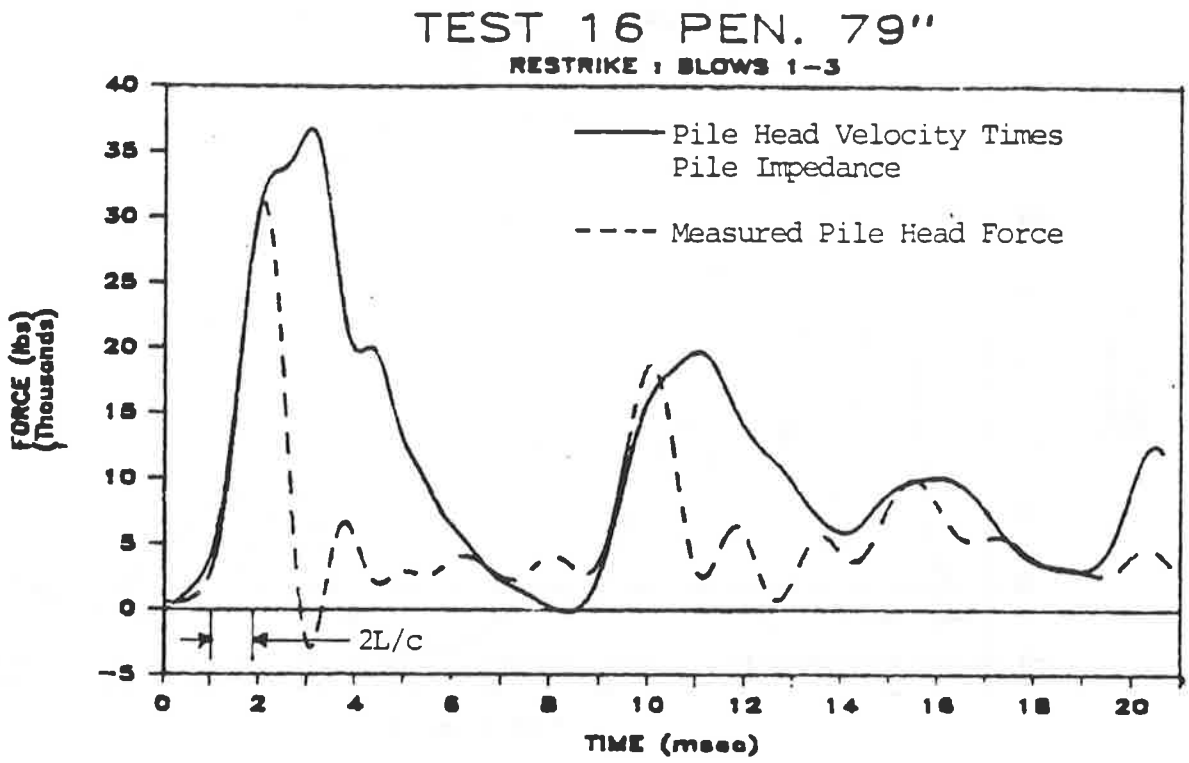

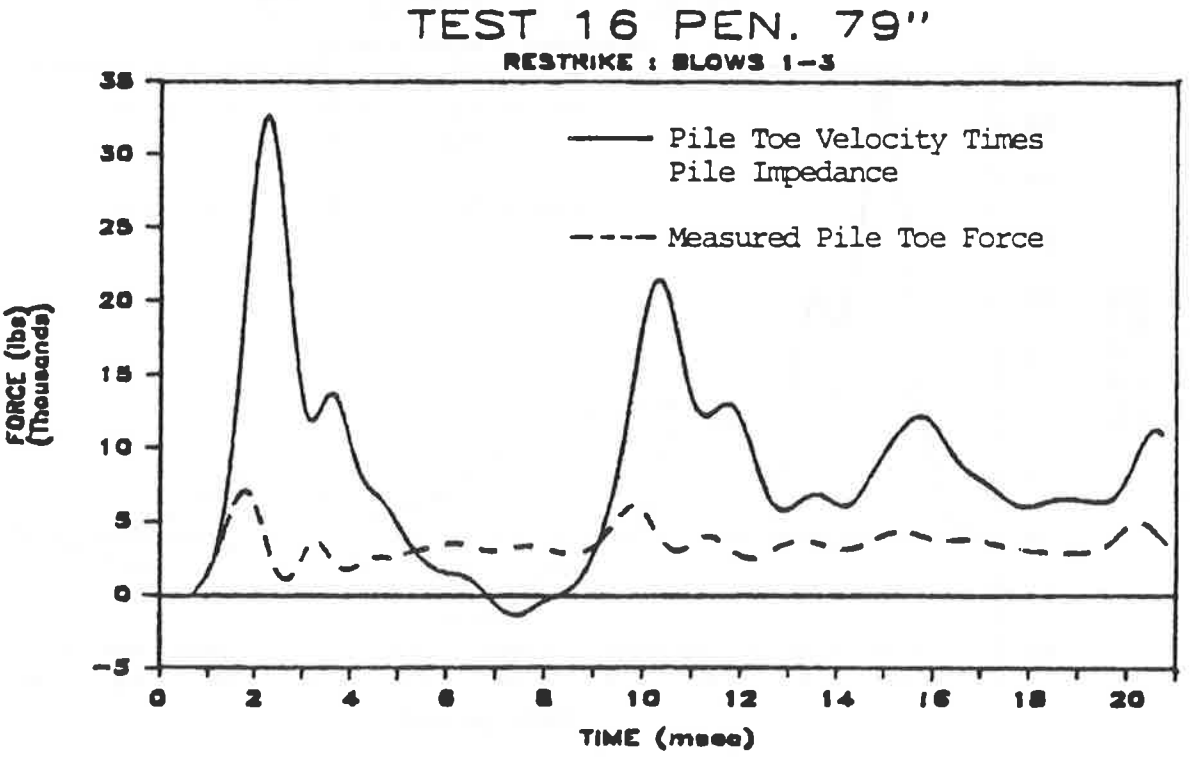

Fig. N.6. Measured Head and Toe Force and Velocity-Impedance Time Histories; Restrike at Full Penetration; Test No. 16 (BLS Sand; 65% Rel. Den.; 10 psi Press.)

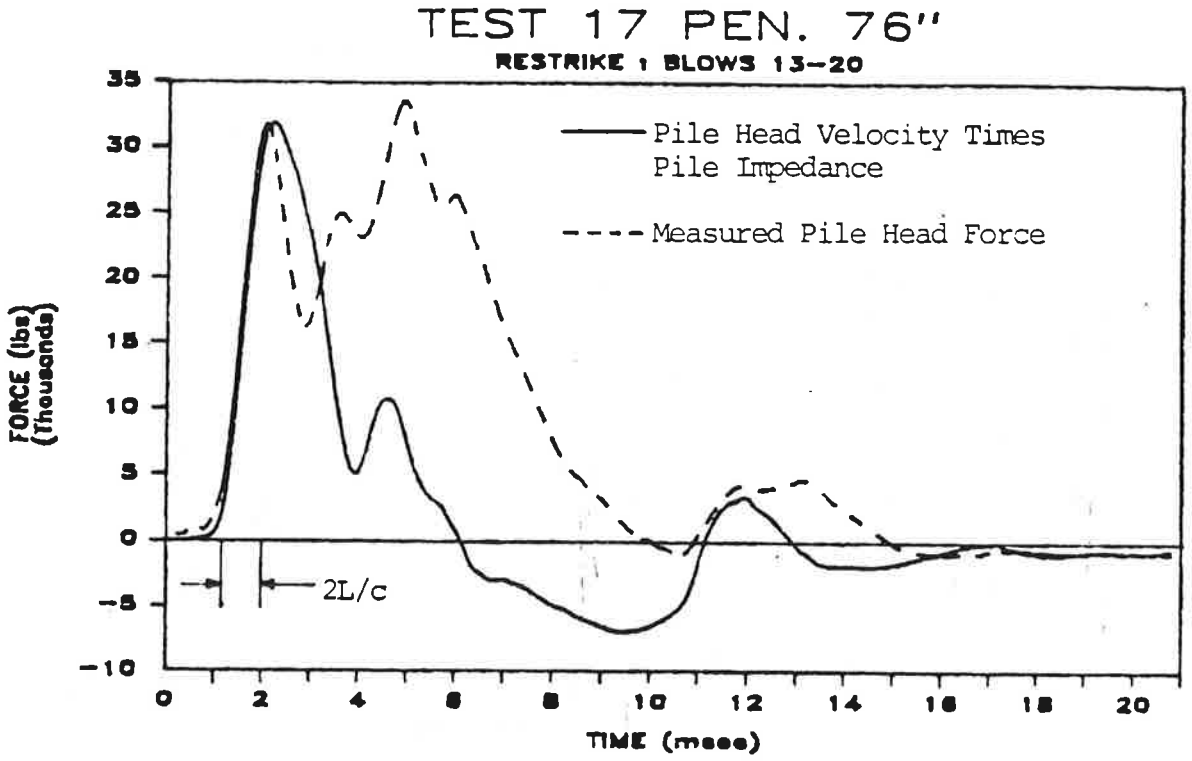

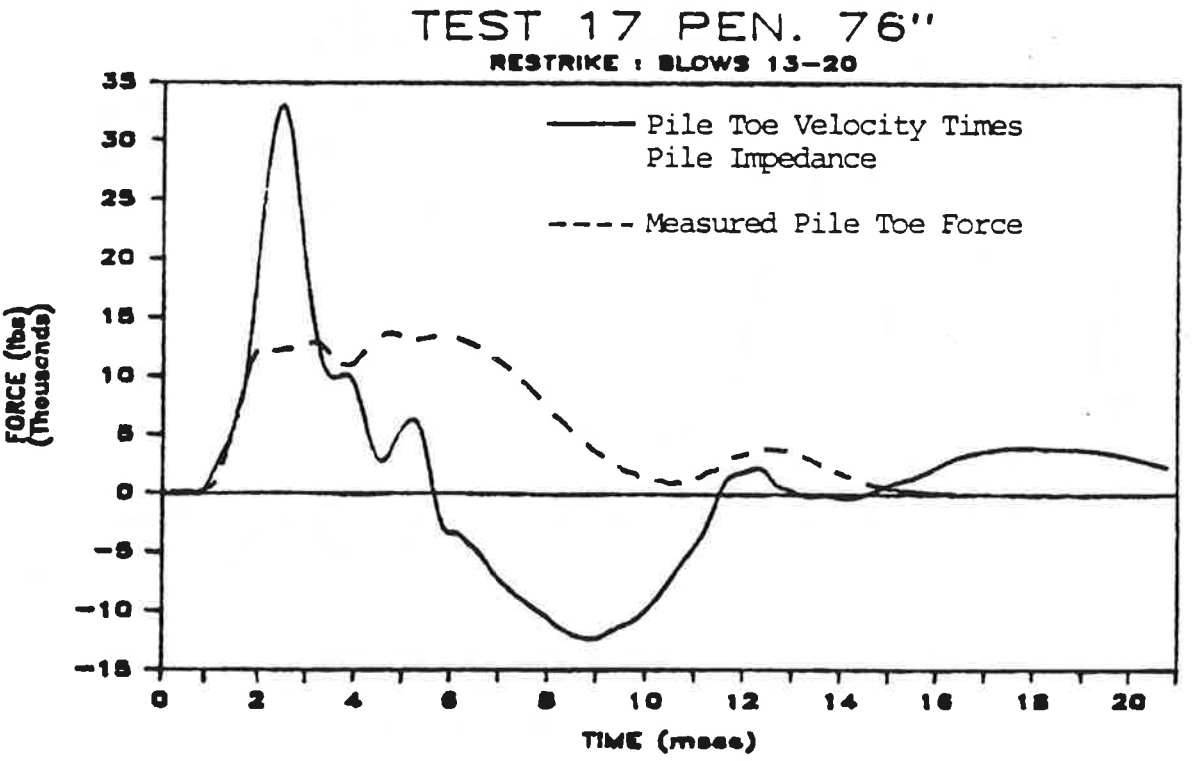

Fig. N.7. Measured Head and Toe Force and Velocity-Impedance Time Histories; Restrike at Full Penetration; Test No. 17 (BLS Sand; 90% Rel. Den.; 20 psi Press.)

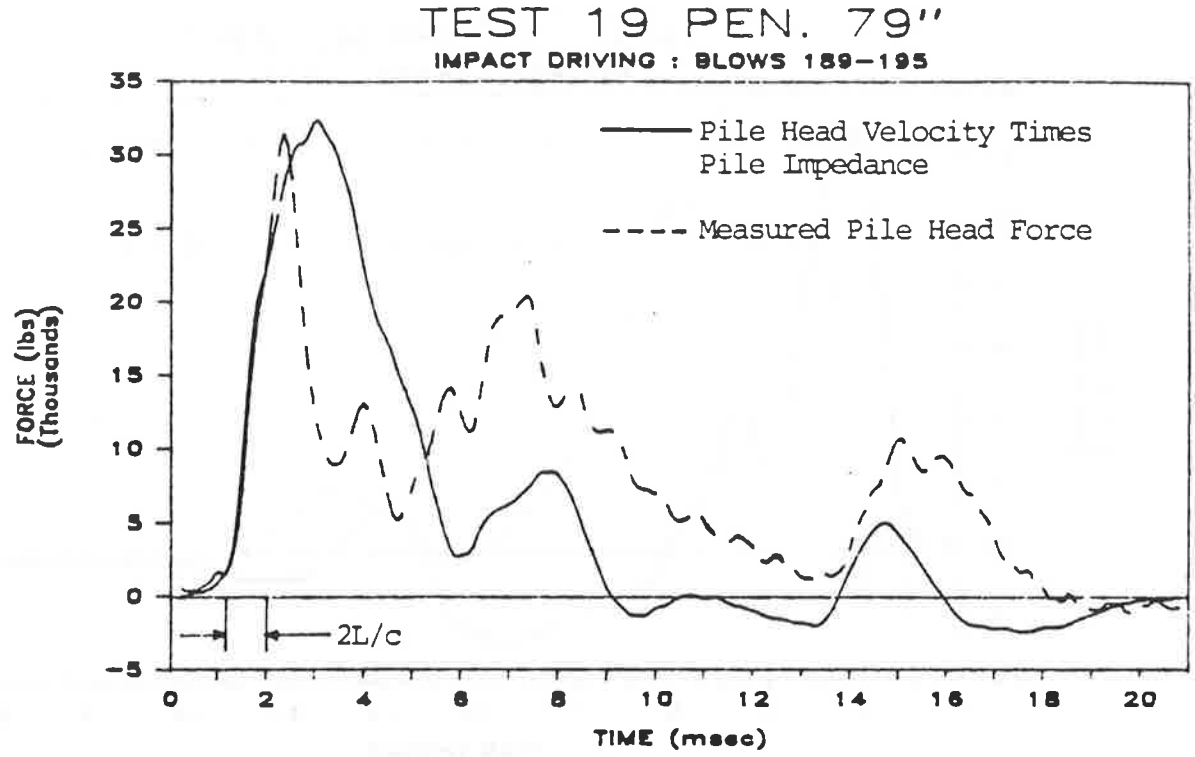

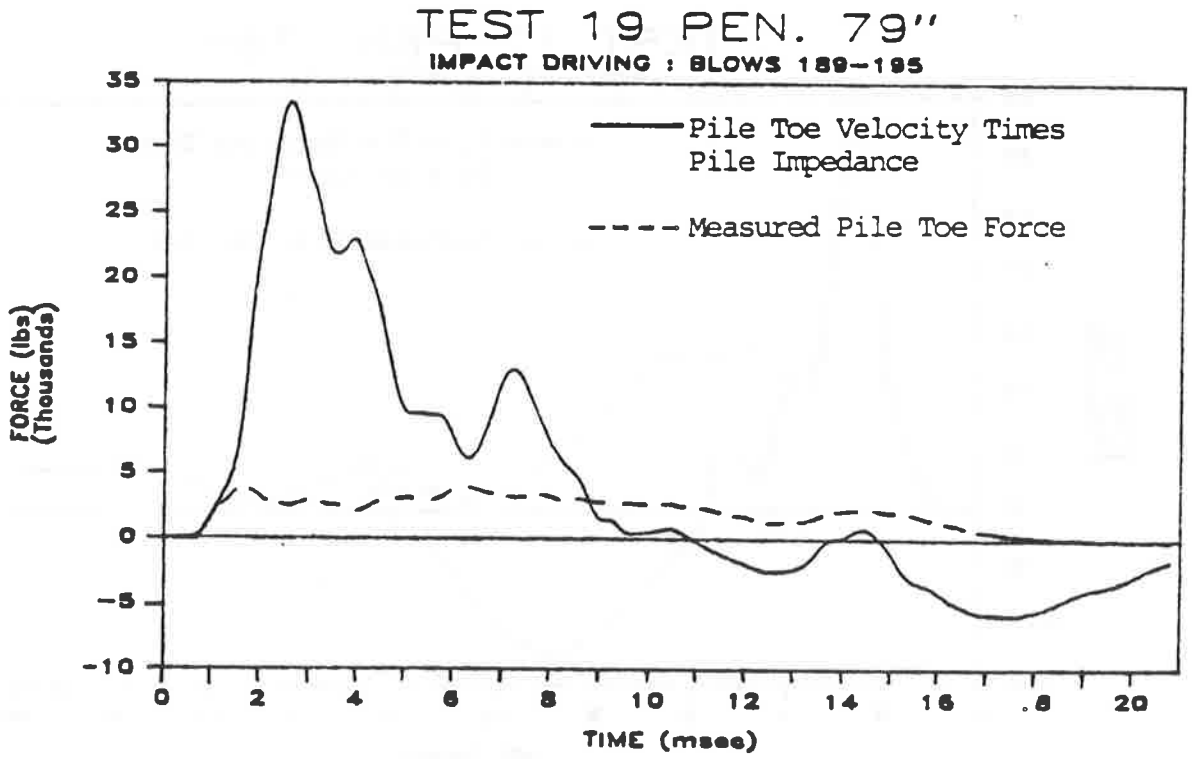

Fig. N.8. Measured Head and Toe Force and Velocity-Impedance Time Histories; Impact-Driving at Full Penetration; Test No. 19 (BLS Sand; 90% Rel. Den.; 10 psi Press.)

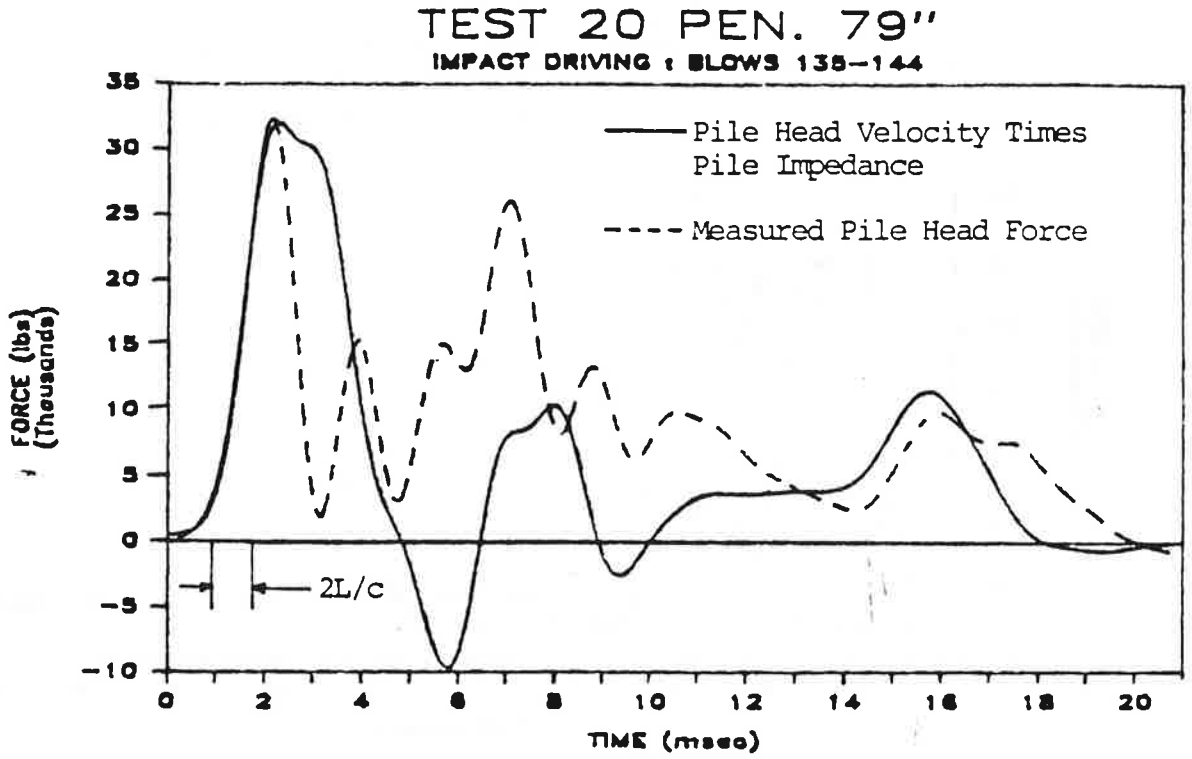

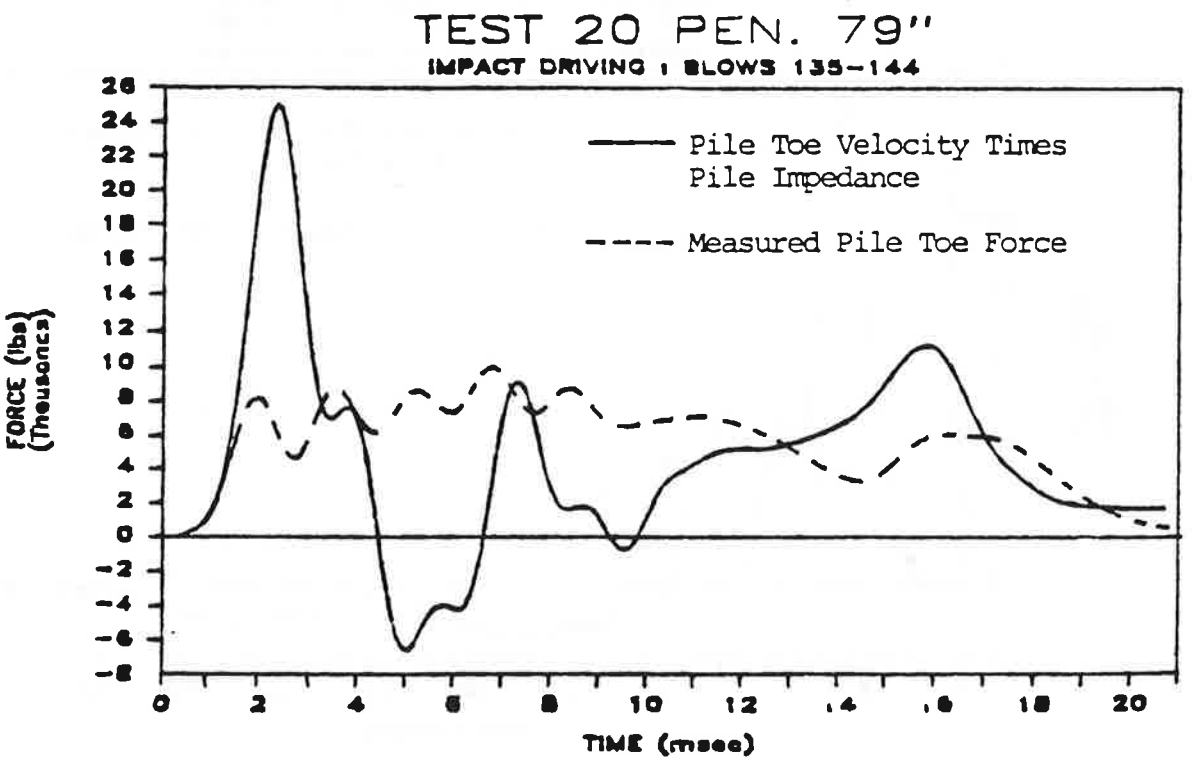

Fig. N.9. Measured Head and Toe Force and Velocity-Impedance Time Histories; Impact-Driving at Full Penetration; Test No. 20 (BLS Sand; 65% Rel. Den.; 10 psi Press.)

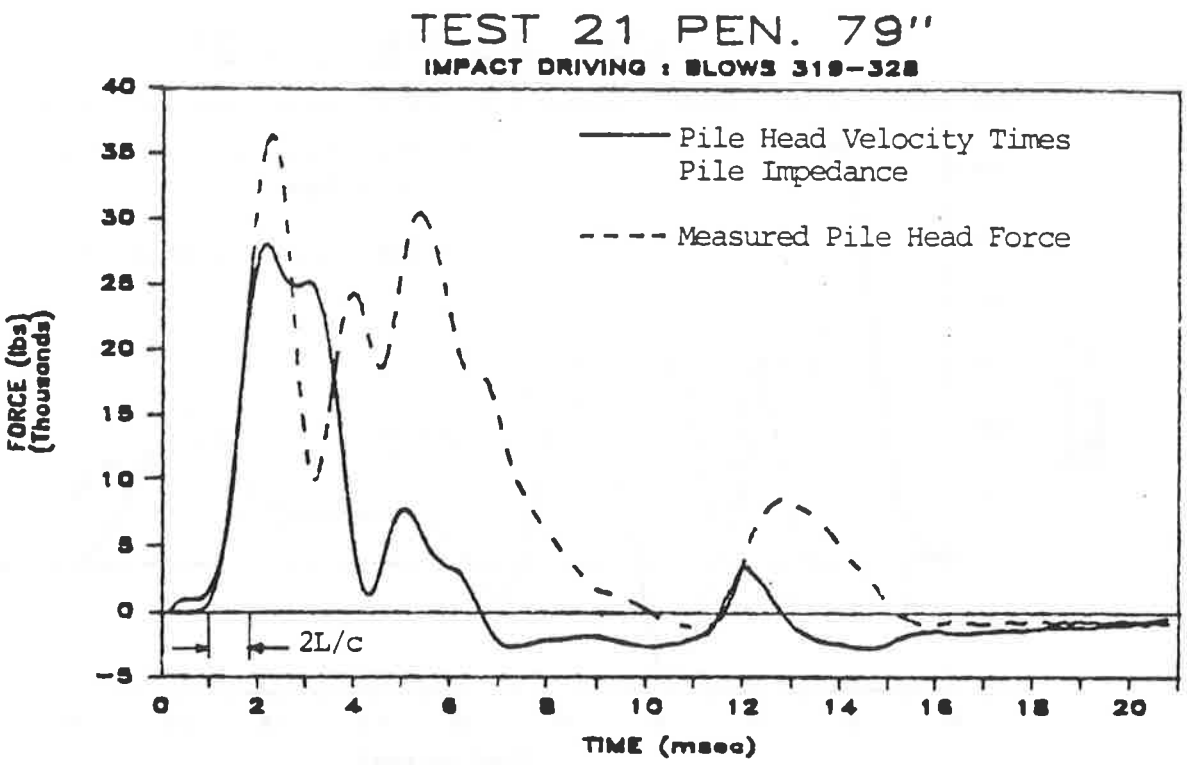

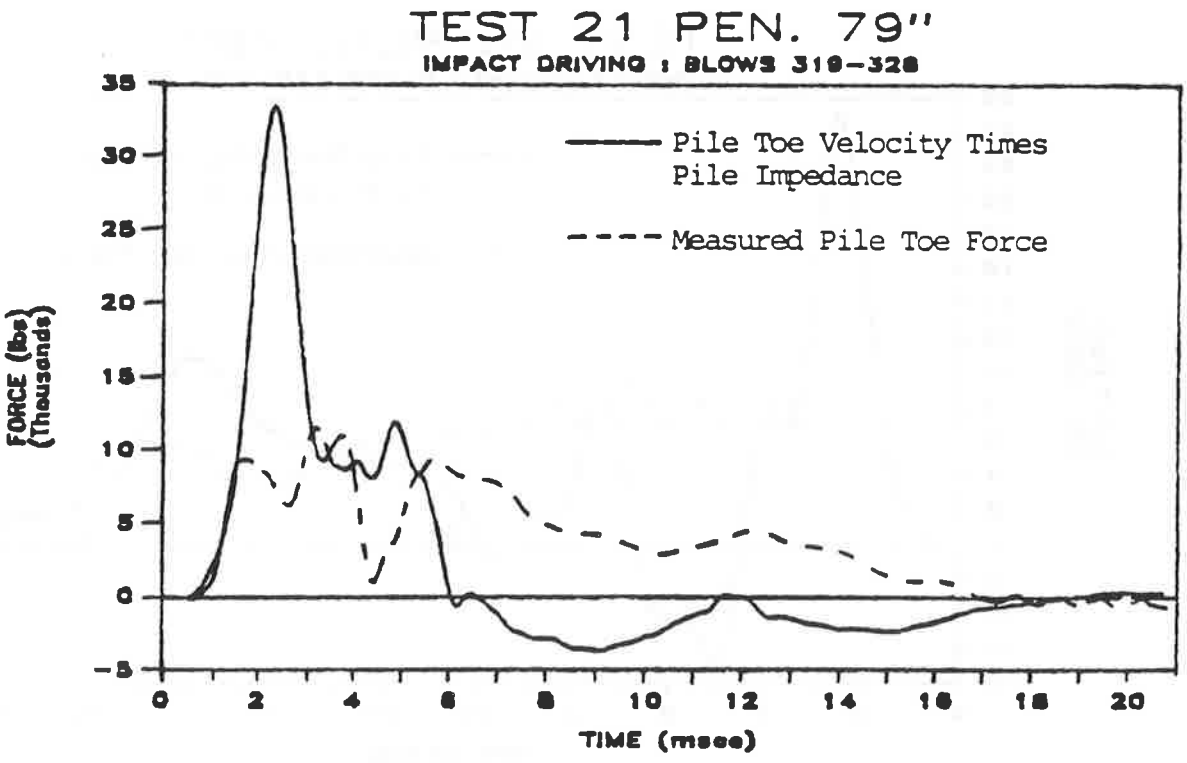

Fig. N.10. Measured Head and Toe Force and Velocity-Impedance Time Histories; Impact-Driving at Full Penetration; Test No. 21 (BLS Sand; 90% Rel. Den.; 20 psi Press.)

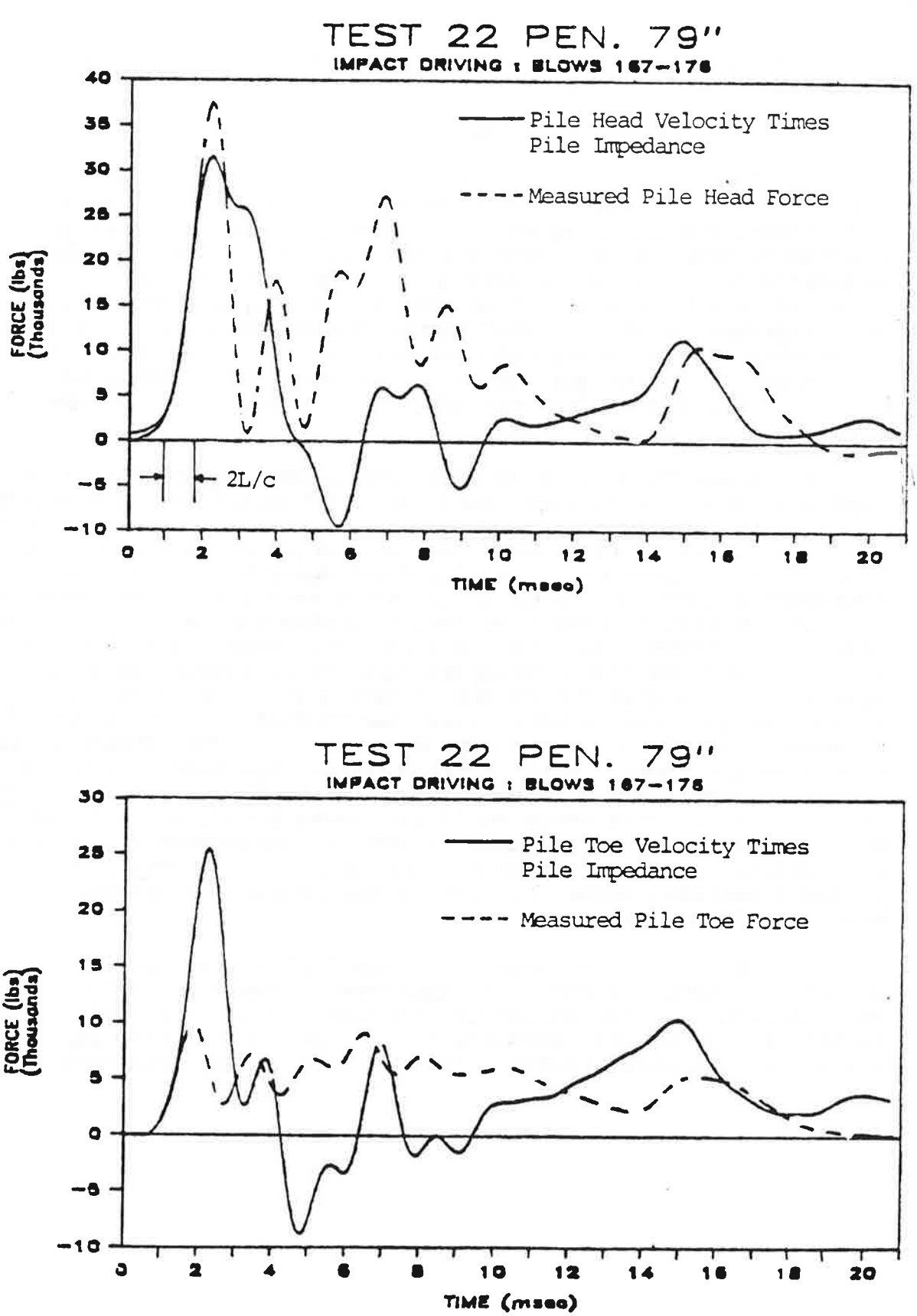

Fig. N.11. Measured Head and Toe Force and Velocity-Impedance Time Histories; Impact-Driving at Full Penetration; Test No. 22 (BLS Sand; 90% Rel. Den.; 10 psi Press.)

reflected back to the transducers at the head. The value of 2L/c for the very short test pile was approximately 0.80 milliseconds.

Several observations can be made from Figs. N.1 - N.11:

1. The force and velocity-impedance traces at the pile head depart from each other at a time of 2L/c from the time of initial rise, with the force generally dropping off more rapidly than the velocity-impedance, indicating that the returning tension wave is reaching the head of the pile before the maximum compression force would have been achieved had the pile been considerably longer. This behavior is not consistent with the behavior of relatively longer piles in the field but is generally consistent among all of the tests conducted in this study, which suggests that conclusions drawn regarding the relative effects of impact driving versus restriking are valid. The consistent time of initial departure of the two traces from one another also suggests that neither impact driving nor vibratory driving had produced drastically different values of static shaft resistance.

2. A relatively strong second positive peak occurs in the force trace and in the velocity-impedance trace at the pile head 3.0 to 4.9 milliseconds after the initial peaks produced by the impact of the ram. These times correlate closely to the times that are required for a compression (p) wave to travel down the pile, through the soil below the pile toe and be reflected back to the toe and up the pile, based on the soil moduli measured in the resonant column test (Appendix I). For the piles installed by vibration, the second peak occurs at a time lapse that is about double that which is computed using the shear moduli from the resonant column test at a shear strain magnitude of 10^{-2}% for the situations in which the relative density was 65% and the effective lateral confining pressure was 10 psi (Figs. N.2 and N.6). Otherwise the lapses for the vibro-driven piles computed using shear moduli at a shear strain magnitude of 10^{-2}% are within 5 to 10 percent of those that are obtained from the time histories. This behavior suggests either a possible loosening effect, generation of very high mean soil strains, or installation-induced reduction in effective soil stress below the pile toe for the conditions of 65% relative density and 10 psi effective lateral pressure, but not for other test conditions. For the impact-driven pile tests, the observed time lapse was always 20% to 40% greater than the computed value, which suggests that one of the phenomena speculated above occurred for all impact-driven piles, regardless of soil density or confining pressure.

3. Under similar soil conditions the peak toe forces were generally similar, regardless of whether the piles were impact-driven or vibro-driven, although some differences in the wave forms are observed. For example, Figs. N.1 and N.11, N.2 and N.9, and N.4 and N.10, and N.5 and N.8 can be compared. This observation suggests that there were no large effects of method of installation on toe capacity during driving.

APPENDIX O

One-Dimensional Wave Equation Analysis

One-dimensional wave equation analyses were employed to attempt to ascertain whether differences could be observed in wave equation parameters for piles that were driven by impact and those that were driven by vibration with restriking. This activity was accomplished primarily with a digital computer program entitled TOPDRIVE, which back-computed the various soil parameters.

Brief Description of the TOPDRIVE Algorithm

The TOPDRIVE algorithm used for back-computing the soil characteristics for impact and restrike tests is based on a finite difference solution to the one-dimensional wave equation, specifically on the version developed by the Texas Transportation Institute (TTI) (23). The program incorporates all of the assumptions in the TTI algorithm and models the soil according to the E. A. L. Smith elastic-plastic representation with velocity-independent viscous damping constants. The soil is thus characterized by a maximum static shaft resistance, a maximum static toe resistance, a shaft quake (Q_s) (yield point), a toe quake (Q_p), a value of shaft damping (J_s), a value of toe damping (J_p) and a ratio of toe resistance to total resistance (R_p/R_T). The pile is characterized by elastic stiffness (EA), length, number of increments (for numerical computation purposes), weight of each increment, circumferential distance around the pile, and cross-sectional area. The weight of the increment representing the part of the pile nearest the toe was increased in this study to account for the added weight of the toe load cell (approximately 8 lb). The shaft resistance may vary in any prescribed manner from head to toe. No plastic offsets (allowances of pile movement before any soil resistance is achieved) are included.

The input forcing function is a force time series, applied at the top of the pile, in place of the usual driving mechanism (e. g., ram impact velocity, weight and cushion and helmet properties). The input function for this study is a force time series measured by strain gage level 1 (averaged over several blows). The static and dynamic soil reactions, pile forces, displacements and velocities are computed at prescribed time steps. When the program-computed integration time step is smaller than the time step of the input force time series at the pile head, the input forces are interpolated linearly with respect to time.

For any given set of soil inputs and distributions of pile stiffness and mass, the following information is output:

a. Permanent set of the pile head,

b. Velocity and force time histories at any pile segment (viz., velocity at the pile head, velocity at the pile toe, and force at the pile toe, which were compared with measurements),

c. Maximum forces and displacements at all pile segments.

Fifteen pile segments were used in the calculations described in this report, and the wave equation computations were stopped (pile permanent set achieved) when the pile

head motion stopped (20 to 25 msec after initial impact). This involved the use of several times the number of time steps normally used in a wave equation analysis. No residual forces were considered in the analyses described, so the back-computed values of quake, damping and resistance ratio must be considered appropriate for the condition of an assumed initially stress-free pile. This condition, while not theoretically correct, is the condition most often assumed in practice.

Values of the soil parameters were varied systematically, and the results (pile-head and toe velocity, pile-toe force, and permanent set) were compared with measured values in order to arrive at the set of soil parameters that most closely satisfied the three time histories described above and the permanent set. This variation was accomplished by making separate runs with numerous combinations of the parameters and comparing the output with the physical measurements manually.

Optimization Study

Tests 9 (vibration with restrike), 17 (vibration with restrike), 21 (impact) and 22 (impact)were studied using TOPDRIVE. It was assumed initially that the shaft resistance was uniform with depth, a reasonable assumption based on analysis of the static test data in Appendix Q. Shaft and toe quake, shaft and toe damping and shaft and toe static resistance were varied, and pile-head set, and pile-head velocity, pile-toe velocity and pile-toe force traces were computed and compared with measured values until an optimum set of inputs was found. The results are summarized in Tables O.1 - O.4, in which only the maximum velocities and force outputs are given. Graphs of the velocity and force traces, both computed and measured, are compared in Figs. O.1 - O.8 for the set of parameters that were selected as optimum. Because the test pile was very short and wave return times could not be scaled, very complex force and velocity traces developed once the reflected tension wave began interfering with the incident compression wave. In fact, it appears that the incident compression wave was not fully developed at the pile head before effects of the return wave were felt. For that reason, emphasis was placed on matching measured and computed wave forms for the first 3 to 4 milliseconds after impact, where pile velocities were highest. [The time required for a stress wave to travel down the pile and return (2 X pile length / compression wave velocity in steel) was about 0.8 milliseconds.] The comparisons of measured and computed wave forms should be considered satisfactory for the case of the very short pile utilized in this study. Further discussions of the force and velocity wave forms for the pile under impact loading are provided in Appendix N.

For Tests 21 and 22, solutions from program WEAP 86 (24), an FHWA-standard program for analysis of pile driving, were also obtained with the optimum set of input parameters derived from TOPDRIVE and are compared with the measured traces and with TOPDRIVE solutions in Figs. O.5 - O.8. It was necessary to input the ram weight and drop height that produced the same energy that was measured at the pile head into WEAP 86, resulting in a hammer efficiency of approximately 85%, rather than measured pile-head force-time history, the stiffness of the plywood cushion (1100 k/inch, as measured in static tests on the plywood cushion) and the coefficient of restitution for the cushion recommended by Goble and Rausche (24) (0.50). Therefore, the boundary conditions for the two solutions were not identical, and identical results were not obtained. However, the results compared well enough to provide confidence that results obtained using TOPDRIVE could be applied to WEAP 86.

The computed results that are presented in this appendix are filtered with a digital filter to remove the effect of mathematical noise that may have resulted from

Trial Values						Computed Values			
Q(s) (in.)	Q(p) (in.)	J(s) (sec/ft)	J(p) (sec/ft)	Toe Resistance (k)	Total Resistance (k)	Set (in.)	V max. Pile Head (ft/sec)	V max. Pile Toe (ft/sec)	F max. Pile Toe (k)
0.10	0.10	0.10	0.15	14	26	0.0089	9.65	8.54	22.23
0.10	0.10	0.10	0.15	14	21	0.0267	10.26	9.30	26.15
0.10	0.10	0.10	0.15	10	18	0.0613	10.35	9.94	20.51
0.10	0.10	0.10	0.10	10	18	0.085	10.43	10.42	17.46
0.10	0.08	0.10	0.10	10	18	0.065	10.29	9.93	20.51
0.10	0.08	0.10	0.10	8	16	0.105	10.43	10.42	17.46
0.08	0.08	0.10	0.10	8	16	0.154	10.14	10.06	15.66
0.06	0.08	0.10	0.10	8	16	0.238	9.71	10.07	13.39
0.08	0.08	0.08	0.10	8	16	0.170	10.26	10.30	15.98
0.08	0.06	0.10	0.10	8	16	0.099	9.98	9.42	19.28
0.08	0.08	0.10	0.08	8	16	0.170	10.16	10.28	14.44
0.08	0.08	0.10	0.10	6	16	0.154	9.92	10.01	12.00
0.08	0.08	0.10	0.10	8	14	0.257	10.52	10.74	16.52
0.08	0.08	0.08	0.08	8	16	0.190	10.29	10.54	14.73
0.06	0.06	0.10	0.10	8	16	0.158	9.59	9.41	16.34
0.06	0.06	0.08	0.08	8	16	0.191	9.74	9.95	15.43
0.06	0.06	0.10	0.10	7	15	0.201	9.65	9.73	14.89
0.06	0.06	0.07	0.07	8	16	0.213	9.81	10.24	14.94
0.06	0.06	0.07	0.07	4	12	0.571	10.11	11.57	9.53
0.04	0.04	0.07	0.07	8	16	0.213	9.05	9.57	15.36
0.04	0.04	0.07	0.07	8	18	0.145	8.69	8.80	15.84
0.05	0.04	0.07	0.07	8	18	0.113	9.02	8.63	17.11
0.04	0.04	0.06	0.07	8	18	0.153	8.76	8.99	14.97
0.04	0.04	0.06	0.06	8	18	0.159	8.77	9.11	14.92
*0.03	*0.03	*0.06	*0.06	*8	*18	0.167	8.26	8.66	14.52
0.03	0.03	0.06	0.06	8	19	0.146	8.09	8.29	14.30
0.03	0.03	0.07	0.07	8	19	0.132	8.01	7.99	14.67
0.03	0.03	0.07	0.07	8	18	0.152	8.18	8.36	14.91
0.03	0.04	0.06	0.06	8	18	0.226	8.36	9.26	12.10
0.03	0.04	0.06	0.06	8	19	0.184	8.18	8.37	11.92
				Measured Values:		0.153	7.62	9.31	14.49

* Selected Parameters

Computed values have time-domain records filtered with A = 0.90

Table O.1. Parameters for Trial Solutions Using TOPDRIVE; Test No. 9

Trial Values						Computed Values			
Q(s) (in.)	Q(p) (in.)	J(s) (sec/ft)	J(p) (sec/ft)	Toe Resistance (k)	Total Resistance (k)	Set (in.)	V max. Pile Head (ft/sec)	V max. Pile Toe (ft/sec)	F max. Pile Toe (k)
0.10	0.10	0.10	0.15	20	43	-0.025	7.70	6.45	18.86
0.10	0.10	0.10	0.15	20	35	-0.012	8.49	7.27	23.45
0.10	0.10	0.10	0.15	15	30	-0.021	8.60	7.86	19.75
0.10	0.10	0.10	0.10	15	30	0.0034	8.63	8.25	17.43
0.10	0.10	0.10	0.10	12	25	0.057	8.98	8.99	16.15
0.10	0.10	0.08	0.10	12	25	0.069	9.15	9.21	16.88
0.08	0.10	0.08	0.10	12	25	0.113	8.73	8.69	14.82
0.08	0.10	0.08	0.08	12	25	0.128	8.74	8.85	14.14
0.08	0.08	0.08	0.08	12	25	0.079	8.66	8.47	16.38
0.08	0.10	0.08	0.08	12	27	0.067	8.45	8.48	13.27
0.08	0.10	0.08	0.08	11	25	0.120	8.62	8.80	13.10
0.09	0.10	0.08	0.08	12	25	0.102	8.97	9.15	15.08
0.07	0.10	0.08	0.08	12	25	0.159	8.47	8.50	13.13
0.08	0.11	0.08	0.08	12	25	0.148	8.77	9.01	13.48
0.08	0.10	0.09	0.08	12	25	0.117	8.65	8.73	14.02
0.08	0.10	0.07	0.08	12	25	0.141	8.83	8.99	14.28
*0.08	*0.10	*0.09	*0.07	*12	*25	0.125	8.66	8.81	13.82
0.08	0.10	0.09	0.06	12	25	0.125	8.66	8.41	13.82
0.08	0.10	0.09	0.07	11	25	0.115	8.53	8.74	12.81
0.08	0.10	0.09	0.07	11	24	0.151	8.68	8.94	13.19
0.08	0.10	0.09	0.07	11	23	0.191	8.84	9.16	13.60
0.04	0.10	0.09	0.07	12	25	0.261	7.31	7.53	9.23
0.04	0.04	0.09	0.07	12	25	0.072	7.08	5.84	16.88
0.08	0.04	0.09	0.07	12	25	0.041	8.29	7.03	24.85
0.08	0.10	0.04	0.07	12	25	0.202	9.15	9.51	14.56
0.08	0.10	0.04	0.04	12	25	0.261	9.18	9.83	13.89
0.08	0.10	0.09	0.04	12	25	0.146	8.67	9.04	13.16
0.08	0.04	0.04	0.04	12	25	0.056	8.72	7.90	25.27
0.04	0.04	0.04	0.04	12	25	0.132	7.61	7.21	16.17
				Measured Values:		0.120	7.95	8.75	13.80

* Selected Parameters

Computed values have time-domain records filtered with A = 0.90

Table O.2. Parameters for Trial Solutions Using TOPDRIVE; Test No. 17

Trial Values						Computed Values			
Q(s) (in.)	Q(p) (in.)	J(s) (sec/ft)	J(p) (sec/ft)	Toe Resistance (k)	Total Resistance (k)	Set (in.)	V max. Pile Head (ft/sec)	V max. Pile Toe (ft/sec)	F max. Pile Toe (k)
0.10	0.10	0.10	0.15	14	32	0.003	9.25	8.36	19.61
0.10	0.10	0.10	0.15	8	25	0.031	9.55	9.50	13.94
0.10	0.10	0.10	0.15	6	23	0.053	9.61	9.92	11.06
0.10	0.10	0.10	0.10	6	23	0.063	9.63	10.19	10.16
0.10	0.08	0.10	0.10	6	23	0.063	9.58	9.92	11.31
0.08	0.08	0.10	0.10	6	23	0.066	9.09	9.17	10.22
0.06	0.08	0.10	0.10	6	23	0.079	8.41	8.18	8.86
0.06	0.06	0.10	0.10	6	23	0.071	8.37	7.88	10.29
0.06	0.06	0.08	0.10	5	22	1.057	8.60	8.45	9.54
0.06	0.04	0.08	0.10	5	22	0.085	8.52	7.93	12.43
0.06	0.04	0.08	0.08	5	22	0.088	8.53	8.06	11.56
0.04	0.04	0.08	0.08	5	22	1.083	7.68	7.38	9.72
0.04	0.04	0.08	0.08	5	21	0.138	7.85	7.73	10.05
*0.04	*0.04	*0.07	*0.08	*5	*21	0.157	7.97	8.07	10.01
0.04	0.04	0.07	0.07	4	21	0.156	7.84	7.99	8.62
0.04	0.04	0.06	0.07	4	21	0.174	7.97	8.29	8.86
0.04	0.04	0.06	0.06	4	21	0.179	7.97	8.35	8.64
0.04	0.06	0.06	0.06	4	21	0.218	8.03	8.73	7.28
0.03	0.05	0.06	0.06	5	22	0.195	7.48	8.12	8.05
0.05	0.03	0.06	0.06	5	22	0.097	8.30	7.82	12.60
0.03	0.03	0.10	0.08	4	20	0.142	7.13	7.01	8.98
0.04	0.04	0.10	0.08	4	20	0.145	7.66	7.49	8.48
				Measured Values:		0.142	6.98	8.82	10.28

* Selected Parameters

Computed values have time-domain records filtered with A = 0.90

Table O.3. Parameters for Trial Solutions Using TOPDRIVE; Test No. 21

Trial Values						Computed Values			
Q(s) (in.)	Q(p) (in.)	J(s) (sec/ft)	J(p) (sec/ft)	Toe Resistance (k)	Total Resistance (k)	Set (in.)	V max. Pile Head (ft/sec)	V max. Pile Toe (ft/sec)	F max. Pile Toe (k)
0.10	0.10	0.15	0.15	6	22	0.024	8.63	8.07	10.34
0.08	0.08	0.10	0.10	6	22	0.057	8.57	8.19	10.44
0.08	0.08	0.10	0.10	5	20	0.076	8.85	8.77	9.55
0.08	0.08	0.10	0.08	5	17	0.122	9.60	10.09	9.88
0.06	0.06	0.10	0.08	5	17	0.135	8.83	9.32	10.20
0.06	0.06	0.10	0.06	5	17	0.141	8.86	9.49	9.53
0.06	0.04	0.10	0.06	4	15	0.166	9.06	9.67	10.94
0.06	0.04	0.10	0.06	4	13	0.221	9.72	10.73	11.59
0.04	0.04	0.10	0.06	4	13	0.265	9.12	10.65	9.48
0.04	0.02	0.10	0.06	4	13	0.190	8.51	9.20	14.05
*0.02	0.02	0.10	0.06	4	13	0.309	7.88	9.61	9.56
0.02	0.02	0.12	0.06	4	13	0.275	7.63	9.16	9.37
0.01	0.01	0.10	0.06	3	11	0.435	7.83	10.10	8.57
0.02	0.02	0.06	0.03	5	16	0.269	7.64	9.41	9.79
				Measured Values:		0.312	7.84	8.52	9.88

* Selected Parameters

Computed values have time-domain records filtered with A = 0.95

Table O.4. Parameters for Trial Solutions Using TOPDRIVE; Test No. 22

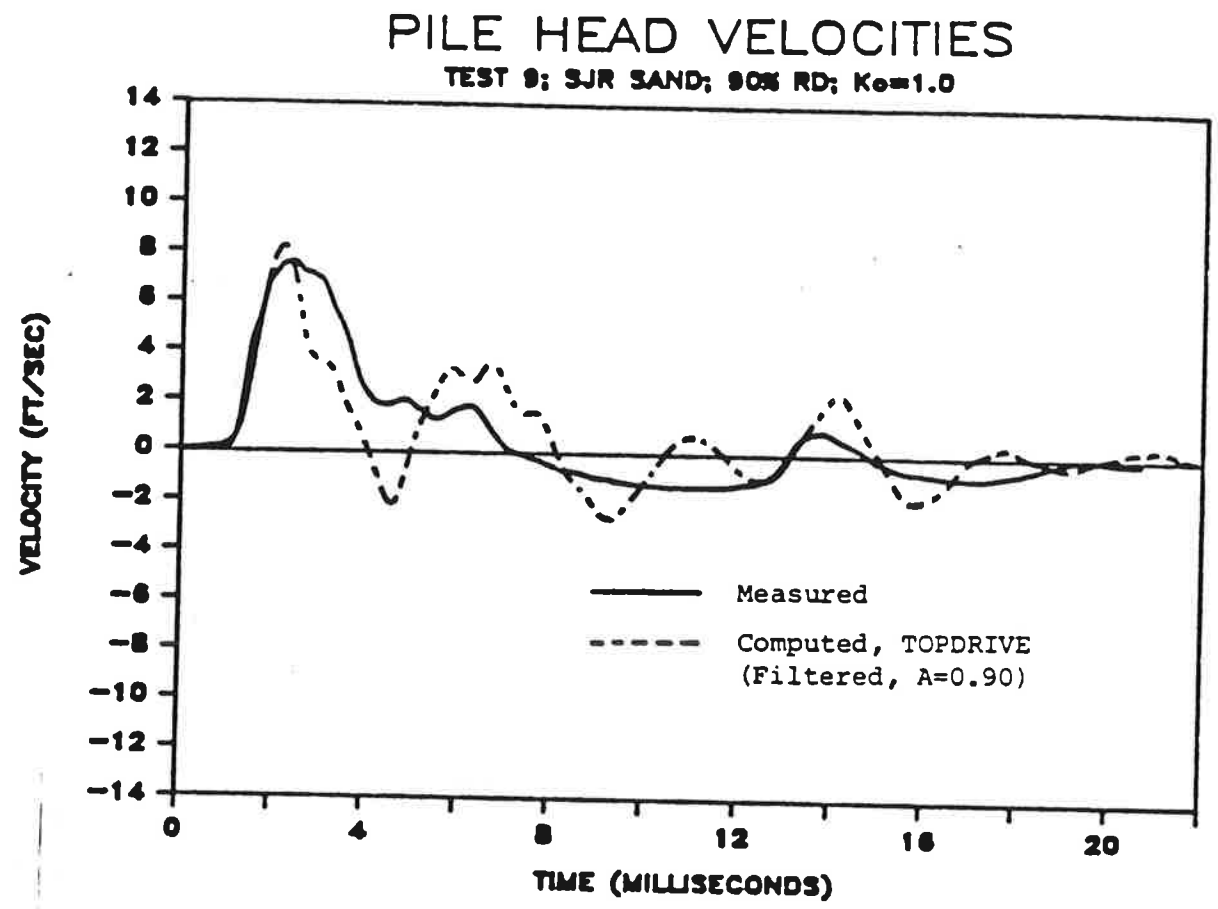

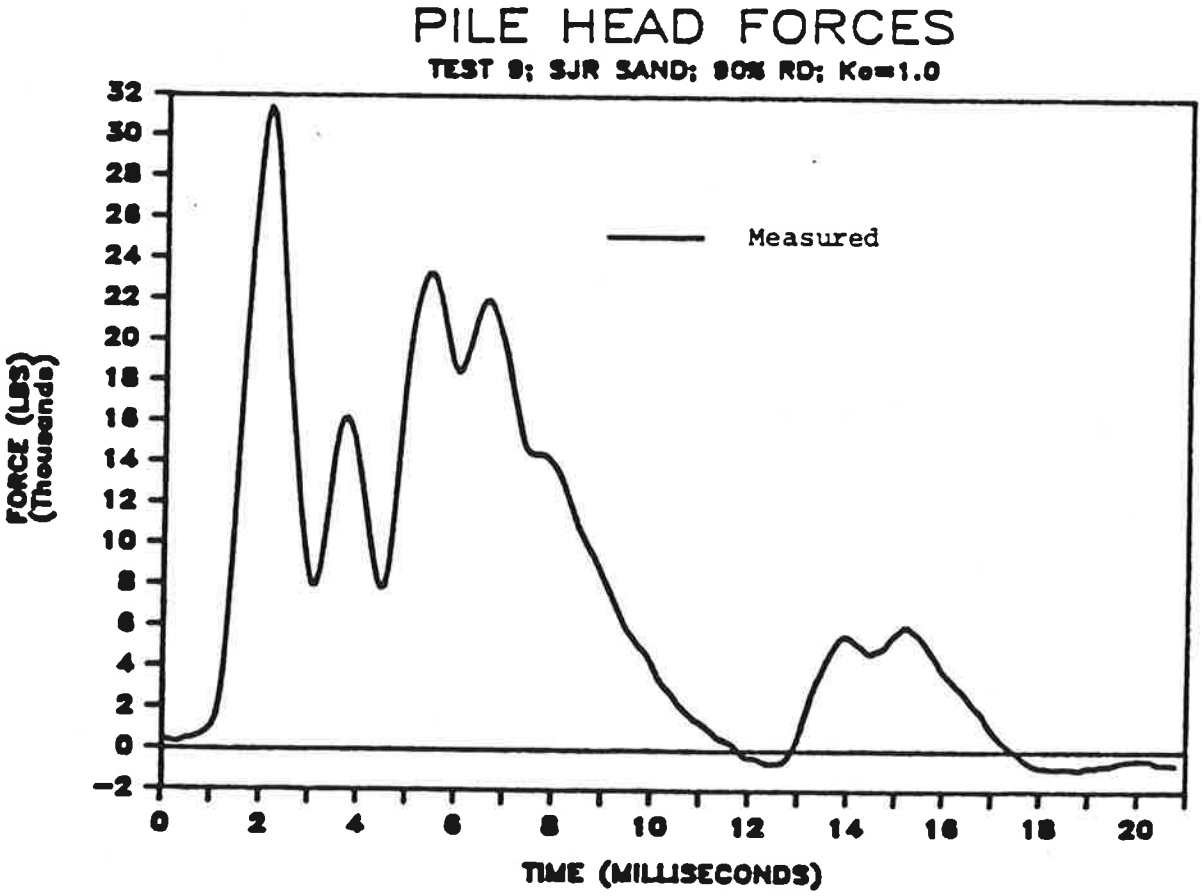

Fig. O.1. Measured and Computed Pile-Head Velocities and Forces; Test No. 9

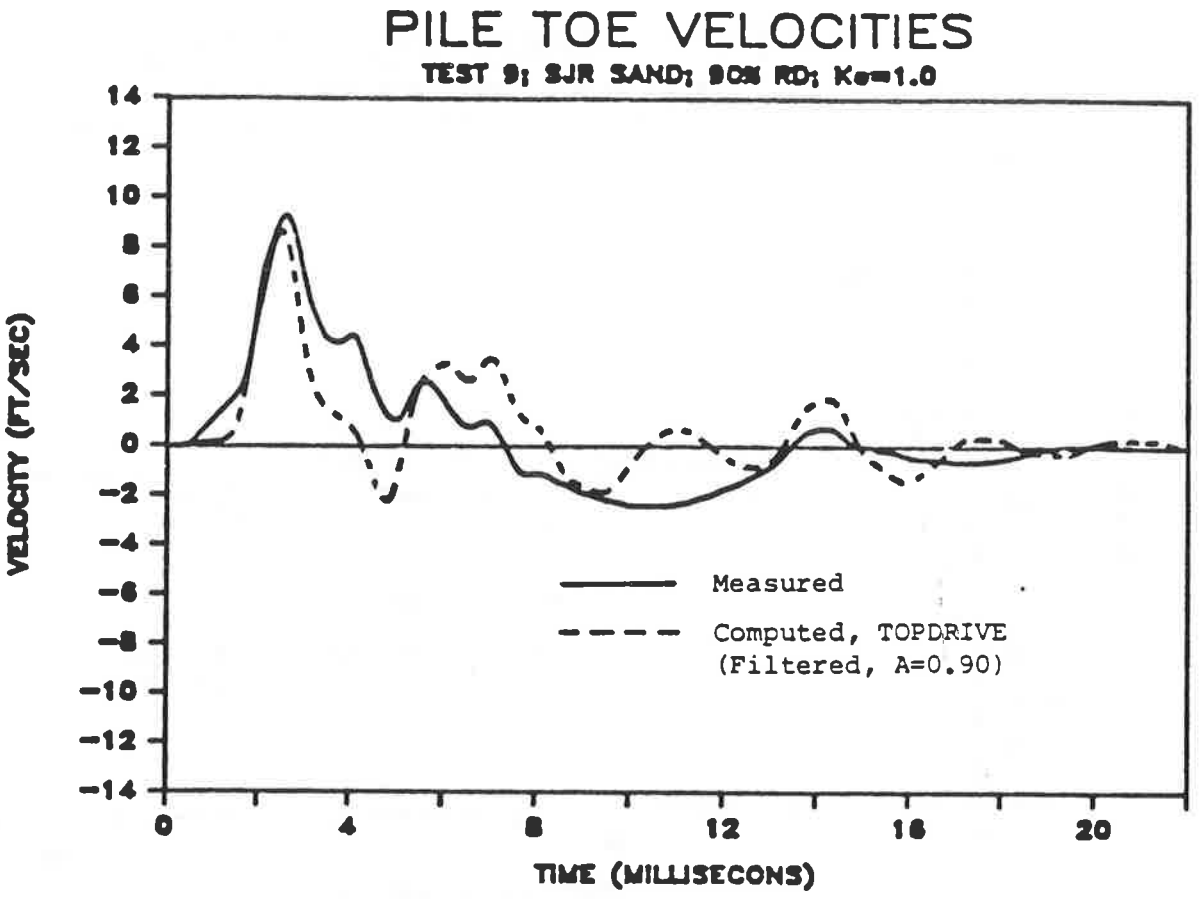

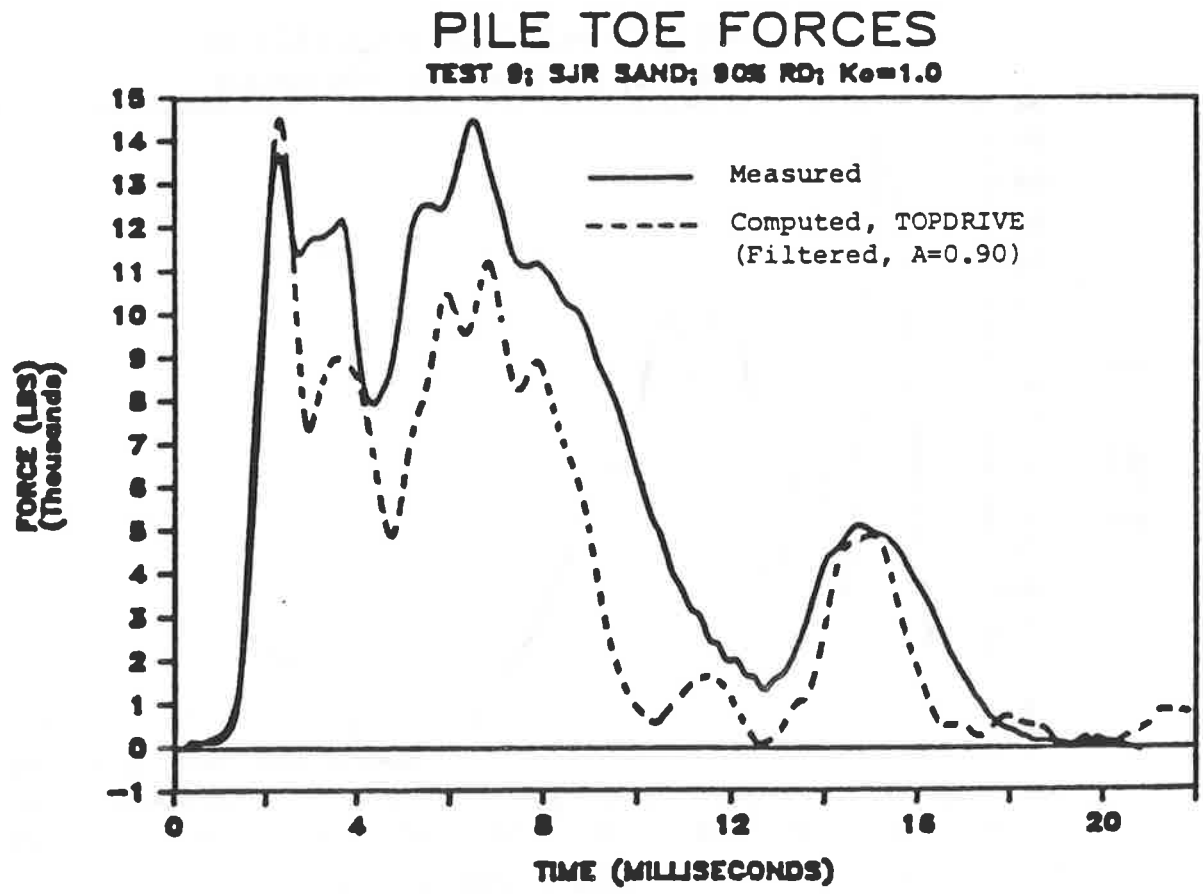

Fig. O.2. Measured and Computed Pile-ToeVelocities and Forces; Test No. 9

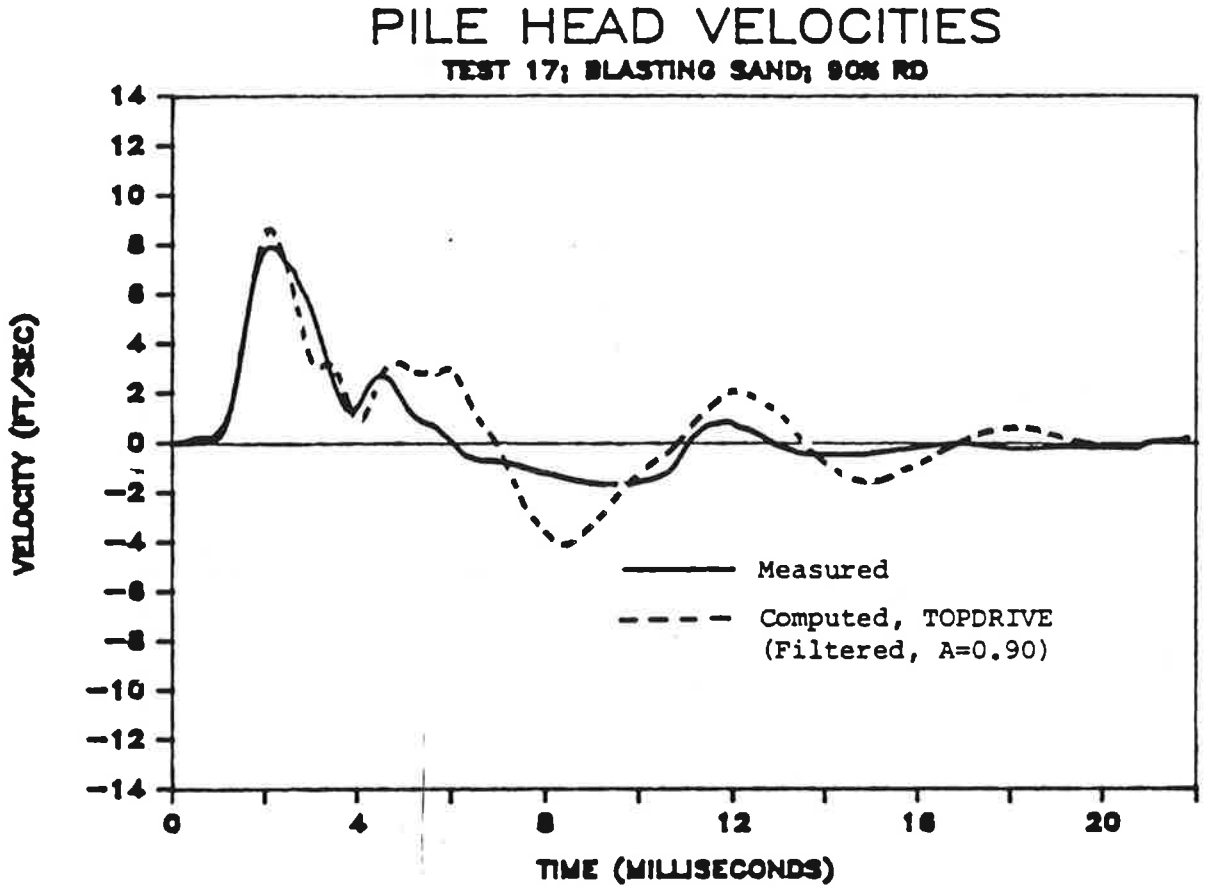

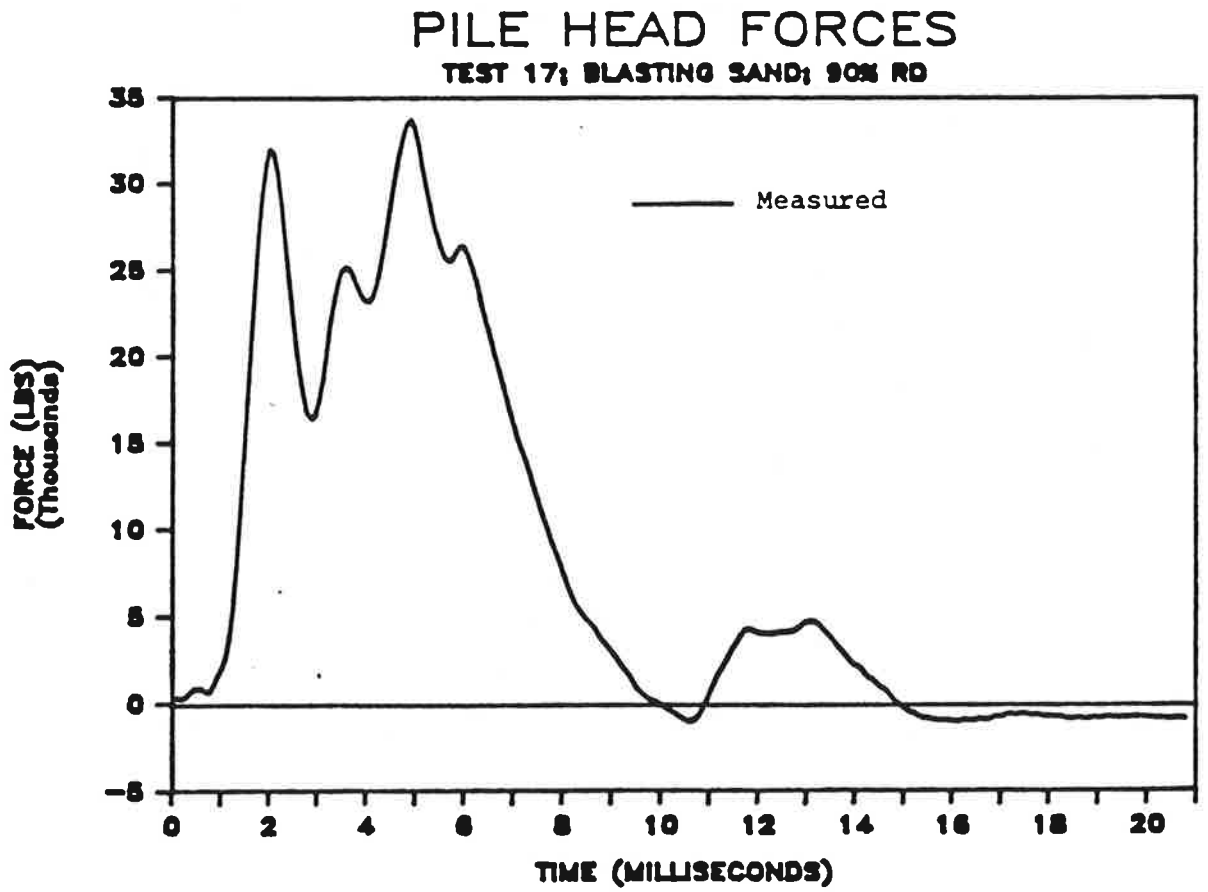

Fig. O.3. Measured and Computed Pile-Head Velocities and Forces; Test No. 17

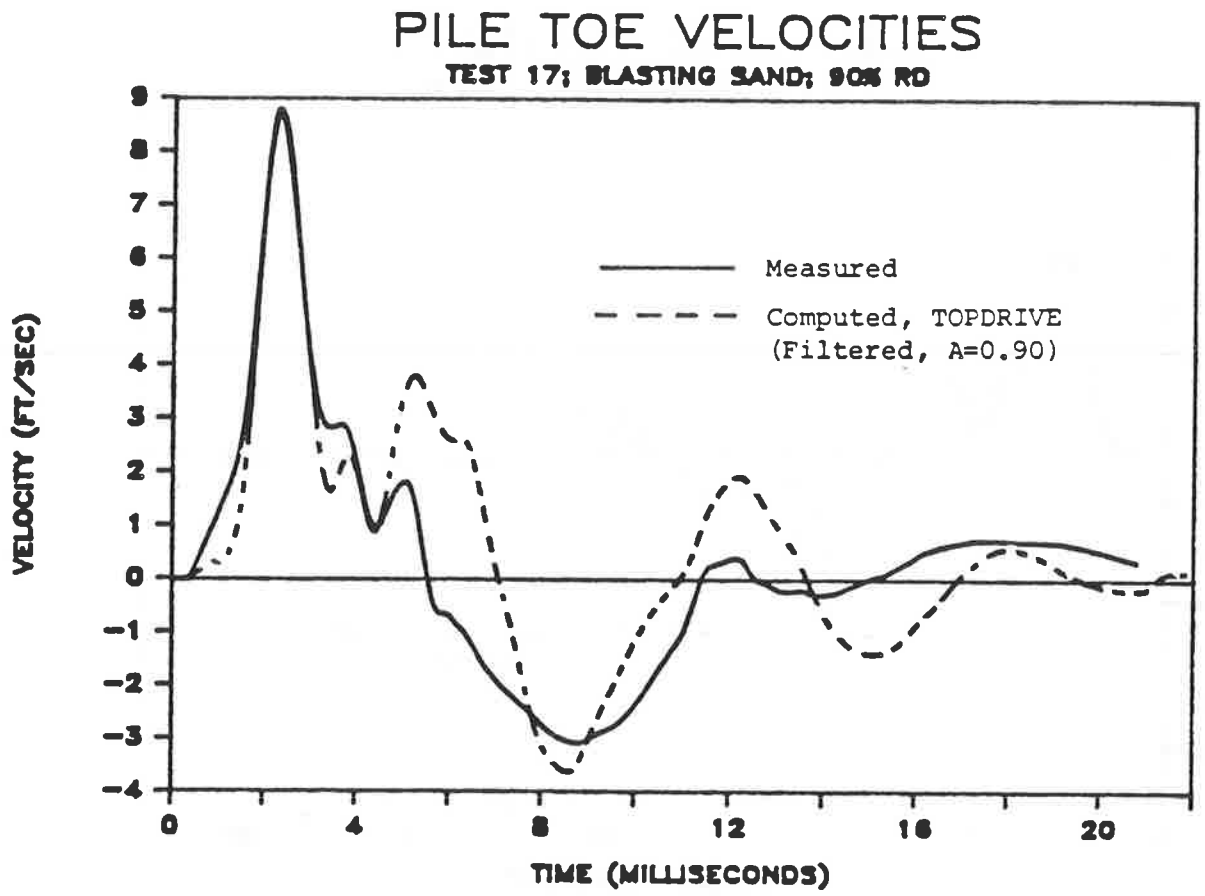

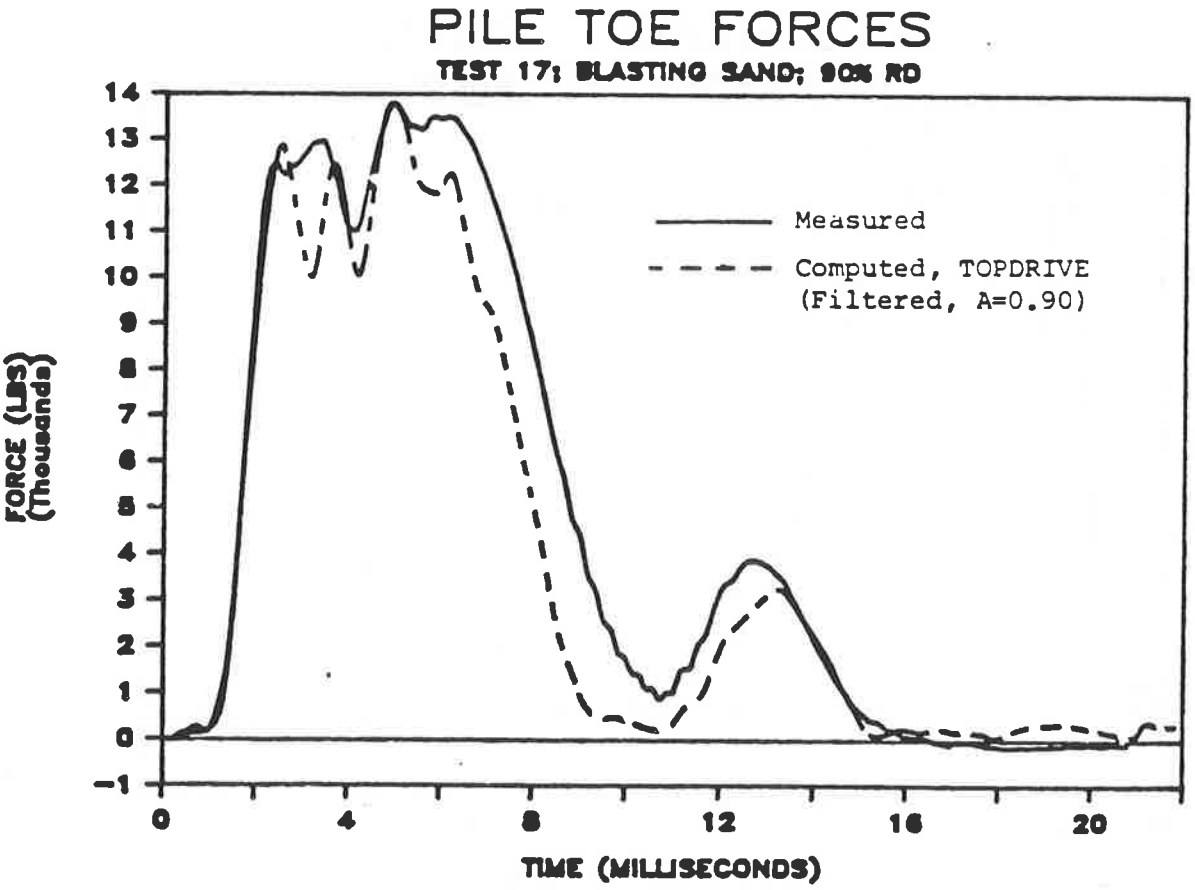

Fig. O.4. Measured and Computed Pile-ToeVelocities and Forces; Test No. 17

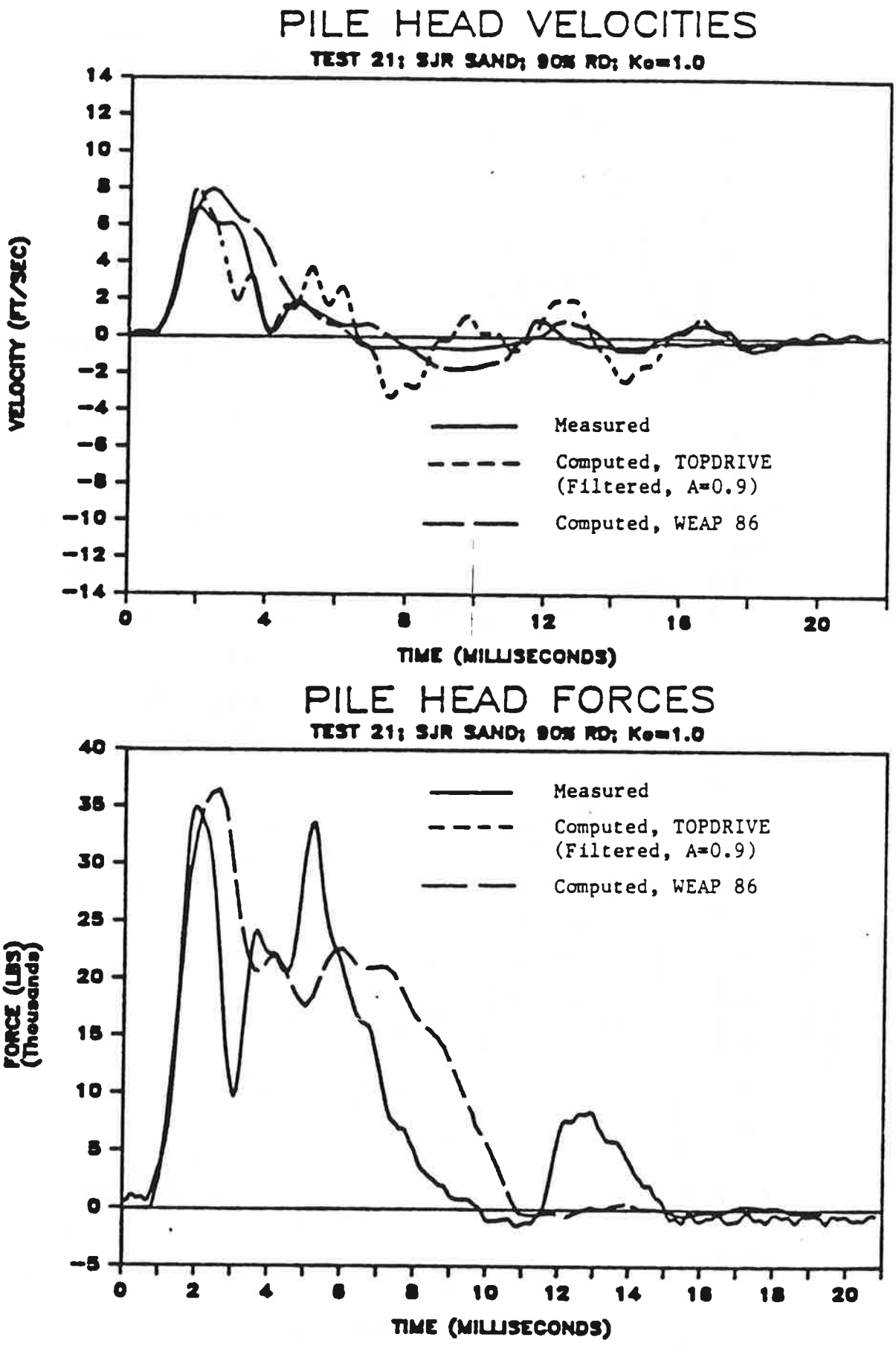

Fig. O.5. Measured and Computed Pile-Head Velocities and Forces; Test No. 21

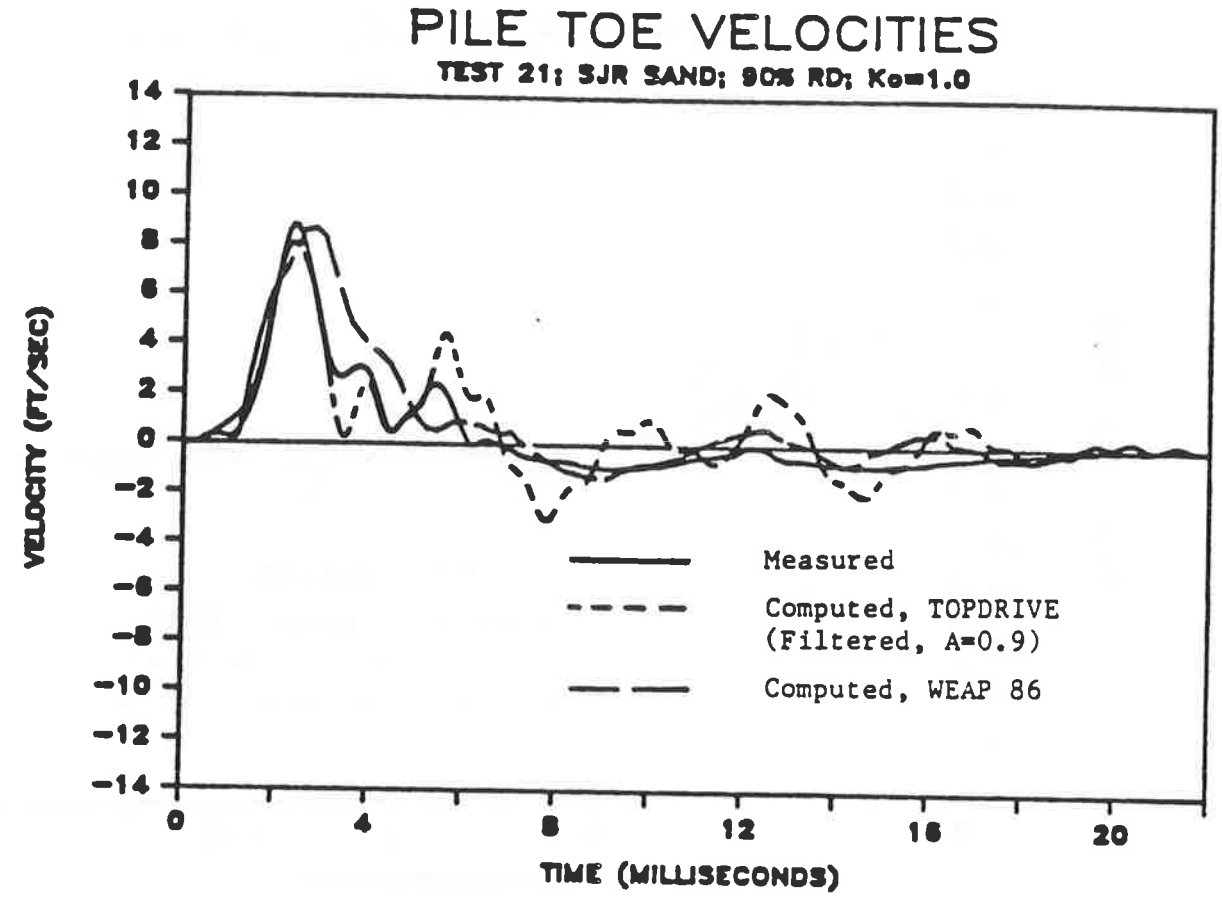

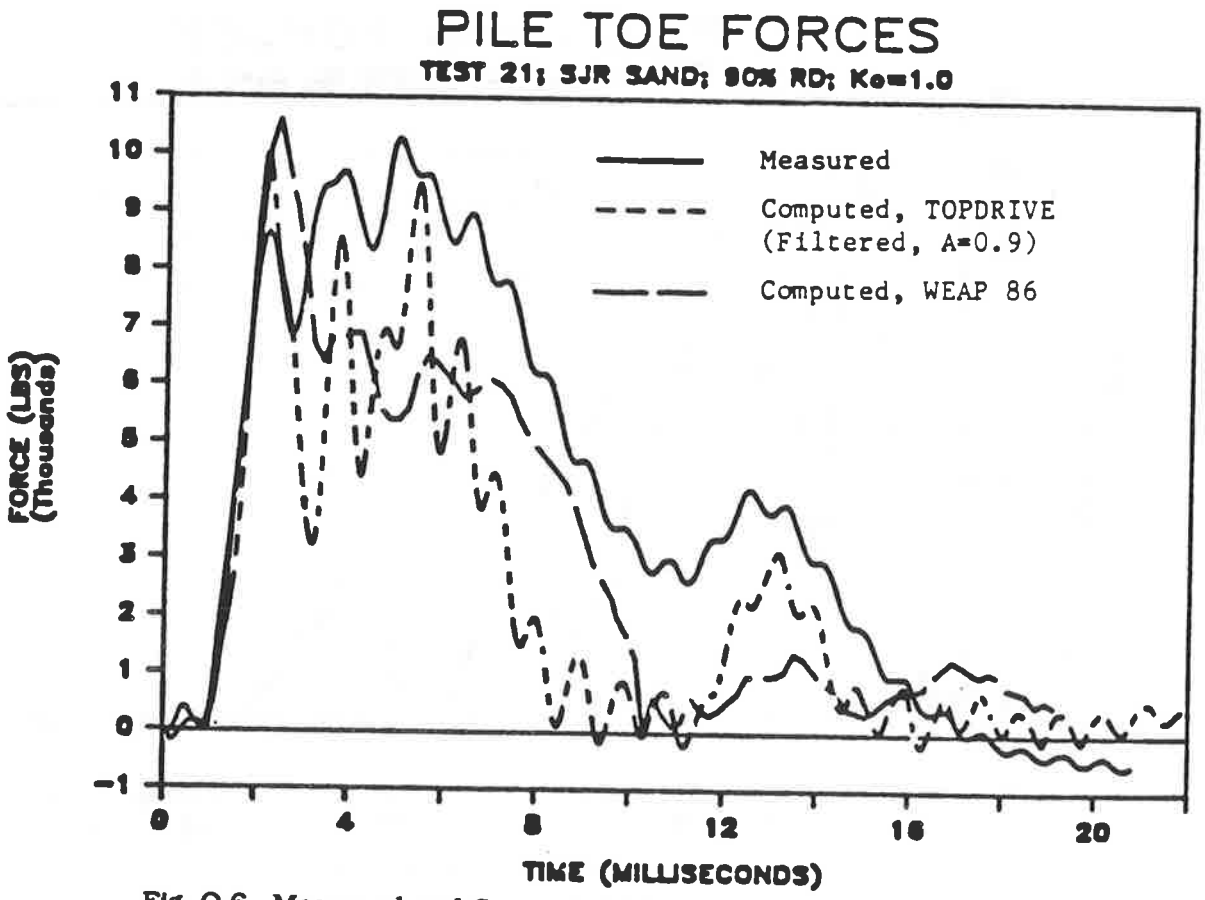

Fig. O.6. Measured and Computed Pile-Toe Velocities and Forces; Test No. 21

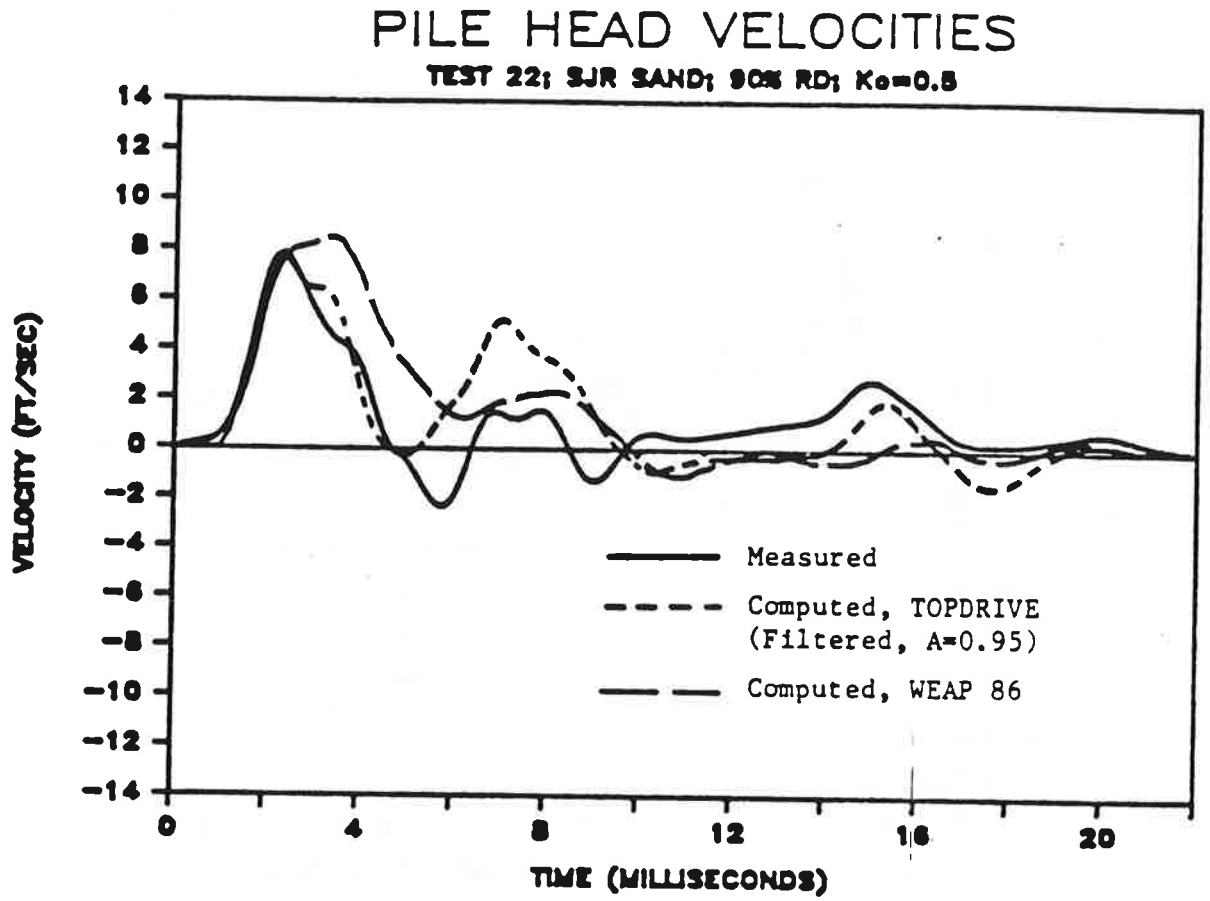

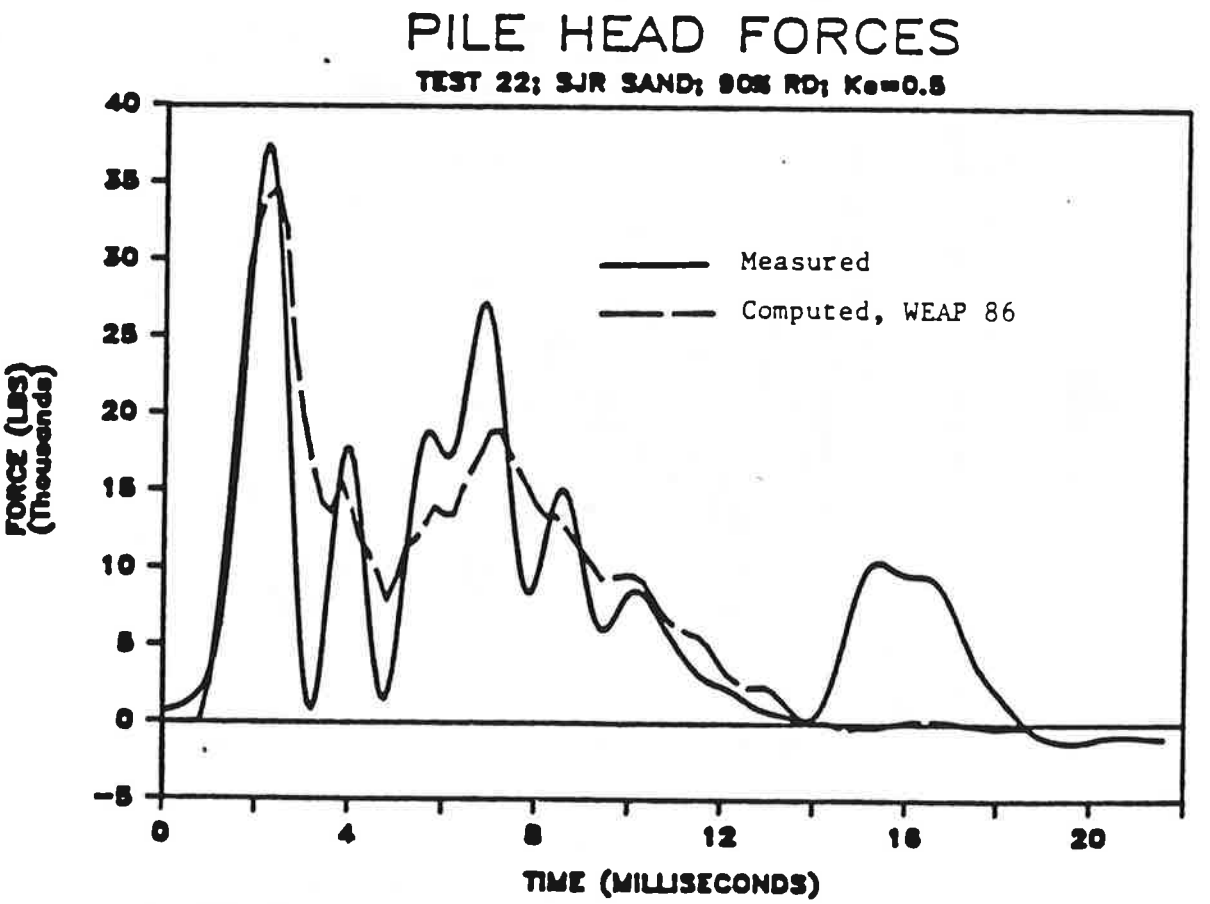

Fig. O.7. Measured and Computed Pile-Head Velocities and Forces; Test No. 22

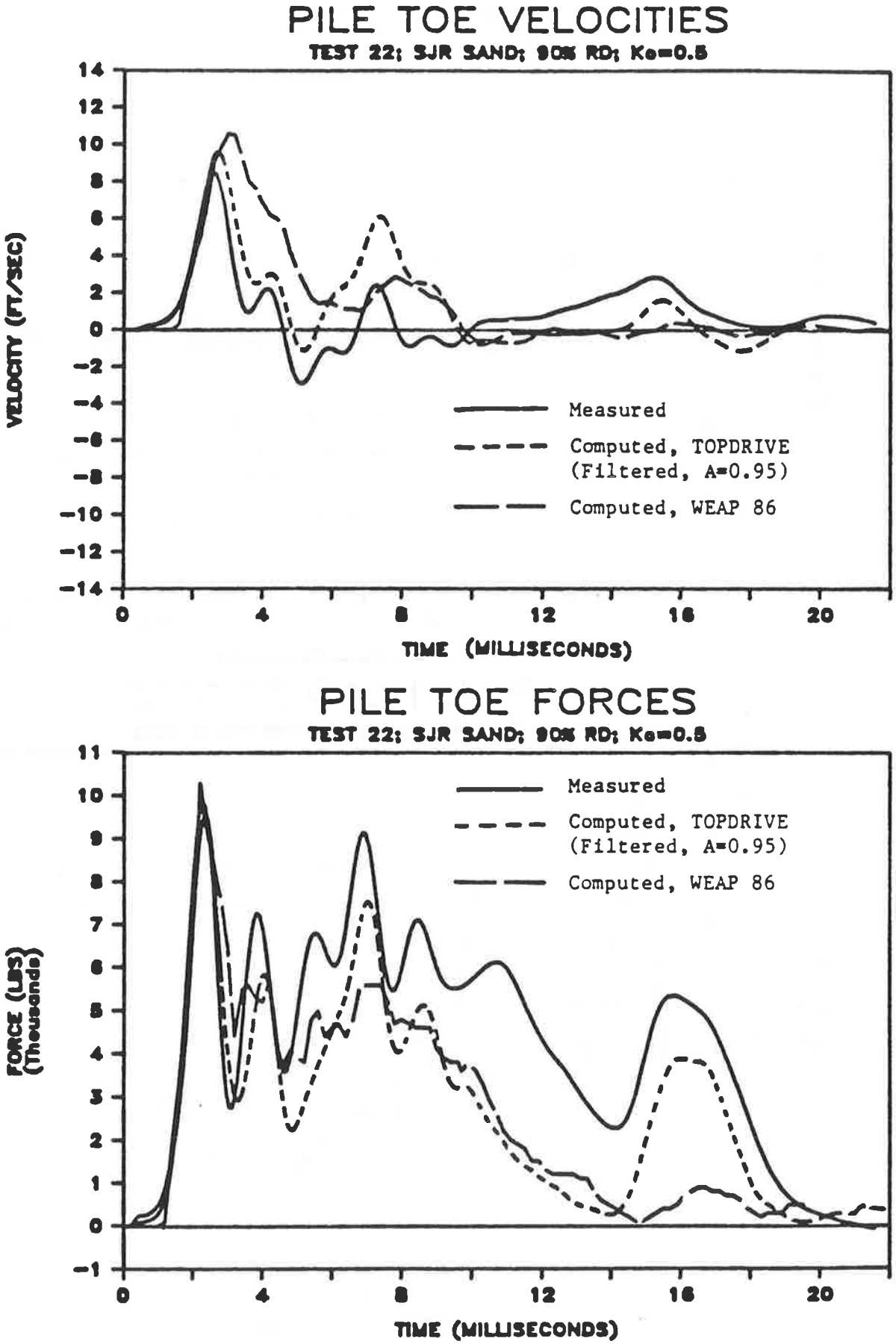

Fig. O.8. Measured and Computed Pile-ToeVelocities and Forces; Test No. 22

modelling of a pile of very short length. The digital filter is of the type described by Eq. O.1.

$$f_n = (1 - A) f'_n + Af'_{n-1} \qquad (O.1)$$

in which f is the filtered value of the function being plotted, f' is the unfiltered value of the function, n is the time step number, and A is the filter coefficient. Values of A are designated on the various graphs.

The optimum Smith-type soil parameters obtained from the TOPDRIVE study are tabulated in Table O.5.

The values of quake and damping are not strikingly different between piles driven by vibration and those driven by continuous impact in SJR sand (all tests except 17 in Table O.5). The ratio of toe force to total force is lower for Test 9, but that may be argued to be due to the fact that in Test 9 a penetration of only 57 inches was developed. It is estimated from simple proportions that had the pile been vibro-driven to a penetration of 77 inches, that ratio would have been about 0.35, which is generally consistent with the ratios from the continuous driving tests in SJR sand.

In the on test in BLS sand that was back-analyzed (Test 17), the ratio of toe resistance to total resistance was relatively higher than in either the vibration or continuous driving tests in SJR sand, and the quake values are noticeably higher than for the tests in SJR sand. This effect indicates that the BLS sand behaved more nearly quasi-elastically at small displacements than did SJR sand. Whether this effect is due to mineralogical differences or to effects of drainage at the toe during a hammer blow is not known.

Sensitivity Analyses

The sensitivity of the TOPDRIVE solution to the variation of certain input parameters was studied through a further analysis of Test 9. This study was conducted to determine the effects of parameters that were not generally varied in the optimization study described in the preceding section, specifically, distribution of shaft resistance along the pile, distribution of weight along the pile (particularly, the addition of extra weight to the toe to simulate soil that might be moving in phase with the pile) and the length of the integration time step. The conditions for the sensitivity analysis are shown in Table O.6. The quake and damping values and ratio of toe resistance to shaft resistance were the optimum values from Table O.5 for Test 9. For purposes of comparison with Table O.6, the values of toe element weight, shaft resistance pattern and time step from the standard solutions reported in Table O.5 were 9.9 lbs, uniform, and 15.6 μsec, respectively.

The time histories that were computed with each of the sets of inputs described in Table O.6 are shown in Figs. O.9 - O.16. By comparing these figures with the results given in Figs. O.1 and O.2, it is observed that the results are relatively insensitive to the parameters that were varied in the sensitivity study, so that the conditions assumed for the standard solutions (for which the optimum parameters are tabulated in Table O.5) appear to be appropriate.

Finally, a small sensitivity study was conducted using WEAP 86 to investigate the effect of the value of cushion stiffness on the pile-head force time history. Results of WEAP 86 solutions for two values of cushion stiffness (the value measured in static

Table O.5. OptimumTOPDRIVE Parmeters

Test/Condition	Q(shaft) (inches)	Q(toe) (inches)	J(shaft) (sec/foot)	J(toe) (sec/foot)	R(toe)/ R(total)
9 / SJR sand $D_r = 90\%$ $K_o = 1$ Ch. Press. = 20 psi (Restrike)	0.03	0.03	0.06	0.06	0.44
17 / BLS sand $D_r = 90\%$ $K_o = 1$ Ch. Press. = 20 psi (Restrike)	0.08	0.10	0.09	0.07	0.48
21 / SJR sand $D_r = 90\%$ $K_o = 1$ Ch. Press. = 20 psi (Continuous impact)	0.04	0.04	0.07	0.08	0.24
22 / SJR sand $D_r = 90\%$ $K_o = 0.5$ Ch. Press. = 20 psi (horiz.) (Continuous impact)	0.02	0.02	0.10	0.06	0.31

Table O.6. Varibles in TOPDRIVE Sensitivity Study (Test 9)

Toe Segment Weight (lbs.)	Shaft Resistance Distribution	Time Step (microsecs)	Figures
16.0	uniform	15.6	O.9, O.10
9.9	step	15.6	O.11,O.12
16.0	step	15.6	O.13,O.14
16.0	step	10.0	O.15,O.16

Note: In the "step" distribution, the bottom half of the pile was assigned twice as much resistance as the top half of the pile.

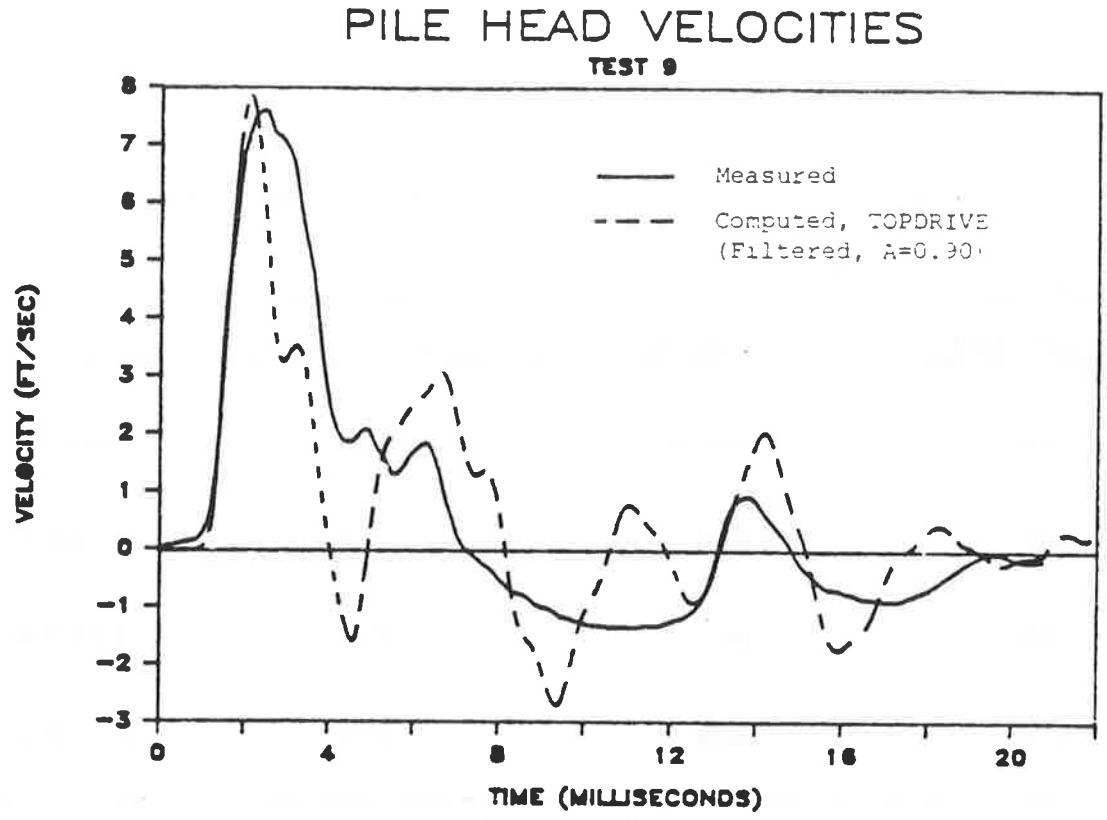

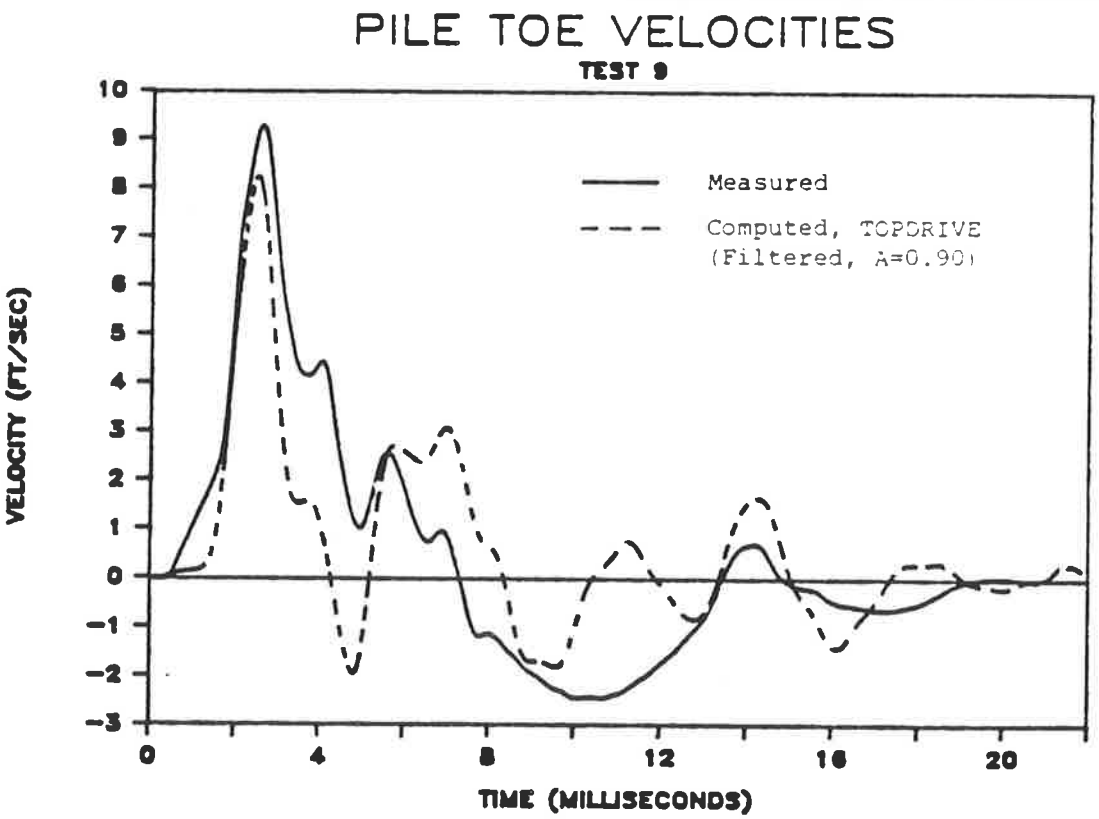

Fig. O.9. TOPDRIVE Analysis of Test No. 9; Increased Toe Weight; Velocities

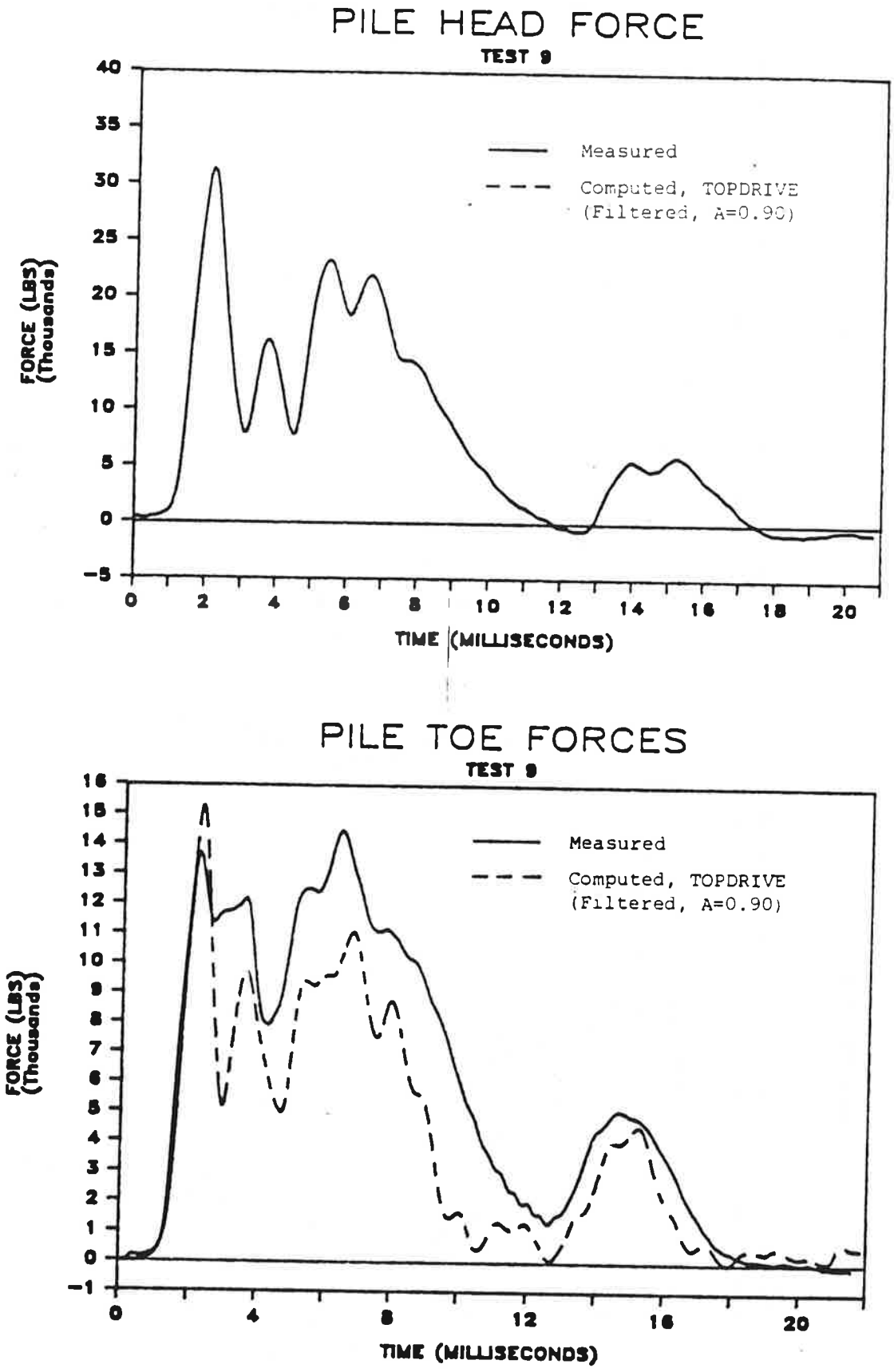

Fig. O.10. TOPDRIVE Analysis of Test No. 9; Increased Toe Weight; Forces

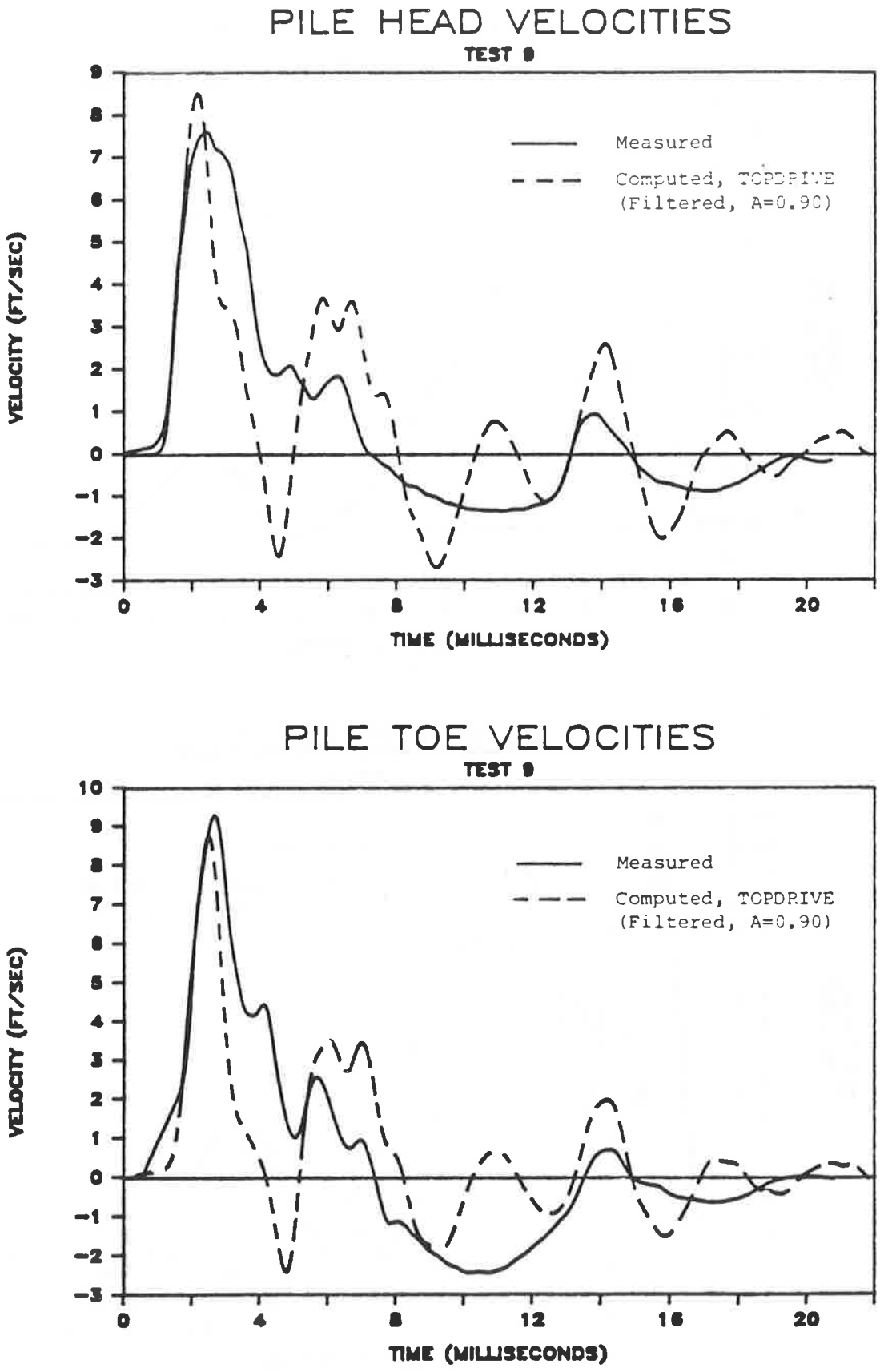

Fig. O.11. TOPDRIVE Analysis of Test No. 9; Variable Shaft Resistance; Velocities

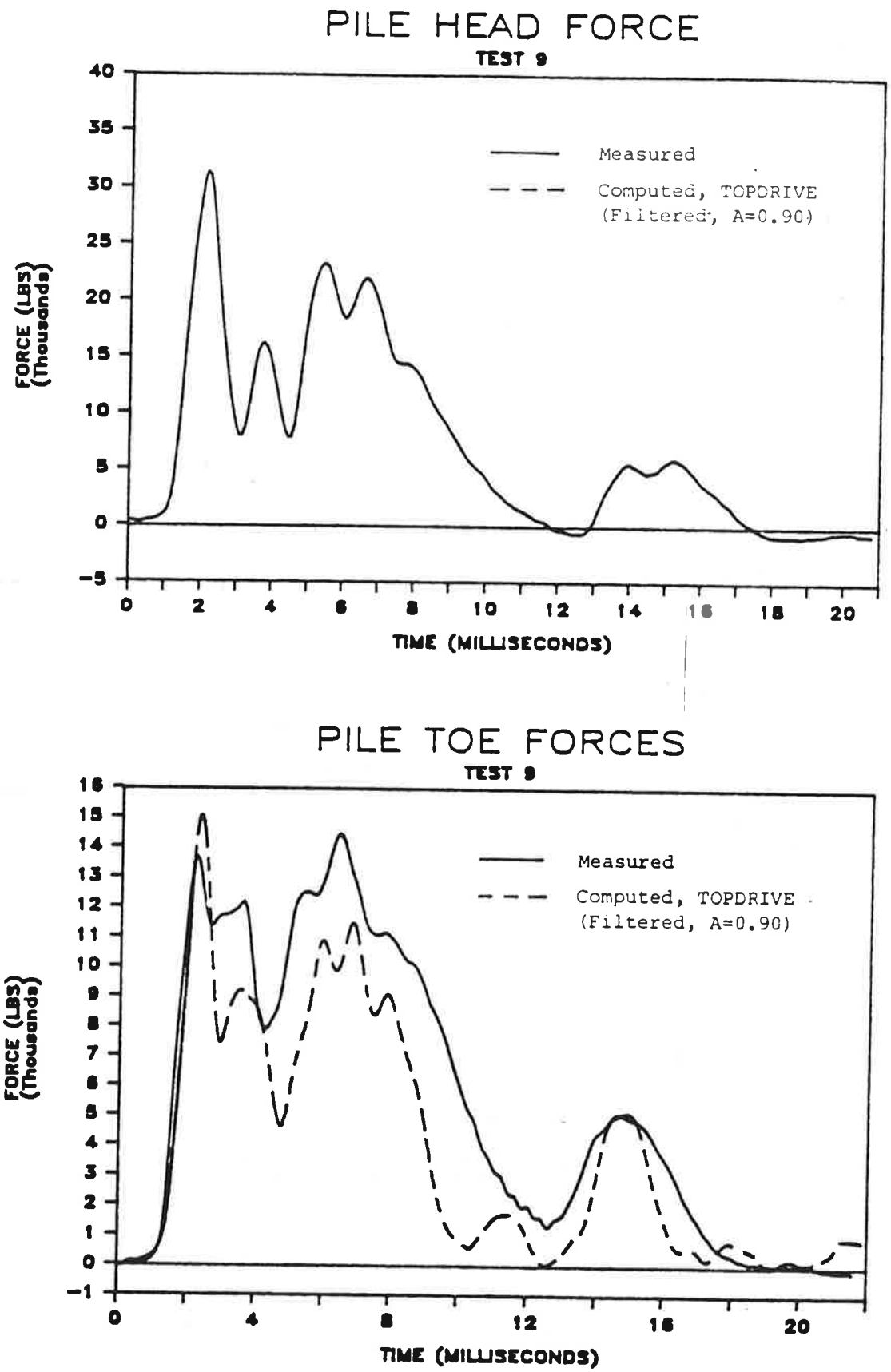

Fig. O.12. TOPDRIVE Analysis of Test No. 9: Variable Shaft Resistance; Forces

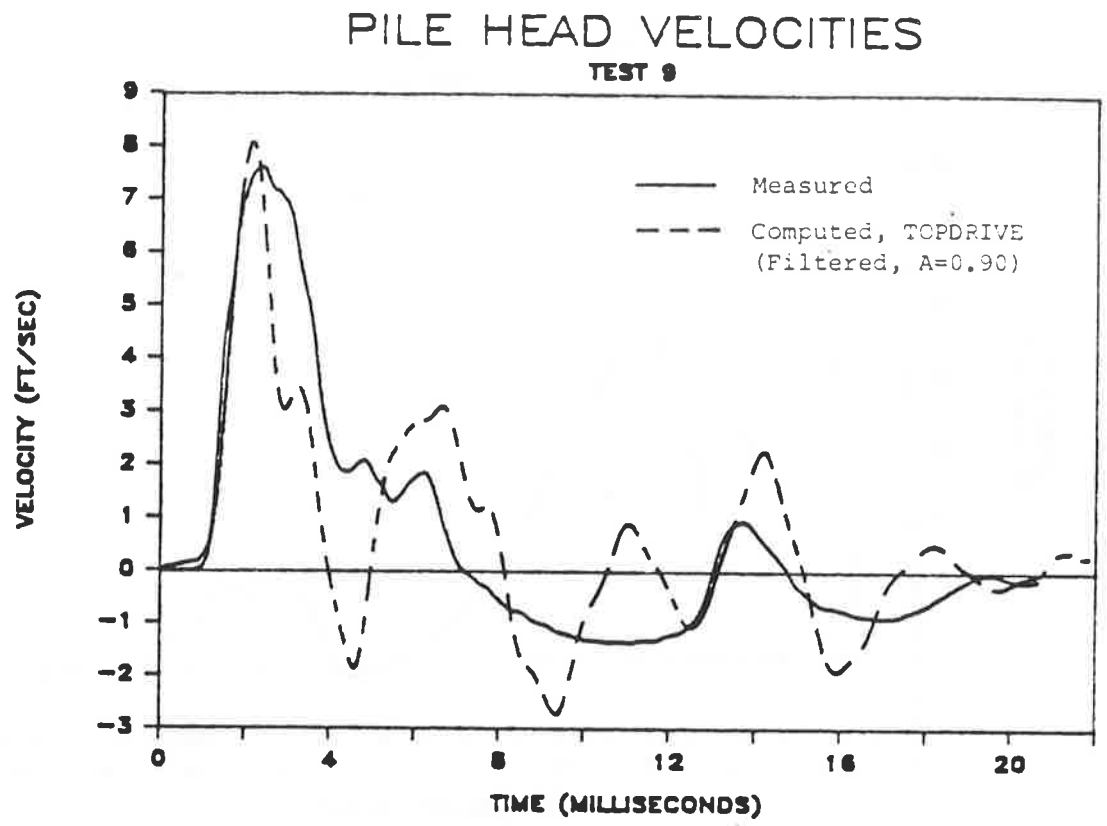

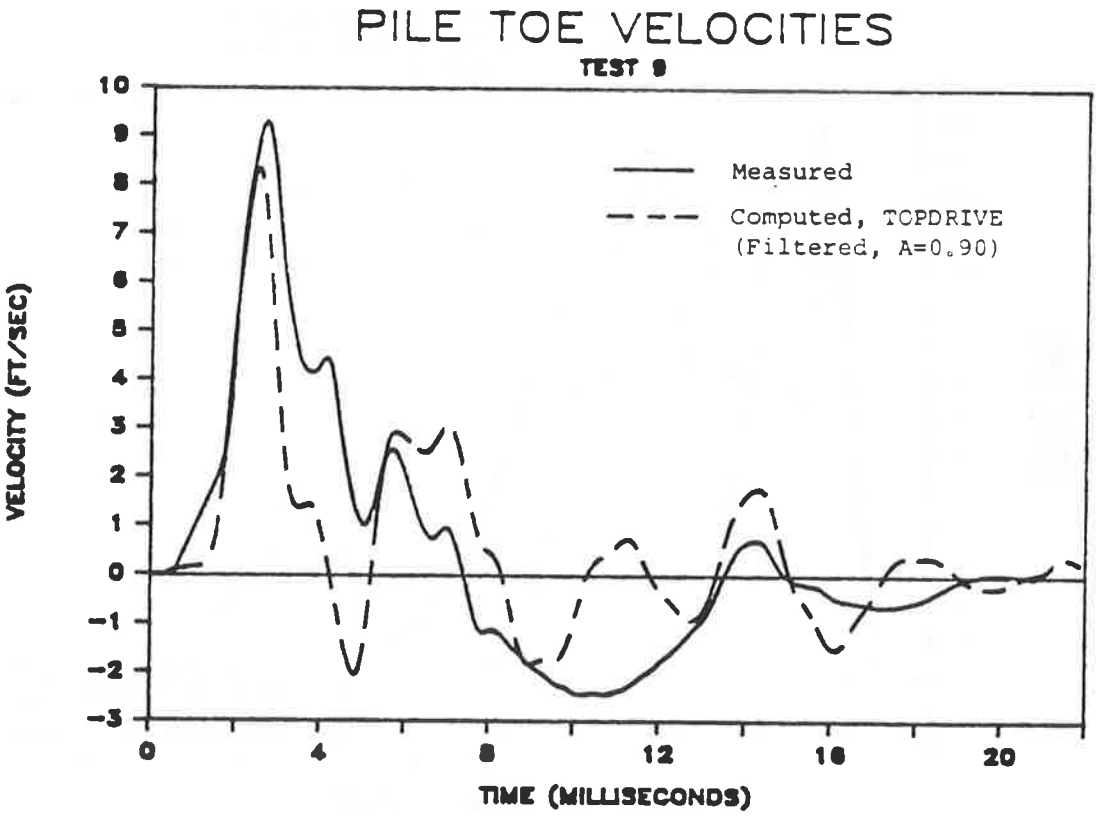

Fig. O.13. TOPDRIVE Analysis of Test No. 9; Increased Toe Weight and Variable Shaft Resistance; Velocities

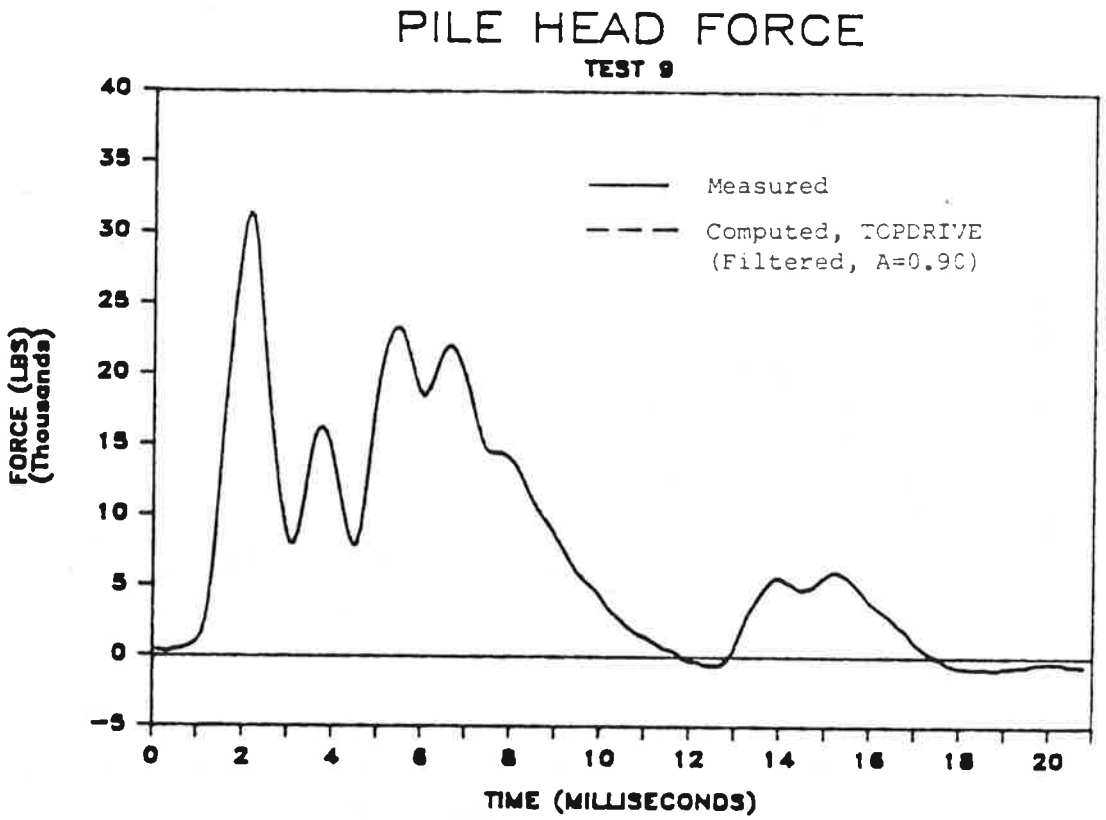

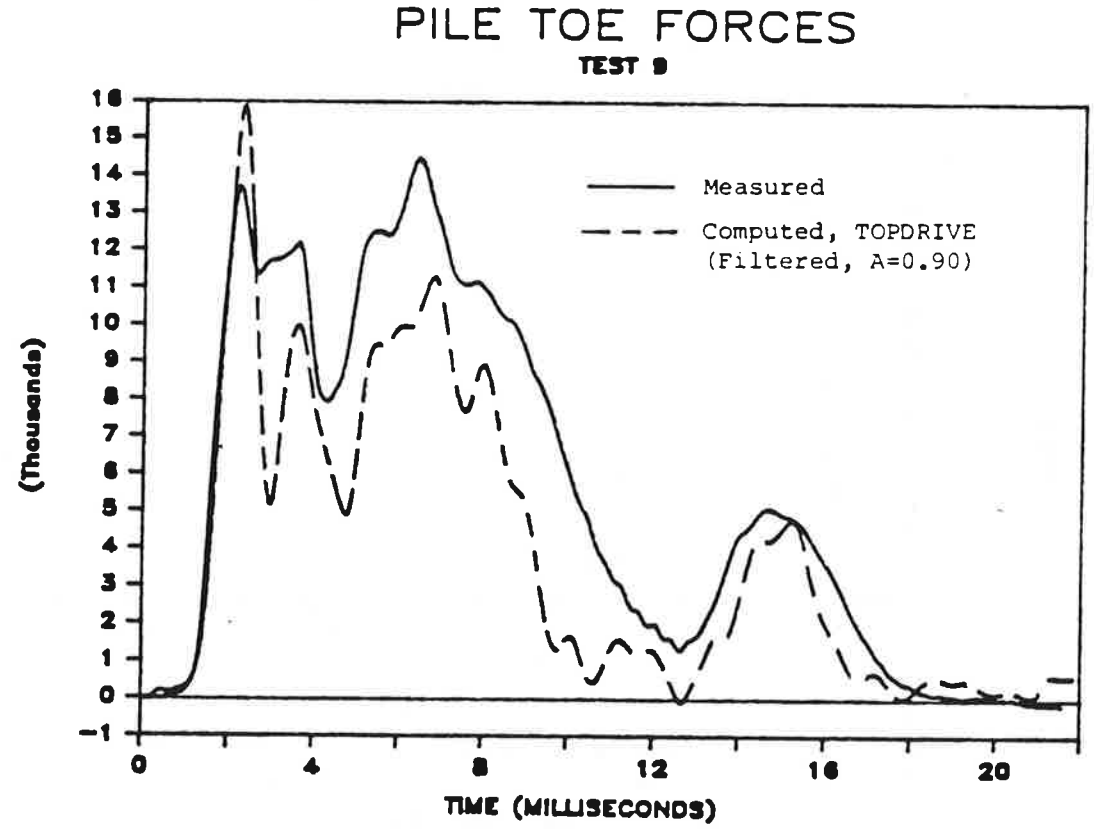

Fig. O.14. TOPDRIVE Analysis of Test No. 9; Increased Toe Weight and Variable Shaft Resistance; Forces

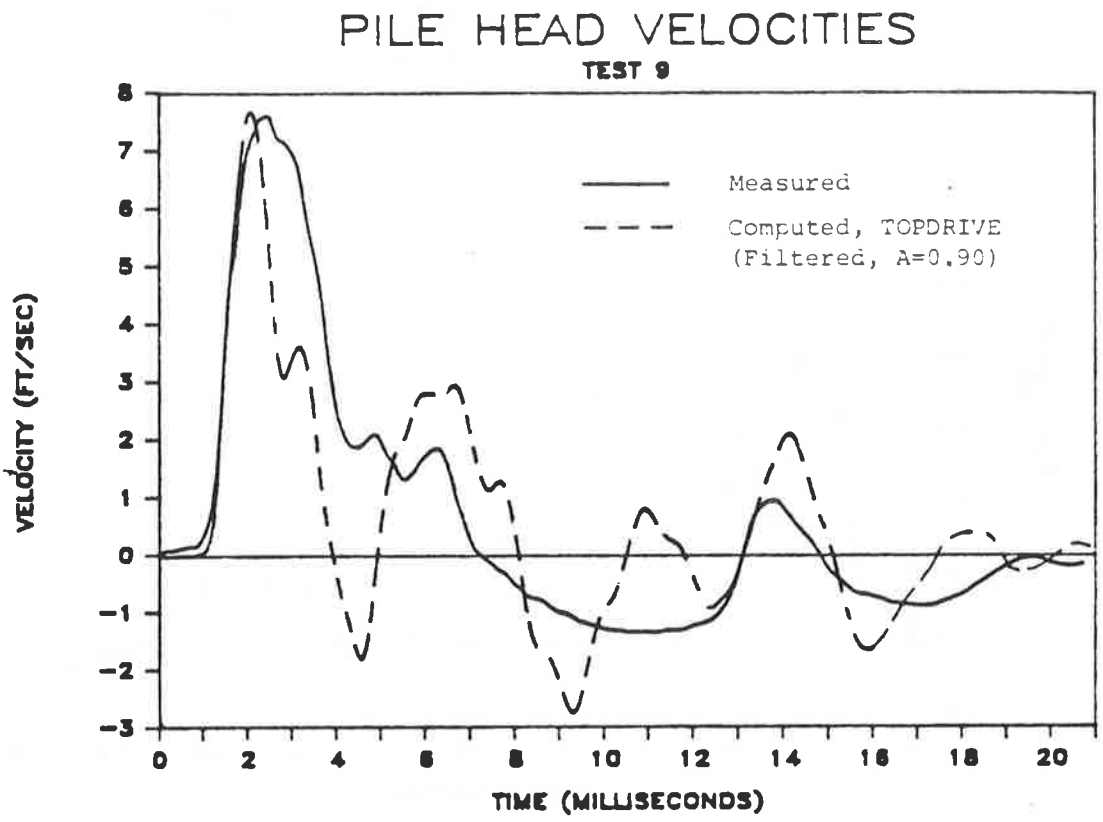

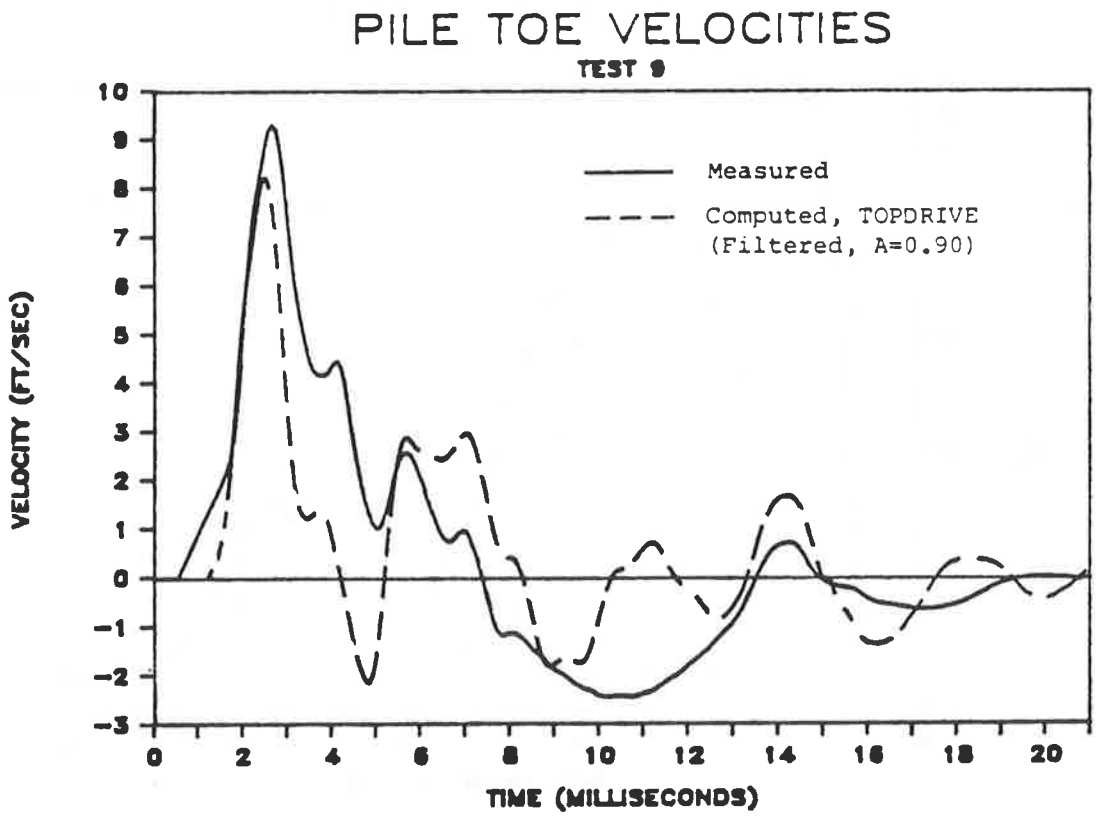

Fig. O.15. TOPDRIVE Analysis of Test No. 9; Increased Toe Weight, Variable Shaft Resistance and Decreased Time Step; Velocities

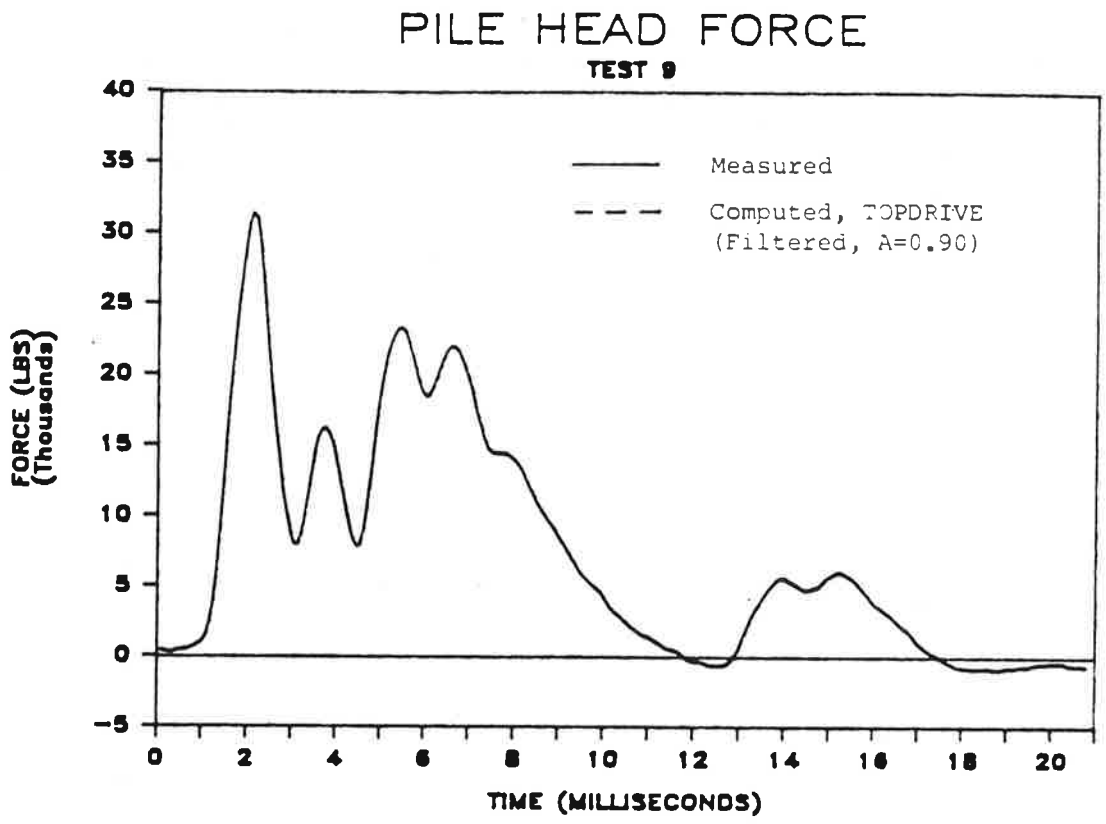

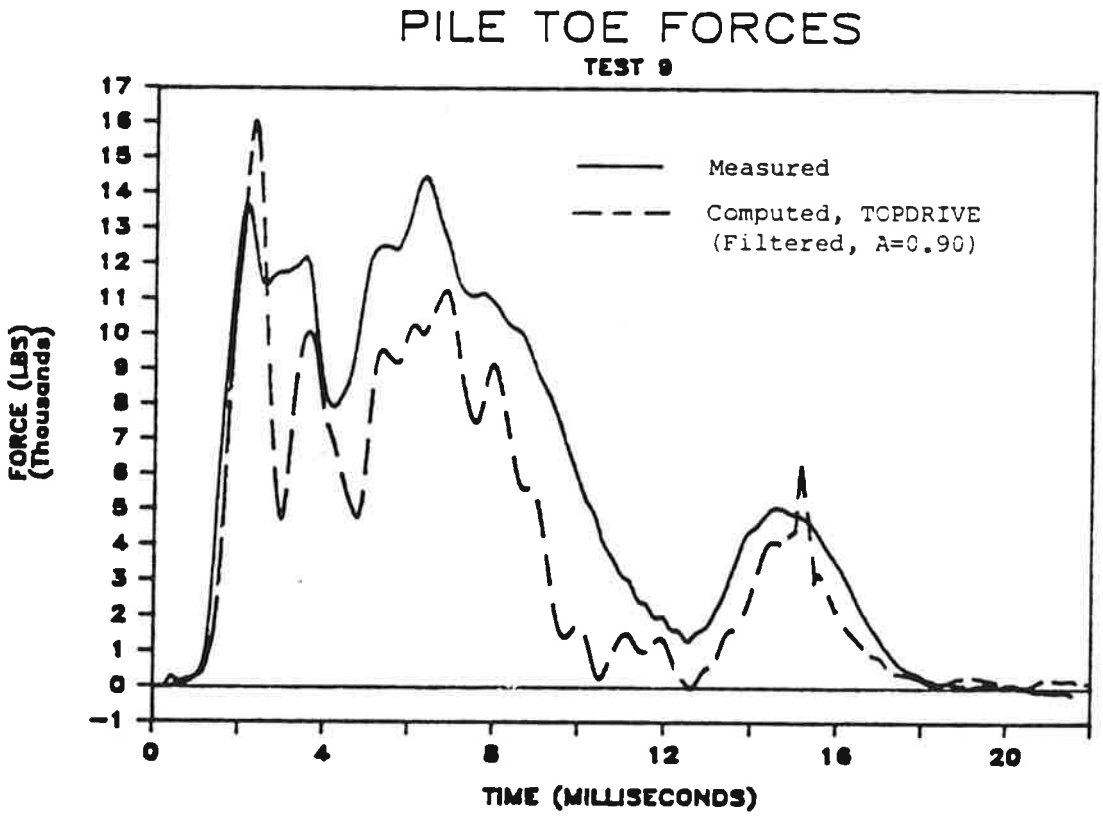

Fig. O.16. TOPDRIVE Analysis of Test No. 9; Increased Toe Weight, Variable Shaft Resistance and Decreased Time Step; Forces

loading tests and the value obtained by using the recommendation of Goble and Rausche (24) of cushion modulus of 30 ksi) are shown in Figs. O.17 and O.18. The measured cushion stiffness of 1100 k/inch, which was used in producing the relations shown in Figs. O.5 - O.8 provided the best match, which suggests that the WEAP 86 solutions shown in those figures are apparently appropriate.

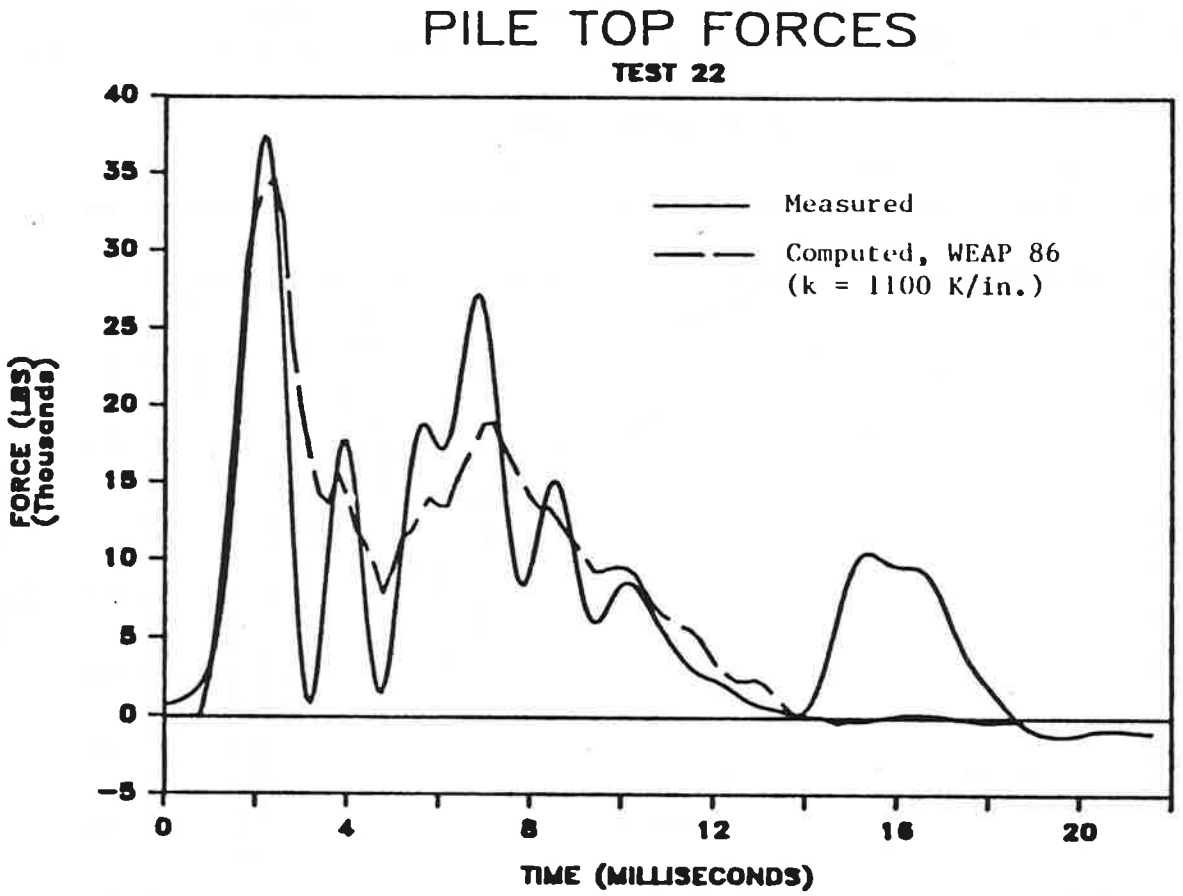

Fig. O.17. WEAP 86 Analysis of Test No. 9 Using Optimum Parameters from TOPDRIVE Analysis (Table O.1), Cushion k = 1100 Kips/Inch

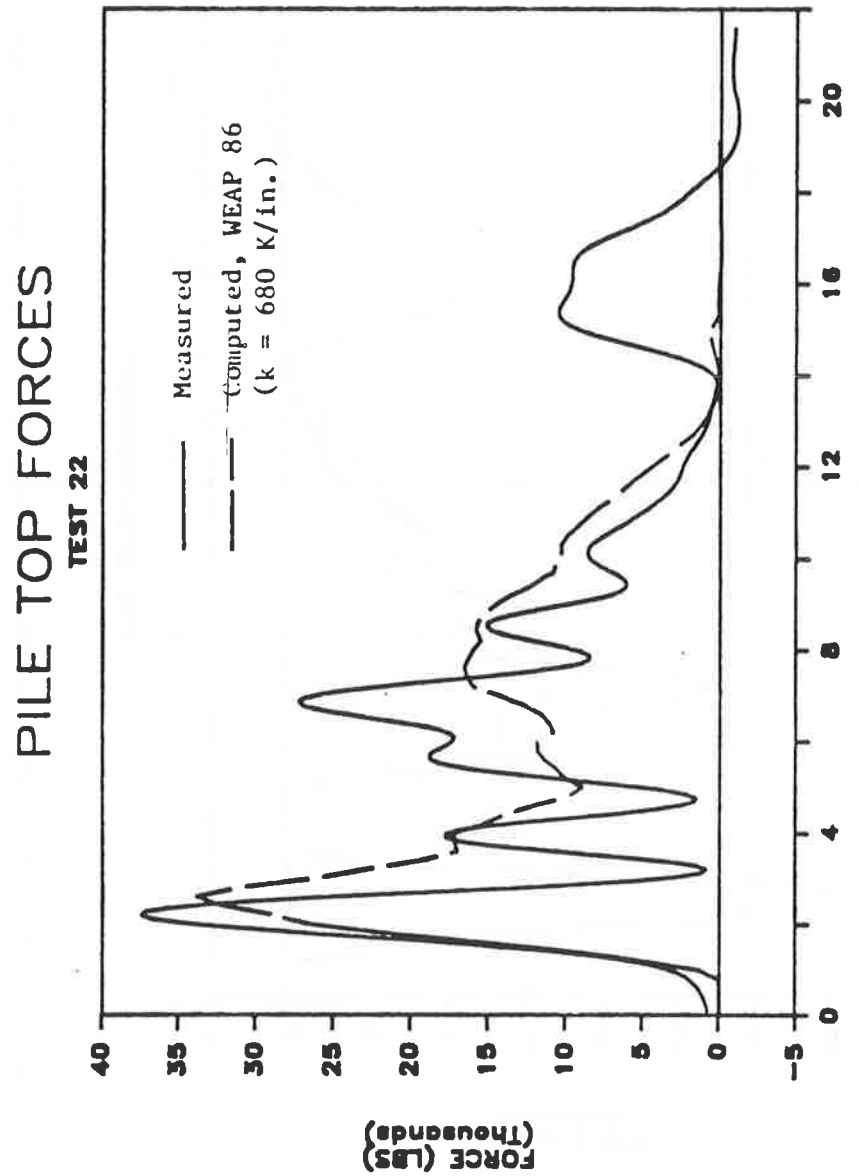

Fig. O.18. WEAP 86 Analysis of Test No. 9 Using Optimum Parameters from TOPDRIVE Analysis (Table O.1), Cushion k = 680 Kips/Inch

APPENDIX P

Static Load Testing Procedures and Interpretation

This appendix describes briefly the procedures used to conduct the static loading tests, which were performed in connection with the "capacity" tests on vibro-driven piles, vibro-driven piles with restriking and impact-driven piles described in Appendix B, Table B.1; documents the static load-movement relations; and discusses the interpretation of failure loads.

Testing Procedures

The following testing protocol was followed:

a. While the pile was sitting vertically on top of the sand column, unstressed except for its own dead weight, all strain gages, pressure cells and load cells were read. These readings constituted the zeroes for all static test data, so that all data taken after installation and during static testing contain the effects of residual stresses that existed in the pile after installation. The instrument leads remained connected to the static data scanner, as well as the dynamic data acquisition system, from the time the predrive zeroes were taken throughout installation and testing, since the static data acquisition system scanner and microcomputer had a very high electrical impedance and did not therefore affect the performance of the dynamic data acquisition system.

b. Once the pile had been driven to its full penetration, the impact hammer or vibro-driver was removed, and the pile head was reconfigured for static testing. This step included, first, the reading of all instruments to check operability with the static data acquisition system and then the removal of the articulated connection (vibratory tests) or extraction of the anvil of the impact hammer (impact or restrike tests). A reaction beam was hoisted into place, and a flat, machined steel loading plate was positioned on the head of the pile.

c. One horizontal instrument arm was attached to each main upright of the service gantry, which served as a deformation-measurement reference for the loading tests. (Vertical deformations in the service gantry were less than 0.02 inches at a load of 45 kips on the pile. Such movements of the reference system were not accounted for in the reduction of the data, but they represent a very small percentage of the movement of the pile and, in any event, were generally consistent from test to test.) At the ends of these arms were attached two linear variable differential transformers (LVDT's), mounted at the northwest and southeast of the pile head, and two mechanical dial gages, mounted at the northeast and southwest of the pile head. The stems of these instruments, which were used to measure settlement (and later uplift), were rested on machined extensions that emanated from the loading plate that had been placed on the head of the pile. The output from the LVDT's fed directly into the static data acquisition system (Appendix F), and the mechanical dial gages were read by eye and recorded manually. The dial gages served to provide a check on the LVDT's, which were the instruments that were ultimately used in the reduction of the data. The dial gages also provided part of a four-point measurement system, which allowed for careful tracking of the rotation of the pile head. No specific data on pile-head rotation are reported for this study, but in

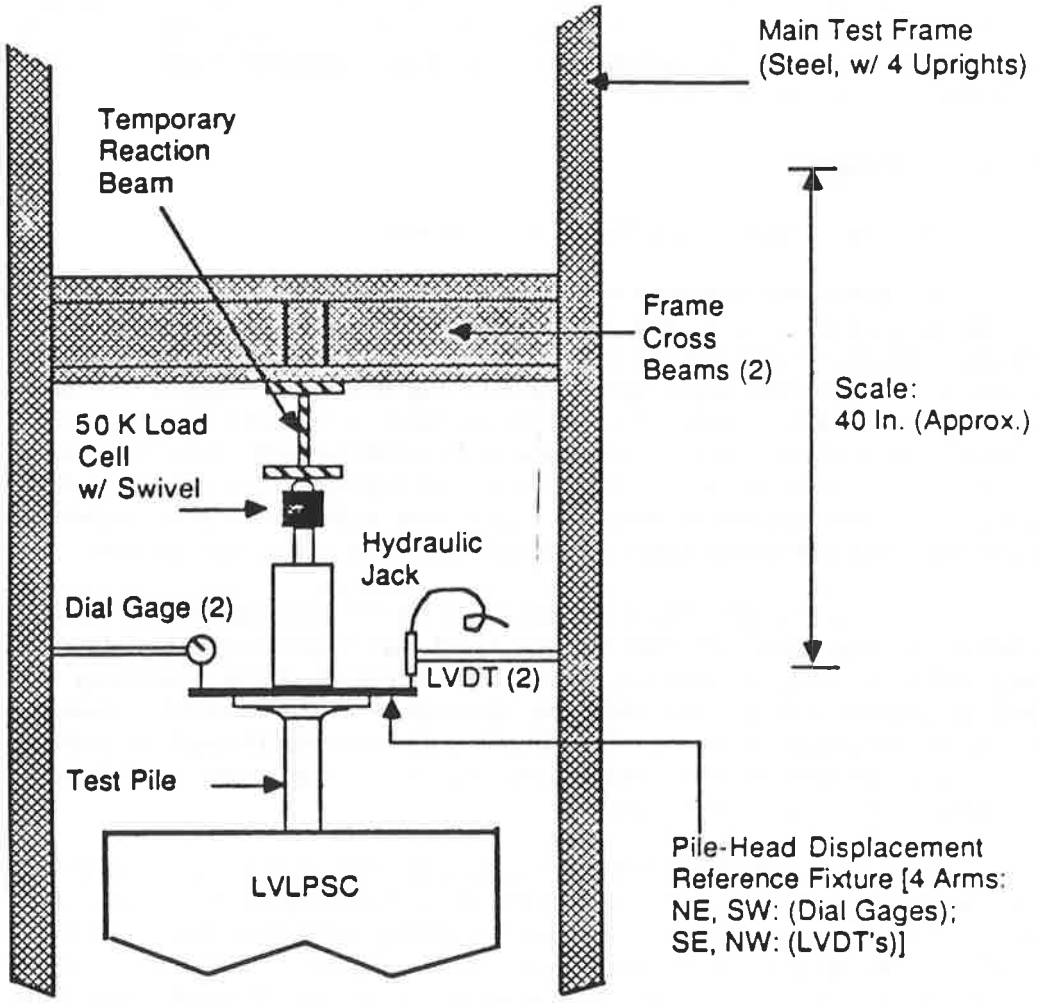

Note: 2 Dial Gages and 2 LVDT's Supported on Aluminum Arms Clamped to Main Frame Uprights

Fig. P.1. Elevation Schematic of Static Compression Testing Arrangement

no case did the rotation exceed 0.003 radians about either axis of measurement during an axial loading test.

d. A hydraulic jack was placed, centered, on the loading head. A 50-k electronic load cell was placed above the jack to measure load, and a simple swivel head was placed between the load cell and the reaction beam. A schematic of the resulting test system is shown in Fig. P.1, and a photograph of the arrangement at the pile head is shown in Fig. P.2. With the load cell in the position shown, it is obvious that the loads recorded were those in excess of the jack weight (about 40 lb.). In Test 9 it was necessary to use the frame cross beams at one level above the level that was normally used as a support for the reaction beam because the pile failed to penetrate to the required depth. During that test it was necessary to place a shim between the swivel head and the reaction beam. Otherwise, shims were not used.

e. Another set of readings was taken, referenced to the predrive zeroes. [At this point, approximately two hours after completion of driving, there were no indicated excess pore water pressures in the sand. In fact, all excess pore water pressures appeared to dissipate within about 90 seconds of the completion of driving, as evidenced by cessation of flow from the lateral drains within the chamber (Appendix C).] The compression loading test then began by manually stroking a small-displacement pump that powered the jack. A constant rate of penetration of 0.033 inches per minute was maintained at the pile head. Initially, readings of all instruments were made at every 0.01 inch of penetration. As the soil began to undergo significant plastic deformation, the interval of data collection was increased to every 0.02 inches of penetration. The loading portion of the test was halted after the pile head had settled 1.0 inches, so that the loading portion of the test required about 30 minutes to complete. The pile was then unloaded in three to four decrements, pausing just long enough at each decrement to make a set of readings.

The electronic instruments that were read during a static test are shown in Fig. F.2. In addition to these instruments, the two dial gages at the top of the pile were read and the readings recorded simultaneously with the acquisition of electronic data. The scanner-computer system that was used could read all instruments in approximately 0.5 seconds, so that a set of readings represents essentially an instantaneous pile state. Tabular values of the loads measured along the pile during each of the static tests are given in Appendix Q, and lateral pressure measurements are also discussed briefly in Appendix Q. In some cases strain gage circuits did not yield variations in readings from load to load that could be rationally explained, and their resistance to ground became low, indicating water intrusion somewhere in the circuit. Readings under such circumstances were excluded when reducing the data, and those readings are absent from the tabulations in Appendix Q.

f. Once the compression test was completed, the head of the pile, the reaction beam and the jack were reconfigured for the uplift test, as shown schematically in Fig. P.3. This procedure required about one hour. The uplift test was then conducted in a manner identical to the compression test, with one exception. An initial frictional failure apparently occurred between the sand and the wall of the pile once the pile had moved upward 0.1 to 0.2 inches. At this point, considerable strain energy was stored in the uplift yoke. That energy was partially dissipated while the pile slid upward momentarily with respect to the soil, apparently as static friction was converted to sliding friction at the wall of the pile. Once a sufficient amount of energy had been released, the pile stopped moving and the pile-soil system was again in equilibrium with

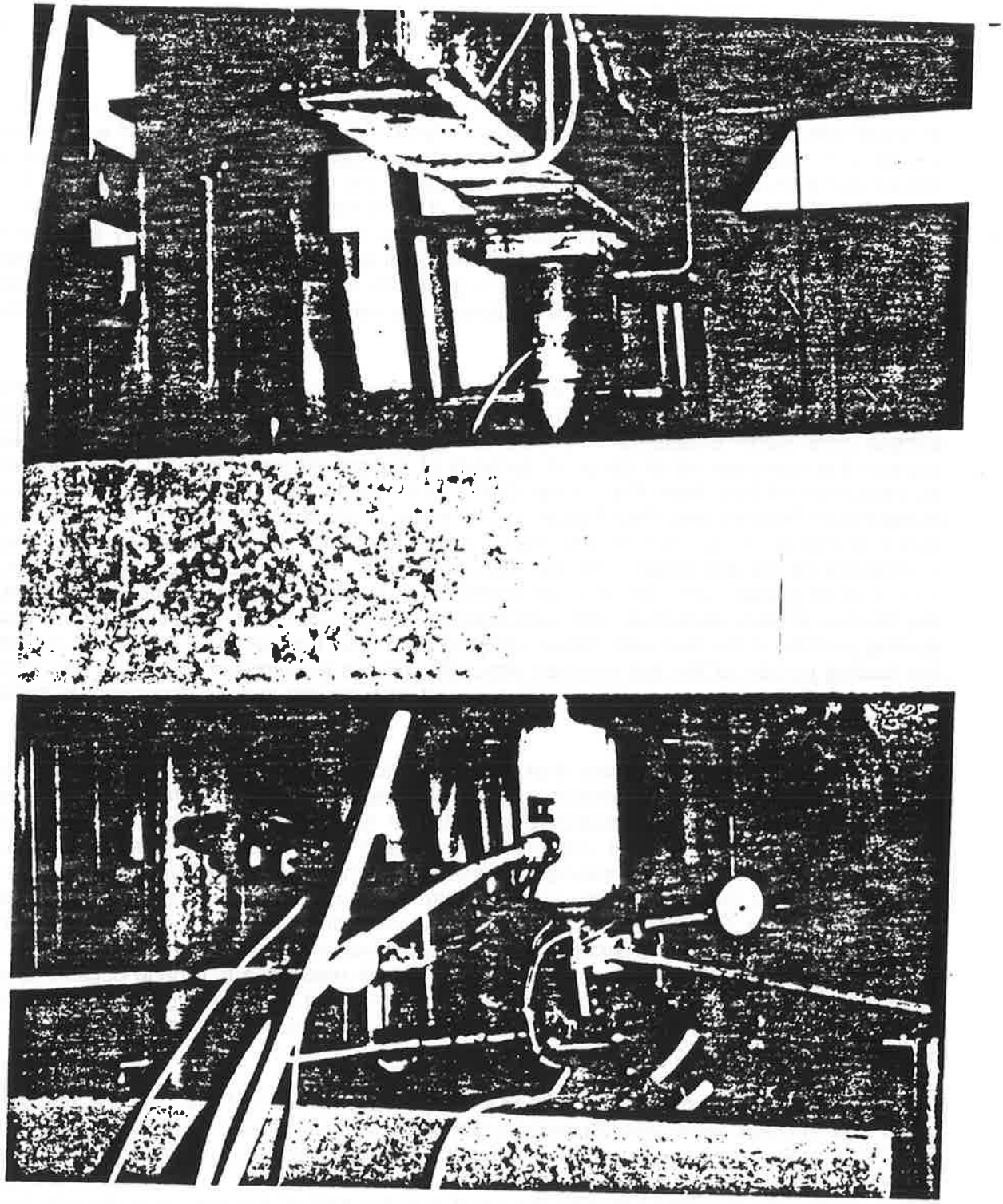

Fig. P.2. Photograph of Pile Head During a Static Load Test, Showing Jack, Load Cell Reaction Beam, Dail Gages and LVDTs

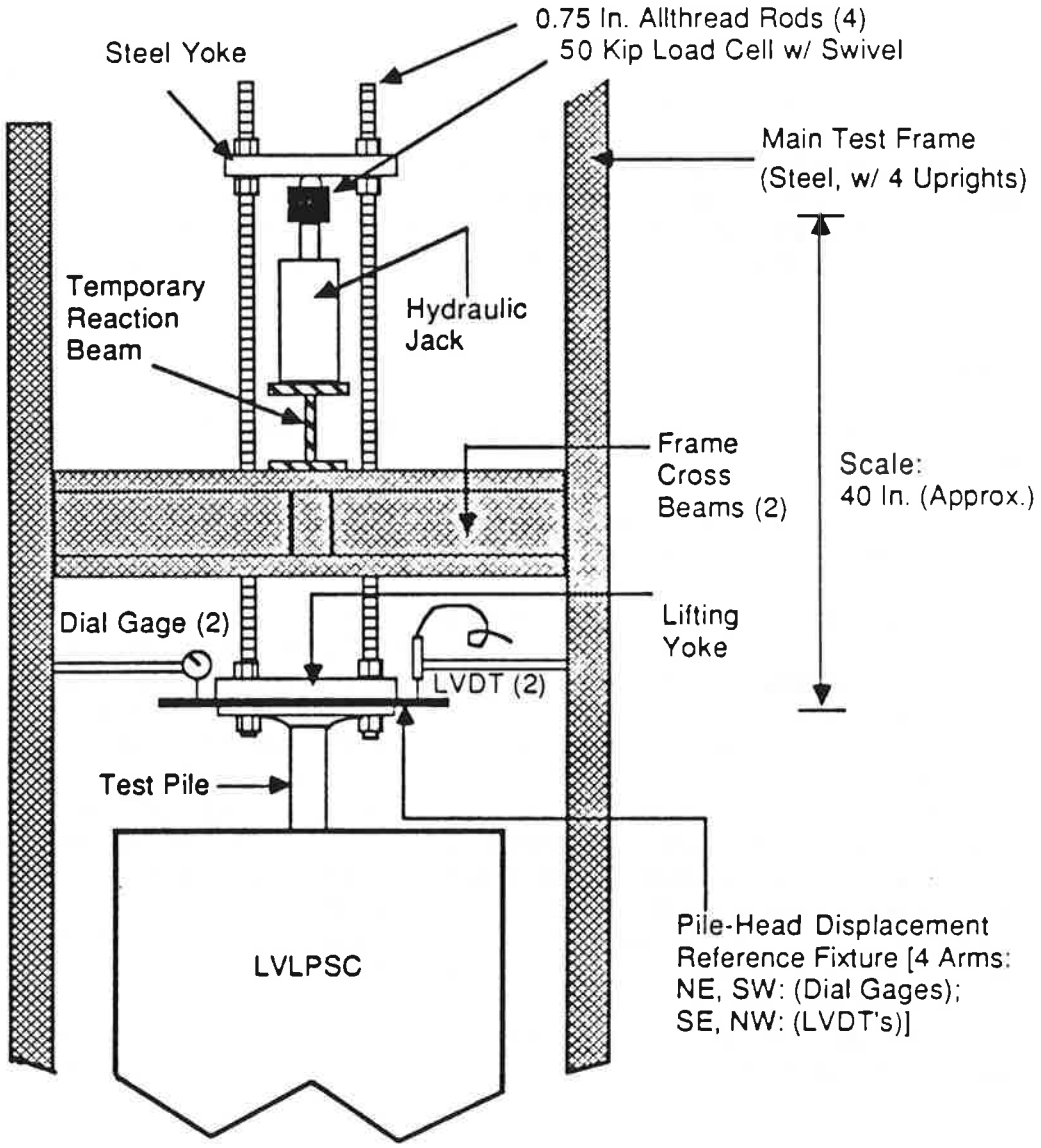

Note: 2 Dial Gages and 2 LVDT's Supported on
Aluminum Arms Clamped to Main Frame Uprights

Fig. P. 3. Elevation Schematic of Uplift Testing Arrangement

the applied load with static friction in force. This process, however, which repeated numerous times as further uplift load was applied, resulted in a series of jerks, in which the pile moved suddenly 0.02 to 0.04 inches on each jerk, making it impossible to maintain a constant rate of uplift of 0.033 inches per minute. That rate was maintained between the jerks, however. Because of this phenomenon, the completion of a typical uplift test to a total pile-head movement of 1.0 inch required only about 20 minutes.

It is of significance to note that the entire process of driving and static load testing required approximately six to seven clock hours from the time the initial zeroes were taken and the installation began. The tests were all conducted in an air conditioned room, with no direct sunlight on any of the components of the test or instrumentation system, so that electronic drift due to temperature changes over the six to seven hours of the maintenance of the zeroes was small enough so that it had essentially no effect on the results.

Load-Movement Relations

Graphical results of the static compression tests are shown in Figs. P.4- P.11, in the following groupings:

(a) all tests of vibro-driven piles with restrike at an effective chamber pressure of 10 psi (Fig. P.4) ;

(b) all tests of vibro-driven piles with restrike at an effective chamber pressure of 20 psi (Fig. P.5). [In Test 9 (SJR Sand) it was possible to drive the pile only to a penetration of 55 inches with the vibrator. The pile was restruck to drive it to a final penetration of 57 inches. In order to compare the results of this test with Test 17 (BLS Sand), a load-movement curve was synthesized for a penetration of 77 inches by using computer program APILE (25), which produces load-settlement relations from pile stiffness and unit load transfer function inputs. The measured shaft unit load transfer relations (f-w curves, Appendix Q) for the top half of the pile and the bottom half of the pile were applied, respectively, to the top and bottom halves of a pile penetrating 77 inches, and the measured toe unit load transfer relation (q-w curve, Appendix Q) at the actual test penetration (57 inches) were used as inputs to APILE to synthesize the load-movement curve shown in Fig. P.5.]

(c) all tests of vibro-driven piles compared with corresponding tests of pile driven with vibration with restrike at an effective chamber pressure of 10 psi (Fig. P.6);

(d) all tests (vibratory and impact) conducted under conditions of K_o = 0.5, with corresponding tests under K_o = 1 (Fig. P.7), in which the lateral effective chamber pressure was 10 psi in each test;

(e) comparison of individual tests of impact-driven piles with tests of vibro-driven piles under corresponding conditions (Figs. P.8 - P.11).

Figures P.12 - P.19 present the load-movement curves from the uplift tests in the same groupings as above.

Several observations can be made from the load-movement results:

(a) The static capacity of vibro-driven piles was much more dependent upon relative density than upon effective grain size at a an effective chamber pressure of 10 psi (Fig. P.4).

(b) The effect of grain size is evident at an effective chamber pressure of 20 psi, as the coarse-grained sand (BLS Sand) produced higher capacity than fine-grained sand (SJR Sand) for the vibro-driven pile with restrike (Fig. P.5).

(c) No conclusive evidence exists that restrike increased the compression capacity of vibro- driven piles (Fig. P.6).

(4) It appears that vibro-driven piles had very slightly greater compression capacities than impact-driven piles under similar conditions at 90% relative density (Figs. P.7, P.8, P.9 and P.11). However, vibro-driven piles yielded a lower capacity than impact-driven piles at 65% relative density (Fig. P.10).

(5) The uplift load-movement results exhibited similar trends to those described for the compression tests. Comparison of compression-test load-movement data at the pile head with corresponding uplift test data and analysis of the toe resistance-movement data for the compression tests from Appendix Q leads to the conclusion that the difference in capacity at 90% relative density between vibro- and impact-driven piles was due to increased toe capacity in the vibro-driven piles, while at 65% relative density the difference was due to somewhat decreased shaft resistance in the vibro-driven piles (e.g., compare Figs. P.7, P.8, P.9, P.10 and P.11 with P.15, P.16, P.17, P.18 and P.19, respectively).

Interpretation of Failure Load

Although the term "capacity" has been used loosely in the preceding section to describe the general trends in the testing program, precise definitions of failure or limiting loads are not readily obvious in Figs. P.4 - P.19. Therefore, several definitions of failure have been employed and compared in tabular form in Chapter 2 for each of the static load tests. Five methods are proposed to define the static failure load from the load-settlement data. In order to employ these definitions, load-movement relations with continuously varying slopes are required. Where sawtooth patterns developed during a test, continuously sloping curves were interpreted by taking the upper envelope to the sawtooth curve. The methods are summarized below.

(a) The offset (or Davisson) method (26), in which the failure load is defined as the intersection of the pile-head load-movement curve and a line intersecting the movement axis at a value of 0.15 + 0.00833B inches (where B is the pile diameter) and having a slope (movement/load) of L/AE where L, A and E are length, cross-sectional area and Young's modulus of the pile material, respectively. While this method was developed for the interpretation of compression loading tests, it has also been applied in this study to the interpretation of uplift loading behavior.

(b) The slope (or Nordlund) method (27), where failure is defined as the point on load-movement curve at which its slope is 0.05 inches/ton.

(c) The Mazurkiewicz method (26), which assumes that the load-movement curve is parabolic at failure. A set of load values are found from a corresponding set of

equally spaced pile-head movement values that are arbitrarily chosen. A 45° line is drawn from each load value on the load axis to intersect with a line drawn parallel to the movement axis at the next larger value of load. These intersections are joined by a straight line which intersects the load axis. That intersection is defined the failure load.

(d) Failure load defined as the load corresponding to a pile-head movement of 0.10 B.

(e) Failure load defined as the load corresponding to a pile-head movement of 1.0 inch (0.25 B).

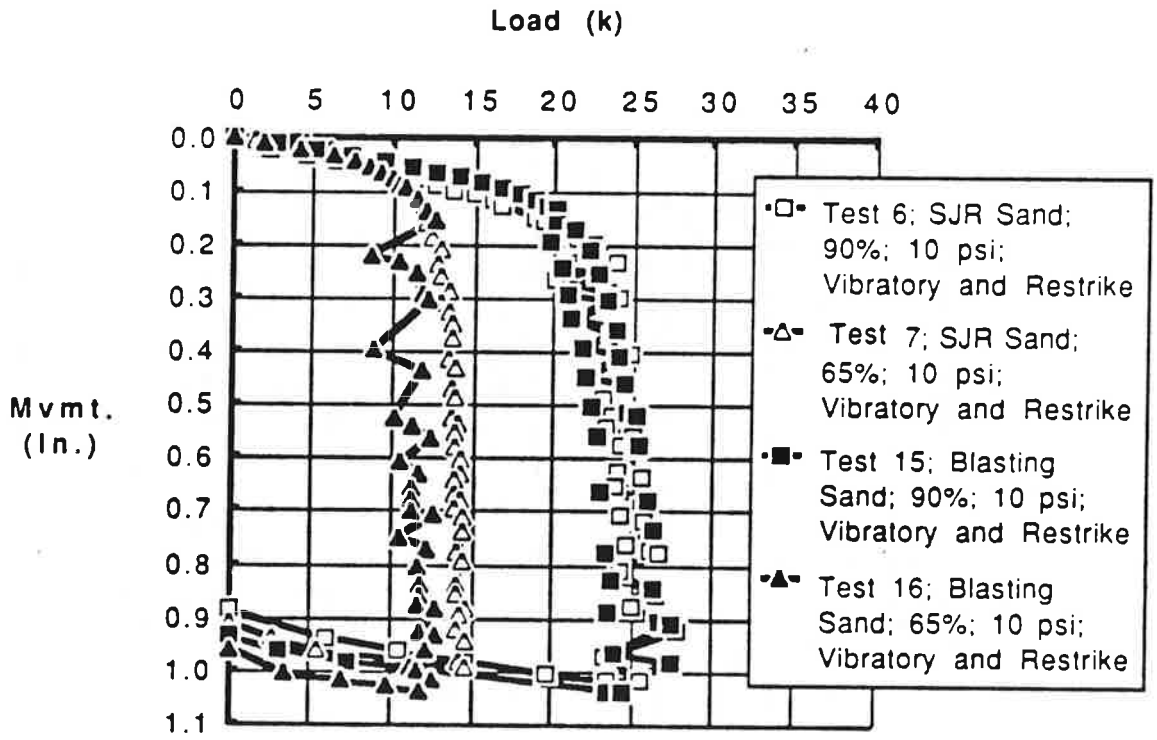

Fig. P.4. Results of Compression Tests: Vibro-Driven Piles with Restrike; Effective Chamber Pressure = 10 psi

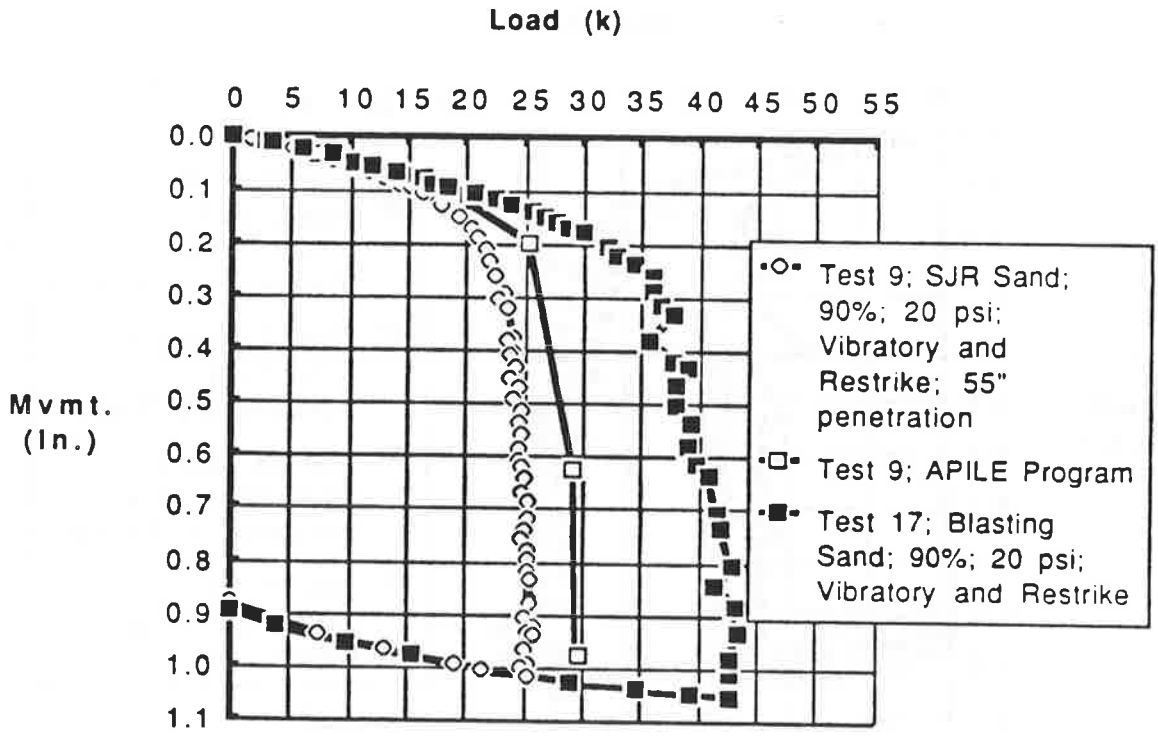

Fig. P.5. Results of Compression Tests: Vibro-Driven Piles with Restrike; Effective Chamber Pressure = 20 psi (Test 9 Synthesized to Full Penetration by Program APILE)

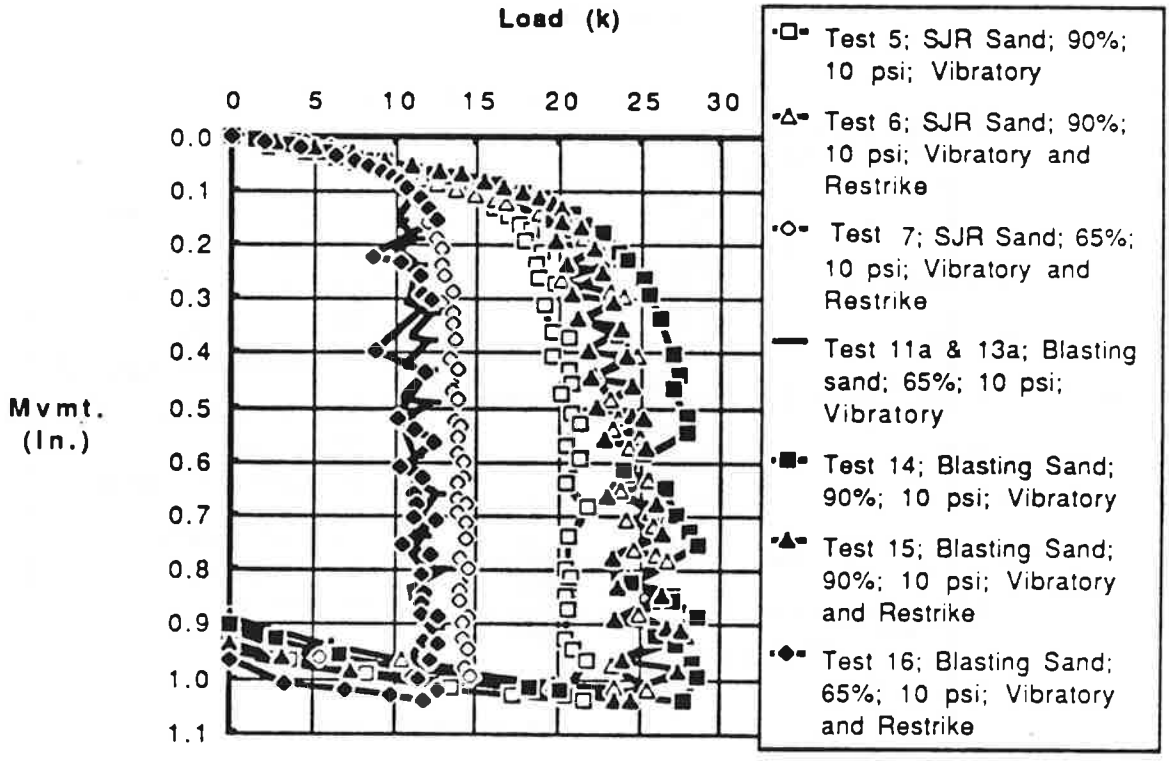

Fig. P.6. Results of Compression Tests: Comparison of Behavior of Vibro-Driven Piles and Restruck Vibro-Driven Piles; Effective Chamber Pressure = 10 psi

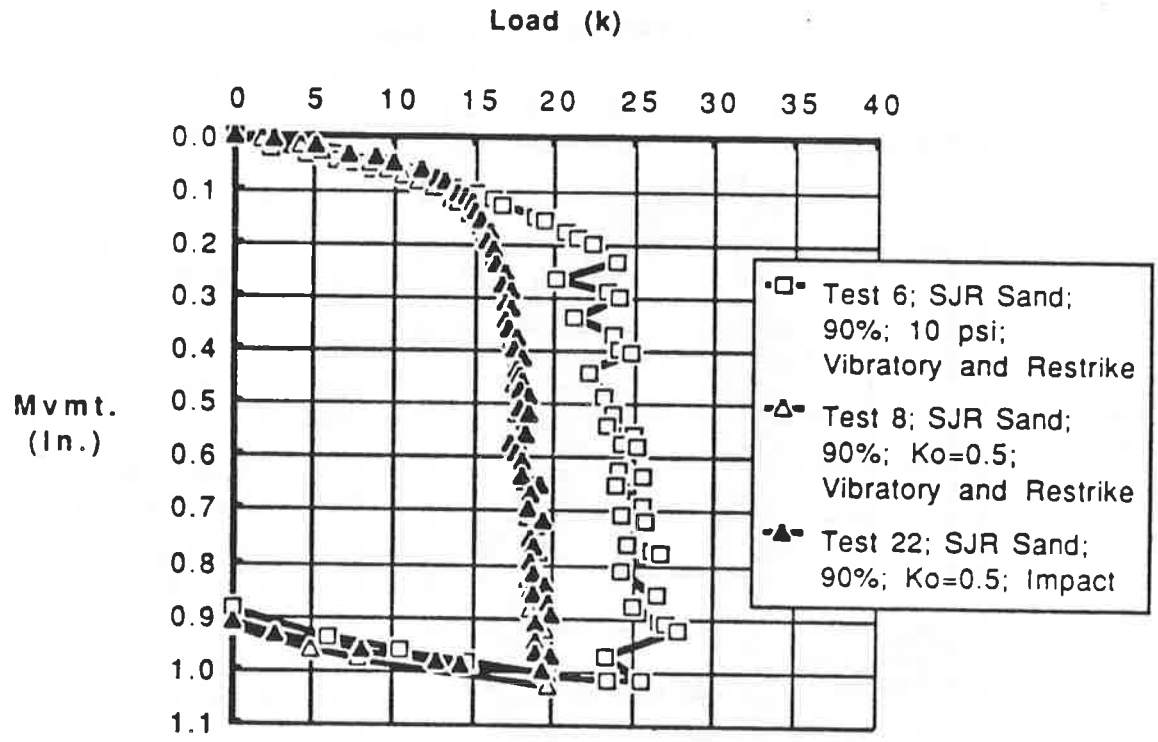

Fig. P.7. Results of Compression Tests: Comparison of Behavior of Piles Tested Under K_o = 0.5 with Piles Tested Under K_o = 1.0; Effective Chamber Pressure = 10 psi

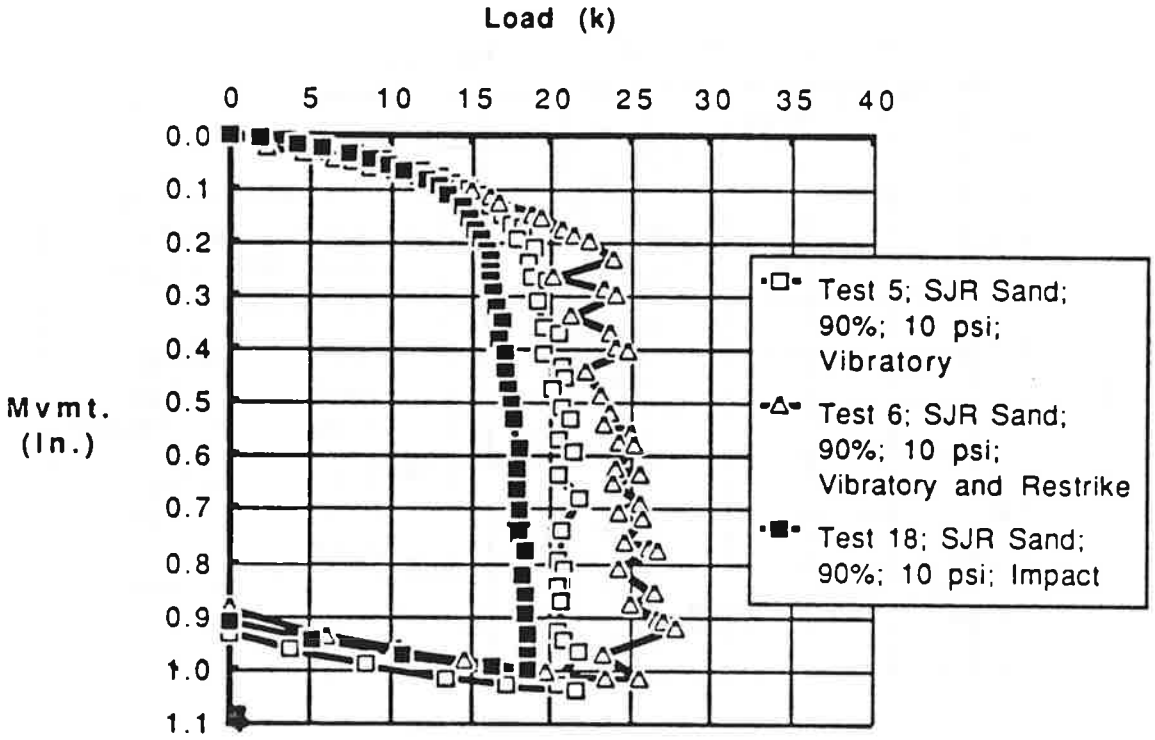

Fig. P. 8. Results of Compression Tests: Comparison of Piles Installed by Vibration, Vibration with Restriking and by Impact; SJR Sand, 90% Relative Density; 10 psi Effective Chamber Pressure

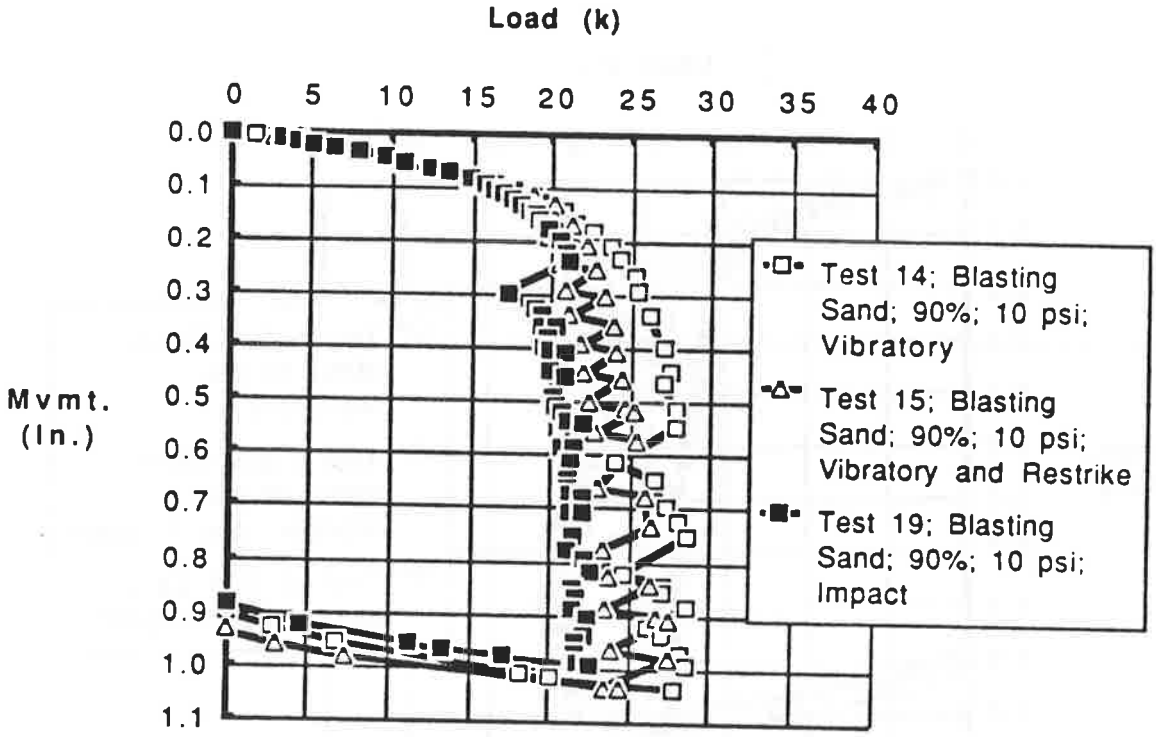

Fig. P. 9. Results of Compression Tests: Comparison of Piles Installed by Vibration, Vibration with Restriking and by Impact; BLS Sand, 90% Relative Density; 10 psi Effective Chamber Pressure

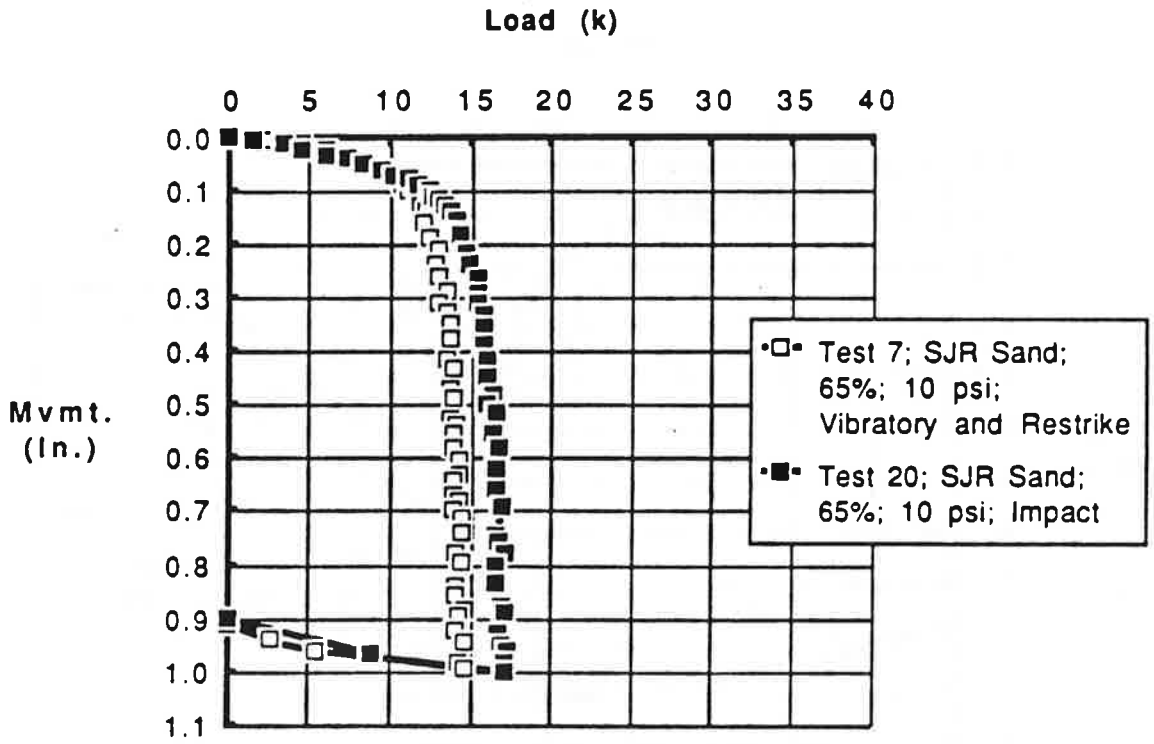

Fig. P.10. Results of Compression Tests: Comparison of Piles Installed by Vibration with Restriking and Impact; SJR Sand, 65% Relative Density; 10 psi Effective Chamber Pressure

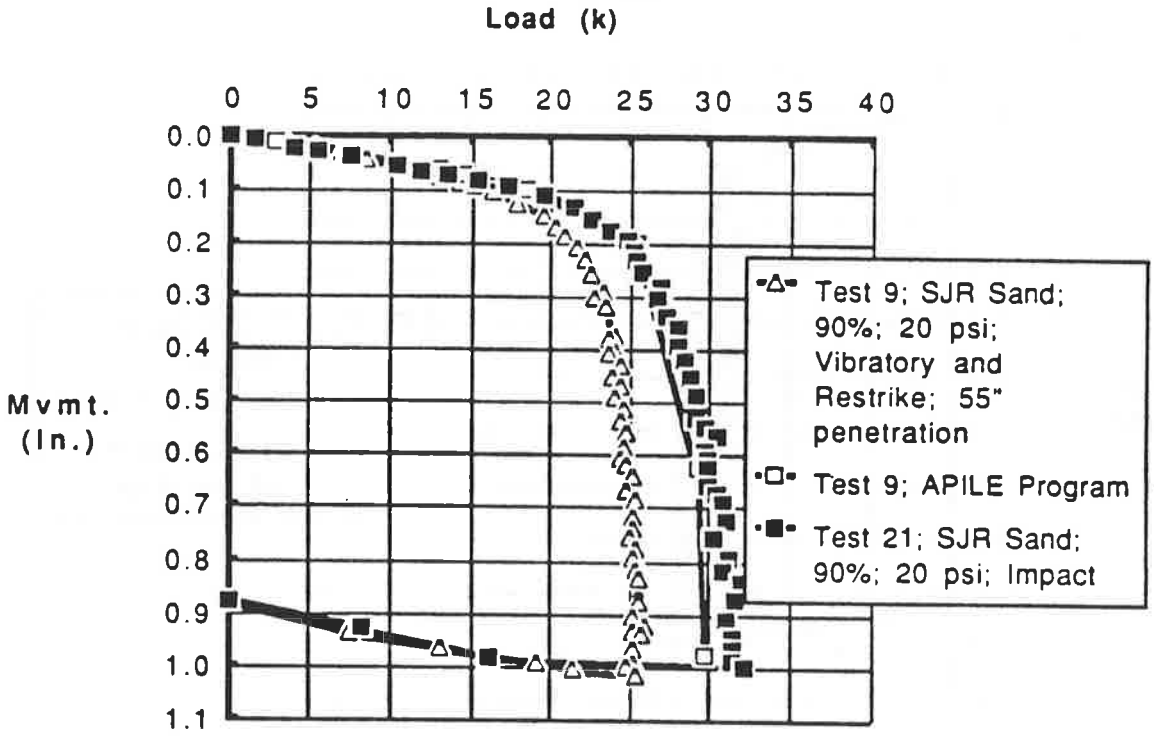

Fig. P.11. Results of Compression Tests: Comparison of Piles Installed by Vibration with Restriking and by Impact; SJR Sand, 90% Relative Density; 20 psi Effective Chamber Pressure

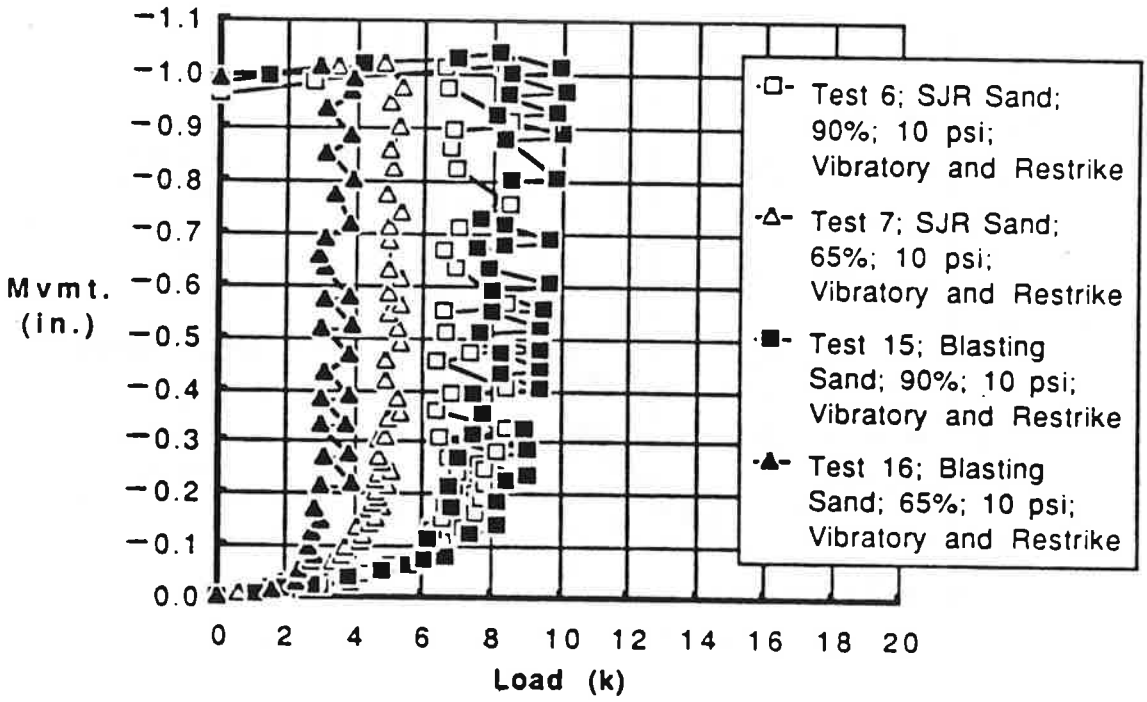

Fig. P.12. Results of UpliftTests: Vibro-Driven Piles with Restrike; Effective Chamber Pressure = 10 psi

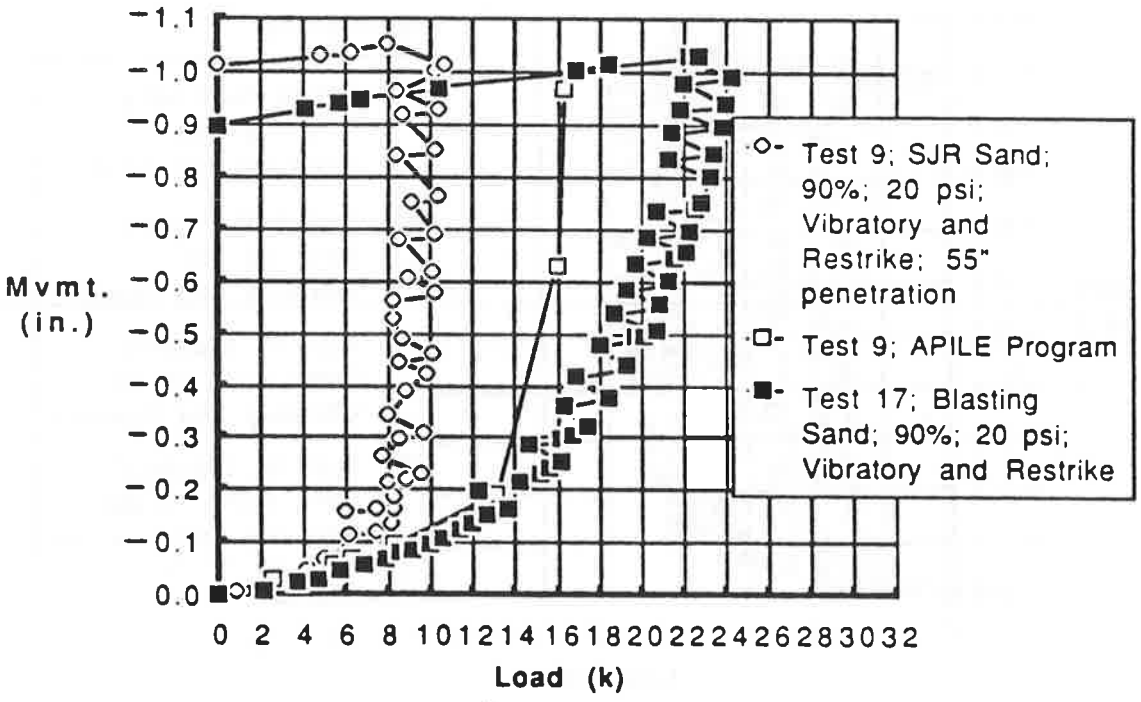

Fig. P.13. Results of UpliftTests: Vibro-Driven Piles with Restrike; Effective Chamber Pressure = 20 psi (Test 9 Synthesized to Full Penetration by Program APILE)

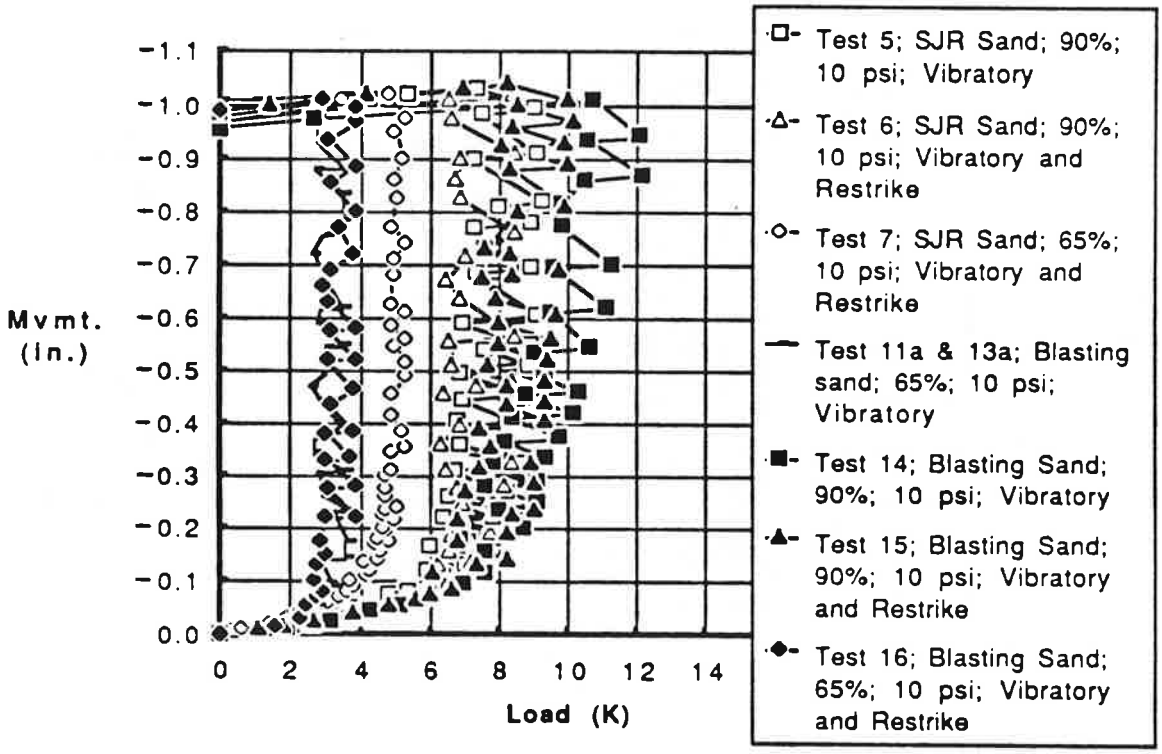

Fig. P.14. Results of Uplift Tests: Comparison of Behavior of Vibro-Driven Piles and Restruck Vibro-Driven Piles; Effective Chamber Pressure = 10 psi

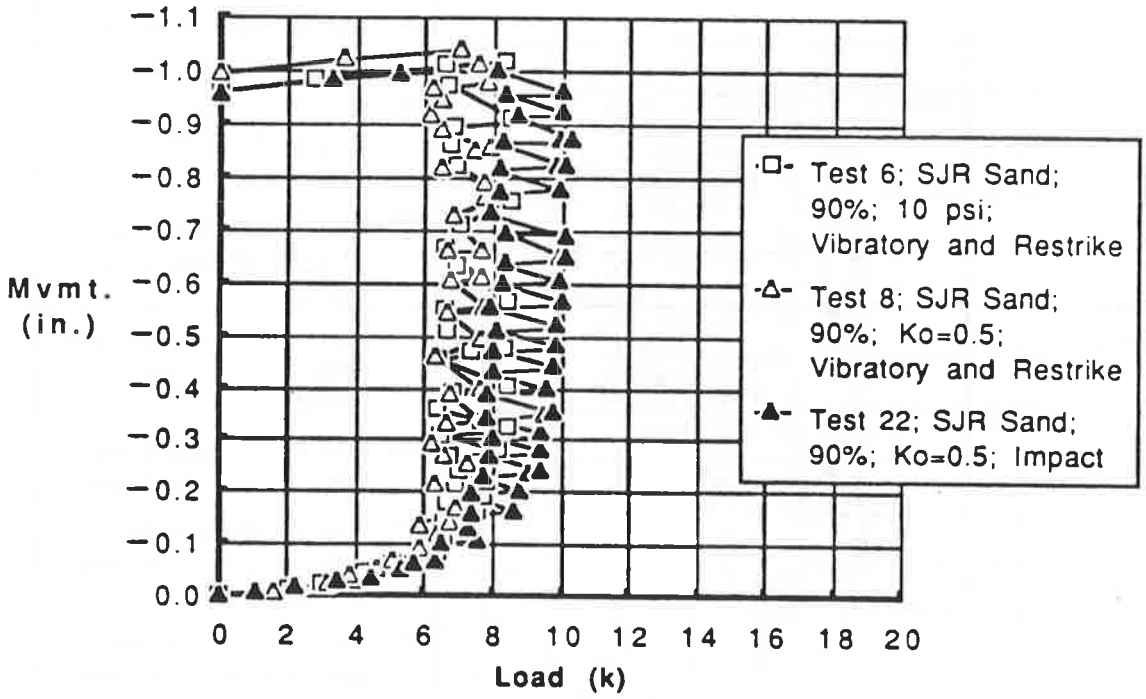

Fig. P.15. Results of Uplift Tests: Comparison of Behavior of Piles Tested Under K_o = 0.5 with Piles Tested Under K_o = 1.0; Effective Chamber Pressure = 10 psi

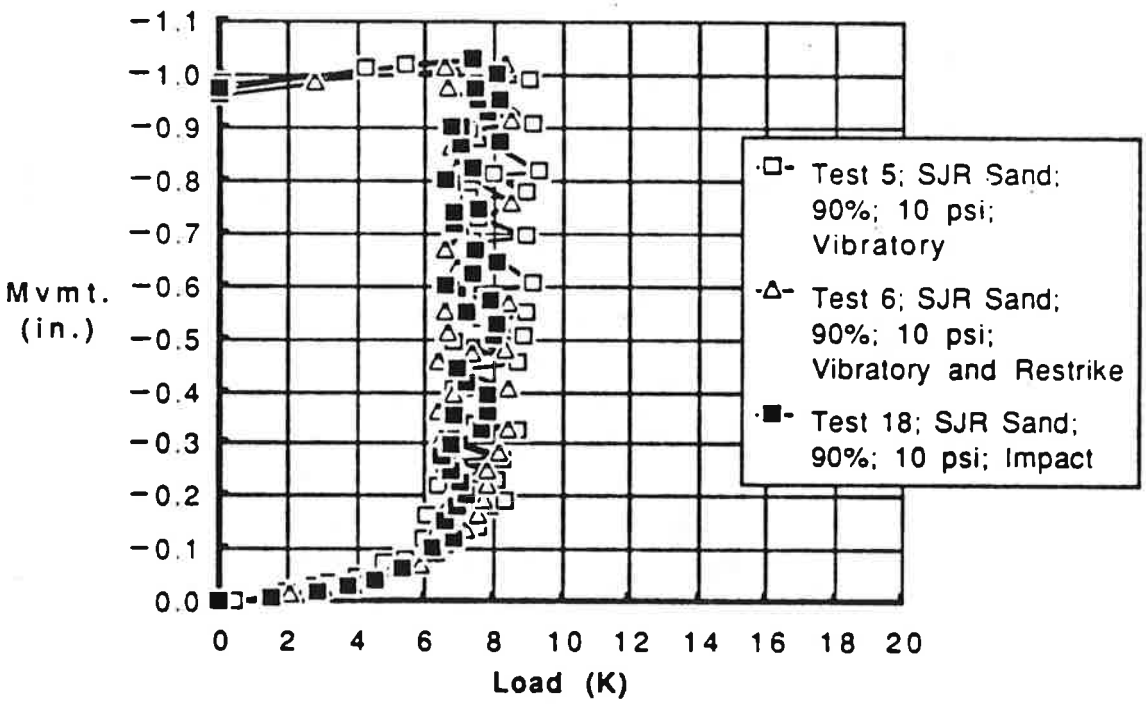

Fig. P. 16. Results of Uplift Tests: Comparison of Piles Installed by Vibration, Vibration with Restriking and by Impact; SJR Sand, 90% Relative Density; 10 psi Effective Chamber Pressure

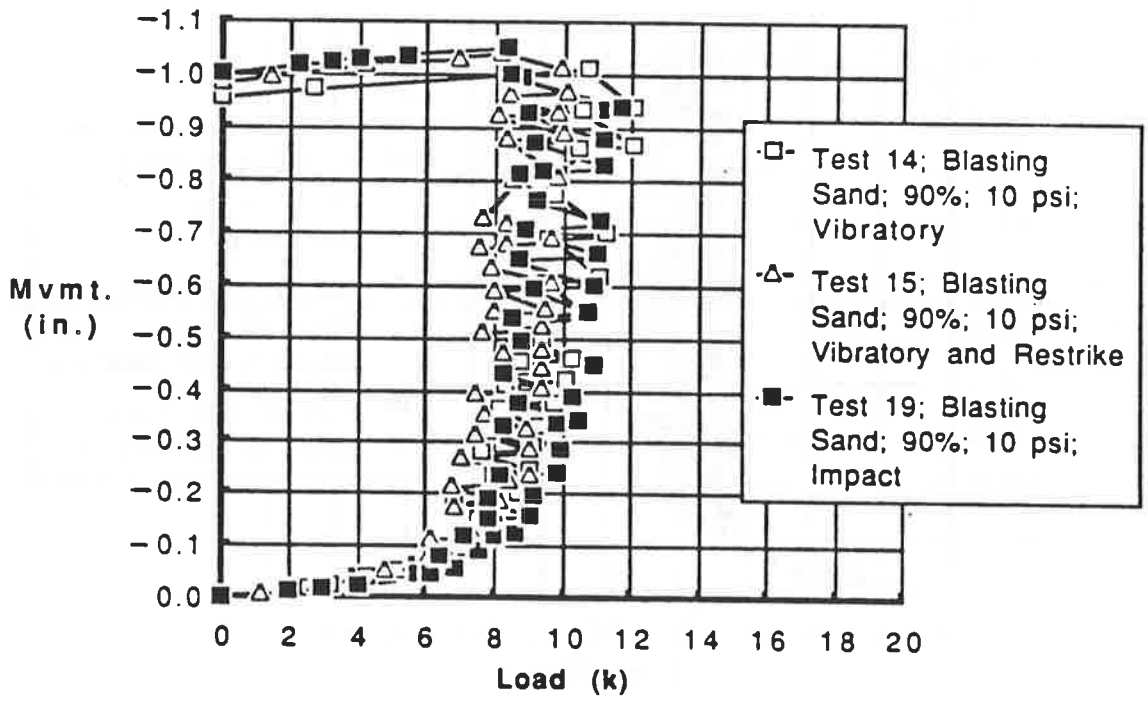

Fig. P. 17. Results of Uplift Tests: Comparison of Piles Installed by Vibration, Vibration with Restriking and by Impact; BLS Sand, 90% Relative Density; 10 psi Effective Chamber Pressure

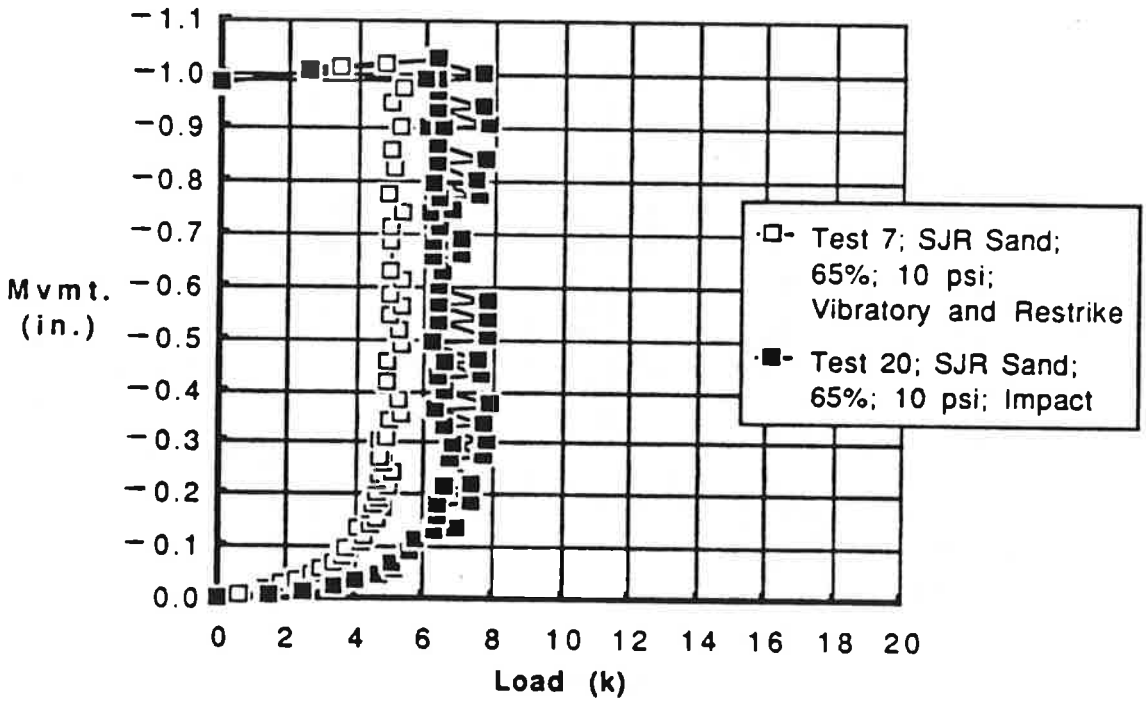

Fig. P.18. Results of UpliftTests: Comparison of Piles Installed by Vibration with Restriking and Impact; SJR Sand, 65% Relative Density; 10 psi Effective Chamber Pressure

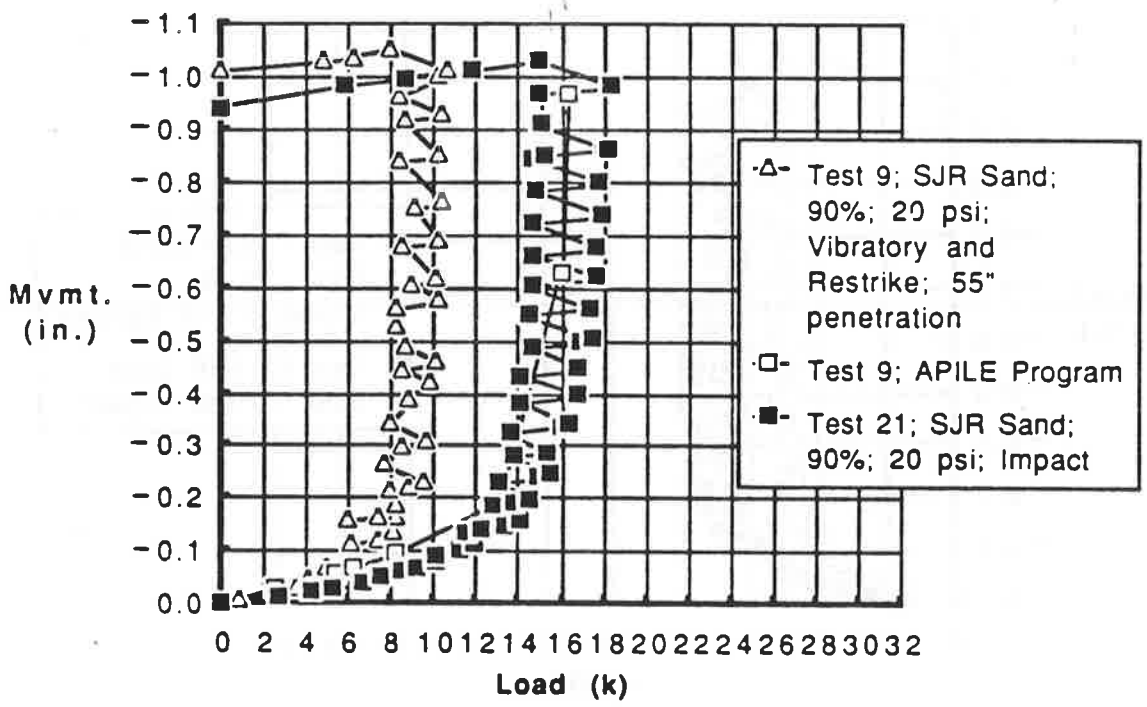

Fig. P.19. Results of Uplift Tests: Comparison of Piles Installed by Vibration with Restriking and by Impact; SJR Sand, 90% Relative Density; 20 psi Effective Chamber Pressure

APPENDIX Q

Static Unit Load Transfer Curves

Relationships of unit shaft shearing resistance (f) to local pile movement (w) and unit toe bearing resistance (q) to toe movement (w) for all static load tests are presented graphically in this appendix. Such information is useful in visually interpreting the maximum load transfer in both shaft shear and toe bearing and the shear and bearing stiffness at the pile-soil interface, particularly in terms of the relative effects of the test parameters. Experimentally derived unit load transfer relationships can also be used to synthesize the static axial behavior of piles of dimensions different from those employed in this study, providing the effective stresses in the system are scaled, which was done in this study. In fact, such synthesis was carried out in the development of the synthesized load-settlement and load-uplift relationships for Test 9 for the condition that the pile could be driven to full penetration. (See Appendix P.)

In order to develop the relationship of f to w and q to w, it is necessary first to determine the load distribution relationships along the pile. This was accomplished for every test by using the calibrated output of the strain gages mounted along the length of the pile, which are described in Appendix D, with calibration constants given in Appendix G. Figs. Q.1 to Q.30 show tabular data for load in pile and the corresponding graphical load distribution relationships for compression and uplift for several selected values of applied load for every test. In those figures, the load measured by the load cell is recorded at the top of each column in the table. Negative values of load indicate tension, while positive values indicate compression. The weight of the pile is not explicitly included in the results, since its effect was zeroed during the initial readings (Appendix F). However, the strain gage readings represent the effects of all other forces acting on the pile during a static load test. It is emphasized that the measured loads are based on zero readings taken before the pile was driven, and the unit load transfer curves that were developed from these load distribution curves therefore contain the effects of any residual stresses that were developed during installation of the pile.

During Tests 5 and 6 it was observed after completion of driving that sand had jammed between the pile and the pile port, which seemed to affect slightly the static load transfer near the point of entry of the pile into the test chamber. (This phenomenon likely had little effect on the vibratory installation, since the sand in that small space would have had to be in a quick state to have been transported there.) The load distributions for Tests 5 and 6 (Figs. Q.1 - Q.4), which, like all load distribution relations, were developed for purposes of deriving the unit load transfer relations through further reduction, were therefore determined by omitting the readings from the top load cell and strain gage level 1 (which were both situated above the top of the port) and including the results of only those instruments that were present below the port. An exception to this correction was the uplift test in Test 6 (Fig. Q.4), in which the strain gage circuit at level 2 malfunctioned, so that the load cell reading was used as load at the top of the pile. For all capacity tests following Test 6, the sand in the annular space between the pile and the pile port was physically removed before conducting the static tests, and the apparent load transfer at that point could no longer be observed.

Since the load distribution data are discrete, it is desirable to develop an analytical expression to fit the data. This was accomplished in this study by passing a series of second order least squares polynomials through the discrete data points. The fitted load

versus depth relations were determined from the expression $Q(z) = A + Bz + Cz^2$, where Q(z) is load in the pile head and z is depth below the chamber, measured from the top of the top cap (Appendix C), and A, B and C are least-squares coefficients. The f-w relations were developed for two depths: 20 inches and 60 inches, which represent the mid-point of the top and bottom halves of the pile, respectively. Unit shaft load transfer, f, was computed from a specified polynomial equation by taking the derivative of the least-squares function at the depth of interest (20 inches or 60 inches) and dividing that derivative by the circumference of the pile. The corresponding w value was calculated by subtracting from the average LVDT reading at the pile head the integral of the least-squares function of load versus depth from the pile head to the depth of interest and dividing the result by the AE of the pile, where A and E are the cross-sectional area and Young's modulus of the pile, respectively. Unit toe bearing, q, was computed at the toe of the pile by dividing the load given by the least-squares function at z = penetration of the toe by the toe area (12.57 square inches). The load at the toe was taken from the least-squares function rather than the direct load cell reading at the toe to minimize the effect of scatter in the data. This process was repeated for each of the several functions shown in Figs. Q.1 - Q.30 to develop sets of points defining the f-w and q-w relations.

Figures. Q.31 to Q.53 present the experimental f-w and q-w relationships for each of the capacity tests. The discrete points developed from the above computations were fit with a convenient function to give a continuous curve; however, no mathematical relations are presented for these functions. Negative values of w indicate upward movement of the pile relative to the soil, while positive values represent downward movement. Correspondingly, negative values of f represent downward-direct shear stresses on the face of the pile shaft, while positive values represent upward-directed shear stresses. Positive q indicates compressive load on the pile toe. The unit loads and movements from these relationships were then normalized by the effective horizontal chamber pressure (σ'_h) and pile diameter (B), respectively, and tests were grouped together according to sand grain size and method of installation, except that tests conducted at 65% relative density were grouped in terms of grain size only. Figs. Q.54 to Q.59 present the normalized f-w curves at 20-inch- (5B) and 60-inch- (15B) depths in the following order: all tests with SJR Sand at 65% relative density (Fig. Q.54); all tests on impact-driven piles with SJR Sand at 90% relative density (Fig. Q.55); all tests on vibro-driven tests with SJR Sand at 90% relative density (Fig. Q.56); all tests with BLS Sand at 65% relative density (Fig. Q.57); all tests on impact-driven piles with BLS Sand at 90% relative density (Fig. Q.58), and all tests on vibro-driven piles with BLS Sand at 90% relative density (Fig. Q.59). Figs. Q.60 to Q.62 show the normalized q-w curves in the following order: all tests with both sands at 65% relative density (Fig. Q.60); all tests with SJR Sand at 90% relative density (Fig. Q.61) and all tests with BLS Sand at 90% relative density (Fig. Q.62). Only the discrete values of f, q and w that are produced by the computations described above are given in Figs. Q.54 - Q.61. Trend lines have been drawn through these points and are presented in Chapter 2, which provides an interpretation of the significance of the results.

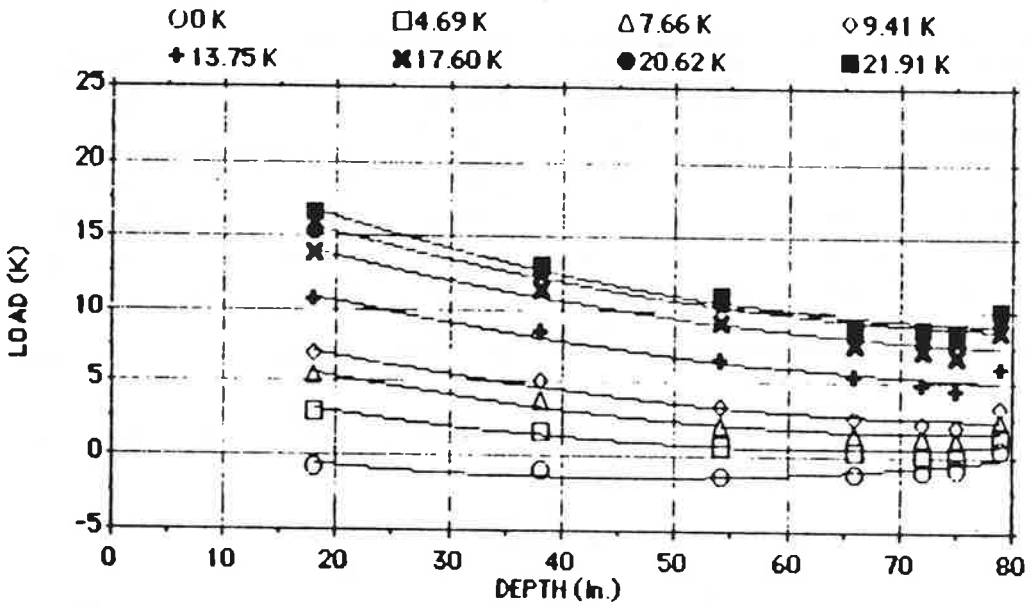

	DEPTH (In.)	0 K	4.69 K	7.66 K	9.41 K	13.75 K	17.60 K	20.62 K	21.91 K
1	0	0	4.69	7.66	9.41	13.75	17.60	20.62	21.91
2	18.00	-.67	3.05	5.46	6.93	10.71	13.76	15.37	16.56
3	38.00	-.98	1.74	3.72	5.07	8.40	11.31	12.68	13.00
4	54.00	-1.31	.81	2.17	3.36	6.62	9.20	10.48	11.08
5	66.00	-1.16	.38	1.57	2.56	5.40	7.73	8.64	8.84
6	72.00	-.92	.26	1.32	2.24	4.90	7.29	8.40	8.70
7	75.00	-.78	.28	1.23	2.06	4.59	6.96	8.19	8.48
8	79.00	.53	1.47	2.44	3.31	6.03	8.55	9.76	10.15

Fig. Q.1. Load Distribution for Test 5; Compression

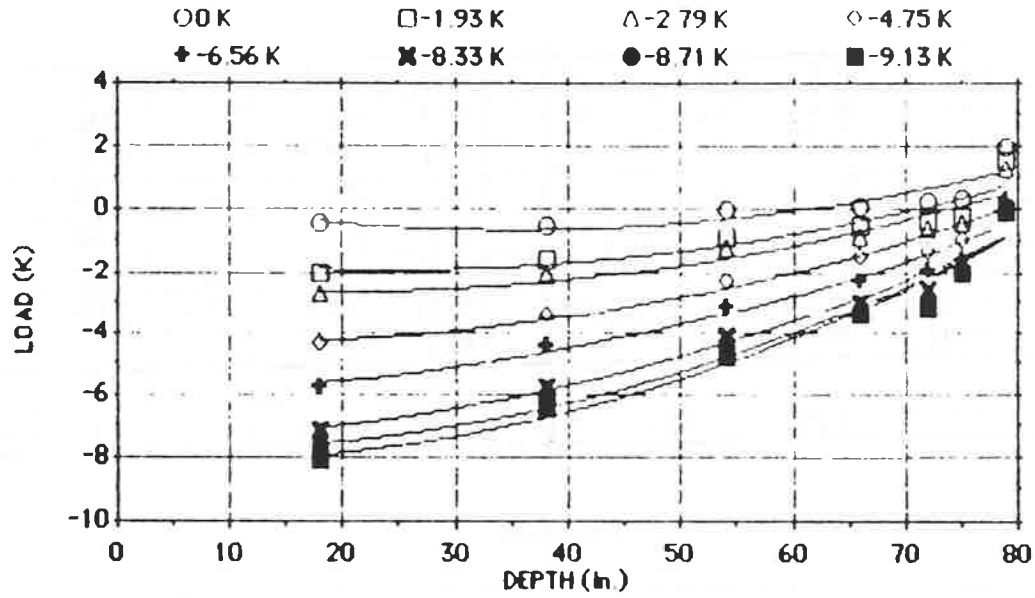

	DEPTH (in.)	0 K	-1.93 K	-2.79 K	-4.75 K	-6.56 K	-8.33 K	-8.71 K	-9.13 K
1	0	0	-1.930	-2.790	-4.750	-6.560	-8.330	-8.710	-9.130
2	18.000	-.460	-1.970	-2.720	-4.390	-5.750	-7.170	-7.690	-8.090
3	38.000	-.560	-1.550	-2.130	-3.420	-4.410	-5.710	-6.190	-6.430
4	54.000	.030	-.860	-1.260	-2.250	-3.150	-4.060	-4.530	-4.750
5	66.000	.130	-.530	-.840	-1.510	-2.250	-2.930	-3.280	-3.360
6	72.000	.240	-.350	-.640	-1.270	-1.870	-2.480	-2.820	-3.120
7	75.000	.310	-.240	-.420	-.980	-1.550	-1.960	-1.920	-1.970
8	79.000	2.010	1.550	1.320	.780	.290	-.090	-.060	-.010

Fig. Q.2. Load Distribution for Test 5; Uplift

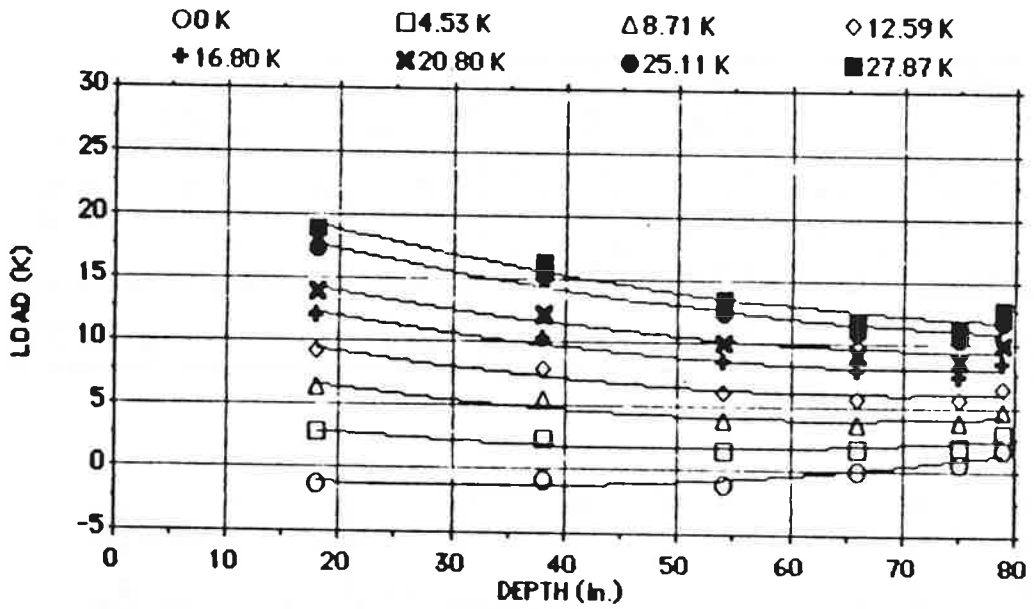

	DEPTH (In.)	0 K	4.53 K	8.71 K	12.59 K	16.80 K	20.80 K	25.11 K	27.87 K
1	0	0	4.53	8.71	12.59	16.80	20.80	25.11	27.87
2	18.00	-1.30	2.74	6.36	9.18	11.99	13.98	17.37	19.00
3	38.00	-.86	2.36	5.34	7.80	10.30	12.21	15.13	16.33
4	54.00	-1.06	1.42	3.87	6.05	8.40	10.02	12.31	13.46
5	66.00	-4.00E-2	1.79	3.77	5.75	7.75	9.19	10.87	11.72
6	75.00	.61	2.01	3.84	5.65	7.45	8.79	10.39	11.27
7	79.00	1.70	2.94	4.75	6.58	8.58	10.02	11.79	12.73

Fig. Q.3. Load Distribution for Test 6; Compression

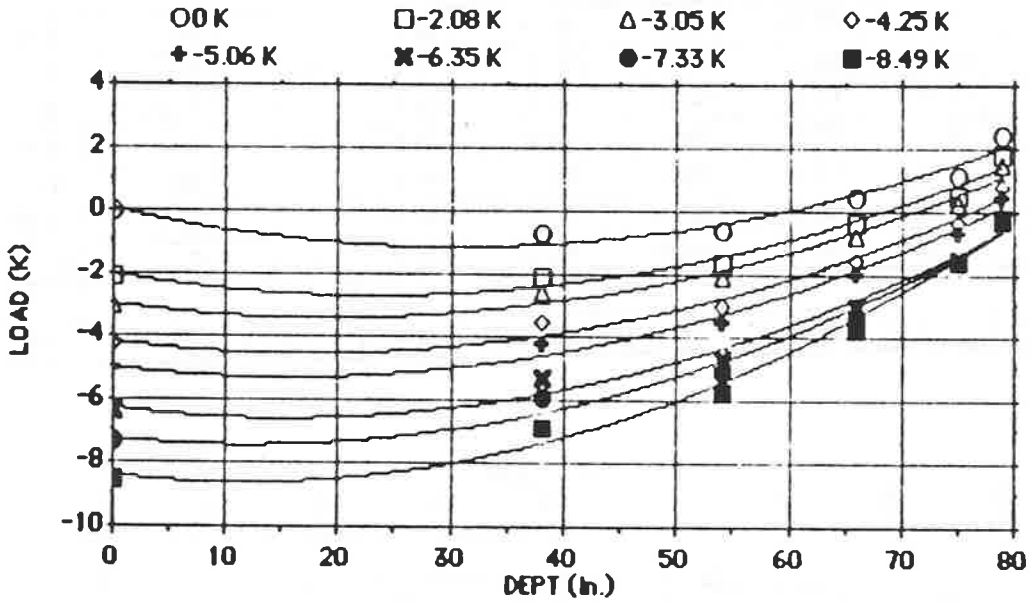

	DEPT (in.)	0 K	-2.08 K	-3.05 K	-4.25 K	-5.06 K	-6.35 K	-7.33 K	-8.49 K
1	0	0	-2.08	-3.05	-4.25	-5.06	-6.35	-7.33	-8.49
2	38.00	-.71	-2.07	-2.58	-3.60	-4.23	-5.32	-5.88	-6.87
3	54.00	-.60	-1.64	-2.13	-3.06	-3.58	-4.71	-5.12	-5.76
4	66.00	.41	-.38	-.80	-1.58	-2.00	-3.07	-3.39	-3.73
5	75.00	1.17	.52	.26	-.38	-.69	-1.49	-1.57	-1.60
6	79.00	2.46	1.81	1.49	.79	47	-.26	-.26	-.21

Fig. Q.4. Load Distribution for Test 6; Uplift

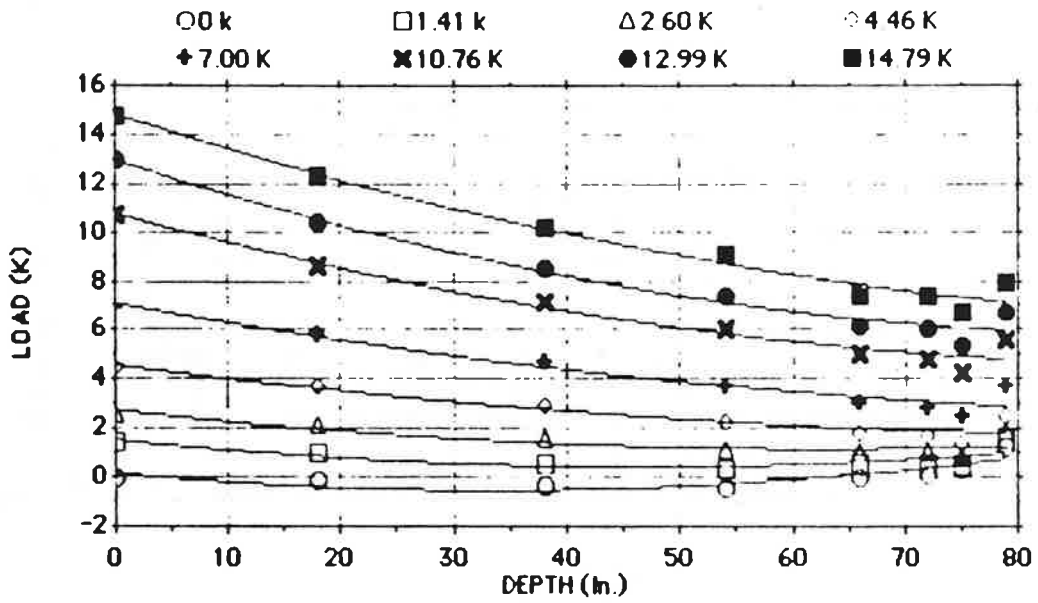

	DEPTH (In.)	0 k	1.41 k	2.60 K	4.46 K	7.00 K	10.76 K	12.99 K	14.79 K
1	0	0	1.41	2.60	4.46	7.00	10.76	12.99	14.79
2	18.00	-.14	1.04	2.15	3.74	5.79	8.61	10.36	12.36
3	38.00	-.35	.62	1.57	2.97	4.73	7.13	8.51	10.23
4	54.00	-.38	.39	1.13	2.25	3.73	6.00	7.42	9.05
5	66.00	0	.57	1.07	1.83	3.07	5.06	6.18	7.36
6	72.00	.11	.58	1.00	1.66	2.86	4.86	6.03	7.35
7	75.00	.37	.44	.79	1.39	2.50	4.31	5.43	6.70
8	79.00	1.26	1.60	1.93	2.52	3.65	5.55	6.68	7.94

Fig. Q.5. Load Distribution for Test 7; Compression

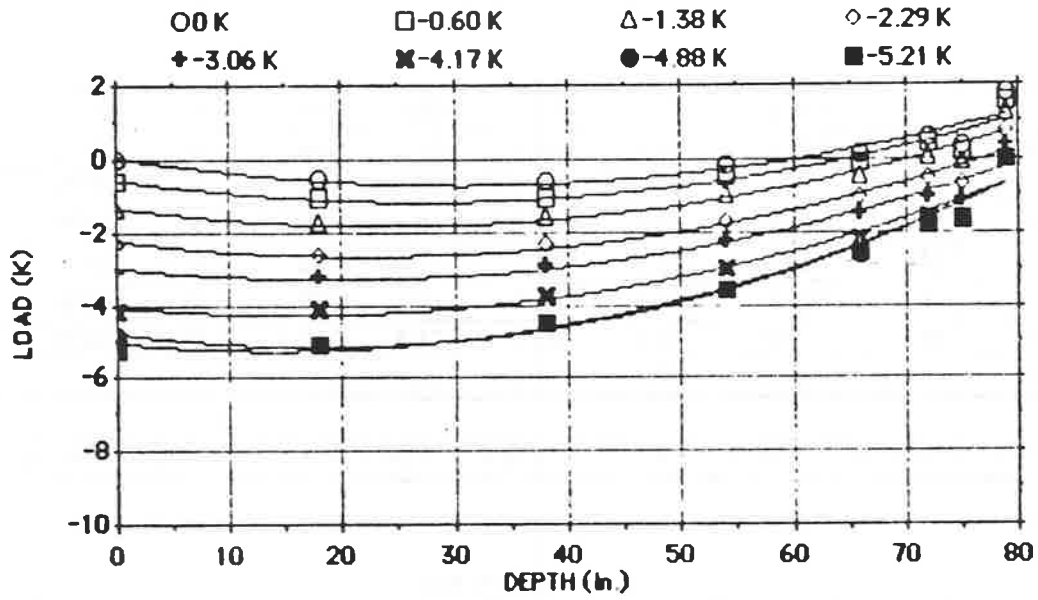

	DEPTH (in.)	0 K	-0.60 K	-1.38 K	-2.29 K	-3.06 K	-4.17 K	-4.88 K	-5.21 K
1	0	0	-.60	-1.38	-2.29	-3.06	-4.17	-4.88	-5.21
2	18.00	-.54	-1.09	-1.76	-2.60	-3.22	-4.12	-5.08	-5.06
3	38.00	-.63	-1.04	-1.61	-2.36	-2.90	-3.72	-4.48	-4.47
4	54.00	-.13	-.44	-.98	-1.73	-2.26	-2.97	-3.60	-3.59
5	66.00	.14	-7.00E-2	-.44	-1.05	-1.53	-2.16	-2.64	-2.54
6	72.00	.60	.41	4.00E-2	-.57	-1.04	-1.59	-1.77	-1.82
7	75.00	.36	.19	-.11	-.67	-1.12	-1.63	-1.62	-1.66
8	79.00	1.74	1.57	1.24	.72	.34	-2.00E-2	-4.00E-2	-8.00E-3

Fig. Q.6. Load Distribution for Test 7; Uplift

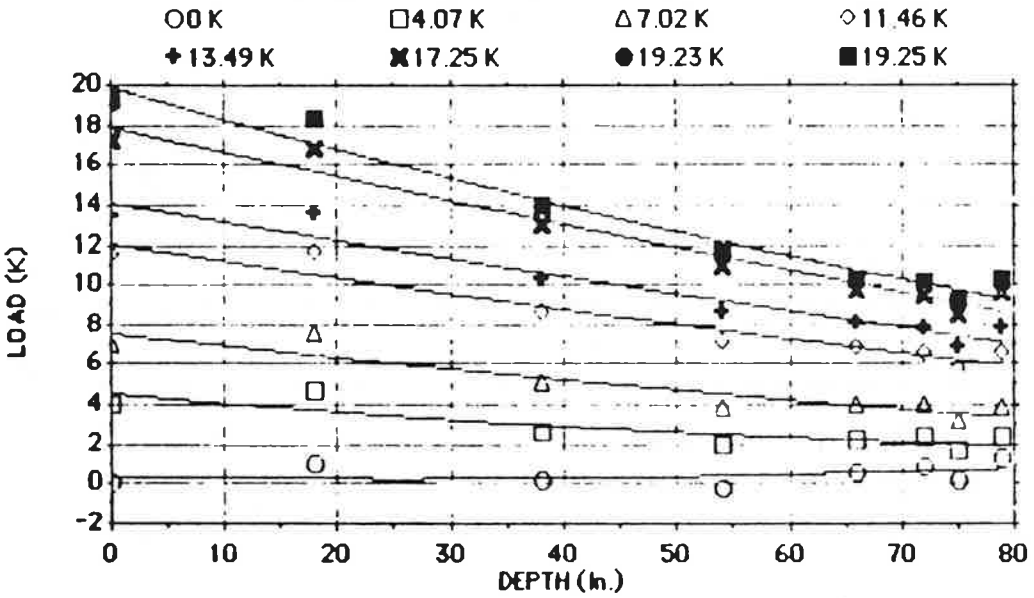

	DEPTH (In.)	0 K	4.07 K	7.02 K	11.46 K	13.49 K	17.25 K	19.23 K	19.25 K
1	0	0	4.07	7.02	11.46	13.49	17.25	19.23	19.25
2	18.00	1.01	4.72	7.57	11.73	13.64	16.91	18.38	18.38
3	38.00	.23	2.71	5.10	8.64	10.36	13.08	13.97	13.95
4	54.00	-.16	1.91	3.90	7.13	8.62	10.94	11.70	11.75
5	66.00	.65	2.26	3.98	6.83	8.10	9.73	10.36	10.35
6	72.00	.91	2.37	3.96	6.66	7.89	9.54	10.17	10.16
7	75.00	.24	1.64	3.17	5.77	6.91	8.49	9.17	9.21
8	79.00	1.24	2.35	3.85	6.57	7.84	9.58	10.23	10.25

Fig. Q.7. Load Distribution for Test 8; Compression

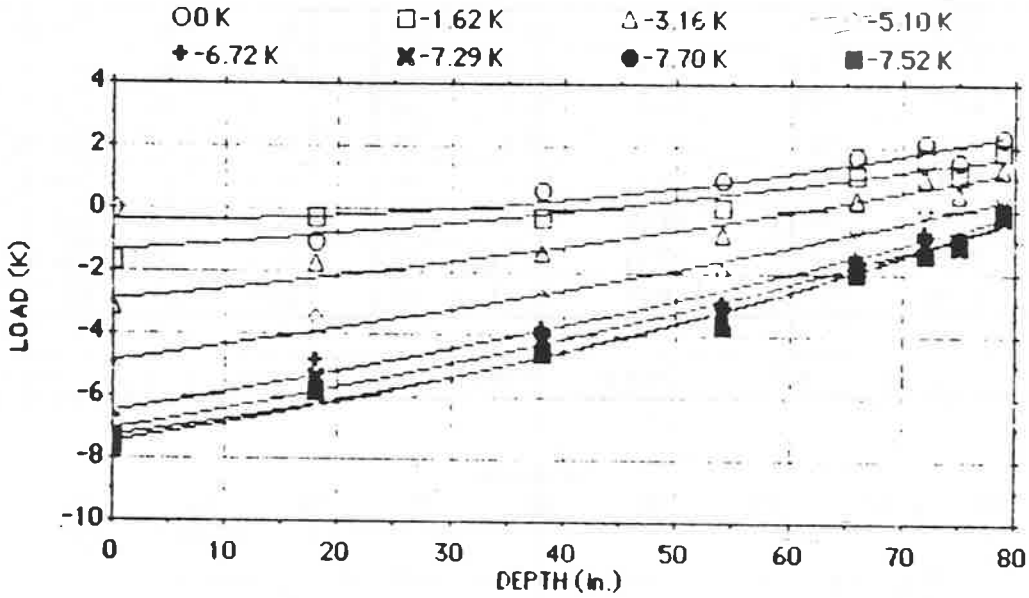

	DEPTH (in.)	0 K	-1.62 K	-3.16 K	-5.10 K	-6.72 K	-7.29 K	-7.70 K	-7.52 K
1	0	0	-1.62	-3.16	-5.10	-6.72	-7.29	-7.70	-7.52
2	18.00	-1.06	-.26	-1.71	-3.46	-4.90	-5.41	-5.86	-5.81
3	38.00	.64	-.26	-1.40	-2.76	-3.83	-4.21	-4.56	-4.57
4	54.00	.93	8.00E-2	-.78	-2.00	-2.94	-3.32	-3.65	-3.65
5	66.00	1.75	1.09	.39	-.65	-1.46	-1.79	-1.99	-1.97
6	72.00	2.16	1.62	1.01	2.00E-2	-.69	-1.01	-1.30	-1.41
7	75.00	1.57	1.11	.54	-.29	-.91	-1.14	-1.08	-.97
8	79.00	2.31	1.91	1.34	.46	-2.00E-2	-.14	-8.00E-2	-3.00E-2

Fig. Q.8. Load Distribution for Test 8; Uplift

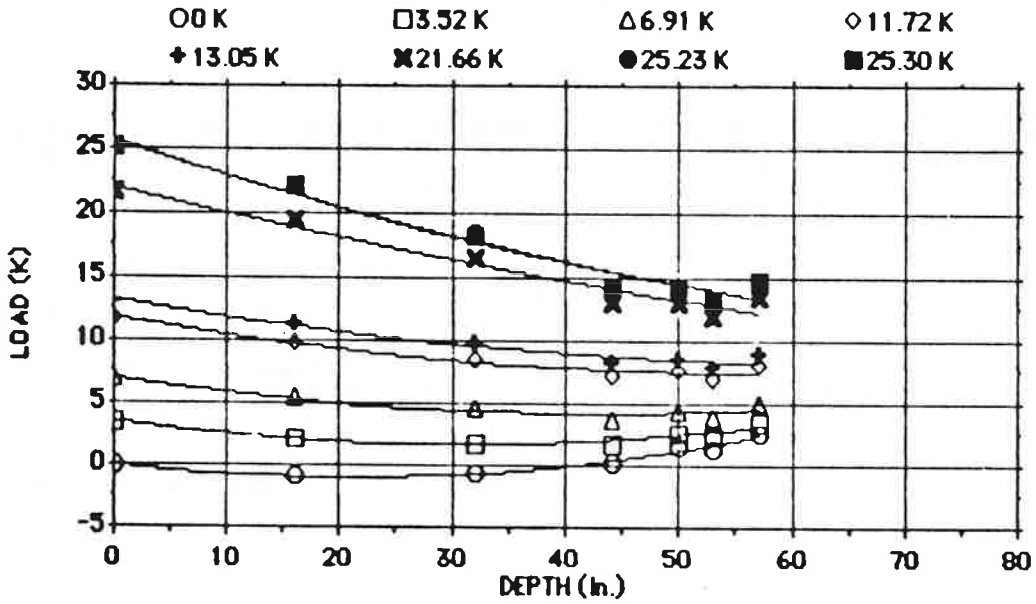

	DEPTH (In.)	0 K	3.52 K	6.91 K	11.72 K	13.05 K	21.66 K	25.23 K	25.30 K
1	0	0	3.52	6.91	11.72	13.05	21.66	25.23	25.30
2	16.00	-.94	2.14	5.34	9.87	11.36	19.52	22.18	22.17
3	32.00	-.64	1.82	4.63	8.57	9.84	16.57	18.54	18.34
4	44.00	.13	1.83	3.80	7.18	8.21	13.07	14.16	14.27
5	50.00	1.43	2.67	4.31	7.52	8.51	13.01	14.13	14.04
6	53.00	1.37	2.44	3.99	6.96	7.86	11.98	13.21	13.20
7	57.00	2.54	3.39	4.90	7.94	8.84	13.44	14.79	14.78

Fig. Q.9. Load Distribution for Test 9; Compression

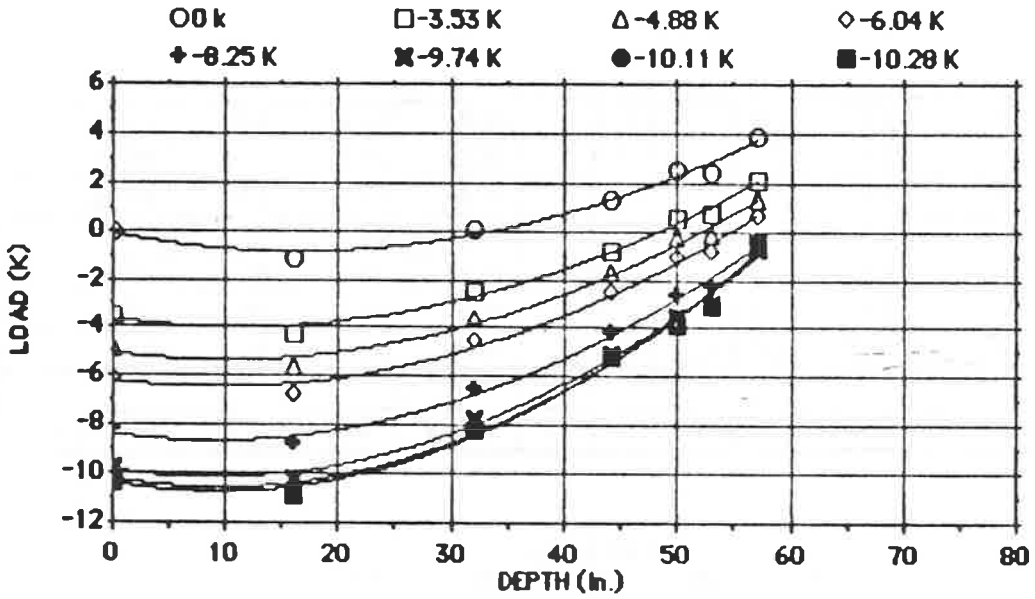

	DEPTH (in.)	0 k	-3.53 K	-4.88 K	-6.04 K	-8.25 K	-9.74 K	-10.11 K	-10.28 K
1	0	0	-3.53	-4.88	-6.04	-8.25	-9.74	-10.11	-10.28
2	16.00	-1.19	-4.26	-5.60	-6.76	-8.81	-10.25	-10.66	-10.83
3	32.00	.11	-2.48	-3.61	-4.55	-6.54	-7.74	-8.10	-8.17
4	44.00	1.35	-.79	-1.72	-2.55	-4.17	-5.04	-5.20	-5.18
5	50.00	2.49	.56	-.30	-1.03	-2.64	-3.49	-3.80	-3.85
6	53.00	2.46	.71	-.11	-.81	-2.31	-3.05	-3.10	-2.90
7	57.00	3.83	2.07	1.30	.66	-.45	-.71	-.54	-.45

Fig. Q.10. Load Distribution for Test 9; Uplift

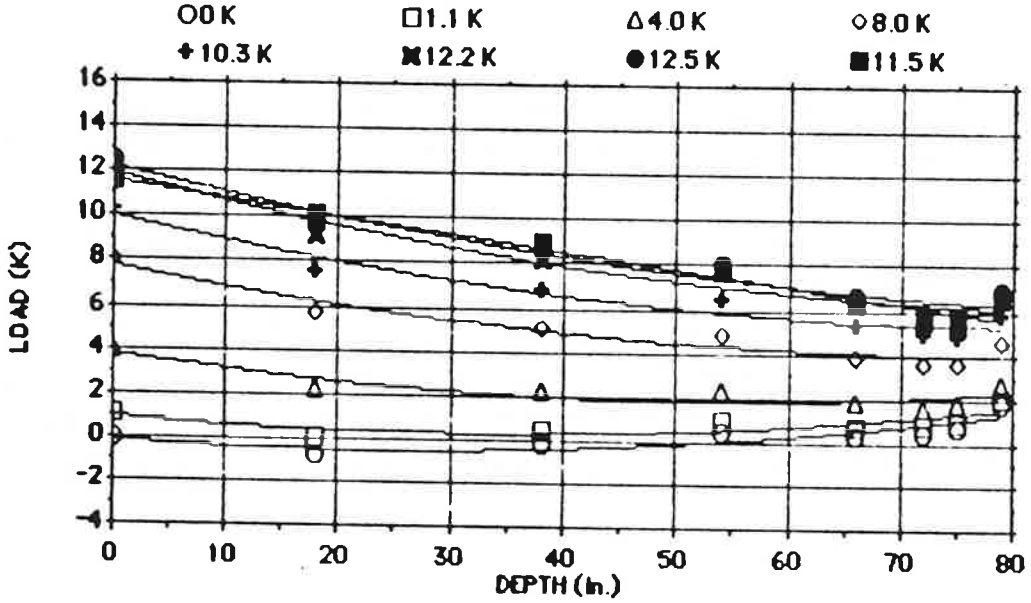

	DEPTH (in.)	0 K	1.1 K	4.0 K	8.0 K	10.3 K	12.2 K	12.5 K	11.5 K
1	0	0	1.10	4.00	8.00	10.30	12.20	12.50	11.50
2	18.00	-.80	6.00E-2	2.17	5.75	7.59	9.16	9.63	10.16
3	38.00	-.20	.46	2.16	5.13	6.83	8.15	8.55	8.90
4	54.00	.41	.95	2.30	4.84	6.49	7.76	8.05	7.67
5	66.00	.33	.76	1.79	3.87	5.35	6.28	6.69	6.26
6	72.00	.47	.80	1.65	3.57	4.89	5.76	5.96	5.59
7	75.00	.72	1.02	1.78	3.55	4.81	5.68	5.84	5.36
8	79.00	1.83	2.05	2.77	4.51	5.80	6.68	6.91	6.56

Fig. Q.11. Load Distribution for Test 11a/13a; Compression

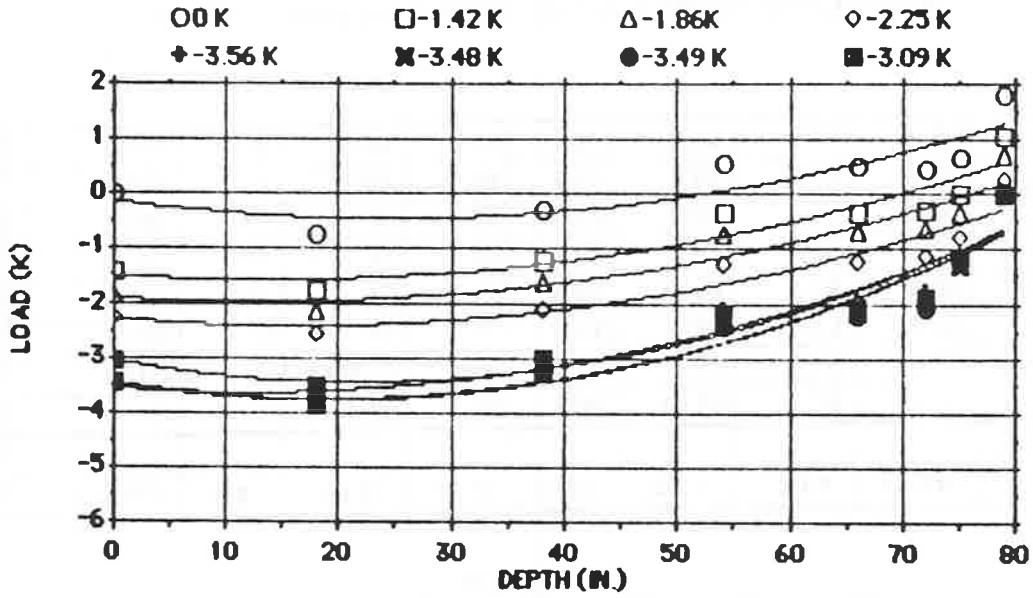

	DEPTH (IN.)	0 K	-1.42 K	-1.86K	-2.25 K	-3.56 K	-3.48 K	-3.49 K	-3.09 K
1	0	0	-1.42	-1.86	-2.25	-3.56	-3.48	-3.49	-3.09
2	18.00	-.71	-1.79	-2.16	-2.57	-3.72	-3.87	-3.87	-3.52
3	38.00	-.31	-1.23	-1.63	-2.12	-3.09	-3.29	-3.26	-3.04
4	54.00	.55	-.34	-.74	-1.26	-2.12	-2.35	-2.42	-2.24
5	66.00	.49	-.32	-.70	-1.22	-1.99	-2.17	-2.22	-2.09
6	72.00	.46	-.27	-.65	-1.13	-1.76	-1.98	-2.07	-1.88
7	75.00	.67	0	-.34	-.80	-1.28	-1.30	-1.23	-1.11
8	79.00	1.79	1.08	.71	.24	-3.80E-2	-1.00E-2	0	1.00E-2

Fig. Q.12. Load Distribution for Test 11a/13a; Uplift

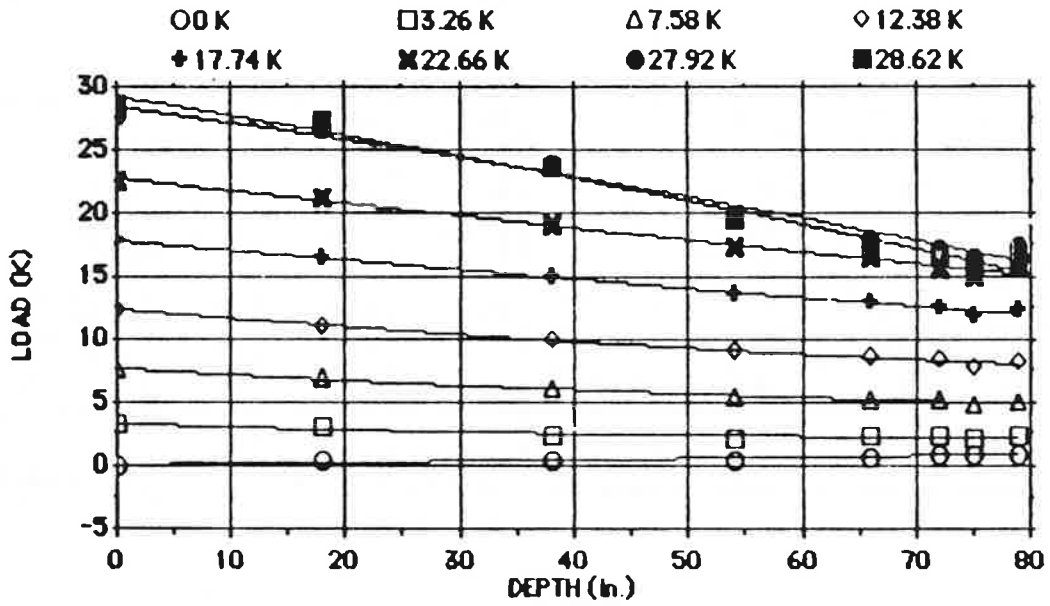

	DEPTH (in.)	0 K	3.26 K	7.58 K	12.38 K	17.74 K	22.66 K	27.92 K	28.62 K
1	0	0	3.26	7.58	12.38	17.74	22.66	27.92	28.62
2	18.00	.36	2.95	6.89	11.12	16.58	21.23	26.75	27.43
3	38.00	.44	2.42	6.01	9.90	14.93	19.14	23.89	23.68
4	54.00	.49	2.27	5.48	9.04	13.67	17.33	19.91	19.48
5	66.00	.70	2.29	5.29	8.65	13.10	16.44	18.11	17.34
6	72.00	.84	2.33	5.21	8.40	12.52	15.70	17.17	16.54
7	75.00	.77	2.17	4.87	7.93	11.86	15.00	16.54	15.80
8	79.00	.92	2.31	5.06	8.23	12.35	15.82	17.40	16.57

Fig. Q.13. Load Distribution for Test 14; Compression

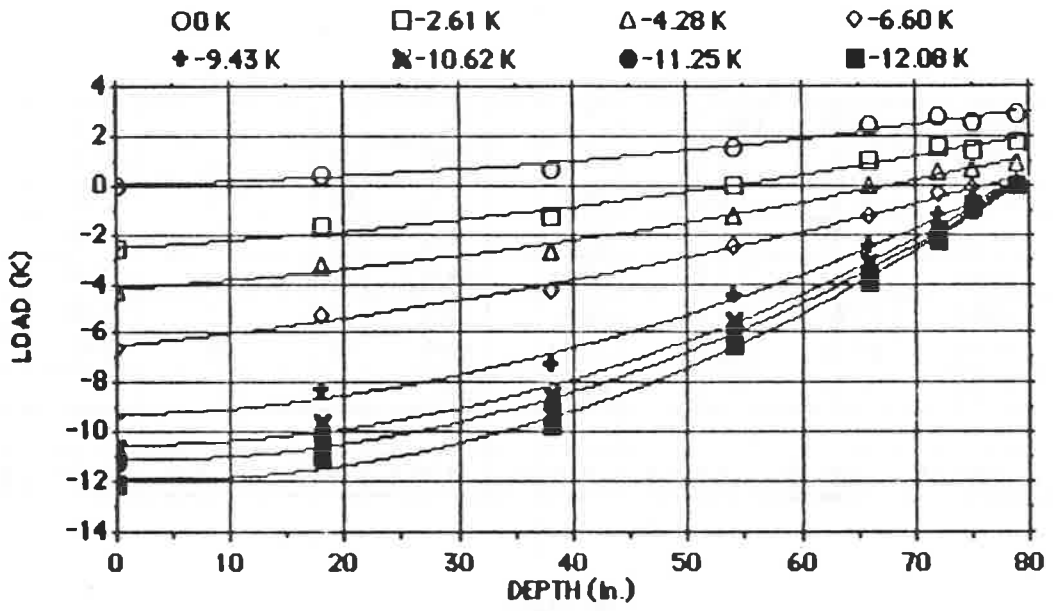

	DEPTH (in.)	0 K	-2.61 K	-4.28 K	-6.60 K	-9.43 K	-10.62 K	-11.25 K	-12.08 K
1	0	0	-2.61	-4.28	-6.60	-9.43	-10.62	-11.25	-12.08
2	18.00	.47	-1.74	-3.27	-5.28	-8.33	-9.67	-10.29	-11.02
3	38.00	.68	-1.28	-2.67	-4.32	-7.27	-8.49	-8.94	-9.71
4	54.00	1.56	-5.00E-2	-1.24	-2.51	-4.46	-5.50	-5.89	-6.50
5	66.00	2.43	1.03	-2.00E-2	-1.20	-2.54	-3.10	-3.52	-3.93
6	72.00	2.72	1.51	.58	-.33	-1.31	-1.78	-2.08	-2.30
7	75.00	2.58	1.47	.62	-.16	-.59	-.81	-1.06	-.97
8	79.00	2.90	1.77	.90	.11	-6.00E-2	-3.00E-2	-3.00E-2	-2.00E-2

Fig. Q.14. Load Distribution for Test 14; Uplift

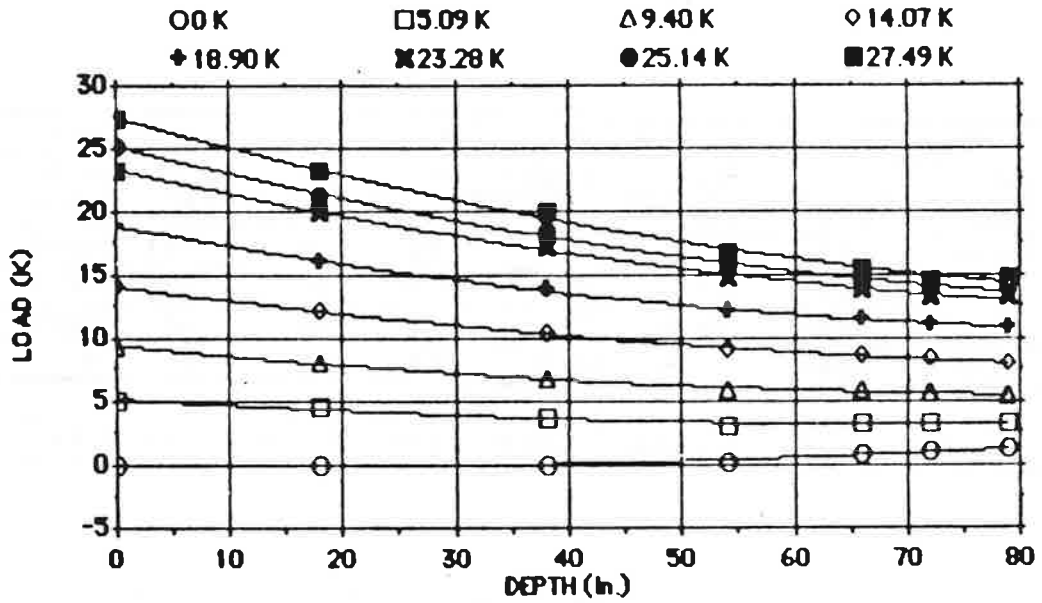

	DEPTH (In.)	0 K	5.09 K	9.40 K	14.07 K	18.90 K	23.28 K	25.14 K	27.49 K
1	0	0	5.09	9.40	14.07	18.90	23.28	25.14	27.49
2	18.00	1.00E-2	4.54	8.08	12.20	16.09	20.06	21.39	23.19
3	38.00	9.00E-2	3.67	6.81	10.47	13.95	17.21	18.40	19.95
4	54.00	.32	3.15	5.91	9.04	12.08	14.82	15.76	16.74
5	66.00	.82	3.27	5.78	8.64	11.49	13.82	14.43	15.53
6	72.00	1.03	3.22	5.64	8.39	11.11	13.29	13.96	14.64
7	79.00	1.26	3.21	5.50	8.14	10.90	13.21	13.98	14.71

Fig. Q.15. Load Distribution for Test 15; Compression

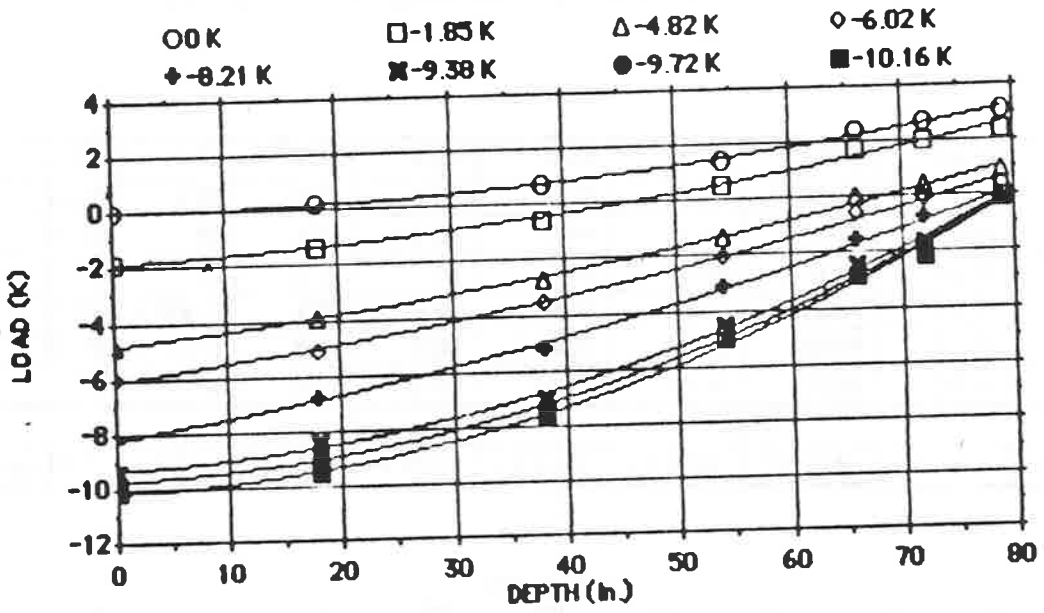

	DEPTH (in.)	0 K	-1.85 K	-4.82 K	-6.02 K	-8.21 K	-9.38 K	-9.72 K	-10.16 K
1	0	0	-1.85	-4.82	-6.02	-8.21	-9.38	-9.72	-10.16
2	18.00	.22	-1.34	-3.94	-5.13	-6.82	-8.44	-9.05	-9.48
3	38.00	.69	-.55	-2.73	-3.60	-5.21	-7.05	-7.34	-7.66
4	54.00	1.37	.50	-1.37	-2.05	-3.17	-4.57	-4.77	-5.08
5	66.00	2.42	1.72	-1.00E-2	-.61	-1.55	-2.42	-2.88	-2.88
6	72.00	2.66	2.03	.46	-4.00E-2	-.79	-1.65	-1.89	-2.21
7	79.00	3.09	2.44	.88	.44	-8.00E-2	-5.00E-2	-3.00E-2	-1.00E-2

Fig. Q.16. Load Distribution for Test 15; Uplift

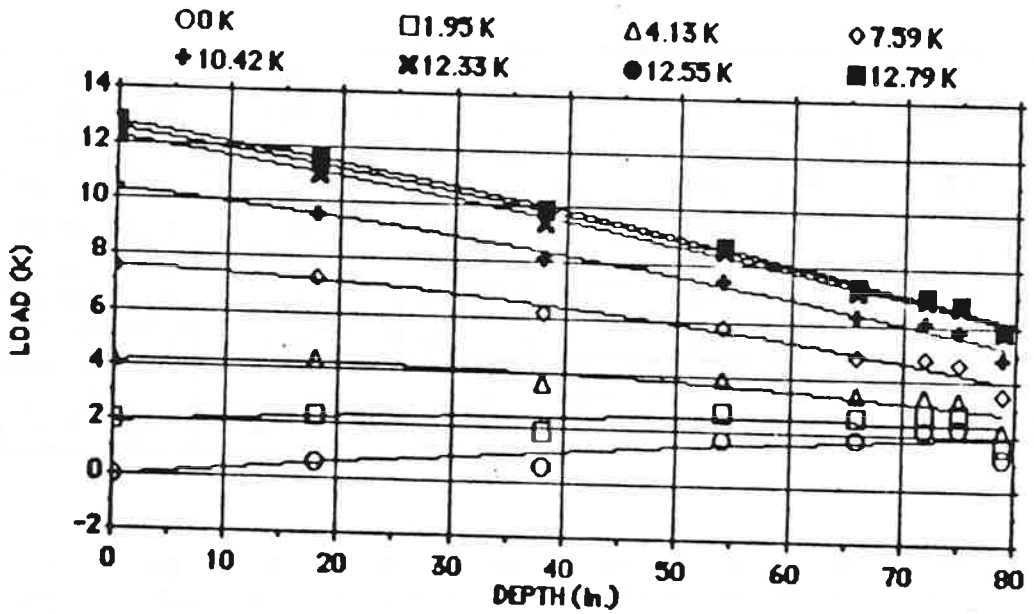

	DEPTH (In.)	0 K	1.95 K	4.13 K	7.59 K	10.42 K	12.33 K	12.55 K	12.79 K
1	0	0	1.95	4.13	7.59	10.42	12.33	12.55	12.79
2	18.00	.61	2.28	4.27	7.28	9.57	11.00	11.41	11.57
3	38.00	.56	1.87	3.52	6.17	8.16	9.46	9.74	9.94
4	54.00	1.65	2.66	3.82	5.74	7.46	8.54	8.60	8.76
5	66.00	1.82	2.58	3.34	4.79	6.25	7.15	7.22	7.36
6	72.00	2.19	2.77	3.40	4.74	6.07	6.87	7.08	7.07
7	75.00	2.25	2.73	3.29	4.53	5.80	6.64	6.70	6.73
8	79.00	1.19	1.61	2.18	3.46	4.80	5.71	5.83	5.90

Fig. Q.17. Load Distribution for Test 16; Compression

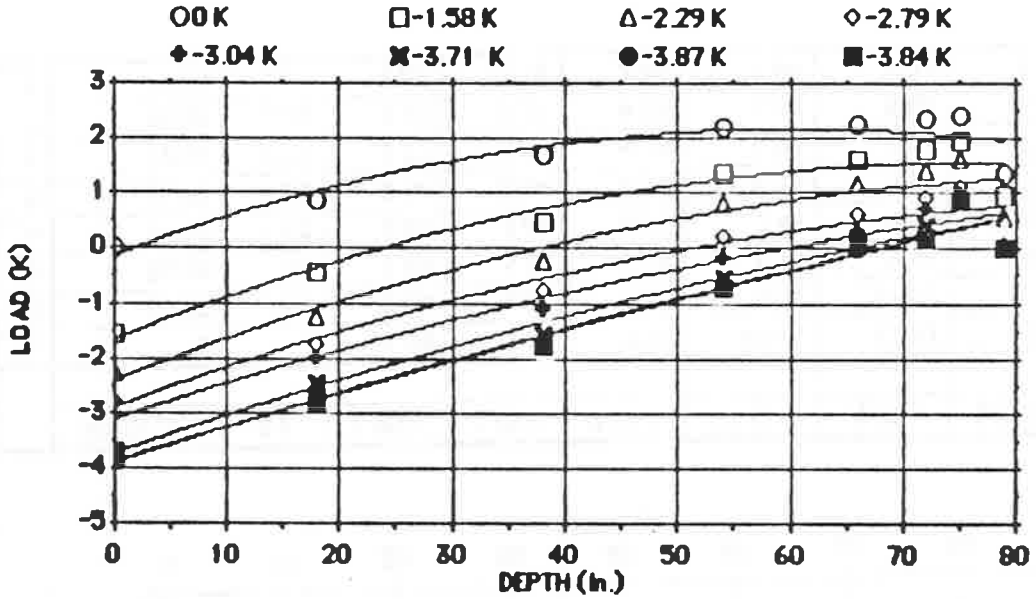

	DEPTH (in.)	0 K	-1.58 K	-2.29 K	-2.79 K	-3.04 K	-3.71 K	-3.87 K	-3.84 K
1	0	0	-1.58	-2.29	-2.79	-3.04	-3.71	-3.87	-3.84
2	18.00	.85	-.44	-1.25	-1.77	-2.04	-2.49	-2.76	-2.79
3	38.00	1.72	.49	-.22	-.77	-1.11	-1.56	-1.74	-1.78
4	54.00	2.22	1.35	.81	.20	-.18	-.51	-.71	-.74
5	66.00	2.24	1.60	1.17	.60	.34	8.00E-2	4.00E-2	.10
6	72.00	2.36	1.83	1.43	.91	.70	.43	.28	.21
7	75.00	2.40	1.94	1.61	1.12	.96	.86	.85	.84
8	79.00	1.37	.94	.59	9.00E-2	0	0	1.00E-2	2.00E-2

Fig. Q.18. Load Distribution for Test 16; Uplift

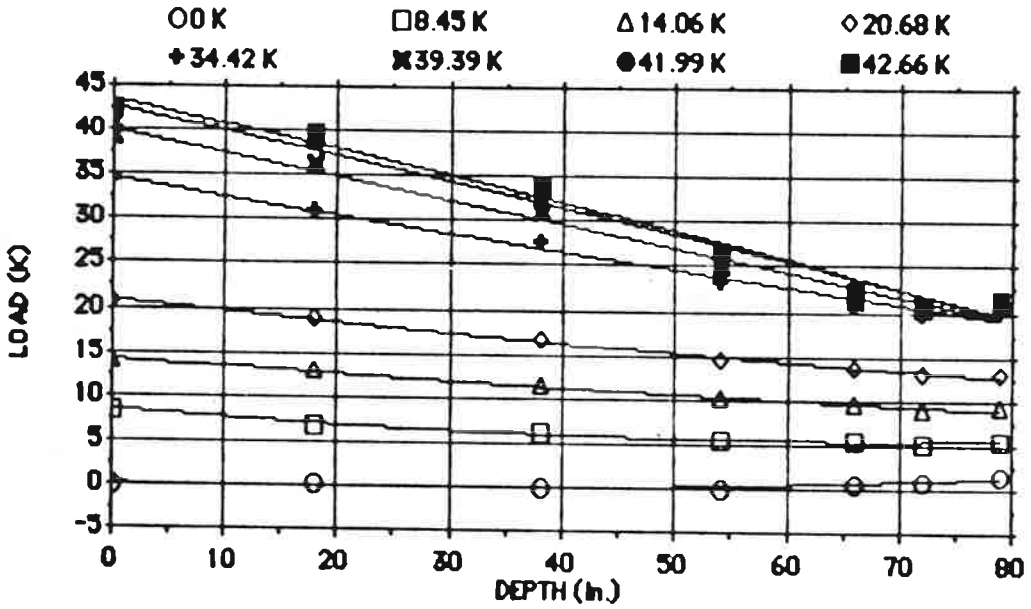

	DEPTH (in.)	0 K	8.45 K	14.06 K	20.68 K	34.42 K	39.39 K	41.99 K	42.66 K
1	0	0	8.45	14.06	20.68	34.41	39.39	41.99	42.66
2	18.00	.14	6.95	12.96	18.98	31.14	36.23	38.76	39.82
3	38.00	2.00E-2	6.10	11.40	16.77	27.66	31.02	33.10	33.79
4	54.00	-8.00E-2	5.49	10.10	14.64	23.34	25.25	26.43	26.69
5	66.00	.59	5.41	9.51	13.56	20.76	21.39	22.54	22.32
6	72.00	.92	5.25	9.05	12.90	19.85	20.32	20.85	20.91
7	79.00	1.38	5.58	9.14	13.00	20.10	20.73	21.46	21.32

Fig. Q.19. Load Distribution for Test 17; Compression

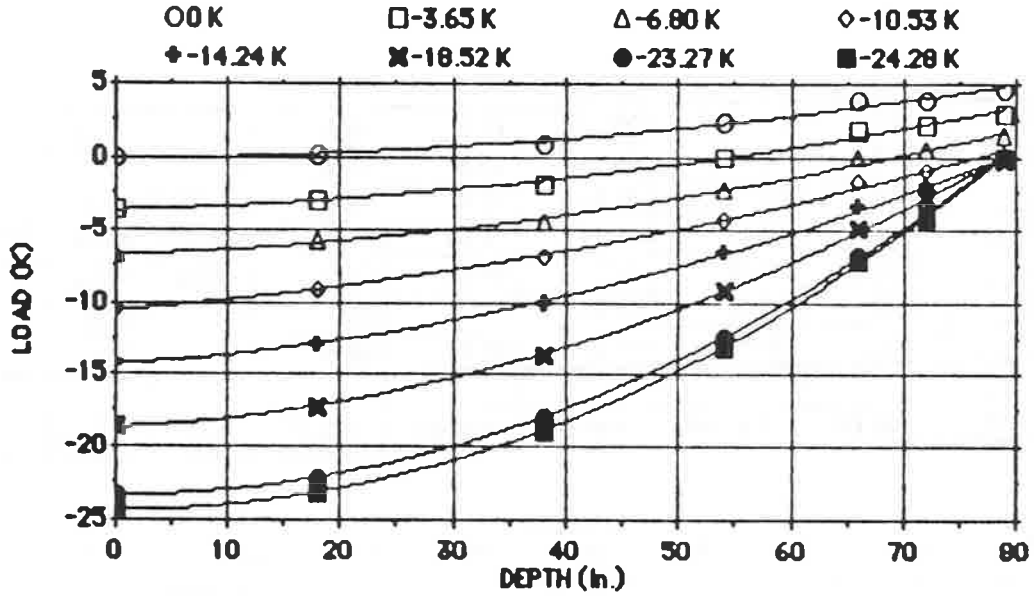

	DEPTH (in.)	0 K	-3.65 K	-6.80 K	-10.53 K	-14.24 K	-18.52 K	-23.27 K	-24.28 K
1	0	0	-3.65	-6.80	-10.53	-14.24	-18.52	-23.27	-24.28
2	18.00	.18	-2.97	-5.88	-9.07	-12.86	-17.23	-22.24	-23.11
3	38.00	.94	-1.85	-4.51	-7.00	-10.08	-13.68	-17.89	-18.82
4	54.00	2.36	-3.00E-2	-2.24	-4.33	-6.63	-9.15	-12.31	-13.12
5	66.00	3.85	1.83	-8.00E-2	-1.71	-3.41	-4.79	-6.68	-7.05
6	72.00	3.91	2.24	.55	-.87	-1.95	-2.84	-3.86	-4.18
7	79.00	4.64	3.01	1.42	.24	-.27	-.21	-.10	-6.00E-2

Fig. Q.20. Load Distribution for Test 17; Uplift

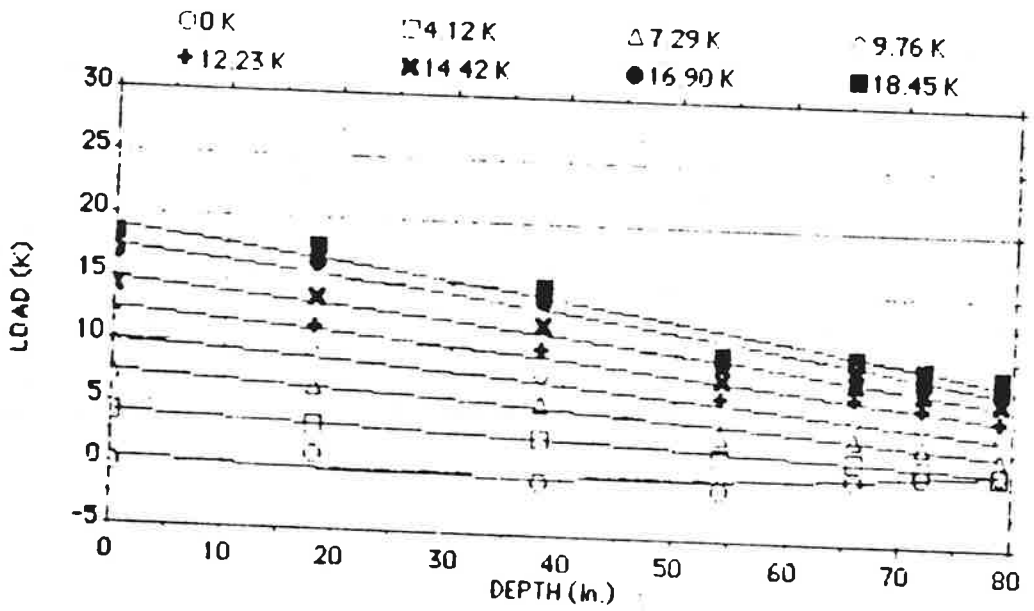

	DEPTH (in.)	0 K	4.12 K	7.29 K	9.76 K	12.23 K	14.42 K	16.90 K	18.45 K
1	0	0	4.12	7.29	9.76	12.23	14.42	16.90	18.45
2	18.00	1.13	3.55	6.61	9.05	11.39	13.73	16.45	17.78
3	39.00	-.68	2.90	5.68	7.86	9.99	11.98	14.00	15.06
4	54.00	-.82	1.79	3.53	5.04	6.54	8.04	9.35	10.02
5	66.00	.20	1.71	3.44	5.03	6.69	8.13	9.28	10.00
6	72.00	.76	1.40	2.95	4.47	6.11	7.47	8.47	9.20
7	79.00	1.01	.94	2.27	3.70	5.27	6.65	7.87	8.65

Fig. Q.21. Load Distribution for Test 18; Compression

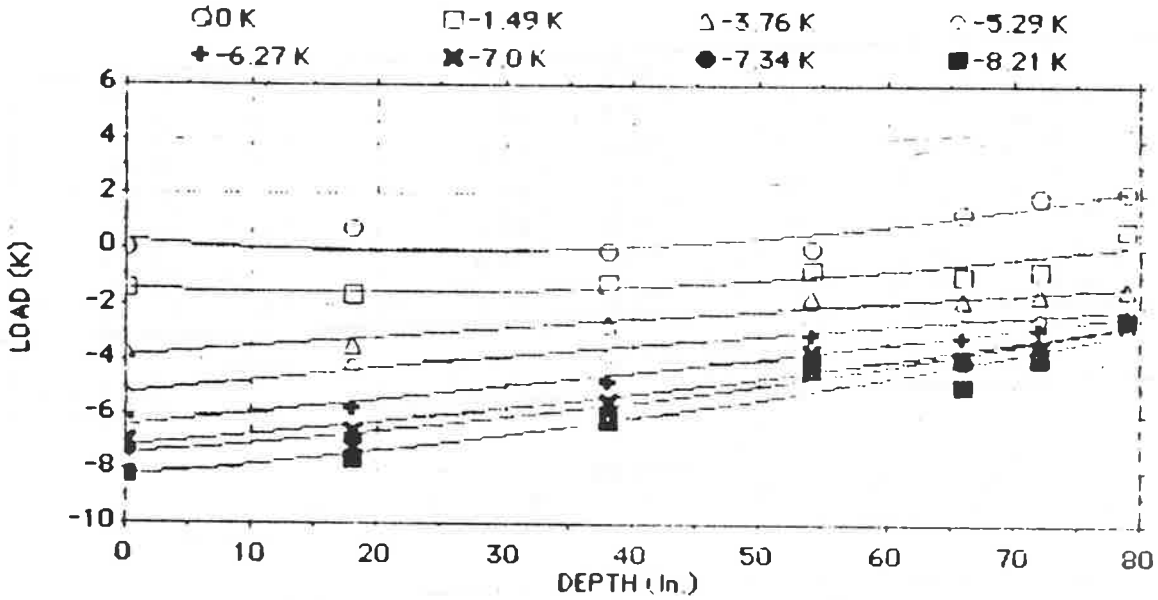

	DEPTH (In.)	0 K	-1.49 K	-3.76 K	-5.29 K	-6.27 K	-7.0 K	-7.34 K	-8.21 K
1	0	0	-1.49	-3.76	-5.29	-6.27	-7.00	-7.34	-8.21
2	18.00	.69	-1.61	-3.54	-4.29	-5.84	-6.67	-6.93	-7.65
3	38.00	-9.00E-2	-1.22	-2.71	-3.90	-4.80	-5.57	-5.97	-6.25
4	54.00	0	-.78	-1.71	-2.63	-3.14	-3.70	-3.97	-4.33
5	66.00	1.28	-.91	-1.86	-2.71	-3.28	-3.92	-4.03	-4.98
6	72.00	1.95	-.77	-1.62	-2.50	-2.97	-3.51	-3.78	-3.97
7	79.00	2.09	.69	-1.42	-2.12	-2.41	-2.65	-2.55	-2.56

Fig. Q.22. Load Distribution for Test 18; Uplift

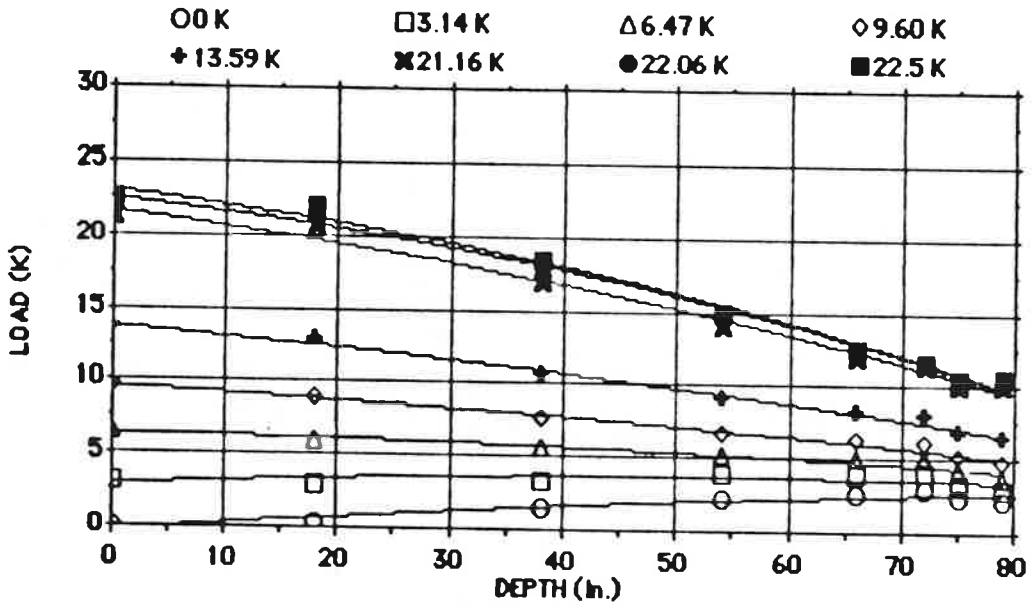

	DEPTH (in.)	0 K	3.14 K	6.47 K	9.60 K	13.59 K	21.16 K	22.06 K	22.5 K
1	0	0	3.14	6.47	9.60	13.59	21.16	22.06	22.50
2	18.00	.29	3.04	6.05	9.00	12.78	20.62	21.45	22.02
3	38.00	1.45	3.42	5.54	7.59	10.66	16.96	18.04	18.38
4	54.00	2.30	3.89	5.26	6.77	9.11	13.92	14.93	14.95
5	66.00	2.57	3.89	4.95	6.25	8.15	11.98	12.50	12.52
6	72.00	2.99	4.05	4.98	6.08	7.96	11.38	11.57	11.63
7	75.00	2.46	3.33	4.20	5.22	6.88	10.14	10.43	10.51
8	79.00	2.27	2.89	3.76	4.82	6.54	10.03	10.41	10.55

Fig. Q.23. Load Distribution for Test 19; Compression

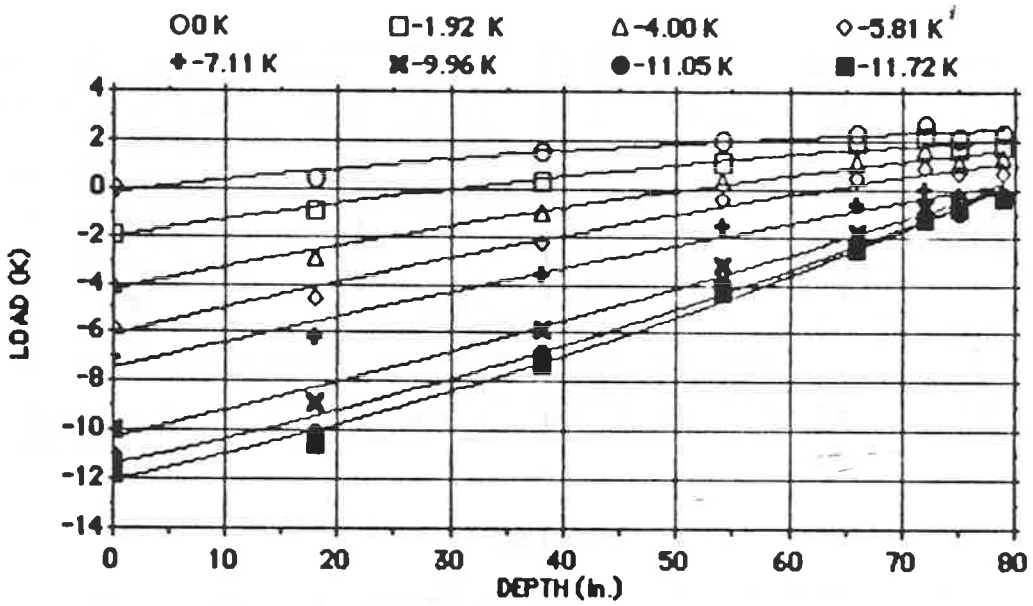

	DEPTH (in.)	0 K	-1.92 K	-4.00 K	-5.81 K	-7.11 K	-9.96 K	-11.05 K	-11.72 K
1	0	0	-1.92	-4.00	-5.81	-7.11	-9.96	-11.05	-11.72
2	18.00	.39	-.93	-2.98	-4.63	-6.18	-8.86	-10.04	-10.55
3	38.00	1.55	.33	-1.00	-2.26	-3.63	-5.81	-6.86	-7.29
4	54.00	2.03	1.14	.35	-.42	-1.55	-3.19	-3.90	-4.27
5	66.00	2.37	1.83	1.12	.46	-.74	-1.82	-2.24	-2.44
6	72.00	2.64	2.21	1.64	.92	-4.00E-2	-.69	-1.11	-1.23
7	75.00	2.06	1.66	1.12	.64	-.28	-.64	-.88	-.76
8	79.00	2.28	1.77	1.27	.69	-.22	-.37	-.29	-.31

Fig. Q.24. Load Distribution for Test 19; Uplift

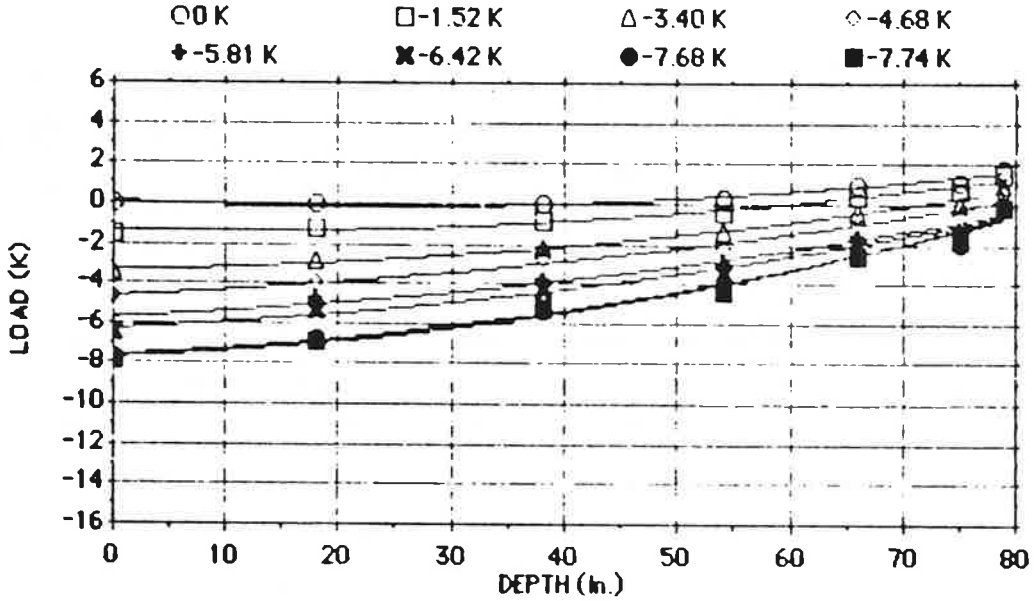

	DEPTH (In.)	0 K	-1.52 K	-3.40 K	-4.68 K	-5.81 K	-6.42 K	-7.68 K	-7.74 K
1	0	0	-1.52	-3.40	-4.68	-5.81	-6.42	-7.68	-7.74
2	18.00	5.00E-2	-1.19	-2.92	-3.97	-4.86	-5.38	-6.65	-6.89
3	38.00	-3.00E-2	-.87	-2.19	-2.81	-3.87	-4.29	-5.28	-5.25
4	54.00	.21	-.48	-1.41	-2.15	-2.97	-3.37	-4.17	-4.33
5	66.00	.98	.46	-.38	-.94	-1.71	-2.04	-2.60	-2.65
6	75.00	1.08	.63	1.00E-2	-.60	-1.35	-1.55	-1.88	-1.75
7	79.00	1.82	1.46	.88	.48	-5.00E-2	-.16	-.20	-.13

Fig. Q.25. Load Distribution for Test 20; Compression

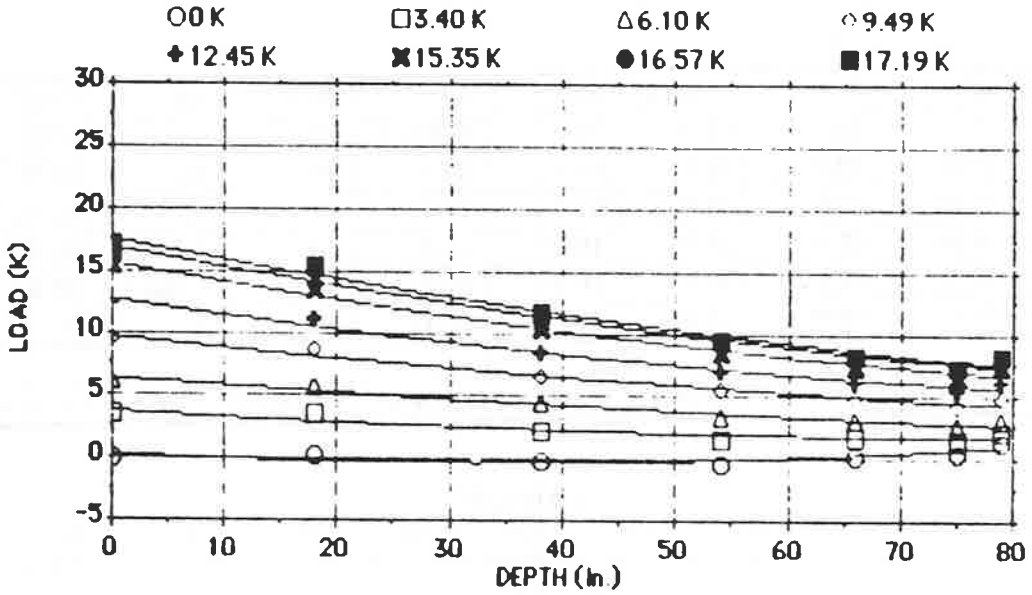

	DEPTH (In.)	0 K	3.40 K	6.10 K	9.49 K	12.45 K	15.35 K	16.57 K	17.19 K
1	0	0	3.40	6.10	9.49	12.45	15.35	16.57	17.19
2	18.00	.30	3.37	5.76	8.60	11.03	13.55	14.90	15.50
3	38.00	-.32	2.27	4.32	6.63	8.52	10.47	11.38	11.84
4	54.00	-.34	1.62	3.28	5.38	6.97	8.49	9.31	9.62
5	66.00	.24	1.73	3.01	4.87	6.19	7.38	8.01	8.23
6	75.00	.45	1.51	2.54	4.20	5.51	6.61	7.29	7.48
7	79.00	1.34	2.14	3.10	4.71	6.07	7.31	8.02	8.25

Fig. Q.26. Load Distribution for Test 20; Uplift

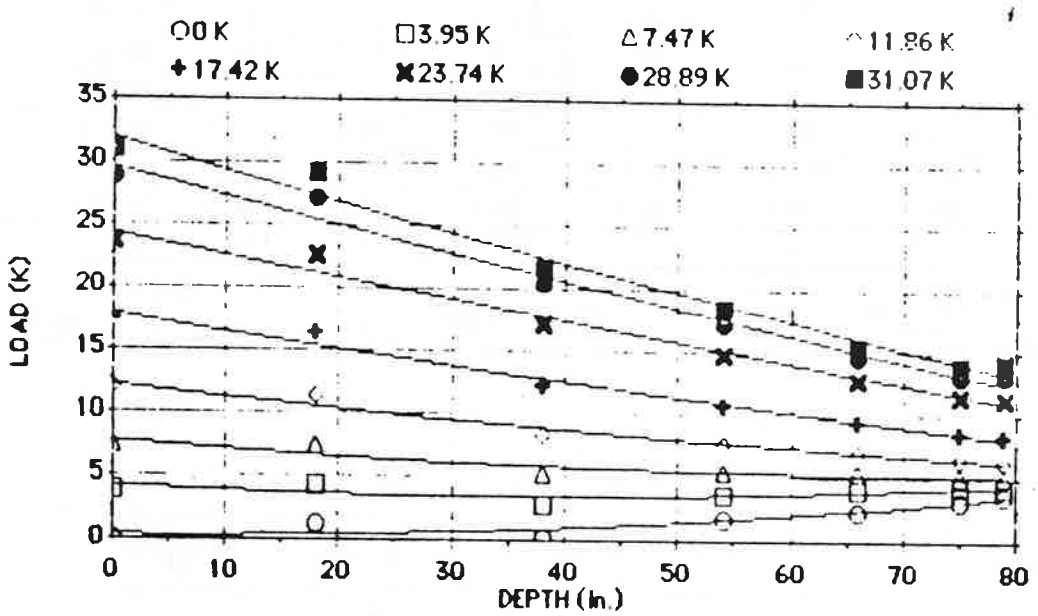

	DEPTH (In.)	0 K	3.95 K	7.47 K	11.86 K	17.42 K	23.74 K	28.89 K	31.07 K
1	0	0	3.95	7.47	11.86	17.42	23.74	28.89	31.07
2	18.00	1.24	4.38	7.40	11.34	16.33	22.56	27.13	29.20
3	38.00	.30	2.76	5.14	8.24	12.22	17.10	20.40	21.83
4	54.00	1.72	3.70	5.47	7.66	10.66	14.81	17.23	18.42
5	66.00	2.46	4.08	5.42	7.02	9.45	12.89	14.53	15.42
6	75.00	3.19	4.30	5.28	6.52	8.56	11.50	12.95	13.96
7	79.00	3.65	4.40	5.24	6.38	8.19	11.38	13.15	14.14

Fig. Q.27. Load Distribution for Test 21; Compression

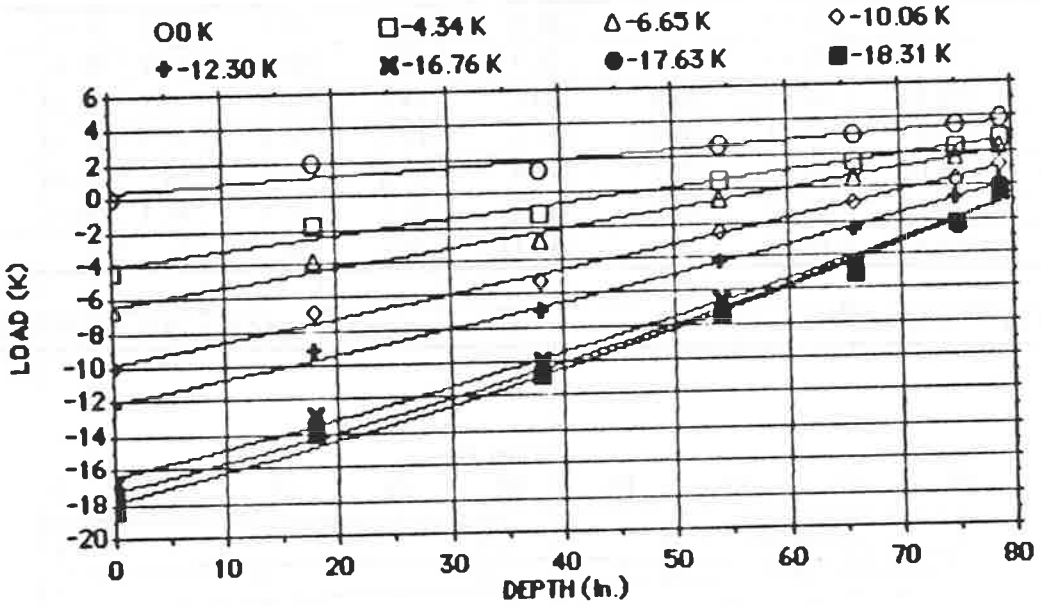

	DEPTH (in.)	0 K	-4.34 K	-6.65 K	-10.06 K	-12.30 K	-16.76 K	-17.63 K	-18.31 K
1	0	0	-4.34	-6.65	-10.06	-12.30	-16.76	-17.63	-18.31
2	18.00	1.95	-1.77	-3.87	-6.99	-9.14	-12.88	-13.64	-14.03
3	38.00	1.37	-1.29	-2.81	-5.24	-7.12	-9.99	-10.50	-10.87
4	54.00	2.53	.55	-.57	-2.57	-4.28	-6.61	-7.07	-7.37
5	66.00	3.02	1.47	.59	-.96	-2.52	-4.60	-4.97	-5.13
6	75.00	3.50	2.28	1.59	.42	-.81	-2.26	-2.41	-2.31
7	79.00	3.89	2.85	2.23	1.21	.18	-.39	-.31	-.23

Fig. Q.28. Load Distribution for Test 21; Uplift

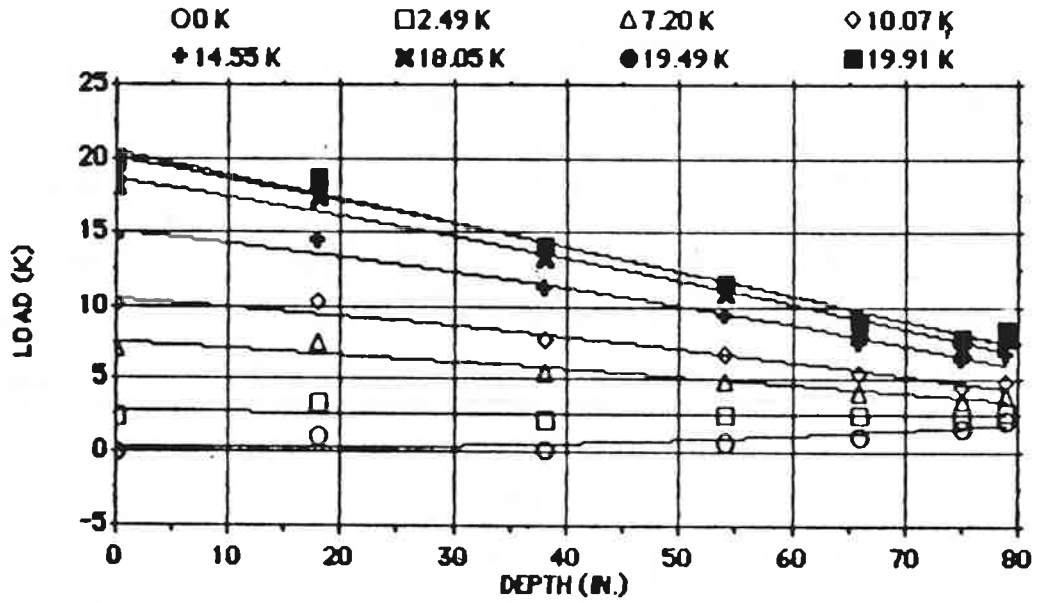

	DEPTH (IN.)	0 K	2.49 K	7.20 K	10.07 K	14.55 K	18.05 K	19.49 K	19.91 K
1	0	0	2.49	7.20	10.07	14.55	18.05	19.49	19.91
2	18.00	1.23	3.36	7.46	10.25	14.43	17.41	18.57	18.70
3	38.00	.30	2.30	5.46	7.67	11.20	13.29	14.03	14.02
4	54.00	.84	2.62	4.89	6.65	9.34	10.90	11.50	11.51
5	66.00	1.19	2.55	4.22	5.44	7.47	8.48	9.02	9.02
6	75.00	1.66	2.45	3.54	4.53	6.32	7.20	7.79	7.78
7	79.00	2.33	2.87	3.94	4.80	6.66	7.80	8.33	8.39

Fig. Q.29. Load Distribution for Test 22; Compression

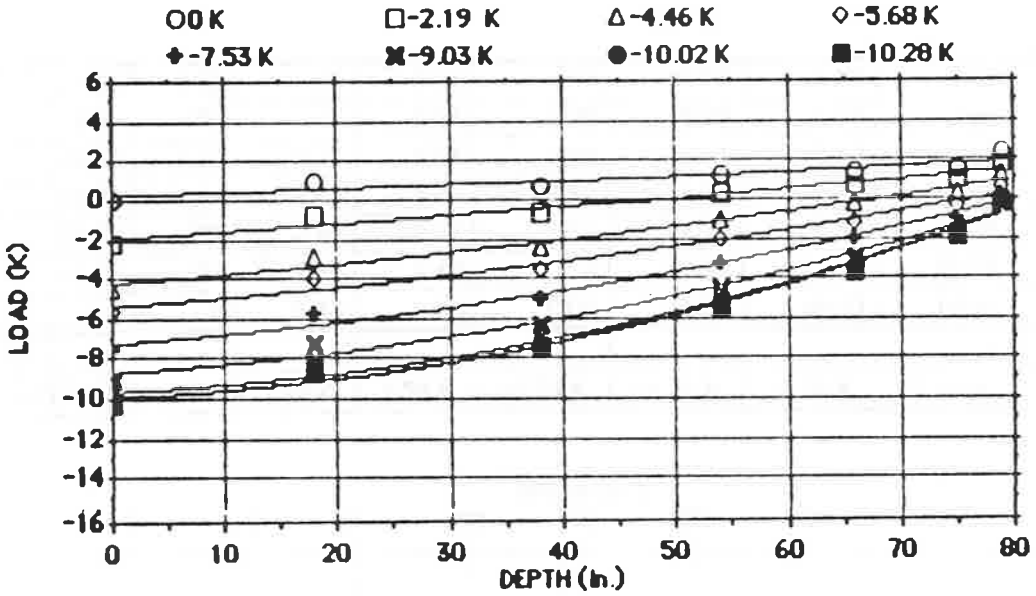

	DEPTH (in.)	0 K	-2.19 K	-4.46 K	-5.68 K	-7.53 K	-9.03 K	-10.02 K	-10.28 K
1	0	0	-2.19	-4.46	-5.68	-7.53	-9.03	-10.02	-10.28
2	18.00	1.01	-.85	-2.92	-4.00	-5.80	-7.20	-8.22	-8.53
3	38.00	.70	-.72	-2.47	-3.56	-5.03	-6.31	-7.21	-7.39
4	54.00	1.28	.24	-1.07	-2.09	-3.26	-4.49	-5.25	-5.43
5	66.00	1.33	.61	-.32	-1.19	-2.10	-3.08	-3.63	-3.73
6	75.00	1.45	.94	.24	-.41	-1.04	-1.75	-1.98	-1.93
7	79.00	2.28	1.82	1.16	.51	8.00E-2	-.22	-.17	-.12

Fig. Q.30. Load Distribution for Test 22; Uplift

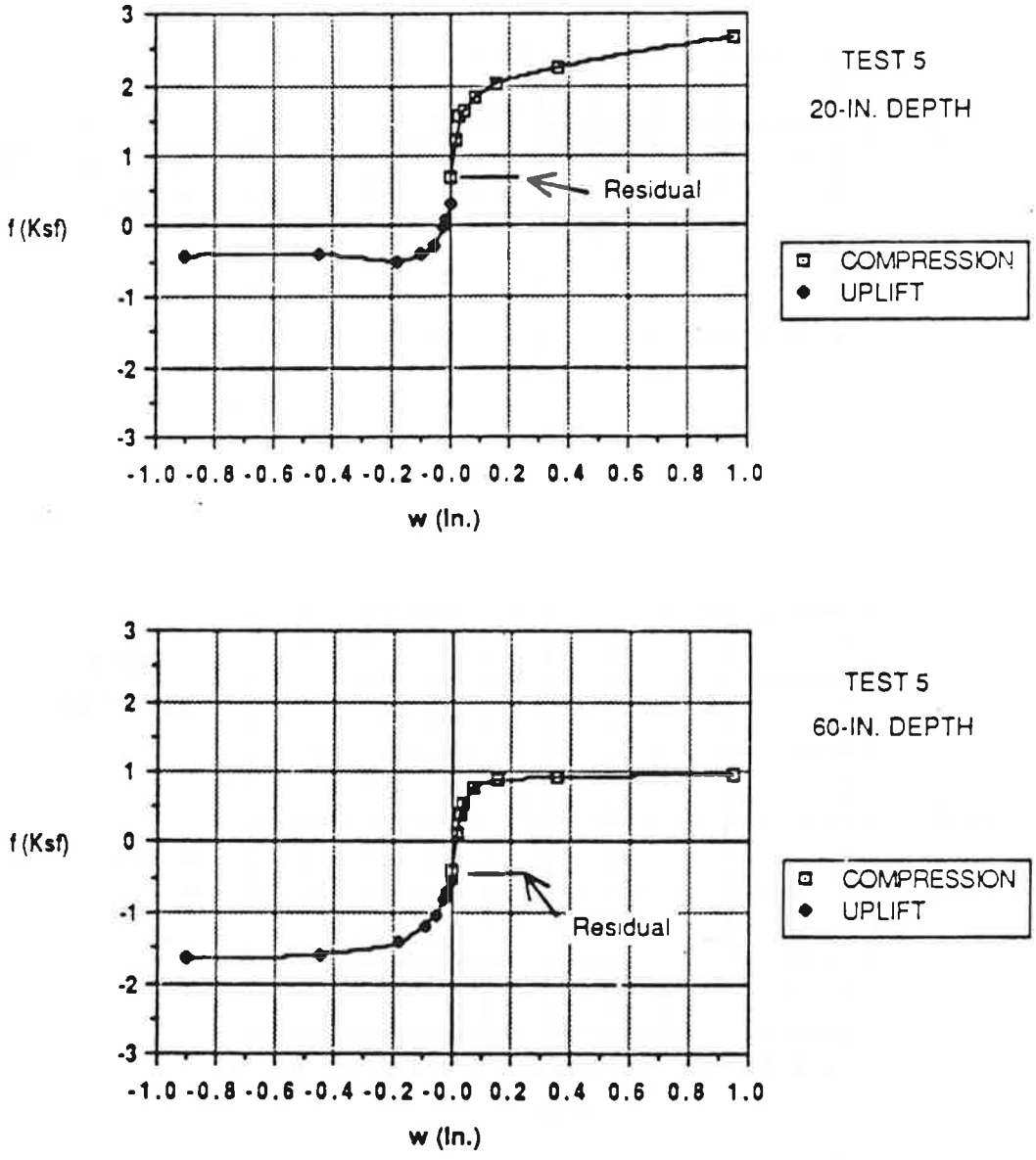

Fig. Q.31. f-w Relationships for Test 5

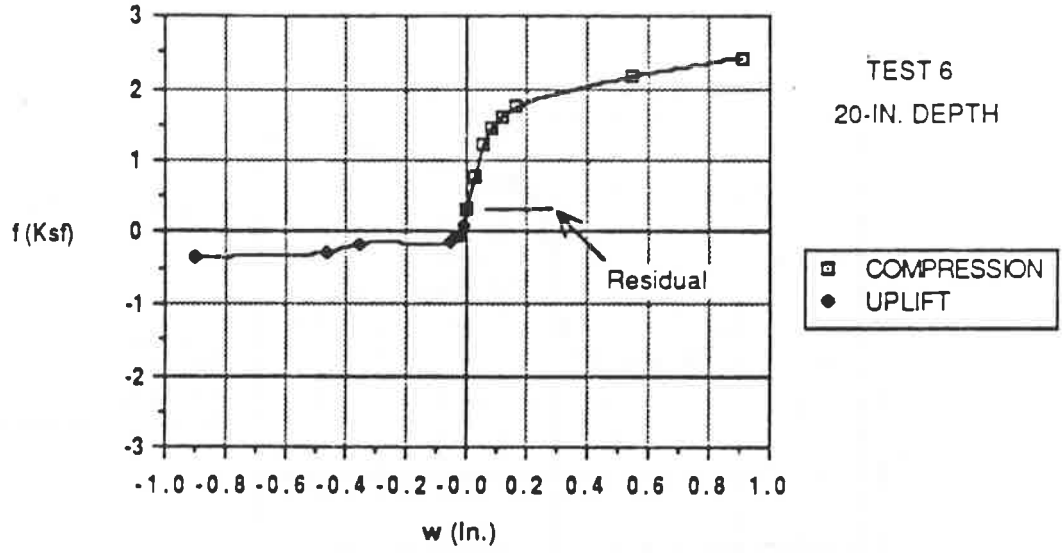

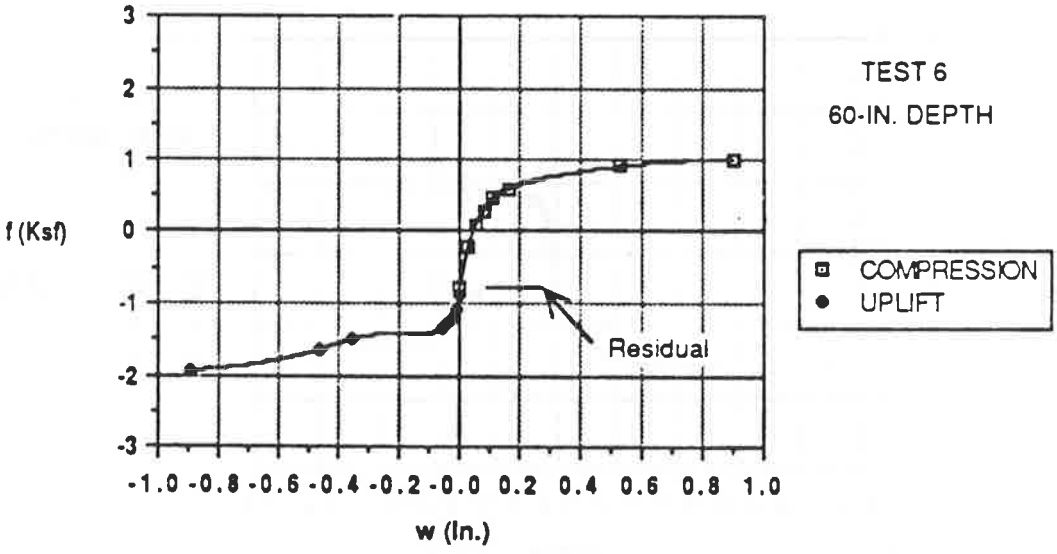

Fig. Q.32. f-w Relationships for Test 6

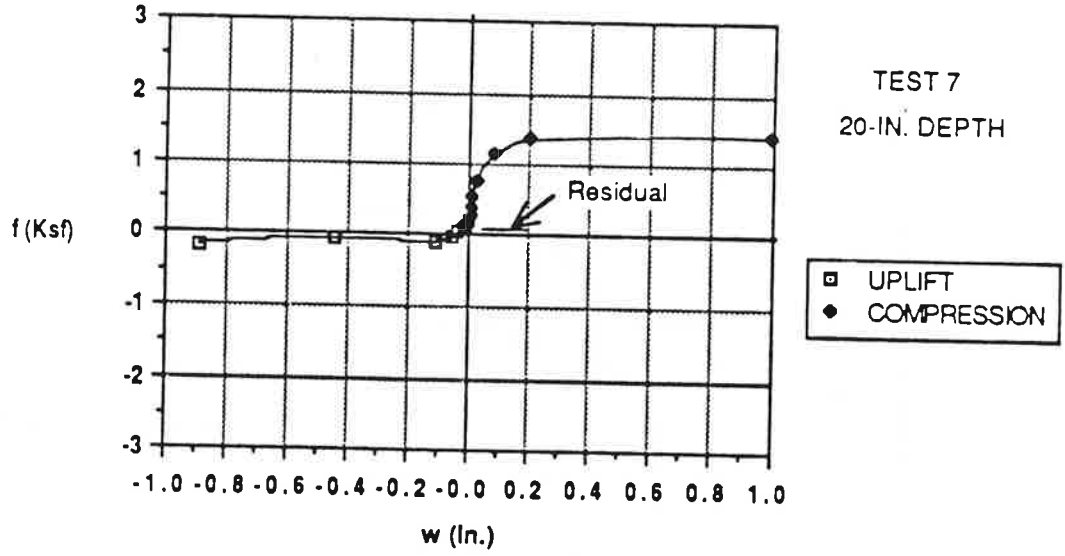

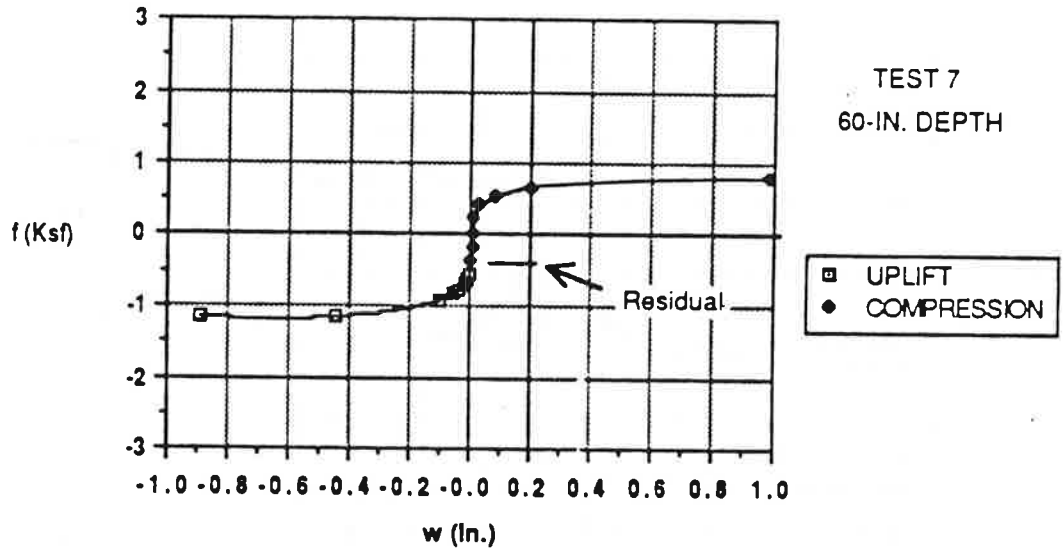

Fig. Q.33. f-w Relationships for Test 7

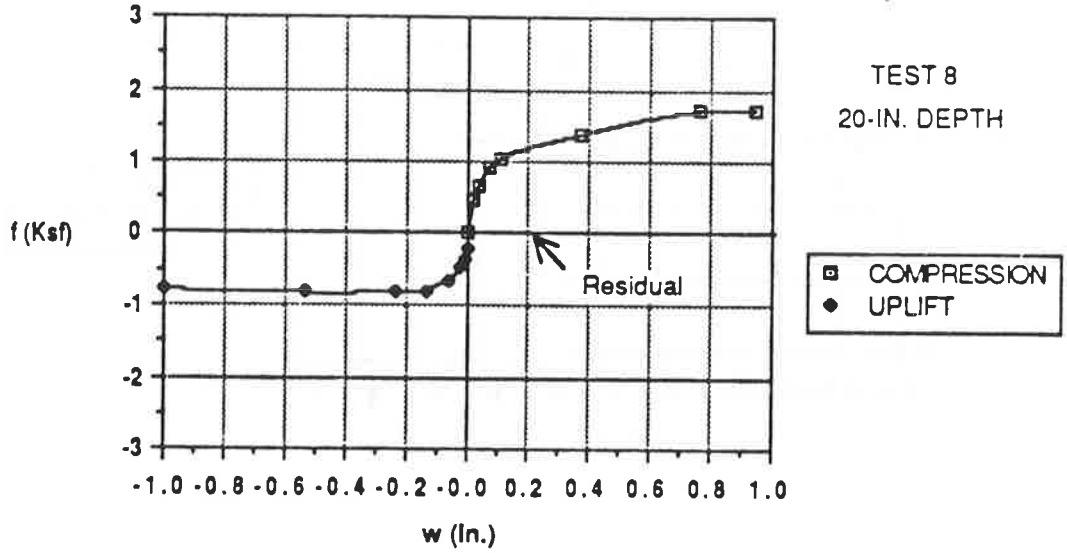

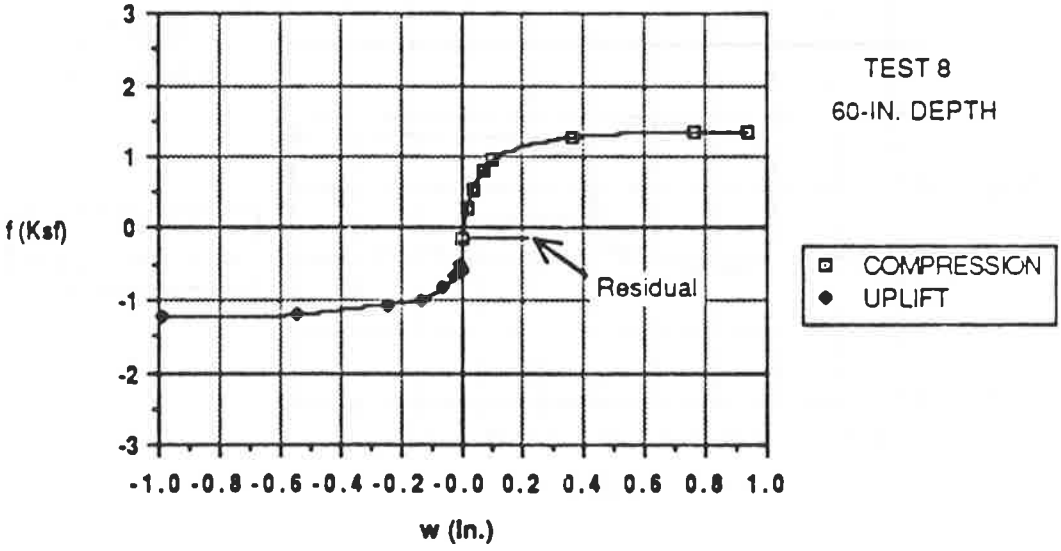

Fig. Q.34. f-w Relationships for Test 8

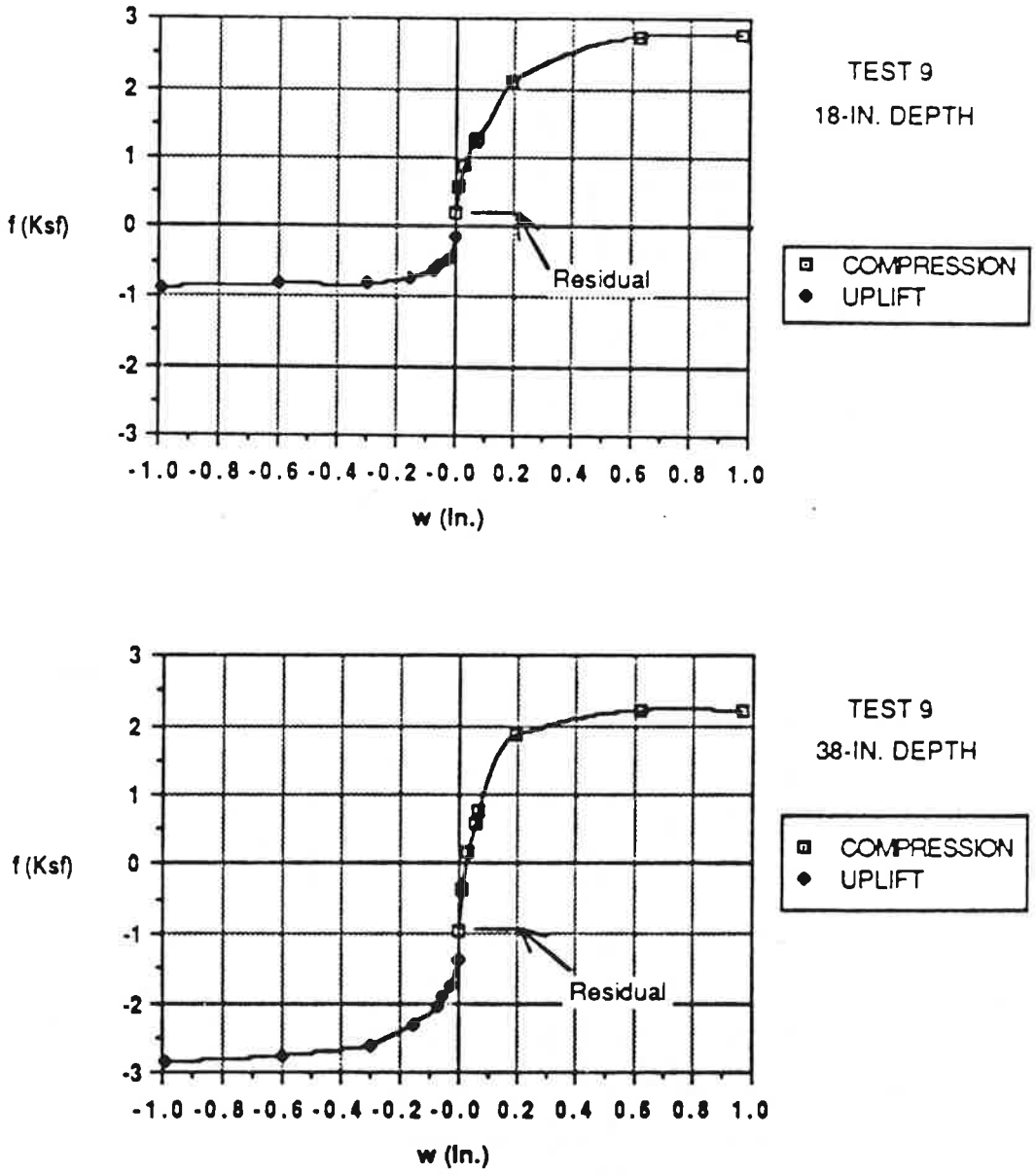

Fig. Q.35. f-w Relationships for Test 9
(Upper and Lower Halves of Pile: Pile Did Not Penetrate Fully)

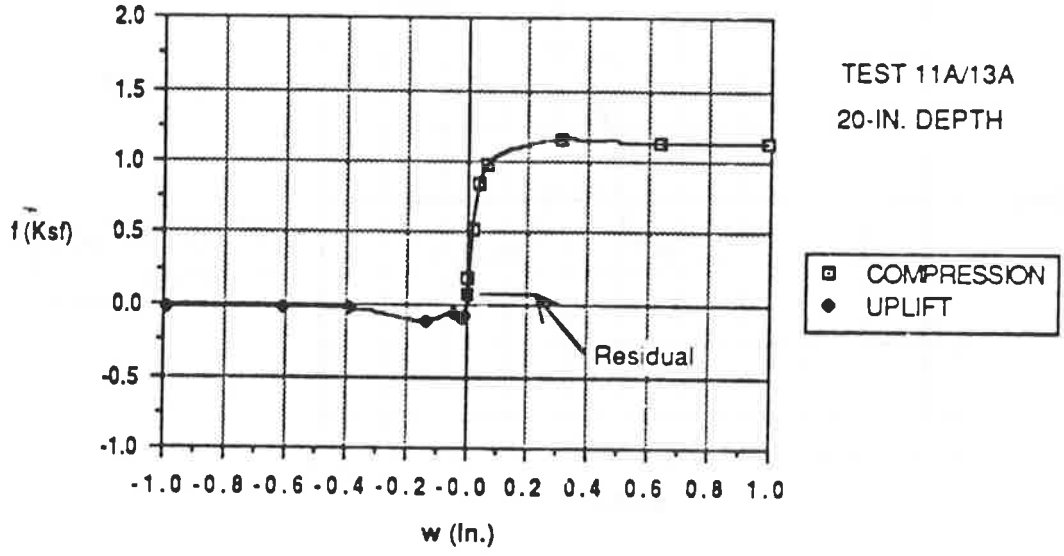

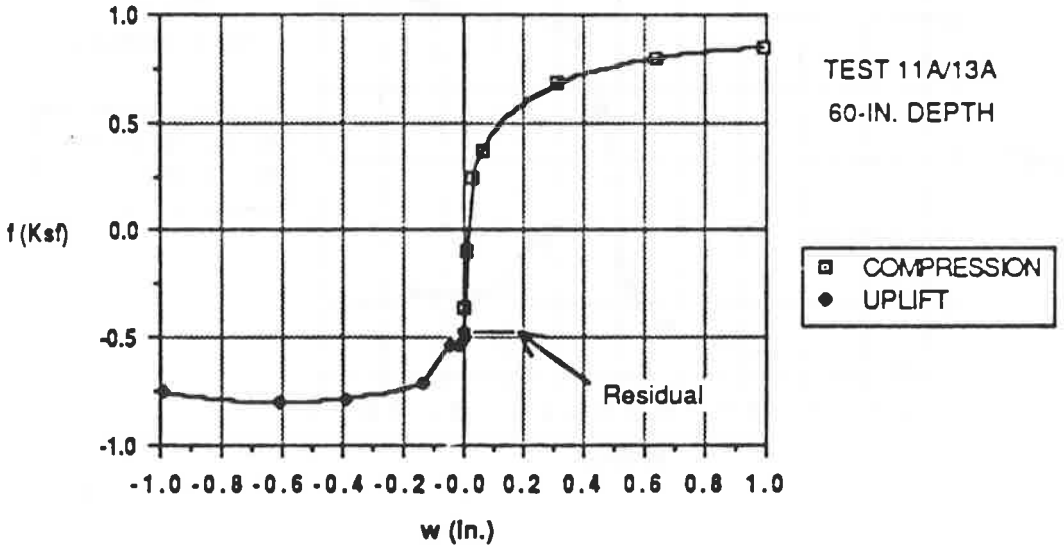

Fig. Q.36. f-w Relationships for Test 11a/13a

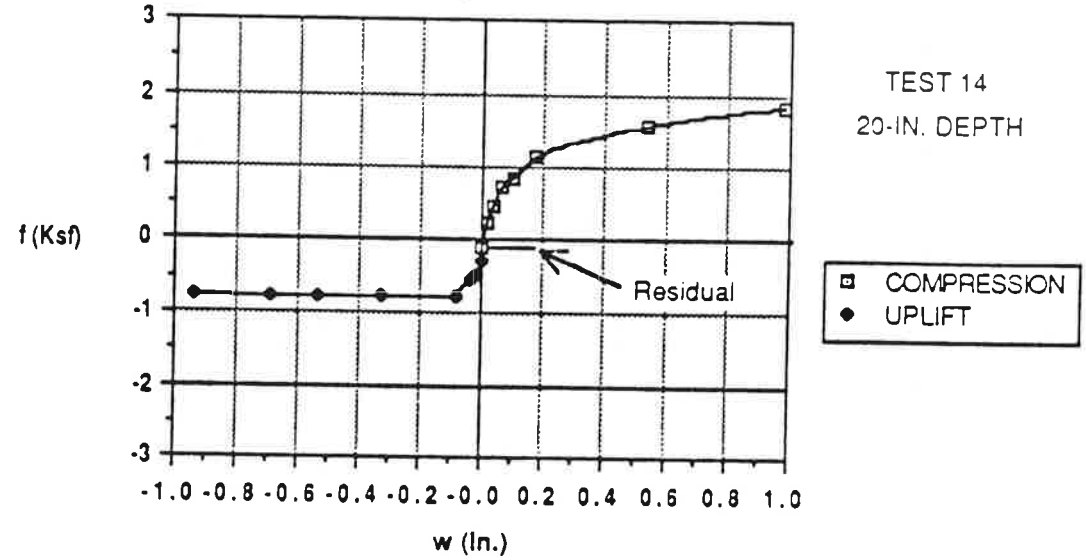

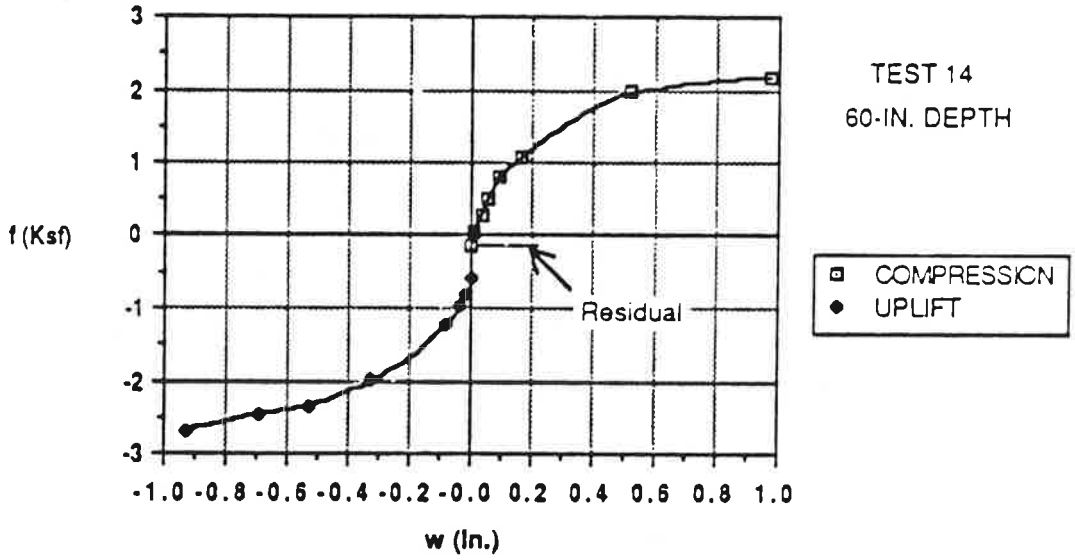

Fig. Q.37. f-w Relationships for Test 14

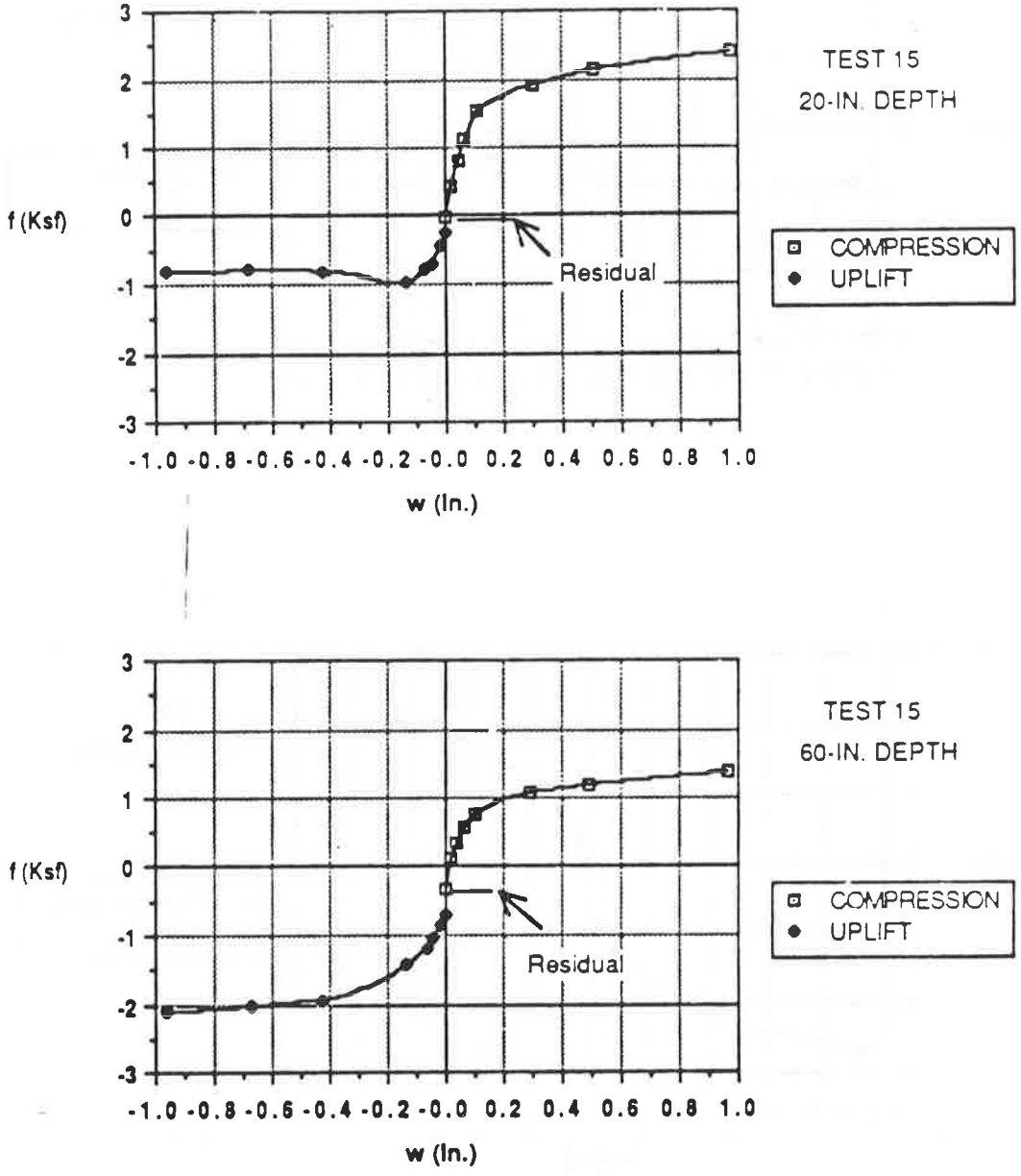

Fig. Q.38. f-w Relationships for Test 15

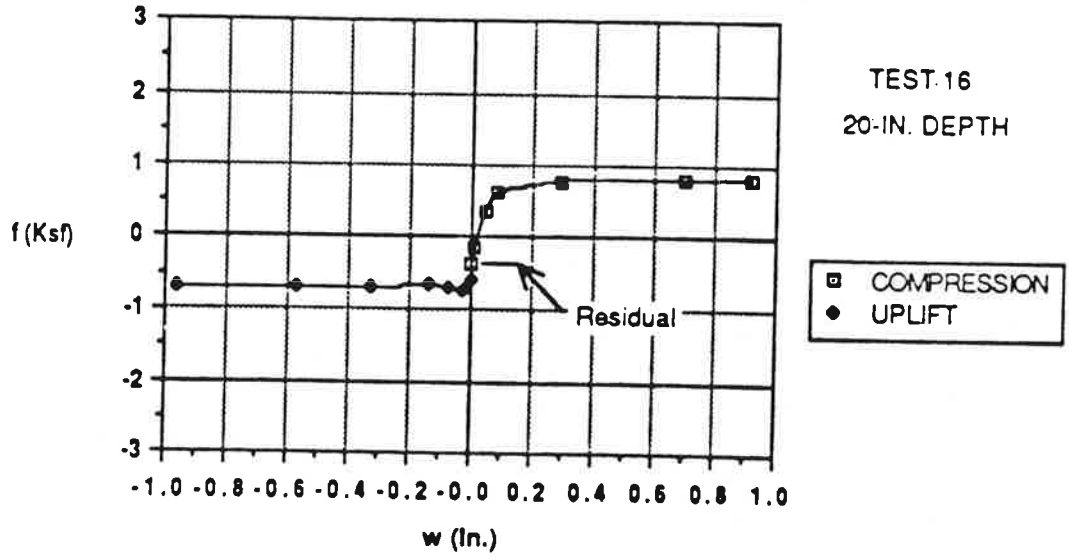

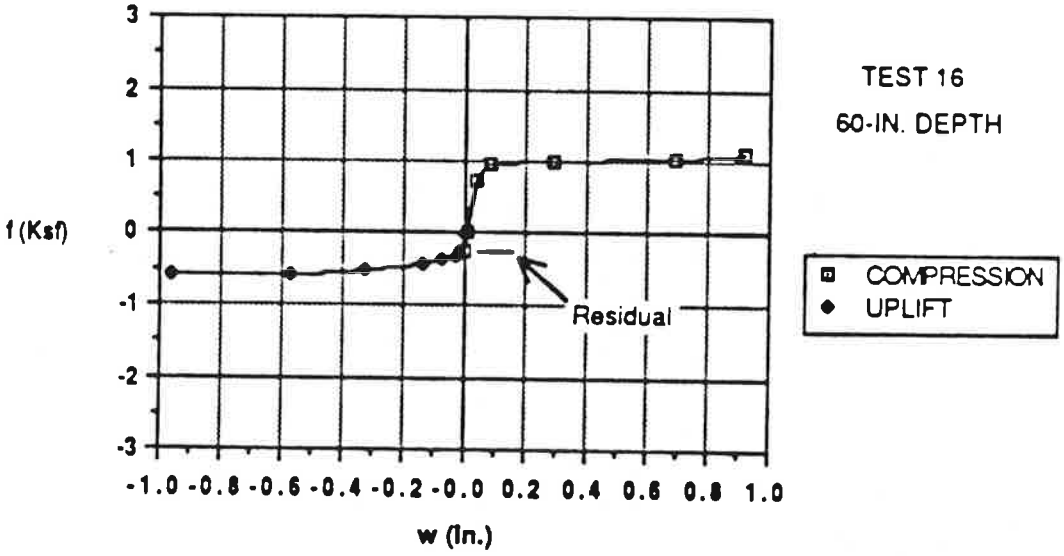

Fig. Q.39. f-w Relationships for Test 16

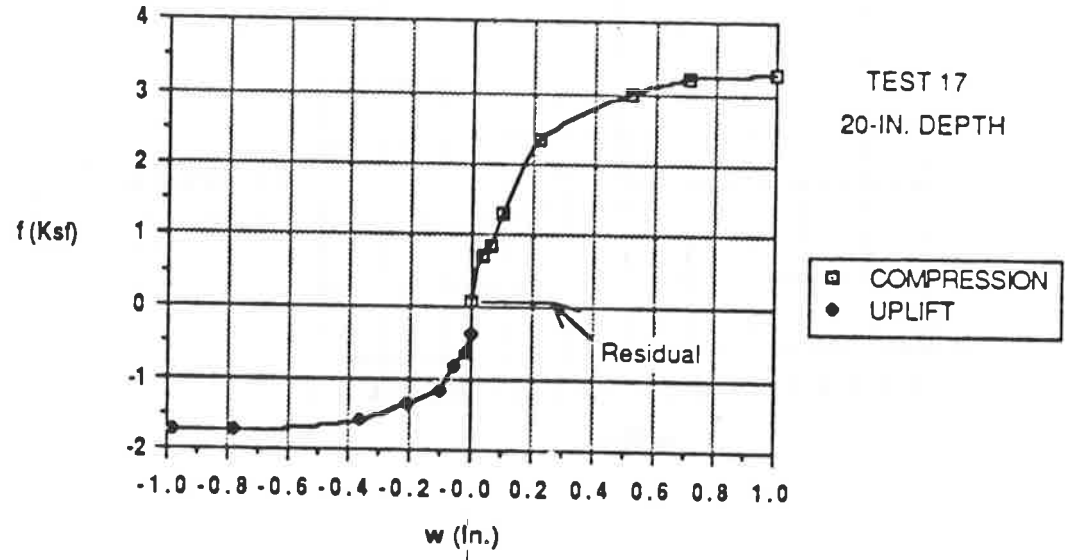

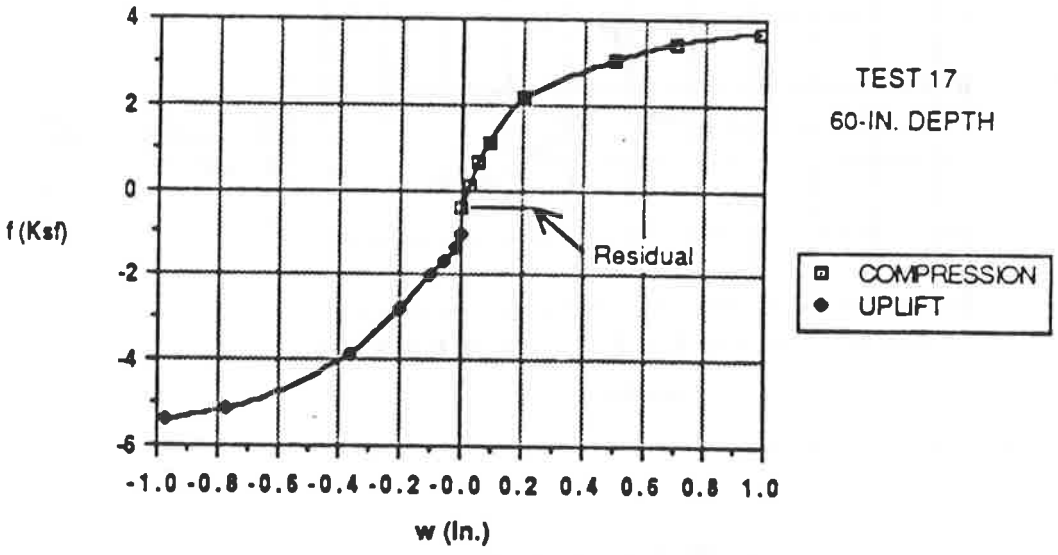

Fig. Q.40. f-w Relationships for Test 17

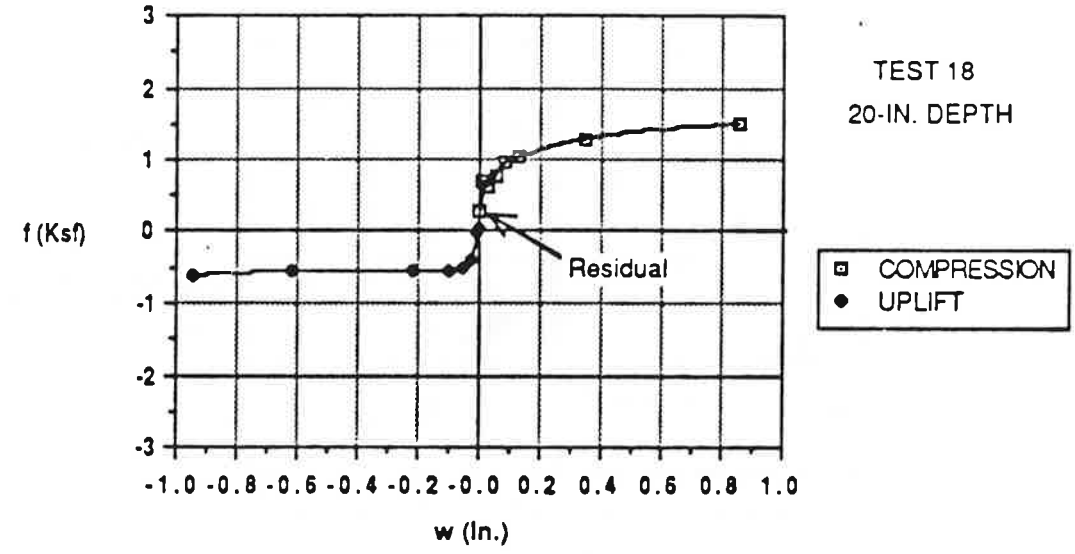

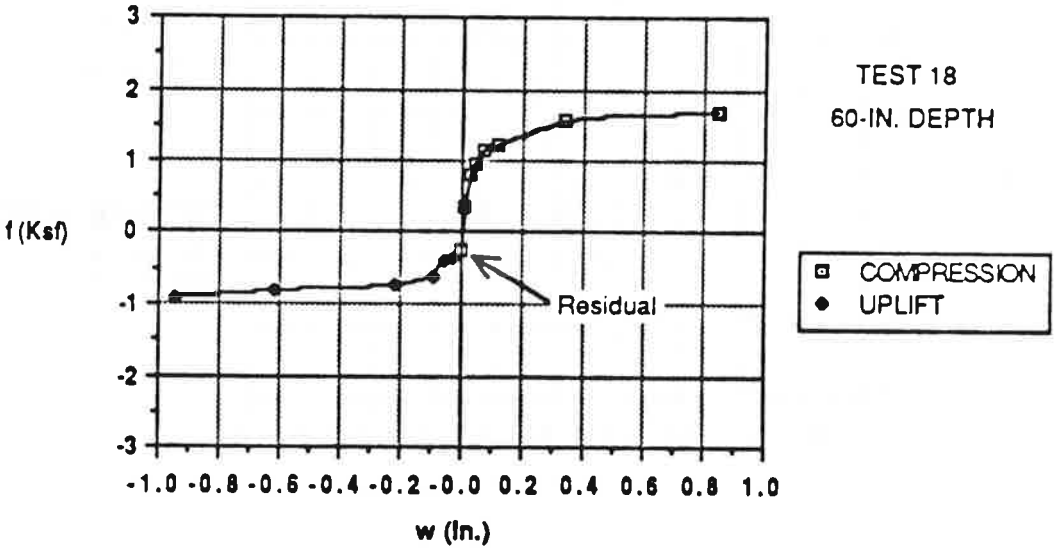

Fig. Q.41. f-w Relationships for Test 18

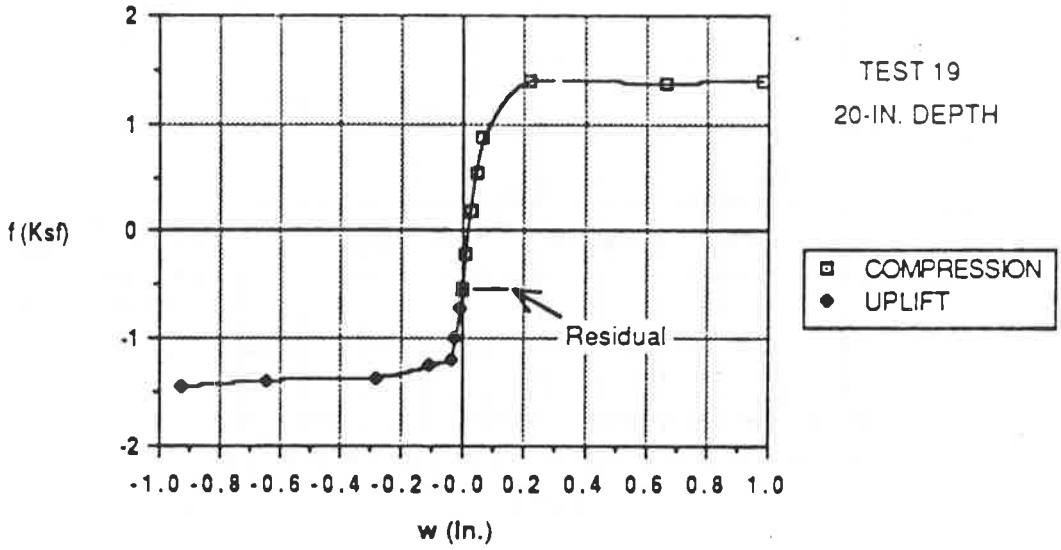

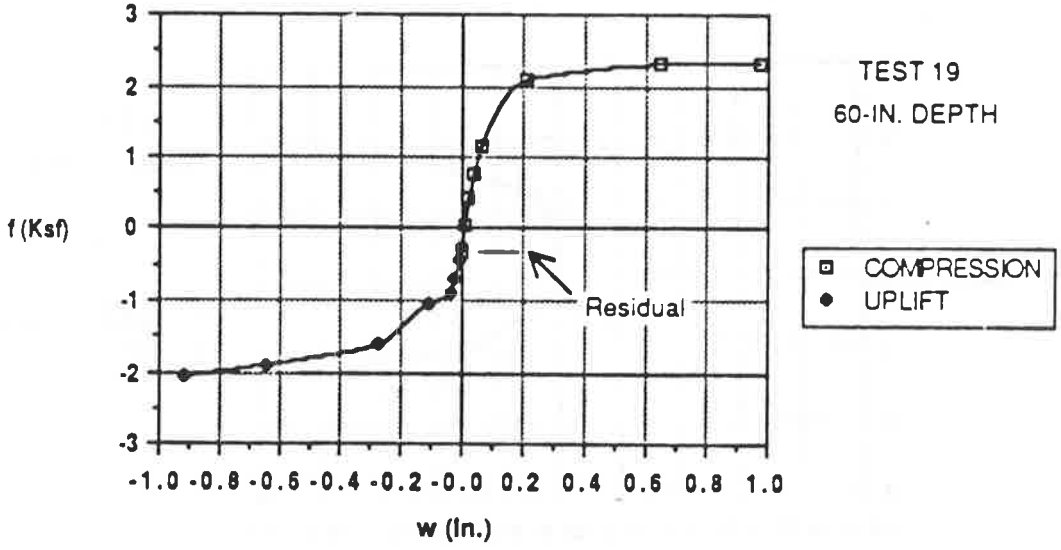

Fig. Q.42. f-w Relationships for Test 19

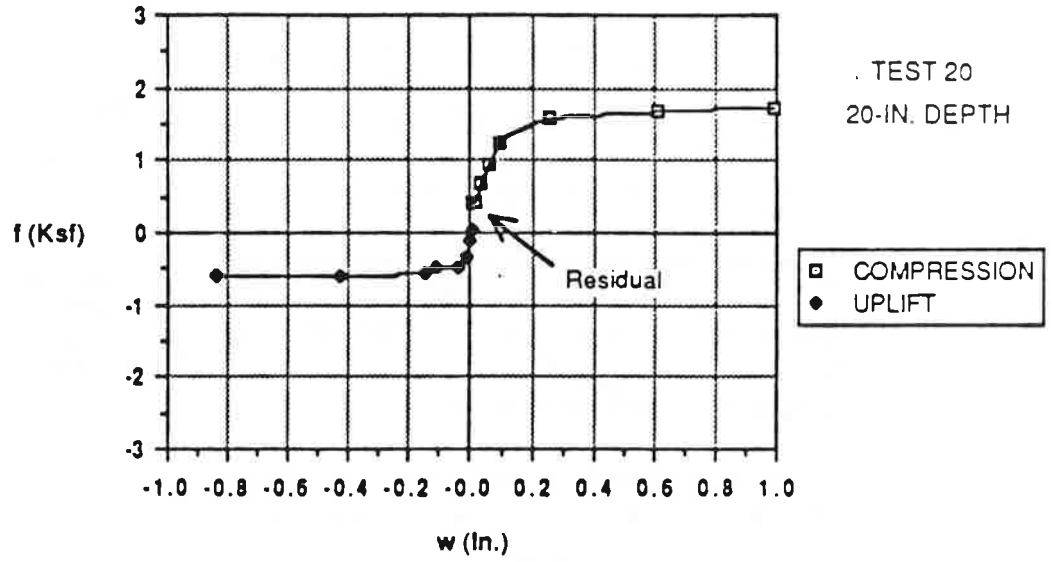

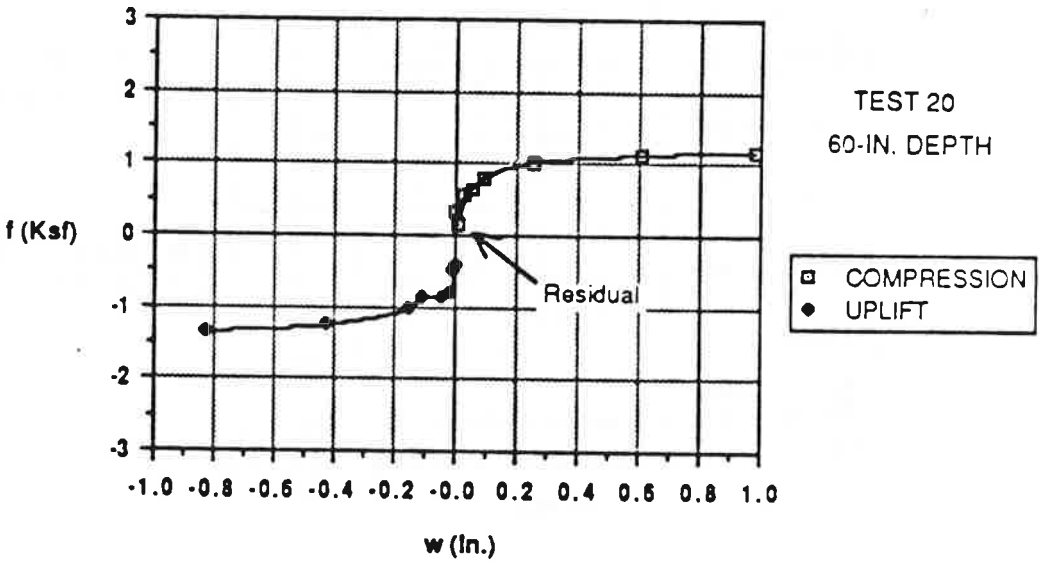

Fig. Q.43. f-w Relationships for Test 20

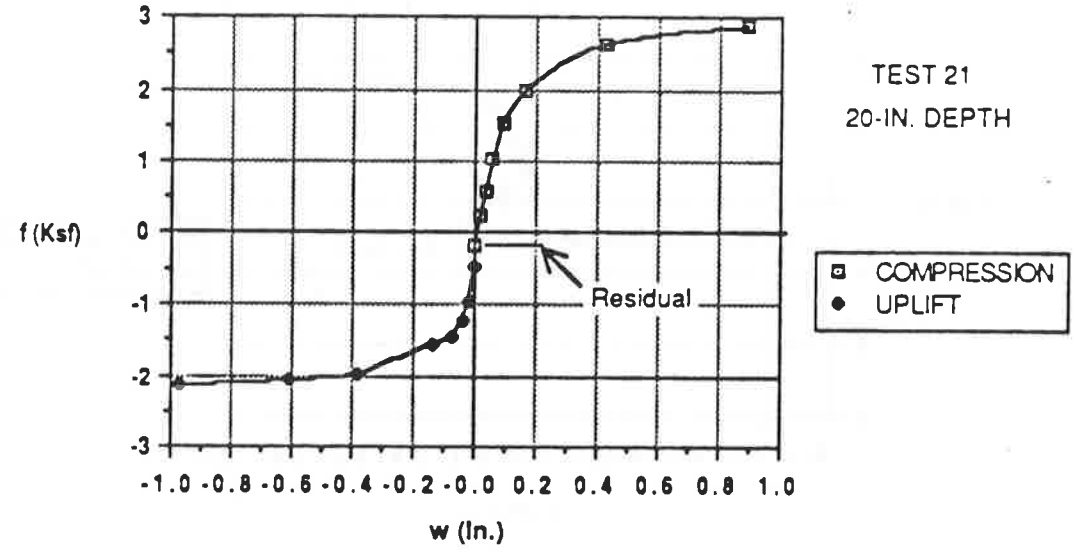

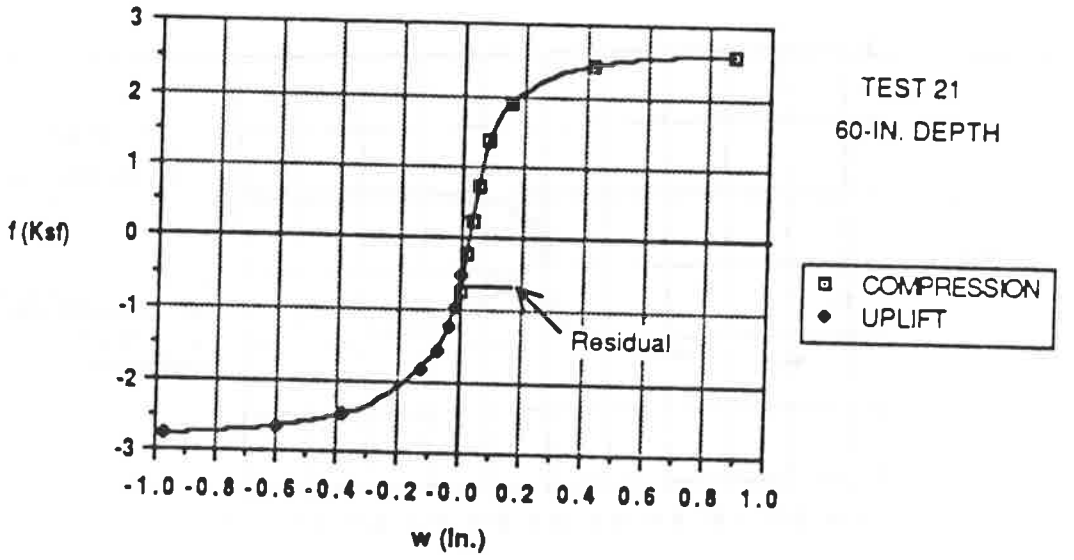

Fig. Q.44. f-w Relationships for Test 21

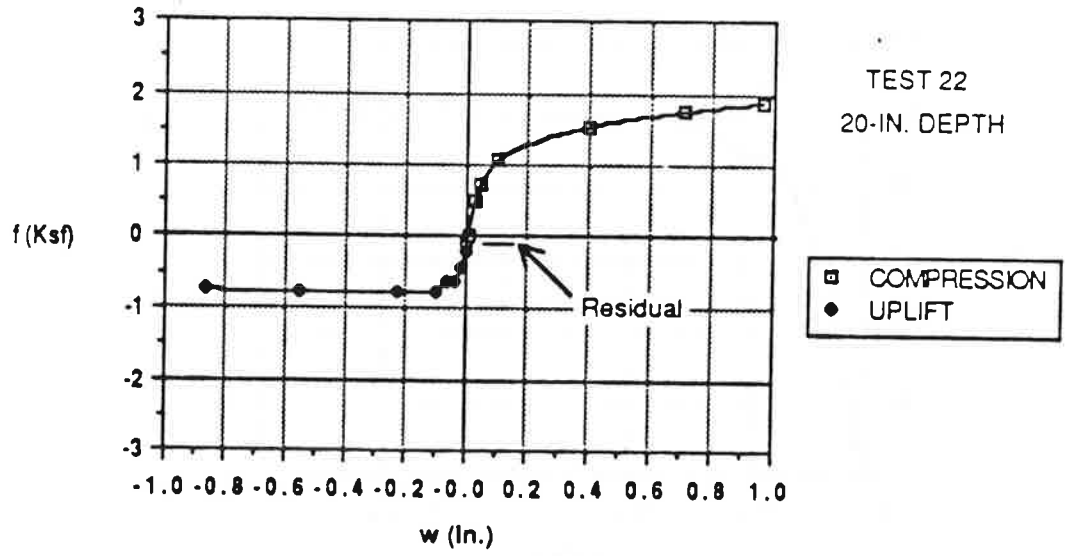

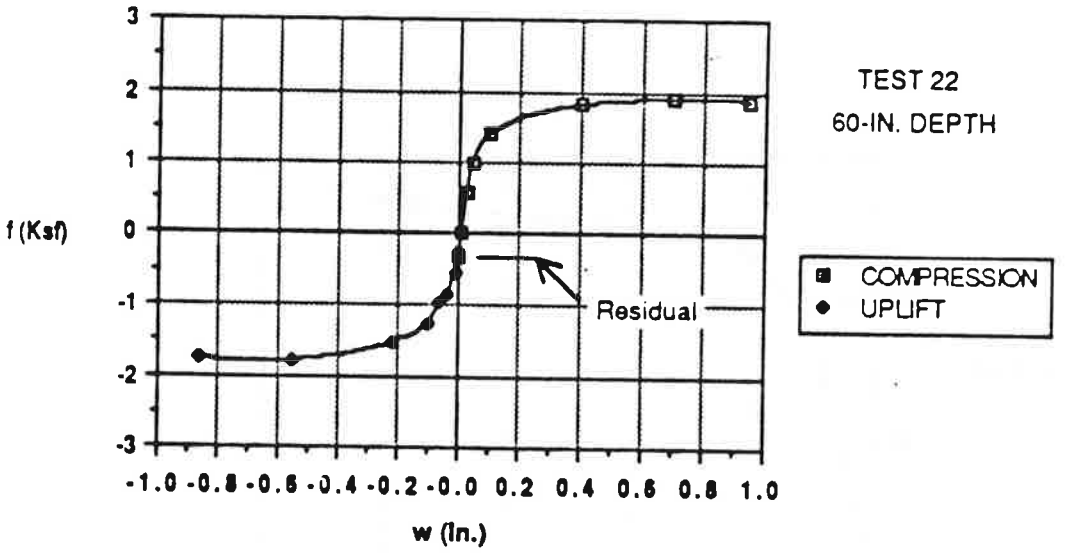

Fig. Q.45. f-w Relationships for Test 22

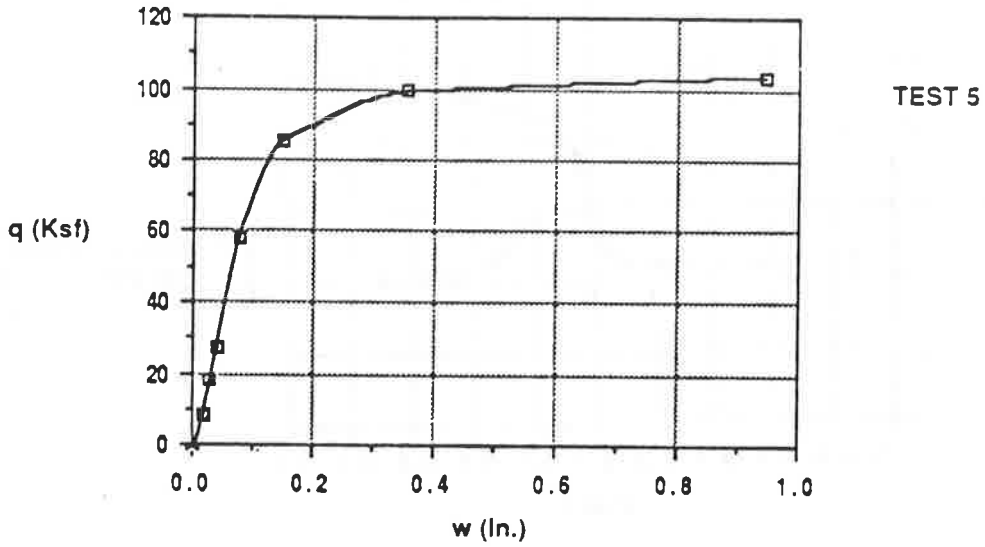

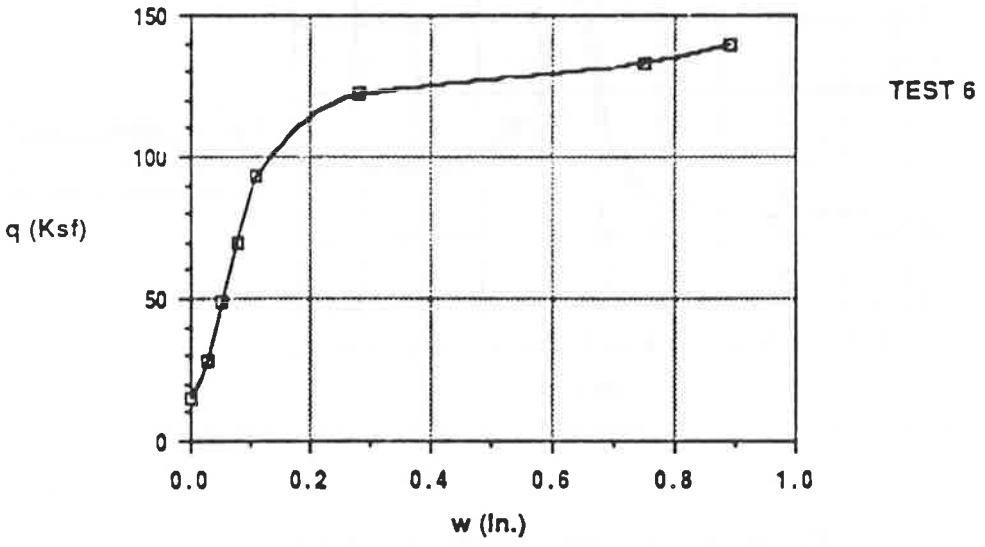

Fig. Q.46. q-w Relationships for Tests 5 and 6

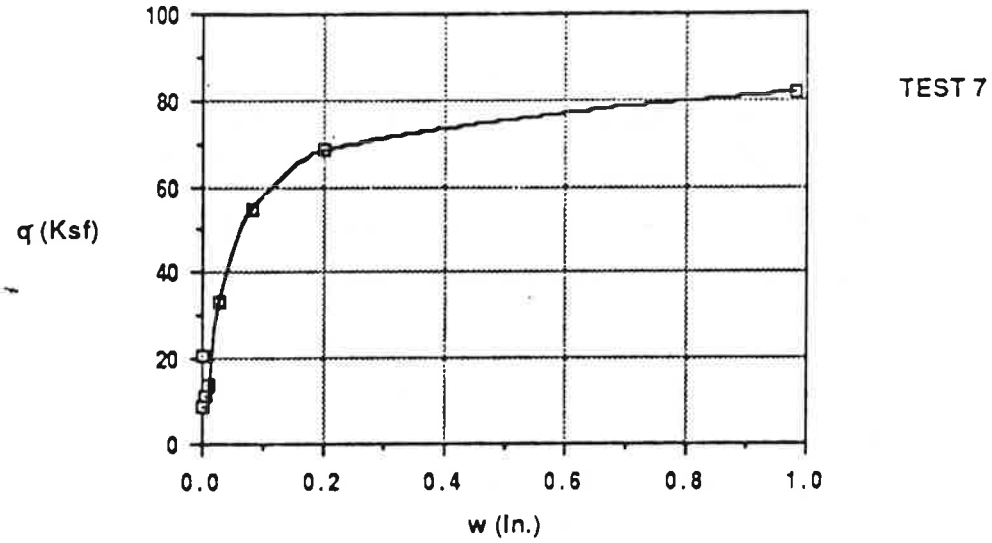

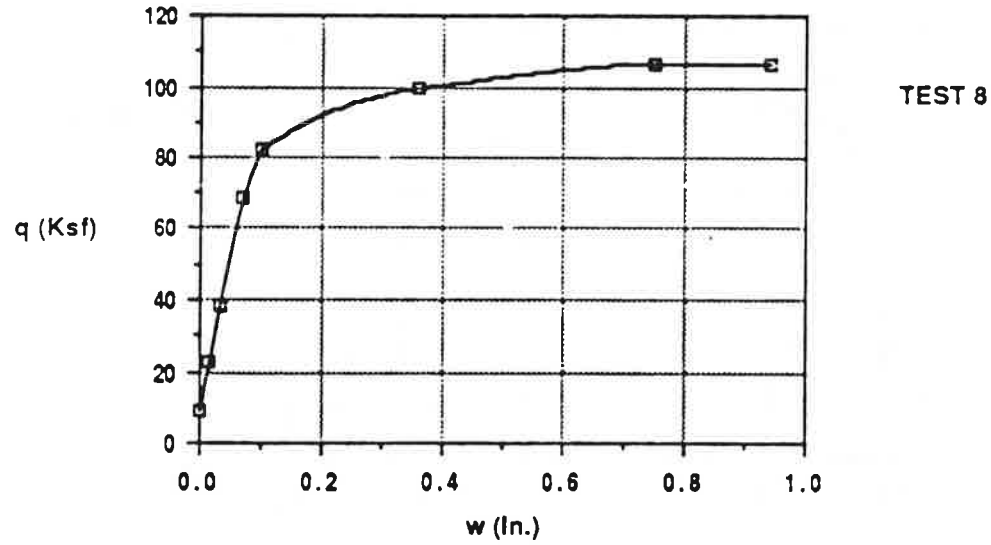

Fig. Q.47. q-w Relationships for Tests 7 and 8

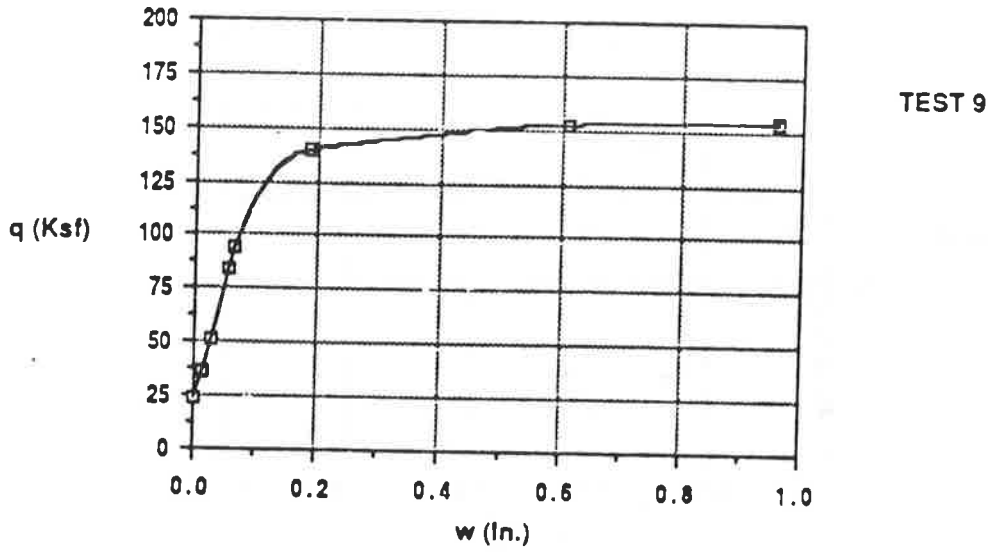

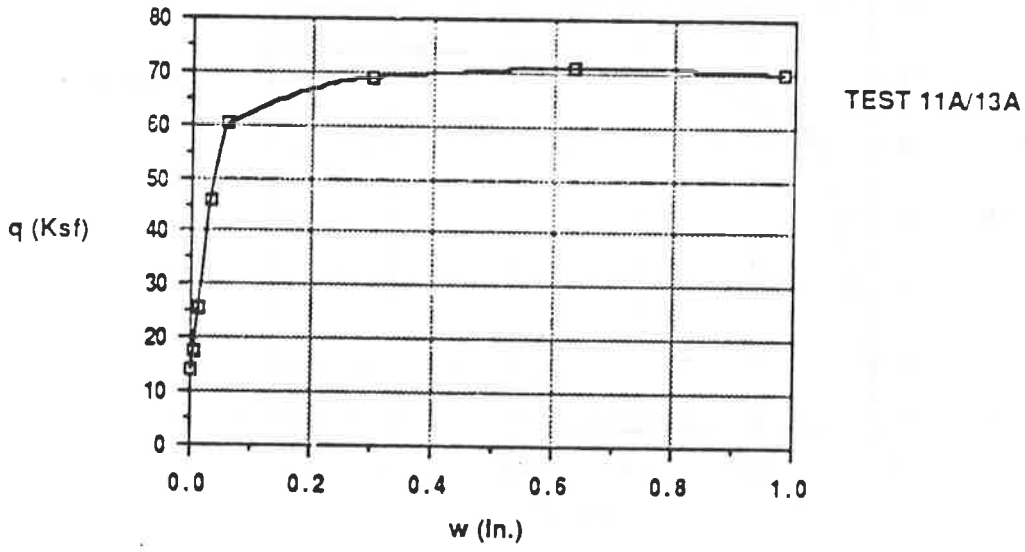

Fig. Q.48. q-w Relationships for Tests 9 and 11a/13a

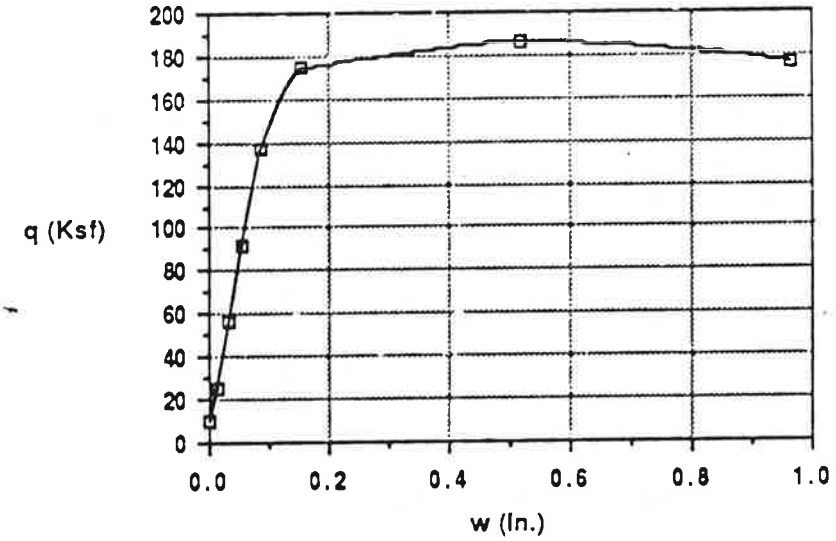

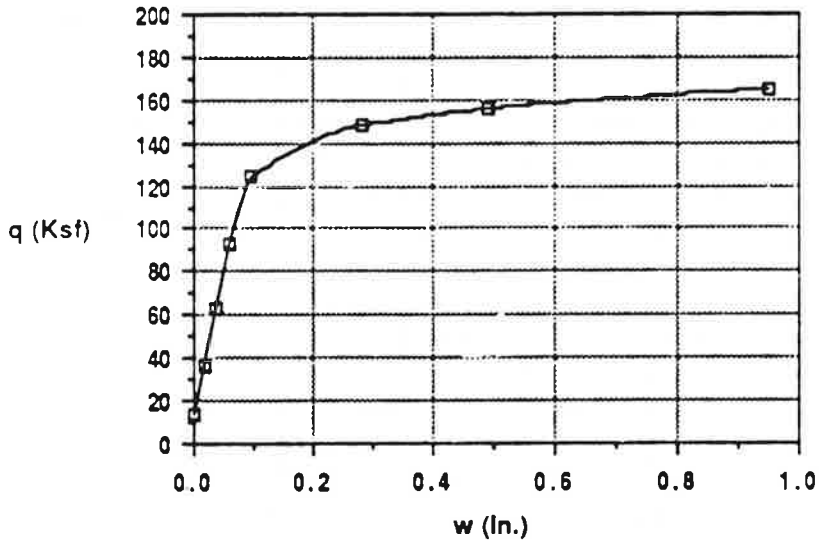

Fig. Q.49. q-w Relationships for Tests 14 and 15

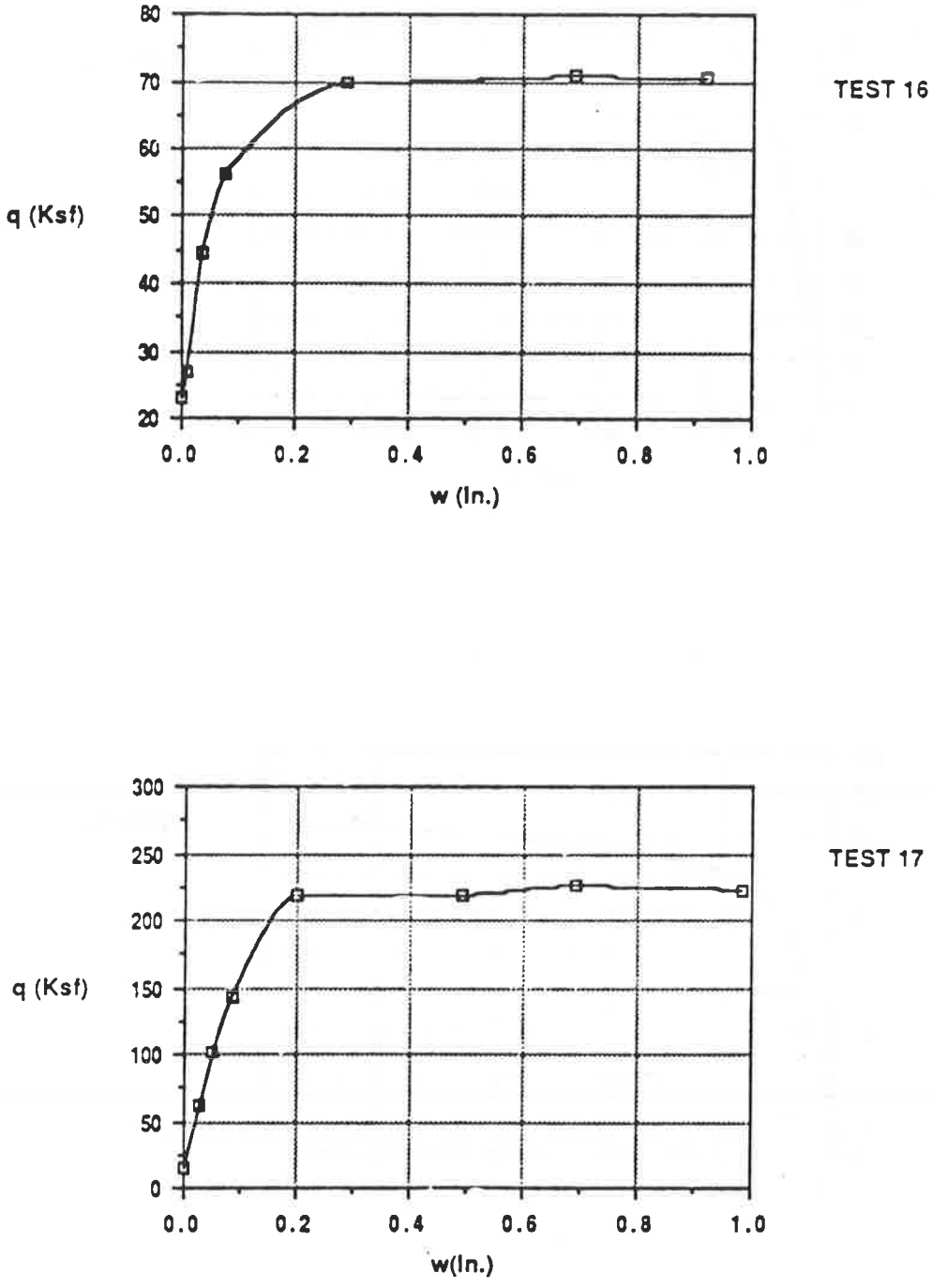

Fig. Q.50. q-w Relationships for Tests 16 and 17

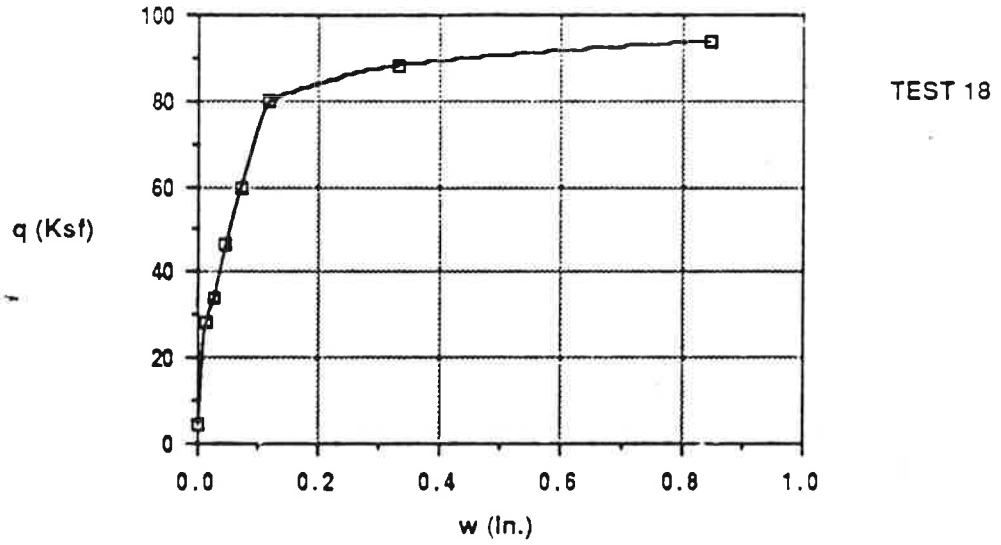

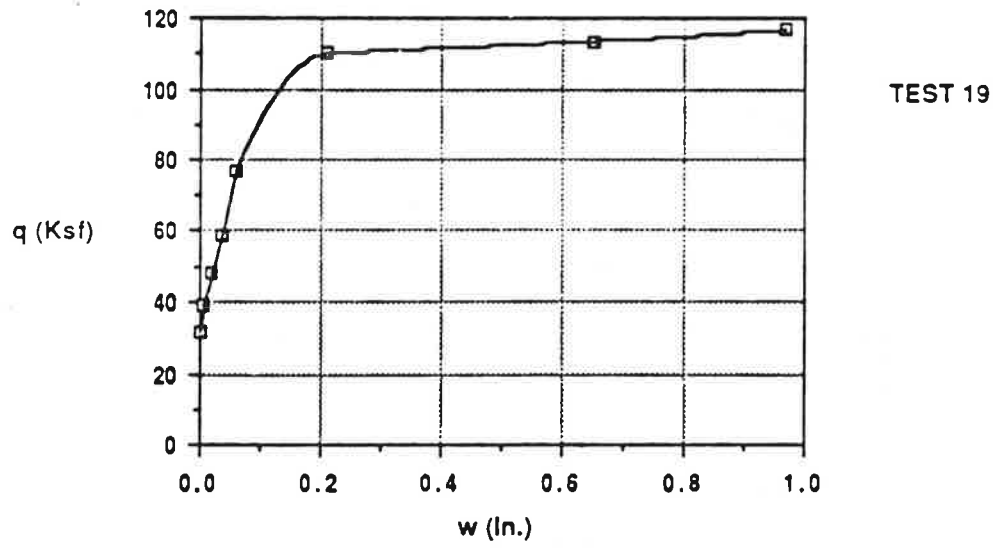

Fig. Q.51. q-w Relationships for Tests 18 and 19

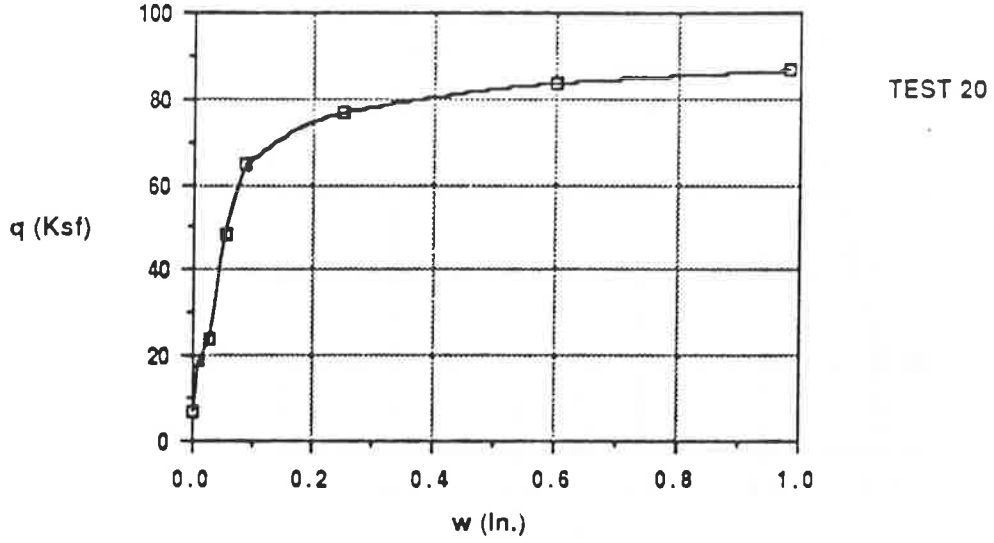

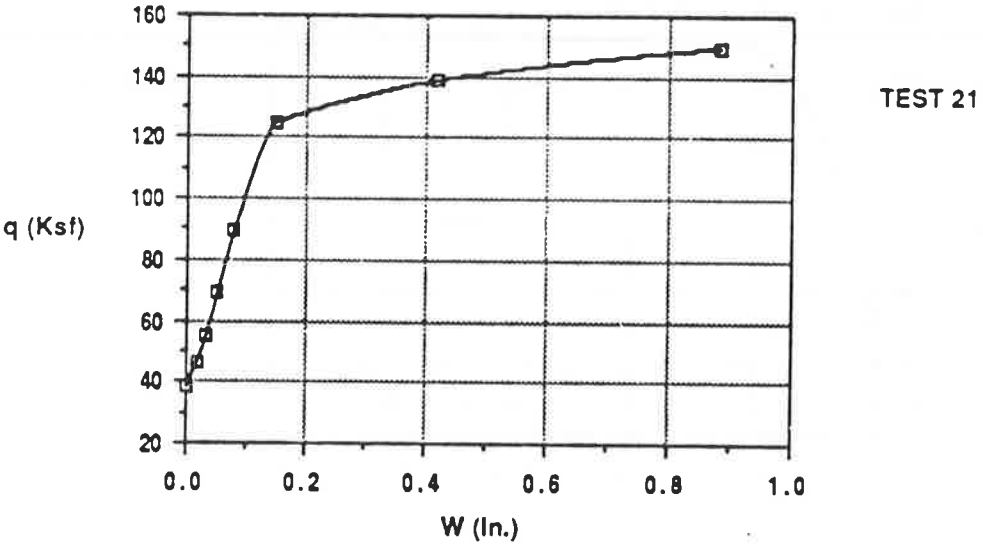

Fig. Q. 52. q-w Relationships for Tests 20 and 21

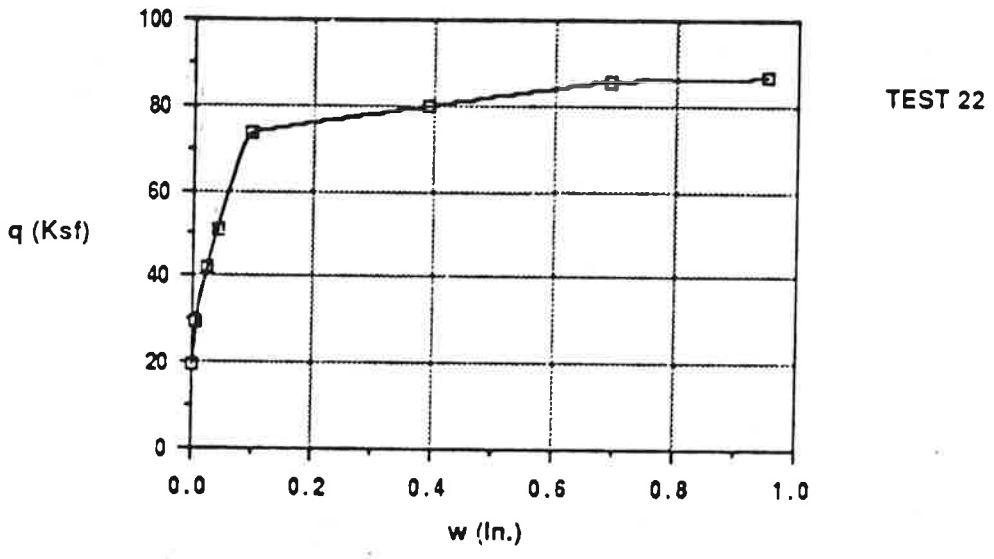

Fig. Q.53. q-w Relationship for Test 22

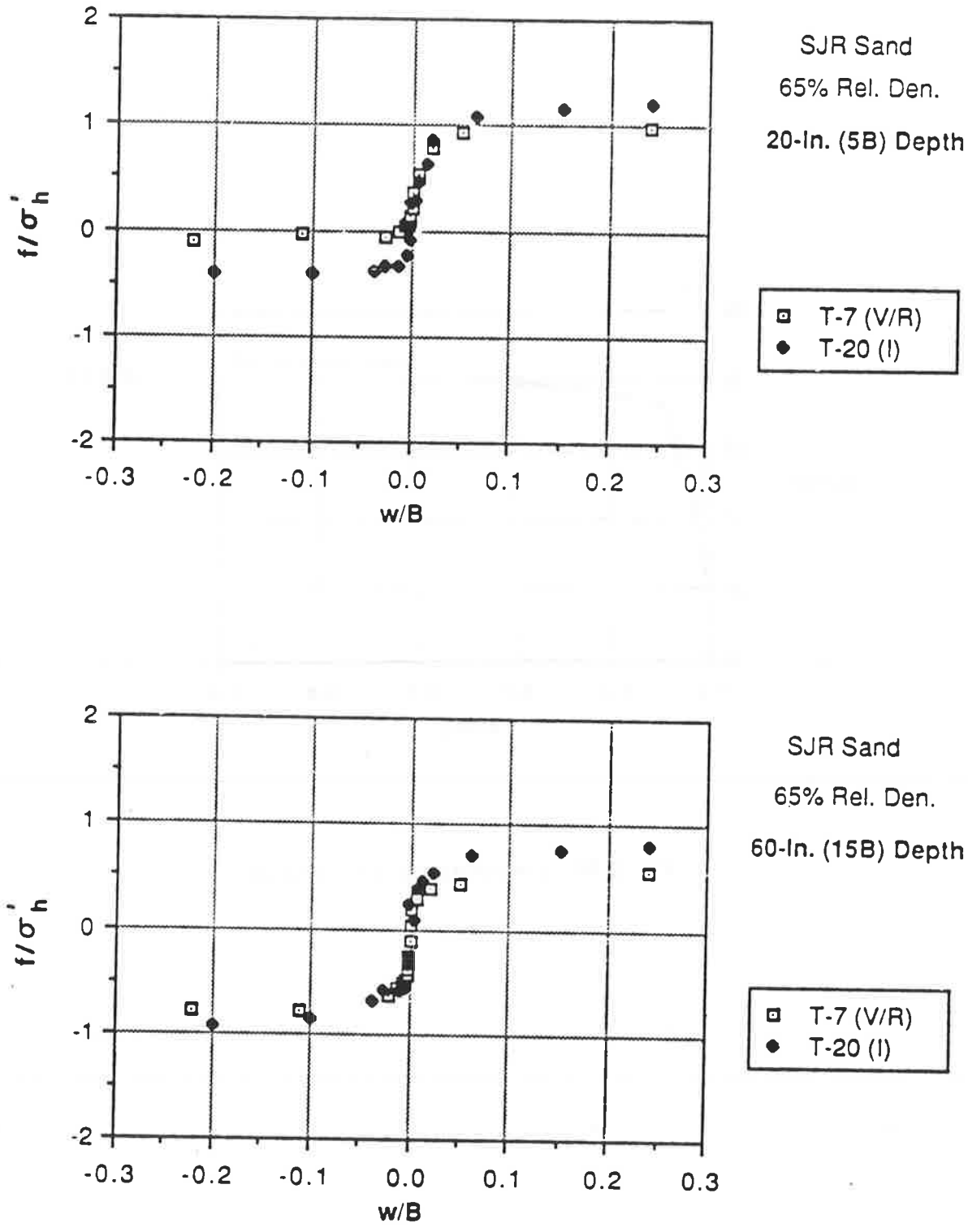

Fig. Q.54. Normalized Discrete f-w Relationships for SJR Sand; 65% Relative Density

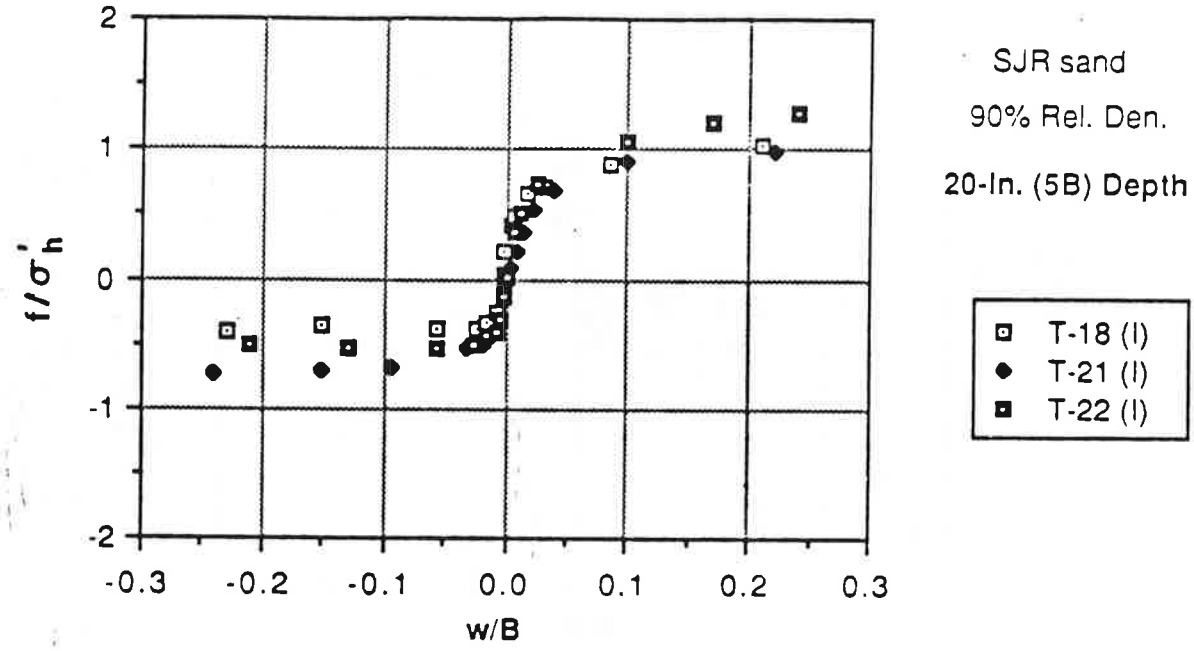

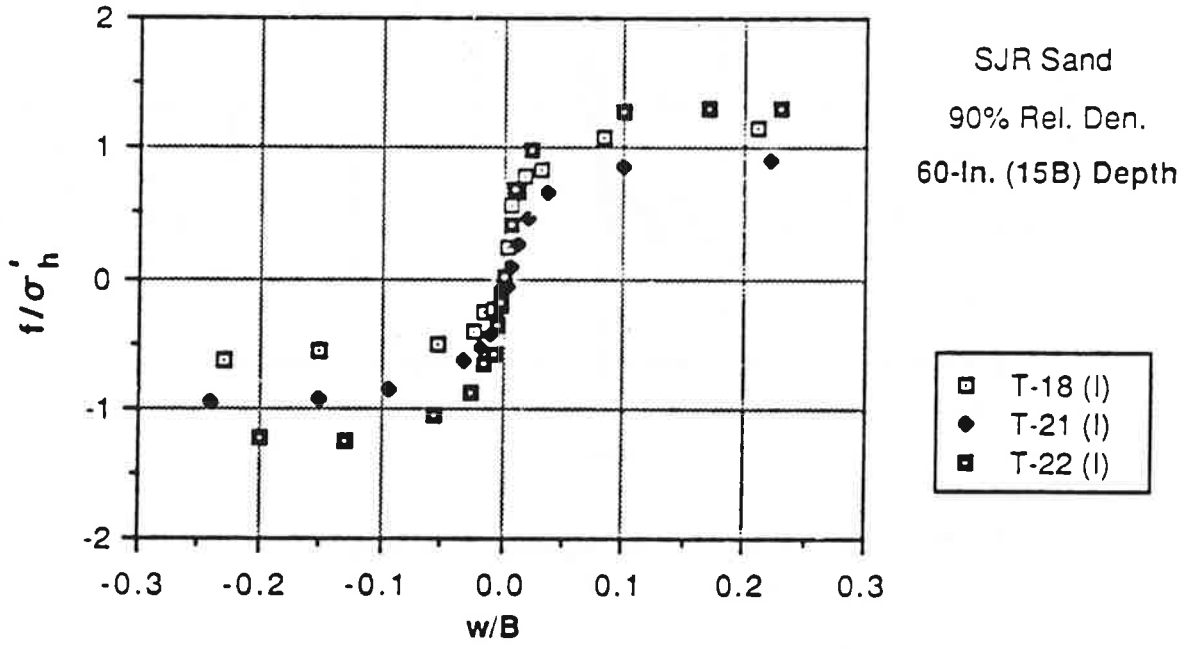

Fig. Q.55. Normalized Discrete f-w Relationships for SJR Sand; 90% Relative Density; Impact-Driven Piles

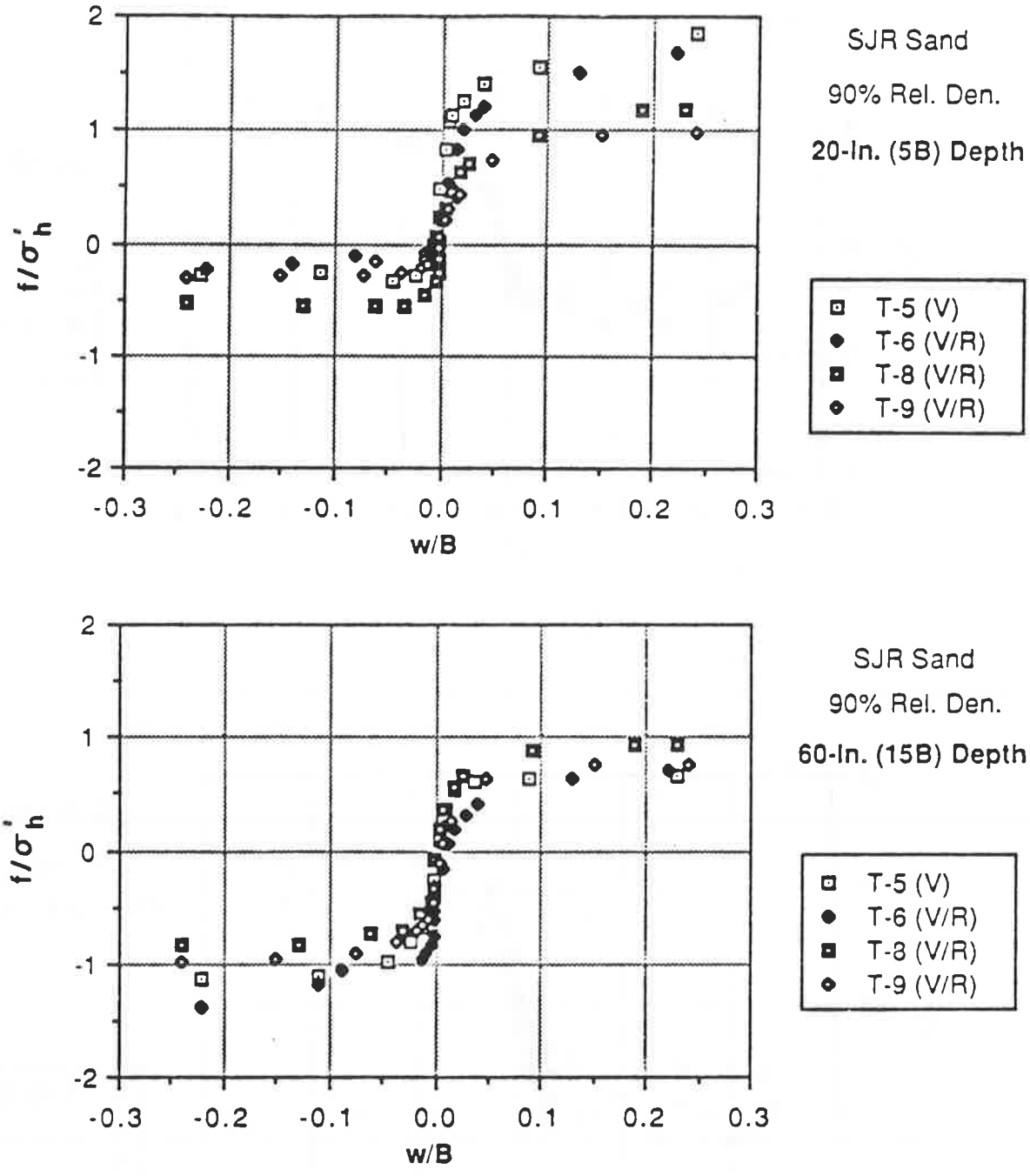

Notes: 1. Data from T-6 disregards head load in curve fit.

2. Final penetration in T-9 was 57 In. (14.25 B).

Fig. Q.56. Normalized Discrete f-w Relationships for SJR Sand; 90% Relative Density; Vibro-Driven Piles

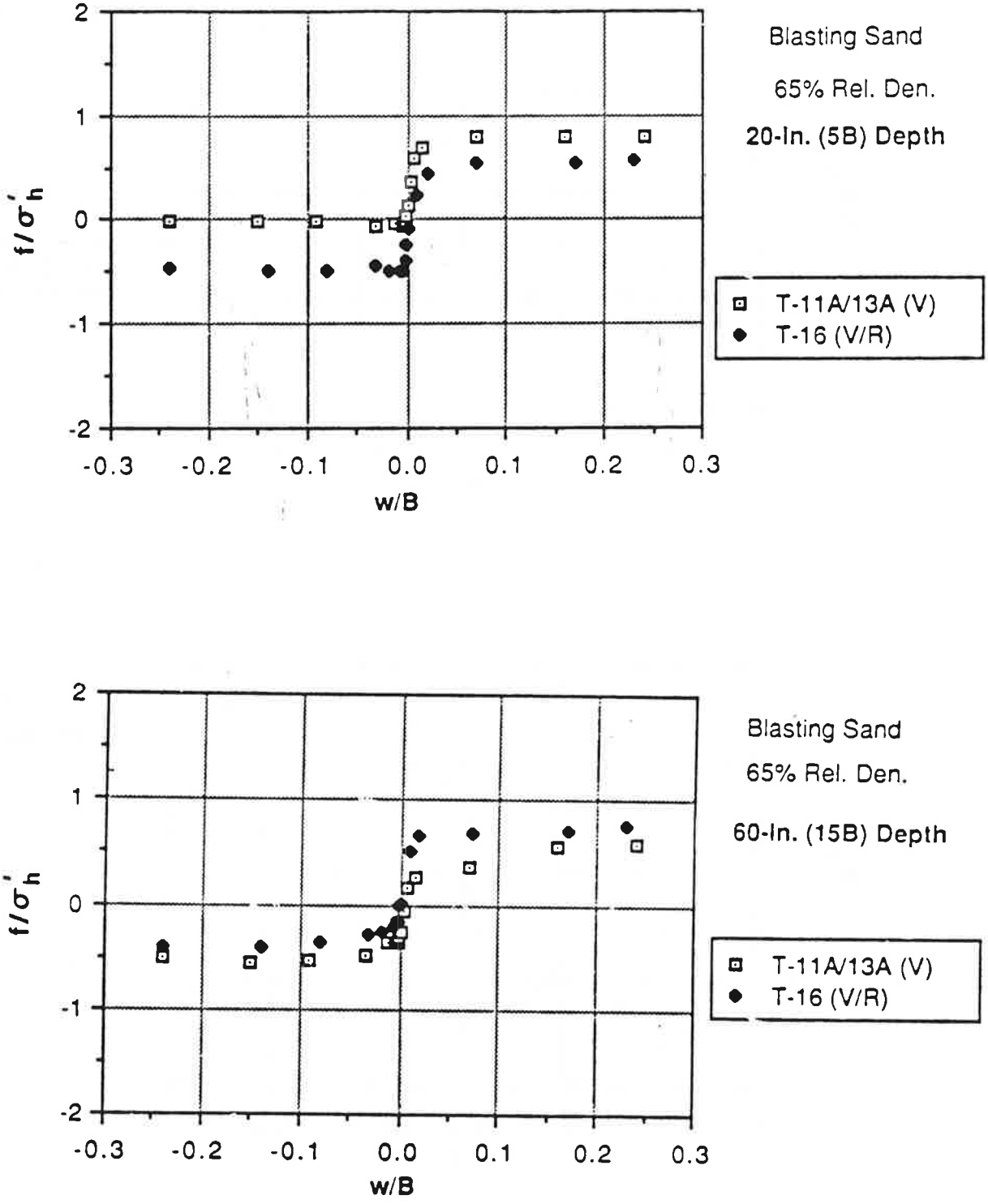

Fig. Q.57. Normalized Discrete f-w Relationships for BLS Sand; 65% Relative Density

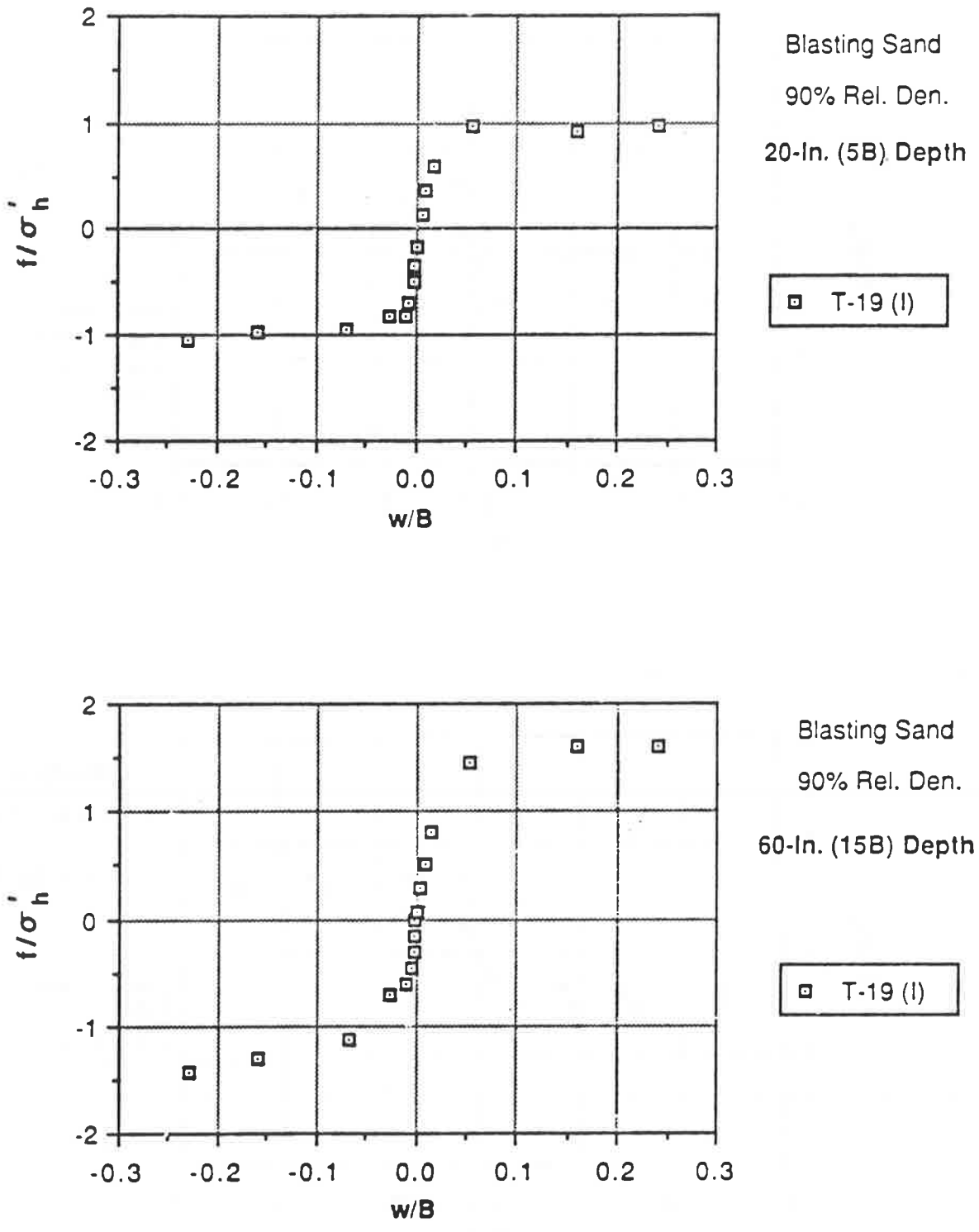

Fig. Q.58. Normalized Discrete f-w Relationships for BLS Sand; 90% Relative Density; Impact-Driven Piles

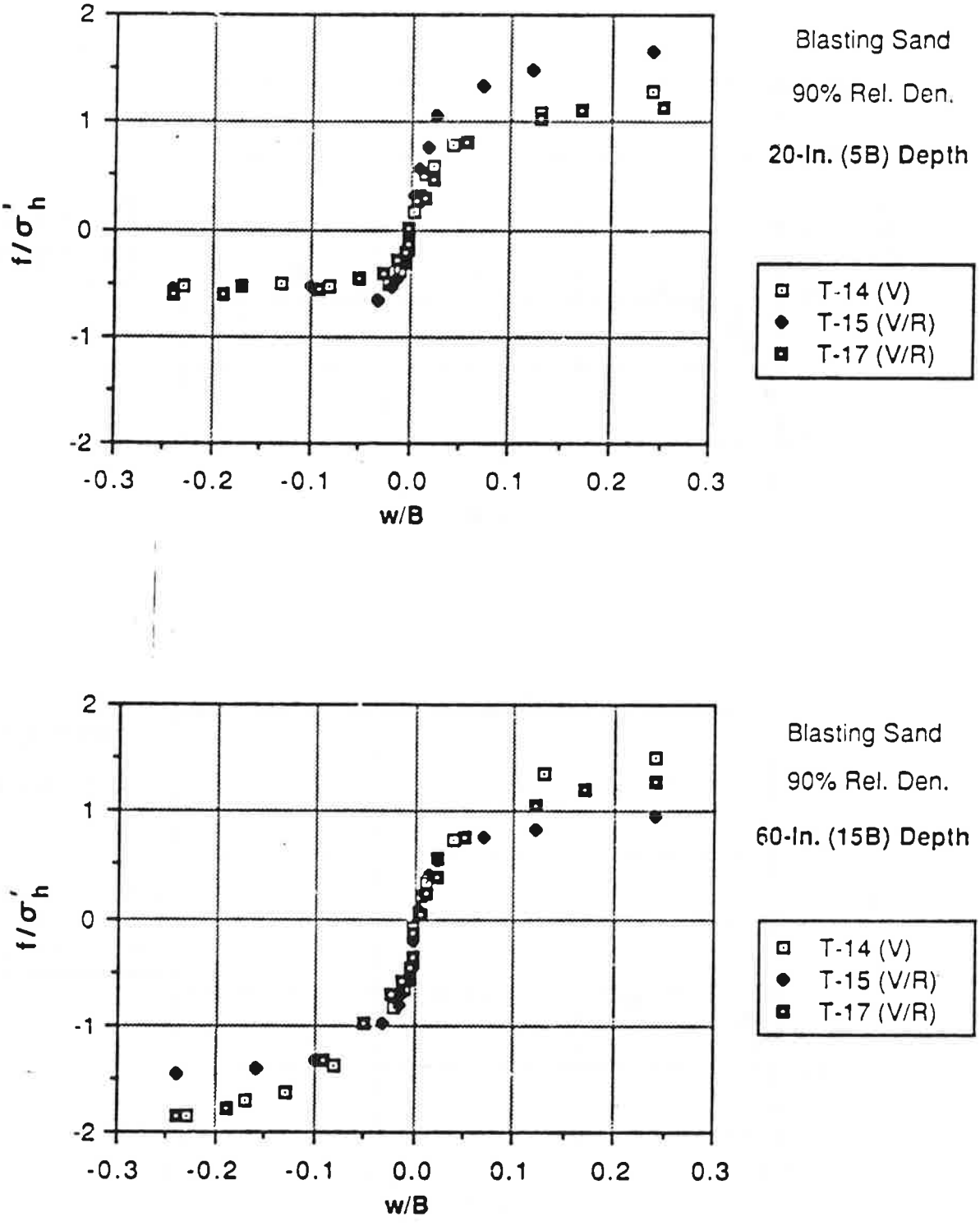

Fig. Q.59. Normalized Discrete f-w Relationships for SJR Sand; 90% Relative Density; Vibro-Driven Piles

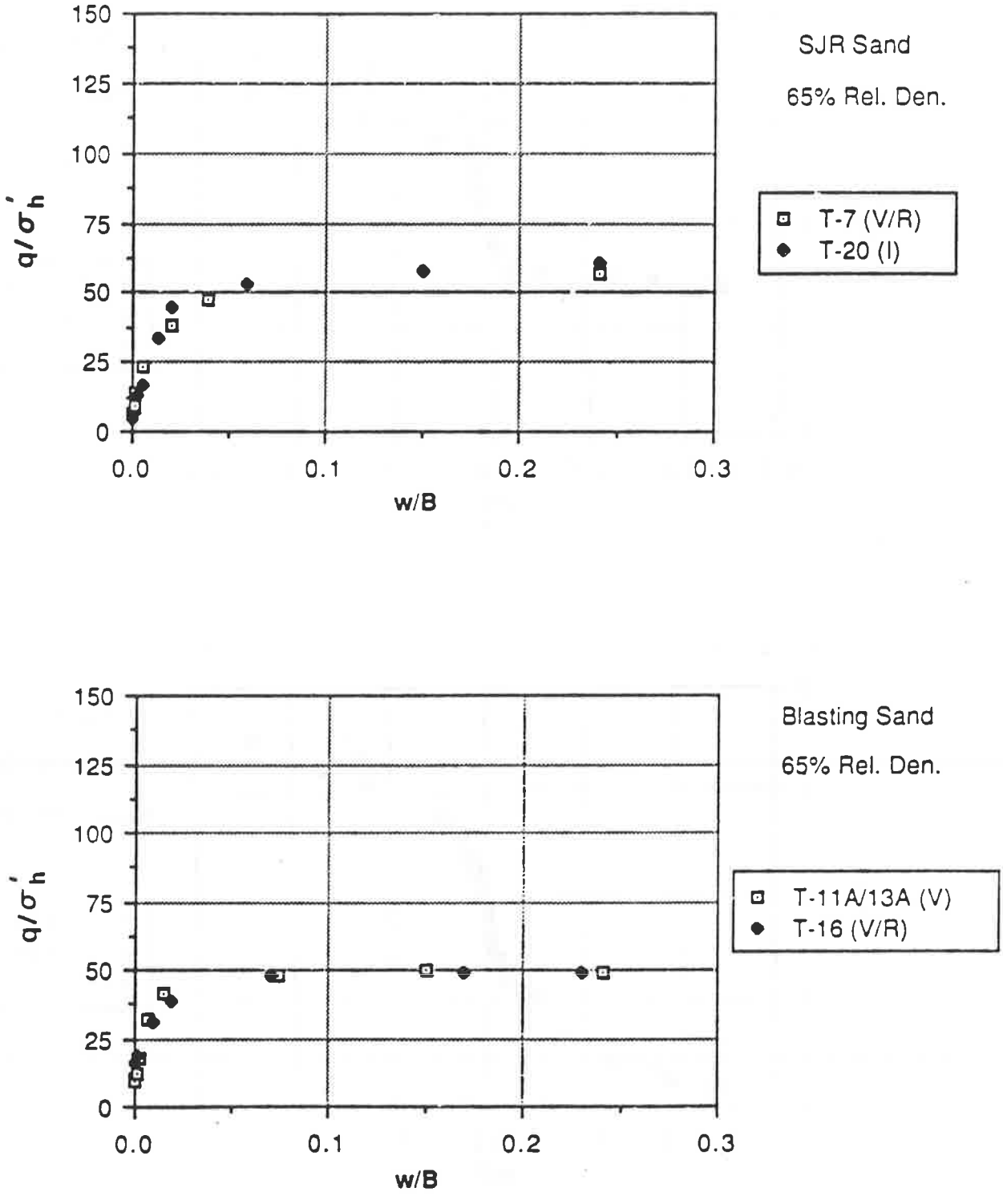

Fig. Q.60. Normalized Discrete q-w Relationships for SJR Sand and BLS Sand: 65% Relative Density

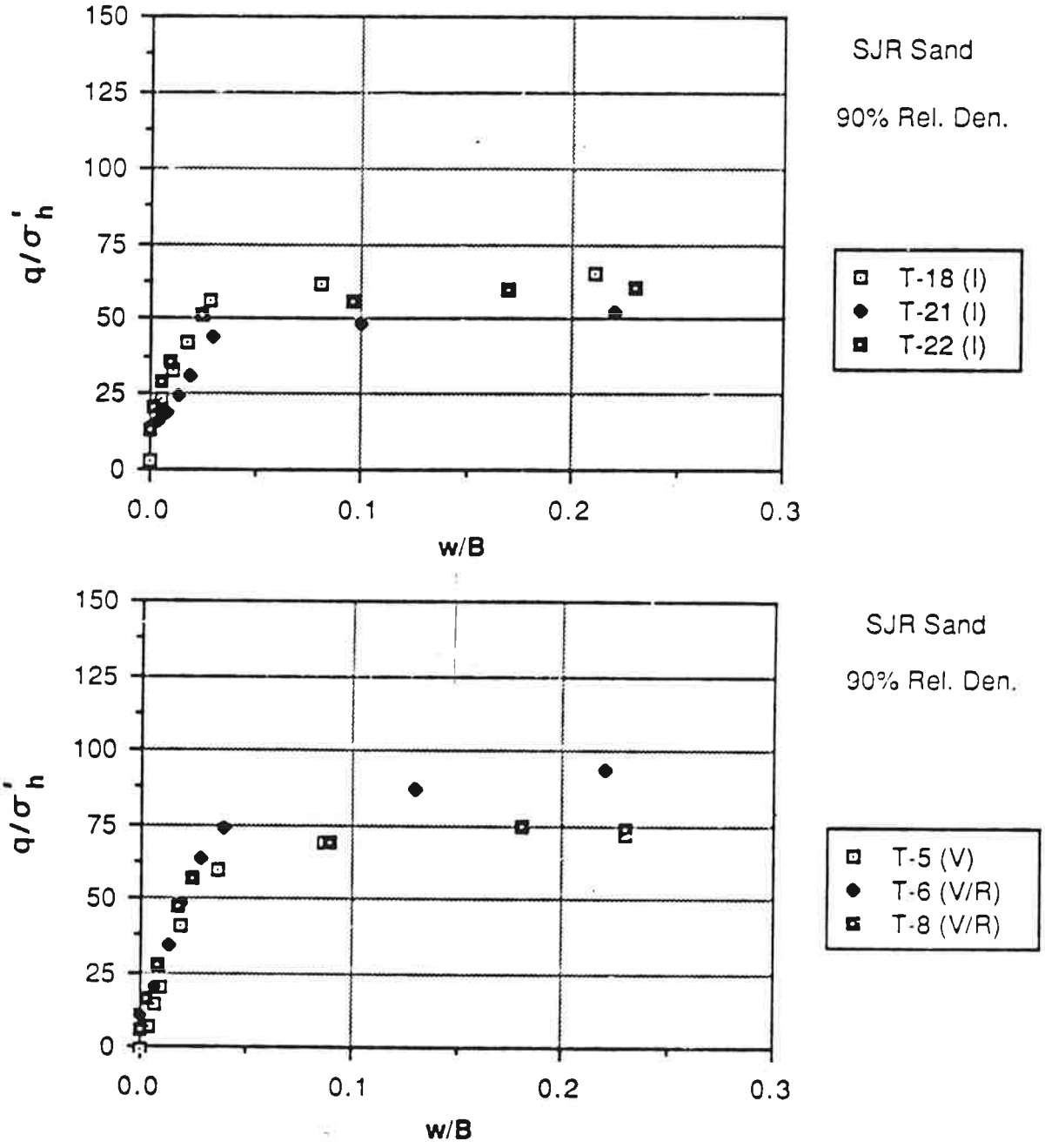

Notes: 1. Data from T-6 disregards head load in curve fit.

2. Data from T-9 not included due to shallow penetration.

Fig. Q. 61. Normalized Discrete q-w Relationships for SJR Sand; 90% Relative Density

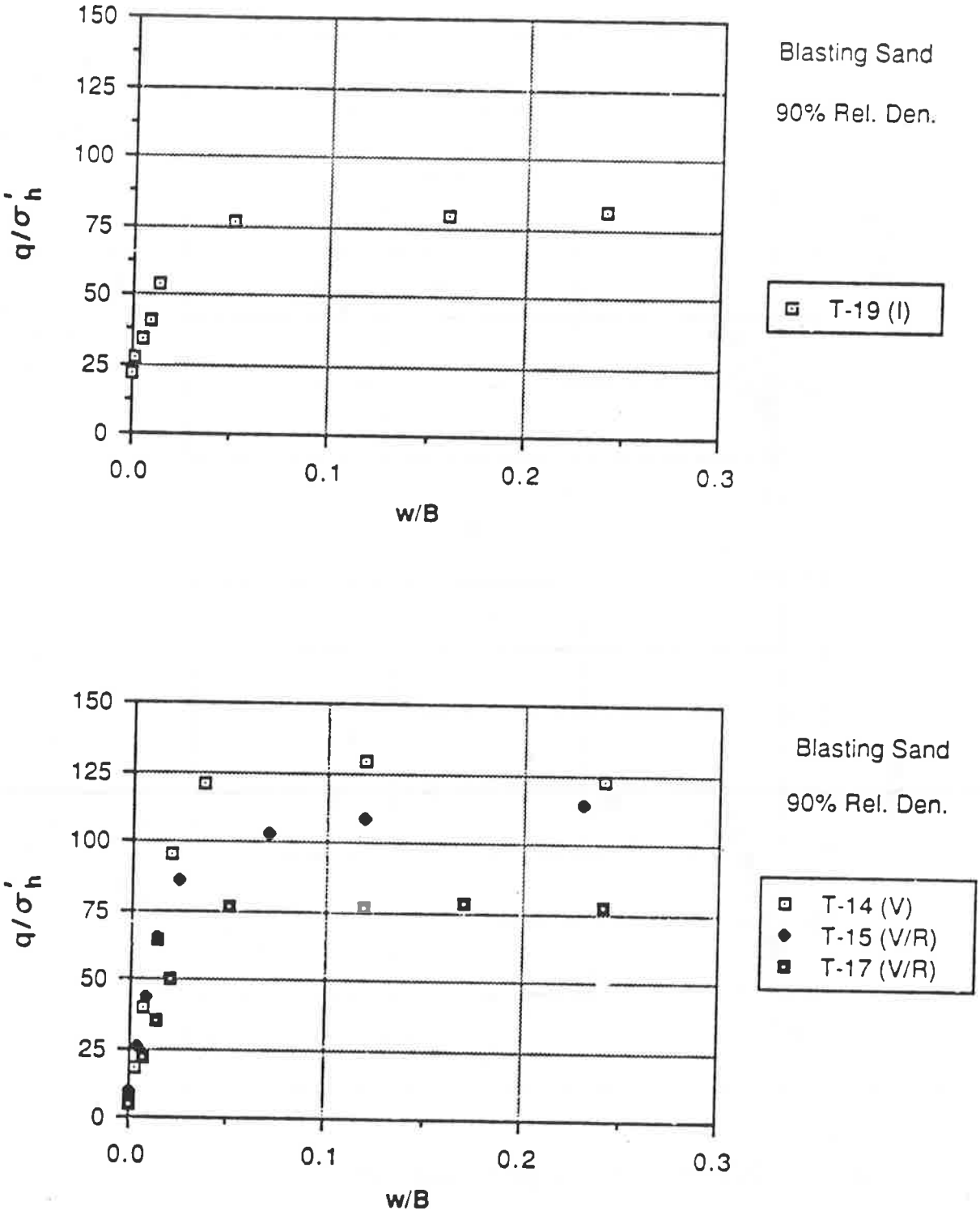

Fig. Q.62. Normalized Discrete q-w Relationships for BLS Sand; 90% Relative Density